

THEORETICAL ASPECTS OF WERNER COMPLEXES AND MOLECULAR
DEVICES

A Dissertation

by

LARS ERIK ANDREAS EHNBOM

Submitted to the Graduate and Professional School of
Texas A&M University
in partial fulfillment of the requirements for the degree of

DOCTOR OF PHILOSOPHY

Chair of Committee,
Co-Chair of Committee,
Committee Members,

Head of Department,

John A. Gladysz
Michael B. Hall
Peter M. Rentzepis
Daniel A. Singleton
Michael Nippe
Simon W. North

December 2021

Major Subject: Chemistry

Copyright 2021 Lars Erik Andreas Ehnbohm

ABSTRACT

This dissertation begins with the first comprehensive review of molecular gyroscopes. The following two chapters feature combined experimental/computational studies. In the first, equilibria involving gyroscope-like complexes and geometric isomers are measured and the data interpreted with molecular dynamics simulations and DFT calculations. In the second, trigonal bipyramidal diiron tetrphosphorus complexes that have parallel P–Fe–P axes and the potential for coupled $\text{Fe}(\text{CO})_3$ rotators are examined. Here the DFT studies focus mainly on electronic structure and IR properties.

The rotators can be removed from the gyroscope-like complexes to give unprecedented dibridgehead diphosphines with long $(\text{CH}_2)_n$ linkers. Their conformational, dynamic, and NMR properties are interrogated by simulated annealing and DFT calculations, helping to rationalize observed behavior and predicting properties of molecules that remain to be synthesized.

Another major class of molecules investigated is polyynes $\text{H}(\text{C}\equiv\text{C})_n\text{H}$ which are of special interest at long chain lengths (models for the polymeric *sp* carbon allotrope carbyne). Nucleus independent chemical shifts are revealing an absence of special shielding regions and DFT calculations provide highly accurate chemical shift values, including polyynes with platinum endgroups. Complexes with four platinum corners and four $-(\text{C}\equiv\text{C})_2-$ edges can be accessed. Electrostatic potential maps show highly negatively charged cores that explain the strong affinities of these species for ammonium salts. DFT calculations also establish very similar energies for planar vs. puckered

conformations, both of which have been observed crystallographically: electronic structures and equilibria involving Pt₃ and Pt₅ homologs are also thoroughly explored.

Werner complexes of the type [Co(en)₃]³⁺ 3X⁻ (*en* = 1,2-ethylenediamine) have also been extensively investigated. In one study, the intricate stereochemical and conformation properties are reviewed including substituted derivatives using conventions from both organic and inorganic chemistry. In another, >150 crystal structures of [Co(en)₃]³⁺ salts have been analyzed with respect to hydrogen bonding between the NH groups and the counteranions. Diverse motifs could be identified and a nomenclature syntax developed.

DEDICATION

To my loving parents Lars and Anita, and my brother Johan. Your love and encouragement gave me the strength I needed to complete this work and fulfill my dreams.

This dissertation is also dedicated to my spouse Dr. Jeffery M. Tharp II – my life would be etiolated without you.

ACKNOWLEDGEMENTS

I would like to thank my advisors, Drs. John A. Gladysz and Michael B. Hall, and my committee members, Drs. Michael Nippe, Daniel A. Singleton, and Peter M. Rentzepis, for their guidance and support throughout the course of this research. I would also like to extend gratitude to former committee members Drs. Marcetta Y. Darensbourg, Donald J. Darensbourg, and Kim R. Dunbar. Special appreciations also go to staff, faculty, and colleagues in the Department of Chemistry for making my time at Texas A&M University enjoyable. I would like to extend special thanks my mother and father for their encouragement during these years far away from home. I also want to thank my spouse for patience and encouragement, from both near and far, during my time in graduate school.

It would require too many pages to list the intra- and extra-departmental personnel who I highly value and who have been extraordinarily helpful. I would however like to extend a special "thank you" to a few key individuals who made this journey possible. Dr. Lisa M. Pérez, for her never-ending patience in helping me learn scripting, Linux, and everything else that computational software can throw at you. Dr. Pérez has been a guiding star and a great role model for me during my time at TAMU. I also extend special thanks to my friend, Prof. Lennart Jönsson, who inspired me to pursue chemistry when I was a student attending his world-class organic chemistry lectures. Who would have known that we would meet again too after I attended your chemistry roadshow during primary school.

I would like to thank my friend, Dr. Isa Doverbratt, for always being there for me and for the endless laughter and great memories that we share from Kemicentrum.

I would like to thank all my current and former co-workers who have taught me so much and with whom I had the fortune to work with. In particular I would like to thank Alex Estrada, Taveechai Wititsuwannakul, and Brenna K. Collins for their friendship.

I would also like to thank Prof. Suzanne A. Blum (UC-Irvine), Prof. Ebbe Nordlander (Lund University), Graeme Hogarth (King's College London), Selwyn Mapolie (Stellenbosch University), Lo Gorton (Lund University), Peter Somfai (Lund University), and all friends and collaborators in these labs. Without the excellent training and support that I gained in these labs, I would not be where I am today.

Finally, I would also like to remember those who are not with us today, but to whom I am eternally grateful. I want to thank Dr. Tobias Fiedler, for his patience teaching the group about graphical design and chemistry, you were an amazing co-worker and friend.

CONTRIBUTORS AND FUNDING SOURCES

Contributors

Part 1. faculty committee recognition

This work was supervised by a dissertation committee consisting of Dr. John A. Gladysz, Dr. Michael B. Hall, Dr. Peter M. Rentzepis, Dr. Daniel A. Singleton, and Dr. M. Nippe.

Part 1. student/collaborator recognition

The experimental work presented in this thesis was performed by Mr. Y. Zhu (section 3), Mr. S. Zarcone and Dr. G. Zhu (section 4). Dr. H. Amini (section 6), Ms. B. K. Collins and Dr. M. Clough Mastry (section 7). The work in section 5 was interpreted together with Mr. Jason E. Kuszynski. The crystallographic data in all applicable sections were resolved by either Dr. N. Bhuvanesh or Dr. J. H. Reibenspies. Part of the analysis in sections 8 and 9 were done together with Dr. Subrata K. Ghosh and Dr. Kyle G. Lewis.

All other work conducted for the dissertation was completed by the author independently.

Funding sources

I thank the US National Science Foundation (CHE-1153085, CHE-1566601, CHE-1900549, 1664866) and the Welch Foundation (A-0648, A-1656) for support. I also thank the Laboratory for Molecular Simulation and Texas A&M High Performance Research Computing for computational resources. The Alexander von Humboldt

Foundation is thanked for enabling research collaborations including visits to RWTH Aachen in Germany.

TABLE OF CONTENTS

	Page
ABSTRACT	ii
DEDICATION	iv
ACKNOWLEDGEMENTS	v
CONTRIBUTORS AND FUNDING SOURCES.....	vii
TABLE OF CONTENTS	ix
LIST OF FIGURES.....	xvi
LIST OF SCHEMES	xxxv
LIST OF TABLES	xxxvii
1. INTRODUCTION.....	1
2. GYROSCOPES AND THE CHEMICAL LITERATURE, 2002–2020: APPROACHES TO A NASCENT FAMILY OF MOLECULAR DEVICES	6
2.1. Introduction to gyroscopes	6
2.2. Scope of review	9
2.3. Strategic considerations: functional molecular gyroscopes	10
2.4. Selected background molecules	14
2.4.1. Molecular turnstiles	14
2.4.2. Species with N–ML ₂ –N rotators where N denotes a disubstituted pyridine ligand.....	18
2.4.3. Other stators in which two bridges connect the termini of the rotator	20
2.5. Summary of coverage	23
2.6. Systems from the Gladysz group	25
2.6.1. Syntheses involving olefin metathesis	25
2.6.2. Reactions that alter the coordination number.....	34
2.6.3. Substitution reactions	38
2.6.4. Dynamic properties: general concepts	43
2.6.5. Measured or bounded rotational barriers.....	48
2.6.6. Key solid state properties	51

2.6.7. Toward molecular gyroscopes.....	56
2.7. Systems from the Setaka group	60
2.7.1. Synthetic strategies	60
2.7.2. Dynamic properties in solution	68
2.7.3. Dynamic properties in the solid state	80
2.7.4. Toward molecular gyroscopes.....	87
2.8. Systems from the Garcia-Garibay group.....	87
2.8.1. Prefatory comments.....	87
2.8.2. Rotors studied in solution	91
2.8.3. Rotors studied in the solid state.....	94
2.8.4. Representative syntheses of the rotors in section 2.8.3.1	129
2.8.5. Toward molecular gyroscopes.....	137
2.9. Systems from other research groups	138
2.9.1. Rotors comprised of covalent bonds	139
2.9.2. Supramolecularly or mechanically bonded systems and MOFs	139
2.9.3. Other rotor motifs	144
2.10. Conclusion.....	147
2.11. References	149

3. PLATINUM(II) ALKYL COMPLEXES OF CHELATING DIBRIDGEHEAD
DIPHOSPHINES $P((CH_2)_N)_3P$ ($N = 14, 18, 22$); FACILE *CIS/TRANS*
ISOMERIZATIONS INTERCONVERTING GYROSCOPE AND PARACHUTE
LIKE ADDUCTS

3.1. Introduction	185
3.2. Results Part I: Experimental [major contribution: Mr. Y. Zhu].....	191
3.2.1. Syntheses and NMR characterization.....	191
3.2.2. Crystallographic characterization.....	198
3.2.3. Additional characterization of equilibria.....	202
3.3. Results Part II: Computational Data [major contribution: Mr. A. Ehnbom]	206
3.4. Discussion	210
3.4.1. Preliminary remarks	210
3.4.2. Coordination geometries: <i>trans</i> /gyroscope versus <i>cis</i> /parachute	212
3.4.3. Further electronic and structural considerations	215
3.4.4. Additional properties of new complexes.....	217
3.5. Conclusions	218
3.6. Experimental [major contribution: Mr. Y. Zhu]	219
3.6.1. General	219
3.6.2. Thermolyses (Table 3.3 and Scheme 3.9)	222
3.6.3. Crystallography	226
3.7. References	228

4. TOWARD FRAMEWORKS WITH MULTIPLE ALIGNED AND INTERACTIVE $\text{Fe}(\text{CO})_3$ ROTATORS: SYNTHESSES AND STRUCTURES OF DIIRON COMPLEXES LINKED BY TWO <i>TRANS</i> -DIAXIAL α,ω -DIPHOSPHINE LIGANDS $\text{AR}_2\text{P}(\text{CH}_2)_N\text{PAR}_2$	239
4.1. Introduction	239
4.2. Results	243
4.2.1. Syntheses of Title Complexes [major contribution: Mr. S. Zarcone, Dr. G. Zhu]	243
4.2.2. Structural Data [major contribution: Mr. A. Ehnбом, Mr. S. Zarcone]	248
4.2.3. DFT Computations [major contribution: Mr. A. Ehnбом]	254
4.3. Discussion	260
4.3.1. Syntheses [major contribution: Mr. S. Zarcone, Dr. G. Zhu]	260
4.3.2. Steric Interactions Diiron Complexes [major contribution: Mr. A. Ehnбом, Mr. S. Zarcone]	261
4.3.3. Related Complexes and Directions	268
4.4. Conclusion	270
4.5. Experimental [major contribution: Mr. S. Zarcone, Dr. G. Zhu]	271
4.5.1. General	271
4.5.2. Crystallography	274
4.5.3. DFT Computations	276
4.6. References	277
5. A COMPUTATIONAL INVESTIGATION OF STRUCTURE, ENERGETICS, HOMEOMORPHIC AND CONFIGURATIONAL ISOMERIZATION, AND NMR PROPERTIES OF MACROCYCLIC ALIPHATIC DIBRIDGEHEAD DIPHOSPHINES EXHIBITING <i>IN/OUT</i> ISOMERISM	288
5.1. Introduction	288
5.2. Results and Discussion	296
5.2.1. Preliminary comments	296
5.2.2. Conformational stability of different dibridgehead diphosphine isomers	299
5.2.3. Justification for the energetic differences between the <i>ii</i> and <i>oo</i> isomers.	306
5.2.4. Structural effects	309
5.2.5. Qualitative analysis of the van der Waals effects (dispersion and sterics)	313
5.2.6. Quantitative analysis of the van der Waals effects (dispersion and sterics)	317
5.2.7. Mechanistic considerations (pathway, intermediates)	322
5.2.8. ^{31}P NMR chemical shifts of selected diphosphines	331

5.3. Conclusions	332
5.4. References	335
6. ORIGIN OF SHIELDING AND DESHIELDING EFFECTS IN NMR SPECTRA OF CONJUGATED POLYIYNES	344
6.1. Introduction	344
6.2. Experimental [major contribution: A. Ehnbom]	347
6.3. Results and Discussion (part 1) [major contribution: A. Ehnbom]	347
6.4. Results and Discussion (part 2) [major contribution: A. Ehnbom, Dr. H. Amini]	355
6.5. Conclusions	365
6.6. References	366
7. MACROCYCLIC COMPLEXES DERIVED FROM FOUR <i>CIS</i>-L₂PT CORNERS AND FOUR BUTADIYNEDIYL LINKERS; SYNTHESSES, ELECTRONIC STRUCTURES, AND SQUARE VERSUS SKEW RHOMBUS GEOMETRIES	374
7.1. Introduction	374
7.2. Results Part I: Experimental [major contribution: Ms. B. K. Collins, Dr. Clough Mastry]	377
7.3. Diphosphine syntheses	377
7.4. Monoplatinum complexes	379
7.5. Syntheses of tetraplatinum complexes	383
7.6. Physical characterization of tetraplatinum complexes	390
7.7. Results Part II: Computations [major contribution: Mr. A. Ehnbom]	395
7.8. Computations: Conformational and constitutional equilibria	395
7.9. Computations: Electronic and electrostatic properties	399
7.10. Discussion	403
7.11. Syntheses and adducts of title complexes	403
7.12. Additional structural and electronic features	405
7.13. Conclusion	408
7.14. Experimental [major contribution: Ms. B. K. Collins, Dr. Clough Mastry]	409
7.14.1. General	409
7.14.2. Crystallography	411
7.15. References	413
8. OCTAHEDRAL WERNER COMPLEXES WITH SUBSTITUTED ETHYLENEDIAMINE LIGANDS: A STEREOCHEMICAL PRIMER FOR A HISTORIC SERIES OF COMPOUNDS NOW EMERGING AS A MODERN FAMILY OF CATALYSTS	426
8.1. Conspectus	426

8.2. Introduction	427
8.3. The chiral $[\text{Co}(\text{en})_3]^{3+}$ trication: cobalt stereocenter	429
8.4. The chiral $[\text{Co}(\text{en})_3]^{3+}$ trication: ligand conformations	432
8.5. Octahedral Werner complexes with monosubstituted ethylenediamine ligands	437
8.5.1. Stereoisomerism at the cobalt center	437
8.5.2. Chelate conformation	437
8.5.3. A Stereoisomers allowing all possible combinations of ligand configurations	441
8.6. Octahedral Werner complexes with symmetrically disubstituted ethylenediamine ligands	441
8.6.1. Stereoisomerism at the cobalt center	443
8.6.2. Ligand conformation: <i>trans</i> -1,2-cyclohexanediamine (<i>trans-chxn</i>) ²⁹	443
8.6.3. Ligand conformation: <i>cis</i> -1,2-cyclohexanediamine (<i>cis-chxn</i>)	447
8.6.4. Ligand conformation: (<i>S,S</i>)- and (<i>R,R</i>)-1,2-diphenylethylenediamine (<i>dpen</i>)	449
8.7. Diastereomer stabilities	452
8.8. Catalysis	455
8.9. Summary and recommendations	457
8.10. References	459

9. HYDROGEN BONDING MOTIFS IN STRUCTURALLY CHARACTERIZED SALTS OF THE TRIS (ETHYLENEDIAMINE) COBALT TRICATION, $[\text{CO}(\text{EN})_3]^{3+}$; AN INTERPRETIVE REVIEW, INCLUDING IMPLICATIONS FOR CATALYSIS

9.1. Introduction	468
9.2. Ethylenediamine ligand conformations	475
9.3. A syntax for hydrogen bonding to the trication $[\text{Co}(\text{en})_3]^{3+}$	480
9.4. Various types of hydrogen bonding motifs for individual anions (or cocrystallized molecules) are summarized in Appendix G (section G.1 and G.2)	482
9.5. Overview of crystallographically characterized salts of the trication $[\text{Co}(\text{en})_3]^{3+}$	487
9.5.1. General procedures and comments	487
9.5.2. Salts with three monoanions (point charge)	488
9.5.3. Salts with three monoanions (delocalized)	494
9.5.4. Salts with three monoanions (two types)	498
9.5.5. Salts with two anions (one monoanion and one dianion)	499
9.5.6. Salts with achiral dianions	502
9.5.7. Salts with chiral tartrate dianions	508

9.5.8. Salts with achiral dianions	515
9.6. Additional structural information and generalizations	527
9.6.1. General remarks and scope of hydrogen bonding	527
9.6.2. Types of hydrogen bonding	528
9.6.3. Possible connections to catalysis	530
9.6.4. Other stereochemical issues	531
9.7. Concluding remarks	532
9.8. References	533
10. SUMMARY	548
APPENDIX A	551
A.1. Additional crystallographic data	551
A.2. Computational section	552
A.2.1. General considerations	552
A.2.2. Details of the simulated annealing (MM/MD) calculations	554
A.2.3. Simulated annealing MM/MD data:	554
A.2.4. Details of the Born-Oppenheimer molecular dynamics (DFT/MD) simulations	559
A.2.5. Benchmark study	561
A.2.6. Electronic structure theory, DFT	563
A.2.7. Energetics of excised diphosphine ligands, single point calculation (DFT)	564
A.3. References	567
APPENDIX B	571
B.1. Computational section	571
B.1.1. General considerations	571
B.1.2. IR spectra	572
B.1.3. Scan calculations and additional data	576
B.2. References	582
APPENDIX C	585
C.1. General considerations	585
C.1.1. Simulated annealing	585
C.1.2. NMR calculations	585
C.2. References	596
APPENDIX D	598
D.1. Computational section for $\text{H}(\text{C}\equiv\text{C})_n\text{H}$ species treated in section 6.3	598
D.1.1. General considerations	598

D.1.2. Procedure for Figure 14.4	602
D.2. Computational details for platinum polyynes in section 6.4	614
D.2.1. General considerations	614
D.3. References	616
APPENDIX E	621
E.1. Computational section	621
E.1.1. General considerations	621
E.1.2. Conformational and constitutional equilibria	624
E.1.3. Computed UV-visible spectra	626
E.1.4. Electrostatic potential surfaces	634
E.1.5. Structural data	635
E.2. References	639
APPENDIX F	642
F.1. Stereoisomers of $[\text{Co}(pn)_3]^{3+}$ trications comprised of all combinations of (<i>R</i>)- <i>pn</i> and (<i>S</i>)- <i>pn</i> ligands	642
F.2. Stereoisomers of $[\text{Co}(cis\text{-}chxn)_3]^{3+}$ trications (i.e. comprised only of <i>R,S</i> - <i>chxn</i> or <i>meso</i> ligands)	645
APPENDIX G	653
G.1. Syntax and nomenclature summaries	653
G.2. Representations of the motifs cataloged in Table 17.1	654
G.3. References	667

LIST OF FIGURES

	Page
Figure 1.1 A graphical summary of the contents of this dissertation and the molecular systems studied.	3
Figure 2.1 Toy mechanical gyroscopes (panels a and b) and some practical applications of gyroscopes (panels c-i).....	8
Figure 2.2 Limiting types of surface mounted rotors, illustrated with literature systems.....	10
Figure 2.3 Representative compounds that have been described as molecular turnstiles.....	17
Figure 2.4 Ring closing metathesis reaction that connects 2,6-disubstituted <i>trans</i> -pyridine ligands (top), ORTEP and space filling representations of the hydrogenation product 8 (middle), and atropisomers arising from restricted pyr–M–pyr rotation in related square planar systems (bottom). ^{87,88}	19
Figure 2.5 Additional complexes with substituted <i>trans</i> -bis(pyridine) ligands prepared by the route in Figure 2.4 (9-11), ⁸⁸ and ORTEP and space filling representations of 9 and 10	19
Figure 2.6 Molecular rotors in which the rotators terminate in tetrahedral or trigonal pyramidal atoms and the stators feature two connecting bridges. ⁹¹⁻⁹⁴	22
Figure 2.7 Additional molecular rotors in which the arylene rotators (denoted Q_y) terminate in tetrahedral atoms and the stators feature two connecting bridges. ^{95,96}	23
Figure 2.8 Three-fold intramolecular ring closing olefin metatheses involving <i>trans</i> heteroatom donor ligands $E(CH_2)_mCH=CH_2$ (top; E usually =P), applications to different metal coordination geometries (middle), and relevant reactant conformations (bottom).....	26
Figure 2.9 Trigonal bipyramidal $Fe(CO)_3$ complexes prepared according to Figure 2.8. An asterisk indicates a yield obtained with Grubbs' second generation catalyst [() indicates $(CH_2)_n$]. ¹⁰⁶	28

Figure 2.10 Thermal ellipsoid and space filling representations of complexes from Figure 2.9 or close relatives thereof (left, 17c ; right, <i>E,E,E</i> -tris(olefinic) precursor of 17a with C=C linkages darkened). ¹⁰⁶	29
Figure 2.11 Square planar complexes prepared according to Figure 2.8. An asterisk indicates a yield obtained with the second generation Hoveyda-Grubbs catalyst [()] indicates (CH ₂) _n . ^{98,100,104,112}	30
Figure 2.12 Thermal ellipsoid and space filling representations of the PtCl ₂ complexes 18c (top) and 18g (bottom) from Figure 2.11. ^{104,112}	32
Figure 2.13 Square planar complexes prepared according to Figure 2.8. An asterisk indicates a yield obtained with the second generation Hoveyda-Grubbs catalyst [()] indicates (CH ₂) _n . ^{98,100,104,112}	33
Figure 2.14 Octahedral complexes prepared according to Figure 2.8. An asterisk indicates that traces of the product were detected by NMR [()] indicates (CH ₂) _n . ^{110,111}	34
Figure 2.15 Thermal ellipsoid and space filling representations of 22c from Figure 2.14 with the P–Re–P axis in (left) and perpendicular to (right) the plane of the image. ¹¹¹	36
Figure 2.16 Trigonal bipyramidal Fe(CO) ₃ complexes prepared according to Figure 2.8, but with arsenic in place of phosphorus [()] indicates (CH ₂) _n . ¹⁰⁷	37
Figure 2.17 Syntheses of trigonal bipyramidal complexes from precursors with different coordination geometries [()] indicates (CH ₂) _n . ^{100,110}	37
Figure 2.18 Syntheses of octahedral complexes from precursors with different coordination geometries [()] indicates (CH ₂) _n . An asterisk indicates an NMR yield for a species generated <i>in situ</i> . ^{100,106,110}	40
Figure 2.19 Reactions of chloride complexes of various coordination geometries with nucleophiles [()] indicates (CH ₂) _n . ¹⁰⁴⁻¹⁰⁶	41
Figure 2.20 Syntheses of complexes with dipolar PhPtCl rotators from precursors with PtCl ₂ rotators [()] indicates (CH ₂) _n . ^{104,109}	41
Figure 2.21 Substitution reactions of carbonyl ligands in iron complexes [()] indicates (CH ₂) _n . ¹⁰⁶⁻¹⁰⁸	42

Figure 2.22 Energy maxima and minima as the rotators in trigonal bipyramidal (top panel), square planar (middle panel), and octahedral complexes (bottom panel) in Figure 2.8 are rotated by 360°. The blue dot represents a marker to help track rotation (and can also be visualized as a unique ligand).....	44
Figure 2.23 Partial $^{13}\text{C}\{^1\text{H}\}$ NMR spectra of the $\text{Fe}(\text{CO})(\text{NO})\text{Cl}$ complex 38c as a function of temperature (CD_2Cl_2 , right) and simulated line shapes with rate constants (left). ¹⁰⁸	49
Figure 2.24 Structures illustrating the concepts of "horizontal clearance" and "vertical clearance" for complexes synthesized in the authors' laboratory.	53
Figure 2.25 Crystal lattice of the $\text{Fe}(\text{CO})_3$ complex 17c viewed along the <i>b</i> axis (top) and perpendicular to the <i>b</i> axis (bottom), iron atoms are depicted in orange and oxygen atoms in red.	54
Figure 2.26 Bis(phosphine) platinum complex with a low barrier H–Pt–H rotator.....	59
Figure 2.27 Gyroscope-like molecules prepared by the Setaka group by three-fold ring closing metatheses of substrates of the type L	63
Figure 2.28 Predicted ratio of hydrogenated ring closing olefin metathesis products LI and LII (Figure 2.27) assuming equal rate constants for metathesis at every branch point (and no reversibility). ¹²⁷	64
Figure 2.29 Gyroscope-like compounds synthesized by a variation of Figure 2.27 in which the number of methylene groups in the $\text{P}(\text{CH}_2)_m$ segments on the "top" and "bottom" in L differ by one [<i>i</i>] indicates $(\text{CH}_2)_n$. ^{131,135}	65
Figure 2.30 Gyroscope-like compounds from the Setaka group prepared by macrocyclizations other than olefin metathesis. ¹³⁹⁻¹⁴¹	65
Figure 2.31 ORTEP and space filling representations of the crystal structure of 50c (lowest temperature modification).....	66
Figure 2.32 Geometric relationships involving the rotators and stators in the <i>p</i> -phenylene and 1,4-naphthalenediyl adducts 50c and 52c-e . In the five compounds 52c-e , the distances d_{AB} and d_{AC} range from 4.43 to 4.48 Å and 5.34 to 5.39 Å, respectively.	67
Figure 2.33 ORTEP and space filling representations of the crystal structures of 52c-e	72

Figure 2.34 Temperature dependence of inverse gated decoupled ^{13}C NMR spectra of 52d in toluene- d_8 (left) and simulated spectra (right, key signals only). ¹²⁶	76
Figure 2.35 ORTEP and space filling representations of the crystal structure of the 2,3-dichloro- <i>p</i> -phenylene adduct 66 (see Figure 2.30). ¹⁴⁰	77
Figure 2.36 Variable temperature ^1H NMR spectra of 66 (SiMe_2 region): left, observed spectra; right, simulated spectra with rate constants for exchange. ¹⁴⁰	78
Figure 2.37 Variable temperature solid-state quadrupolar echo ^2H NMR spectra of 50c-d₄ showing characteristic Pake patterns. () indicates $(\text{CH}_2)_n$. ¹²³	83
Figure 2.38 <i>p</i> -Phenylene adduct 50c* (top), crystal structures at 300 and 340 K, with the latter showing <i>p</i> - C_6H_4 disorder (middle), and heterocycle adducts studied by solid state ^2H NMR (bottom, () indicates $(\text{CH}_2)_n$). ¹²⁵	84
Figure 2.39 4,4'-Biphenylene adduct 58e [() indicates $(\text{CH}_2)_n$], and space filling representations of the crystal structures at 200 K (left), 280 K (center), and 320 K (right).	85
Figure 2.40 Combinations of different types of radially bulky stators (blue) and low-volume-demand rotators (orange) and possible packing motifs.	89
Figure 2.41 Synthetic approaches to gyroscope-like molecules 101 and 103 studied by Garcia-Garibay, and space filling representations of the molecular structures (with solvate molecules omitted, the rotator in 101 is disordered and only one conformation is depicted).	92
Figure 2.42 Molecular rotors consisting of $-\text{C}\equiv\text{C}-(p\text{-arylene})-\text{C}\equiv\text{C}-$ rotators and trityl stators studied by Garcia-Garibay.	93
Figure 2.43 Variable temperature ^{13}C CP/MAS NMR spectra of 106-d₃₀ (<i>p</i> -phenylene CH signals) recorded with a contact time of 50 μs (black traces) and simulations (blue traces). ¹⁷⁸ The asterisks denote residual signals due to the <i>ipso</i> <i>p</i> -phenylene carbon atoms and one of the trityl carbon atoms.	95
Figure 2.44 Representations of the crystal structure of the <i>p</i> -phenylene containing rotor 106 · $2\text{C}_6\text{H}_6$	101
Figure 2.45 Additional molecular rotors studied by Garcia-Garibay, most with heteroatom containing endgroups. ¹⁸² For the significance of the geometric	

shapes, see the text and Figure 2.46. Deuterated compounds are normally not displayed, but 128-<i>d</i>₂ has not been reported in nondeuterated form.	102
Figure 2.46 First row of structures: cross sections of rotators of C_n symmetries (solid orange) and packing motifs that saturate the van der Waals surface boundaries (dashed blue lines). Second row: packing environments that would be generated upon rotation of the rotators by $360^\circ/2n$. Top: idealized qualitative energy profiles.	104
Figure 2.47 Steric interactions in the crystal structure of the 1,4-cubane-diyl adduct 125 (see also text). ¹⁸²	107
Figure 2.48 Molecular rotors with substituted trityl endgroups studied by Garcia-Garibay (part 1).....	110
Figure 2.49 Molecular rotors with substituted trityl endgroups studied by Garcia-Garibay (part 2).....	110
Figure 2.50 Comparison of packing coefficients (C_k) and E_a values (kcal/mol) for <i>p</i> -phenylene rotation in four molecules. ^a Consult the references in Table 2.5 for additional details regarding the composition of the solvate.....	113
Figure 2.51 Additional molecular rotors studied by Garcia-Garibay, all with at least one triptycyl or substituted triptycyl endgroup.....	113
Figure 2.52 Additional molecular rotors studied by Garcia-Garibay, all of which incorporate a pentiptycene moiety.....	117
Figure 2.53 Additional molecular rotors studied by Garcia-Garibay.....	118
Figure 2.54 Supramolecular rotors studied by Garcia-Garibay and collaborators: top, halogen bonded DABCO adducts; bottom, hydrogen bonded DABCO adducts.	122
Figure 2.55 MOFs in which rotators have been incorporated into the connectors studied by Garcia-Garibay or others (part 1).....	126
Figure 2.56 MOFs in which rotators have been incorporated into the connectors studied by Garcia-Garibay or others (part 2).	127
Figure 2.57 Reactions used to access molecular rotors with deuterated trityl or triptycyl groups.....	130

Figure 2.58 Molecular rotors accessed by postsynthetic modification of certain compounds in Table 2.6. ^a Rapidly decomposes in solution.....	132
Figure 2.59 Syntheses of molecular rotors with silicon (123-126 , top) or phosphorus (127-130 , bottom) containing endgroups.	132
Figure 2.60 Syntheses of molecular rotors 151-157 (top) and 159 (bottom).....	135
Figure 2.61 Syntheses of key precursors to the molecular rotors 160-166	135
Figure 2.62 Final steps in the syntheses of molecular rotors 160-164 (top), 166 (middle), and 165 (bottom).....	136
Figure 2.63 Synthesis of the dendrimer like molecular rotor 167	137
Figure 2.64 Synthesis and structural representations of a "gyroscope inspired" hemicryptophane (300).....	138
Figure 2.65 Syntheses and molecular structures of 304 and 305 , which were reported as molecular gyroscopes.	141
Figure 2.66 Self-assembly of gyroscope-like supramolecular systems 307-317 , rotational barriers of guest molecules, and crystallographic representations of the dimethoxy substituted adduct 309	142
Figure 2.67 An assembly described as a supramolecular gyroscope (318) with a water molecule serving as a dipolar rotator.....	143
Figure 2.68 Solid endohedral fullerene C ₂ Sc ₂ @C ₈₄ (319), considered an example of a quantum gyroscope.....	143
Figure 2.69 Tris(<i>o</i> -phenylenedioxy)cyclotriphosphazene (TPP; 320), a space filling representation of the molecular structure (CCCV), and a top view of the crystal lattice (CCCVI).	145
Figure 2.70 Typical molecular rotors (321-327) that have been intercalated into the channels of CCCVI (Figure 2.69) and representations of intercalated adducts of 327 (CCCVII , reproduced from ref 235 . Copyright 2015 American Chemical Society) and 324 (CCCVIII).	146
Figure 3.1 Thermal ellipsoid plots of the molecular structure of <i>cis</i> - 4c (50% probability level, dominant conformation).	201
Figure 3.2 Thermal ellipsoid plots of the molecular structure of <i>trans</i> - 5c (50% probability level, dominant conformation).	201

Figure 3.3 Thermal ellipsoid plots of the molecular structure of <i>trans-7c</i> (50% probability level, one of three independent molecules).....	201
Figure 3.4 Thermal ellipsoid plots of the molecular structure of <i>trans-10c</i> (50% probability level, dominant conformation).....	201
Figure 3.5 Relative energies (ΔG , kcal mol ⁻¹) of isomeric <i>cis</i> /parachute and <i>trans</i> /gyroscope platinum complexes as computed by DFT (gas phase or toluene or <i>o</i> -C ₆ H ₄ Cl ₂ solutions) preceded by molecular dynamics and semi-empirical (PM7) computations.	208
Figure 3.6 Relative energies (ΔG , kcal mol ⁻¹) of isomeric <i>cis</i> and <i>trans</i> platinum complexes with acyclic triethylphosphine ligands as computed by DFT (gas phase or toluene or <i>o</i> -C ₆ H ₄ Cl ₂ solutions) preceded by molecular dynamics and semi-empirical (PM7) computations.....	209
Figure 3.7 Platinum–ligand bond lengths (Å) for computed <i>trans</i> /gyroscope and <i>cis</i> /parachute complexes.	216
Figure 4.1 IR spectra (ATR/powder film, $\nu_{C\equiv O}$ region) of the new diiron complexes V with principal features highlighted.	243
Figure 4.2 Thermal ellipsoid plots (50% probability) of the molecular structures of 3 (two independent molecules (1 and 2)), 4a (two independent molecules (1 and 2)), and 4b . Solvent molecules in the lattices have been omitted.....	250
Figure 4.3 Thermal ellipsoid plots (50% probability) of the molecular structure of 6' (left) and a relevant complex from the literature, 6'' (right; see the Discussion section 4.3). Solvent molecules in the lattices have been omitted.....	253
Figure 4.4 Thermal ellipsoid plots (50% probability) of the previously reported molecular structure of 5 (top) ⁹ and a plot of the computed structure for the yet unknown higher homolog 6 (bottom). The primed atoms in the latter (employed for uniformity with the other structures) are misleading, as there are no symmetry elements.	258
Figure 4.5 Space-filling side views of the Fe(CO) ₃ rotators in 3 (two independent molecules (1 and 2)), 4a (two independent molecules (1 and 2)), and 4b , 5 , and 6 (computed structure) illustrating the offset between the two Fe(CO) ₃ planes and iron–iron and (when constant) P–Fe–P axis–axis distances.....	258
Figure 4.6 Computed IR $\nu_{C\equiv O}$ bands for monoiron and diiron carbonyl complexes. ...	259

Figure 4.7 Space-filling "top" views of the Fe(CO) ₃ rotators of 3 (top, both independent molecules), 4a (middle, both independent molecules), and 4b (bottom) at van der Waals radii.	264
Figure 4.8 Analyses of interactions in hypothetical conformations of complexes with two coplanar Fe(CO) ₃ rotators (see text).....	265
Figure 4.9 Minimum iron/iron spacing required (6.79 Å) for rotation of a Fe(CO) ₃ rotator with no van der Waals (vdW) interactions with a neighboring Fe(CO) ₃ rotator.....	267
Figure 5.1 Representative dibridgehead diamines I and II (A), and principal diprotonated forms of II (B,C).	289
Figure 5.2 Conventions for representing methylene linkers (CH ₂) _n (A), criteria for assigning <i>in/out</i> orientations to E–X bridgeheads (B), homeomorphic isomerization illustrated for <i>ii</i> and <i>oo</i> isomers including the two limiting "crossed-chain" (<i>cs</i>) intermediates IV and IV' (C), and the onset of what would be classified as a crossed-chain species in analyses below (D ; the "peekaboo" limit).....	291
Figure 5.3 The first macrocyclic aliphatic dibridgehead diphosphines.	294
Figure 5.4 Related systems studied by the Wheeler (A), von Delius (B), and Setaka groups (C).	295
Figure 5.5 A pictorial overview of the calculation pipeline and workflow of this study.....	298
Figure 5.6 The relative energy (stability, potential energy, E_p) of the lowest energy species (panel A) for each cage size of <i>ii</i> _n vs. <i>oo</i> _n ($n = 4-20$). The average energy (potential energy, E_p) of all species of the <i>ii</i> _n and <i>oo</i> _n ($n = 4-20$) type from the annealing data set (panel B).	302
Figure 5.7 Whisker plots of the <i>ii</i> _n (A) and <i>oo</i> _n (B) for the $n = 6-20$ data sets showing the 25-75% energetic range as the average represented. The diamond symbol represents the average energy of each n data set. The horizontal solid black lines (whiskers) indicate the range of outliers (one standard deviation) and the horizontal orange lines indicate extreme values.	302
Figure 5.8 All data frames of <i>ii</i> _n ($n = 6-20$) and <i>oo</i> _n ($n = 4-20$). This three dimensional plot has the potential energy given on the y-axis, the annealing cycles (frames in ns) given on the z-axis and the cage size (n) on the x-axis.....	305

Figure 5.9 An illustration of the repulsive part (steric interactions) of the E_{vdW} term between two E–X groups of a ii_n species (A) whereas B shows the attractive dispersion forces between a solvent molecule (S) and a tether. Experimentally observed single crystal structures of macrobicyclic cages (C–F). All species crystallize in oo_n and several structures contain guest molecules in the assembly. ^{10,29-31}	307
Figure 5.10 A selection of topologically different computed structures.....	311
Figure 5.11 Correlation between surface area, void space, and dispersion interactions (part of E_{vdW}) for a topologically relevant $ii_{14, f12}$ (top) and $ii_{14, f86}$ (bottom).	315
Figure 5.12 A rendition of a Connolly surface onto an arbitrary three-atom molecule.	316
Figure 5.13 The distribution of computed solvent-accessible surface areas (A2) of ii_{14} and oo_{14} (A), and all ii_{14}/oo_{14} species as a function of the computed A2 (B). The computed A2 as a function of E_{vdW} for all ii_{14} and oo_{14} species (C, D) with linear regression analysis.	318
Figure 5.14 The two trajectories of ii_{14} and oo_{14} a function of potential energy (E_p) with selected frames depicted.....	321
Figure 5.15 Probing the inversion barrier of a macrobicyclic phosphine ($n = 7$) from ii_7 vs. an acyclic trimethyl phosphine model compound (A). The io_n can undergo inversion to form ii_n or oo_n (B). The io_n species can have a chain threading through to form two new species with crossing chains (ii_n^{CS} and oo_n^{CS}) (C).	324
Figure 5.16 Synchronicity of the homeomorphic pathway. Note that the E–X bond in the left center panel showing IV have been omitted as both bridgehead groups would need to have a directionality facing the reader, which is difficult to depict.....	328
Figure 5.17 Cross-chain intermediates as a function of cage size (A), and the average energies of the ii_n , oo_n , and io_n^{CS} isomers (B). The two hypothesized pathways with different synchronicity for interconverting ii_{14} and oo_{14} (C and D). Experimentally characterized cross-chain species (E,F).....	329
Figure 5.18 Probing the cutoff for homeomorphic isomerism by performing extended trajectories for ii_{13} and oo_{13}	330

Figure 5.19 Experimental and computed ^{31}P NMR chemical shifts for ii_{14} , io_{14} , and oo_{14} .	332
Figure 5.20 A summary of all intermediates including hypothesized species.	334
Figure 6.1 Classical ring-current-based shielding/deshielding models for benzene (I) and ethyne (II). ^{1,2}	345
Figure 6.2 Computed NICS about benzene (III) and ethyne (IV), with red and green spheres indicating shielding and deshielding, respectively. The data are from ref 5, which can be consulted for the scales represented by the spheres.	345
Figure 6.3 Representative diplatinum polyyne diyl complexes.	347
Figure 6.4 Representative NICS grid plots for ethyne and the diterminal polyynes $\text{H}(\text{C}\equiv\text{C})_n\text{H}$ ($n = 2-10$). The distances are not to scale. The grid points on the y -axis represent increments of 0.50 \AA , and those on the x -axis represent increments of $1.19-1.21$ or $1.35-1.37 \text{ \AA}$ (for $\text{C}\equiv\text{C}$ and $\equiv\text{C}-\text{C}\equiv$ linkages, respectively) or $1.06-1.11 \text{ \AA}$ (for $\text{C}-\text{H}$ linkages and points extending further out from the carbon chain).	348
Figure 6.5 Computed ^1H and ^{13}C NMR chemical shifts of ethyne and the diterminal polyynes $\text{H}(\text{C}\equiv\text{C})_n\text{H}$ vs. TMS and (when available) experimental values [in brackets].	350
Figure 6.6 Computed ^1H NMR chemical shifts for ethyne and the diterminal polyynes $\text{H}(\text{C}\equiv\text{C})_n\text{H}$ vs. TMS (blue rhomb) and experimental values (open circle).	351
Figure 6.7 Organic conjugated polyynes used for chemical shift comparisons. ^{11a,b,21}	352
Figure 6.8 Computed ^{13}C NMR chemical shifts for ethyne and the diterminal polyynes $\text{H}(\text{C}\equiv\text{C})_n\text{H}$ ($\text{HC1}\equiv\text{C2}-\text{C3}\equiv\text{C4}\dots$) vs. TMS as a function of n (green square = C1; open circle = C2; blue rhomb = C3; black triangle = C4; black plus sign = C5; orange triangle = C6; purple filled circle = C7; black cross = C8).	353
Figure 6.9 Correlation of ^{13}C NMR chemical shifts trends computed for $\text{H}(\text{C}\equiv\text{C})_n\text{H}$ (blue diamond) vs. those observed experimentally for $\text{Ar}^*(\text{C}\equiv\text{C})_n\text{Ar}^*$ (6; open circle; acetone- d_6). The C7/C8 and C9/C10 signals of $\text{Ar}^*(\text{C}\equiv\text{C})_{10}\text{Ar}^*$ were reported as overlapping singlets at δ 63.97 and 63.84 ppm, respectively.	354

Figure 6.10 Experimental $^{13}\text{C}\{^1\text{H}\}$ NMR spectrum of the $\text{PtC}\equiv\text{C}$ and $\text{C}\equiv\text{CSi}$ segments of $\text{Pt}^{\text{T}}\text{C}_8\text{TIPS}$ (125 MHz, CDCl_3 , cryoprobe).....	359
Figure 7.1 Thermal ellipsoid plots (50% probability level) of the crystal structure of $\mathbf{3a}\cdot\text{CH}_2\text{Cl}_2$ with the solvate molecule omitted. Bond lengths (\AA) and angles ($^\circ$) associated with platinum or the butadiynyl ligands: Pt1–C4 1.998(4), Pt1–C8 2.004(4), Pt–P2 2.2912(10), Pt–P3 2.2870(9), C4 \equiv C5 1.212(5), C5–C6 1.387(5), C6 \equiv C7 1.178(5), C8 \equiv C9 1.211(5), C9–C10 1.376(6), C10 \equiv C11 1.188(5), P2–Pt1–P3 96.06(3), Pt1–C4–C5 174.2(3), Pt1–C8–C9 175.6(3), C4–C5–C6 175.1(4), C5–C6–C7 179.8(6), C8–C9–C10 178.2(4), C9–C10–C11 178.9(4).....	380
Figure 7.2 UV-visible spectra of the Pt_4C_{16} complexes $\mathbf{4a,b}\cdot([\text{H}_2\text{NET}_2]^+ \text{Cl}^-)_n$, the precursor $\text{Pt}(\text{C}_4\text{H})_2$ species $\mathbf{3a,b}$, and the PtC_4Pt species $\mathbf{5}$ (3.0×10^{-5} M in CH_2Cl_2). λ_{max} (nm) [ϵ ($\text{M}^{-1} \text{cm}^{-1}$)]: $\mathbf{4a}$, 266 [564,000], 327 [602,000], 350 [454,000]; $\mathbf{4b}$, 266 [639,000], 330 [635,000], 351 [525,000]; $\mathbf{3a}$, 268 [130,000], 277 [138,000], 304 [166,000]; $\mathbf{3b}$, 268 [128,000], 277 [136,000], 304 [165,000]; $\mathbf{5}$, 330 [17,500], 350 [13,600]. The ϵ values for $\mathbf{4a,b}$ are calculated including the formula weight of the $[\text{H}_2\text{NET}_2]^+ \text{Cl}^-$ present (see text and experimental section 7.6 and 7.14).	392
Figure 7.3 Thermal ellipsoid plots (50% probability) of the molecular structures of the Pt_4C_{16} complexes $\mathbf{4a}$. Solvate molecules have been omitted.....	394
Figure 7.4 Limiting geometries of the model compounds $\mathbf{4'a}$ (PMe in place of PPh of $\mathbf{4a}$) and $\mathbf{4''}$ (2PH_3 in place of each diphosphine of $\mathbf{4a}$), and the intervening transition state for the latter.	397
Figure 7.5 ΔG_{gas} values, computed at the CAM–B3LYP/6-311G(d) level of theory, associated with hypothetical isodesmic equilibria involving $\mathbf{4'a}$, $\mathbf{7'a}$, and $\mathbf{8'a}$ (top), and the corresponding structures (bottom).	397
Figure 7.6 Computed UV-visible spectra (top, $\mathbf{7'a}$; middle, $\mathbf{3'a}$ and $\mathbf{4'a}$ bottom $\mathbf{8'a}$) and orbitals that are dominant contributors to selected transitions.....	400
Figure 7.7 The HOMO and LUMO of $\mathbf{4'a}$	401
Figure 7.8 Electrostatic potential surface maps of $\mathbf{7'a}$, $\mathbf{4'a}$, $\mathbf{8'a}$, and other relevant species.....	402
Figure 7.9 Previously reported "tweezer" complexes.	404

Figure 8.1 Representations of the enantiomeric Λ and Δ -[Co(en) ₃] ³⁺ trications (a-c) and the related bis(chelates) [Co(en) ₂ (A) ₂] ³⁺ and [Co(en) ₂ (A)(B)] ⁿ⁺ (d).....	430
Figure 8.2 Chelate conformations of ethylenediamine.	433
Figure 8.3 Accommodation of ethylenediamine ligands with three λ or three δ conformations in the coordination sphere of an octahedral cobalt atom with a Δ configuration.....	434
Figure 8.4 All possible stereoisomers of the [Co(en) ₃] ³⁺ trication.....	435
Figure 8.5 The <i>fac/mer</i> isomers of the [Co((<i>R</i>)- <i>pn</i>) ₃] ³⁺ trication.	438
Figure 8.6 Chelate conformations of (<i>R</i>)- <i>pn</i> and (<i>S</i>)- <i>pn</i>	438
Figure 8.7 Principal stereoisomers of the [Co((<i>R</i>)- <i>pn</i>) ₃] ³⁺ trication.....	440
Figure 8.8 Configurational stereoisomers of 1,2-cyclohexanediamine.....	444
Figure 8.9 Diamine chelate conformations and principal stereoisomers of the [Co(<i>trans</i> - <i>chxn</i>) ₃] ³⁺ trication with homochiral (all <i>S,S</i> or all <i>R,R</i>) ligands.	444
Figure 8.10 Stereoisomers of the [Co(<i>trans</i> - <i>chxn</i>) ₃] ³⁺ trication with all possible combinations of (<i>R,R</i>)- <i>chxn</i> and (<i>S,S</i>)- <i>chxn</i> ligands.	446
Figure 8.11 Diamine chelate conformations and representative stereoisomers of the [Co(<i>cis</i> - <i>chxn</i>) ₃] ³⁺ trication; axial and equatorial are used to designate C–N bond positions on the cyclohexane ring, and pseudoaxial and pseudoequatorial are used to designate C–CH ₂ bond positions on the chelate ring.....	447
Figure 8.12 Diamine chelate conformations and principal configurational stereoisomers of the [Co(<i>dpen</i>) ₃] ³⁺ trication with homochiral (all <i>S,S</i> or all <i>R,R</i>) ligands.....	450
Figure 8.13 Stereoisomers of the [Co(<i>dpen</i>) ₃] ³⁺ trication with all possible combinations of (<i>R,R</i>)- <i>dpen</i> and (<i>S,S</i>)- <i>dpen</i> ligands.....	451
Figure 8.14 Thermal equilibration of racemic [Co(<i>trans</i> - <i>chxn</i>) ₃] ³⁺ 3Cl ⁻ in the presence of excess ligand.....	454

Figure 8.15 Thermal equilibration of enantiopure Δ -[Co((<i>R,R</i>)- <i>dpen</i>) ₃] ³⁺ 3Cl ⁻ in the presence of excess ligand.....	454
Figure 8.16 Organic transformations that can be catalyzed by cobalt(III) complexes with ethylenediamine or substituted ethylenediamine ligands (BAr _f ⁻ = B(3,5-C ₆ H ₃ (CF ₃) ₂) ₄ ⁻ ; BAr _{f20} ⁻ = B(C ₆ F ₅) ₄ ⁻).....	456
Figure 9.1 Representations of the enantiomeric Λ - and Δ -[Co(<i>en</i>) ₃] ³⁺ trications.	472
Figure 9.2 Chelate conformations of ethylenediamine.	474
Figure 9.3 Accommodation of ethylenediamine ligands with three λ or three δ conformations in the coordination sphere of an octahedral cobalt atom with a Δ configuration.....	476
Figure 9.4 All possible stereoisomers of the [Co(<i>en</i>) ₃] ³⁺ trication.....	479
Figure 9.5 Representations of the C ₂ and C ₃ binding sites of the Δ - $\lambda\lambda\lambda$ -[Co(<i>en</i>) ₃] ³⁺ trication, and a general nomenclature system for hydrogen bonding to an anion or molecule.	481
Figure 9.6 Anion binding modes involving hydrogen bonding to both the C ₂ and C ₃ sites of the Δ - $\lambda\lambda\lambda$ -[Co(<i>en</i>) ₃] ³⁺ trication.....	484
Figure 9.7 Representative hydrogen bonding motifs for the Δ - $\lambda\lambda\lambda$ -[Co(<i>en</i>) ₃] ³⁺ trication (<i>lel</i> ₃ , <i>D</i> ₃) and the nitrate anion.	486
Figure 9.8 Hydrogen bonding interactions in Λ - $\delta\delta\delta$ -[Co(<i>en</i>) ₃] ³⁺ 3Cl ⁻ ·H ₂ O (<i>lel</i> ₃) viewed along the C ₃ axis (left) and a C ₂ axis (right).....	489
Figure 9.9 Hydrogen bonding interactions in Λ - $\delta\delta\delta$ -[Co(<i>en</i>) ₃] ³⁺ 3Cl ⁻ ·2.8H ₂ O (<i>lel</i> ₃) viewed along the C ₃ axis (left) and a C ₂ axis (right).....	490
Figure 9.10 Hydrogen bonding interactions in Λ - $\delta\delta\delta$ -[Co(<i>en</i>) ₃] ³⁺ 3Cl ⁻ (<i>lel</i> ₃) viewed along the C ₃ axis (left) and a C ₂ axis (right).	491
Figure 9.11 Hydrogen bonding interactions in Λ - $\delta\delta\delta$ -[Co(<i>en</i>) ₃] ³⁺ 3Br ⁻ ·H ₂ O (<i>lel</i> ₃) viewed along the C ₃ axis (left) and a C ₂ axis (right).....	492

- Figure 9.12 Hydrogen bonding interactions in Λ - $\delta\delta\delta$ -[Co(en)₃]³⁺ 3I⁻·H₂O (*oblel*₃) viewed along the pseudo C₃ axis (left) and a C₂ axis (right).494
- Figure 9.13 Hydrogen bonding interactions in Λ - $\delta\delta\delta$ -[Co(en)₃]³⁺ 3NO₃⁻ (*lel*₃) viewed along the C₃ axis (left) and a C₂ axis (right). The distal oxygen atoms of the NO₃⁻ anions have been omitted for clarity.....495
- Figure 9.14 Hydrogen bonding interactions in the Λ - $\lambda\delta\delta$ -[Co(en)₃]³⁺ 3ReO₄⁻ (*oblel*₂) viewed along the pseudo C₃ axis (left) and the C₂ axis (right). Non-interacting oxygen atoms of the ReO₄⁻ anions have been omitted for clarity.496
- Figure 9.15 Hydrogen bonding interactions in the Λ - $\delta\delta\delta$ -[Co(en)₃]³⁺ 3SCN⁻ (*lel*₃) viewed along the C₃ axis (left) and the C₂ axis (right). Non-coordinating atoms of the anions have been omitted for clarity.....497
- Figure 9.16 Hydrogen bonding interactions in the Λ - $\delta\delta\delta$ -[Co(en)₃]³⁺ Cl⁻2I⁻·H₂O (*lel*₃) viewed along the C₃ axis (left) and the C₂ axis (right).498
- Figure 9.17 Hydrogen bonding interactions in the Λ - $\lambda\delta\delta$ -[Co(en)₃]³⁺ I⁻CO₃²⁻·4H₂O (*oblel*₂) viewed along the pseudo C₃ axis (left) and the C₂ axis (right). One non-interacting oxygen atom of each carbonate anion has been omitted for clarity.....500
- Figure 9.18 Hydrogen bonding interactions in the Λ - $\lambda\delta\delta$ -[Co(en)₃]³⁺ B₅O₆(OH)₄⁻ B₈O₁₀(OH)₆²⁻·5H₂O (*oblel*₂) viewed along the pseudo C₃ axis (left) and the C₂ axis (right). The larger borate dianion is colored orange and the smaller borate monoanion is colored light green. In both cases, some non-interacting atoms have been omitted for clarity. ^a Two of the hydrogen bonds involve BOB linkages, and one a BOH linkage. ^b Two of the hydrogen bonds involve BOB linkages, and two BOH linkages.....501
- Figure 9.19 Hydrogen bonding interactions in the Λ - $\lambda\delta\delta$ -[Co(en)₃]³⁺ 1.5C₄O₄²⁻·4.5H₂O (*oblel*₂) viewed along the pseudo C₃ axis (left) and the C₂ axis (right). Several non-interacting atoms of the squarate anions have been omitted for clarity.503
- Figure 9.20 Hydrogen bonding interactions in the Λ - $\delta\delta\delta$ -[Co(en)₃]³⁺ 1.5*p*-C₆H₄(CO₂)₂²⁻·10H₂O (*lel*₃) viewed along the C₃ axis (left) and the C₂ axis

(right). The hydrogen atoms of the H₂O molecules and the C₆H₄ moieties of the terephthalate dianions have been omitted for clarity.....504

Figure 9.21 Hydrogen bonding interactions in the Λ - $\delta\delta\delta$ -[Co(en)₃]³⁺ 1.5HPO₄²⁻·4.5H₂O (*lel*₃) viewed along the C₃ axis (left) and the C₂ axis (right). The hydrogen atoms of the H₂O molecules and HPO₄²⁻ dianions, and non-interacting oxygen atoms of the latter, have been omitted for clarity.506

Figure 9.22 Hydrogen bonding interactions in the Λ - $\delta\lambda\lambda$ -[Co(en)₃]³⁺ 1.5C₅H₅²⁻·3H₂O (*lelob*₂) viewed along the pseudo C₃ axis (left) and the C₂ axis (right). Several atoms of the C₅O₅²⁻ dianions have been omitted for clarity.508

Figure 9.23 Hydrogen bonding interactions in the Λ - $\delta\delta\delta$ -[Co(en)₃]³⁺ Cl⁻(*R,R*)-tart²⁻·5H₂O (*lel*₃) viewed along the C₃ axis (left) and the C₂ axis (right). Most non-interacting atoms of the tartrate dianions have been omitted for clarity. 510

Figure 9.24 Hydrogen bonding interactions in the two independent trications of Δ - $\lambda\lambda\lambda$ -[Co(en)₃]³⁺ 1.5(*R,R*)-tart²⁻·5.75H₂O (*lel*₃) viewed along the C₃ axis (left middle, left bottom) and a C₂ axis (right middle, right bottom), or as linked together (top). In the middle and bottom representations, most non-interacting atoms of the tartrate dianions have been omitted for clarity.512

Figure 9.25 Hydrogen bonding interactions in the two independent trications of Λ - $\delta\delta\delta$ -[Co(en)₃]³⁺ 1.5(*R,R*)-tart²⁻·9.5H₂O (*lel*₃) viewed along the C₃ axis (left middle, left bottom) and a C₂ axis (right middle, right bottom). Most non-interacting atoms of the tartrate dianions have been omitted for clarity.514

Figure 9.26 Hydrogen bonding interactions in Λ - $\delta\delta\delta$ -[Co(en)₃]³⁺ AsO₄³⁻·3H₂O (*lel*₃) viewed along the C₃ axis (left) and a C₂ axis (right). Non-interacting oxygen atoms of the arsenate trianion have been omitted for clarity.516

Figure 9.27 Hydrogen bonding interactions in Λ - $\lambda\delta\delta$ -[Co(en)₃]³⁺ AsS₄³⁻ (*oblel*₂) viewed along the C₃ pseudoaxis (left) and a C₂ axis (right). Non-interacting sulfur atoms of the tetrathioarsenate trianion have been omitted for clarity. .517

Figure 9.28 Hydrogen bonding interactions in Λ - $\delta\delta\delta$ -[Co(en)₃]³⁺ GaF₆³⁻ (*lel*₃) viewed along the C₃ axis (left) and a C₂ axis (right). Non-interacting fluorine atoms of the hexafluorogallate trianion have been omitted for clarity.518

- Figure 9.29 Hydrogen bonding interactions in Λ - $\lambda\delta\delta$ -[Co(en)₃]³⁺ Co(CN)₆³⁻·5H₂O (*oblel*₂) viewed along the pseudo C₃ axis (left) and the C₂ axis (right). Except for the interacting CN units, the Co(CN)₆³⁻ trianions have been omitted for clarity. Disordered H₂O molecules are denoted with an X. ^a Although this salt has a stoichiometry of five H₂O molecules per trication, there are seven H₂O molecules in the second coordination sphere, four of which are shared with neighboring trications and disordered over two positions (each highlighted with an "X").....520
- Figure 9.30 Hydrogen bonding interactions in Λ - $\delta\delta\delta$ -[Co(en)₃]³⁺ Δ -Rh(C₂O₄)₃³⁻ (*lel*₃) viewed along the C₃ axis (left) and a C₂ axis (right). Non-interacting atoms of the trianion have been omitted for clarity.521
- Figure 9.31 Hydrogen bonding interactions in Λ - $\delta\delta\delta$ -[Co(en)₃]³⁺ Δ -Rh(C₂O₄)₃³⁻ (*lel*₃) viewed along the C₃ axis (left) and a C₂ axis (right). Non-interacting atoms of the trianion have been omitted for clarity.522
- Figure 9.32 Hydrogen bonding interactions in Λ - $\lambda\delta\delta$ -[Co(en)₃]³⁺ (C₆H₃)(CO₂)₃³⁻·5.55H₂O (*oblel*₂) viewed along the pseudo C₃ axis (left) and a C₂ axis (right). Non-interacting atoms of the trianion have been omitted for clarity. 524
- Figure 9.33 Hydrogen bonding interactions in Λ - $\delta\delta\delta$ -[Co(en)₃]³⁺ P₃O₉³⁻·2H₂O (*lel*₃) viewed along the C₃ axis (left) and a C₂ axis (right). Most non-interacting atoms of the trianion have been omitted for clarity.525
- Figure 9.34 Hydrogen bonding interactions in Λ - $\delta\delta\delta$ -[Co(en)₃]³⁺ P₃O₉³⁻·2H₂O (*lel*₃) viewed along the C₃ axis (left) and a C₂ axis (right). Most non-interacting atoms of the trianion have been omitted for clarity.526
- Figure 11.1 Thermal ellipsoid plots of the molecular structure of *trans*-**7c** (50% probability level, three independent molecules).551
- Figure 11.2 A graphical overview of the computational sequence used in this study. ...553
- Figure 11.3 Molecular dynamics simulations (MM/MD, simulated annealing) of *cis*-**2c** (×) and *trans*-**2c** (○). The trajectories are run in the gas phase.555
- Figure 11.4 Molecular dynamics simulations (MM/MD, simulated annealing) of *cis/trans*-**5c**, **7c**, **8**, **4c**, **6c**, **3c**. The trajectories are run in the gas phase.556

Figure 11.5 Molecular dynamics simulations (MM/MD, simulated annealing) of acyclic <i>cis-2</i> " (×) and <i>trans-2</i> " (○). The trajectories are run in the gas phase.	557
Figure 11.6 Molecular dynamics simulations (MM/MD, simulated annealing) of acyclic <i>cis/trans-5</i> ", <i>7</i> ", <i>8</i> ", <i>4</i> ", <i>6</i> ", <i>3</i> ". The trajectories are run in the gas phase.	558
Figure 11.7. Views of gyroscope like complexes showing attractions between two (CH ₂) _n bridges if dispersion corrections are used.	564
Figure 11.8. Structures and relative electronic energies from single point energy calculations on P((CH ₂) ₁₄) ₃ P scaffolds excised from the platinum complexes indicated.	565
Figure 11.9. Structures and relative electronic energies from single point energy calculations of the diphosphines H ₂ P(CH ₂) ₁₄ PH ₂ , HP((CH ₂) ₁₄) ₂ PH, and P((CH ₂) ₁₄) ₃ P derived from the parent platinum complexes <i>cis/trans-2c</i>	566
Figure 12.1 A graphical overview of the computational methods employed in this study.	571
Figure 12.2 Computed structures and vibrational modes of <i>monoiron</i> complexes. The lengths of the arrows indicate the relative amplitude.	573
Figure 12.3 Computed structures and vibrational modes of <i>diiron</i> complexes. The lengths of the arrows indicate the relative amplitudes.	574
Figure 12.4 Three different setups for scanning the energy vs. Fe1...Fe1' interatomic distance with single point calculations at each increment.	577
Figure 12.5 Computed structures of the <i>monoiron</i> complexes overlaid with crystal structures when available (RMSD values).	578
Figure 12.6 Computed structures of the <i>diiron</i> complexes overlaid with crystal structures when available (RMSD values).	579
Figure 13.1 The ten lowest and highest energy (<i>E_p</i>) molecular mechanics <i>ii</i> ₁₄ frames have been DFT optimized.	596
Figure 14.1 Graphical outline of the calculation sequence.	598
Figure 14.2 Validation of the computational methods: benchmarking vs. literature results.	601

Figure 14.3 Graphical depiction of the different distances typically used in the NICS grid plots.	602
Figure 14.4 NICS grid plot for $\text{H}(\text{C}\equiv\text{C})_n\text{H}$ ($n = 10, 9$).	603
Figure 15.1 Views of computed structures.....	623
Figure 15.2 Computed UV-visible spectra of 3'a , 3b , 4'a , 7'a , and 8'a	627
Figure 15.3 Selected frontier molecular orbitals of 3'a relevant to Table 15.2.	630
Figure 15.4 Selected frontier molecular orbitals of 7'a relevant to Table 15.2.	631
Figure 15.5 Selected frontier molecular orbitals of 4'a relevant to Table 15.2.	632
Figure 15.6 Selected frontier molecular orbitals of 8'a relevant to Table 15.2.	633
Figure 15.7 Electrostatic potential surface plots for selected DFT optimized species. .	634
Figure 15.8 Overlays of experimental and computed structures, truncating the former for atoms not included in the latter. The hydrogen atoms have been removed for clarity.	635
Figure 16.1 Conventions used in designating chelate stereochemistry (<i>R</i> vs. <i>S</i> ; λ vs. δ ; <i>ob</i> vs. <i>lel</i>) in the structural representations in Figure 16.2 and some "short cuts" involving these relationships.	643
Figure 16.2 The 24 stereoisomers of the $[\text{Co}(\text{pn})_3]^{3+}$ trication summarized in Table 16.1, allowing all combinations of <i>R</i> (purple labels) and <i>S</i> (turquoise labels) <i>pn</i> ligands. The methyl groups are depicted in blue for <i>fac</i> isomers, and in vermilion for <i>mer</i> isomers.	644
Figure 16.3 Conventions used in designating chelate stereochemistry in the structural representations in Figure 16.4. The procedure is analogous to that in Figure 16.1 except it is important to consistently view the C_3 axes from in front of the plane of the paper to "order" the <i>SR/RS</i> configurations of the chelate ring stereocenters.	646
Figure 16.4 The 24 stereoisomers of the $[\text{Co}(\text{cis-}chxn)_3]^{3+}$ trication (<i>cis-}chxn = <i>R,S-}chxn</i>) summarized in Table 16.1. In each vertical series, the λ/δ configuration of the chelate at apex 1 (Figure 16.3) is kept constant while the configurations in the remaining chelates are varied, as denoted by the arrows \Leftarrow/\Rightarrow (for $\lambda\delta\delta$ and $\delta\lambda\lambda$ systems apex 1 is also set as the unlike configuration). Bold lines separate the families of isomers described in the</i>	

preceding text. There is extensive color-coding that carries over to Table 16.1, but the conventions are left to be empirically discerned.647

LIST OF SCHEMES

	Page
Scheme 3.1 Generalized syntheses of gyroscope like (<i>trans</i> - II) and parachute like (<i>cis</i> - II) metal complexes.....	186
Scheme 3.2 Previously studied isomerizations of parachute and gyroscope like complexes.	188
Scheme 3.3 Stereospecific substitution of chloride ligands by phenyl ligands in <i>trans</i> and <i>cis</i> platinum complexes.....	190
Scheme 3.4 Substitution of the chloride ligands in <i>trans</i> - 2c,e,g by methyl ligands with isomerization.....	193
Scheme 3.5 Introduction of halide ligands and attendant isomerization.....	194
Scheme 3.6 Substitution and isomerization reactions involving ethyl ligands.	195
Scheme 3.7 Substitution and isomerization reactions involving phenyl ligands.	197
Scheme 3.8 Halide substitution reactions.	197
Scheme 3.9 Thermolyses that afford well defined complex/solvent reactions.	206
Scheme 3.10 Potential equilibria that may play a role in substitution reactions.....	211
Scheme 4.1 Syntheses of gyroscope-like complexes (II) and new targets with two ML_y rotators with parallel axes (III and IV).....	240
Scheme 4.2 Some possible products derived from equimolar amounts of $Fe(CO)_3$ sources and α,ω -diphosphines $Ar_2P(CH_2)_nPAR_2$ (V and VI).	242
Scheme 4.3 Syntheses of new diiron and monoiron complexes.	242
Scheme 4.4 Computed ΔG values for the hypothetical equilibrium between monoiron and diiron complexes classical.	262
Scheme 4.5 A triphosphine that templates the synthesis of trinickel complexes with three approximately parallel rotators.	269
Scheme 7.1 Some previously characterized polygon shaped molecules with butadiynediyl or $-(C\equiv C)_2-$ edges. ⁶	375

Scheme 7.2 Previously reported Pt ₄ C ₁₆ complexes with four like corners.	378
Scheme 7.3 The 1,3-diphosphine ligands used in this study, and syntheses of those not previously reported (1c,d,f).....	378
Scheme 7.4 Syntheses of monoplatinum complexes.	380
Scheme 7.5 Syntheses of Pt ₄ C ₁₆ complexes that are admixed with 1-2 equiv. of ammonium salts (see text).	393
Scheme 9.1 Resolution of the enantiomeric Λ and Δ -[Co(en) ₃] ³⁺ trications. ^{3e,4a}	470

LIST OF TABLES

	Page
Table 2.1 Activation parameters for Fe(CO)(NO)(X) or Fe(CO) ₃ H rotation within E((CH ₂) _n) ₃ E cages in solution as determined by variable temperature ¹³ C{ ¹ H} NMR [() Indicates (CH ₂) _n].	50
Table 2.2 Structural data for gyroscope-like complexes of the formula <i>trans</i> -M(L)(L')(L'')(E(CH ₂) ₁₄ E) ₂ .	57
Table 2.3 Data for the reactions represented in Figure 2.27.	69
Table 2.4 Activation parameters for rotation of 1,4-naphthalenediyl rotators in toluene- <i>d</i> ₈ .	79
Table 2.5 Arrhenius parameters for the solid-state rotation of rotators in compounds studied by Garcia-Garibay and related systems.	98
Table 2.6 Syntheses of -C≡C-arylene-C≡C- containing rotors with identical trityl or substituted trityl endgroups.	131
Table 3.1 Summary of crystallographic data.	199
Table 3.2 Key crystallographic bond lengths [Å] and angles [°].	200
Table 3.3 Summary of thermolysis experiments.	205
Table 4.1 Experimental and computed IR ν _{C≡O} bands for monoiron (1' - 6') and diiron (3 , 4a,b , 5 , and 6) complexes.	247
Table 4.2 General crystallographic data.	249
Table 4.3 Key interatomic distances (Å) and bond angles (°) for crystallographically characterized complexes.	256
Table 4.4 Additional structural features of crystallographically or computationally characterized diiron complexes. ^a	257
Table 5.1 Relative energies of <i>ii</i> _n vs. <i>oo</i> _n (<i>n</i> = 5-20) for the lowest energy structures.	300

Table 5.2 Percent difference in the contribution of individual terms of E_p for ii_n vs. oo_n of $n = 5-7$ and 14 . A positive value indicates that the value for ii_n is greater than oo_n	312
Table 6.1 Experimental $^{13}\text{C}\{^1\text{H}\}$ and computed [brackets] ^a ^{13}C NMR chemical shifts (δ/ppm ; CDCl_3 , referenced to TMS).....	356
Table 6.2 Correlation of ^{13}C NMR chemical shifts computed for the compounds in Table 6.1 (blue diamonds) versus those observed experimentally (open circles).....	361
Table 7.1 $^{31}\text{P}\{^1\text{H}\}$ NMR data for 1a-1f , 2a-2f , 3a-3f , and 4a-4f	381
Table 7.2 $^{13}\text{C}\{^1\text{H}\}$ NMR data for 3a-3f and 4a-4f (δ , ppm; CDCl_3 unless noted).....	385
Table 7.3 General crystallographic data.....	386
Table 7.4 Key crystallographic distances [\AA] and angles [$^\circ$] for new Pt_4C_{16} complexes.	387
Table 7.5 Views of the puckered hinge like Pt_4C_{16} cores of 4a (middle) and 4b (bottom), and plane/plane angles ($^\circ$) and platinum-platinum distances (\AA) in these and related complexes.	389
Table 8.1 Stereoisomers of $[\text{Co}(pn)_3]^{3+}$ trications comprised of all combinations of (<i>R</i>)- <i>pn</i> and (<i>S</i>)- <i>pn</i> ligands (rows in bold are for tris((<i>R</i>)- <i>pn</i>) adducts as analyzed in Figure 8.7).	442
Table 11.1 Computed stability differences (kcal/mol) of key pairs of <i>cis/trans</i> species.....	562
Table 12.1 Computed IR $\nu_{\text{C}\equiv\text{O}}$ bands and energies for iron carbonyl complexes.	575
Table 12.2 Key interatomic distances (\AA) and angles ($^\circ$) for computed structures of diiron complexes. ^a	580
Table 12.3 Key interatomic distances (\AA) and angles ($^\circ$) for the computed structures of di iron complexes. ^a	581
Table 13.1 Molecular dynamics simulation (simulated annealing) of ii_n , $n = 4, 5, 6, \dots, 20$. The different species are denoted as follows: \times (cross-chain) o (<i>out-out</i>) (<i>in-in</i>) \diamond (<i>in-out</i>). The <i>x</i> -axes represent cumulative molecular structures and the <i>y</i> -axes represent potential energy (kcal/mol).....	586

Table 13.2 Molecular dynamics simulation (simulated annealing) of oo_n , $n = 4, 5, 6, \dots, 20$. The different species are denoted as follows: \times (cross-chain) o (<i>out-out</i>) l (<i>in-in</i>) \diamond (<i>in-out</i>). The x -axes represent cumulative molecular structures and the y -axes represent potential energy (kcal/mol).....	591
Table 13.3 Boltzmann averaged energies ($T = 298.15$ K) of ii_n vs. oo_n for $n = 5-20$	595
Table 14.1 The sum of (1) the percent difference in average C-C bond lengths, and (2) the percent difference in average C \equiv C bond lengths for those in the crystal structure of t -Bu(C \equiv C) $_8$ t -Bu versus those computed for H(C \equiv C) $_8$ H with various functionals. ¹¹	600
Table 14.2 Carbon-carbon bond distances (\AA) in optimized structures of H(C \equiv C) $_8$ H using nine different functionals compared to experimentally determined values in t -Bu(C \equiv C) $_8$ t -Bu.....	608
Table 14.3 The effect of basis set on NICS values at three distances from the centers of the C1 and C2 atoms of H(C \equiv C) $_4$ H using the CAM-B3LYP functional...	610
Table 14.4 The effect of functional on NICS values at three distances from the centers of the C1 and C2 atoms of H(C \equiv C) $_4$ H using the 6-311++G(d,p) basis set. ...	611
Table 14.5 Summary of the ^1H and ^{13}C NMR chemical shifts for H(C \equiv C) $_n$ H ($n = 1-10$). All isotropic values have been corrected using TMS and the GIAO method at the CAM-B3LYP/6-311++G(d,p) level. The TMS isotropic ^1H and ^{13}C values are 31.9766 and 187.8458, respectively.	612
Table 14.6 Summary of optimized bond lengths (\AA) for H(C \equiv C) $_n$ H ($n = 1-10$) at the CAM-B3LYP/6-311++G(d,p) level.	613
Table 15.1 Computed stability differences (kcal/mol) between planar and puckered isomers of 4'a . ^a	625
Table 15.2 Computed wavelengths (λ , nm), oscillator strengths (f), main compositions, and main assignments for the UV-visible electronic excitations of 3'a , 7'a , 4'a , and 8'a . Unless noted, only contributions larger than 10% are presented. The associated orbitals are plotted in Figures 15.3-15.6.	628
Table 15.3 Key crystallographic distances (\AA) and angles ($^\circ$) for 3a ·CH $_2$ Cl $_2$ and the corresponding metrics computed for 3a , 3'a , 3b , and 3'b . ^a Computed data are have compound numbers shown in brackets.	636

Table 15.4 Key crystallographic distances (Å) and angles (°) for 4a , and corresponding metrics computed for 4'a , 7'a , and 8'a . ^a Computed data are have compound numbers shown in brackets.	637
Table 16.1 Summary of the stereoisomers of the $[\text{Co}(\text{cis-}chxn)_3]^{3+}$ trication.....	651
Table 16.2 A grid of the structure numbers for the 24 stereoisomers in Figure 16.4 with "×" indicating those that can be interconverted by a single cyclohexane "ring flip". The specific ring can be inferred from additional coding in Figure 16.4. The sets of structures interconverted by "×" are considered families of conformational stereoisomers.....	652
Table 17.1 Syntax for hydrogen bonding interactions between the $[\text{Co}(en)_3]^{3+}$ trication and anions or solvent molecules.....	653
Table 17.2 Syntax using Λ - $\delta\delta\delta$ - $[\text{Co}(en)_3]^{3+}$ (<i>lel</i> ₃) and a hypothetical triatomic anion (green) in which all atoms are capable of hydrogen bonding.....	654
Table 17.3 Crystal structures containing the $[\text{Co}(en)_3]^{3+}$ trication in the Cambridge Structural Database (CSD) minus duplicates. ^a The identities of the salts can be found in the supplementary information of the published article.	662
Table 17.4 Duplicate crystal structures containing the $[\text{Co}(en)_3]^{3+}$ trication in the Cambridge Structural Database (CSD).....	666

1. INTRODUCTION

The introduction of computer-aided simulations has profoundly changed many fields of chemical research. More recent innovations such as machine-learning and artificial intelligence are increasingly important, and are becoming widely used in many fields. This dissertation aims to demonstrate the synergism between experiments and computations. Herein, I employ computer models to predict properties of different chemical systems that are summarized graphically in Figure 1.1, and the references therein provide additional literature background.

The systems studied in this dissertation vary from simple *sp* carbon chains (Figure 1.1A) of the type $\text{H}(\text{C}\equiv\text{C})_n\text{H}$ (**I**) (section 6), to more complex platinum end-capped models that have the general formula $\text{L}_y\text{M}(\text{C}\equiv\text{C})_n\text{Z}$ ($\text{Z} = \text{SiR}_3, \text{H}$) (**II**), as well as dimetallic species of the type $\text{L}_y\text{M}(\text{C}\equiv\text{C})_n\text{ML}_y$ ($\text{M} = \text{Pt}; \text{L} = \text{Ar}, \text{PAr}_3$). The spectroscopic signatures of these carbon chains are convoluted; however, computations presented herein (second half of section 6) unambiguously determine *all* NMR spectroscopic signals of these complexes. Interestingly, the monometallic species can be coupled together to form larger molecular entities commonly termed *molecular polygons*. Specifically, molecular *tetragons* (**III**) were of interest (Figure 1.1B). These can take multiple shapes, i.e. they can be flat as in a *square* or non-planar as in *puckered*. Both these forms have been observed crystallographically. In this thesis, the interconversion of these two geometric shapes was computationally studied. The mechanism of this interconversion was determined to be analogous to the wing

movement of a butterfly (section 7) with two diagonal platinum atoms moving towards the reader and the two remaining atoms away from the reader in a concerted motion. An even more important part of the latter work showed that these molecular assemblies contain a negatively charged core, which can attract and bind to positively charged entities. This was later confirmed through crystallization experiments where the rendering species had positively charged ammonium ions binding in the center of the core and, notably, computations predicted the experimental findings in advance.

A completely different molecular array termed *molecular gyroscopes* (*trans-IV*) is also examined in this thesis (Figure 1.1C). These systems are so named due to their resemblance to macroscale objects such as a toy gyrotop. The physical properties of molecular gyroscopes follow those of their macroscale counterparts. A review of these systems is presented in section 2 and new computational studies related to these species are presented in sections 3-5. One aspect of the current work regards the interconversion of the isomers *cis-IV* and *trans-IV* ($M = \text{Pt}$; $L_y = \text{halides, alkyl and phenyl groups}$); this interconversion was observed by experimentalists at elevated temperatures. The relative stabilities of both of these forms were evaluated and the underlying reasons for the observed stability patterns were elucidated.

When the core units of two molecular gyroscopes are coupled and linked together by tethers of their backbone ligands, molecular constructs (*V*) akin to gearboxes result (Figure 1.1C). These systems are therefore termed *molecular gearboxes*. The movements of the two (possibly) rotating parts, called rotators, ML_y and $M'L_y$, can be independent or coupled, with correlations corresponding to macroscopic gears. Herein,

the steric features of these systems were evaluated using computational models. The spectroscopic features of the monometallic starting materials vs. the bimetallic iron systems, both containing Fe–(CO) groups, were very similar. Computational efforts distinguished the starting material from the products and allowed for definitive characterization with diagnostic computed IR bands (section 4).

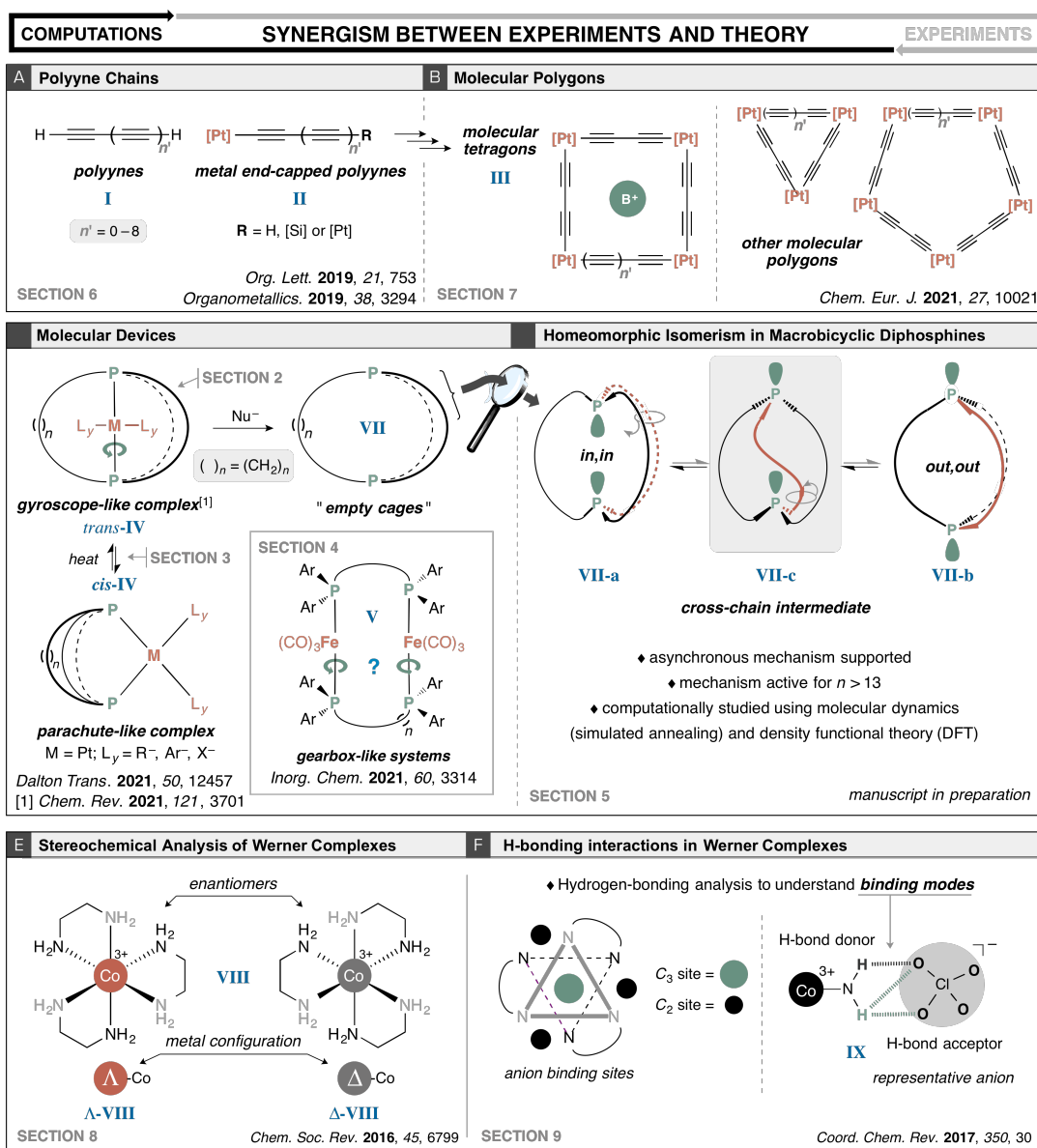


Figure 1.1 A graphical summary of the contents of this dissertation and the molecular systems studied.

The last molecular systems studied in this work are so-called "empty cages" (**VII**) (Figure 1.1C). The metallic fragment can be extruded when molecular gyroscopes containing platinum centers are treated with an appropriate nucleophile. Only the peripheral "stator" components, consisting of three methylene strands adjoined at two bridgehead atoms, remain. Prompted by unexpected experimental data, macrobicyclic cage compounds of the formula $P((CH_2)_{14})_3P$, where the phosphorous bridgeheads hold the three strands together, were investigated computationally (section 5). Early reports suggested peculiar spectroscopic patterns for these compounds; specifically, the spectra contained multiple peaks when, in principle, only one peak was expected. This phenomena was attributed to an ability of these cage compounds to turn themselves "inside out" (Figure 1.1D). In these compounds, the two phosphorous atoms at each bridgehead carry a lone pair which can face inwards (**VII-a**) or outwards (**VII-b**). Much like a T-shirt can be turned inside out, by threading one of the strand through the two remaining strands (**VII-c**) these compounds can invert to give rise to a new manifestation of *in/out isomerism*. Herein, the mechanism of this *in/out isomerism* was fully investigated and computationally observed (section 5). The specific cage sizes for which this phenomenon was predicted to occur were also established.

The last two sections (8 and 9) (Figure 1.1E,F) study a completely different chemical system: a new family of molecular catalysts featuring a stereogenic cobalt stereocenter such that two non superimposable mirror images can exist, $\Lambda, \Delta-[CoL_3]^{3+} nA^{y-}$ (**Λ -VIII**, **Δ -VIII**), where the Λ and Δ notation indicates either or a mixture of two stereoisomers. L is a 1,2-diamine, and nA^{y-} (A = anion) represents $3A^-$, A^{3-} , $A^{2-} \cdot A^{-}$,

or other higher order pairings. These Werner complexes are named after a pioneer in the field (Alfred Werner) who reported them in the early 20th century. The stereochemistry and nomenclature syntax of these novel systems are detailed in the first of these two sections (section 8) (Figure 1.1E). The second section analyzes the hydrogen bonding motifs of these cobalt cations to a host of anions nA^{y-} , and introduces a nomenclature standard for these interactions (Figure 1.1F). Highly specific and reoccurring binding modes are found in these species (**IX**). Furthermore, the ligands themselves often adopt specific conformations which can have a tremendous impact on catalysis. Unpublished work not disclosed herein applies the concepts described in these last two sections to understand a selectivity dichotomy, wherein one type of anion will generate only one form of the catalyst (Λ configuration of a diastereomer) whereas another type of anion promotes the opposite form of the catalyst (Δ configuration of a diastereomer).

"2. GYROSCOPES AND THE CHEMICAL LITERATURE, 2002–2020:
APPROACHES TO A NASCENT FAMILY OF MOLECULAR DEVICES[†]

2.1. Introduction to gyroscopes

Gyroscopes are ubiquitous in everyday life¹⁻³ although they are often kept out of view, in part due to the general desirability of shielding moving components in mechanical assemblies. Thus, they are less familiar to the public than other types of machines and devices. Nonetheless, many children have been introduced to toy mechanical gyroscopes, typical examples of which are illustrated in Figure 2.1 (panels **a** and **b**). With a little practice, these can be coaxed into a number of "tricks", such as tabletop precession or funambulism (tightrope walking). However, these phenomena do not play roles in the numerous practical applications of gyroscopes.¹⁻³

The practical applications usually involve some aspect of the orientation of an object. They include antiroll stabilizers in seagoing vessels and high speed trains, railroad track occupancy monitors, automotive safety systems, gyrocompasses in drones and airplane autopilots, space station orientation and navigational systems, virtual reality headsets and other wearable technology (e.g. relating to fitness or fall protection), wireless computer pointing devices, and the display orientation and gaming controls of mobile phones (panels **c-i**, Figure 2.1).¹⁻¹¹ Some non-everyday applications that

[†] Reproduced with permission from Ehnbohm, A.; Gladysz, J. A. Gyroscopes and the Chemical Literature, 2002-2020: Approaches to a Nascent Family of Molecular Devices. *Chem. Rev.* **2021**, *121*, 3701-3750. Copyright 2021 American Chemical Society.

underscore the broad applicability of gyroscopes include stabilizing the horizontal surfaces of pool tables¹² and Iron Man's flying suit.¹³ Furthermore, properties associated with gyroscopes are exploited in various aspects of racecar and motorcycle stabilization.^{1,14}

The useful attributes of mechanical gyroscopes derive from the conservation of angular momentum,¹⁵⁻¹⁷ and the toy version in panel **a** of Figure 2.1 provides a useful point of reference. The most critical component is the flywheel. As with many devices with rotating elements, the flywheel is typically sterically insulated with a "belt" and "spokes". However, these are not essential for function. When the rotating flywheel is tilted from the plane in which it is initially set in motion, there is a restoring force to realign the flywheel with the original plane. This can easily be felt in the wrist when so slanting a spinning toy gyroscope.



Figure 2.1 Toy mechanical gyroscopes (panels **a** and **b**) and some practical applications of gyroscopes (panels **c-i**).

There are a variety of newer designs for gyroscopes, many of which are based upon vibrating as opposed to rotating components.¹⁷⁻²¹ These can have exotic sounding names, such as "wine glass resonator" or "Coriolis vibrating" gyroscopes. Some can furthermore be designated as "microelectromechanical systems" (MEMS)²² or "quantum" gyroscopes.²³⁻²⁸ Regardless of type,²⁹ molecular analogs remain unknown. When Steve Jobs gave his roll out presentation of the iPhone gyroscope, which controls the orientation of the screen display and enables various gaming functions, an image of a

mechanical gyroscope was projected onto the screen at the rear of the stage.³⁰ However, in reality, one of the newer vibrating architectures was utilized.

Importantly, the physics of a mechanical gyroscope¹⁵⁻¹⁷ holds at a molecular level.³¹ Thus, in the ongoing quest to miniaturize devices, molecular gyroscopes would seem to be unbeatable. They also constitute a subclass of an extensive body of molecules that have been termed "molecular rotors".^{31,32} Formally, rotors are comprised of rotating and nonrotating substructures. However, motion is always a function of the frame of reference. Thus, the convention is to consider the substructure with the greater moment of inertia to be stationary and hence termed the "stator". Similarly, the substructure with the lower moment of inertia is termed the "rotator". Some stators consist of two non-bonded components that cap the termini of a rotator, and these will often be referred to as "endgroups".

2.2. Scope of review

As follows from the previous paragraph, molecular rotors are ubiquitous, with a compound as simple as ethane qualifying. Accordingly, the universe of molecules that might be able to function as gyroscopes is enormous. It is not the purpose of this review to collect all examples. Rather, the focus is on studies where the investigators have explicitly sought to access molecules or families of molecules that in their view hold promise as functional molecular gyroscopes. In most cases, these have featured sterically shielded rotators.

In an earlier review,³³ the authors sought to comprehensively cover the interface of gyroscopes and the chemical literature through 2002. This included all compounds for

which any type of link to a gyroscope was claimed. As would be expected, some were more relevant than others, and a few especially germane systems are treated again below. The coverage in the present review is also quite liberal with respect to author claims. A cutoff date of 01 July 2020 is generally applied to cited literature.

In order to help readers appreciate the basis for selecting the new literature, the next section describes, in general terms, the currently most popular approaches to achieving functional molecular gyroscopes. Additional strategies have been suggested³¹ but seem to have a greater number of practical obstacles.

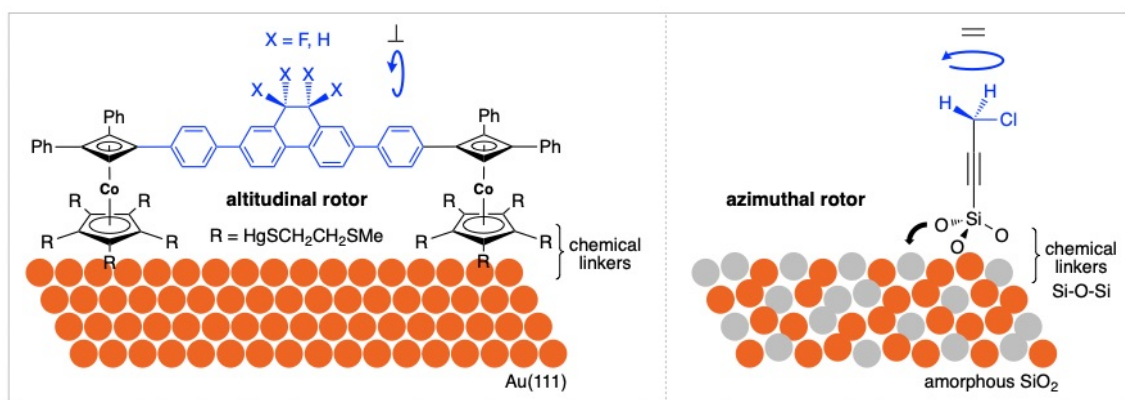


Figure 2.2 Limiting types of surface mounted rotors, illustrated with literature systems.

2.3. Strategic considerations: functional molecular gyroscopes

For a molecular rotor or a suitable ensemble or bulk sample thereof to function as a gyroscope, all rotators must rotate unidirectionally, that is, clockwise or counterclockwise, as opposed to randomly (Brownian). This generates angular momentum analogously to a macroscopic mechanical gyroscope. Thus, something that

will enforce non-Brownian rotation, akin to pulling the string on the toy gyroscope in panel **a** of Figure 2.1, is required.

The most frequently presented and easily visualized means of implementing such unidirectional rotation requires the introduction of a dipole moment on the rotator, giving what is termed a "dipolar rotator" or, considering the entire molecule, a "dipolar rotor".³¹ A static electric field can then orient the rotator. Rotors thus treated have been termed molecular compasses.³⁴⁻³⁷ Similarly, an electric field that rotates at an appropriate frequency can drive unidirectional rotation of the rotator.^{31,38-46} However, any compound with a dipolar rotator also possesses a molecular dipole. A complication in these scenarios is that the electric field may drive "whole molecule" orientation or rotation, processes that would often be of lower energy than the rotation of a rotator embedded in a stator. Although there may be ways to exploit whole molecule rotation, this would frequently be a deal-killer. Furthermore, in many types of ensembles or bulk samples the axes of the rotators would be arrayed in different directions, leading to variable degrees of interaction with an electric field.

An alternative approach would involve immobilizing the molecules in a manner that renders all rotator axes parallel and only the rotators capable of rotating. One strategy would involve mounting the rotors on a surface.^{31,38,42-51} Two limiting orientations can be envisioned, altitudinal (rotator axes parallel to the surface) and azimuthal (axes perpendicular to the surface).^{38,42,43} Several elegantly designed systems have been studied by Michl,^{31,38,39,42-46,49-51} both experimentally and computationally.

Examples are illustrated in Figure 2.2. Sykes has also published a number of relevant studies.⁵²⁻⁵⁷

However, with surfaces to which multiple altitudinal rotors have been attached, there is no a priori means of ensuring that the rotators are mutually parallel. In contrast, the rotator axes in any ensemble of rigorously azimuthal rotors must be parallel (some types of surfaces and anchoring moieties may be more amenable to this idealized orientation than others).

Since the specific rotors illustrated in Figure 2.2 are dipolar, there are opportunities for various experiments involving electric fields. Detailed molecular dynamics simulations of the response of the azimuthal rotor in Figure 2.2 to rotating electric fields have been carried out, with particular attention to the effects of field strength, frequency, and temperature.⁴⁴ The altitudinal rotor in Figure 2.2 has been studied experimentally in static electric fields and computationally in oscillating electric fields.⁴⁶ Another goal with the altitudinal system has been to drive the rotator using a flowing stream of molecules.^{38,42,43,58,59} For some of these studies, computational simulations (movies) are available.^{58,59} The electrical stimulation of surface bound rotators with STM tips has also been investigated.⁵²⁻⁵⁷

A second approach to realizing ensembles of rotors with parallel rotators would involve crystallization. Naturally, molecules can crystallize in numerous ways, and substrates would need to be engineered to yield lattices not only with parallel axes, but also with voids or other features that allow the rotator to rotate with a minimal energy barrier. Both intra- and intermolecular van der Waals contacts must be avoided or

minimized. Cage-like superstructures or scaffolding would be one approach to enforcing voids.

Crystals in which components or subunits of the molecules can rotate are said to be amphidynamic, a term coined by Garcia-Garibay.³⁴⁻³⁷ Although some luck is involved in any effort to tailor a crystal lattice, there have been some notable successes in the direction of molecular gyroscopes, as described below. Furthermore, there is an ever growing body of MOFs and related species that offer geometrically well defined scaffolding for rotators and often feature large void spaces,^{60,61} as detailed below. Porous materials can also be exploited as hosts for dipolar rotors, as illustrated in section 2.9.3.

Some other design considerations merit emphasis. For example, nonionic compounds are preferred. Any counterions can electrostatically interact with dipolar rotators as they rotate. The resulting attractive and repulsive domains can lead to increased rotational barriers. Also, any structural or electronic modification that can lower the rotational barrier, sometimes spoken of as "intramolecular friction", is desirable. For example, if the rotating electric field were disengaged, the rotators of systems with lower barriers would continue their unidirectional trajectories for longer periods of time. Indeed, rotors that are essentially barrierless are being increasingly documented,⁶² as further exemplified in section 2.8.3 below.

An additional consideration is the means by which electric fields can be applied to samples. To the authors' knowledge, there is no "off the shelf" instrumentation capable of delivering a rotating electric field, although experimental protocols have been

described.³¹ However, there is an established technique, dielectric spectroscopy, that delivers an oscillating electric field, that is, one that "flips" back and forth by 180°. ⁶³⁻⁶⁵ This instrumentation is commercially available and has numerous applications, although it is not very familiar to chemists and the review literature is geriatric. ⁶³⁻⁶⁵ Typically, the change in capacitance, which is a function of the molecular dipoles in the bulk sample, is measured. The resonance frequency that would be established for dipole oscillation would be correlated to the rotational frequency of an electric field necessary to drive unidirectional rotation.

Functional molecular gyroscopes would be characterized by a number of testable properties. Probably the most intuitive are associated with the conservation of angular momentum. Thus, with respect to the "flywheel" component, if this plane were to be tilted, a measurable force would be required. Similarly, there would be a comparable driving force for restoring the original orientation of the flywheel plane.

2.4. Selected background molecules

2.4.1. Molecular turnstiles

Of the types of molecules treated in the previous review,³³ one class deserves emphasis. Specifically, compound **1** in Figure 2.3, which was synthesized by Moore,⁶⁶ represents what is often termed a "molecular turnstile". These are now being exploited in various contexts by a vigorous community of researchers,⁶⁷⁻⁸⁶ of which the Hosseini group is the most prolific.⁷³⁻⁸⁶

Definitions of molecular turnstiles have been given in several papers.^{71,72,77,82,83,85,86} These can, in the context of this review, be paraphrased as "molecular rotors that exhibit bistability in the sense of the rotator being able to adopt what can be viewed as open and closed states". In the most common motif, exemplified by **1** and **2** in Figure 2.3, both the stator and rotator are roughly planar or two-dimensional.^{66,67} The turnstile is "open" when these planes are perpendicular, and "closed" when they are parallel or nearly so. There are also a fair number of what might be termed "half turnstiles", as illustrated by **3** in Figure 2.3.⁶⁹⁻⁷¹ The rotators in these systems are not entirely circumnavigated by the stators but can still be perpendicular or parallel with respect to the plane of the stator.

In another variant, the stator or rotator becomes complete only when an "effector" is added. For example, **3** is prepared by combining the palladium(II) effector $(\text{MeCN})_2\text{PdCl}_2$ with the free bis(alkynylpyridine) ligand.⁷⁰ In a more complex variant, **4** can be viewed as a half turnstile with a 4-pyridyl-C \equiv C-Pt-C \equiv C-4-pyridyl rotator and a P-Pt-P axis.⁸¹ When the appropriate palladium species is added, **5** results. This can be viewed as a "full" turnstile with a 4-pyridyl rotator and a Pt-C \equiv C-4-pyridyl-Pt axis, and now with the P-Pt-P axis "locked down".

In these efforts, there have not to the authors' knowledge been any connections to the molecular gyroscope literature, although there is one study that involves the interaction of a dipolar rotator with an electric field.⁷² An issue would be the lack of "steric protection" for the rotator when it is in the "open" position, with the plane

perpendicular to that of the stator. Thus, molecular turnstiles are not included in the sections below detailing the main avenues of approach to molecular gyroscopes. However, there are probably ways to engineer sterically more protected systems, for example, by introducing appropriately bulky R' groups in **1** (Figure 2.3), so this class of molecules merits consideration for future research.

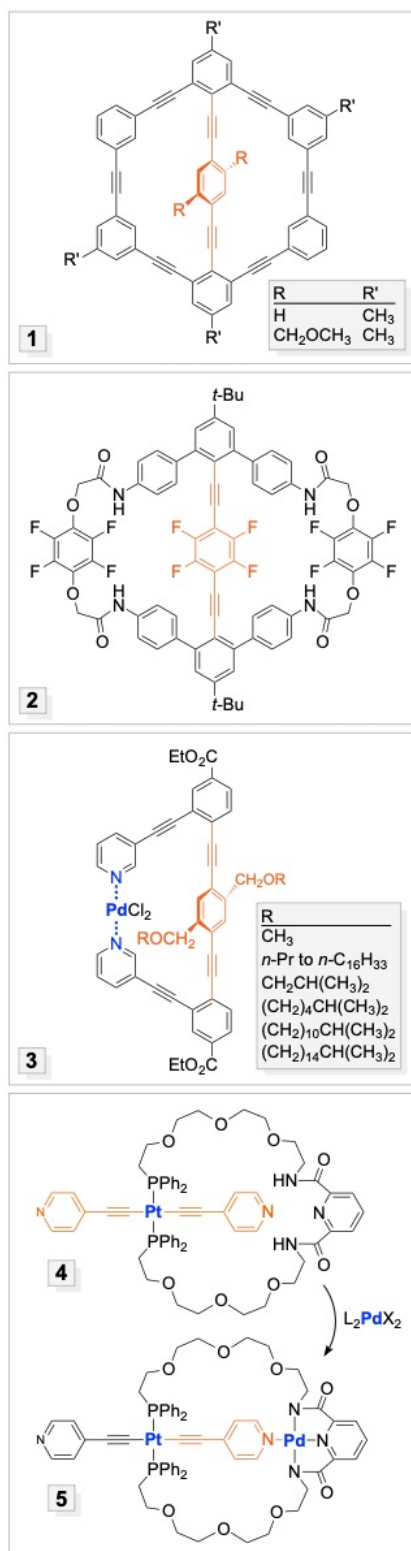


Figure 2.3 Representative compounds that have been described as molecular turnstiles.

2.4.2. Species with N-ML₂-N rotators where N denotes a disubstituted pyridine ligand

An important compound topologically related to the preceding turnstile systems was reported in 1999 by Lambert,⁸⁷ who left academia shortly thereafter. He first prepared the *trans* palladium bis(pyridine) complex **6** shown in Figure 2.4 (top), in which the 2 and 6 pyridine positions (adjacent to the nitrogen atom) feature alkene containing CH₂CH₂CH=CH₂ substituents. This complex underwent two-fold *interligand* ring closing olefin metathesis with Grubbs' first generation catalyst to yield what could be termed a pyridinophane adduct (**7**). Such ring closing metatheses commonly give *cis/trans* C=C mixtures, but the *cis,cis* isomer crystallized, and an X-ray structure could be obtained.

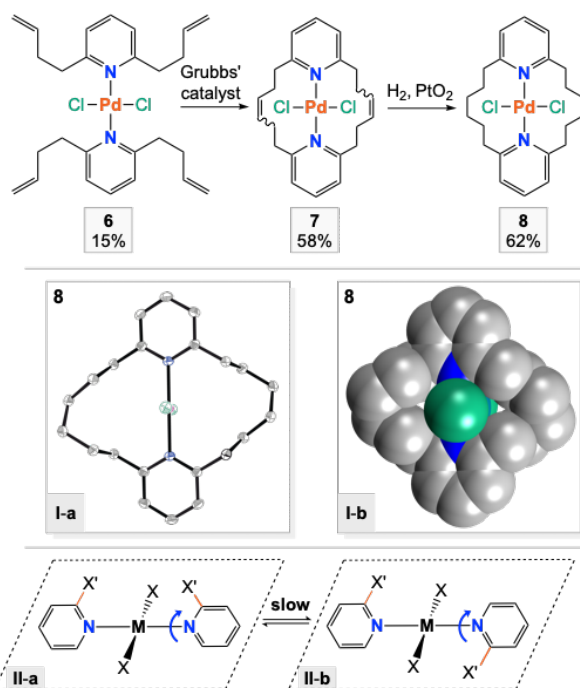


Figure 2.4 Ring closing metathesis reaction that connects 2,6-disubstituted *trans*-pyridine ligands (top), ORTEP and space filling representations of the hydrogenation product **8** (middle), and atropisomers arising from restricted pyr–M–pyr rotation in related square planar systems (bottom).^{87,88}

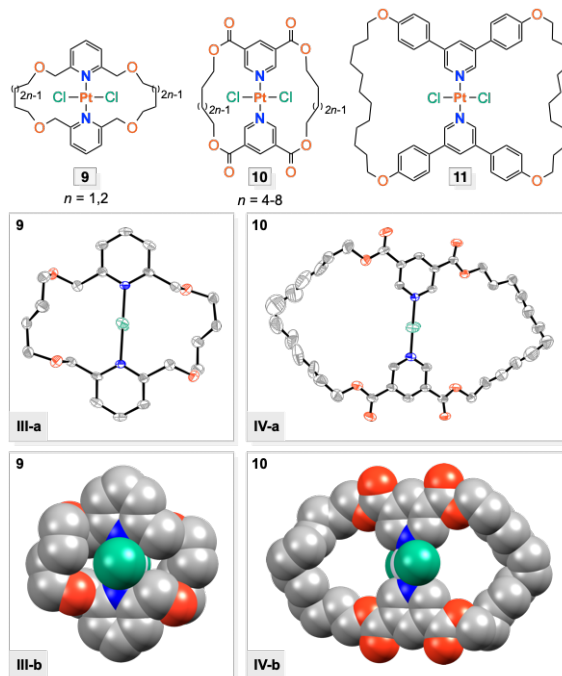


Figure 2.5 Additional complexes with substituted *trans*-bis(pyridine) ligands prepared by the route in Figure 2.4 (**9-11**),⁸⁸ and ORTEP and space filling representations of **9** and **10**.

In subsequent efforts in the authors' laboratory,⁸⁸ **7** was hydrogenated to give **8**. The crystal structure is shown in Figure 2.4 (**I-a**). As can best be appreciated from space filling models (**I-b**),⁸⁸ any 2,6-pyridine substituents effectively block PdCl₂ rotation. This is reflected by the perpendicular orientation of the Cl–Pd–Cl vector with respect to the pyridine ligand planes in crystalline **8** (as well as **6** and *cis,cis-7*; not depicted). Accordingly, atropisomers have been observed for a number of square planar complexes featuring two *trans*-2-monosubstituted pyridine ligands (Figure 2.4, bottom).^{89,90}

In follow up efforts, the authors similarly prepared the dichloroplatinum pyridinophane complexes **9-11** shown in Figure 2.5.⁸⁸ In particular, **10** and **11** were viewed as attractive families of molecular rotors, as replacing 2,6-substituents by 3,5-substituents should allow PtCl₂ rotation. Thus, they represent functional molecular turnstiles. Also, the introduction of appropriate substituents at the 4 position ("para" to nitrogen) could enable surface mounting with an azimuthal rotator orientation. However, for several reasons, such as the absence of three-dimensional shielding of the rotator by the stator, these systems were not further pursued.

2.4.3. Other stators in which two bridges connect the termini of the rotator

With most of the compounds in Figure 2.3, Figure 2.4, and Figure 2.5, the axes of the rotators terminate with *sp*² hybridized carbon or nitrogen atoms. This leaves two atoms or substituents for architectural purposes — i.e. creating the two bridges ("spokes") that comprise the stator connecting the termini of the rotator.

One can also consider the generation of two bridges between atoms that bear three substituents, which would generally have tetrahedral or (for heteroatoms with a lone pair substituent) trigonal pyramidal geometries (approximate sp^3 hybridization). Such systems have in fact been crafted, as summarized in Figure 2.6 and Figure 2.7.⁹¹⁻⁹⁶ In some cases, the syntheses were carried out as intermediate feasibility studies⁹¹ associated with the preparation of analogs with three bridges connecting the rotator termini (treated in following sections). Compounds **15** and **16**, in which the rotators, substituted *p*-phenylenes, lack a transition metal (Figure 2.7), were synthesized by the Setaka group.^{95,96}

Note that these syntheses are capable of giving two isomeric products, as generalized in the bottom panel of Figure 2.6. In one, the positions of the non-bridging substituents (or lone pairs) on opposite termini are antiperiplanar, and in the other, they are synperiplanar. Usually the latter dominates, and rationales have been proposed.⁹¹⁻⁹³ Although the resulting rotors have a lower degree of planarity than those in Figure 2.3, Figure 2.4, and Figure 2.5, they still do not effectively shield the rotators in a three-dimensional sense. Hence, the authors have never applied the term "gyroscope like" to these systems in their own writings.

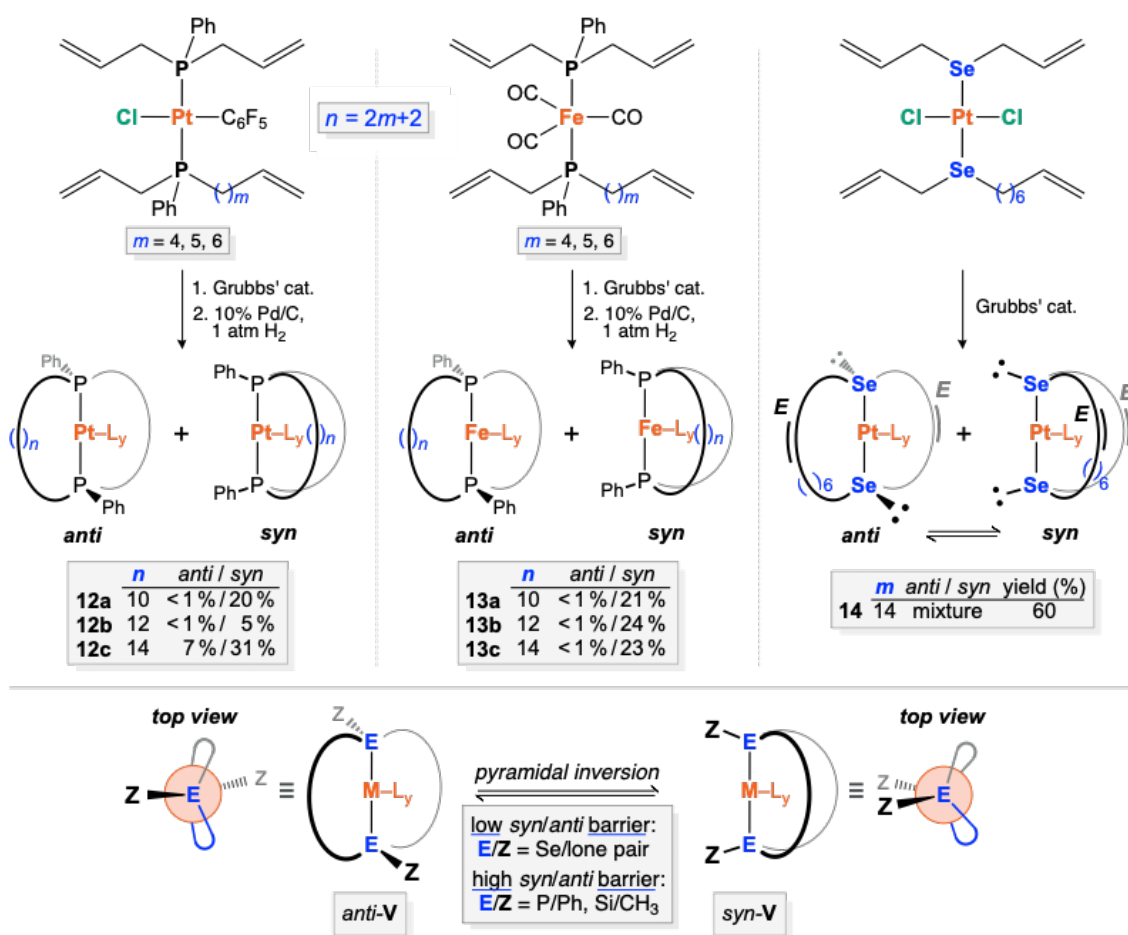


Figure 2.6 Molecular rotors in which the rotators terminate in tetrahedral or trigonal pyramidal atoms and the stators feature two connecting bridges.⁹¹⁻⁹⁴

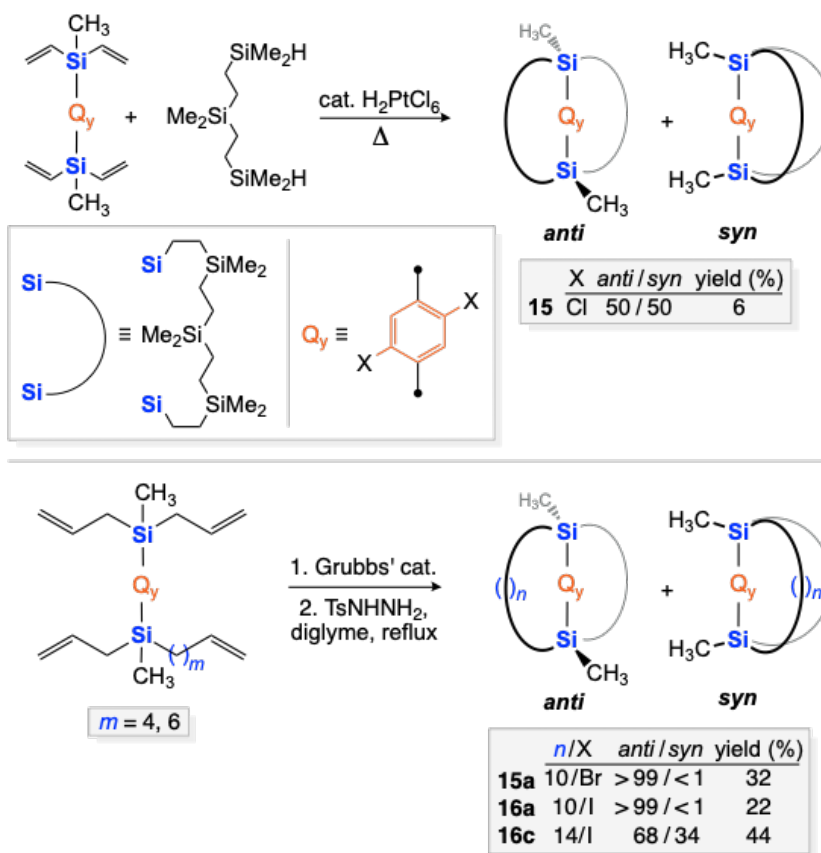


Figure 2.7 Additional molecular rotors in which the arylene rotators (denoted Q_y) terminate in tetrahedral atoms and the stators feature two connecting bridges.^{95,96}

2.5. Summary of coverage

In the following three sections, results from the major groups pursuing candidates for molecular gyroscopes are presented in turn. A fourth section collects relevant systems from other laboratories. In each case, the text progresses from simpler to more complex structures. At the same time, attempts are made to highlight phenomena common to substrates that do not hold adjacent positions in this hierarchy.

Coverage begins with studies from the authors' laboratory.⁹⁷⁻¹¹³ All of the underlying syntheses involve olefin metatheses, as first communicated in 2004.⁹⁷ These

were preceded by investigations of other modes of olefin metathesis in metal coordination spheres.¹¹⁴⁻¹¹⁹ A more detailed description of the chemical phenomena associated with this work will be provided in a later review.¹²⁰ Also, the broader topic of multifold ring closing metatheses in metal coordination spheres has been separately reviewed.¹²¹

Efforts from the Setaka laboratory are then treated.¹²² This group has also made extensive use of olefin metathesis in their syntheses,¹²²⁻¹³⁸ but has employed other macrocyclizations as well (e.g. Figure 2.7, top).^{94,139-141} Attention is then turned to the Garcia-Garibay laboratory.³⁴⁻³⁷ This ordering does not do justice to the intellectual and experimental leadership that has distinguished this group. However, it was felt that the data could best be highlighted and analyzed in this position. As noted above, systems where other researchers have attempted connections to molecular gyroscopes are presented in a subsequent section.

Finally, mention should be made of the Michl group, which has had a marked influence upon the field of molecular rotors.³¹ In addition to the surface mounted systems described above (Figure 2.2), Michl (sometimes in collaborations) has studied a wide variety of dipolar rotors in numerous contexts. However, none of these studies have targeted molecular gyroscopes *per se*. As a result, descriptions of relevant studies are dispersed throughout the text.

2.6. Systems from the Gladysz group

2.6.1. Syntheses involving olefin metathesis

The signature reaction sequence of the authors' group is depicted in Figure 2.8 (top). The starting materials are usually metal complexes with two alkene containing *trans* phosphine ligands of the formula $P((CH_2)_mCH=CH_2)_3$ (see **VI**).¹⁰³ Analogous arsine and stibine adducts can also be employed. Then three-fold intramolecular and interligand ring closing olefin metatheses are carried out, most commonly with Grubbs' first generation catalyst. To avoid dealing with mixtures of *cis/trans* C=C isomers, these are followed by hydrogenations to give the cage-like products **VII**.

To minimize side reactions, spectator ligands in the equatorial plane of the substrates must be "small", meaning monatomic and linear diatomic species such as halides, CN, and CO. High overall yields of products have been obtained with trigonal bipyramidal (**VII-a**, Figure 2.8), square planar (**VII-b**), and octahedral coordination geometries (**VII-c**). The number of methylene groups in the chains connecting the *trans* phosphorus atoms, n , is related to the number of methylene groups in each substituent of the phosphine ligand, m , by the equation $n = 2m + 2$. The authors commonly refer to such complexes as "gyroscope-like". The conservative phrasing reflects that functional molecular gyroscopes have yet to be realized.

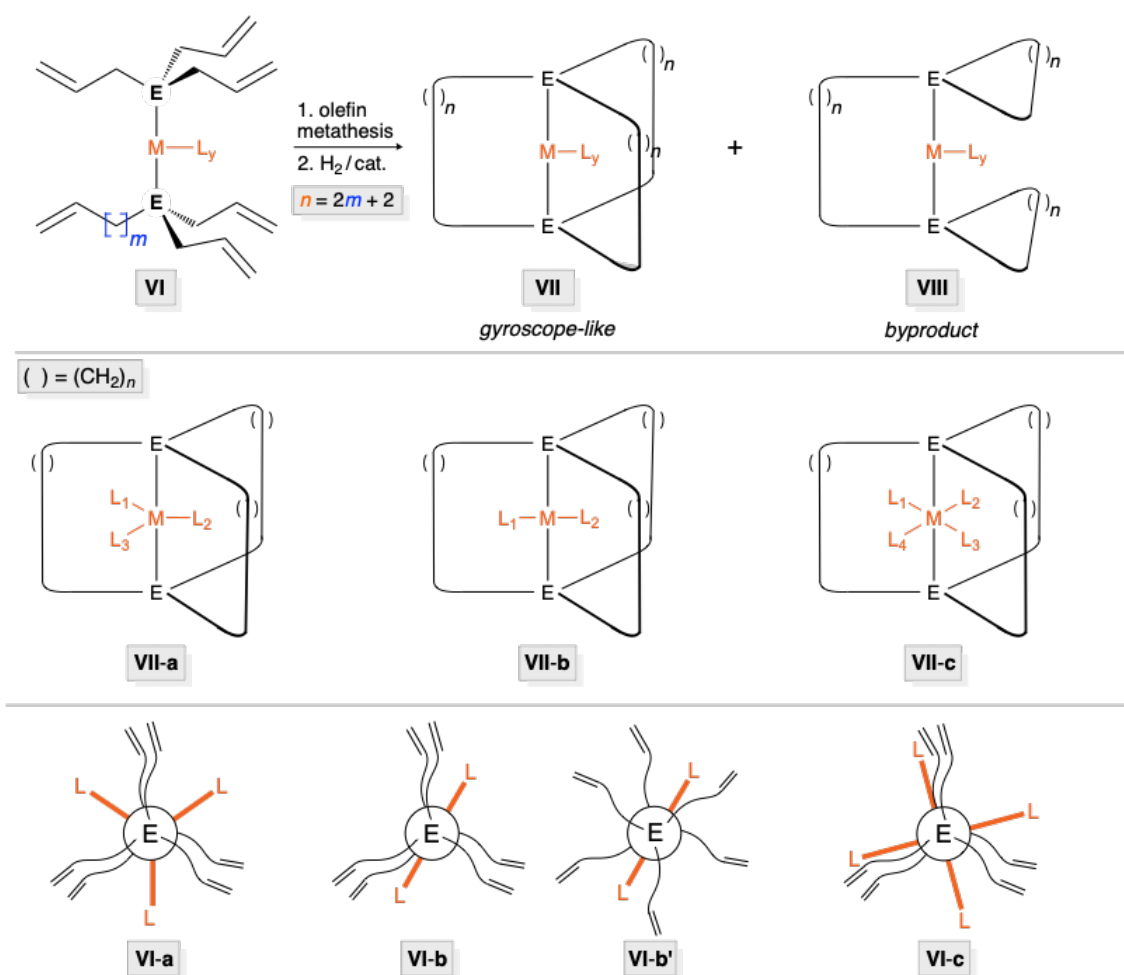


Figure 2.8 Three-fold intramolecular ring closing olefin metatheses involving *trans* heteroatom donor ligands $\text{E}(\text{CH}_2)_m\text{CH}=\text{CH}_2$ (top; E usually =P), applications to different metal coordination geometries (middle), and relevant reactant conformations (bottom).

The alternative monometallic products in Figure 2.8, **VIII**, are derived from mixtures of interligand and intraligand ring closing metatheses. While such species are sometimes observed with square planar and octahedral coordination geometries, they are seldom the major product. Any other byproducts are presumed to be oligomers or polymers. In the case of square planar products, authentic samples of some *cis* isomers have been synthesized.^{112,113} However, in all systems studied to date, *cis/trans*

isomerization only takes place at elevated temperatures, with the *trans* isomers being more stable.^{112,113} Thus, it is believed that *cis/trans* isomerization plays no role in any of the phenomena described below.

The sequence in Figure 2.8 will first be analyzed as a function of coordination geometry. In subsequent sections, ligand substitution, addition, and elimination reactions will be examined. The last two increase and decrease the coordination numbers, respectively. Thus, there is more than one pathway to any given coordination geometry.

To date, the only phosphine based trigonal bipyramidal complexes accessed via the sequence in Figure 2.8 (**VII-a**, E = P) are the Fe(CO)₃ adducts **17** shown in Figure 2.9.¹⁰⁶ The overall yields (47-64%) are higher than those obtained with square planar or octahedral substrates (*vide infra*). In fact, **17a** and **17b** are the only complexes so far accessed with shorter (CH₂)₁₀ and (CH₂)₁₂ connecting bridges. The enhanced yields may be due to unique conformational properties of the reactants. By analogy to the energy minima of ethane or other species with C_{sp3}-C_{sp3} linkages, the three olefinic phosphine substituents should stagger with respect to the three iron-carbon bonds of the Fe(CO)₃ fragment, as shown in **VI-a** in Figure 2.8. This P-Fe-P conformation "preorganizes" the CH=CH₂ groups that are required to undergo ring closing metathesis.

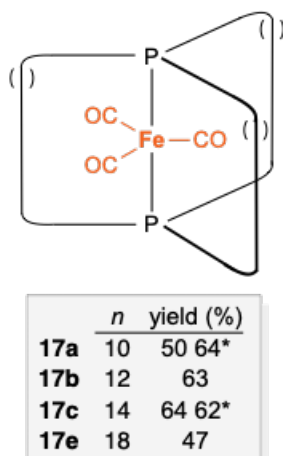


Figure 2.9 Trigonal bipyramidal $\text{Fe}(\text{CO})_3$ complexes prepared according to Figure 2.8. An asterisk indicates a yield obtained with Grubbs' second generation catalyst $[(\text{CH}_2)_n]^{106}$.

Crystal structures provide visual clues as to how these systems would behave as molecular rotors. Two representations of the complex with three $(\text{CH}_2)_{14}$ bridges (**17c**) are shown in Figure 2.10 (**IX-a,b**). Counting the P–Fe–P linkages, this makes for three 17-membered macrocycles. It is a simple matter to calculate the van der Waals radius of $\text{Fe}(\text{CO})_3$ as well as other ML_y rotators (see section 2.6.6). The macrocycles indeed offer sufficient lateral or horizontal "clearance" for $\text{Fe}(\text{CO})_3$ rotation, although top/bottom or vertical interactions are tighter.

In contrast, the opposite conclusion is easily reached when viewing the crystal structure of a related complex with three 10-carbon bridges (**X-a,b** in Figure 2.10; 13-membered macrocycles). Actually, this structure is that of the precursor to **17a** prior to hydrogenation, with three *E*- $(\text{CH}_2)_4\text{CH}=\text{CH}(\text{CH}_2)_4$ bridges. In any case, the $\text{Fe}(\text{CO})_3$ rotator is clearly held in a "straight jacket" that only allows a back and forth oscillation

over a few degrees. Phosphite analogs of **17** have been synthesized, but these were obtained as oils and could not be rigorously purified.¹⁰²

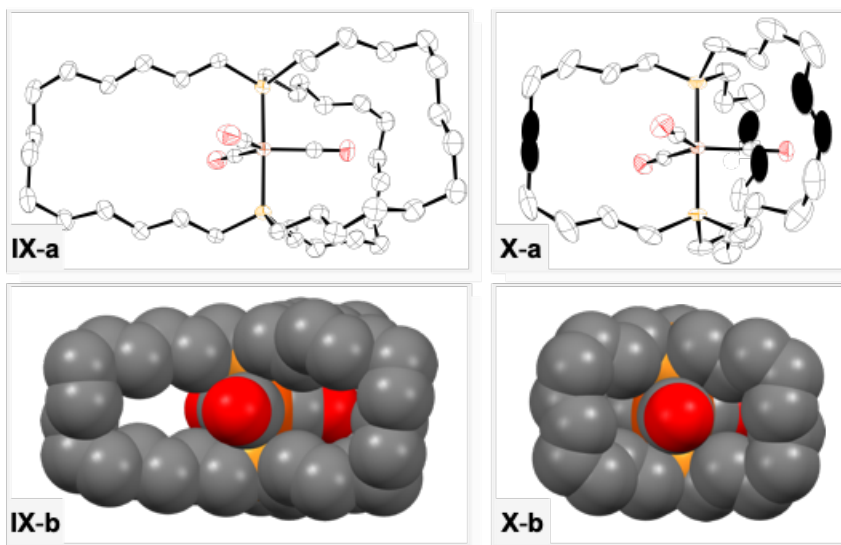


Figure 2.10 Thermal ellipsoid and space filling representations of complexes from Figure 2.9 or close relatives thereof (left, **17c**; right, *E,E,E*-tris(olefinic) precursor of **17a** with C=C linkages darkened).¹⁰⁶

Analogous sequences can be carried out with square planar *trans*-phosphine adducts of PtCl₂, PdCl₂, and Rh(CO)Cl.^{98,100,104,112} The resulting products are shown in Figure 2.11. In these cases, the reactants lack P–M–P conformations that "preorganize" the CH=CH₂ groups as in **VI-a** in Figure 2.8. Although **VI-b** depicts a conformation that is favorable for the desired three-fold ring closing metathesis, an alternative in which one P–M bond is rotated by 180° (**VI-b'**) would have approximately the same energy and a greater propensity for side reactions. In any case, the overall yields are diminished relative to those for the trigonal bipyramidal complexes, and phosphine ligands P((CH₂)_mCH=CH₂)₃ with *m* ≥ 6 (corresponding to *n* ≥ 14) are

required. Otherwise only oligomeric and polymeric products are obtained. A crystal structure of the PtCl₂ complex with $n = 14$ (**18c**) is shown in Figure 2.12 (**XI-a,b**). This molecule features the same macrocycle size (17-membered) as **17c** in Figure 2.10.

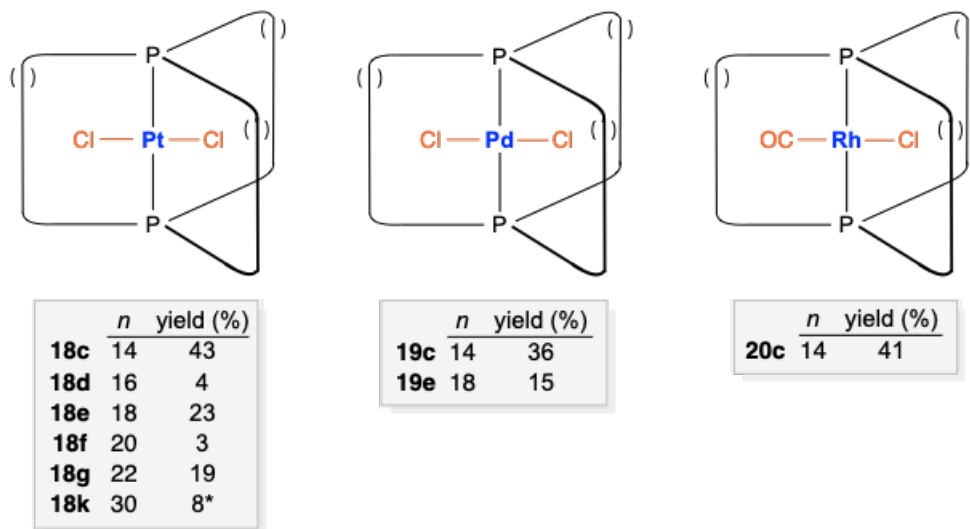


Figure 2.11 Square planar complexes prepared according to Figure 2.8. An asterisk indicates a yield obtained with the second generation Hoveyda-Grubbs catalyst [() indicates (CH₂)_n].^{98,100,104,112}

So far no upper bound on m has been reached with the square planar precursors. Phosphine adducts of PtCl₂ with $m = 10$ and 14 have been successfully employed, leading to complexes with $n = 22$ (**18g**) and 30 (**18k**), or 25- and 33-membered macrocycles. The crystal structure of the former is depicted in Figure 2.12 (**XII-a,b**). This represents the complex with the longest (CH₂)_n bridges that has been structurally characterized to date.

The Rh(CO)Cl adduct **20c** in Figure 2.11 constitutes the first complex in this section with a dipolar rotator. This sequence has been extended to precursors with *trans*-

triarylphosphine ligands of the formula $P(p\text{-C}_6\text{H}_4\text{O}(\text{CH}_2)_m\text{CH}=\text{CH}_2)_3$.⁹⁹ The complexes **21b,c** in Figure 2.13 (top), which feature 25- and 27-membered macrocycles, can be isolated in 41-26% overall yields. The crystal structures of both have been determined, and the latter is depicted in Figure 2.13. The interior of the cage-like stator is clearly much more spacious than in the aliphatic systems (*cf.* **XIII-b** vs. **XI-b**), although in the solid state neighboring molecules interdigitate as treated in greater detail below.

To the authors' initial surprise, it also proved possible to conduct analogous olefin metatheses with octahedral complexes, as reflected by the rhenium and osmium adducts in Figure 2.14.^{110,111} This requires the six $(\text{CH}_2)_m\text{CH}=\text{CH}_2$ groups to "wrap" around an equatorial coordination plane that contains four ligands. Again, m must be at least 6, but substrates with $m \geq 9$ have not yet been studied. Since the yields of byproducts of the type **VIII** in Figure 2.8 are often comparable (and in a few cases higher), both are tabulated in Figure 2.14. A crystal structure of a representative complex with $n = 14$ (**22c**) is provided in Figure 2.15.

Finally, the iron tricarbonyl diphosphine systems in Figure 2.9 have been extended to the diarsine complexes **26a-c** in Figure 2.16.¹⁰⁷ The overall yields are slightly lower. X-ray diffraction shows the adduct with $n = 14$ to be isostructural with the diphosphine homolog in Figure 2.10. The volume of the unit cell is only 0.7% greater, but the iron–heteroatom bonds are 4.0% longer, which will have consequences as seen below.

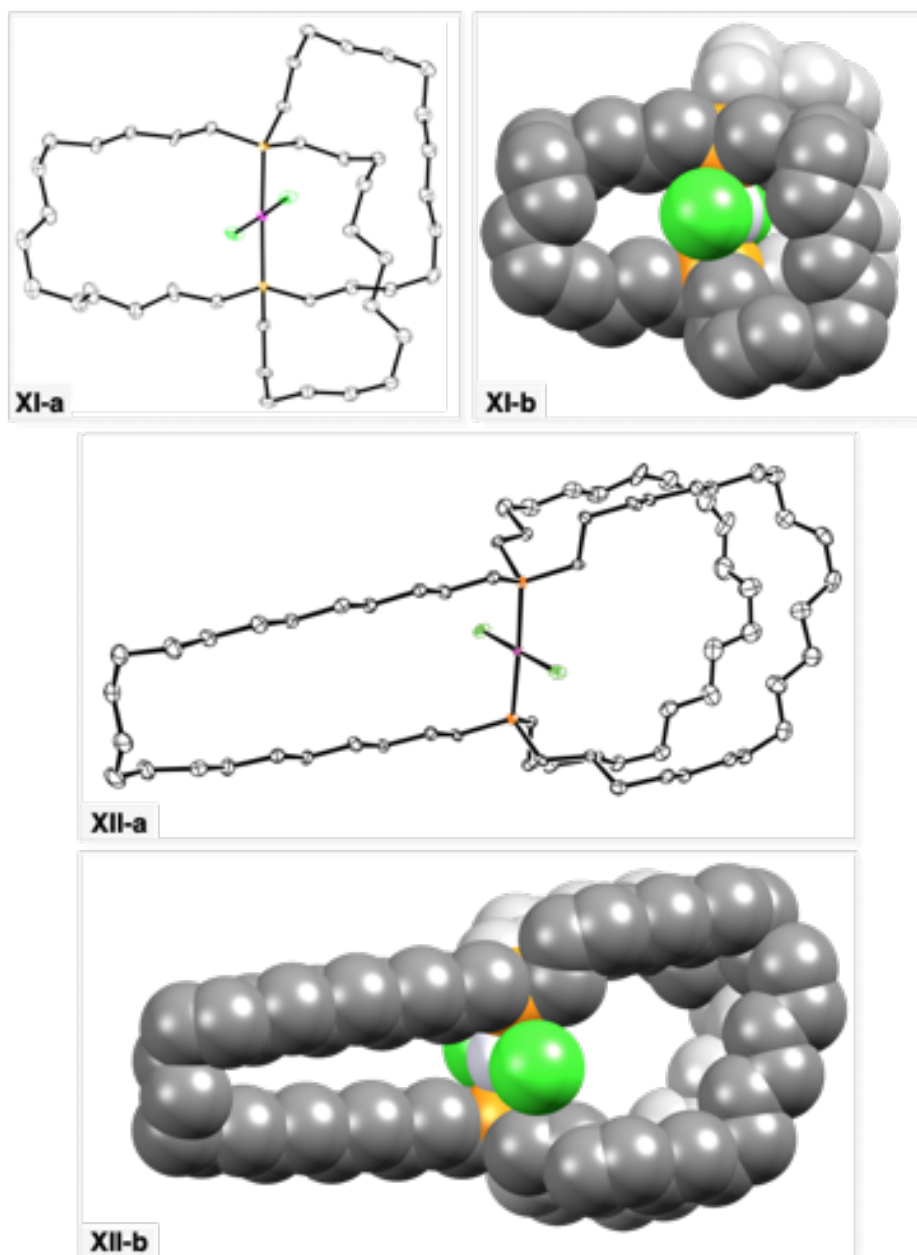


Figure 2.12 Thermal ellipsoid and space filling representations of the PtCl₂ complexes **18c** (top) and **18g** (bottom) from Figure 2.11.^{104,112}

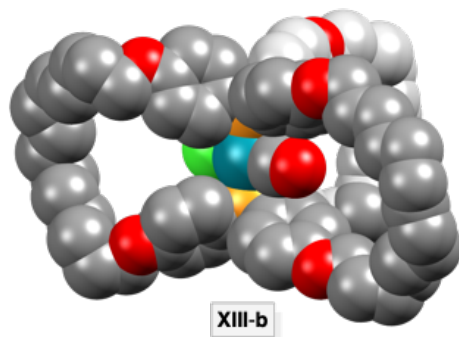
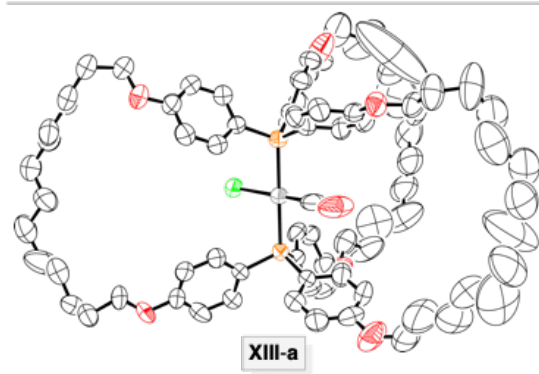
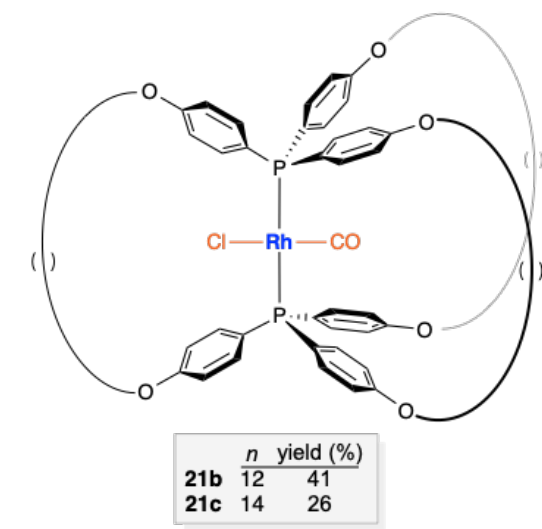


Figure 2.13 Square planar complexes prepared according to Figure 2.8. An asterisk indicates a yield obtained with the second generation Hoveyda-Grubbs catalyst [(O indicates $(\text{CH}_2)_n$].^{98,100,104,112}

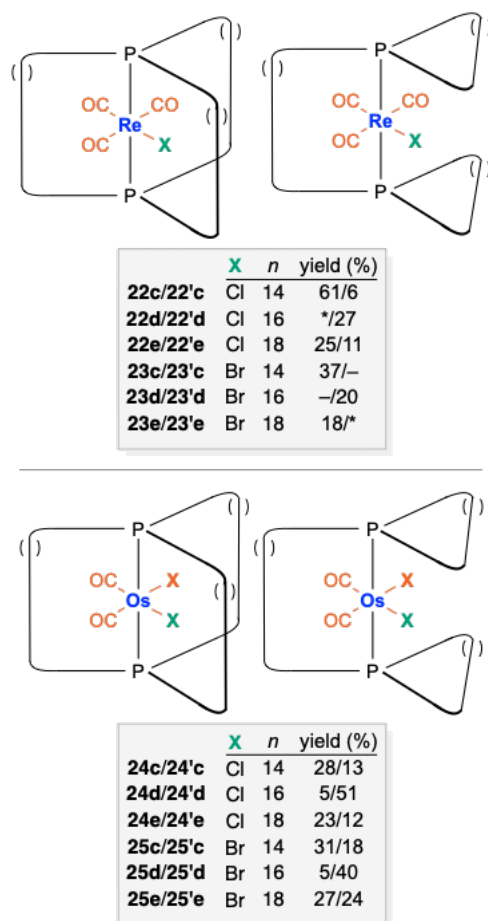


Figure 2.14 Octahedral complexes prepared according to Figure 2.8. An asterisk indicates that traces of the product were detected by NMR [() indicates $(\text{CH}_2)_n$].^{110,111}

2.6.2. Reactions that alter the coordination number

The metathesis/hydrogenation sequences in the previous section provide only a fraction of the molecular rotors of interest to the authors' group. Importantly, they can be elaborated to a variety of other rotors, some of which are viewed as particularly attractive candidates for molecular gyroscopes. Addition and elimination reactions that alter the coordination numbers of the complexes are treated in this section. Substitution

reactions that modify the rotators but retain the coordination numbers are summarized in the following section.

As shown in Figure 2.17 (top), the octahedral osmium(II) dicarbonyl dichloride ($\text{Os}(\text{CO})_2\text{Cl}_2$) complex **24c** prepared in Figure 2.14 can be reduced with potassium graphite under a CO atmosphere to give the trigonal bipyramidal osmium(0) tricarbonyl ($\text{Os}(\text{CO})_3$) complex **27c**.¹¹⁰ The corresponding dibromide complex, as well as higher homologs, reacts similarly. X-ray diffraction establishes that this complex is isostructural with the iron analog depicted in Figure 2.10. As would be expected from the longer osmium–phosphorus versus iron–phosphorus bond (Os–P 2.3626(6) Å, Fe–P 2.2056(5) Å), the unit cell volume is slightly larger (4693.71(16) vs. 4633.5(3) Å³, or 1.3%). However, it cannot (yet) be analogously synthesized, as the authors have never been able to access the necessary precursor *trans*- $\text{Os}(\text{CO})_3(\text{P}((\text{CH}_2)_6\text{CH}=\text{CH}_2)_3)_2$.

Trigonal bipyramidal complexes can also be generated by additions to square planar species. Several bis(phosphine) rhodium(I) carbonyl iodide complexes, *trans*- $\text{Rh}(\text{CO})\text{I}(\text{PR}_3)_2$, have been noted to (reversibly) add a second carbonyl ligand to give *trans*- $\text{Rh}(\text{CO})_2\text{I}(\text{PR}_3)_2$.^{142,143} As shown in Figure 2.17 (bottom), the gyroscope-like carbonyl iodide complex **28c** can be generated by a chloride ligand substitution of **20c**.¹⁰⁰ When **28c** is treated with CO (1 atm), the trigonal bipyramidal dicarbonyl addition product **29c** is quantitatively generated. It was possible to crystallize **29c**, but the CO addition is readily reversed under a nitrogen stream.

Reactions that convert square planar d^8 complexes to octahedral d^6 complexes are ubiquitous. Thus, as shown in Figure 2.18 (top), the rhodium carbonyl chloride complex and CBrCl_3 combine to give the rhodium(III) oxidative addition product **30c**.¹⁰⁰ In unpublished work, several platinum(IV) adducts have been synthesized and crystallographically characterized.

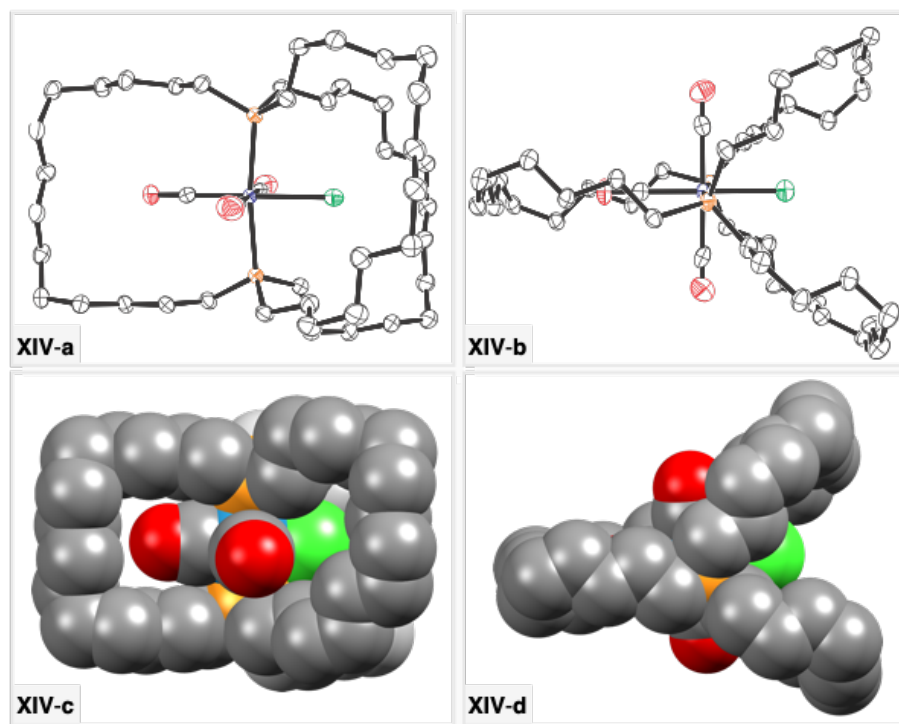
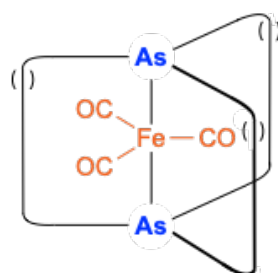
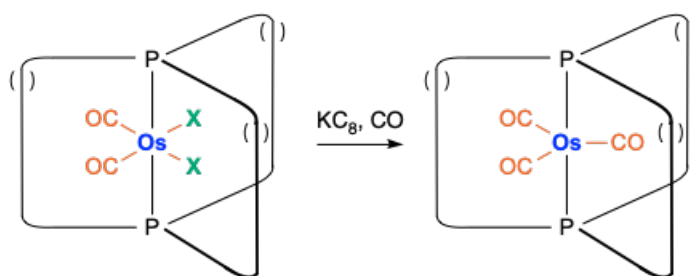


Figure 2.15 Thermal ellipsoid and space filling representations of **22c** from Figure 2.14 with the P–Re–P axis in (left) and perpendicular to (right) the plane of the image.¹¹¹



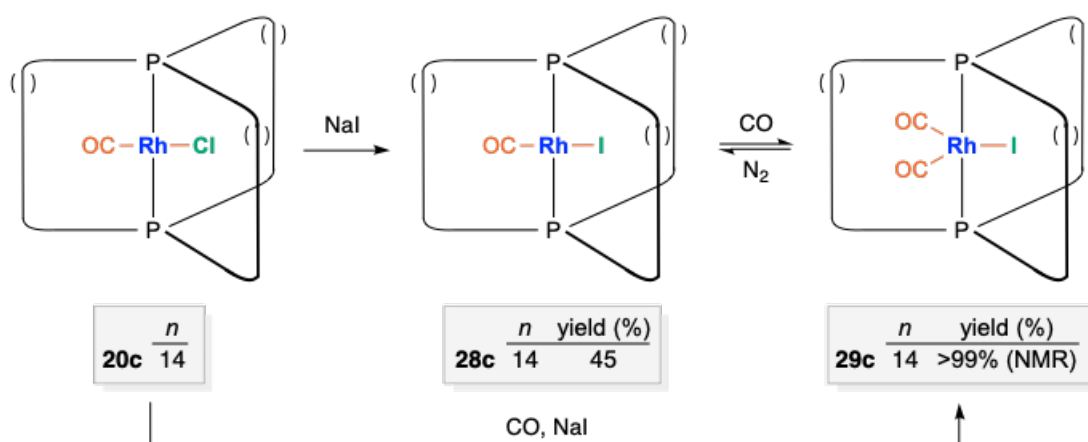
	<i>n</i>	yield (%)
26a	10	41
26b	12	54
26c	14	59

Figure 2.16 Trigonal bipyramidal $\text{Fe}(\text{CO})_3$ complexes prepared according to Figure 2.8, but with arsenic in place of phosphorus [() indicates $(\text{CH}_2)_n$].¹⁰⁷



	X	<i>n</i>
24c	Cl	14
25c	Br	14
25e	Br	18

	<i>n</i>	yield (%)
27c	14	87
27c	14	82
27e	18	79



	<i>n</i>
20c	14

	<i>n</i>	yield (%)
28c	14	45

	<i>n</i>	yield (%)
29c	14	>99% (NMR)

Figure 2.17 Syntheses of trigonal bipyramidal complexes from precursors with different coordination geometries [() indicates $(\text{CH}_2)_n$].^{100,110}

Some protonation reactions that convert trigonal bipyramidal complexes described above to cationic octahedral complexes have been reported. For example, the iron and osmium $M(\text{CO})_3$ species shown in Figure 2.18 (bottom) have been treated with the strong acids $\text{CF}_3\text{SO}_3\text{H}$ and/or $[\text{H}(\text{OEt}_2)]^+\text{BARf}^-$.^{106,110} The corresponding iron or osmium hydride salts $\mathbf{31}^+\text{X}^-$ are obtained in high yields.

2.6.3. Substitution reactions

2.6.3.1. Replacements of chloride ligands

The syntheses described above afford a variety of square planar and octahedral chloride complexes. This has helped to develop a rich substitution chemistry that will be fully described in a future review.¹²⁰ There are also tantalizing mechanistic questions. For example, how can such displacement reactions occur within the confines of the stator cages?

The chloride ligands can be replaced by a variety of halide and pseudohalide nucleophiles such as Br^- , I^- , CN^- , and NCS^- (Figure 2.19).^{98,100,104,111} Both linkage isomers have been obtained with NCS^- . It has never been problematic to use aryl (e.g. ZnPh_2)^{98,104,105,110,111} or alkynyl ($\text{MC}\equiv\text{CR}$)^{99,100} nucleophiles. In contrast, methyl groups are easily introduced in some systems^{105,110,111} but this requires extensive optimization in others. Complexes with hydride ligands have not yet been generated, but a rhodium $\text{H-BH}_2\text{-H}$ chelate derived from NaBH_4 has been isolated ($\mathbf{33c}$, Figure 2.19).¹⁰⁵ A few substitution reactions of analogous bromide complexes have been reported,^{104,111} but they are much less developed.

With dichloride complexes such as the PtCl₂ species **18** in Figure 2.11, there is interest in monosubstitution reactions. These would yield dipolar rotators. To date, all efforts in the authors laboratory have yielded difficultly separable mixtures of products. Part of the problem is that the rate constant for the first substitution often appears to be similar to the second. However, alternative routes can sometimes be developed. For example, Figure 2.20 shows an initial disubstitution of the chloride ligands in **18c,e** by phenyl ligands.¹⁰⁴ When the diphenyl complexes **34c,e** are then treated with HCl, the phenyl chloride complexes **35c,e** can be isolated in 93-98% yields.¹⁰⁹ Presumably, the introduction of the first electron withdrawing chloride ligand diminishes the rate of further electrophilic attack by HCl.

The variation of the sizes of the ligands on the rotator, or alternatively the radius of the rotator, allows the rotational barrier to be modulated. Some might state that the substitution of a chloride ligand by a large (or "long") ligand introduces a "brake". However, the authors prefer to reserve this term for ligands that can be reversibly introduced by addition reactions. Although rotational barriers are treated more quantitatively below, some brief remarks here may be helpful.

First, for any square planar PtX₂ adduct, not all of the (CH₂)_n bridges or stator spokes are equivalent. By symmetry, two sets of ¹³C NMR signals would be expected (2:1 ratio). However, for the PtCl₂ complex with *n* = 14 (**18c**), only one set is observed, even at temperatures as low as -120 °C.¹⁰⁴ This indicates rapid rotation of the PtCl₂ rotator, often qualified as "on the NMR time scale". The same limiting spectra are

obtained with the PtBr_2 , PtI_2 , and $\text{Pt}(\text{CN})_2$ analogs, at least at room temperature. However, multiple signals can be observed with longer pseudohalide ligands, such as NCS adducts.^{104,105}

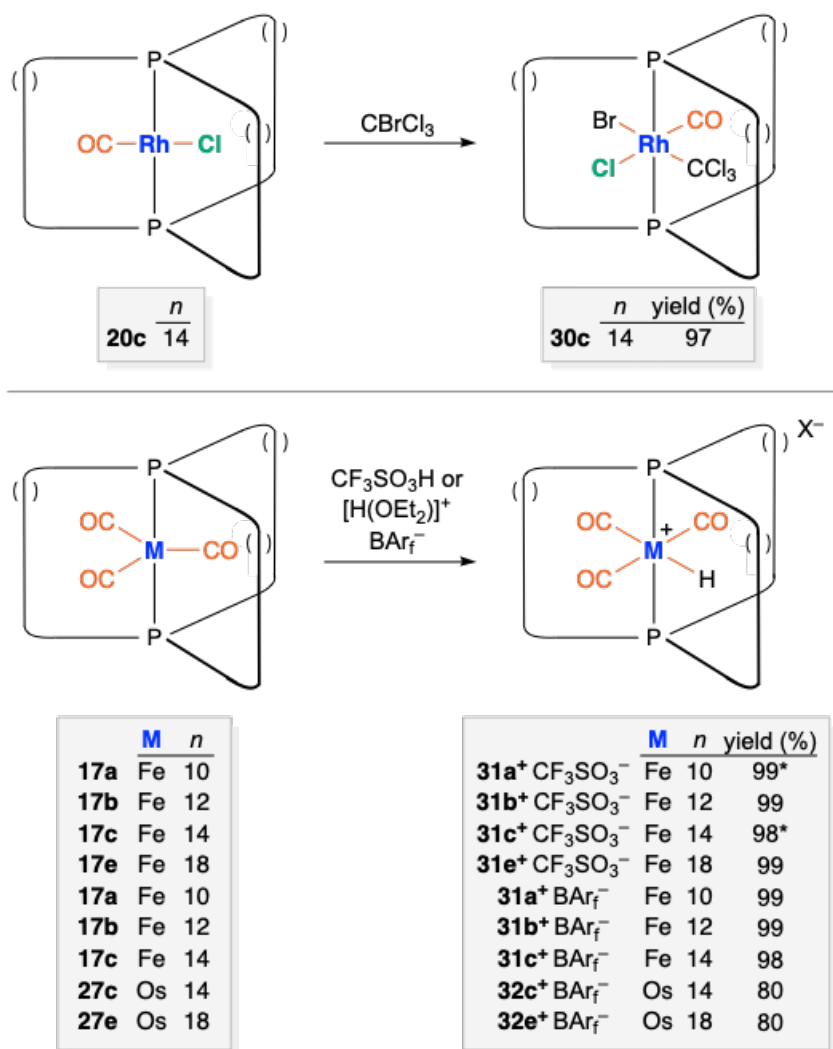


Figure 2.18 Syntheses of octahedral complexes from precursors with different coordination geometries [() indicates $(\text{CH}_2)_n$]. An asterisk indicates an NMR yield for a species generated *in situ*.^{100,106,110}

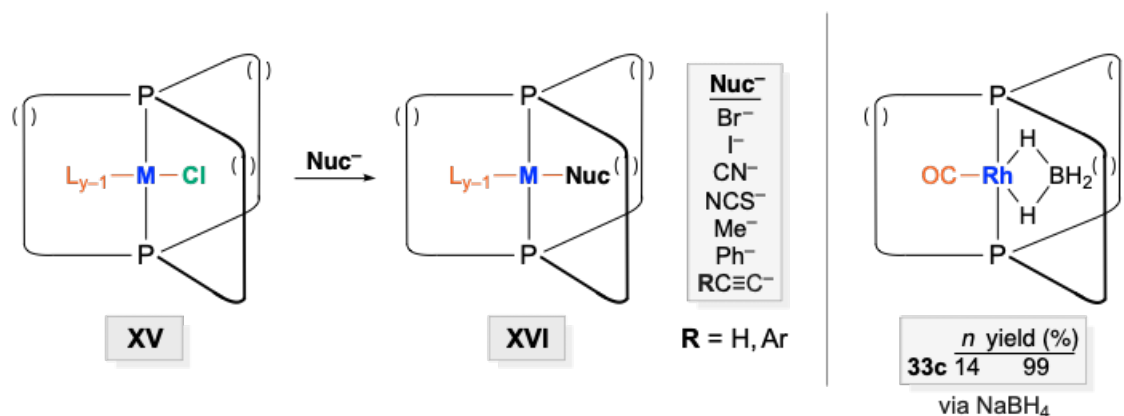


Figure 2.19 Reactions of chloride complexes of various coordination geometries with nucleophiles [() indicates (CH₂)_n].¹⁰⁴⁻¹⁰⁶

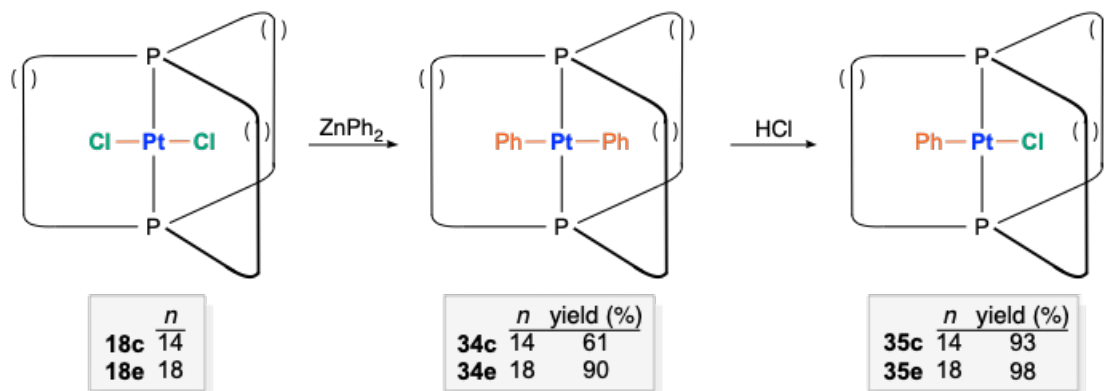


Figure 2.20 Syntheses of complexes with dipolar PhPtCl rotators from precursors with PtCl₂ rotators [() indicates (CH₂)_n].^{104,109}

Similar scenarios are encountered with other complexes. For example, when the chloride ligand in the RhCl(CO) adduct **21b** (Figure 2.13) is replaced with the phenylethynyl ligand C≡CC₆H₅, the number of ¹³C NMR signals (room temperature) is unaffected.⁹⁹ However, when the chloride ligand is replaced by the slightly more extended *p*-tolylethynyl ligand, C≡C-*p*-C₆H₄CH₃, multiple sets of signals are observed.

2.6.3.2. Replacements of carbonyl ligands

Although the photochemical substitution of carbonyl ligands has abundant precedent, all attempts to effect well-defined reactions with any of the preceding carbonyl complexes have been unsuccessful. However, with all $\text{Fe}(\text{CO})_3$ (but not $\text{Os}(\text{CO})_3$) complexes, the addition of NO^+BF_4^- leads to CO/NO⁺ exchange as shown in Figure 2.21.^{106,107} The cations of the resulting salts, **36a-c**⁺ BF_4^- , and **37a-c**⁺ BF_4^- are isoelectronic and isostructural with their precursors, and the NMR properties are further detailed below.

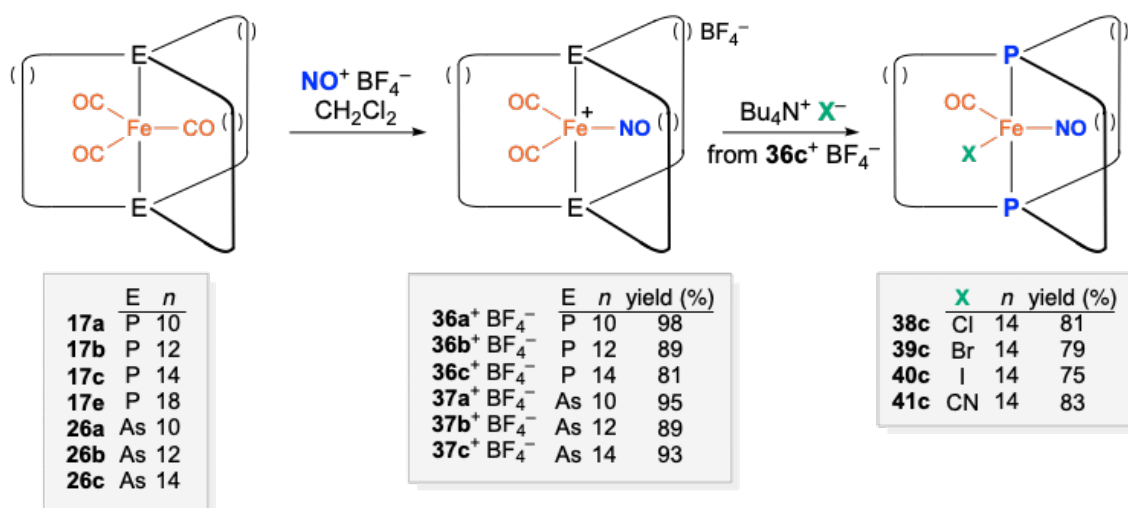


Figure 2.21 Substitution reactions of carbonyl ligands in iron complexes [() indicates $(\text{CH}_2)_n$].¹⁰⁶⁻¹⁰⁸

The dipolar rotators in **36a-c**⁺ BF_4^- and **37a-c**⁺ BF_4^- are potentially useful, but as noted above there are complications with molecular gyroscopes derived from ionic systems. However, with the diphosphine complexes **36a-c**⁺ BF_4^- , halide and

pseudohalide nucleophiles (Cl^- , Br^- , I^- , CN^-) readily displace one of the remaining carbonyl ligands, giving neutral complexes with $\text{Fe}(\text{CO})(\text{NO})(\text{X})$ rotators as shown in Figure 2.21 (**38c-41c**).¹⁰⁸ This sequence has not yet been attempted with the diarsine complexes **37a-c**⁺ BF_4^- , but parallel chemistry is anticipated.

With this series of complexes, it was studied whether carrying out CO ligand substitution prior to the metathesis/hydrogenation sequence in Figure 2.8 might be advantageous.¹⁰⁸ In all cases, it proved better to effect substitution after installing the dibridgehead diphosphine ligand, per Figure 2.21.

2.6.4. Dynamic properties: general concepts

As mentioned above, some aspects of the dynamic behavior of the rotators in the preceding complexes can be gleaned from routine NMR spectra. In this context, one should note that trigonal bipyramidal complexes in which all rotator ligands are identical should adopt ground state conformations in which the three M–L bonds are staggered with respect to the P–C bonds. As depicted in the top panel of Figure 2.22, these would have idealized D_3 or D_{3h} symmetry in which all three $\text{P}(\text{CH}_2)_n\text{P}$ bridges are homotopic (i.e. interchangeable by a C_n rotational axis).

Square planar and octahedral complexes can be similarly considered, as illustrated in the middle and bottom panels of Figure 2.22. There are no ML_y conformations in which all three $\text{P}(\text{CH}_2)_n\text{P}$ bridges are related by symmetry. However, for each energy minimum, two bridges qualify as homotopic.

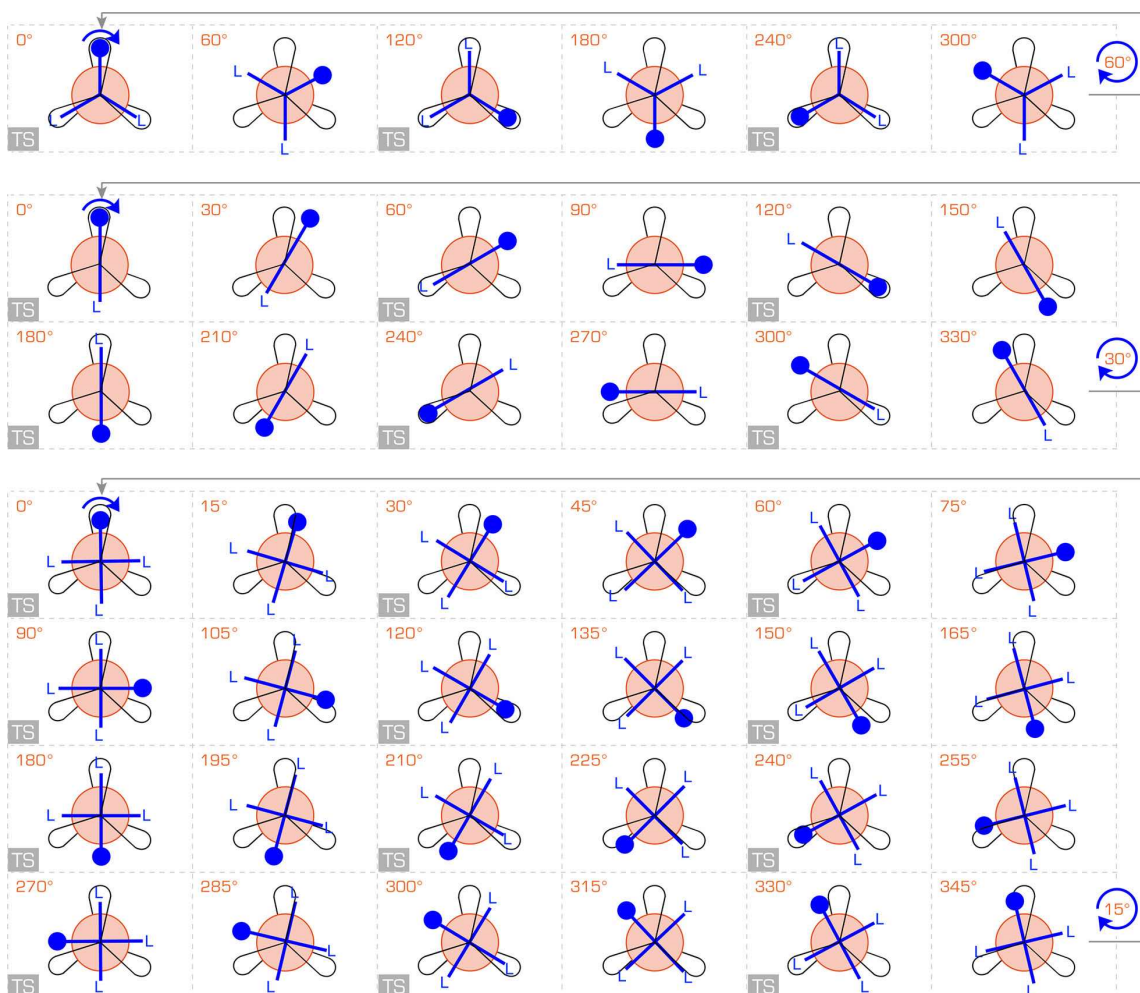


Figure 2.22 Energy maxima and minima as the rotators in trigonal bipyramidal (top panel), square planar (middle panel), and octahedral complexes (bottom panel) in Figure 2.8 are rotated by 360°. The blue dot represents a marker to help track rotation (and can also be visualized as a unique ligand).

These situations of course change when the rotator ligands are not identical. In the case of trigonal bipyramidal complexes, there will be two homotopic $P(CH_2)_nP$ bridges for rotators of the type ML_2L' , and none for MLL'' rotators. The former case is easily visualized by treating the blue marker or dot in the top panel of Figure 2.22 as L' . There are no homotopic bridges for square planar complexes with MLL' rotators or octahedral complexes with ML_3L' rotators.

In any case, if only one set of $\text{P}(\text{CH}_2)_n\text{P}$ ^{13}C NMR signals is observed for a square planar or octahedral complex, there must be a mechanism for exchange of the $\text{P}(\text{CH}_2)_n\text{P}$ units that is rapid on the NMR time scale. The most intuitive would involve a simple rotation of the rotator. Other possibilities, such as multistep processes involving ligand dissociation, can be ruled out by NMR or other data.

As a point of calibration, one can consider the most intensively studied cage size with $n = 14$, corresponding to 17-membered macrocycles. In brief, rotators bearing only halide, cyanide, CO, NO^+ , and CH_3 ligands generally remain in the fast exchange limit, even at -100 °C, regardless of coordination geometry. However, the introduction of phenyl substituents usually supplies sufficient bulk to "brake" rotation, as evidenced by two or more sets of $\text{P}(\text{CH}_2)_{14}\text{P}$ signals.^{98,105} Also, the slow exchange regime is easier to reach with trigonal bipyramidal complexes (i.e. T_{coal} at less negative (higher) temperatures), for example, with a $\text{Fe}(\text{CO})(\text{NO})\text{Cl}$ rotator¹⁰⁸ as opposed to a $\text{Re}(\text{CO})_3\text{Cl}$ rotator.¹¹¹ How can this be understood?

First, return to the trigonal bipyramidal species in the top panel of Figure 2.22. The transition state for rotator rotation entails a three-fold ligand/ $\text{P}(\text{CH}_2)_n\text{P}$ (L–M–P–C) eclipsing interaction. Furthermore, as the rotator passes through 360° , three minima and three maxima are encountered. Their idealized L–M–P–C torsion angles are 60° and 0° , respectively (considering only the nearest L/ $\text{P}(\text{CH}_2)_n\text{P}$ moieties). Although each set of three is degenerate, it remains instructive to view the entire coordinate as in Figure 2.22, where the blue dot aids the tracking of rotation. As noted above, it can also be regarded

as a unique ligand, facilitating recognition of the two types of symmetry inequivalent $P(CH_2)_nP$ bridges.

As the ML_2 rotator of a square planar complex passes through 360° (middle panel, Figure 2.22), six degenerate maxima and six degenerate minima are encountered. Now there is only one L–M–P–C eclipsing interaction present in each transition state. Furthermore, in the minima, the idealized L–M–P–C torsion angles associated with the nearest $L/P(CH_2)_nP$ moieties are only 30° , increasing the possibility of van der Waals interactions that would slightly destabilize the ground state. Thus, intrinsically lower rotational barriers as compared to trigonal bipyramidal analogs would be expected.

The considerations raised with the square planar complexes become more pronounced with the octahedral complexes. As shown in the bottom panel of Figure 2.22, there are 12 degenerate maxima and 12 degenerate minima as the rotator passes through 360° . Again, there is only one eclipsing interaction associated with each transition state, with idealized L–M–P–C torsion angles of 0° , $2 \times 30^\circ$, and 60° for the nearest $L/P(CH_2)_nP$ moieties. The minima feature idealized L–M–P–C torsion angles of $2 \times 15^\circ$ and $2 \times 45^\circ$ for the nearest $L/P(CH_2)_nP$ moieties. The compressed 15° torsion angles are likely to introduce van der Waals interactions that would contribute to ground state strain. Hence, the rotational barriers should be further reduced relative to the cases above.

The preceding concepts are well recognized in the physical organic literature,^{144,145} where it is common to refer to the foldedness, N , of a rotational barrier about a covalent bond A–B.

$$N = (p \cdot q) / w \quad (\text{eq. 1})$$

in which p is the foldedness of the fragment A (often corresponding to a C_n axis), q is the foldedness of the fragment B, and w is the number of eclipsed bonds in the transition state.

As N becomes larger, rotational barriers tend to diminish. Another way to view this trend is that for a higher fold system to have a rotational barrier comparable to a lower fold system, a similar energy change must take place over a much more restricted range of torsion angles. Accordingly, the trigonal bipyramidal systems exhibit three-fold barriers $[(3 \times 3) / 3]$ whereas the square planar and octahedral systems exhibit six- and twelve-fold barriers, respectively.

In qualitative agreement with the preceding analysis, low temperature ^{13}C NMR spectra of the trigonal bipyramidal $\text{Rh}(\text{CO})_2\text{I}$ complex **29c** exhibit two sets of $\text{P}(\text{CH}_2)_n\text{P}$ signals (ca. 2:1 area ratio, $-25\text{ }^\circ\text{C}$, CD_2Cl_2), but spectra of the square planar $\text{Rh}(\text{CO})\text{I}$ complex **28c** exhibit only one (CDFCl_2 , $-120\text{ }^\circ\text{C}$).¹⁰⁰ When the former sample is warmed, the signals coalesce. In this case, other data suggest that the mechanism by which the $\text{P}(\text{CH}_2)_n\text{P}$ bridges become equivalent involves CO dissociation. Nonetheless, it can be concluded that the $\text{Rh}(\text{CO})_2\text{I}$ rotational barrier is higher than that for $\text{Rh}(\text{CO})\text{I}$.

With the other carbonyl complexes studied, the maintenance of certain couplings precludes dissociative processes.

2.6.5. Measured or bounded rotational barriers

As summarized in Table 2.1, a number of barriers to rotator rotation in the preceding complexes have been measured or bounded using variable temperature ^{13}C NMR data. Note that to exchange the positions of all of the $\text{P}(\text{CH}_2)_n\text{P}$ bridges in a trigonal bipyramidal complex with a $\text{ML}_2\text{L}'$ or $\text{MLL}'\text{L}''$ rotator, a 240° rotation is necessary (corresponding to the structures labeled 60° and 300° in the top panel of Figure 2.22). However, to exchange the positions of all the $\text{P}(\text{CH}_2)_n\text{P}$ bridges in a square planar complex with a ML_2 rotator, only a 120° rotation is necessary (see structures labeled 30° and 150° in the middle panel of Figure 2.22). With a MLL' rotator, a 300° rotation becomes necessary (structures labeled 30° and 330°). For octahedral complexes with ML_4 or $\text{ML}_3\text{L}'$ rotators, the equivalent values are 60° and 330° , respectively. Thus, the rate constants employed in the Eyring plots used to generate the activation parameters can represent varying degrees of rotation.

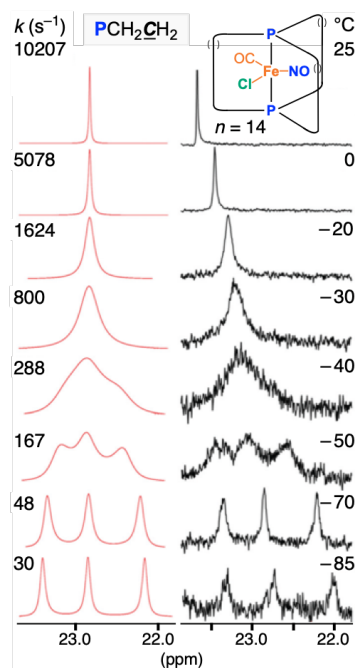


Figure 2.23 Partial $^{13}\text{C}\{^1\text{H}\}$ NMR spectra of the $\text{Fe}(\text{CO})(\text{NO})\text{Cl}$ complex **38c** as a function of temperature (CD_2Cl_2 , right) and simulated line shapes with rate constants (left).¹⁰⁸

A typical series of spectra used to generate the data in Table 2.1 is shown in Figure 2.23. At each temperature, the line shapes are simulated with standard programs, and the rate constants are extrapolated. The negative ΔS^\ddagger values in Table 2.1 suggest quite ordered transition states, consistent with ligands traversing through the otherwise unoccupied macrocycle cavities. Also, consistent with expectations involving barrier foldedness, the trigonal pyramidal complexes with $\text{Fe}(\text{CO})_2(\text{NO})^+$ rotators exhibit higher ΔG^\ddagger values than the corresponding octahedral complexes with $\text{Fe}(\text{CO})_3\text{H}^+$ rotators (e.g. at 383 K, 19.2 vs. 15.1 kcal/mol for **36b**⁺ BF_4^- and **31b**⁺ BAR_f^- , or 16.2 vs. 14.1 kcal/mol for **37b**⁺ BF_4^- and **42b**⁺ BAR_f^-). Other trends in Table 2.1 are interpreted below.

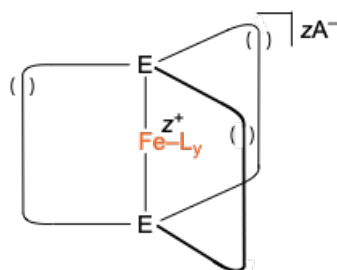


Table 2.1 Activation parameters for Fe(CO)(NO)(X) or Fe(CO)₃H rotation within E((CH₂)_n)₃E cages in solution as determined by variable temperature ¹³C{¹H} NMR [() Indicates (CH₂)_n].

complex	L _y	E	n	zA ⁻	ΔH^\ddagger (kcal mol ⁻¹)	ΔS^\ddagger (eu) ^a	ΔG^\ddagger_{298K} (kcal mol ⁻¹)	ΔG^\ddagger_{383K} (kcal mol ⁻¹)	ref
38c^b	CO, NO, Cl	P	14	0	5.9	-20.4	11.9	13.6	108
40c^c	CO, NO, I	P	14	0	7.6	-23.9	14.7	16.8	108
36b⁺ BF₄^{-c}	(CO) ₂ , NO	P	12	1BF ₄ ⁻	8.3	-28.4	16.7	19.2	106
36c⁺ BF₄^{-d}	(CO) ₂ , NO	P	14	1BF ₄ ⁻	9.5	-6.5	11.4	11.9	106
37a⁺ BF₄^{-c}	(CO) ₂ , NO	As	10	1BF ₄ ⁻	—	—	—	>19.4	107
37b⁺ BF₄^{-b}	(CO) ₂ , NO	As	12	1BF ₄ ⁻	7.7	-22.1	14.2	16.2	107
31b⁺ BAr_f^{-b}	(CO) ₃ , H	P	12	1BAr _f ⁻	6.1	-23.5	13.0	15.1	107
42a⁺ BAr_f^{-c}	(CO) ₃ , H	As	10	1BAr _f ⁻	—	—	—	>18.9	107
42b⁺ BAr_f^{-b}	(CO) ₃ , H	As	12	1BAr _f ⁻	5.4	-22.7	12.2	14.1	107

^a Units of cal·mol⁻¹·K⁻¹. ^b CD₂Cl₂ solution. ^c C₆D₅Cl solution. ^d CDFCl₂ solution.

2.6.6. Key solid state properties

The authors have determined the crystal structures of large numbers of the preceding complexes. In some cases, there is disorder in the $(\text{CH}_2)_n$ segments, but well over half the time, this can be modeled. The authors have also made frequent use of geometric analyses of the types illustrated in Figure 2.24.^{104,106-108,110,111} Various features of these diagrams are examined in turn.

The first step with each crystal structure is to calculate the radius (or "horizontal steric demand") of the rotator. One simply takes the distance from the metal to the terminal atom of each ligand and adds the van der Waals radius of the terminal atom. The largest of these values is considered the radius. As would be expected, the radius of any ML_y rotator or individual M–L bond length does not significantly vary with the lengths of the $\text{P}(\text{CH}_2)_n\text{P}$ moieties (and could often in theory be taken from appropriate model compounds in the literature).

Next, the "horizontal clearance" provided by the three $\text{P}(\text{CH}_2)_n\text{P}$ bridges is considered. The syntheses in Figure 2.8 always give an even number for n , which places the midpoint between two atoms. Hence, the authors have focused on the two innermost CH_2 groups (Figure 2.24, left), for example, the seventh and eighth from either terminus in a $\text{P}(\text{CH}_2)_{14}\text{P}$ bridge. Thus, the distances of six carbon atoms from the metal are calculated, and the van der Waals radius of a carbon atom (1.70 Å) is subtracted from each. Although a number of ways to treat these data can be considered, the authors have always taken (as the most conservative estimate) the shortest of the resulting distances as

the "clearance" (while also tabulating the average distance). When this value is greater than the radius of the rotator, rotation is always rapid on the NMR time scale and only a single set of $\text{P}(\text{CH}_2)_n\text{P}$ ^{13}C NMR signals are observed.

The qualitative nature of the preceding analysis deserves emphasis. First, in the crystal lattice, the three $\text{P}(\text{CH}_2)_n\text{P}$ units usually exhibit different conformations. However, in solution, they all have the same ensemble of conformations available. Furthermore, these conformations will change during the course of rotator rotation. Second, this treatment also ignores the hydrogen atoms of the stator. However, it is often found that hydrogen atoms can be neglected when evaluating the feasibility of dynamic processes from space filling models.

Similar analyses of the "vertical" or "top/bottom" clearance can be carried out.^{106,107} Several approaches with largely equivalent results have been taken. The first step is to consider the *trans*- $\text{CH}_2\text{-P-M-P-CH}_2$ linkages or $(\text{CH}_2)_3\text{P-M-P}(\text{CH}_2)_3$ units. The distances between the closest CH_2 groups on opposite termini can then be calculated. These are not quite eclipsed, as is evident from the views shown in the crystal structure in Figure 2.25 (bottom panel). Alternatively, the distance between the two planes defined by the three $\text{P}(\text{CH}_2)_3$ carbon atoms can be calculated (Figure 2.24, right; these are often parallel due to crystallographic symmetry). In either case, the van der Waals radii of two carbon atoms are then subtracted to give a clearance. The values are then compared to the van der Waals *diameter* (or "vertical steric demand" or "fatness") of the atoms bound to the rotator.

Consider the structurally characterized neutral iron complexes with dipolar rotators, $\text{Fe}(\text{CO})(\text{NO})(\text{X})$ (**38c**, **39c**, **41c**).¹⁰⁸ In the case of the chloride complex **38c**, diameters of the ligating atoms are 3.10 Å (NO), 3.40 Å (CO), and 3.50 Å (Cl) versus a vertical clearance of ≥ 2.62 Å. In the case of the bromide complex **39c**, the vertical clearance is nearly unchanged (≥ 2.68 Å), but the bromide ligand has a larger diameter (3.70 Å) than chloride. In the case of the cyanide complex **41c**, the diameters of the ligating atoms are all ≤ 3.40 Å, while the clearance is little changed (≥ 2.58 Å). Despite the pronounced van der Waals interactions that clearly must accompany rotator rotation in these three compounds, rotation remains fast on the NMR time scale. Thus, concurrent conformational processes that attenuate these interactions are presumably taking place (e.g. $\text{P}(\text{CH}_2)_n\text{P}$ bond rotations). This would be another contributor to the negative ΔS^\ddagger values in Table 2.1 (avg. ca. -21 eu). In any case, a major portion of the activation energy must be due to poor vertical clearance. Possible means of ameliorating these interactions are discussed below.

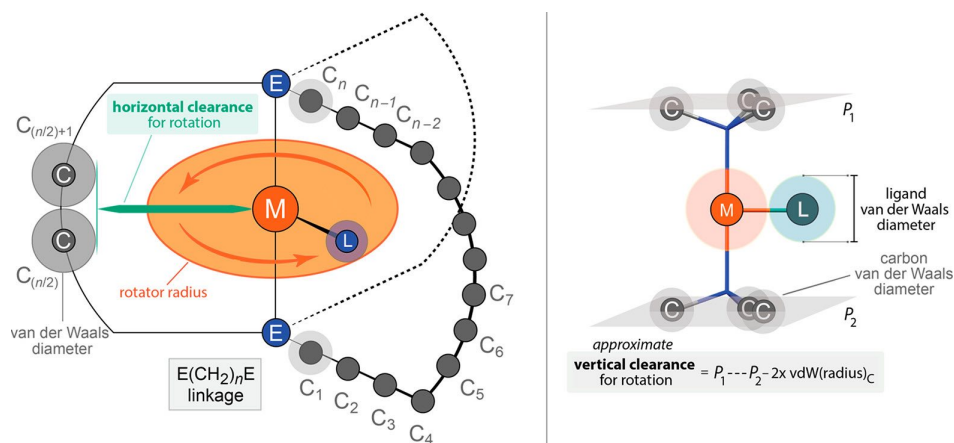
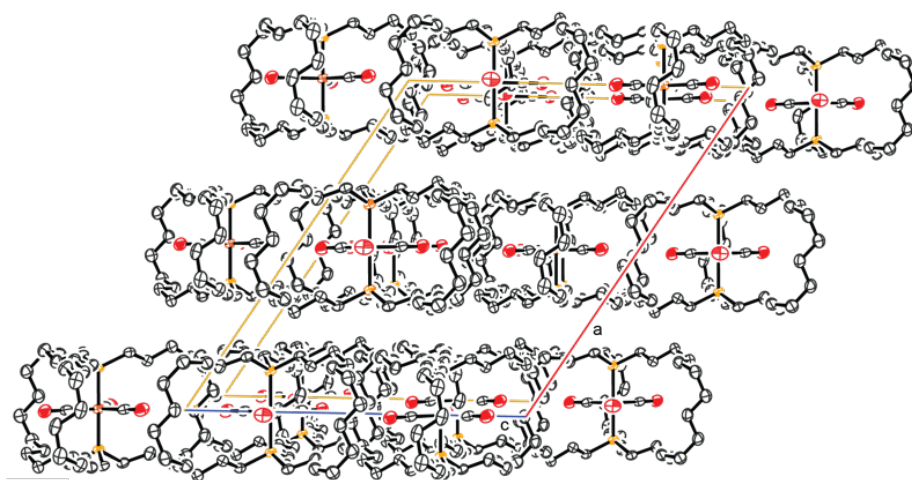


Figure 2.24 Structures illustrating the concepts of "horizontal clearance" and "vertical clearance" for complexes synthesized in the authors' laboratory.



XVII-a

XVII-b

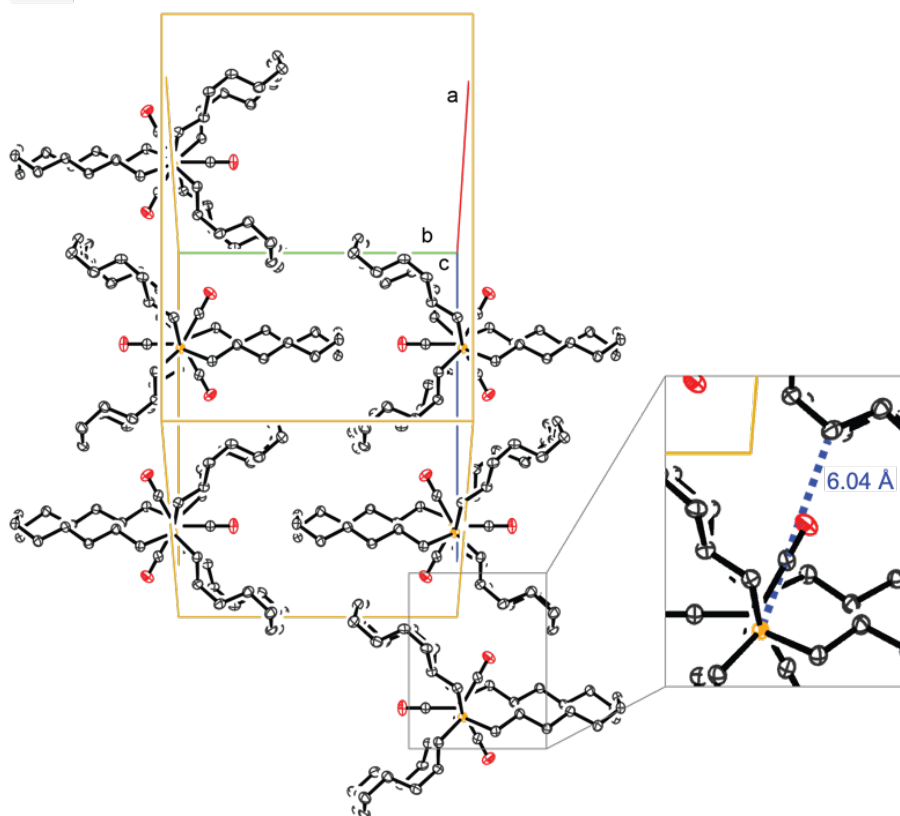


Figure 2.25 Crystal lattice of the $\text{Fe}(\text{CO})_3$ complex **17c** viewed along the b axis (top) and perpendicular to the b axis (bottom), iron atoms are depicted in orange and oxygen atoms in red.

Of course, under the solution phase conditions used to measure the rotational barriers in Table 2.1, the molecules are oriented randomly, and none of the approaches to functional molecular gyroscopes outlined in section 2.3 apply. Accordingly, the authors have sought crystalline samples of the preceding compounds in which the rotators (1) exhibit parallel axes, (2) have no *intermolecular* steric impediments to rotation, and (3) have significant dipole moments so that they can strongly interact with electric fields. Among the many square planar and octahedral complexes that have been structurally characterized, not one has crystallized with parallel rotator axes (although there are always subsets of molecules with parallel rotator axes). However, both criteria 1 and 2 are fulfilled with all *neutral* trigonal bipyramidal complexes with $\text{E}(\text{CH}_2)_{14}\text{E}$ bridges and CO/NO/X ligands prepared to date, that is, species of the general formula $\overline{\text{M}(\text{L})(\text{L}')(\text{L}'')(\text{E}(\text{CH}_2)_{14}\text{E})_2}$.^{97,106-108,110} These include $\text{Fe}(\text{CO})_3$ rotators for $\text{E} = \text{P}$ and As and $\text{Os}(\text{CO})_3$, $\text{Fe}(\text{CO})(\text{NO})\text{Cl}$, $\text{Fe}(\text{CO})(\text{NO})\text{Br}$, and $\text{Fe}(\text{CO})(\text{NO})(\text{CN})$ rotators for $\text{E} = \text{P}$. For the last three rotators, DFT calculations indicate dipole moments of 2.68 to 1.38 D (decreasing as $\text{X} = \text{CN}, \text{Br}, \text{Cl}$).¹⁴⁶ These are in the range of dipolar rotators that have previously been driven by electrical fields.^{132,147,148}

As summarized in Table 2.2, these six complexes crystallize in identical space groups ($C_{2/c}$) with very similar monoclinic lattice dimensions. Two perspectives of an abbreviated packing diagram for *trans*- $\text{Fe}(\text{CO})_3(\text{P}(\text{CH}_2)_{14}\text{P})_2$ (**17c**) are given in Figure 2.25. The upper view illustrates both the parallel rotator axes and a pronounced layering of molecules. The lower view illustrates the spacing between the $\text{Fe}(\text{CO})_3$ rotators and

neighboring molecules within the same layer. The individual CO ligands are directed at the stators of the neighbors. For all six complexes, it is a simple matter to calculate the distances between the metal atoms of one molecule and the closest stator atom of a neighboring molecule, which as easily inferred visually always turn out to be carbon atoms. The values range from 6.09 to 5.99 Å or 4.39 to 4.29 Å after subtracting the van der Waals radius of a carbon atom. In each case, this *intermolecular clearance* comes very close to accommodating the radius of the rotator (4.38-4.59 Å).

2.6.7. Toward molecular gyroscopes

In assessing the crystalline forms of these complexes as candidates for molecular gyroscopes, the Fe(CO)(NO)Cl adduct **38c** would be preferred to the corresponding iodide species **40c** given the lower barrier to rotation in Table 2.1. However, the cyanide ligand in **41c** extends only slightly farther from iron than chloride (4.53 vs. 4.38 Å; there is ample free volume in this dimension) and is slightly more "svelte" (3.40 vs. 3.50 Å). The latter may help in the more congested vertical dimension, and as noted in section 2.6.6, the cyanide substituted rotator exhibits the highest dipole moment. Thus, the Fe(CO)(NO)Cl and Fe(CO)(NO)(CN) complexes **38c** and **41c** will serve as the leads in future experimental investigations. However, hydride or fluoride ligands would be smaller yet, and synthetic routes are currently under investigation.

Table 2.2 Structural data for gyroscope-like complexes of the formula $\overline{\text{trans-M(L)(L')(L'')(E(CH}_2\text{)}_{14}\text{E)}}_2$.

complex ^a	E/rotator	radius ^b [Å]	M··· CH ₂ [Å] ^b	M···CH ₂ - vdW _C [Å] ^d	a [Å]	b [Å]	c [Å]	β (°)	ref
26c	As/Fe(CO) ₃	4.45	6.01	4.31	21.438(3)	13.9810(17)	18.227(2)	121.3	107
17c	P/Fe(CO) ₃	4.45	6.04	4.34	21.5104(8)	13.9765(6)	18.3436(8)	122.8	106
27c	P/Os(CO) ₃	4.59	6.09	4.39	21.6848(5)	14.0336(2)	18.2091(4)	122.1	110
38c	P/Fe(CO)(NO)Cl	4.38	5.99	4.29	21.4367(4)	13.8586(4)	18.3518(5)	122.5	108
39c	P/Fe(CO)(NO)Br	4.47	6.06	4.36	21.2190(8)	13.9660(8)	18.1727(2)	121.0	108
41c	P/Fe(CO)(NO)(CN)	4.53	6.04	4.34	21.4114(6)	13.9998(2)	18.2960(5)	122.7	108

^a All complexes crystallize in the space group $C_{2/c}$ as monoclinic crystal systems ($\alpha = \gamma = 90^\circ$). ^b The distance from the metal to the terminal atom of each ligand is calculated, and the van der Waals radius of the terminal atom is added. The largest of the three values is taken as the radius. The distances used are from Skaper, D. doctoral thesis, Universität Erlangen-Nürnberg, 2010, Table 2-9. ^c The distance from the metal to the nearest carbon atom of a neighboring molecule in the crystal lattice (see example in Figure 2.25). ^d The previous distance minus the van der Waals radius of a carbon atom (intermolecular horizontal clearance).

The diantimony and dibismuth analogs of the trigonal bipyramidal iron complexes would also be attractive synthetic targets. Iron–heteroatom and heteroatom–carbon bonds progressively lengthen upon descending group 15. For example, in the crystallographically characterized series $\text{Fe}(\text{CO})_4(\text{E}(t\text{-Bu})_3)$, the Fe–P, –Sb, and –Bi bonds lengthen from 2.364(1) to 2.547(1) to 2.6269(9) Å, and the P–, Sb–, and Bi–C bonds lengthen from 1.93 to 2.22 to 2.32 Å (averages; the Fe–E–C angles remain in the narrow range 107.2–106.0°).¹⁴⁹⁻¹⁵¹ The rotational barriers ($\Delta G_{298\text{K}}^\ddagger$) for the isostructural diphosphine and diarsine complexes $\mathbf{36b}^+ \text{BF}_4^-$ and $\mathbf{42b}^+ \text{BF}_4^-$ in Table 2.1 are 16.7 and 14.2 kcal/mol, respectively, a 2.5 kcal/mol reduction. Thus, longer Fe–E bond lengths appear to greatly relieve rotator/stator steric interactions in the vertical dimension.

Osmium analogs would also greatly improve the vertical clearance. However, as noted above, the authors have so far been unable to effect substitution reactions of the $\text{Os}(\text{CO})_3$ complexes in Figure 2.17. It may also be advantageous to introduce some type of "belt" in the equatorial plane, connecting the spokes of the stators in a manner analogous to the stationary ring in Figure 2.1a. This would further shield the rotator from neighboring molecules and inhibit intercalation. A possible synthetic approach would be to construct the stator by alkyne instead of olefin metathesis¹⁵² and then introduce linkers between the alkyne moieties.

With an eye on critical issues in realizing metal based molecular gyroscopes, Fekl and Schurko alertly pointed to H–M–H units as "low barrier rotators".¹⁵³ They

studied the platinum dihydride complex **43** in Figure 2.26, which features two bulky *trans* disposed phosphine ligands. A variety of low temperature *solid-state* NMR experiments were carried out and interpreted with the aid of a crystal structure and DFT calculations. The rotational barrier, estimated as ca. 3 kcal/mol, is one of the lowest in this review. Interestingly, each energy minimum features an eclipsed H–Pt–P–C segment with a torsion angle of ca. 0°, as opposed to the 30° idealized torsion angles shown for the square planar complexes in Figure 2.22 (middle). But when one hydride ligand is replaced by a chloride ligand (affording a dipolar rotator), the solid-state rotational barrier increases considerably.

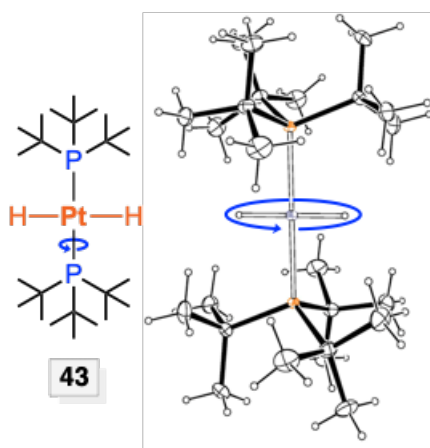


Figure 2.26 Bis(phosphine) platinum complex with a low barrier H–Pt–H rotator.

2.7. Systems from the Setaka group

2.7.1. Synthetic strategies

The Setaka group has also been prolific with regard to embedding rotators within cage-like stators of three-fold symmetry.¹²²⁻¹⁴¹ They have focused upon arenediyl rotators, denoted Q_y in figures and tables herein, for which *p*-phenylene ($p\text{-C}_6\text{H}_4$) represents the parent case (Q_1). These are anchored by silicon or occasionally germanium atoms,¹²⁸ affording dibridgehead disilane (digermane) stators that are akin to the dibridgehead diphosphine stators in many of the transition metal containing rotors in section 2.6. The Setaka group often refers to their systems as "gyrotops".

Most of their syntheses feature three-fold intramolecular ring closing olefin metathesis of species of the formula $Q_y[E((\text{CH}_2)_m\text{CH}=\text{CH}_2)_3]_2$ (\mathbf{L} ; $E = \text{Si}, \text{Ge}$).¹²³⁻¹³⁸ As depicted in Figure 2.27, two types of products are possible following hydrogenation: the gyroscope-like compounds \mathbf{LI} , derived exclusively from metatheses of olefins tethered to different silicon atoms, and \mathbf{LII} , derived in part from metatheses of olefins tethered to the same silicon atom. Per the convention in section 2.6, the former are given unprimed numbers and the latter primed ones (the alphabetical indices \mathbf{a} , \mathbf{b} , \mathbf{c} , etc. for m and n are also kept constant). Compounds available by this route are summarized in Table 2.3. In about half of the cases, \mathbf{LI} is the dominant product.

As shown in Figure 2.28, Setaka has considered the product distribution that would be expected if the rate constants at each branch point in the metathesis sequences leading to \mathbf{LI} and \mathbf{LII} were identical.¹²⁷ Interestingly, the latter is favored statistically,

with an idealized 1:3 ratio (20% vs. 60%, with 20% oligomer or incomplete metathesis). In Table 2.3, this ratio is realized (or exceeded) only for **50d'**, **52d'**, **54d'**, **58e'**, **59e'**, **60d'**, **61e'**, **61g'**, and **63e'**.

Thus, the rate constants for metatheses involving olefins tethered to different silicon atoms generally appear to be greater. However, for **50c** and **50c'**, the dominant product depends upon the temperature at which metathesis is carried out (**LI/LII** 1.0:0.8, 0 °C; 1.0:1.0, 20 °C; 1.0:1.7, 40 °C).¹²⁷ This suggests that, at least in this case, some macrocyclization steps are reversible, with **50c'** (or the triolefin precursor **LVIII** in Figure 2.28) representing the thermodynamically more stable product.

Setaka has also been able to prepare starting substrates in which the two anchoring silicon atoms bear different substituents.^{131,135} For example, an endgroup $\text{Si}(\text{CH}_2)_m\text{CH}=\text{CH}_2$ can be paired with one in which each silicon substituent has an additional methylene spacer, $\text{Si}(\text{CH}_2)_{m+1}\text{CH}=\text{CH}_2$. This allows access to methylene bridges with an odd number of carbon atoms, that is, $\text{Si}(\text{CH}_2)_{2m-1}\text{Si}$. Such products are depicted in Figure 2.29 and are designated with a double index (**cd** or **de**), denoting an intermediate (odd) value of n .

Setaka has also employed other types of three-fold macrocyclizations to access dibridgehead disilanes. That shown in Figure 2.30 involves stitching together the terminal hydrosilane moieties of substituents of the formula $(\text{Si})\text{CH}_2\text{CH}_2\text{Si}(\text{CH}_3)_2\text{CH}_2\text{CH}_2\text{Si}(\text{CH}_3)_2\text{H}$ with aqueous NaOH to give bridges with siloxane $(\text{Si}(\text{CH}_3)_2\text{O}(\text{CH}_3)_2\text{Si})$ linkages.¹³⁹⁻¹⁴¹ As in Figure 2.29, this protocol also

affords an odd number of atoms in the spokes between the bridgehead silicon atoms. Another macrocyclization method that was used to install two bridges between the anchoring silicon atoms was depicted in Figure 2.7 in section 2.4.3. All of the gyroscope-like compounds in Figure 2.27, Figure 2.29, and Figure 2.30 exhibit six-fold rotational barriers, with six maxima and six minima as the rotator is rotated through 360° (see section 2.6.4). Those with symmetrically substituted or non-dipolar rotators like *p*-phenylene share many features with the square planar complexes with ML₂ rotators from the authors' laboratory (e.g. **18c-g,k** in Figure 2.11). Those with less symmetrical or dipolar rotators such as 2,3-dichloro-*p*-phenylene (**66** in Figure 2.30) would be conceptually related to square planar complexes with MLL' rotators (e.g. **20c** in Figure 2.11 or **35c,e** in Figure 2.20).

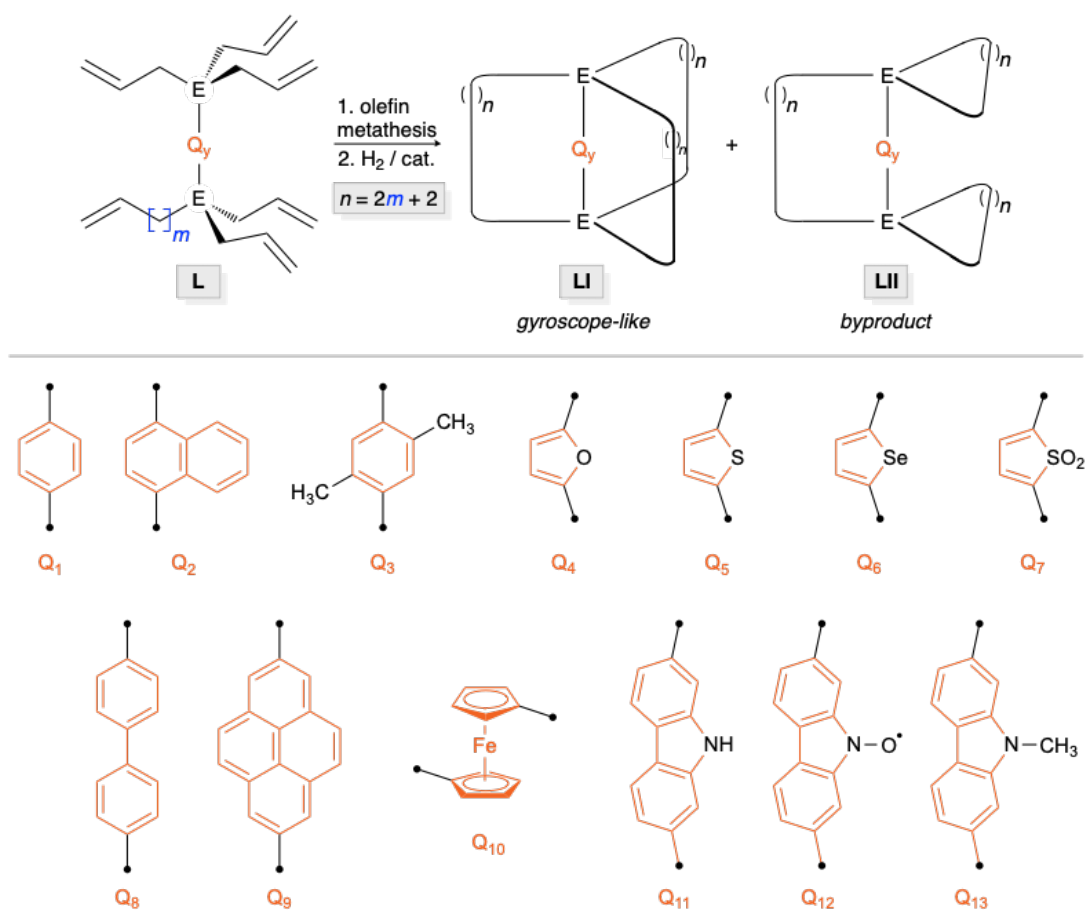


Figure 2.27 Gyroscope-like molecules prepared by the Setaka group by three-fold ring closing metatheses of substrates of the type **L**.

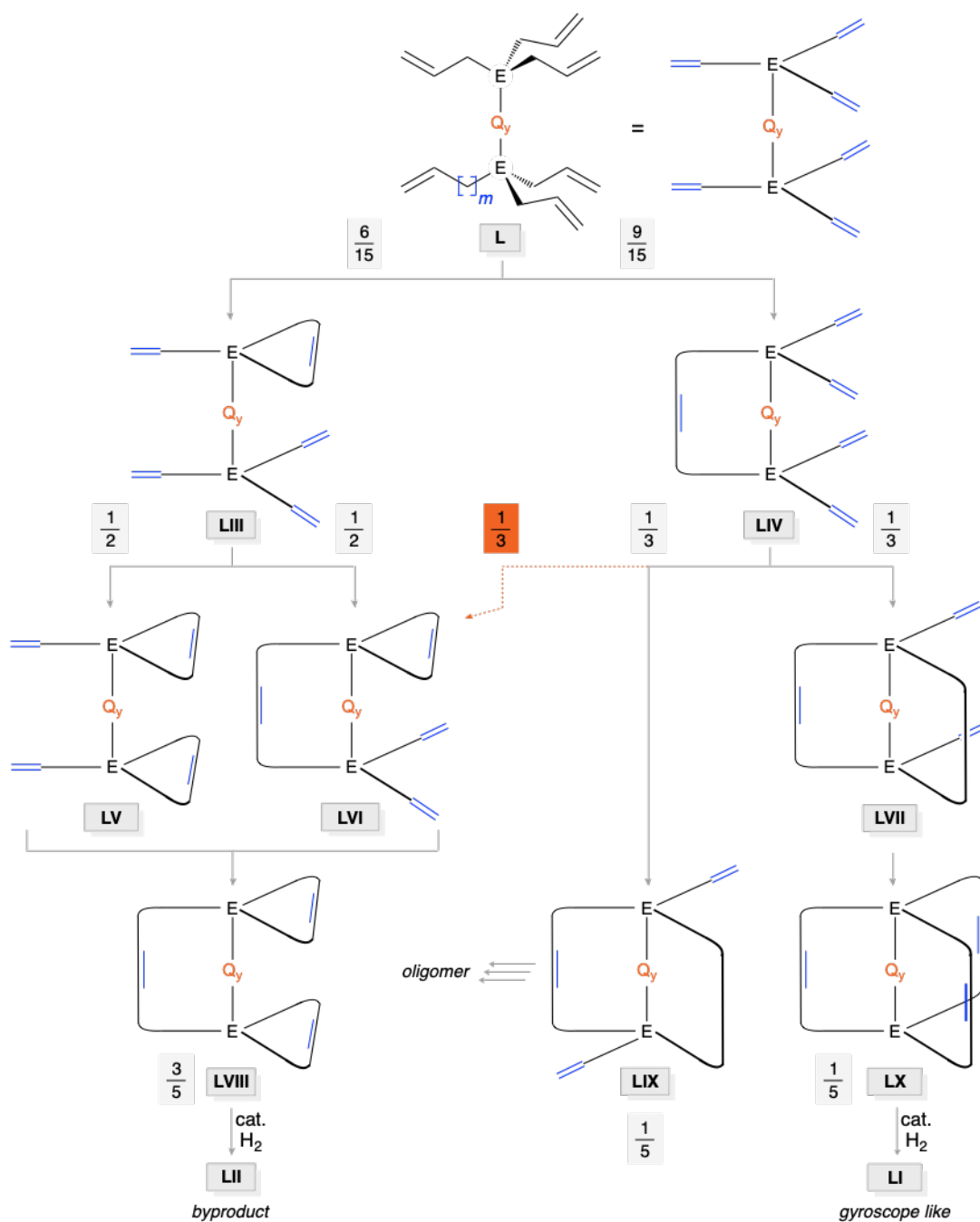


Figure 2.28 Predicted ratio of hydrogenated ring closing olefin metathesis products **LI** and **LII** (Figure 2.27) assuming equal rate constants for metathesis at every branch point (and no reversibility).¹²⁷

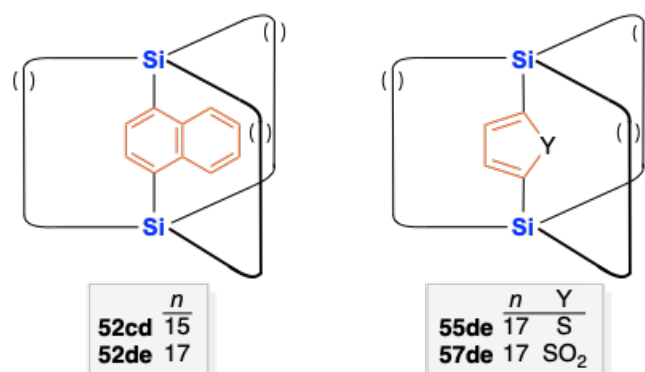


Figure 2.29 Gyroscope-like compounds synthesized by a variation of Figure 2.27 in which the number of methylene groups in the $P(CH_2)_m$ segments on the "top" and "bottom" in **L** differ by one [O] indicates $(CH_2)_n$.^{131,135}

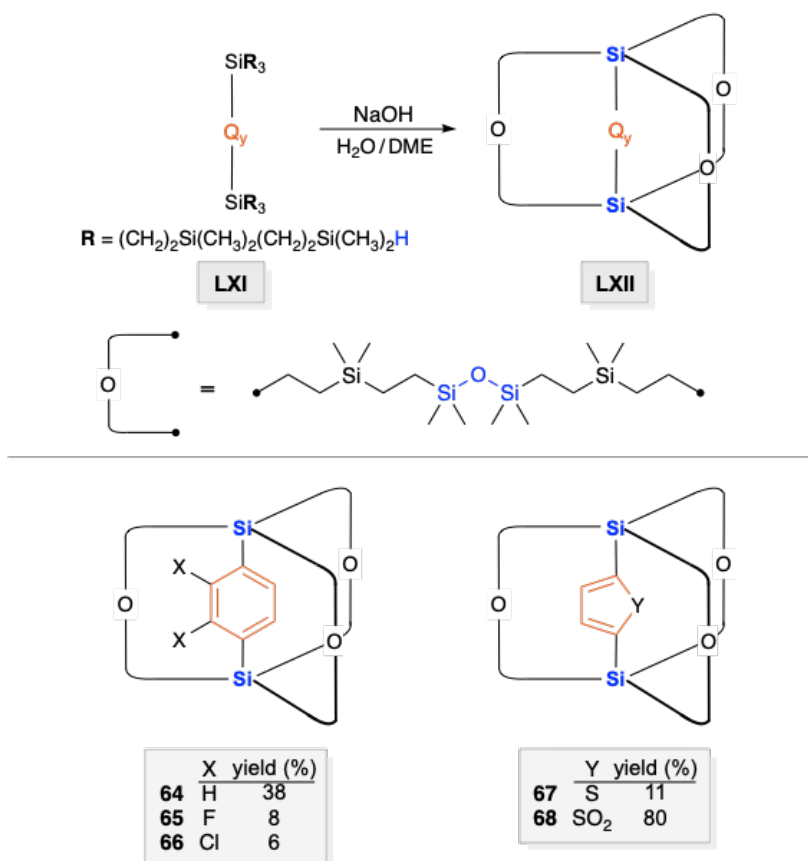


Figure 2.30 Gyroscope-like compounds from the Setaka group prepared by macrocyclizations other than olefin metathesis.¹³⁹⁻¹⁴¹

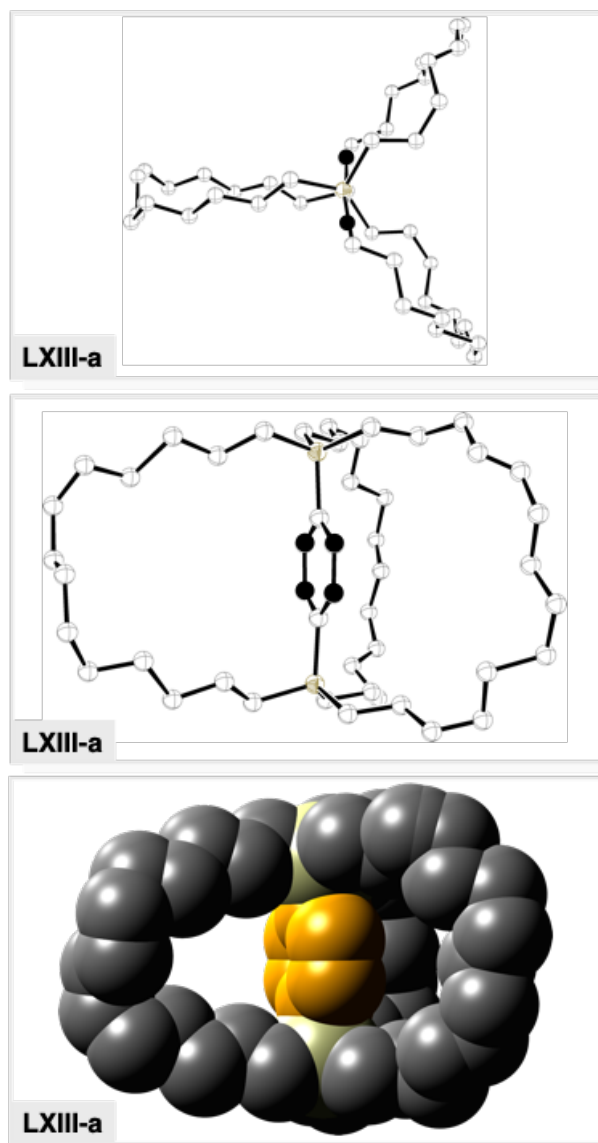


Figure 2.31 ORTEP and space filling representations of the crystal structure of **50c** (lowest temperature modification).

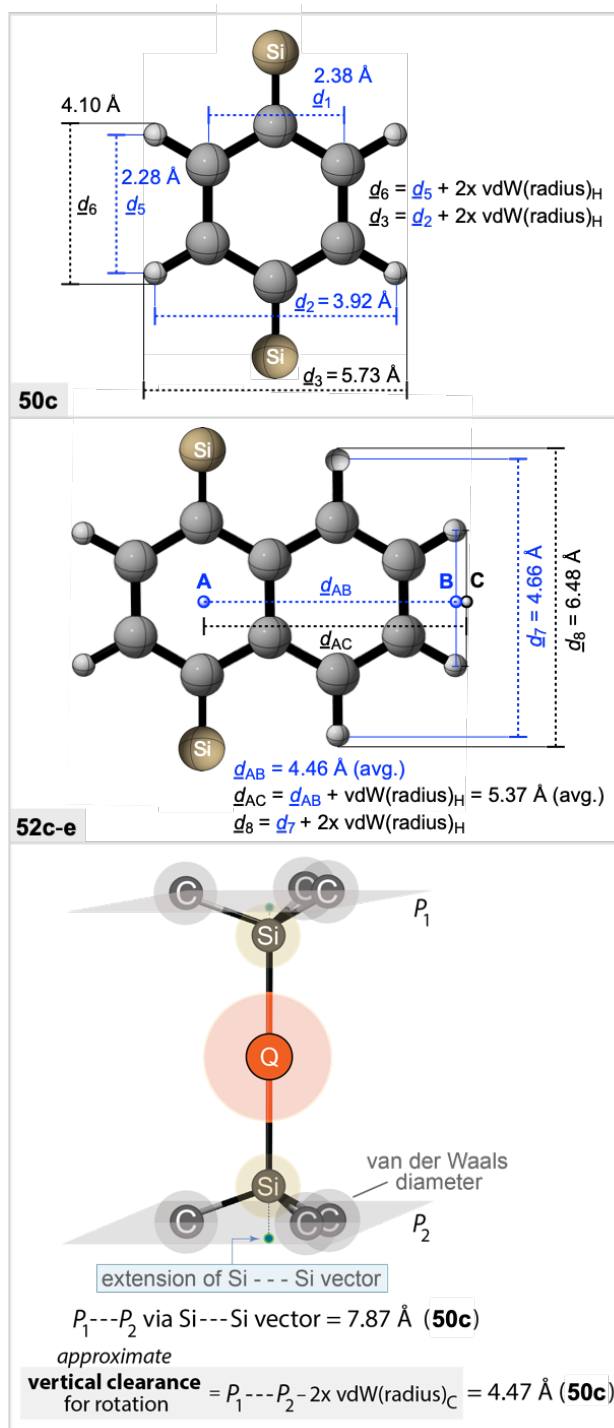


Figure 2.32 Geometric relationships involving the rotators and stators in the *p*-phenylene and 1,4-naphthalenediyl adducts **50c** and **52c-e**. In the five compounds **52c-e**, the distances d_{AB} and d_{AC} range from 4.43 to 4.48 Å and 5.34 to 5.39 Å, respectively.

2.7.2. Dynamic properties in solution

For several of his compounds, Setaka has probed the barriers to rotator rotation in solution by variable temperature NMR. Consider first the *p*-phenylene adduct **50c**, which features fourteen methylene groups in each spoke connecting the bridgehead silicon atoms. Given the symmetry and the analysis in Figure 2.22 (middle panel), two sets of $^{13}\text{C}\{^1\text{H}\}$ NMR signals would be expected (ca. 2:1 area ratio). However, only a single set is observed in CDCl_3 at ambient probe temperature, indicative of rapid rotation on the NMR time scale.¹²³

Such phenomena can be qualitatively analyzed in a manner analogous to Figure 2.24. However, one difference is that for most *p*-arylene rotators, the atoms that must pass through the macrocycles, for example, the $\text{HC}\cdots\text{CH}$ units derived from *ortho* carbon and hydrogen atoms of *p*-phenylene, are no longer in the equatorial plane. In any case, the crystal structure of **50c** provides important reference points. Several views of the lowest temperature modification are depicted in Figure 2.31 (the rotator is disordered in higher temperature modifications).

Table 2.3 Data for the reactions represented in Figure 2.27.

Q _y	E	n	product type LI	yield (%) ^a	product type LII	yield (%) ^a	ref
Q ₁	Si	12	50b	<i>b</i>	50b'	<i>b</i>	129
Q ₁	Si	14	50c	24	50c'	—	123,125,129
Q ₁	Si	16	50d	10	50d'	43	129
Q ₁	Si	18	50e	23 ^c	50e'	39	127,129
Q ₁	Ge	14	51c	24	51c'	8	128
Q ₂	Si	14	52c	29	52c'	27	126,131
Q ₂	Si	15	52cd	14	52cd'	29	131
Q ₂	Si	16	52d	7	52d'	32	126,131
Q ₂	Si	17	52de	13	52de'	28	131
Q ₂	Si	18	52e	18	52e'	15	126,131
Q ₃	Si	14	53c	7	53c'	—	123
Q ₄	Si	14	54c	5	54c'	2	138
Q ₄	Si	16	54d	4	54d'	19	132
Q ₅	Si	14	55c	25	55c'	2	124
Q ₅	Si	16	55d	15	55d'	24	132
Q ₅	Si	17	55de	17	55de'	18	135
Q ₆	Si	16	56d	18	56d'	38	132
Q ₇	Si	16	57d	66	57d'	—	135
Q ₇	Si	17	57de	60 ^d	57de'	—	135
Q ₈	Si	18	58e	3	58e'	45	133
Q ₉	Si	18	59e	5	59e'	51	130
Q ₁₀	Si	14	60c	8	60c'	19	134
Q ₁₀	Si	16	60d	12	60d'	44	134
Q ₁₀	Si	18	60e	15	60e'	17	134
Q ₁₀	Si	22	60g	12	60g'	15	134
Q ₁₁	Si	18	61e	5	61e'	46	136
Q ₁₁	Si	22	61g	9	61g'	28	136
Q ₁₂	Si	18	62e	<i>e</i>	62e'	<i>e</i>	136
Q ₁₂	Si	22	62g	<i>e</i>	62g'	<i>e</i>	136
Q ₁₃	Si	18	63e	3	63e'	34	137

^a Isolated yields following metathesis and hydrogenation. ^b No disilicon products could be detected. ^c The highest yield among several conditions screened. ^d This yield is for the oxidation of **55de** using *m*-CPBA. ^e Due to the short half-life of these radical species, yields could not be established.

In **50c**, the average distance between the *ortho* carbon atoms on opposite sides of the rotator axis is 2.38 Å, and that for the corresponding hydrogen atoms is 3.92 Å. These relationships are depicted in Figure 2.32 (top; d_1 and d_2). When twice the van der Waals radius of a hydrogen atom is added, a wingspan of 5.73 Å (d_3) is obtained. This is halved to obtain the corresponding radius or "horizontal steric demand", 2.87 Å. For reference, the radius is much shorter than that of the iron or osmium rotator in the trigonal bipyramidal complexes in Table 2.2 (4.38-4.59 Å).

In the vertical dimension, the average distance between the two pairs of HC...CH hydrogen atoms is 2.28 Å (d_5), as shown in Figure 2.32 (top). When twice the van der Waals radius of a hydrogen atom is added, a "vertical steric demand" of 4.10 Å is obtained (d_6).

As in Figure 2.24, the horizontal and vertical "clearance" afforded by the stator is estimated from the crystal structure (Figure 2.31). For the former, the distance from the centroid of the *p*-phenylene ring to the two innermost CH₂ groups of each (CH₂)_{*n*} bridge [here (CH₂)₁₄] is calculated, and the van der Waals radius of carbon is subtracted. The shortest of the six resulting distances is then used as the most conservative estimate, which for **50c** is 4.74 Å as compared to an average of 5.42 Å. Thus, the radius of the *p*-phenylene rotator can be comfortably accommodated within the spokes of the stator (2.87 Å vs. 4.74 Å), as would be intuitively expected by viewing the crystal structure. As noted above, there are several alternative approaches to estimating horizontal clearances, but since all are intrinsically qualitative, the authors stick with Figure 2.24.

For the vertical clearance, it is a simple matter to define the two planes that contain the three Si(CH₂)₃ carbon atoms bound to each terminus of the rotator (Figure 2.32, bottom; *cf.* Figure 2.24, right). When these are not parallel, the plane/plane distance that runs through the silicon-silicon vector is calculated (7.87 Å). The van der Waals radii of two carbon atoms are then subtracted. For **50c**, the clearance so obtained (4.47 Å) is greater than the vertical steric demand of the *p*-phenylene rotator computed in Figure 2.32 (4.10 Å). Hence, in **50c** the rotator/stator steric interactions are greatly attenuated relative to the metal diphosphine complexes with (CH₂)₁₄ bridges in section 2.6. For comparison, the distance between the two E(CH₂)₃ planes of the analogous Fe(CO)₃ adduct **17c** is 6.00 Å versus 7.87 Å for **50c**.

In a tour-de-force, Setaka was able to synthesize and crystallographically characterize five dibridgehead disilicon compounds with 1,4-naphthalenediyl rotators and progressively longer (CH₂)_{*n*} bridges (*n* = 14, **52c**; 15, **52cd**; 16, **52d**; 17, **52de**; 18, **52e**).^{126,131} The structures of the compounds with bridges where *n* is an even number are shown in Figure 2.33. This rotator is much more sterically demanding than *p*-phenylene in both the horizontal and vertical dimensions.

To estimate the radius or horizontal steric demand, the centroid of the C₆H₂ ring that spans the bridgehead silicon atoms is first defined. As shown in Figure 2.32, the distance to the midpoint between the two remote hydrogen atoms of the C₆H₄ ring is then calculated. The van der Waals radius of a hydrogen atom is subsequently added to

give the radius of the rotator (d_{AC}). As would be expected, very similar quantities are obtained for each compound (5.34-5.39 Å; average 5.37 Å).

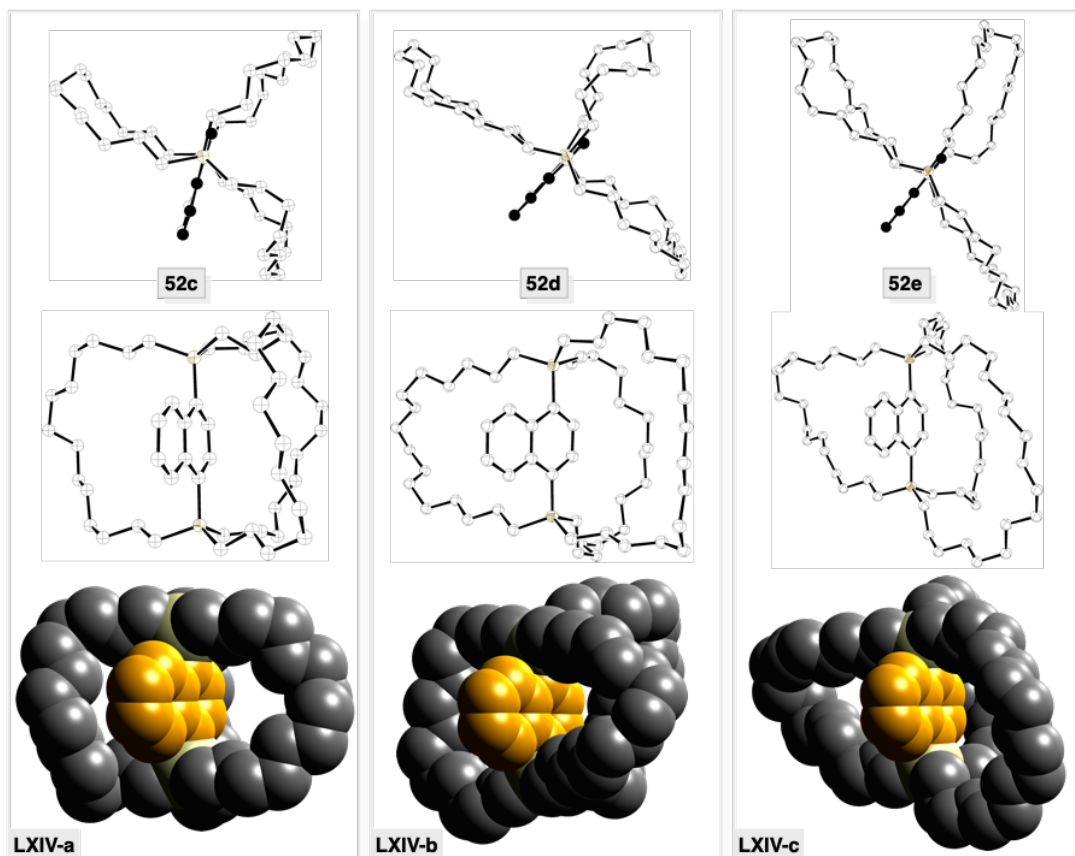


Figure 2.33 ORTEP and space filling representations of the crystal structures of **52c-e**.

The horizontal clearance associated with the stators is calculated as with **50c**, except that for **52cd** and **52de** (for which n in $(CH_2)_n$ is odd), the distances from the centroid of the C_6H_2 ring to a total of nine CH_2 groups (the three innermost of each bridge) are considered. After subtracting the van der Waals radius of a carbon atom, the shortest and average clearances are as follows: **52c**, 4.38/5.22 Å; **52cd**, 4.33/5.77 Å;

52d, 5.39/6.43 Å; **52de**, 5.39/6.40 Å; **52e** 6.42/7.33 Å. With the three largest macrocycles, the values exceed the radius of the 1,4-naphthalenediyl moiety (5.34-5.39 Å), auspicious for rotation.

For the vertical steric demand, the distances between the *para* hydrogen atoms of the C₆H₄ rings are first calculated (4.66 Å). As depicted in Figure 2.32 (middle), the van der Waals radii of two hydrogen atoms are then added, giving 6.48 Å (*d*₇). The vertical clearances, calculated from the planes of the Si(CH₂)₃ carbon atoms as described for **50c** in Figure 2.32, average 4.57 Å (**50c**, 4.55 Å; **52cd**, 4.70 Å; **52d**, 4.53 Å; **52de**, 4.52 Å; **52de**, 4.55 Å). These values are significantly lower than the 6.48 Å vertical steric demand, impeding rotation.

Thus, rotation of the rotators will need to be correlated to conformational changes in the macrocycles that "open up" the vertical dimension. The crystal structures in Figure 2.33 allow one possible modus to be visualized. In **52c**, all six of the C_{*ipso*}-Si-CH₂-CH₂ linkages adopt gauche conformations. However, in **52e** there are two anti C_{*ipso*}-Si-CH₂-CH₂ linkages (one at each terminus), presumably facilitated by the longer methylene chain. The *anti* disposition widens the vertical dimension of the "hole" in the macrocycle.

Variable temperature NMR spectra of **52c**, **52cd**, **52d**, **52de**, and **52e** give results consistent with the preceding analyses. In the case of **52c**, ¹³C{¹H} NMR spectra show two sets of Si(CH₂)₁₄Si signals (ca. 2:1 area ratios) in toluene-*d*₈, both at ambient probe temperatures and upon heating to 340 K.¹³¹ These data allow a lower limit of 15.4

kcal/mol to be set for $\Delta G_{340\text{K}}^\ddagger$ (calculated by the present authors from two non-coalescing SiCH₂ signals with a frequency difference of 202 Hz), as indicated in Table 2.4.

In the case of **52d**, the longer methylene chains allow the coalescence of ¹³C NMR signals to be observed (260-280 K), as shown in Figure 2.34.¹²⁶ The data give ΔH^\ddagger and ΔS^\ddagger values of 9.42 kcal/mol and -12.0 eu, respectively, as noted in Table 2.4. In the case of **52e**, the slow exchange limit cannot be realized, even at 220 K. However, when toluene-*d*₈ solutions of the compound with an intermediate methylene chain length, **52de**, are cooled, decoalescence can be observed (230 K). The data give ΔH^\ddagger and ΔS^\ddagger values of 7.49 kcal/mol and -11.0 eu, respectively. Finally, **52cd** has been studied by ¹³C-¹³C EXSY, a technique that allows dynamic processes with a broader range of time scales to be characterized. The data give ΔH^\ddagger and ΔS^\ddagger values of 14.6 kcal/mol and -11.9 eu, respectively.

The activation parameter trends in Table 2.4 reflect the increasing abilities of the longer methylene chains to "open up" in the horizontal and vertical dimensions to accommodate the 1,4-naphthalenediyl rotators. In this context, an interesting feature can be seen in the top views of the crystal structures in Figure 2.33 (also with **52cd** and **52de**, which are not depicted). Namely, the rotators adopt conformations that maximize the distance of the sterically demanding C₆H₄ ring from the two nearest macrocycles. This has the consequence of positioning the C₆H₂ ring within the cavity of the remaining macrocycle. Such eclipsing interactions are rarely observed in the crystal structures of

the many other dibridgehead diheteroatom rotors in this review. Interestingly, there are intermolecular π -stacking interactions between rotators in crystalline **52c**, **52d**, and **52e**, but not in **52cd** or **52de**.

Setaka has similarly studied a second series of compounds, this time varying the rotators. As shown in Figure 2.30 above, the *p*-phenylene, 2,3-difluoro-*p*-phenylene, and 2,3-dichloro-*p*-phenylene adducts **64-66** feature silicon atoms that are spanned by 13 atom bridges, each with four SiMe₂ groups. The additional methyl groups render the steric topology of these compounds much different from those discussed above. Thus, analyses of "clearances" and related properties are not attempted. Some views of the crystal structure of the dichloro species **66** are given in Figure 2.35.¹⁴⁰ The top representation shows that the rotator adopts a conformation that maximizes the distance the ClC...CCl moiety from the nearest macrocycles. In a phenomenon similar to that seen in Figure 2.33, this directs the smaller HC...CH moiety into a macrocycle cavity.

When NMR spectra of the *p*-phenylene compound **64** or difluoro analog **65** are recorded at 173-175 K in CDCl₃, only a single set of signals is observed. However, for the dichloro analog **66**, the SiMe₂ ¹H NMR signals decoalesce upon cooling as shown in Figure 2.36. Line shape analyses and application of a three-site exchange model give ΔH^\ddagger and ΔS^\ddagger values of 12.8 kcal/mol and -4.6 eu, respectively.^{139,140} The radii of the rotators in this series of compounds increase from 2.87 Å (**64**) to 3.84 Å (**65**, approximated from 1,2-difluorobenzene)¹⁵⁴ to 4.47 Å (**66**). A computational study of **64** suggests a miniscule barrier of 1.2 kcal/mol.¹⁵⁵

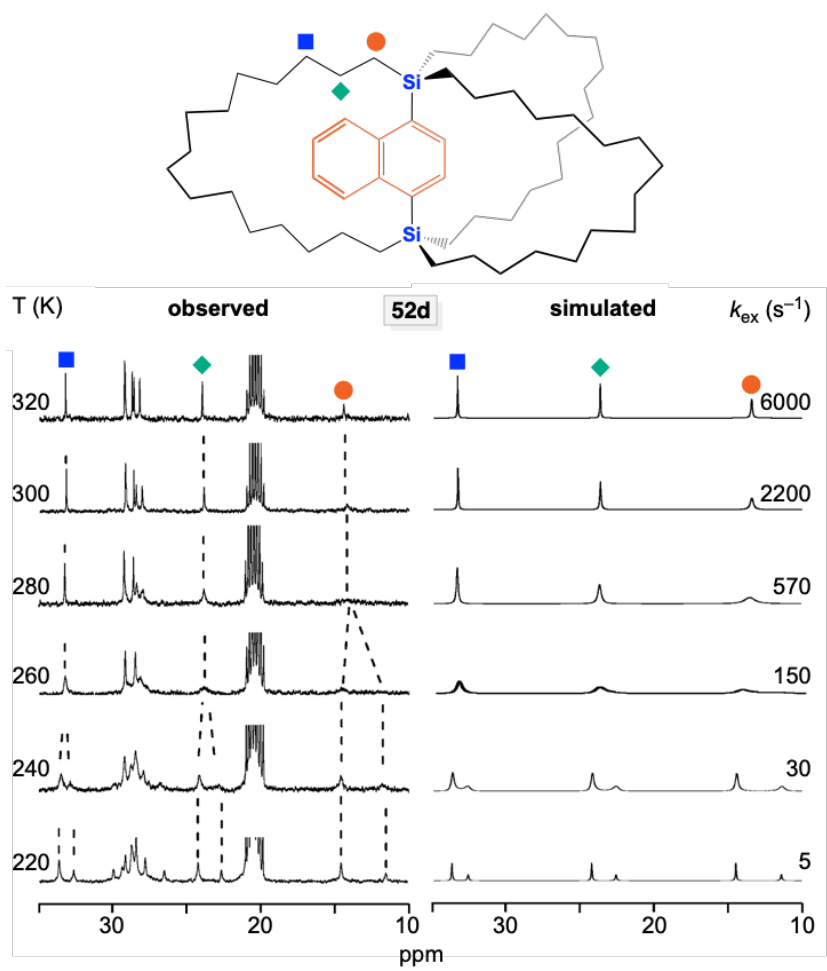


Figure 2.34 Temperature dependence of inverse gated decoupled ¹³C NMR spectra of **52d** in toluene-*d*₈ (left) and simulated spectra (right, key signals only).¹²⁶

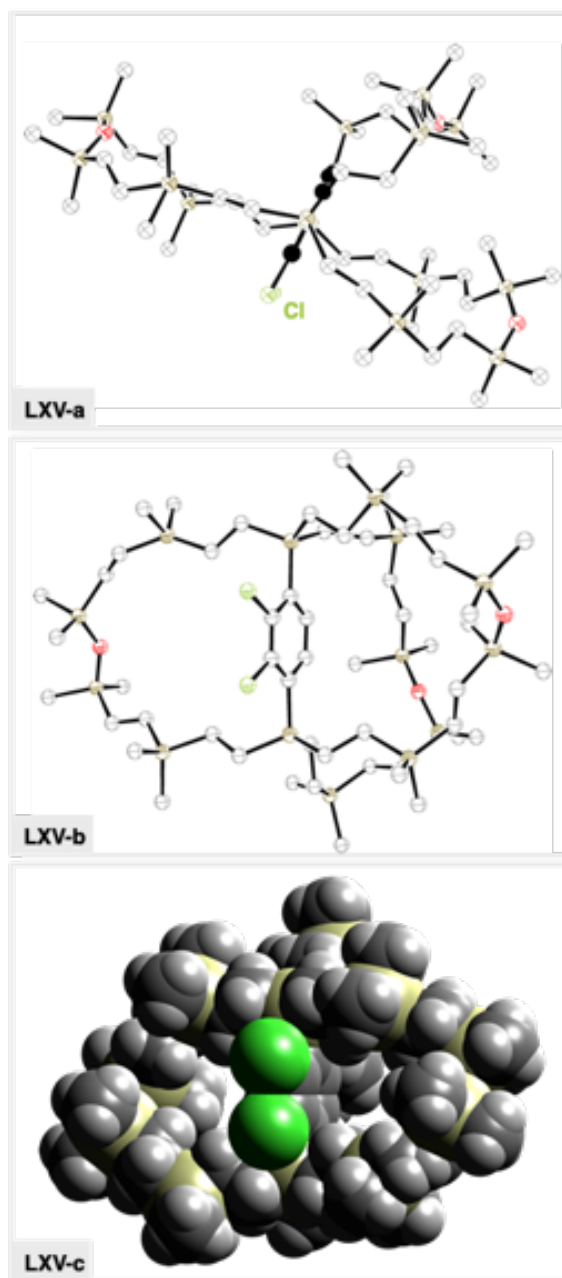


Figure 2.35 ORTEP and space filling representations of the crystal structure of the 2,3-dichloro-*p*-phenylene adduct **66** (see Figure 2.30).¹⁴⁰

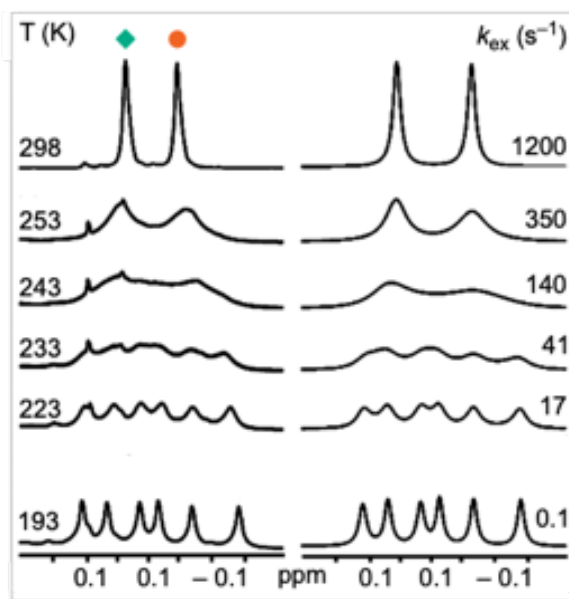
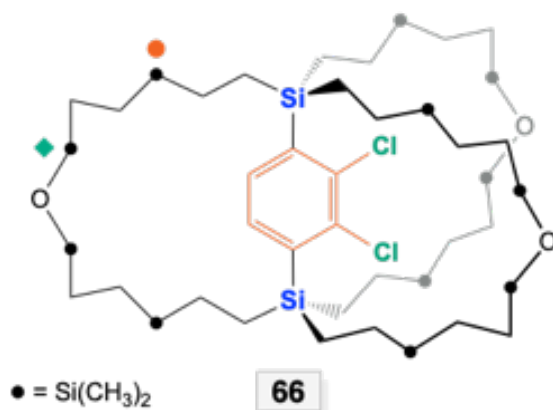


Figure 2.36 Variable temperature ¹H NMR spectra of **66** (SiMe₂ region): left, observed spectra; right, simulated spectra with rate constants for exchange.¹⁴⁰

Table 2.4 Activation parameters for rotation of 1,4-naphthalenediyl rotators in toluene-*d*₈.

compound	<i>n</i>	experiment	ΔH^\ddagger (kcal mol ⁻¹)	ΔS^\ddagger (eu) ^a	ΔG^\ddagger_{340K} (kcal mol ⁻¹)	ref
52c	14	¹³ C NMR	>14.6 ^b	—	>15.4 ^c	126,131
52cd	15	¹³ C- ¹³ C EXSY NMR	14.6 ^d	-11.9 ^d	17.0	131
52d	16	¹³ C NMR (220-320 K)	9.42	-12.0	11.8	126,131
52de	17	¹³ C NMR (210-270 K)	7.49	-11.0	9.7	131
52e	18	estimate based on 52d	<7.46 ^b	—	—	126,131

^a Units of cal·mol⁻¹·K⁻¹. ^b Estimated as described in the reference cited. ^c Limit calculated as described in the text. The highest yield among several conditions screened. ^d These values were assigned appreciable error limits.

2.7.3. Dynamic properties in the solid state

The Setaka group has also probed the rotation of the rotators of many of the preceding compounds in the solid state. There are several variable temperature solid-state NMR methods that are widely applicable to the investigation of molecular dynamics within crystals, as reviewed by Garcia-Garibay, who first applied these techniques to gyroscope-like molecules.³⁵ In the Setaka group, the workhorse has been quadrupolar echo solid state ^2H NMR, which requires that the motional units be labeled with deuterium atoms. Most researchers concerned with dynamics in crystals express barriers as E_a values (from Arrhenius plots), as opposed to ΔH^\ddagger or ΔG^\ddagger values (from Eyring plots). It is also common to speak of a group "flipping" as opposed to undergoing rotation.

As in section 2.7.2, the *p*-phenylene adduct **50c** provides a logical starting point. This compound crystallizes with all rotator axes (Si-*p*-C₆H₄-Si) parallel, and the C₆D₄ analog (**50c-d₄**) has been similarly synthesized.¹²³ When the entire crystal lattice is considered, the two DC...CD linkages occupy inequivalent sites (although the environments appear similar when a single molecule is viewed, as in Figure 2.31). Variable temperature quadrupolar echo ^2H NMR spectra give the Pake patterns depicted in Figure 2.37. Simulation of the line shapes for the data at 230-260 °C give rate constants that are used in an Arrhenius plot, affording an E_a of 10.3 kcal/mol for "flipping" the C₆D₄ moiety by 180°.

Above 270 °C, the narrower line widths indicate an additional oscillatory or librational degree of freedom. This is substantiated by crystal structures over a parallel temperature range, which reveals increased anisotropic thermal parameters followed by structural disorder. A reduced E_a of 9.0 kcal/mol could be computed from the data. Setaka also documented the temperature dependent birefringence of the crystals, a property exhibited by several other compounds below.

The analogous species with a dideuterated *p*-xylene based rotator (**53c-d₂**; see Figure 2.37) has been similarly studied. Although the radius of this rotator is significantly greater than that of *p*-phenylene (4.25 Å vs. 2.87 Å), the crystal structures and lattices of the two compounds (as their non-deuterated analogs) are similar. As noted in section 2.7.2, a conservative estimate of the horizontal clearance in crystalline **50c** is 4.74 Å. However, the ²H NMR data indicate that the rotator in **53c-d₂** is static within the crystal.

The digermanium analog of **50c-d₄**, **51c-d₄**, has also been synthesized.¹²⁸ Again, the molecular structures and crystal lattices (of the non-deuterated counterparts) are virtually identical. As expected, the Ge-C_{ipso} bond is longer than the Si-C_{ipso} bond (1.958(4) Å vs. 1.885(4) Å, or 3-4%). Consistent with the vertically more spacious stator, the E_a for C₆D₄ rotation associated with the higher temperature dynamic regime decreases to 8.0 kcal/mol from 9.0 kcal/mol. In another follow up to the NMR study of **50c-d₄**, Setaka examined the analog in which the saturated (CH₂)₁₄ bridges were replaced by monoolefinic (*E*)-(CH₂)₆CH=CH(CH₂)₆ bridges (**50c^{*}-d₄**).¹²⁵ The parent

compound **50c**^{*} (see Figure 2.38) proved isolable in 24% yield when the sequence in Figure 2.27 was worked up after olefin metathesis but prior to hydrogenation. It also crystallized with parallel rotator axes. In any case, ²H NMR experiments (**50c**^{*}-*d*₄, 280-300 K) established an E_a of 11.4 kcal/mol for a 180° flip of the rotator. The increase over that of **50c**-*d*₄ (10.3 kcal/mol under comparable conditions) was attributed to steric constraints imposed by the (*E*)-C=C linkages.

As with **50c**-*d*₄, a higher temperature dynamic regime (>300 K) distinguished by narrower line widths was also characterized. These data could be simulated by a six-site exchange model with the *p*-phenylene moiety populating three minima spaced by 120° about the rotator axis. The barrier dramatically decreased, and to help gain insight, crystal structures of **50c**^{*} were determined at a series of temperatures. As shown in Figure 2.38, between 300 and 340 K the rotator became disordered over three positions (differing by 120° about the rotator axis; occupancies 0.24, 0.63, 0.29). In addition, the macrocycle conformations became more spherical or "horizontally extended". This could potentially be quantified in a number of ways, but only the data set collected at 100 K has been made available in the CCDC. These distortions were proposed to account for the faster *p*-phenylene rotation and provide a welcome "snapshot" of the "correlated conformational changes" frequently invoked above during rotator rotation.

The expansions of the macrocycles were also reflected in the unit cell dimensions, which were determined at closely spaced temperature intervals. All of these

phenomena remained fully reversible below 355 K. Setaka likened the overall changes in macrocycle conformations to the inflation and deflation of a balloon.

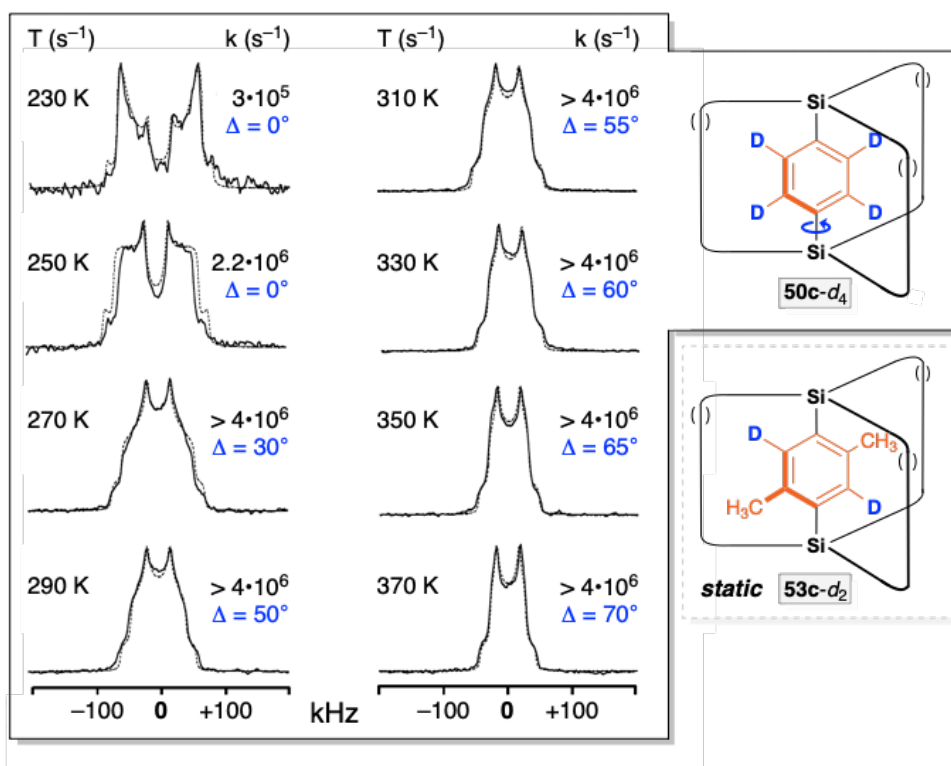


Figure 2.37 Variable temperature solid-state quadrupolar echo 2H NMR spectra of $50c-d_4$ showing characteristic Pake patterns. () indicates $(CH_2)_n$.¹²³

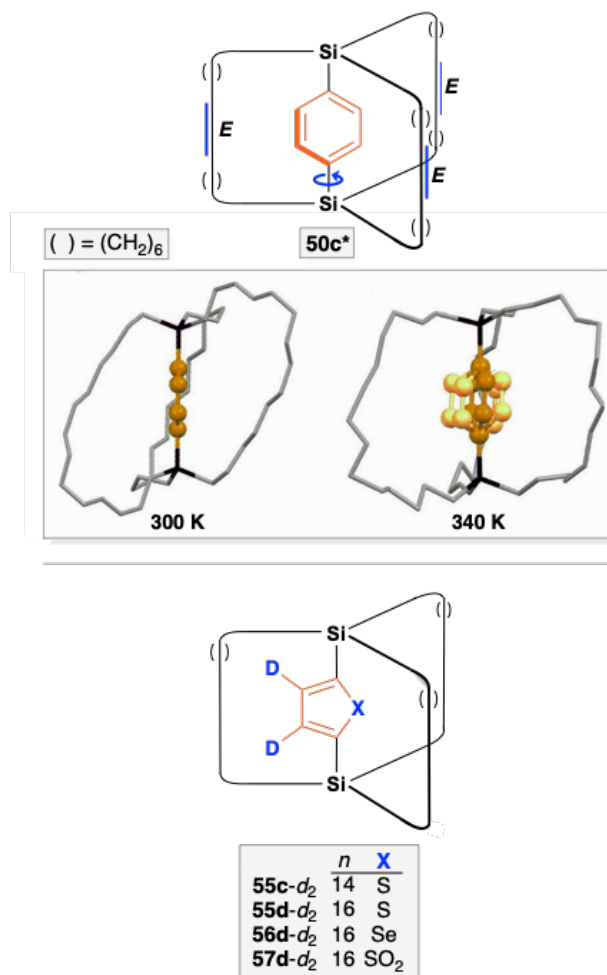


Figure 2.38 *p*-Phenylene adduct **50c*** (top), crystal structures at 300 and 340 K, with the latter showing *p*-C₆H₄ disorder (middle), and heterocycle adducts studied by solid state ²H NMR (bottom, () indicates (CH₂)_{*n*}).¹²⁵

Various compounds with heterocyclic rotators and saturated (CH₂)_{*n*} bridges have also been studied by Setaka. For example, crystal structures of the dipolar 2,5-thiophenediyl rotor **55c** (see *d*₂ analog, Figure 2.38, bottom)¹²⁴ have been determined at a series of temperatures. Again, all rotator axes are parallel in the lattice. At 200 K, the rotators exhibit two orientations such that the molecular dipoles cancel. At 270 K, a different modification with two alternative dipole orientations is obtained, but the

dipoles again cancel. At 300 K, a third modification is obtained in which the dipoles are randomly distributed between two orientations but with an overall 50:50 population. A number of ^2H NMR experiments have been carried out with **55c-d₂**. The thiophenediyl rotator is static in the low temperature crystalline form but undergoes slow and fast exchange in the higher temperature crystalline forms. However, it is not possible to obtain quantitative activation energies.

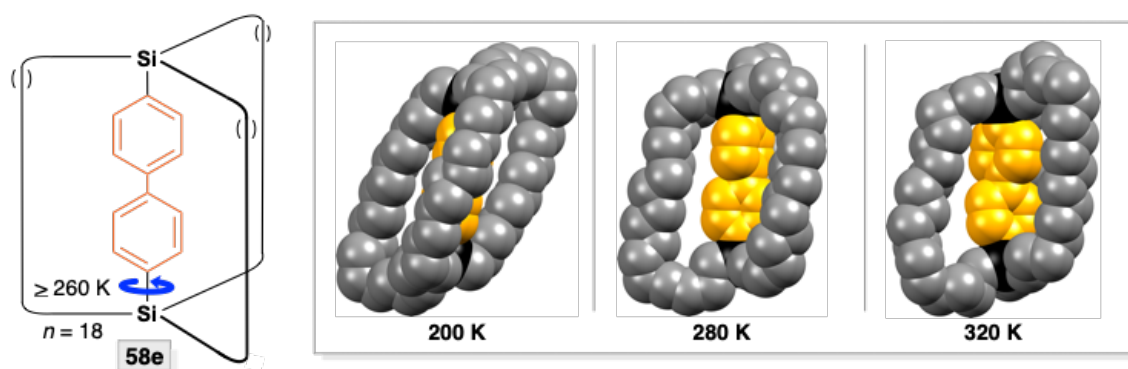


Figure 2.39 4,4'-Biphenylene adduct **58e** (□ indicates $(\text{CH}_2)_n$), and space filling representations of the crystal structures at 200 K (left), 280 K (center), and 320 K (right).

Setaka has also expanded this effort to the higher $(\text{CH}_2)_{16}$ homolog of **55c-d₂**, namely, **55d-d₂**¹³² and the corresponding 2,5-selenophenediyl species **56d-d₂** in Figure 2.38.¹³² Again, the non-deuterated analogs crystallize with parallel rotator axes. Once more, technical issues render quantitative activation energies elusive, but it is possible to establish a lower rotational barrier for the selenium compound. This counterintuitive result has been rationalized based upon subtle effects derived from Si-C(aryl) bonds, leading to a greater silicon-silicon separation in **56d** (6.31 Å vs. 6.09 Å at 200 K).

However, it has proven possible to obtain E_a values for rotation of the heterocyclic rotator in the analogous 2,5-thiophene(dioxide)diyl species **57d**- d_n .¹³⁵ That determined by ^2H NMR is 9.0 kcal/mol, and that measured by dielectric spectroscopy is 9.1 kcal/mol. It seems likely that the barriers in the thiophenediyl analog **55d** would be lower. Interestingly, **57d** also crystallizes with parallel rotator axes.

The compound **58e** shown in Figure 2.39 features a 4,4'-biphenylene (*p*-C₆H₄-*p*-C₆H₄) rotator, which is among the longest studied by Setaka (see Figure 2.27).¹³³ Extended (CH₂)₁₈ chains are required to bridge the silicon atoms. Three crystalline phases could be characterized (Figure 2.39), all with parallel rotator axes and silicon-silicon distances of 10.68 Å, 10.88 Å, and 10.87 Å. The angles defined by the planes of the C₆H₄ rings increase from 42° in the lowest temperature modification to 66° in the higher temperature forms.

A variety of ^2H NMR experiments have been carried out with **58e**- d_4 . The rotators in the lowest temperature modification are static at 220 K, but "flipping" can be detected at 260 K. In the higher temperature modifications, the macrocycles adopt more spherical (less ovoid) conformations, although not to the extent in Figure 2.38, and rotation becomes immeasurably fast. Interestingly, the data require that only one type of rotation is operational, either (1) synchronous rotation of the two *p*-phenylene moieties or (2) independent (asynchronous) rotation, but not both.

Finally, there have been some attempts to model the rotational dynamics of selected disilicon compounds by computational methods (**50c,d,e**;¹²⁹ **64**¹⁵⁵). These

initial efforts have been able to reproduce certain features in a qualitative sense (e.g. conformational energy minima), but have not given quantitatively reliable data. As noted above, the barrier computed for **64** is a very low 1.2 kcal/mol.

2.7.4. Toward molecular gyroscopes

Despite the steric interactions that attend rotation of the rotators in many of the above disilicon (and digermanium) compounds, there are also species that seemingly lack significant steric contacts (e.g. **50c**). Furthermore, most compounds crystallize in motifs with all rotator axes parallel, and dipolar rotators are easily accommodated. As such, this remains a very promising class of compounds for engineering very small barriers to rotator rotation, and application as molecular gyroscopes. Setaka's compounds also seem to be particularly prone to phase transitions in the solid state, affording multiple allotropes for study.

2.8. Systems from the Garcia-Garibay group

2.8.1. Prefatory comments

It hardly seems fitting that studies by the Garcia-Garibay group, which is responsible for so much intellectual and experimental leadership regarding molecular gyroscopes, are not treated in the leadoff section. Nonetheless, from a narrative standpoint it seemed more natural to transition from groups that have emphasized solution phase investigations to those that have emphasized solid phase investigations. Garcia-Garibay has also introduced the allied concept of "molecular compasses", in which dipolar rotators are oriented by static electric fields.¹⁵⁶⁻¹⁶⁰ Unsurprisingly, he has reviewed some aspects of his work himself.³⁴⁻³⁷

The broad interests of the Garcia-Garibay group in molecular rotors and amphidynamic crystals present some complications. Some of these studies directly target molecular gyroscopes and others less so, although there remains an obvious relevance. Thus, most of the groups' work involving molecular rotors has been covered but with a few exclusions: (1) rotors that feature large biomolecules such as steroids as stators¹⁶¹⁻¹⁶⁷ are not treated, as these have generally been prepared with goals other than molecular devices in mind, (2) rotors that are restricted to crankshaft type motions¹⁶⁸ or are comprised of multiple nonparallel rotators^{169,170} are likewise not treated.

Several design elements helped to drive these studies. In general, a svelte rotator with rod-like segments is paired with a bulky stator, usually in the form of two endgroups with appreciable radial extensions. The hope, aided by design elements familiar in crystal engineering, such as the "sextuple phenyl embrace",^{171,172} is that the molecule will crystallize in a motif with all rotator axes parallel. It is furthermore hoped that the endgroups will enforce spacings between the axes that allow for facile rotation of the rotators in the solid state. One optimistic scenario is shown in **C** in Figure 2.40. However, as illustrated in **CI**, packing motifs remain in which the stator can sterically interact with the rotator of a neighboring molecule. This can be ameliorated by stators with enhanced shielding capabilities, as illustrated in **CII**.

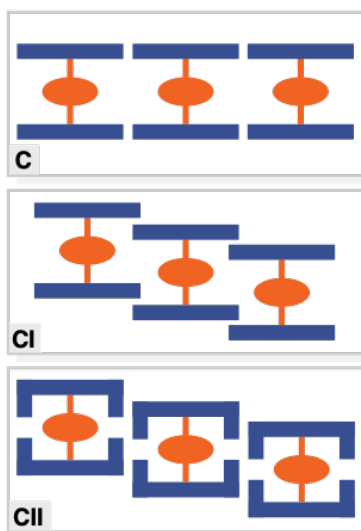


Figure 2.40 Combinations of different types of radially bulky stators (blue) and low-volume-demand rotators (orange) and possible packing motifs.

Said differently, the objective is the creation of "free space" about a rotator with a "low volume demand". As this work has progressed, additional concepts such as "packing coefficients" (C_k : the van der Waals volumes of all molecules in the unit cell divided by the unit cell volume, typically 0.80-0.65 for organic molecules)¹⁷³ and "crystal fluidity" (the ability of the rotator surroundings to distort, creating transient cavities),³⁷ have been introduced. To fast-forward to where this line of inquiry winds up today, Garcia-Garibay concludes that the creation of free space alone does not always result in ultrafast dynamics.³⁷ In closed packed crystals (low free volumes), dynamics can also be rapid, but this requires substantial crystal fluidity.

One "wild card" in crystal engineering is the potential for solvent to occupy void spaces, so special attention must be paid to the composition of any crystal studied. Apropos to their chemical heritages, the authors refer to these as solvates, whereas Garcia-Garibay employs the more general term clathrates. Furthermore, polymorphism

or pseudopolymorphism¹⁷⁴ can be observed, as seen in section 2.7 with a number of Setaka's molecular rotors.

As noted above, Garcia-Garibay has reviewed the NMR methods that are most widely applied to the study of molecular dynamics within crystals.³⁵ He most frequently employs variable temperature solid-state ^{13}C CP/MAS NMR (cross-polarization/magic angle spinning) and quadrupolar echo ^2H NMR. Error limits are not quoted in the text for the resulting Arrhenius activation energies (E_a), but when these have been reported, they are incorporated into tabular summaries herein. The Arrhenius pre-exponential factors are also tabulated.

Well over half of the rotators studied by Garcia-Garibay incorporate $-\text{C}\equiv\text{C}-(p\text{-arylene})-\text{C}\equiv\text{C}-$ linkages. The individual sp carbon atoms are presumed to undergo barrierless rotation. In the case of p -phenylene, the distance between the $\text{C}_{sp}/\text{C}_{sp}$ or $-\text{C}\equiv\text{C}-(p\text{-C}_6\text{H}_4)-\text{C}\equiv\text{C}-$ termini is typically 8.06 Å. Thus, Garcia-Garibay's rotators are generally much longer than those studied by Setaka or the authors. The distance between the $\text{C}_{sp2}/\text{C}_{sp2}$ termini of the 4,4'-biphenylene rotators in Setaka's compound **58e** (Figure 2.39) is 7.16-7.22 Å (depending upon modification).

Most of Garcia-Garibay's stators or endgroups feature C_3 symmetry axes. Many of the rotors used for solid state studies are assembled by similar sequences. Hence, to enhance continuity, their syntheses are grouped in a later section (section 2.8.4).

2.8.2. Rotors studied in solution

Garcia-Garibay has prepared a few molecular rotors with topologies evocative of those emphasized in the authors' and Setaka's groups, as opposed to the motifs depicted in Figure 2.40. These systems, **101** and **103** in Figure 2.41, consist of $\text{-C}\equiv\text{C-(}p\text{-C}_6\text{H}_4\text{)-C}\equiv\text{C-}$ rotators capped by two trityl-based endgroups.^{175,176} The endgroups are in turn connected, via one *meta* carbon atom of each aryl ring, by three ethereal spokes of the formulas $\text{O(CH}_2\text{)}_{10}\text{O}$ or $\text{OCH}_2\text{-(}p\text{-C}_6\text{H}_4\text{)-CO-(}p\text{-C}_6\text{H}_4\text{)CH}_2\text{O}$.

As shown in Figure 2.41, the best way to access **101** is from the tris(phenol) **100** via a three-fold intramolecular Williamson ether synthesis. Attempts to effect a six-fold variant from the hexaphenol **102** and the α,ω -dibromide $\text{Br(CH}_2\text{)}_{10}\text{Br}$ or a three-fold interligand ring closing metathesis/hydrogenation sequence starting from the hexaalkene **104**, give instead **105**, derived from an alternative ring closing mode. However, under high dilution conditions, the hexaphenol **102** condenses with the appropriate dibenzylic α,ω -dibromide to give the target rotor **103**. A number of related species have been prepared in which the trityl endgroups were spanned by a single bridge.^{175,176}

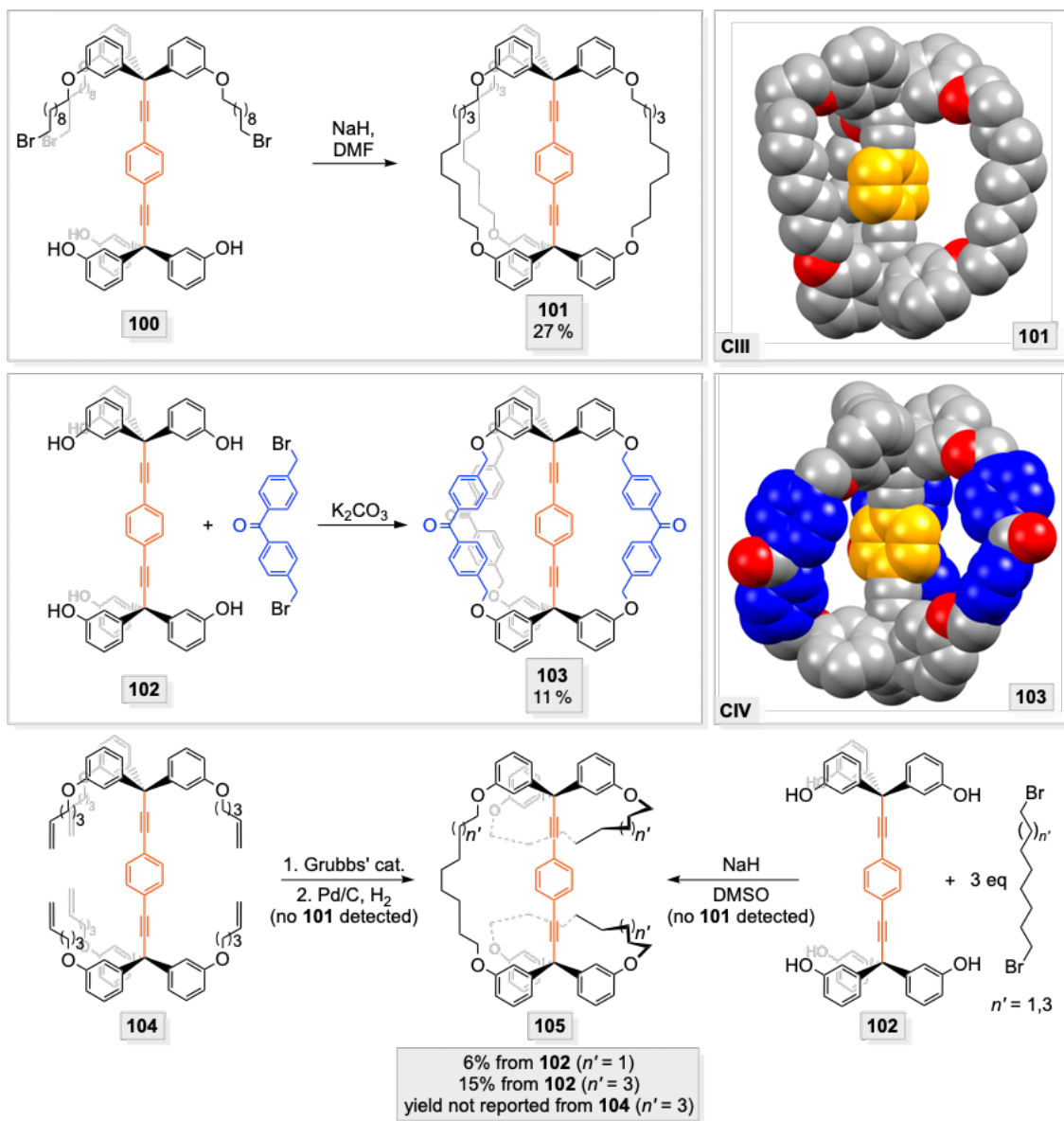


Figure 2.41 Synthetic approaches to gyroscope-like molecules **101** and **103** studied by Garcia-Garibay, and space filling representations of the molecular structures (with solvate molecules omitted, the rotor in **101** is disordered and only one conformation is depicted).

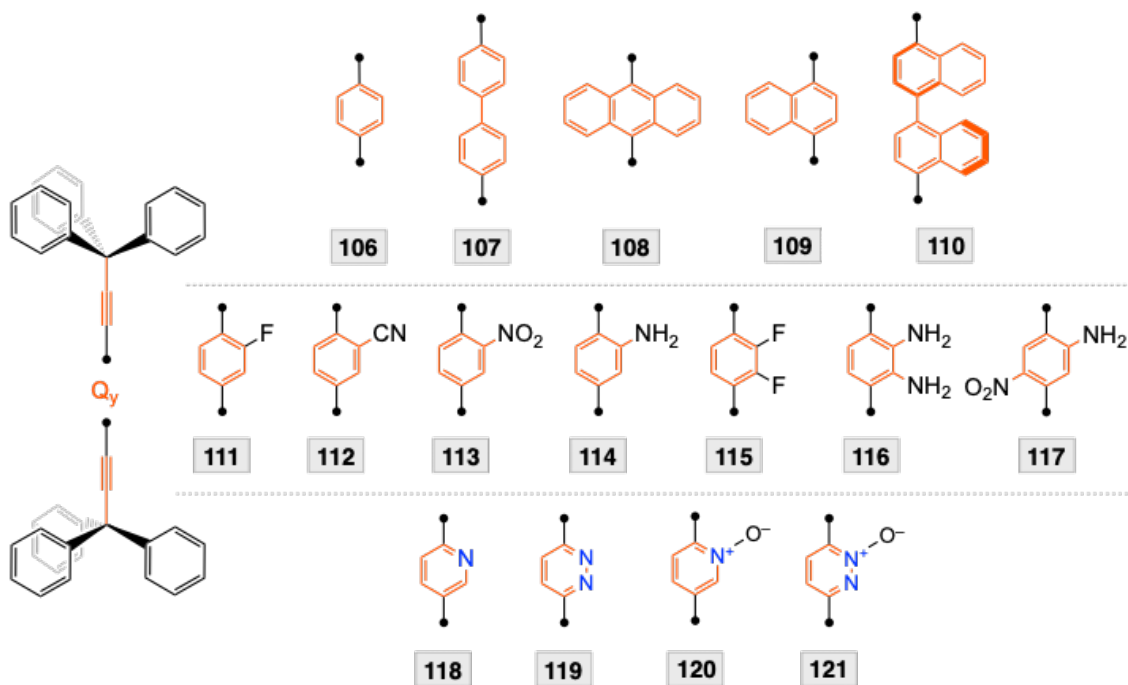


Figure 2.42 Molecular rotors consisting of $-\text{C}\equiv\text{C}-(p\text{-arylene})-\text{C}\equiv\text{C}-$ rotators and trityl stators studied by Garcia-Garibay.

The rotators in **101** and **103** rapidly rotate in solution on the NMR time scale, so no quantitative data are available for these systems. The crystal structures of solvates of **101** and **103** have been determined, and space-filling representations are provided in Figure 2.41 (**CIII**, **CIV**). In both cases, the interstices between the ethereal spokes are fully occupied by solvent molecules or the spokes of neighboring molecules. Due to the two $\text{C}\equiv\text{C}$ linkages in the rotators of **101** and **103**, the "vertical clearance" is much greater than those in the systems studied by the authors and Setaka. As analyzed in Figure 2.32 above, the *p*-phenylene moiety has a rather modest "horizontal steric demand" (2.87 Å radius). Thus, the low rotational barriers in solution are not surprising.

2.8.3. Rotors studied in the solid state

2.8.3.1. Rotors comprised of covalent bonds

Just as many of the molecular rotors studied by Setaka can be viewed as modifications of a benchmark compound with a *p*-phenylene rotator (**50c**, Figure 2.31 and Figure 2.32), many rotors studied by Garcia-Garibay can be formally derived from **106** (Figure 2.42).^{156,158,159,177,180,181} This relatively simple compound, which features a $\text{-C}\equiv\text{C-(}p\text{-C}_6\text{H}_4\text{)-C}\equiv\text{C-}$ rotator and two trityl stators, was first reported in 2002.¹⁵⁶ Compound **102** in Figure 2.41 represents a hexahydroxylated derivative. In any case, **106** has spawned the large family of *p*-arylene or arenediyl analogs shown in Figure 2.42.^{156,158,159,177,180,181}

Solvent free crystals of **106** could be grown from CH_2Cl_2 , and a benzene disolvate ($\text{106}\cdot 2\text{C}_6\text{H}_6$) was obtained from benzene.^{156,158} Their dynamic properties were probed by variable temperature ^{13}C CP/MAS NMR and quadrupolar echo solid state ^2H NMR. Per the measurements in section 2.7, the latter required the deuterated $\text{-C}\equiv\text{C-(}p\text{-C}_6\text{D}_4\text{)-C}\equiv\text{C-}$ analog (**106-d**₄).¹⁵⁸ A more extensively deuterated species with two $(\text{C}_6\text{D}_5)_3\text{C}$ endgroups (**106-d**₃₀) was prepared to remove interfering signals in the ^{13}C CP/MAS NMR measurements.¹⁷⁸ Since representative solid-state ^2H NMR spectra were depicted in Figure 2.37, partial ^{13}C CP/MAS NMR spectra of **106-d**₃₀ are shown in Figure 2.43. The two main signals at low temperature are due to the *p*-phenylene CH carbon atoms.

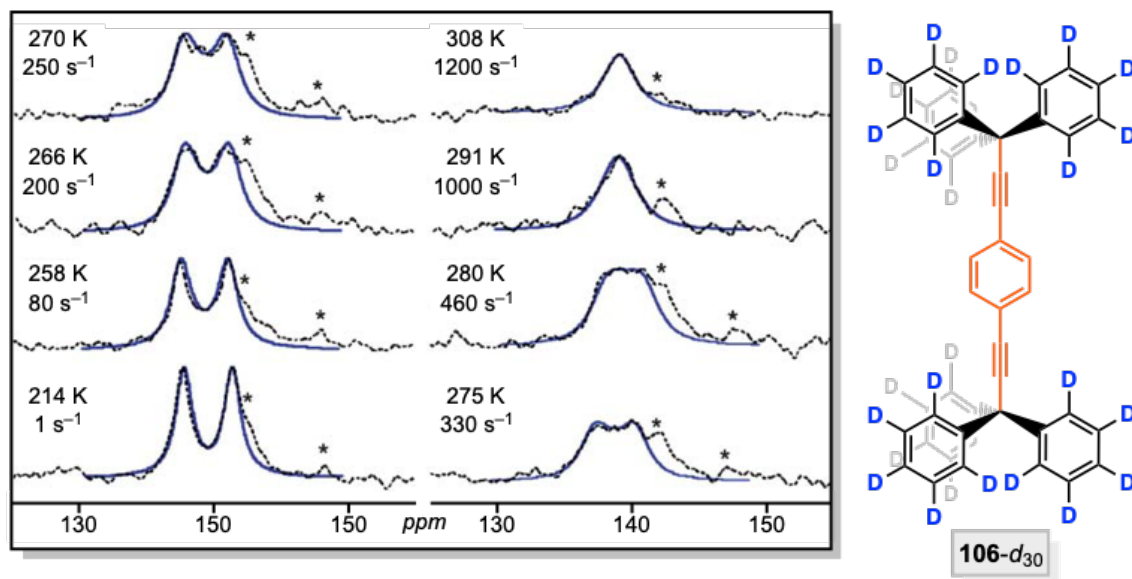


Figure 2.43 Variable temperature ^{13}C CP/MAS NMR spectra of **106-d₃₀** (*p*-phenylene CH signals) recorded with a contact time of $50\ \mu\text{s}$ (black traces) and simulations (blue traces).¹⁷⁸ The asterisks denote residual signals due to the *ipso* *p*-phenylene carbon atoms and one of the trityl carbon atoms.

The NMR experiments clearly established two-fold flipping of the $p\text{-C}_6\text{H}_4$ moiety. As summarized in Table 2.5, the data for solvent-free **106-d₄** gave an E_a of 14.6 kcal/mol, and that for solvent-free **106-d₃₀** gave (from rate constants derived from the simulated spectra in Figure 2.43) an E_a of 11.3 kcal/mol. The 3.3 kcal/mol difference was attributed¹⁷⁸ to "the use of different temperatures, different isotopologues, or the accumulated errors of the two techniques." The principal component of the barrier involved interactions with neighboring molecules in the lattice.

The situation with **106·2C₆H₆** was potentially more complex, as benzene molecules are capable of facile six-fold rotation (discrete six-fold flipping) in the solid state. There was the question as to whether this might be coupled to *p*-phenylene rotation, and the possibility for gearing was considered. To aid visualization, several

views of the crystal lattice are given in Figure 2.44. Two (**CV-a**, **CV-c**) are reminiscent of motif **C** in Figure 2.40, with both trityl endgroups of neighboring rotor molecules in van der Waals contact. The benzene molecules help to fill the void space between the rotators. There are six arrayed around each, but in the interest of clarity, only two are depicted in Figure 2.44. Also, the space filling representation **CV-a** helps to visually calibrate readers as to what a packing coefficient (C_k) of ca. 0.7 can look like.

In depth NMR analyses did not provide any evidence for coupled rotation. Thus, independent *p*-phenylene rotation could be assigned an E_a of 12.8 kcal/mol (Table 2.5). Another investigator, Gardinier, has carried out similar studies with salts of the isoelectronic diboron compound $[\text{Ph}_3\text{B}-\text{C}\equiv\text{C}-(p\text{-C}_6\text{H}_4)-\text{C}\equiv\text{C}-\text{BPh}_3]^{2-}$.¹⁷⁹ The accompanying cations result in packing motifs in which all rotator axes are no longer parallel. Although fewer details for this system are available, the rate of *p*-phenylene rotation appears to be somewhat faster.

Figure 2.42 also depicts compounds **107-110**, in which the *p*-phenylene moiety of **106** has been replaced by other unfunctionalized arylenes.¹⁷⁷ In the case of **107**, the 4,4'-biphenylene containing rotator would have the same radius as that in **106**. However, for the others (**108-110**), the radii are much greater. Hence, in the absence of new (favorable) crystal packing motifs, much higher rotational barriers would be expected. Indeed, the 9,10-anthracenediyl moiety in crystalline **108** is locked into a narrow pocket created by the stators of neighboring molecules.

Only the dynamic properties of the deuterated 4,4'-biphenylene systems **107-*d*₈** and **107-*d*₃₀** have been studied in depth.¹⁷⁷ Solid-state NMR experiments were carried out with (1) an *o*-xylene monosolvate in which the linked *p*-phenylene units were not quite coplanar and (2) a disordered solvent-free solid. Two-fold flipping processes were implicated with E_a values of 7.4 and 8.7 kcal/mol, respectively (Table 2.5). The data did not distinguish whether this was synchronous, involving both C₆D₄ rings or only one. With the *o*-xylene monosolvate, the data were best modeled when a barrier-free $\pm 15^\circ$ librational motion was included. Garcia-Garibay noted that the 7.4 kcal/mol barrier was 4-5 kcal/mol lower than that of the benzene solvate of **106**. However, there was no correlation to packing coefficients or any obvious geometric explanation. In response to other aspects of the data, it was speculated that rotational motion in solvated crystals may take advantage of long-range lattice vibrations that couple with molecular modes.

Table 2.5 Arrhenius parameters for the solid-state rotation of rotators in compounds studied by Garcia-Garibay and related systems.

compound	E_a (kcal mol ⁻¹)	pre-exponential factor, A (s ⁻¹)	variable temperature technique	ref
106-d₄ ·2C ₆ H ₆	12.8	—	¹³ C CP/MAS NMR ^b	158,159
106-d₄	14.6±2.5	7.96 × 10 ¹⁴	quad. echo ² H NMR ^c	37,158,159
106-d₃₀	11.3±1	2.9 × 10 ¹¹	¹³ C CP/MAS NMR ^b	178
107-d₈ · <i>o</i> -C ₆ H ₄ (CH ₃) ₂	7.4	2.5 × 10 ¹²	quad. echo ² H NMR ^c	177
107-d₃₀	8.7	4.9 × 10 ⁹	¹³ C CP/MAS NMR ^b	177
111 ·2C ₆ H ₆ ^d	13.7±0.9 ^{d,e}	—	dielectric spectroscopy	37,147
111-d₃	13±2 ^e	(1.0±0.7) × 10 ¹⁴	quad. echo ² H NMR ^c	37,147
115	14.1±0.2 to 15.1±0.5	(4±1) × 10 ¹³ to (8±4) × 10 ¹³	dielectric spectroscopy	148
115-d₂	14.8±1	(8±6) × 10 ¹³	quad. echo ² H NMR ^c	148
118-d₂ ·2THF	8.5	6.2 × 10 ¹²	quad. echo ² H NMR ^c	37,181
123-d₄	8.5±2.5	1.07 × 10 ¹³	quad. echo ² H NMR ^c	37,182
124	3.55±0.2	3.59 × 10 ¹⁰	¹ H spin-lattice relax. ^f	37,182
125	12.6±2.5	9.63 × 10 ¹¹	¹³ C CP/MAS NMR ^b	37,182
126	3.0±0.1	6.39 × 10 ¹⁰	¹ H spin-lattice relax. ^f	37,182
127-d₄	5.21	5.8 × 10 ¹⁰	quad. echo ² H NMR ^c	37,185
128-d₂	3.3-6.7	2.6 × 10 ¹¹ to 3.6 × 10 ⁸	quad. echo ² H NMR ^c	186
131	4.1	2.2 × 10 ¹¹	¹ H spin-lattice relax. ^f	37,187
131-d₃₀	13.7±1.1	(5.1±4.5) × 10 ¹¹	¹³ C CP/MAS NMR ^b	37,187
140-d₄ ·C ₆ H ₆	11.6±2.0	(3.5±3.0) × 10 ¹³	quad. echo ² H NMR ^c	34,192
140 ·C ₆ H ₆	11.7	1.7 × 10 ¹²	¹³ C CP/MAS NMR ^b	34,192
140 ·C ₆ H ₆	8.0-10.3	—	X-ray ADP ^g	192
148-d₄ ·8(solvent) ^{h,i}	15.7	3.5 × 10 ¹⁸	quad. echo ² H NMR ^c	37,191
148-d₂₄ ·8(solvent) ^{h,i}	15.5 (14.7) ^j	7.8 × 10 ¹⁷ (5.3 × 10 ¹³) ^j	quad. echo ² H NMR ^c	37,191
148-d₉₀ ·8(solvent) ^{h,i}	13.7	7.8 × 10 ¹⁵	quad. echo ² H NMR ^c	37,191
149-d₄ ·2CH ₂ Cl ₂ ^k	<5 ^k	—	quad. echo ² H NMR ^c	34,160,210
150-d₄ ·2EtOAc ^l	5.0 (7.0) ^l	9.7 × 10 ¹¹ (4.3 × 10 ¹⁰) ^l	quad. echo ² H NMR ^c	37,194
156-d₄ ·2C ₆ H ₅ Br	4.4	1.6 × 10 ¹²	quad. echo ² H NMR ^c	37,195,196
159-d₄	7.9±1.6	2.75 × 10 ¹¹	quad. echo ² H NMR ^c	37,197
165-d₈ ·4C ₆ H ₅ CH ₃	9.0	2.4 × 10 ¹³	quad. echo ² H NMR ^c	37,199
167-d₆	10.2	1.1 × 10 ¹⁰	quad. echo ² H NMR ^c	200
168-d₈	5.5	3.6 × 10 ⁹	quad. echo ² H NMR ^c	202
170a-e	2.4-4.8	1.1 × 10 ¹² to 9.9 × 10 ¹²	¹ H spin-lattice relax. ^f	205

Table 2.5 continued.

compound	E_a (kcal mol ⁻¹)	pre-exponential factor, A (s ⁻¹)	variable temperature technique	ref
171	1.15±0.04	$(1.3±0.3) \times 10^{12}$	¹ H spin-lattice relax. ^f	206
172	0.71±0.04	$(1.2±0.4) \times 10^{12}$	¹ H spin-lattice relax. ^f	206
173	4.5	1.8×10^{12}	¹ H spin-lattice relax. ^f	209
174	8±2	—	¹ H spin-lattice relax. ^f	209
174-d₁₂	9.5	4.2×10^{13}	quad. echo ² H NMR ^c	209
175	2.63 (0.5) ^m	4.4×10^{12} (1.1 × 10 ⁷) ^g	¹ H spin-lattice relax. ^f	203
180-d₄	11.3	1.6×10^{12}	quad. echo ² H NMR ^c	37,210
181	7.3	5×10^{11}	dielectric spectroscopy	37,212
182	5.0±0.2	1.3×10^7	¹ H spin-lattice relax. ^f	37,211
185-d₈	13.5	8.7×10^{15}	quad. echo ² H NMR ^c	37,213
186	0.18	4.7×10^{10}	¹ H spin-lattice relax. ^f	37,214
187-d₄	8.6	7×10^{11}	quad. echo ² H NMR ^c	216
188-d₂	6.8±0.1	5.4×10^{12}	quad. echo ² H NMR ^c	215
188	7.1±0.5	1.7×10^{14}	dielectric spectroscopy	215

^a Error limits are given when provided in the paper cited. ^b ¹³C Cross-polarization magic angle spinning NMR. ^c Quadrupolar echo ²H NMR, also referred to as spin-echo ²H NMR. ^d The same barrier was obtained using a desolvated sample. ^e This value represents the barrier for conversion of the higher energy to the lower energy rotator conformation, which differ in energy by 0.7 kcal/mol. ^f ¹H NMR spin-lattice relaxation (T_1). ^g Anisotropic displacement parameters from crystal structures. ^h In this series, the deuterium atoms are located on the central *p*-phenylene rotator, the six trityl based *p*-phenylene rotators, or the twelve phenyl rotators, respectively; the E_a values pertain to the deuterated rotator. ⁱ These crystals feature mixtures of 2,4,6-trimethylpyridine and 2,2,4-trimethylpentane solvent molecules. ^j This value is for an amorphous sample. ^k During sample preparation (grinding), desolvation occurred; due to this and other complications, the E_a value could only be estimated. ^l The two values are for two independent molecules of **150-d₄** in the unit cell. ^m This value is for a high temperature phase.

A number of derivatives of **106** have been prepared in which the *p*-phenylene rotator has been substituted with one or two heteroatom containing functional groups.^{159,180} These are shown as **111-117** in Figure 2.42, and nearly all feature dipolar rotators. However, only the rotational dynamics of the two dipolar fluorinated compounds have been studied.

The monofluoro compound **111** crystallized analogously to **106**.¹⁵⁹ Either an unsolvated form or the benzene disolvate, **111**·2C₆H₆, could be obtained. In the latter, there was a belt of four benzene dimers about each rotator, somewhat akin to view **CV-a** of **106**·2C₆H₆ in Figure 2.44. In both cases, the fluorine atoms exhibited positional disorder (i.e. CH···CF/CH···CH exchange), which was initially fit to a 50:50 occupancy ratio.¹⁵⁹ Nonetheless, the possibility of domains in which the dipoles of neighboring molecules would be favorably aligned could not be excluded,

In any case, **111** and **111**·2C₆H₆ were studied both by dielectric spectroscopy and (following deuteration) solid state ²H NMR.¹⁴⁷ Each probe indicated that the two fluoro-*p*-phenylene orientations were not isoenergetic but differed slightly. Thus, the crystal structure of **111** was redetermined at 296 K, and an 80:20 positional disorder was now found, corresponding to a difference of 0.7 kcal/mol. The *E_a* values, 13.7 and 13 kcal/mol, respectively (Table 2.5), represent the barriers for transiting from the higher energy to the lower energy well. Possible reasons for the ca. 1 kcal/mol discrepancy between the two techniques have been analyzed.¹⁴⁷

The related 2,3-difluoro-*p*-phenylene compound **115** in Figure 2.42 could be crystallized in an unsolvated form that was isomorphous with those of **106** and **111**. The dynamic properties were analogously studied, and a very similar rotational potential with E_a values of 14-15 kcal/mol was obtained (Table 2.5).^{37,148}

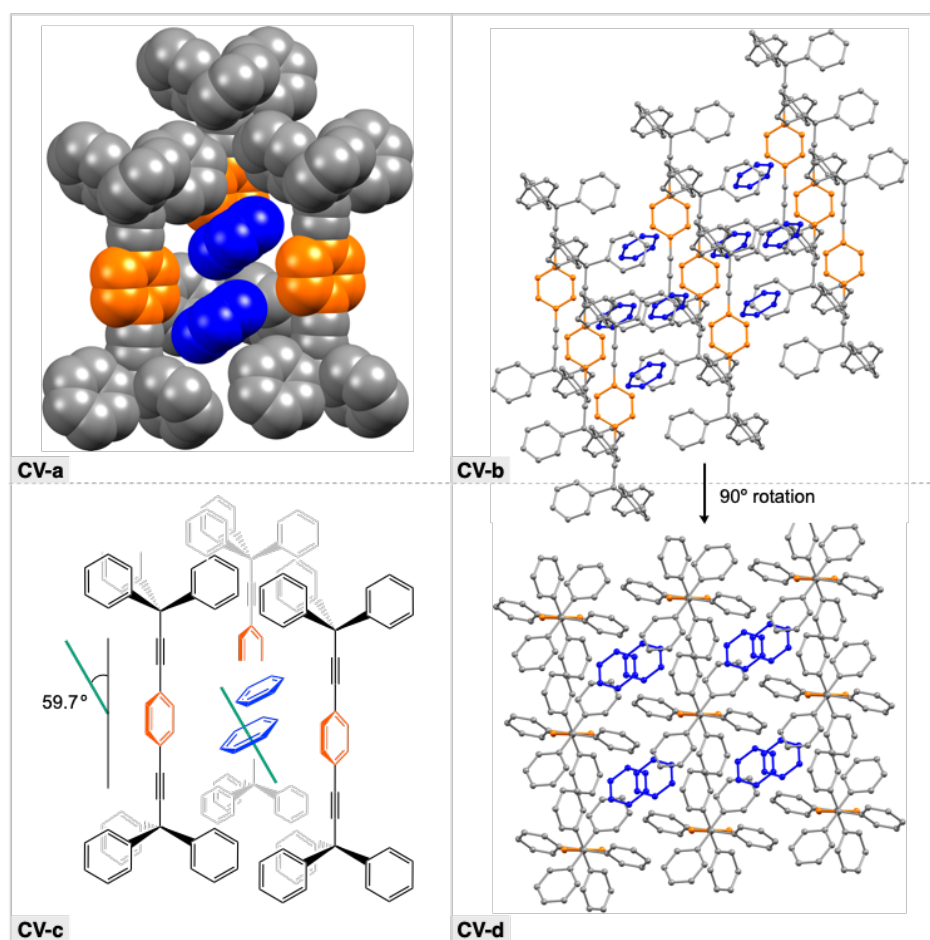


Figure 2.44 Representations of the crystal structure of the *p*-phenylene containing rotor **106**·2C₆H₆.

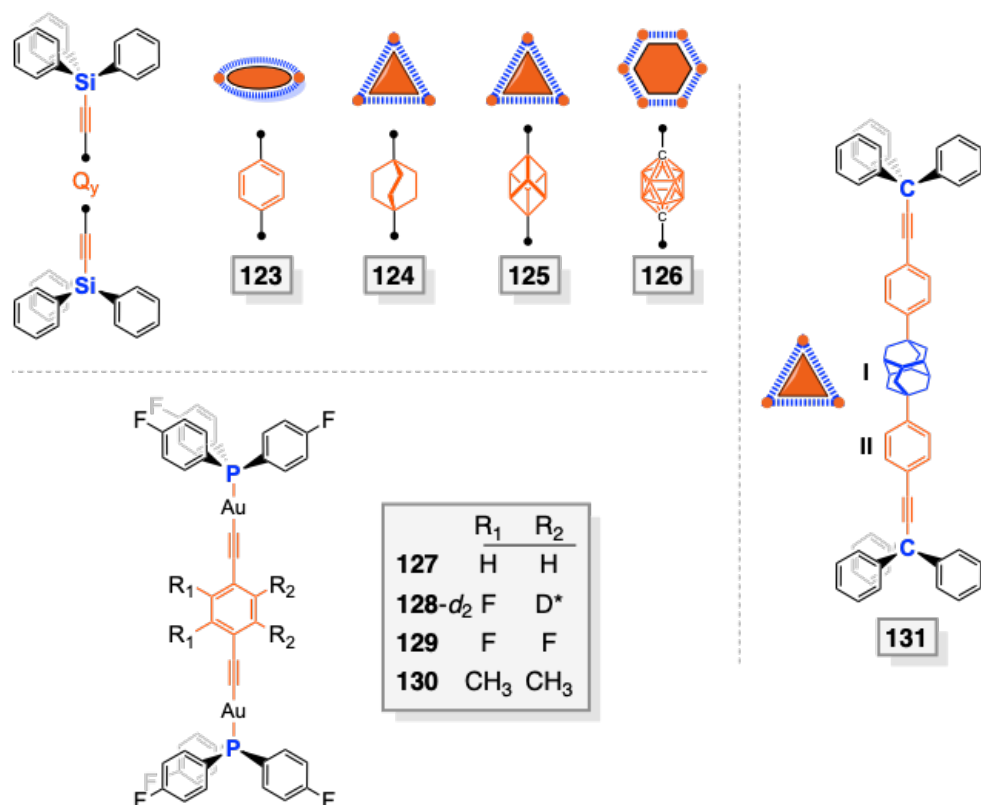


Figure 2.45 Additional molecular rotors studied by Garcia-Garibay, most with heteroatom containing endgroups.¹⁸² For the significance of the geometric shapes, see the text and Figure 2.46. Deuterated compounds are normally not displayed, but **128-d₂** has not been reported in nondeuterated form.

Several compounds with dipolar nitrogen heterocycle rotators are also depicted in Figure 2.42 (**118-121**).¹⁸¹ In most of these, the dipole moments of the rotators are greater than those of the mono- and difluorinated *p*-phenylenes in **111** and **115**. Crystals of the 2,5-pyridinediyl (**118**·THF) and 3,6-pyridazinediyl (**119**, **119**·CHCl₃) adducts have been structurally characterized. The packing motifs are quite similar to those of **106**, **111**, and **115**, consistent with the similar dimensions of the rotators. Garcia-Garibay estimates the volumes of the *p*-arylene units in **118** and **119** as 0.5-1.1% less than that of **106**.¹⁸¹

Quantitative studies of dynamic properties are so far limited to the 2,5-pyridinediyl system **118**·THF.¹⁸¹ Solid-state ²H NMR experiments (**118**-*d*₂·THF) afford an E_a of 8.5 kcal/mol for rotational site exchange. The higher E_a values for the monofluorine rotators in **111** and **111**·2C₆H₆ have been ascribed to the larger fluorine substituent, the lesser steric demand of the pyridinediyl moiety, and the smaller size of the occluded THF. The first two would also apply to the higher barrier in the difluorinated compound **115**.

Figure 2.45 collects other types of rotors examined by Garcia-Garibay. One subset (**123**-**126**) features triphenylsilyl endgroups.¹⁸² The first compound, **123**, represents a disilicon analog of **106**. The *p*-phenylene segment is then replaced by a polycyclic hydrocarbodiyl moiety derived from either bicyclo[2.2.2]octane or cubane, both of which feature a C_3 symmetry axis, as shown by **124** or **125**. A *p*-carboranediyl moiety with an even higher symmetry axis (C_6) can be introduced, as shown by **126**.

Silicon–carbon bonds are typically 21% longer than carbon–carbon bonds,¹⁸³ and this is a potential factor when comparing the rotational barriers in these compounds to those of analogs with trityl endgroups. However, another property is in play in this series. Namely, rotators with higher rotational symmetry should generally exhibit diminished solid-state rotational barriers. The reasoning is as follows.¹⁸² First, note the geometric representations of the rotators in Figure 2.45. Those with C_3 symmetry axes are depicted as orange triangles, and those with C_2 and C_6 symmetry axes are depicted

as orange ovals and hexagons, respectively. These shapes are repeated in Figure 2.46, together with some corresponding to rotators with other C_n symmetries.

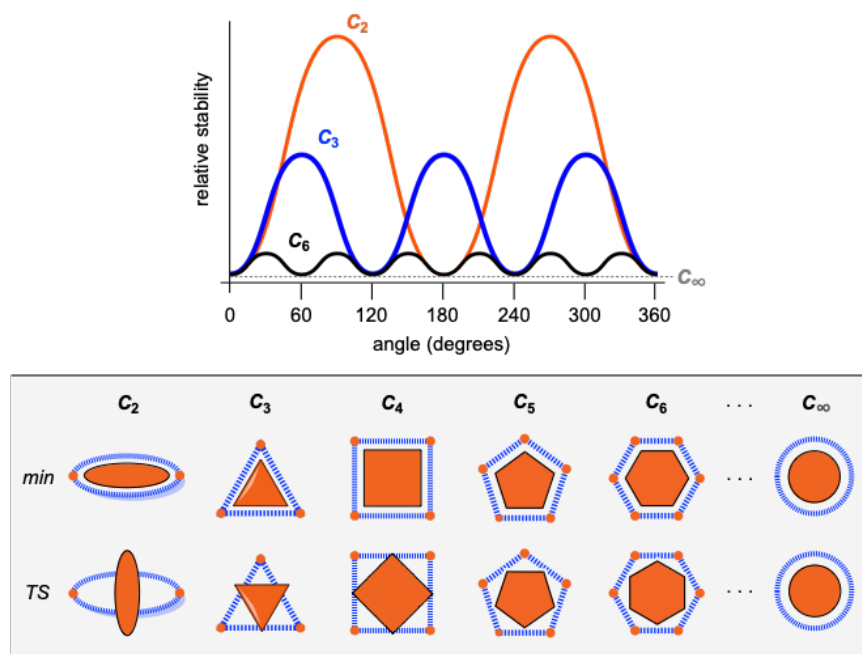


Figure 2.46 First row of structures: cross sections of rotators of C_n symmetries (solid orange) and packing motifs that saturate the van der Waals surface boundaries (dashed blue lines). Second row: packing environments that would be generated upon rotation of the rotators by $360^\circ/2n$. Top: idealized qualitative energy profiles.

Consider first the solid-state environments of the C_∞ and C_6 rotators. One might expect that the neighboring molecules in the lattice would pack in a complementary, roughly cylindrically symmetrical manner about the C_∞ axis. In any event, rotation of the rotator by 30° or 60° or 90° (etc.) would not generate increased steric interactions. With the C_6 rotator, the adjacent molecules would pack with nearly cylindrical symmetry. A rotation of 30° ($360^\circ/2n$) would likely lead to an energy maximum (TS in

Figure 2.46), but the increased steric interactions would be moderate. A further rotation of 30° would restore the energy minimum.

Now consider a rectangular or ovoid rotator with C_2 symmetry. If the adjacent molecules pack about the rotator in a complementary manner, there is the likelihood of severe steric interactions upon a 90° rotation. Intermediate situations are obtained with C_3 , C_4 , or C_5 symmetric rotators. There are a number of conceptual parallels with the trends associated with n -fold rotational barriers detailed in section 2.6.4 (Figure 2.22). In any case, one would expect energy profiles with the relationships qualitatively expressed in Figure 2.46 (top) as the C_n symmetry of the rotator decreases.

The series of rotors **123-126** with varying rotator symmetries (Figure 2.45) crystallize without solvent.¹⁸² Despite some differences in unit cell dimensions and crystal symmetries, they pack in relatively similar manners. Each crystal consists of long chains of molecules aligned by interactions between the aryl rings of the endgroups (SiPh₃/Ph₃Si). These entail attractive edge/face motifs and sextuple phenyl embraces. The structures are disorder-free, except for **124** in which the bicyclo[2.2.2]octane moiety occupies two positions (50:50) that differ by a 60° rotation.

The NMR properties of the disilyl analog of **106**, **123**, have been studied in detail.¹⁸² Experiments with **123-*d*₄** give an E_a of 8.5 kcal/mol (Table 2.5), somewhat lower than that of nonsolvated **106-*d*₄** (11.6 kcal/mol) and intuitively in line with the longer silicon–carbon bonds. Much lower barriers are obtained for **124** and **126** (E_a 3.5 and 3.1 kcal/mol, respectively), consistent with expectations from the higher C_n -

symmetries of their rotators. There is no correlation to the radii of the *p*-phenylene, bicyclo[2.2.2]octanediyl, and *p*-dicarboranediyl segments of the rotators (2.87, 3.05, and 3.42 Å, respectively, as estimated from their crystal structures including the van der Waals radii of the hydrogen atoms).

However, the barrier is much higher with the 1,4-cubane diyl adduct **125** ($E_a = 12.6$ kcal/mol), in which the radius of the rotator is 3.14 Å. This has been attributed to steric features of the tight rotator pocket formed by four neighboring molecules, as shown in Figure 2.47. The six cubane carbon atoms not connected to the $-C\equiv C-$ units can be represented by a pair of triangles, as depicted in **CVI** and **CVII** (Figure 2.47; the dark background represents a van der Waals boundary). In particular, two phenyl hydrogen atoms (blue and orange semicircles in **CVI**) extend into the rotator pocket. As the six carbon atoms rotate, one hydrogen atom (orange) is poised to strongly interact with the atoms in the upper triangle, and the other (blue) in the lower triangle (see **CVII**).

The various geometric relationships embodied in **123-126** and their implications for rotational barriers have also been probed computationally by other investigators.¹⁸⁴ In general, good agreement with the experimental results were realized.

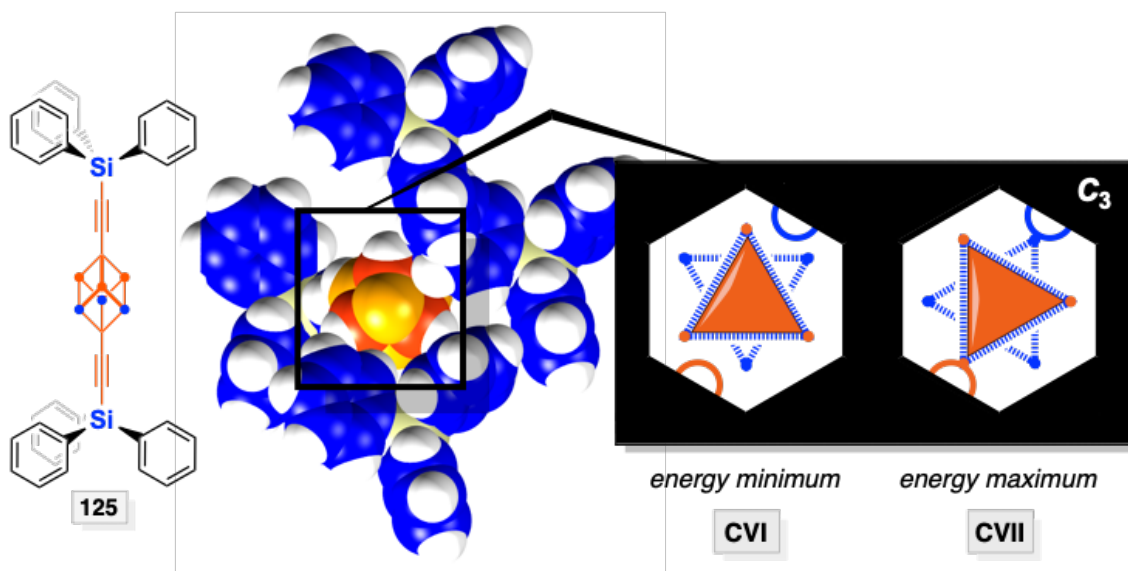


Figure 2.47 Steric interactions in the crystal structure of the 1,4-cubane diyl adduct **125** (see also text).¹⁸²

A second subgroup of rotors in Figure 2.45 feature tri(*p*-fluorophenyl) phosphine endgroups as opposed to triphenylsilyl endgroups.^{185,186} The phosphines in turn anchor digold rotators of the formula $\text{AuC}\equiv\text{C}-(p\text{-C}_6\text{R}_4)\text{-C}\equiv\text{CAu}$, with $\text{R}_4 = \text{H}_4$ (**127**), Me_4 (**130**), F_2D_2 (**128-d**₂), and F_4 (**129**). Outside of the MOF systems described below, these represent the only metal containing rotors studied in the Garcia-Garibay group, with one underlying goal being the modulation of phosphorescence emission. All of these adducts can be crystallized in solvent-free forms.^{185,186} Auophilic interactions between neighboring molecules are evident (Au-Au 2.95-3.36 Å) and are clearly a factor in the packing motifs.

In **127**, two of the *p*-phenylene hydrogen atoms exhibit weak $\text{CH}\cdots\pi$ -interactions with the fluorophenyl groups from the triarylphosphine stators of neighboring molecules. Despite these attractive interactions, NMR experiments (**127-d**₄) indicate a low E_a of 5.2

kcal/mol. However, rotational site exchange could not be established for the sterically more demanding tetramethyl-*p*-phenylene rotator in **130**. The difluoro compound **128-*d*₂** crystallizes analogously to **127** but with two-fold rotationally disordered *p*-C₆F₂D₂ units. The packing motif of the tetrafluoro compound **129** is very similar.

The interpretation of the dynamic behavior of the difluoro compound **128-*d*₂** was complicated by a nonlinear Arrhenius plot.¹⁸⁶ This was attributed to reversible expansion/compression of the distances between the axes, giving E_a values of 3.3-6.7 kcal/mol. There were additional challenges in the case of the tetrafluoro compound **129**, but solid state ¹⁹F NMR experiments provided evidence for a similar dynamic range.

Finally, in the last and quite unique rotor **131** in Figure 2.45, a C_3 symmetric 4,9-diamantanediyl moiety has been inserted into the C₆H₄-C₆H₄ linkage of **107** (Figure 2.42).¹⁸⁷ The 4,9-diamantanediyl unit is conceptually related to the 1,4-cubanediyyl unit of **125**, with the six four-membered rings of the latter now expanded to six-membered rings. This is the first compound in this review where there are two symmetry inequivalent components of the rotator that can independently rotate, the two *p*-phenylene groups (C_2) and the central 4,9-diamantanediyl group (C_3).

Solvent-free crystals of **131** could be obtained. NMR experiments with appropriately deuterated samples gave an E_a of 13.7 kcal/mol for two-site exchange of the *p*-phenylene groups. Consistent with the expectations from Figure 2.46, the E_a associated with three-site exchange of the 4,9-diamantanediyl moiety was much lower,

4.1 kcal/mol. Interestingly, the radii of the rotator segments trend in the opposite direction (*p*-phenylene, 2.87 Å; 4,9-diamantanediyl, 3.28 Å).

Another series of rotors studied by Garcia-Garibay is collected in Figure 2.48.^{175,188} These feature (1) trityl endgroups with one or two oxygen-bound *meta* substituents (OH, OMe, OTIPS) and (2) *p*-phenylene, 2,3-difluoro-*p*-phenylene, or 2,5-pyridinediyl rotators. Solid-state NMR experiments have been carried out with **132**, the difluorinated derivative **133**, and deuterated analogs.¹⁸⁸ The data indicate extremely slow rotation of the rotators, with E_a values much higher than 12-14 kcal/mol. The crystal structures of **132** and **133** have also been determined, and the isomorphous packing motifs were analyzed in detail. The high barriers could be ascribed to steric effects arising from the TIPS group and stabilizing edge/face interactions of the rotators with neighboring aryl groups.

Some of the other compounds in Figure 2.48 represent stepping-stones to more complicated species that were viewed as outside the scope of this review (see section 2.8.1).^{175,188} Nonetheless, they are presented in the interest of a complete record. A related group of rotors is depicted in Figure 2.49. Each contains a $-C\equiv C-(p-C_6H_4)-C\equiv C-$ rotator, and all except **145** and **146** have multiply substituted trityl endgroups of C_3 symmetry.^{160,175,176,189-191,194}

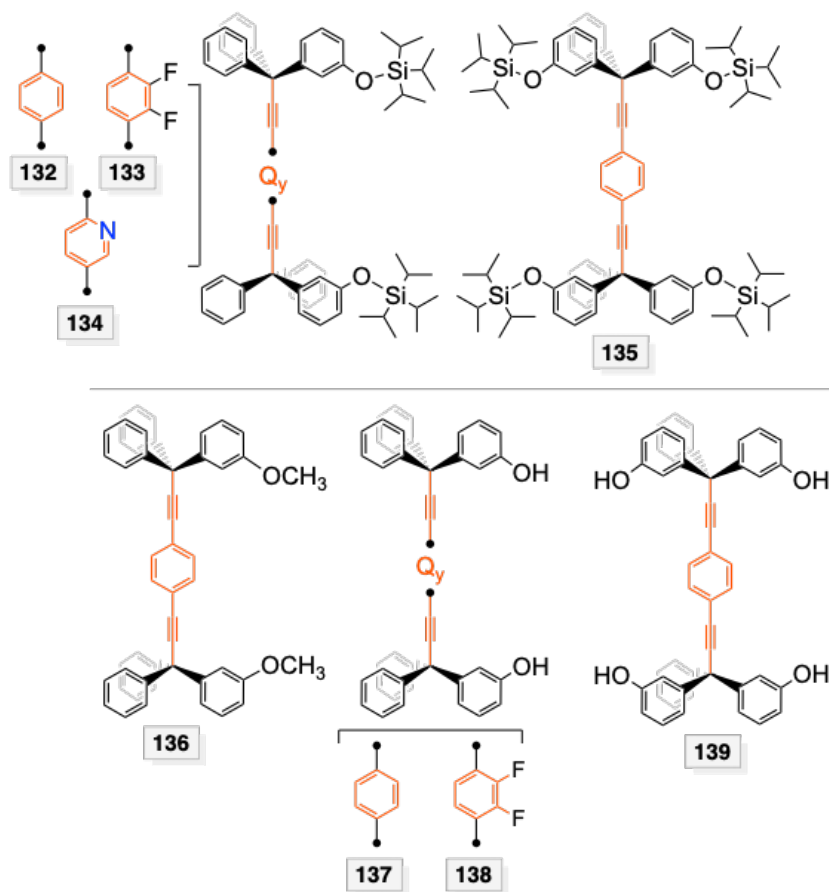


Figure 2.48 Molecular rotors with substituted trityl endgroups studied by Garcia-Garibay (part 1).

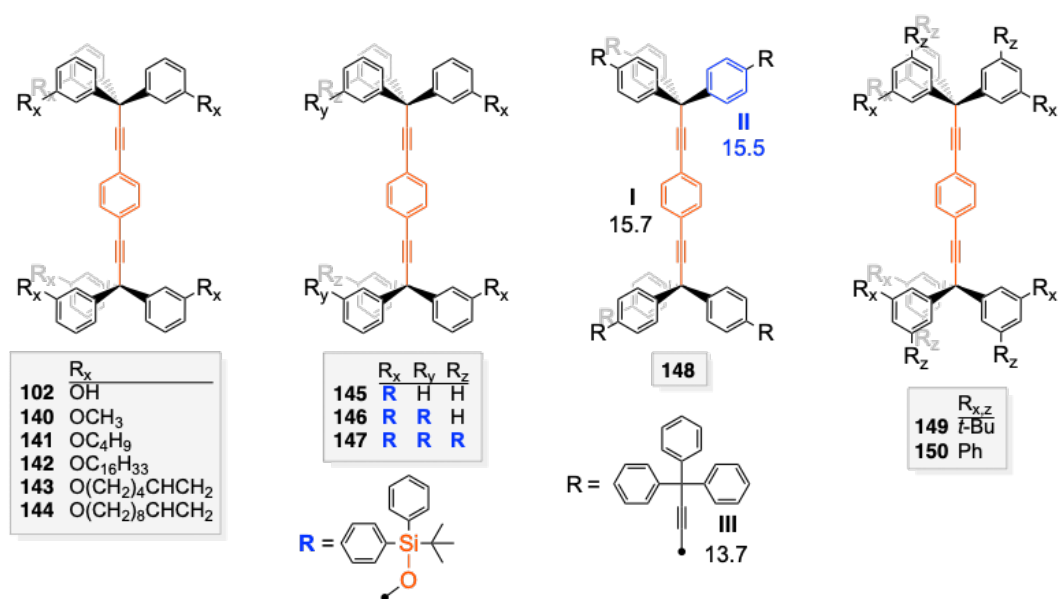


Figure 2.49 Molecular rotors with substituted trityl endgroups studied by Garcia-Garibay (part 2).

One subset of rotors in Figure 2.49 features a single *meta* hydroxy or alkoxy substituent on each trityl aryl ring (**102,140-144**). Compound **140** has received particular attention as a candidate for a crystalline molecular gyroscope.^{189,192,193} It is challenging to condense the full breadth of this study, as seven polymorphs have been characterized. Some of these arise from conformational degrees of freedom about the C–C–O–Me or $C_{sp}-C_{sp^3}-C_{ipso}-C_{ortho}$ linkages, and others by incorporating different solvent molecules (pseudopolymorphs).¹⁷⁴

The monobenzene solvate **140**·C₆H₆ has been extensively examined by the solid state NMR techniques described above. The data yield E_a values of 11.5-11.7 kcal/mol, close to those of the unsolvated and benzene solvated forms of the parent compound **106** (Table 2.5). In addition, a crystallographic approach to assaying rotational barriers has been investigated. This entails analyzing the anisotropic displacement parameters as a function of temperature, particularly with respect to librational motion and amplitudes. Readers are referred to the article for further details.¹⁹² In any event, E_a values of 10.3, 10.1, and 8.0 kcal/mol could be derived from data collected at 100, 200, and 300 K, respectively. The lower value at 300 K has been attributed to an increased anharmonicity of the potential energy surface at higher temperature.

In another subset of rotors in Figure 2.49 (**145-147**), a *meta*-OSiPh₂*t*-Bu substituent can be found on one, two, or three of the aryl rings of each trityl endgroup.¹⁹⁰ The stator in the last compound is particularly bulky, but a crystal structure could not be determined. NMR experiments with **147**-*d*₄ provide evidence for very slow

rotation of the *p*-phenylene moiety, but various issues preclude the determination of an E_a .

In the rotors **149** and **150** in Figure 2.49, both *meta* positions of all six aryl rings of the trityl endgroups are substituted with *t*-butyl or phenyl groups. In the latter, each endgroup can be viewed as having three *m*-terphenyl substituents. Both compounds can be seen as an effort to transition from packing motif **CI** to packing motif **CII** in Figure 2.40. The former crystallizes as the disolvate, **149**·2CH₂Cl₂, with one of the dichloromethane molecules located close to the *p*-phenylene group.¹⁶⁰ The solvent molecules could be removed without complete loss of crystalline order. Solid-state NMR experiments with **149**-*d*₄ could attain both the fast (293 K) and slow exchange limits (≤ 193 K), but a number of complications prevent the quantitative measurement of the E_a value.

Compound **150** could be crystallized as the disolvate, **150**·2EtOAc.¹⁹⁴ The unit cell contained two independent molecules of **150**. Although the solid-state NMR data (**150**-*d*₄·2EtOAc) and attendant modeling required complex analysis, it was possible to estimate the E_a values for rotation of the *p*-phenylene groups of the two molecules as 5 and 7 kcal/mol.³⁷ In the former, there were no close contacts involving the rotator, whereas in the latter sources of steric hindrance were apparent. Also, the *p*-phenylene units underwent essentially barrierless librations of ± 15 -20°.

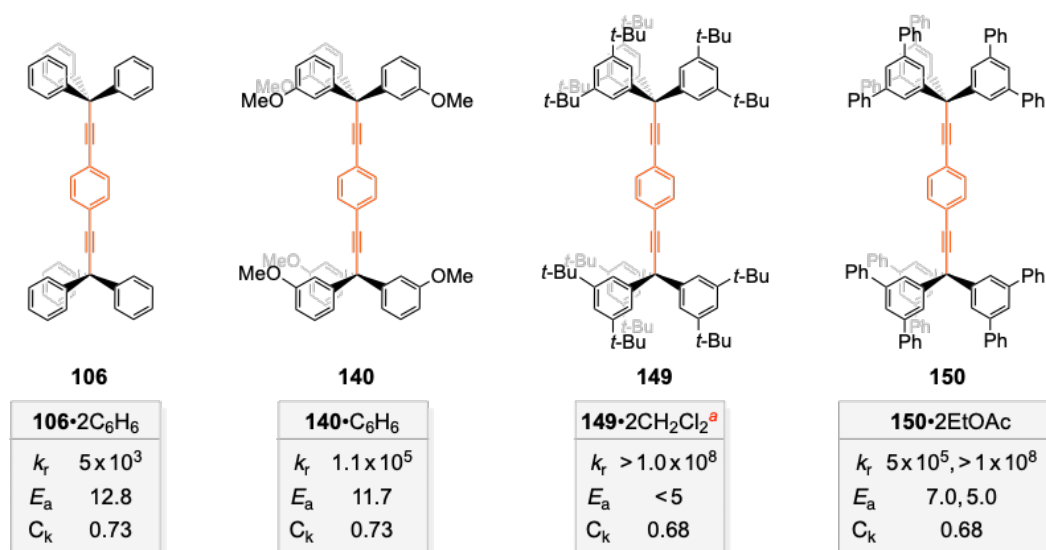


Figure 2.50 Comparison of packing coefficients (C_k) and E_a values (kcal/mol) for *p*-phenylene rotation in four molecules. ^aConsult the references in Table 2.5 for additional details regarding the composition of the solvate.

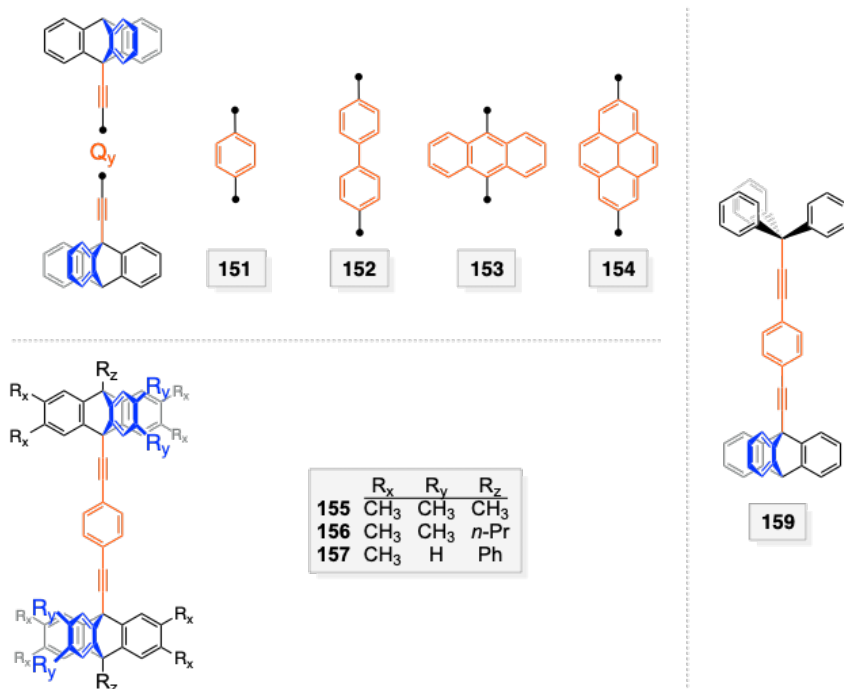


Figure 2.51 Additional molecular rotors studied by Garcia-Garibay, all with at least one triptycyl or substituted triptycyl endgroup.

Although Garcia-Garibay later integrated this analysis over a broader spectrum of compounds,³⁷ it is instructive to compare the four structurally related rotors in Figure 2.50, three of which come from Figure 2.49.¹⁹⁴ As the packing coefficients, C_k (which include the solvent molecules), decrease from 0.73 to 0.68, there is an overall (although not proportional) decrease in the E_a values. However, this relationship does not hold as well in other series of compounds, and additional relevant factors are treated below.

For the unique rotor **148** in Figure 2.49,¹⁹¹ the *para* positions of all six trityl aryl groups have been substituted with bulky $C\equiv CPh_3$ substituents, making for a dendrimer like adduct with a total of eight trityl moieties. Compound **148** could be crystallized from an unusual solvent mixture (2,4,6-trimethylpyridine/2,2,4-trimethylpentane) as a highly disordered tetrasolvate. The radius of the stator can be estimated as ca. 12 Å, which is unsurpassed in all of the preceding adducts. Ignoring the solvent molecules, the packing coefficient (C_k) is only 0.46. Accordingly, there are very few contacts involving the rotator.

Clearly, the hope was that there would be a low barrier to $-C\equiv C-(p-C_6H_4)-C\equiv C-$ rotation in solid **148**. However, analysis of the NMR data proved complicated. Using **148- d_4** , Garcia-Garibay reported an *apparent* E_a of 15.7 kcal/mol,¹⁹¹ greatly increased relative to that of **106** (12.8, 14.6, or 11.3 kcal/mol depending upon solvation, Table 2.5). However, other observations prompted him to adjust this value to 7.9 kcal/mol (253 K) and 6.9 kcal/mol (293 K). The temperature dependence was ascribed to crystal fluidity effects. The more heavily deuterated substrates **148- d_{24}** and **148- d_{90}** were used

to probe the rotational barriers of the $C_{sp^3}-(p-C_6H_4)-C\equiv C$ and C_6H_5 units. The apparent E_a values (15.5 and 13.7 kcal/mol) as well as the corrected values were similar to those obtained from **148-*d*₄**. The possibility of various types of correlated rotation or gearing was considered, but in the end it was concluded that rotation was primarily associated with a temperature induced softening of the packing structure.

For the series of rotors in Figure 2.51, one or both of the trityl endgroups in molecules treated earlier have been replaced by triptycyl or substituted triptycyl moieties.^{157,195-197} These have fewer degrees of freedom and are incapable of propeller chirality, a feature that can play a role in crystal packing. The compounds **151-154**, two of which are homologs of **106** and **107** in Figure 2.42, were among the first studied by Garcia-Garibay.¹⁵⁷ Only solution phase NMR spectra were reported, and rotator rotation was always fast on the NMR time scale. In the crystalline *m*-xylene monosolvate **151**·C₈H₁₀, the protruding triptycene units of one molecule interdigitated into voids proximal to the *p*-phenylene unit of another, blocking rotation.¹⁹⁵

Similar compounds have been prepared in which subsets of the triptycyl hydrogen atoms are replaced by methyl, *n*-propyl, or phenyl groups, as exemplified by **155-157**.¹⁹⁵⁻¹⁹⁷ It was hoped that the additional substituents would hamper interdigitation. The *n*-propyl substituted compound **156** could be crystallized as a bromobenzene disolvate, **156**·2C₆H₅Br.¹⁹⁵ NMR experiments using **156-*d*₄**·2C₆H₅Br showed that the barrier to *p*-phenylene rotation was sharply reduced to 4.4 kcal/mol, the second lowest with respect to the other compounds described above. Garcia-Garibay

noted that this is only 1.4 kcal/mol higher than the barrier to carbon–carbon bond rotation in ethane in the gas phase.¹⁹⁵ The crystal structure of **156**·2C₆H₅Br revealed that the *p*-phenylene rotators were very well insulated from neighboring rotors, although in close proximity to six solvent molecules.

The rotor **159** in Figure 2.51 represents a mixed system with one trityl and one triptycyl endgroup¹⁹⁷ and constitutes a "hybrid" of **106** and **151**. It crystallizes as the monosolvate **159**·CHCl₃, but samples lose chloroform during solid-state NMR measurements. However, it can be desolvated while retaining crystallinity at 110 °C. NMR data with **159**-*d*₄ indicate an *E*_a of 7.9 kcal/mol for *p*-phenylene flipping. Notably, this is 6 kcal/mol lower than that measured for solvent-free samples of **106**. Although the crystal structure of desolvated **159** is unknown, Garcia-Garibay observes that the packing coefficient of **159**·CHCl₃ (0.69) is lower than those of **106** (0.74) and **151** (0.85).

Figure 2.52 depicts a series of compounds with -C≡C-(*p*-C₆H₄)-C≡C- rotators and substituted pentiptycene endgroups (**160-164**).¹⁹⁸ The wingspan associated with these endgroups is greater than those of triptycyl analogs such as **151** in Figure 2.51. However, in the three adducts that can be crystallized, it is obvious that intermolecular contacts strongly impede any rotation of the *p*-phenylene moiety. It has been suggested that bulky groups at the periphery of the pentiptycene stators would help prevent interdigitation.

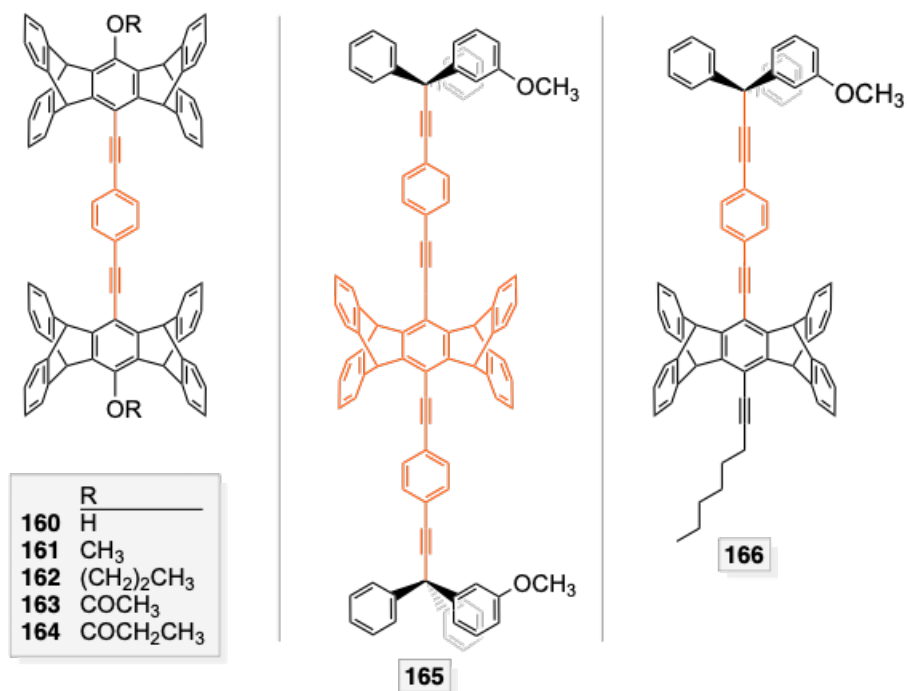


Figure 2.52 Additional molecular rotors studied by Garcia-Garibay, all of which incorporate a pentiptycene moiety.

The pentiptycene moiety has been moved to the "middle" in the adduct **165** in Figure 2.52.¹⁹⁹ Although this is the customary position for the rotator, the moment of inertia of the pentiptycene group is comparable to those of the triarylmethyl endgroups. Hence, **165** is better viewed as a "dirotor" with two $-\text{C}\equiv\text{C}-(p\text{-C}_6\text{H}_4)-\text{C}\equiv\text{C}-$ rotators that have collinear axes. Although there are a number of interesting properties to appreciate in **165**, the bottom line is that NMR experiments with the toluene monosolvate **165**- $d_8\cdot\text{C}_7\text{H}_8$ (C_k 0.71) establish an E_a of 9.0 kcal/mol for p -phenylene rotation. To the authors' knowledge, the rotor properties of **166** remain uninvestigated, although the photophysical properties of **165** and **166** have been studied in detail.¹⁹⁹

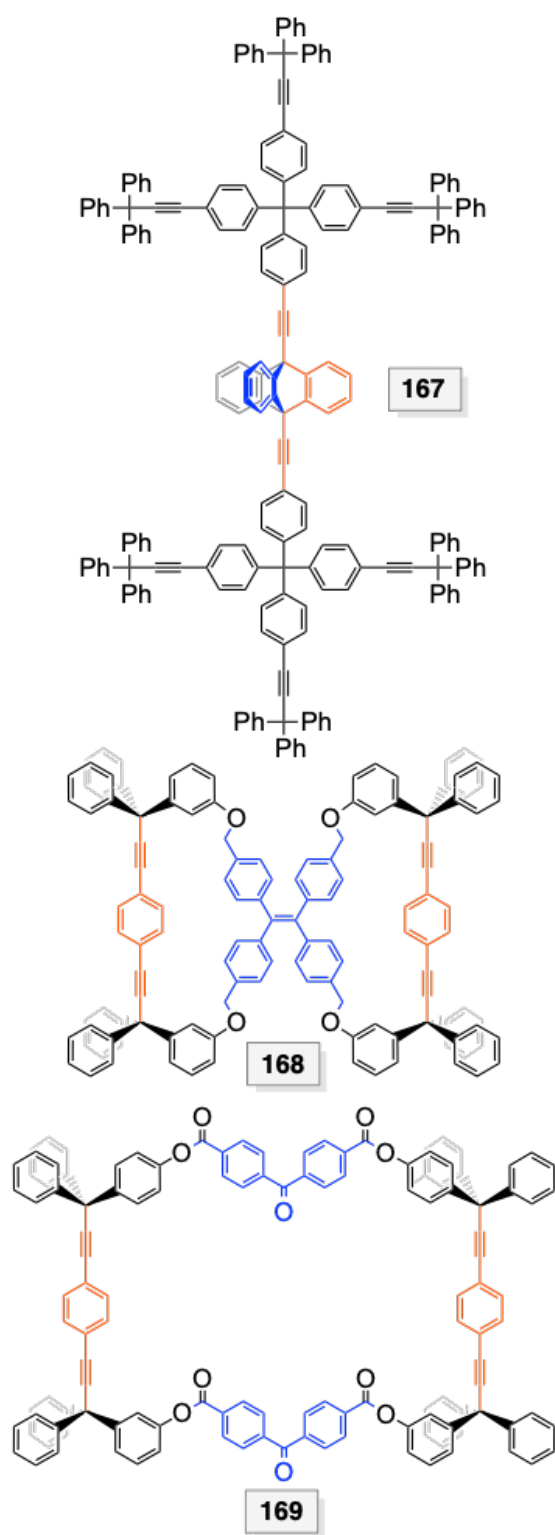


Figure 2.53 Additional molecular rotors studied by Garcia-Garibay.

Compound **167** in Figure 2.53 (top)²⁰⁰ represents a return to the extremely bulky dendrimer like stators first encountered with **148** in Figure 2.49. The rotator features a central triptycenediyl moiety, flanked by two C≡C-*p*-phenylene domains. The radius of the triptycenediyl segment (ca. 5.52 Å, estimated from crystal structures of related molecules and including hydrogen atoms²⁰¹) is much greater than those of the *p*-phenylene segments (2.87 Å, from Figure 2.32). Due to splintering and other problems, it has not proved possible to determine the crystal structure. However, solid-state NMR studies of **167-*d*₈** (deuterated on two of the three benzenoid triptycene rings) establish, following in depth analyses, an E_a of 10.2 kcal/mol for a 120° rotation of the triptycenediyl segment.

As noted above, compound **165** in Figure 2.52 features two rotators with collinear axes. Garcia-Garibay has also studied adducts that feature two rotators with parallel axes, as exemplified by **168** in Figure 2.53 (middle).²⁰² This compound was prepared with the idea that the fluorescence intensity of the tetraarylethylene core might be a function of the rotator mobilities. Solid-state NMR experiments with **168-*d*₈** indicate a low E_a , 5.5 kcal/mol, for *p*-phenylene rotation. However, a crystal structure could not be determined. Compound **169** in Figure 2.53 represents a byproduct in the synthesis of a monorotor precursor to **168**.¹⁷⁵ Compounds with more than one rotator for which the axes are not collinear or parallel¹⁶⁹ are considered beyond the scope of this review.

2.8.3.2. Rotors based upon supramolecular assemblies or MOFs

2.8.3.2.1. Supramolecular systems

Garcia-Garibay, sometimes together with collaborators, has also studied supramolecular rotators.²⁰³⁻²⁰⁹ Although connections to gyroscopes are briefly mentioned in his papers, other investigators have emphasized potential relationships (section 2.9.2). One advantage of supramolecular rotors is that many can be synthesized by simple self-assembly of the rotator and stator components.²⁰⁵

Figure 2.54 (top) depicts a series of halogen bonded 1:2 adducts of DABCO and fluorinated phenyl iodides (**170a-e**).²⁰⁵ The moments of inertia of the components are comparable, so the rotator and stator cannot be assigned by the criteria in section 2.1. Most of these crystallize as represented in Figure 2.54, although **170c** adopts an alternative connectivity. The crystal structures of **170a,e** have been studied in particular detail, and show numerous reversible phase transitions between 100 K and room temperature. The crystal packing motif remains intact throughout, but the DABCO moiety exhibits increasing rotational disorder over two positions differing by 60°. The rotator axes in **170a,e** are aligned in a parallel manner, as seen with virtually all of the rotors in section 2.8.3.1. However, this motif is not always observed in the halogen bonded rotors.

NMR experiments and other data confirm the preferential rotation of the C_3 symmetric DABCO moiety as opposed to the C_2 symmetric fluorinated aryl groups, consistent with the concepts embodied in Figure 2.46. The aryl groups can therefore be regarded as stators. The E_a values are quite low, ranging from 2.4 to 4.8 kcal/mol. A

variety of properties have been analyzed, including the origin of the higher rotational barrier (8.2 kcal/mol) in pure crystalline DABCO.

In a subsequent study,²⁰⁶ the 1:1 adducts **171** and **172** in Figure 2.54, derived from DABCO and the corresponding trityl substituted haloalkynes, were examined. Despite the absence of steric protection, NMR experiments established an E_a of only 0.71 kcal/mol for DABCO rotation in bromine containing **172**, aptly likened to "a spinning top on a tripod". At that time, this was the lowest rotational barrier measured in an amphidynamic crystal. A slightly higher E_a was found for iodine containing **171** (1.15 kcal/mol) and attributed to subtle differences in the crystal lattices that result in a more hindered DABCO cavity. Both potential energy surfaces consisted of six local minima and six local maxima. Garcia-Garibay also studied the solid state behavior of bis(alkynyl iodides) containing DABCO or *p*-phenylene rotators, for which halogen bonding between like molecules is possible.^{204,207}

Hydrogen bonding is ubiquitous in supramolecular systems. As shown in Figure 2.54 (bottom), Garcia-Garibay has also employed DABCO as a component of (1) a 1:2 adduct with the monocarboxylic acid **B1**, affording **173**, and (2) a 1:1 adduct with the dibridgehead dicarboxylic acid **B2**, affording the one-dimensional polymer **174**.²⁰⁹ These are structurally complex systems; with the crystallographic data indicating that the DABCO in **173** (1) is protonated on one nitrogen atom and hydrogen bonded on the other and (2) resides in a pseudo-four-fold symmetric cavity formed by aromatic residues from neighboring molecules. The mismatch with the C_3 symmetry axis of DABCO suggests the possibility of twelve nearly degenerate minima, which should help

lower the rotational barrier. In contrast, in **174** the DABCO occupies a packing environment of pseudo-three-fold symmetry, which should enhance the rotational barrier.

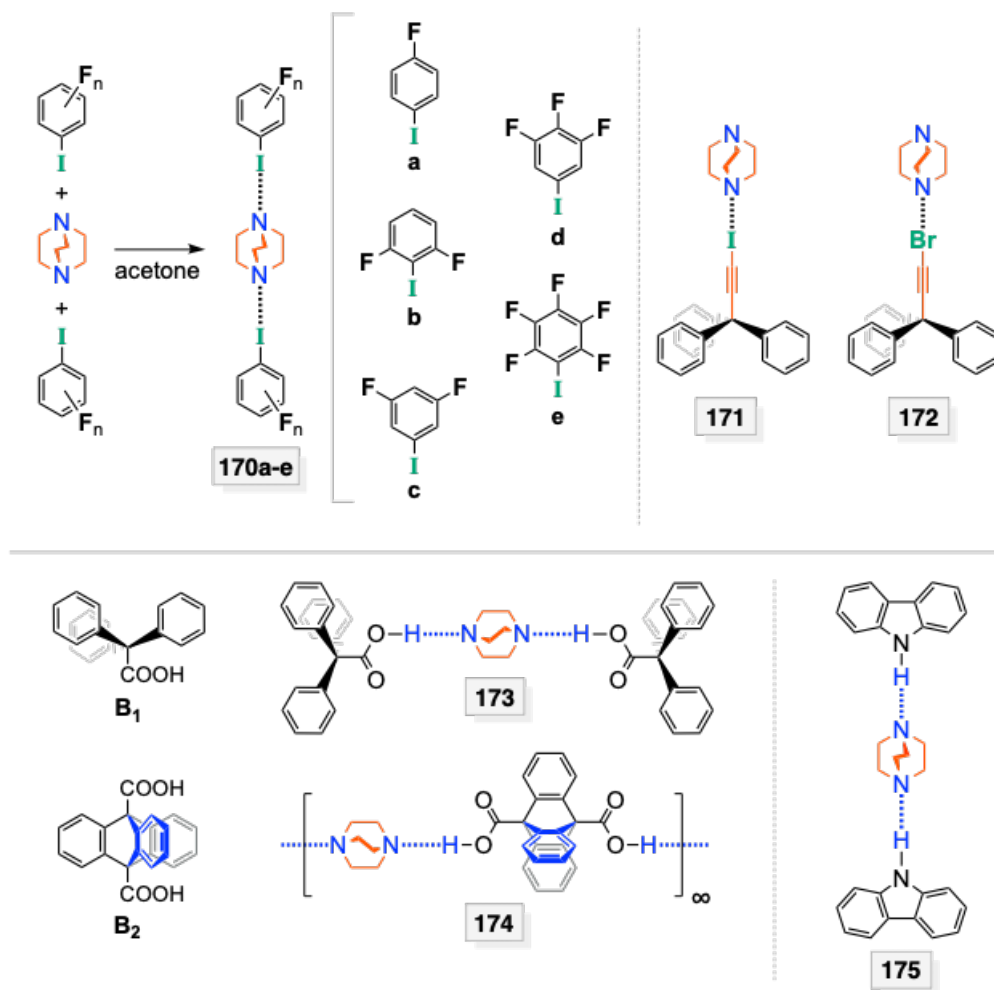


Figure 2.54 Supramolecular rotors studied by Garcia-Garibay and collaborators: top, halogen bonded DABCO adducts; bottom, hydrogen bonded DABCO adducts.

NMR experiments (with d_{12} analogs) indicated rapid DABCO rotation in **173**, faster than 10^7s^{-1} at 148 K, but an exact E_a could not be obtained. In contrast, that for **174** was 9.2 kcal/mol (ca. 10^4s^{-1} at 243 K). However, the primary objective of this study

concerned the prospects of exploiting dipoles generated by thermal proton transfer to attain transient ferroelectric domains. This undertaking also entailed a variety of dielectric measurements.

The 1:2 adduct of DABCO and carbazole, **175** in Figure 2.54 (bottom), has also been investigated.²⁰³ Two crystalline phases can be characterized, with the symmetry of the crystal lattice and cavity hosting the C_3 rotator increasing at higher temperature. This leads to a reduction in the E_a value for DABCO rotation from 2.6 to 0.5 kcal/mol. However, due to a large decrease in the pre-exponential factor, the rate slows considerably at higher temperatures.

2.8.3.2.2. MOF systems

Another obvious research direction would be to extend the preceding types of studies to MOFs and other porous materials. Of course, such assemblies would not qualify as molecular rotors or gyroscopes. However, the situation is not all that different from a crystal lattice of molecular rotors. Some of the MOFs studied by Garcia-Garibay and collaborators or close associates are given in Figure 2.55.

The first system studied by Garcia-Garibay was Yaghi's MOF-5 (**180**), also known as IMROF-1.²¹⁰ All horizontal and vertical connectors feature a *p*-phenylene rotator in the form of a terephthalate dianion. Each carboxylate is anchored to two zinc atoms (one for each oxygen atom). NMR experiments using **180** with deuterated rotators yield an E_a of 11.3 kcal/mol. This represents a relatively large barrier, especially in view of the void space (see **CVIII** or **CIX**, Figure 2.55) and miniscule packing coefficient (C_k 0.20). It has been attributed to an electronic effect, namely, to a loss of conjugation

between the ideally coplanar *p*-phenylene and carboxylate groups, as depicted in **CX** in Figure 2.55.²¹⁰ Other probes of rotator dynamics are also surveyed in this work.

This effort was followed by studies of analogous MOFs with dipolar monosubstituted *p*-phenylene rotators, *p*-C₆H₃X.^{211,212} In the case of bromo-*p*-phenylene (IMROF-2 or **181**), Price and Michl measured an E_a of 7.3 kcal/mol by dielectric spectroscopy.²¹² In the case of amino-*p*-phenylene (IMROF-3 or **182**), Garcia-Garibay and Yaghi measured an E_a of 5.0 kcal/mol by ¹H spin-lattice relaxation.²¹¹ Additional properties were characterized by further solid state ¹³C and ¹⁵N NMR experiments. The positions of the bromine atoms in **181** were disordered, and the dipole-dipole interactions were not strong enough to produce an observable polar ordering,²¹¹ a topic further treated in section 2.9.3.

The trends in E_a values have been rationalized by Garcia-Garibay and Yaghi.²¹¹ The larger bromine and amino substituents in **181** and **182** are thought to sterically destabilize the otherwise coplanar *p*-phenylene/carboxylate units in which conjugation is maximized (**CX**, Figure 2.55). This of course will lower barriers relative to that of **180**. Also, the NH₂ moiety, which undergoes independent rotation (E_a 1.8 kcal/mol), can hydrogen bond to the neighboring carboxylate group, and this is potentially a stronger interaction in the transition state.

Garcia-Garibay has also synthesized a series of three MOFs depicted in Figure 2.56, UCLA-R1 (**183**), UCLA-R2 (**184**), and UCLA-R3 (**185**).²¹³ These feature dizinc as opposed to tetrazinc junctions (**B**). The horizontal connectors (**C1**) are the

terephthalate dianion, the 4,4'-biphenyl analog, or the dibridgehead dicarboxylate of triptycene, respectively. The vertical connectors (**A1**; pillars) are now capped by nitrogen donor atoms in the form of 9,10-bis(4-pyridylethynyl)-triptycene, these directly bind to zinc.

The first two MOFs crystallize in catenated motifs, such that what would be a cavity in the basic rectangular building block (top structure, Figure 2.56) is occupied by components of additional offset rectangular assemblies. The third, UCLA-R3 (**185**), crystallizes in an uncatenated motif with ten DMF molecules in each cavity. It has been termed a pillared paddlewheel MOF. NMR experiments with deuterated analogs establish an E_a for rotation of 13.5 kcal/mol. A substantial portion of this barrier is attributed to interactions of the triptycene blades and the DMF molecules.

Applying insight from the studies in section 2.8.3.1, Garcia-Garibay designed the "BODCA MOF" (**186**) in Figure 2.55.²¹⁴ This can be viewed as an analog of MOF-5 (**180**) in which the *p*-phenylene unit of the terephthalate dianion has been replaced by a bicyclo[2.2.2]octanediyl moiety. There are two principal effects: (1) the destabilization associated with rotating the *p*-phenylene moiety "out of conjugation" is removed (**CX**, **CXI**; Figure 2.55); (2) a rotator with a local two-fold symmetry axis is replaced by one with a local three-fold symmetry axis. As analyzed above, this is conducive to lower rotational barriers.

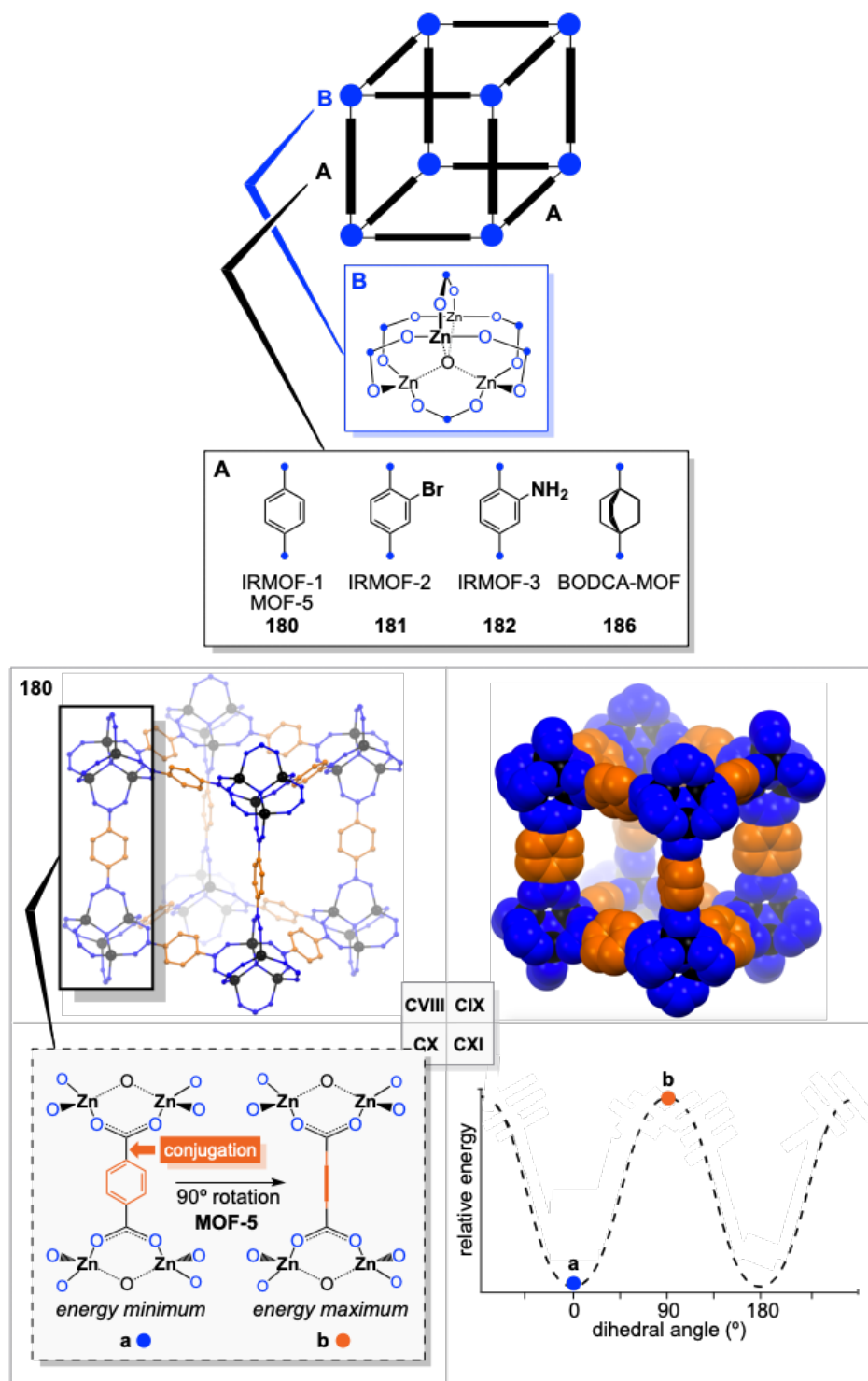


Figure 2.55 MOFs in which rotators have been incorporated into the connectors studied by Garcia-Garibay or others (part 1).

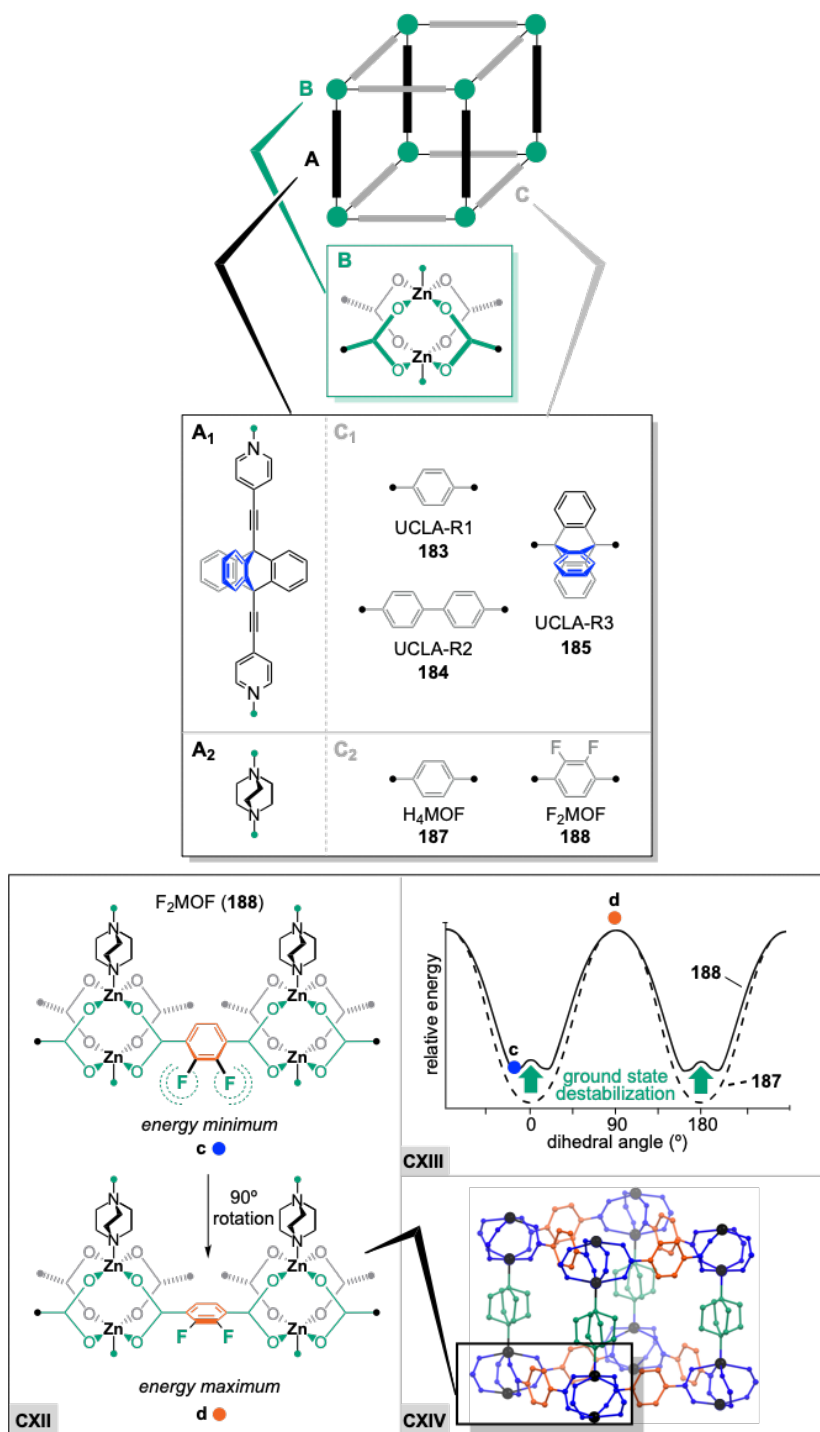


Figure 2.56 MOFs in which rotators have been incorporated into the connectors studied by Garcia-Garibay or others (part 2).

Accordingly, solid-state ^1H NMR measurements at 2.3-80 K establish the amazingly low E_a of 0.185 kcal/mol for rotation of the bicyclo[2.2.2]octanediyl segment. This is supported by ^2H NMR studies of deuterated analogs between 292 and 50 K, as well as molecular dynamics simulations. Garcia-Garibay notes that this represents the engineering of rotational dynamics in the solid state to a rapidity commensurate with a high-density gas or low-density liquid phase.

In his most recent efforts, Garcia-Garibay²¹⁵ has combined design elements from several of the above studies. As shown in Figure 2.56, the dizinc based MOFs **187** and **188** feature either the usual horizontal connector, the terephthalate dianion (H_4MOF), or the dipolar 2,3-difluorinated analog (F_2MOF). For the nitrogen donor pillars, DABCO is used, providing a much lower spacing than with the bis(pyridyl) units in UCLA-R3 (**185**).

For **188**, NMR and dielectric spectroscopy measurements indicate E_a values of 6.8 and 7.1 kcal/mol, respectively, for rotation of the difluorinated *p*-phenylene rotators. NMR measurements with *nonfluorinated* **187** indicate a higher E_a , 8.6 kcal/mol.^{215,216} Data from crystal structures and DFT calculations suggest that steric interactions involving the two fluorine substituents destabilize the planar conjugated conformations of the $-\text{O}_2\text{C}-(p\text{-C}_6\text{H}_2\text{F}_2)-\text{CO}_2-$ units, leading to a lower barrier. Garcia-Garibay's representation of this phenomenon is sketched in **CXIII** in Figure 2.56. Similar interactions with bromine or amino substituents are invoked above to rationalize, at least in part, the lower barriers of **181** and **182** versus **180**.

2.8.4. Representative syntheses of the rotors in section 2.8.3.1

Many of the molecular rotors studied by Garcia-Garibay in section 8.3.1, such as those in Figure 2.42, are of a modular structural nature. Thus, one would anticipate that modular syntheses would also be possible. For that reason, preparative routes have been collected into this separate section. As would be expected from the type of adducts in Figure 2.42, Figure 2.45, and Figure 2.48 to Figure 2.53, the syntheses make particular use of coupling, addition, and displacement reactions of terminal alkynes. Appropriately substituted trityl, triptycyl, and pentiptycene building blocks are also required.

This section does not attempt to exhaustively treat the syntheses of deuterated rotors. However, accessing deuterated triptycyl and trityl groups is less routine, so the dominant routes are sketched in Figure 2.57. For example, 9,10-anthroquinone- d_8 (**190**) is commercially available and can be elaborated by addition/reduction sequences to various 9,10-bis(alkynyl) anthracenes (**191**). Subsequent reactions with benzyne afford triptycyl- d_8 species with bridgehead alkynyl substituents (**192**).²⁰⁰ Alternatively, a three-fold Friedel-Crafts reaction can be carried out with CCl_4 , excess benzene- d_6 , and AlCl_3 .¹⁷⁷ The resulting perdeuterated product $(\text{C}_6\text{D}_5)_3\text{CCl}$ (**193**) is easily ethynylated and carried on to d_{30} rotor molecules.

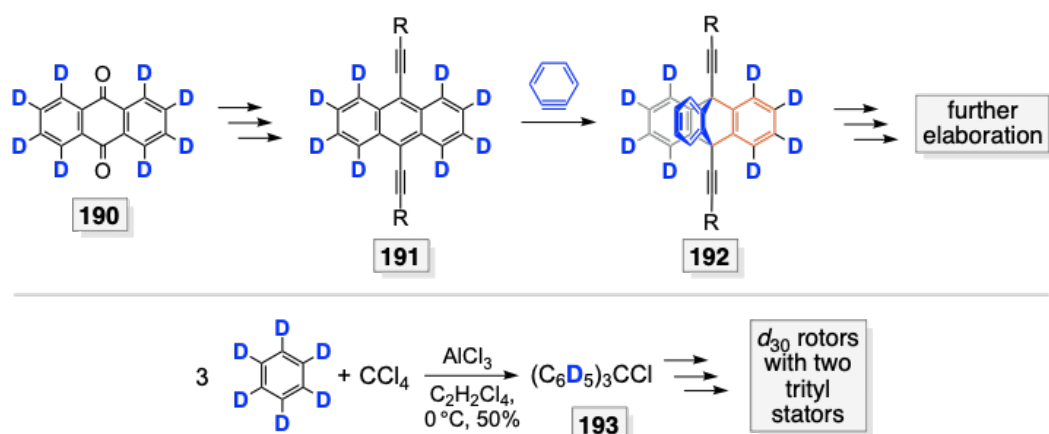
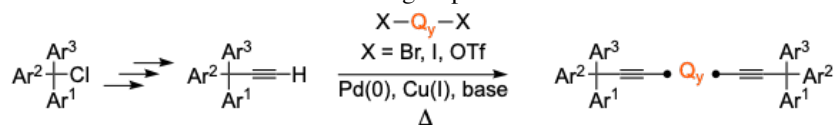


Figure 2.57 Reactions used to access molecular rotors with deuterated trityl or triptycyl groups.

All rotors with $-\text{C}\equiv\text{C}-(p\text{-arylene})-\text{C}\equiv\text{C}-$ rotators and identical trityl endgroups (Figure 2.42) or substituted trityl endgroups (Figure 2.48 and Figure 2.49) have been synthesized via palladium catalyzed Sonogashira type reactions as summarized in Table 2.6.^{147,148,156,159,160,175,177,180,181,187-191,194} The requisite $\text{X}-(p\text{-arylene})-\text{X}$ and $\text{Ar}^1\text{Ar}^2\text{Ar}^3\text{CCl}$ building blocks can be accessed by routine procedures. In several cases, the $p\text{-arylene}$ moieties or endgroups have been subjected to postsynthetic functionalization.^{175,176,181,188} These transformations are depicted in Figure 2.58.

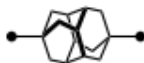
The related disilicon and bis(triaryl phosphine) digold rotors in Figure 2.45 (**123-126** and **127-130**) have been accessed as shown in Figure 2.59.^{182,185,186} In the final step in the disilicon series, the diconjugate dibase of a $\text{HC}\equiv\text{C}-(p\text{-arylene})-\text{C}\equiv\text{CH}$ species is treated with an excess of Ph_3SiCl . In the diphosphorus series, the electrophile is switched to Ar_3PAuCl . Some of the α,ω -diynes required several steps to access, and readers are referred to the cited literature for further details.

Table 2.6 Syntheses of -C≡C-arylene-C≡C- containing rotors with identical trityl or substituted trityl endgroups.



compound	Q _y	Ar ₁ ^a	Ar ₂ ^a	Ar ₃ ^a	yield (%)	ref
106	<i>p</i> -phenylene	Ph	Ph	Ph	15	156
107	4,4'-biphenylene	Ph	Ph	Ph	47	177
108	9,10-anthracenediyl	Ph	Ph	Ph	56	177
109	1,4-naphthalenediyl	Ph	Ph	Ph	68	177
110	4,4'-binaphthalenediyl	Ph	Ph	Ph	92	177
111	fluoro- <i>p</i> -phenylene	Ph	Ph	Ph	23	147
112	cyano- <i>p</i> -phenylene	Ph	Ph	Ph	10	159
113	nitro- <i>p</i> -phenylene	Ph	Ph	Ph	40	159
114	amino- <i>p</i> -phenylene	Ph	Ph	Ph	26	159
115	2,3-difluoro- <i>p</i> -phenylene	Ph	Ph	Ph	38	148,180
116	2,3-diamino- <i>p</i> -phenylene	Ph	Ph	Ph	22	159
117	2-amino-5-nitro- <i>p</i> -phenylene	Ph	Ph	Ph	12	159
118	2,5-pyridenediyl	Ph	Ph	Ph	22	181
119	3,6-pyridazinediyl	Ph	Ph	Ph	75	181
131	<i>p</i> -C ₆ H ₄ -X'- <i>p</i> -C ₆ H ₄ ^b	Ph	Ph	Ph	40	187
132	<i>p</i> -phenylene	<i>m</i> -TIPS	Ph	Ph	77	188
133	2,3-difluoro- <i>p</i> -phenylene	<i>m</i> -TIPS	Ph	Ph	82	188
134	2,5-pyridenediyl	<i>m</i> -TIPS	Ph	Ph	81	188
135	<i>p</i> -phenylene	<i>m</i> -TIPS	<i>m</i> -TIPS	Ph	86	188
136	<i>p</i> -phenylene	<i>m</i> -OCH ₃	Ph	Ph	73	175
139	<i>p</i> -phenylene	<i>m</i> -OH	<i>m</i> -OH	Ph	92	188
140	<i>p</i> -phenylene	<i>m</i> -OCH ₃	<i>m</i> -OCH ₃	<i>m</i> -OCH ₃	70	175,189
145	<i>p</i> -phenylene	<i>m</i> -TBDPS	Ph	Ph	74	190
146	<i>p</i> -phenylene	<i>m</i> -TBDPS	<i>m</i> -TBDPS	Ph	73	190
147	<i>p</i> -phenylene	<i>m</i> -TBDPS	<i>m</i> -TBDPS	<i>m</i> -TBDPS	75	190
148	<i>p</i> -phenylene	<i>p</i> -C≡CCPh ₃	<i>p</i> -C≡CCPh ₃	<i>p</i> -C≡CCPh ₃	70	191
149	<i>p</i> -phenylene	3,5-(<i>t</i> -Bu) ₂	3,5-(<i>t</i> -Bu) ₂	3,5-(<i>t</i> -Bu) ₂	64	160
150	<i>p</i> -phenylene	3,5-Ph ₂	3,5-Ph ₂	3,5-Ph ₂	87	194

^a Only the substituents are given for substituted phenyl groups. ^b X' =



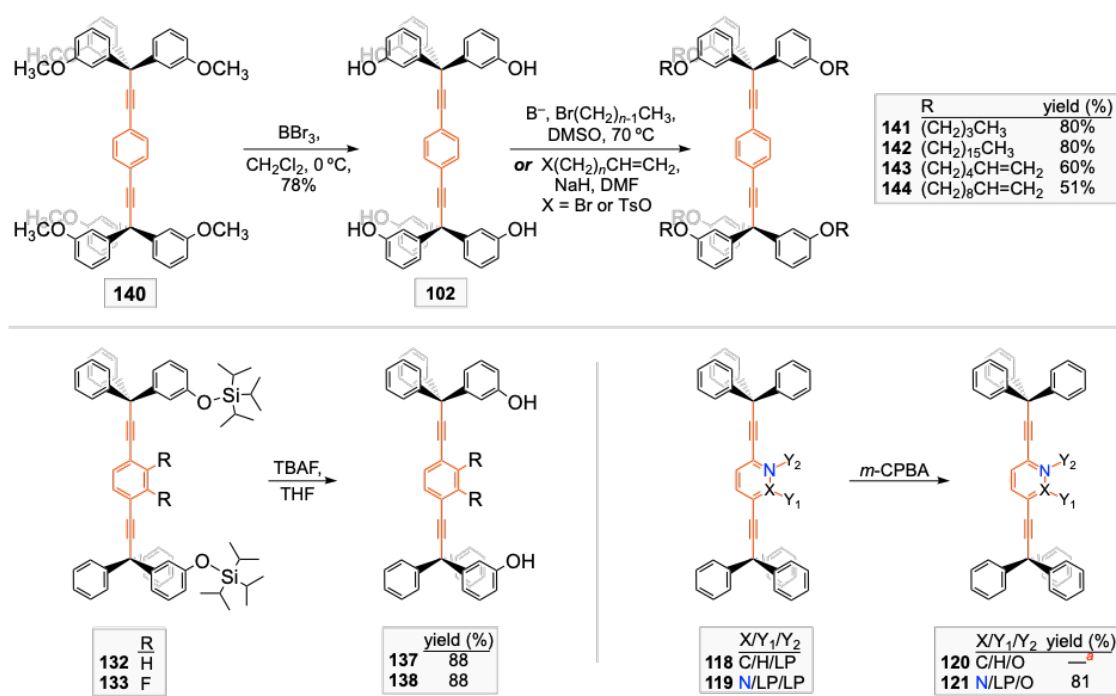


Figure 2.58 Molecular rotors accessed by postsynthetic modification of certain compounds in Table 2.6.
^aRapidly decomposes in solution.

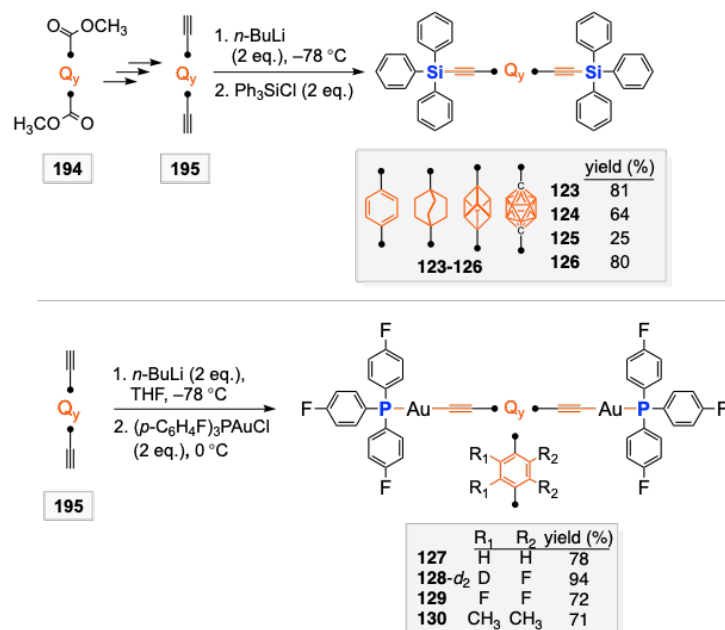


Figure 2.59 Syntheses of molecular rotors with silicon (**123-126**, top) or phosphorus (**127-130**, bottom) containing endgroups.

Accessing rotors with triptycyl or substituted triptycyl endgroups requires somewhat more steps. As shown in Figure 2.60 (top), triptycyl precursors with bridgehead $-C\equiv C-CMe_2OH$ substituents (**198**) are first prepared.^{157,196} These syntheses involve benzyne additions similar to that introduced in Figure 2.57. In a standard protocol for generating terminal alkynes or transient conjugate bases, compounds **198** are treated with KOH. Subsequent Sonogashira couplings of the resulting alkynes **199** afford the target molecules **151-157**. As shown in Figure 2.60 (bottom), a stepwise approach involving *p*-diiodobenzene and two Sonogashira couplings is used for the mixed trityl/triptycyl adduct **159**.¹⁹⁷

Some of the designer rotor architectures featured in Garcia-Garibay's later studies require somewhat more involved syntheses. Cases in point include the pentiptycene adducts **160-166** in Figure 2.52.^{198,199} The final steps of the syntheses of **160-164** are analogous to those used for other $-C\equiv C-(p\text{-arylene})-C\equiv C-$ rotors in Table 2.6.¹⁹⁸ The trick is to prepare the requisite pentiptycene building blocks.

Figure 2.61 shows how these are accessed from **203**, derived from the two-fold Diels-Alder adduct of anthracene and *p*-quinone.^{198,199,217} Using $LiC\equiv CTMS$, an alkynyl group is first introduced, and reduction installs a *para* hydroxy group, giving **204**. The alkyne can be protodesilylated (\rightarrow **205**) and the hydroxy group can be replaced by methoxy or *n*-propoxy groups (**206**, **207**). Alternatively, two alkynyl groups can be introduced using excess $LiC\equiv CTMS$, with subsequent reduction and protodesilylation giving **208**. In a variant, two different alkynyl groups can be introduced, giving **209** via a

parallel sequence. These building blocks are then applied as depicted in Figure 2.62.^{198,199} First, the monoethynyl compounds **205-207** are combined with *p*-diiodobenzene under Sonogashira conditions to give **160-162**. The hydroxyl groups in **160** can also be derivatized, for example, by acylation to give **163** and **164**. Second, the mixed ethynyl/octynyl compound **209** can be combined with the iodoarene **210** under Sonogashira conditions. This affords **166**, which is comprised of a $-\text{C}\equiv\text{C}-(p\text{-C}_6\text{H}_4)-\text{C}\equiv\text{C}-$ rotator and substituted trityl and pentiptycene endgroups. Third, an excess of **210** can be combined with the bis(ethynyl) compound **208** under Sonogashira conditions to give the bis(rotor) **165**, with a central pentiptycene unit.

Finally, as depicted in Figure 2.63, the dendrimer like rotor **167**, which features a triptycyl rotator, can be prepared in four linear steps from anthraquinone in quite high overall yield.²⁰⁰ These utilize conditions similar to those applied in the preceding figures.

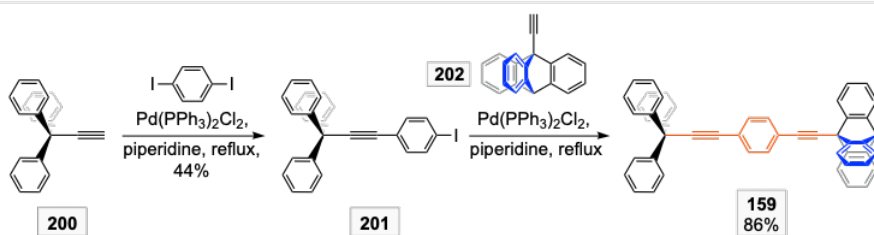
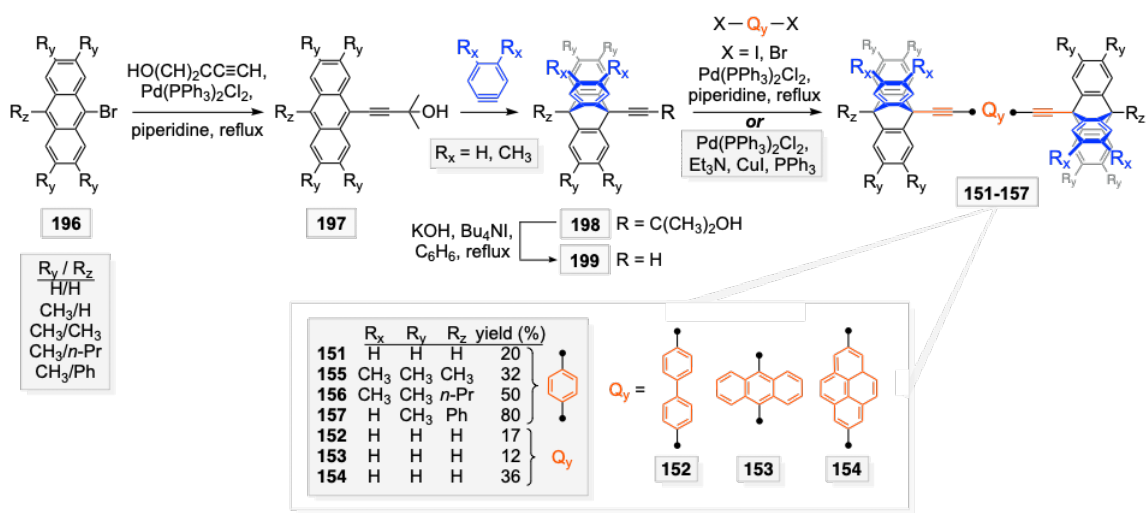


Figure 2.60 Syntheses of molecular rotors **151-157** (top) and **159** (bottom).

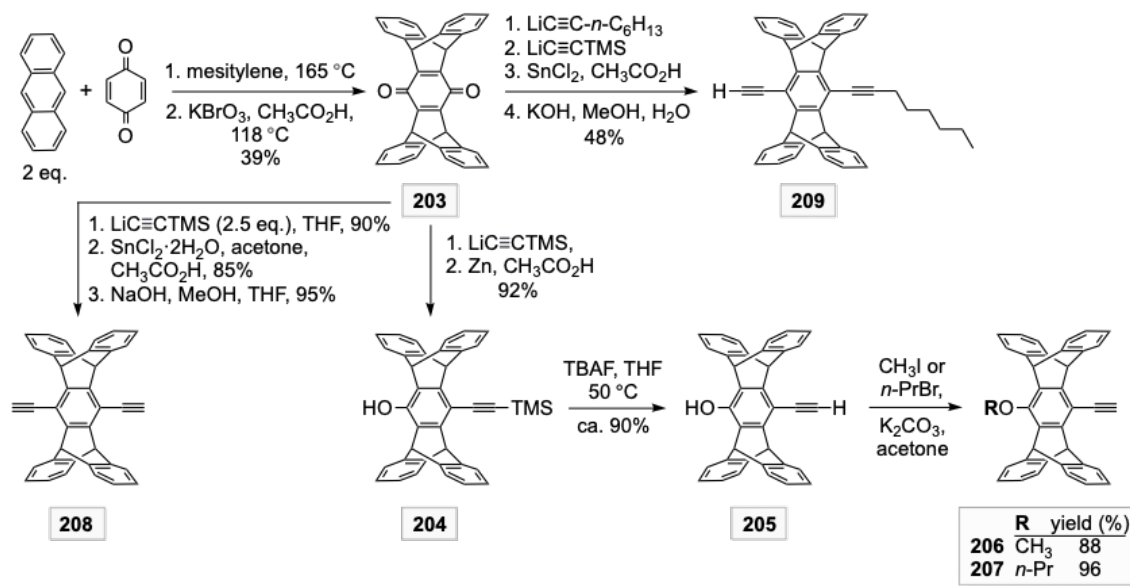


Figure 2.61 Syntheses of key precursors to the molecular rotors **160-166**.

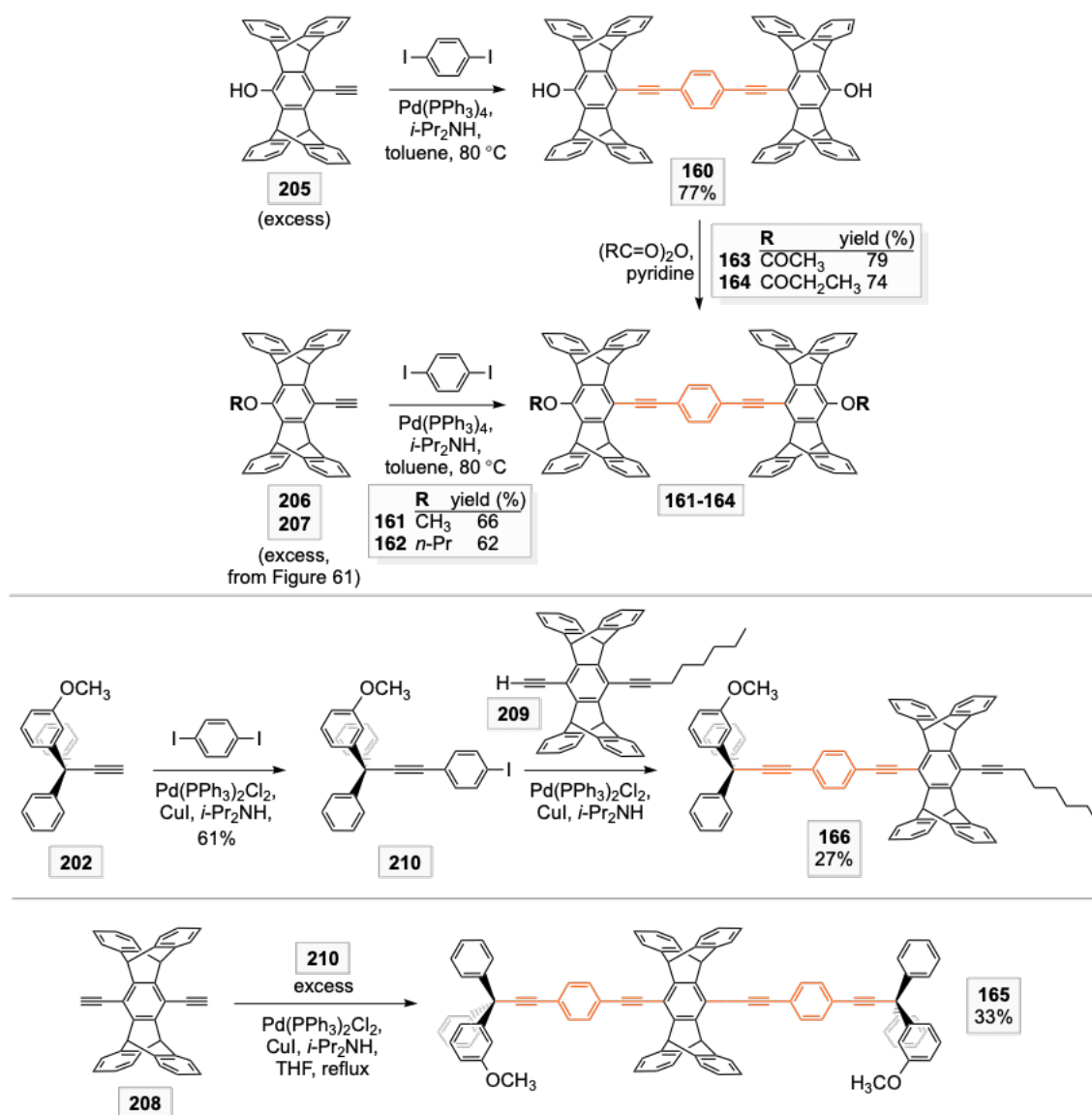


Figure 2.62 Final steps in the syntheses of molecular rotors **160-164** (top), **166** (middle), and **165** (bottom).

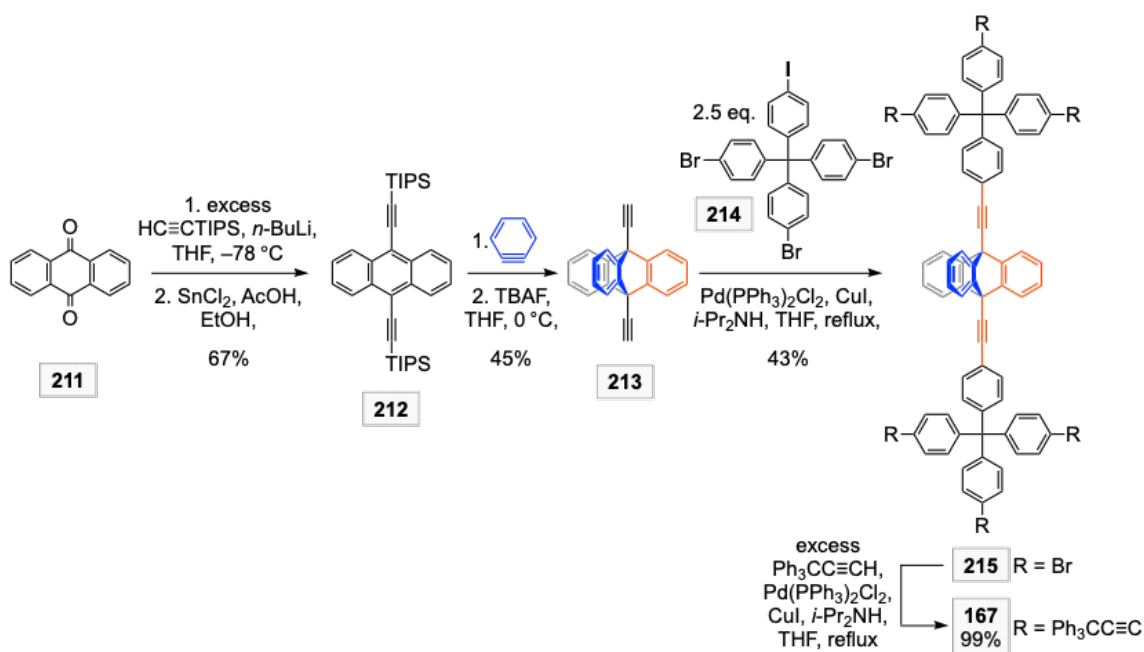


Figure 2.63 Synthesis of the dendrimer like molecular rotor **167**.

2.8.5. Toward molecular gyroscopes

The wide-ranging studies of the Garcia-Garibay group have provided a number of tantalizing leads with respect to molecular gyroscopes, especially within the context of amphidynamic crystals. Diverse types of rotors have been engineered with very low E_a values, and dipolar rotators, particularly fluorinated *p*-phenylenes, are easily introduced. For most any compound or crystal lattice, the principal factors affecting the rotational barriers can be identified. Certain generalizations, such as those embodied in Figure 2.46, have considerable applicability. However, exceptions can also be identified (e.g. Figure 2.47). These complicating factors render the realization of molecular gyroscopes more challenging, but the detailed road map provided by the preceding data should nevertheless facilitate future efforts.

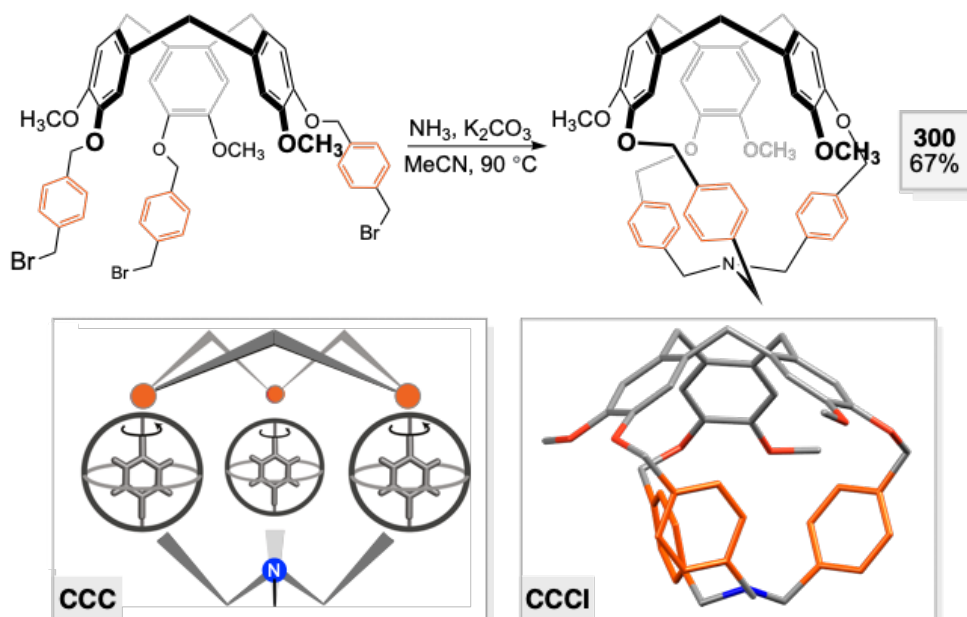


Figure 2.64 Synthesis and structural representations of a "gyroscope inspired" hemicyptophane (**300**).

2.9. Systems from other research groups

This section collects other reports subsequent to the previous review³³ featuring molecules that have been described as gyroscopes or in some way related to gyroscopes. Since some readers or researchers have need of a comprehensive bibliography, this includes compounds where the connection to gyroscopes may be tenuous. The authors also note (1) a study where the investigators formulated targets viewed as molecular gyroscopes but then encountered synthetic obstacles²¹⁸ and (2) papers viewed as germane by reviewers, some of which represent expansions of the scope of this review and in an even handed treatment would necessitate many additional citations.^{219,220}

2.9.1. Rotors comprised of covalent bonds

In a study stated as "gyroscope inspired", the hemicryptophane **300** has been prepared by the three-fold alkylation of ammonia as shown in Figure 2.64.²²¹ This molecule contains three *p*-phenylene rotators. Variable temperature NMR studies establish a ca. 10 kcal/mol activation energy for rotation in CD₂Cl₂. Rotation of the three rotators appears not to be strongly correlated (i.e. little or no gearing). In this context, compounds with multiple *p*-phenylene rotators are not intrinsically rare, all appropriately sized [*n.n*]paracyclophanes qualify.

A report with a title claim of molecular gyroscopes is excerpted in Figure 2.65.²²² The macrocycles **301** and **302**, each of which feature two 2,6-disubstituted aniline moieties, have been condensed with the *trans*-cyclohexane-1,4-dicarboxaldehyde **303** to give the bis(imines) or Schiff bases **304** and **305**. Rotation about the aryl–nitrogen bonds is rapid on the NMR time scale at 298 K in CDCl₃. The authors of this review see a closer relationship of **304** and **305** to molecular turnstiles (section 2.4.1).

2.9.2. Supramolecularly or mechanically bonded systems and MOFs

Capsules or container molecules comprised of two hemispheric components linked by hydrogen bonds are now well known.²²³ These are often ovoid in shape, as exemplified by the empty capsule **306** in Figure 2.66.^{224,225} Compound **306** can accommodate a single 1,4-acetoxybenzene guest (adduct **307**) or various disubstituted derivatives (**308-317**). The crystal structure of dimethoxy substituted **309** in Figure 2.66, as well as much supporting NMR data, establish that the acetoxy groups and

disubstituted *p*-phenylene ($p\text{-C}_6\text{H}_2\text{R}_2$) rotators are oriented along the long axis of the ovoid capsule.

NMR studies show that for adducts with small 1,4-diacetoxybenzene substituents (R), rotation remains rapid on the NMR time scale even at 218 K (**307**, **308**, **316**, **317**), whereas in others with bulky substituents, rotation remains slow even at 323 K (**314**, **315**). For adducts where the guest substituents have intermediate sizes (**309-313**), $\Delta G^\ddagger_{298\text{K}}$ values of 11.3-17.4 kcal/mol have been determined. It is noteworthy that the adduct with a dipolar difluorinated rotor (**317**) falls into the low barrier group. However, interactions of these assemblies with electric fields will be complicated by the fact that the stator (capsule) is also dipolar, as the top and bottom hemispheres are not identical.

A crystalline supramolecular gyroscope has been claimed in another report.²²⁶ The investigators were able to synthesize an adduct of 18-crown-6, the cation $t\text{-BuNH}_3^+$, and the anion $\text{ZnCl}_3(\text{H}_2\text{O})^-$. Two crystalline phases could be obtained, and the one of most interest (200 K) is depicted in Figure 2.67. The oxygen atom of the water molecule binds to zinc, and the two hydrogen atoms hydrogen bond to two oxygen atoms of the crown ether that have a 1,3-relationship. At the opposite face of the crown ether, the three hydrogen atoms of the NH_3^+ moiety hydrogen bond to three oxygen atoms that have a 1,3,5-relationship.

The $\text{O}\cdots\text{HOH}\cdots\text{O}$ hydrogen bonds are disordered over three symmetry related sites, suggesting that the water molecule is capable of rotation. Indeed, variable temperature dielectric spectroscopy, molecular dynamics simulations, and other

experiments provide strong support for such behavior. An E_a of 10.1 kcal/mol could be established. The $\text{NH}\cdots\text{O}$ hydrogen bonds are said to remain static. In view of the "tilt" of the water molecule, **318** qualifies as a dipolar rotator. Similarly to the capsule molecules in Figure 2.66, the endgroups in **318** are inequivalent, thereby affording a dipolar stator.

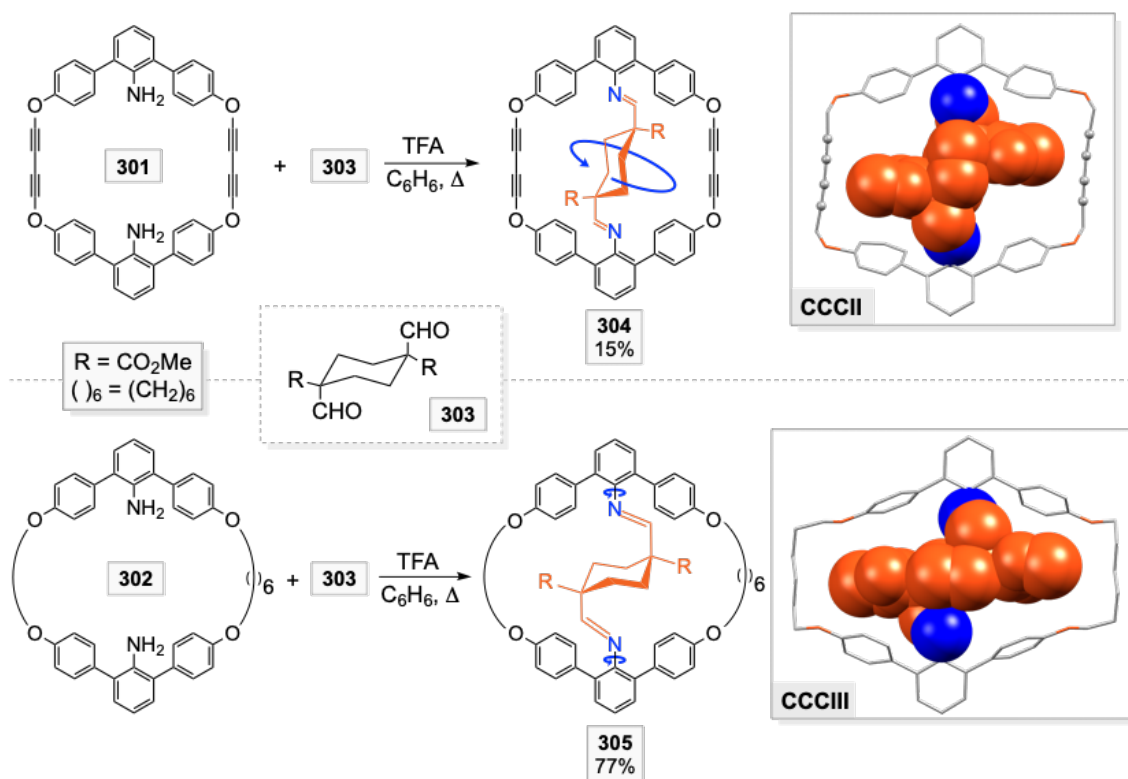


Figure 2.65 Syntheses and molecular structures of **304** and **305**, which were reported as molecular gyroscopes.

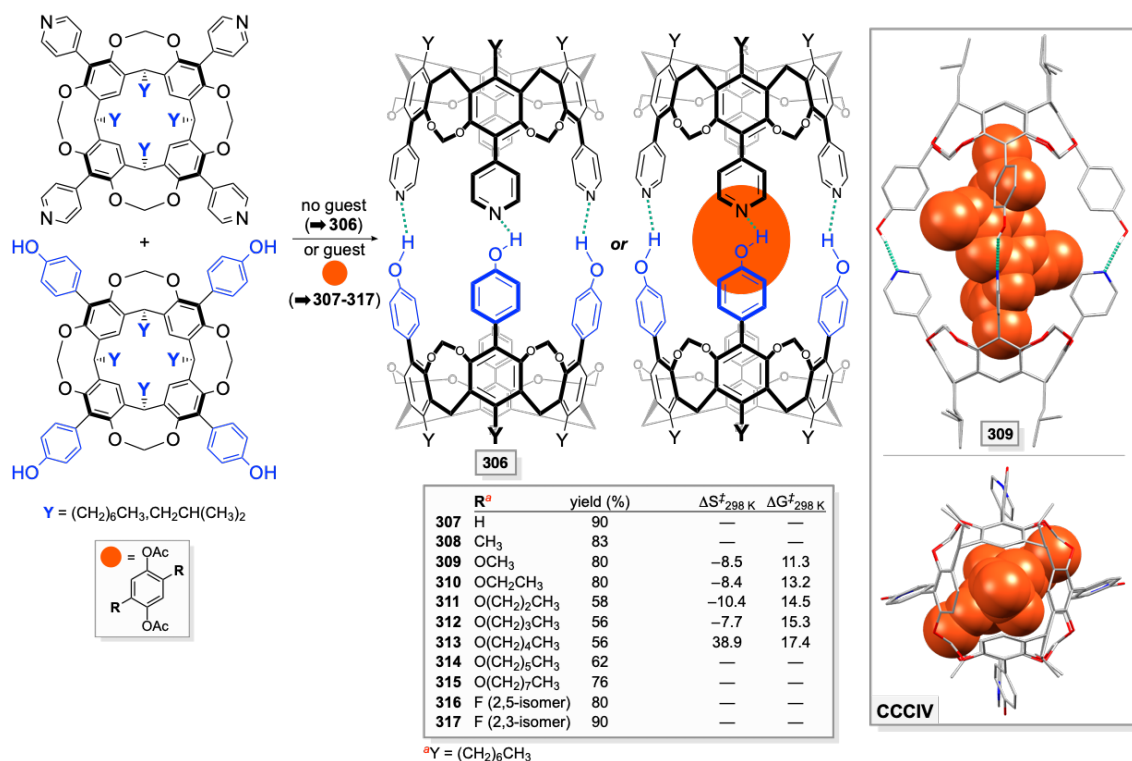


Figure 2.66 Self-assembly of gyroscope-like supramolecular systems **307-317**, rotational barriers of guest molecules, and crystallographic representations of the dimethoxy substituted adduct **309**.

Other supramolecular rotators have been reported in the literature, and selected references are supplied.^{227,228} There is furthermore additional and often quite informative literature dealing with rotators imbedded in MOFs,⁶² some of which is cited in the references for section 8.3.2. However, as emphasized above, coverage is restricted to systems for which the authors have sought connections to molecular gyroscopes.

The solid endohedral fullerene C₂Sc₂@C₈₄ (**319**)²²⁹ in Figure 2.68 represents a mechanically bonded system. In an experimental and computational study, the authors observe quantized rotational states for the C₂ unit and other attributes befitting a

quantum gyroscope. In the quantum gyroscope literature, introduced in section 2.1,²³⁻²⁸ most examples are not molecular in nature.

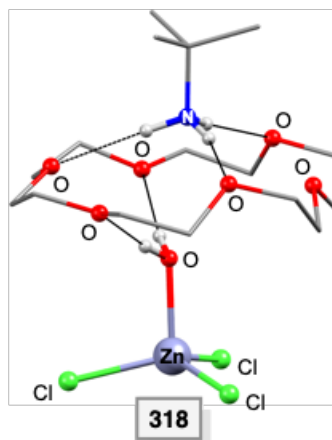


Figure 2.67 An assembly described as a supramolecular gyroscope (**318**) with a water molecule serving as a dipolar rotator.



Figure 2.68 Solid endohedral fullerene $C_2Sc_2@C_{84}$ (**319**), considered an example of a quantum gyroscope.

2.9.3. Other rotor motifs

There has also been great interest in incorporating molecular rotors into porous materials.^{220,230} In particular, Michl has explored the use of inclusion compounds to generate arrays of dipolar molecular rotors.²³¹⁻²³⁶ His workhorse systems are derived from tris(*o*-phenylenedioxy)cyclotriphosphazene (TPP) (**320**), the structure of which is provided in Figure 2.69. As illustrated by **CCCVI**, this compound can be crystallized with well-defined parallel channels of 4.5-5.0 Å internal diameter located ca. 11.5 Å apart.

Michl has synthesized a variety of complementary shaft like rotors, most of which are dipolar. Representative examples include **321-326** in Figure 2.70. Some of these are designed to fully intercalate, whereas others have "stoppers" that limit the depth of penetration. The schematic representation **CCCVII** features the rotor **327**, and **CCCVIII** represents an interpretation of NMR and other data with the rotor **324**.

The overarching goal of this work is to characterize rotor dipole/rotor dipole interactions, with the hopes of achieving systems with ferroelectric ground states (dipoles of all rotators aligned). Such materials hold particular promise for certain types of ultrafast microelectronic devices. Dielectric spectroscopy measurements establish very low rotational barriers of 1.2 to 9 kcal/mol. Importantly, these values pertain only to the dipolar subunit of the guest molecules, other segments of which may remain static. In any event, the dipole moments of the embedded rotors respond to an oscillating electric field. Hence, they should also be responsive to a rotating electric field.

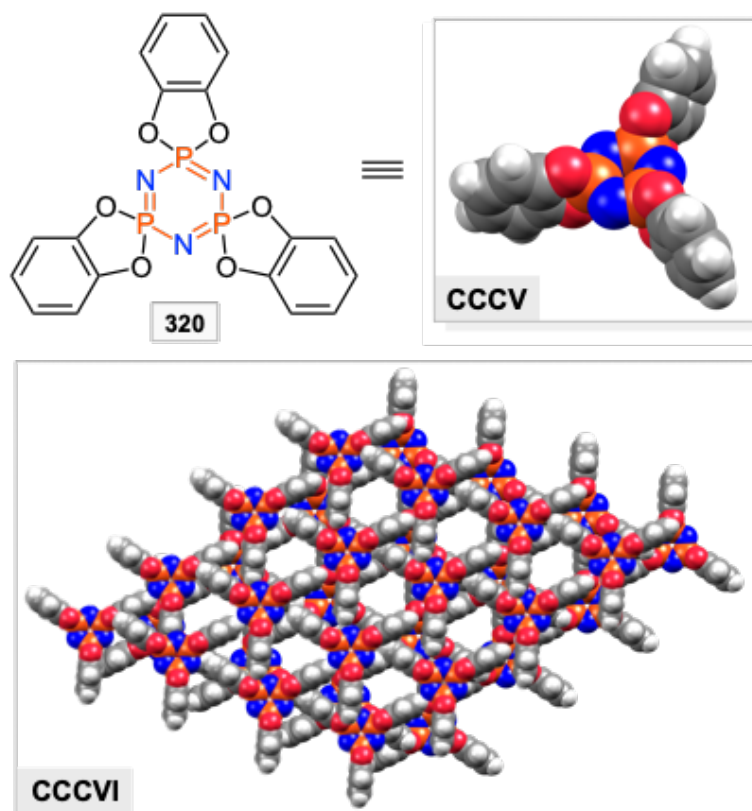


Figure 2.69 Tris(*o*-phenylenedioxy)cyclotriphosphazene (TPP; **320**), a space filling representation of the molecular structure (**CCCV**), and a top view of the crystal lattice (**CCCVI**).

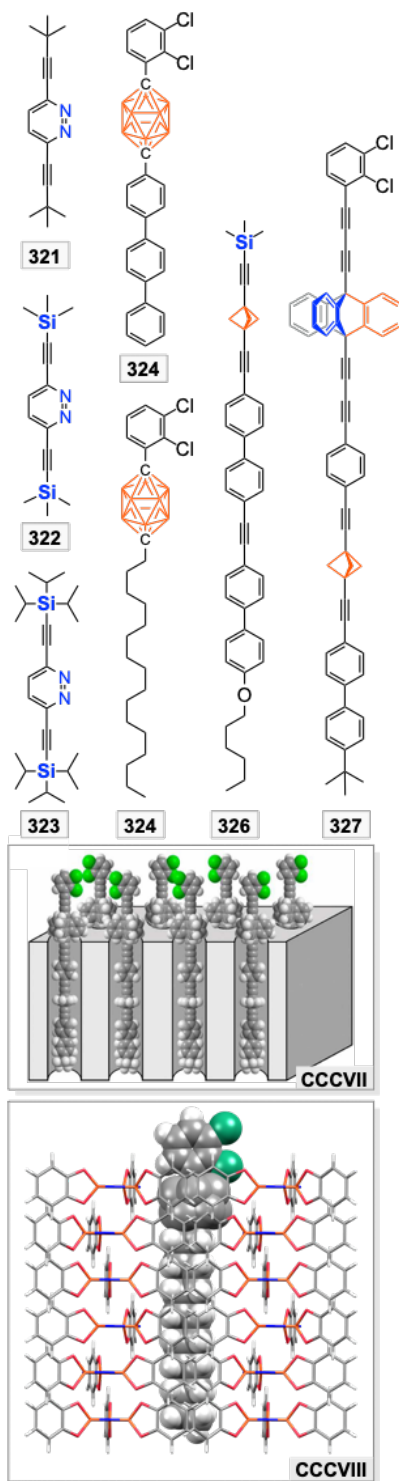


Figure 2.70 Typical molecular rotors (**321-327**) that have been intercalated into the channels of **CCCVI** (Figure 2.69) and representations of intercalated adducts of **327** (**CCCVII**, reproduced from ref [235](#). Copyright 2015 American Chemical Society) and **324** (**CCCIII**).

2.10. Conclusion

This review has outlined the considerable progress made during the period 2002-2020 toward the realization of functional molecular gyroscopes. A variety of general strategies for sterically protecting rotators and minimizing their rotational barriers have been identified, both in solution and the solid state. These in turn require significant degrees of molecular or crystal engineering. Toward these ends, an impressive underpinning of synthetic methodology has been developed. However, it should also be noted that a few rotors with very low barriers have more or less been identified by serendipity (e.g. **172** in Figure 2.54), and that fundamental, curiosity driven research may lead to unanticipated breakthroughs.

In the interest of providing readers with a full bibliography, this review has also included studies where an investigator has claimed to prepare a molecular gyroscope, or some related species, but has not fully substantiated or defined what is meant by the claim. For example, the authors have always applied "gyroscope-like" to the compounds from their laboratory highlighted in section 2.6. For some of the "faux gyroscopes" depicted above, a variety of similar compounds can be found in the literature, but it is beyond the scope of this review to treat them.

Appreciable numbers of the preceding dipolar molecules and assemblies have been studied by dielectric spectroscopy, in which an oscillating electric field is applied to "flip" the orientation of the dipole, or otherwise subjected to electric fields. However, extensions to rotating electric fields or alternative means of promoting unidirectional rotation (more demanding types of experiments)³¹ have not yet been reported. This

review represents the second installment of a projected trilogy,³³ and based upon the broad scope of progress and interest evident above, it is anticipated that the concluding article will be able to include examples of functional molecular gyroscopes. This will constitute a watershed event in the evolution of molecular devices.

2.11. References

(1) See <http://www.gyroscopes.org/uses.asp> (accessed November 21, 2020). The authors are unaware of any books or peer-reviewed articles that match the diverse examples on the gyroscope.org website, which is maintained by G. Turner.

(2) Crabtree, H. An elementary treatment of the theory of spinning tops and gyroscopic motion. Merchant Books, unrevealed location (<http://merchantbooksonline.com>), **2007**. ISBN 1-933998-95-4.

(3) Armenise, M. N.; Ciminelli, C.; Dell'Olio, F.; Passaro, V. M. N. Advances in gyroscope technologies. Springer, Berlin, **2010**. ISBN: 978-3-642-15493-5.

(4) This citation and references **5** and **6** involve medical technologies: Najafi, B.; Aminian, K.; Loew, F.; Blanc, Y.; Robert, P. A. Measurement of stand-sit and sit-stand transitions using a miniature gyroscope and its application in fall risk evaluation in the elderly. *IEEE Trans. Biomed. Eng.* **2002**, *49*, 843-851.

(5) Lim, Y. P.; Brown, I. T.; Khoo, J. C. T. An accurate and robust gyroscope-based pedometer. *2008 30th Annual International Conference IEEE EMBS Conference*, **2008**, 4587-4590.

(6) Kim, T. S.; Park, D. D. H.; Lee, B. Y.; Han, D. G.; Shim, J. S.; Lee, Y. J. Kim, P. C. W. A study on the measurement of wrist motion range using the iPhone 4 gyroscope application. *Ann. Plast. Surg.* **2014**, *73*, 215-218.

(7) Delporte, B.; Perroton, L.; Grandpierre, T.; Trichet, J. Accelerometer and magnetometer based gyroscope emulation on smart sensor for a virtual reality application. *Sensors & Transducers Journal*, **2012**, *14*, 32-47.

(8) Desai, P. R.; Desai, P. N.; Ajmera, K. D.; Mehta, K. A review paper on oculus rift-a virtual reality headset. *IJETT*. **2014**, 13, 175-179.

(9) Broquetas, A.; Comerón, A.; Gelonch, A.; Fuertes, J. M.; Castro, J. A.; Felip, D.; López, M. A.; Pulido. J. A. Track detection in railway sidings based on MEMS gyroscope sensors. *Sensors*, **2012**, 12, 16228-16249.

(10) Aroganam, G.; Manivannan, N.; Harrison, D. Review on wearable technology sensors used in consumer sport applications. *Sensors*, **2019**, 19, 1983-2008.

(11) Kumar, N.; Dixit, A. Nanotechnology in futuristic warfare, in *Nanotechnology for Defence Applications*, Springer; **2019**, section 8.4.2, ISBN-13: 978-3-030-29879-1.

(12) Gyroscope self-leveling pool table on the cruise ship *Radiance of the Seas*. (YouTube) <https://www.youtube.com/watch?v=N-aE5oszXyQ> (accessed November 21, 2020).

(13) Fictional characters are often useful in outreach lectures. The use of gyroscopic stabilizers in Iron Man's flying suit was first described in Iron Man, April 1976, Vol. 1, #85 (see <https://www.quora.com/How-do-Tony-Starks-Iron-Man-suits-generate-lift-for-horizontal-flight>, accessed November 21, 2020).

(14) This BMW motorcycle balances itself. <https://www.usatoday.com/story/money/2016/10/11/bmws-future-vision-includes-self-balancing-motorcycle/91908774/> (accessed November 21, 2020). This new motorcycle uses a gyroscope sensor that allows the rider to never have to put down a foot, even at a standstill.

(15) Butikov, E. Precession and nutation of a gyroscope. *Eur. J. Phys.* **2006**, *27*, 1071-1081.

(16) Kleppner, D.; Kolenkow, R. An introduction to mechanics. Cambridge University Press: Cambridge, UK; 2010; Chapters 7.3-7.5.

(17) Passaro, V. M. N.; Cuccovillo, A.; Vaiani, L.; De Carlo, M.; Campanella, C. E. Gyroscope technology and applications: a review in the industrial perspective. *Sensors*, **2017**, *17*, 2284-2305.

(18) Yazdi, N.; Ayazi, F.; Najafi, K. Micromachined inertial sensors. *Proc. IEEE*, **1998**, *86*, 1640-1659.

(19) See https://en.wikipedia.org/wiki/Vibrating_structure_gyroscope (accessed November 09, 2020). This site has a diverse set of applications of Coriolis Vibratory Gyroscope (CVG).

(20) Wen, H.; Daruwalla, A.; Ayazi, F. Resonant pitch and roll silicon gyroscopes with sub-micron-gap slanted electrodes: breaking the barrier toward high-performance monolithic inertial measurement units. *Microsyst. & Nanoeng.* **2017**, *3*, 16092.

(21) Wen, H.; Daruwalla, A.; Liu, C. S.; Ayazi, F. A high-frequency resonant framed annulus pitch or roll gyroscope for robust high-performance single-chip inertial measurement units. *J. Microelectromech. Syst.* **2018**, *27*, 995-1008.

(22) Jin, L.; Qin, S.-Y.; Zhang, R.; Li, M.-W. High-sensitivity tunneling magneto-resistive micro-gyroscope with immunity to external magnetic interference. *Sci. Rep.* **2020**, *10*, 16441.

- (23) This citation and references 24-28 are provided as recent lead references: Landon-Cardinal, O.; MacKenzie, R. Decoherence of a quantum gyroscope. *Phys. Rev. A* **2012**, *85*, 022333.
- (24) Toro, C.; Liu, Q.; Echebiri, G. O.; Mullin, A. S. Inhibited rotational quenching in oriented ultra-high rotational states of CO₂. *Mol. Phys.* **2013**, *111*, 1892-1901.
- (25) Kok, P.; Dunningham, J.; Ralph, J. F. Role of entanglement in calibrating optical quantum gyroscopes. *Phys. Rev. A* **2017**, *95*, 012326.
- (26) Song, X.; Wang, L.; Diao, W.; Duan, C. Quantum gyroscope based on Berry phase of spins in diamond. *Proc. SPIE* **2018**, *10697*, 106974K; DOI: 10.1117/12.2309334.
- (27) Song, X.; Wang, L.; Feng, F.; Lou, L.; Diao, W.; Duan, C. Nanoscale quantum gyroscope using a single ¹³C nuclear spin coupled with a nearby NV center in diamond. *J. Appl. Phys.* **2018**, *123*, 114301.
- (28) Tian, T.; Wang, Z.; Song, L. J. Rotation sensing in two coupled whispering-gallery-mode resonators with loss and gain. *Phys. Rev. A* **2019**, *100*, 043810.
- (29) Zhang, K.; Zhao, N.; Wang, Y.-H. Closed-loop nuclear magnetic resonance gyroscope based on Rb–Xe. *Sci. Rep.* **2020**, *10*, 2258.
- (30) iPhone 4's new gyroscope. Jobs, S. (YouTube) <https://www.youtube.com/watch?v=ORcu-c-qnjg> (accessed November 21, 2020).
- (31) Kottas, G. S.; Clarke, L. I.; Horinek, D.; Michl, J. Artificial molecular rotors. *Chem. Rev.* **2005**, *105*, 1281-1376.

- (32) Dattler, D.; Fuks, G.; Heiser, J.; Moulin, E.; Perrot, A.; Yao, X.; Giuseppone, N. Design of collective motions from synthetic molecular switches, rotors, and motors. *Chem. Rev.* **2020**, *120*, 310-433.
- (33) Skopek, K.; Hershberger, M. C.; Gladysz, J. A. Gyroscopes and the chemical literature: 1852-2002. *Coord. Chem. Rev.* **2007**, *251*, 1723-1733.
- (34) For reviews by Garcia-Garibay, see references [35-37](#) and Garcia-Garibay, M. A. Crystalline molecular machines: encoding supramolecular dynamics into molecular structure. *Proc. Natl. Acad. Sci. U.S.A.* **2005**, *102*, 10771-10776.
- (35) Karlen, S. D.; Garcia-Garibay, M. A. Amphidynamic crystals: structural blueprints for molecular machines. *Top. Curr. Chem.* **2005**, *262*, 179-227.
- (36) Khuong, T.-A. V.; Nuñez, J. E.; Godinez, C. E.; Garcia-Garibay, M. A. Crystalline molecular machines: a quest toward solid-state dynamics and function. *Acc. Chem. Res.* **2006**, *39*, 413-422.
- (37) Howe, M. E.; Garcia-Garibay, M. A. The roles of intrinsic barriers and crystal fluidity in determining the dynamics of crystalline molecular rotors and molecular machines. *J. Org. Chem.* **2019**, *84*, 9835-9849.
- (38) Magnera, T. F.; Michl, J. Altitudinal surface-mounted molecular rotors. *Top. Curr. Chem.* **2005**, *262*, 63-97.
- (39) Vacek, J.; Michl, J. Molecular dynamics of a grid-mounted molecular dipolar rotor in a rotating electric field. *Proc. Natl. Acad. Sci. U.S.A.* **2001**, *98*, 5481-5486.

(40) Arcenegui, J. J.; García-Sánchez, P.; Morgan, H.; Ramos, A. Electric-field-induced rotation of Brownian metal nanowires. *Phys. Rev. E* **2013**, *88*, 033025.

(41) Kopperger, E.; List, J.; Madhira, S.; Rothfischer, F.; Lamb, D. C.; Simmel, F. C. A self-assembled nanoscale robotic arm controlled by electric fields. *Science* **2018**, *359*, 296-301.

(42) Vacek, J.; Michl, J. Artificial surface-mounted molecular rotors: molecular dynamic simulations. *Adv. Funct. Mater.* **2007**, *17*, 730-739.

(43) Horansky, R. D.; Magnera, T. F.; Price, J. C.; Michl, J. Artificial dipolar molecular rotors. *Lect. Notes Phys.* **2007**, *711*, 303-330.

(44) Horinek, D.; Michl, J. Molecular dynamics simulation of an electric field driven dipolar molecular rotor attached to a quartz glass surface. *J. Am. Chem. Soc.* **2003**, *125*, 11900-11910.

(45) Zheng, X.; Mulcahy, M. E.; Horinek, D.; Galeotti, F.; Magnera, T. F.; Michl, J. Dipolar and nonpolar altitudinal molecular rotors mounted on an Au(111) surface. *J. Am. Chem. Soc.* **2004**, *126*, 4540-4542.

(46) Horinek, D.; Michl, J. Surface-mounted altitudinal molecular rotors in alternating electric field: single-molecule parametric oscillator molecular dynamics. *Proc. Natl. Acad. Sci. U.S.A.* **2005**, *102*, 14175-14180.

(47) Jian, H.; Tour, J. M. En route to surface-bound electric field-driven molecular motors. *J. Org. Chem.* **2003**, *68*, 5091-5103.

(48) Hutchison, J. A.; Uji-i, H.; Deres, A.; Vosch, T.; Rocha, S.; Müller, S.; Bastian, A. A.; Enderlein, J.; Nourouzi, H.; Li, C.; Herrmann, A.; Müllen, K.; De

Schryver, F.; Hofkens, J. A surface-bound molecule that undergoes optically biased Brownian rotation. *Nat. Nanotechnol.* **2014**, *9*, 131-136.

(49) Mulcahy, M. E.; Bastl, Z.; Stensrud, K. F.; Magnera, T. F.; Michl, J. Mercury-mediated attachment of metal-sandwich-based altitudinal molecular rotors to gold surfaces. *J. Phys. Chem. C* **2010**, *114*, 14050-14060.

(50) Caskey, D. C.; Michl, J. Toward self-assembled surface-mounted prismatic altitudinal rotors. A test case: trigonal and tetragonal prisms. *J. Org. Chem.* **2005**, *70*, 5442-5448.

(51) Mulcahy, M. E.; Magnera, T. F.; Michl, J. Molecular rotors on Au(111): rotator orientation from IR spectroscopy. *J. Phys. Chem. C* **2009**, *113*, 20698-20704.

(52) Tierney, H. L.; Baber, A. E.; Jewell, A. D.; Iski, E. V.; Boucher, M. B.; Sykes, E. C. H. Mode-selective electrical excitation of a molecular rotor. *Chem. Eur. J.* **2009**, *15*, 9678-9680.

(53) Jewell, A. D.; Tierney, H. L.; Baber, A. E.; Iski, E. V.; Laha, M. M.; Sykes, E. C. H. Time-resolved studies of individual molecular rotors. *J. Phys. Condens. Matter* **2010**, *22*, 264006.

(54) Tierney, H. L.; Calderon, C. E.; Baber, A. E.; Sykes, E. C. H.; Wang, F. Understanding the rotational mechanism of a single molecule: STM and DFT Investigations of dimethyl sulfide molecular rotors on Au(111). *J. Phys. Chem. C* **2010**, *114*, 3152-3155.

(55) Murphy, C. J.; Smith, Z. C.; Pronschinski, A.; Lewis, E. A.; Liriano, M. L.; Wong, C.; Ivimey, C. J.; Duffy, M.; Musial, W.; Therrien, A. J. Thomas III, S. W.;

Sykes, E. C. H. Ullmann coupling mediated assembly of an electrically driven altitudinal molecular rotor. *Phys. Chem. Chem. Phys.* **2015**, *17*, 31931-31937.

(56) Wasio, N. A.; Slough, D. P.; Smith, Z. C.; Ivimey, C. J.; Thomas III, S. W.; Lin, Y.-S.; Sykes, E. C. H. Correlated rotational switching in two-dimensional. *Nat. Commun.* **2017**, *8*, 16057-16062.

(57) Balema, T. A.; Ulumuddin, N.; Murphy, C. J.; Slough, D. P.; Smith, Z. C.; Hannagan, R. T.; Wasio, N. A.; Larson, A. M.; Patel, D. A.; Gordon, K. McEwen, J.-S.; Lin, Y.-S.; Sykes, E. C. H. Controlling molecular switching via chemical functionality: ethyl vs methoxy rotors. *J. Phys. Chem. C* **2019**, *123*, 23738-23746.

(58) Vacek, J.; Chocholousova, J.; Michl, J. Calculations for a gas-flow driven molecular rotor. *IEEE*, **2007**, 153-157.

(59) Prokop, A.; Vacek, J.; Michl, J. Friction in carborane-based molecular rotors driven by gas flow or electric field: classical molecular dynamics. *ACS Nano*, **2012**, *6*, 1901-1914.

(60) Zhou, H.-C.; Long, J. R.; Yaghi, O. M. Introduction to metal-organic frameworks. *Chem. Rev.* **2012**, *112*, 673-674. This article represents the introduction to a thematic issue with many relevant reviews.

(61) Zhou, H.-C.; Kitagawa, S. Metal-organic frameworks (MOFs). *Chem. Soc. Rev.* **2014**, *43*, 5415-5418. This article represents the introduction to a thematic issue with many relevant reviews.

- (62) Perego, J.; Bracco, S.; Negroni, M.; Bezuidenhout, C. X.; Prando, G.; Carretta, P.; Comotti, A.; Sozzani, P. Fast motion of molecular rotors in metal-organic framework struts at very low temperatures. *Nat. Chem.* **2020**, *12*, 845-851.
- (63) von Hippel, A. R. *Dielectrics and waves*. John Wiley & Sons, New York, **1954**.
- (64) Daniel, V. V. *Dielectric relaxation*. Academic Press: London, **1967**.
- (65) McCrum, N. G.; Read, B. E.; Williams, G. *Anelastic and dielectric effects in polymeric solids*. John Wiley & Sons, New York, **1967**.
- (66) Bedard, T. C.; Moore, J. S. Design and synthesis of a "molecular turnstile". *J. Am. Chem. Soc.* **1995**, *117*, 10662-10671.
- (67) Hirata, O.; Takeuchi, M.; Shinkai, S. Allosteric binding of anionic guests to a bicyclic host which imitates the action of a 'turnstile'. *Chem. Commun.* **2005**, 3805-3807.
- (68) Carella, A.; Launay, J.-P.; Poteau, R.; Rapenne, G. Synthesis and reactivity of [penta(4-halogenophenyl)cyclopentadienyl][hydrotris(indazolyl)borato]ruthenium(II) complexes: rotation-induced Fosbury flop in an organometallic molecular turnstile. *Chem. Eur. J.* **2008**, *14*, 8147-8156.
- (69) Weibel, N.; Mishchenko, A.; Wandlowski, T.; Neuburger, M.; Leroux, Y.; Mayor, M. Catechol-based macrocyclic rods: en route to redox-active molecular switches. *Eur. J. Org. Chem.* **2009**, 6140-6150.

- (70) Yu, C.; Ma, L.; He, J.; Xiang, J.; Deng, X.; Wang, Y.; Chen, X.; Jiang, H. Flexible, linear chains act as baffles to inhibit the intramolecular rotation of molecular turnstiles. *J. Am. Chem. Soc.* **2016**, *138*, 15849-15852.
- (71) Wang, G.; Xiao, H.; He, J.; Xiang, J.; Wang, Y.; Chen, X.; Che, Y.; Jiang, H. Molecular turnstiles regulated by metal ions. *J. Org. Chem.* **2016**, *81*, 3364-3371.
- (72) Le Pleux, L.; Kapatsina, E.; Hildesheim, J.; Häussinger, D.; Mayor, M. A molecular turnstile as an *E*-field-triggered single-molecule switch: concept and synthesis. *Eur. J. Org. Chem.* **2017**, *2017*, 3165-3178.
- (73) Lang, T.; Guenet, A.; Graf, E.; Kyritsakas, N.; Hosseini, M. W. Porphyrin based molecular turnstiles. *Chem. Commun.* **2010**, *46*, 3508-3510.
- (74) Lang, T.; Graf, E.; Kyritsakas, N.; Hosseini, M. W. Open and closed states of a porphyrin based molecular turnstile. *Dalton Trans.* **2011**, *40*, 3517-3523.
- (75) Lang, T.; Graf, E.; Kyritsakas, N.; Hosseini, M. W. An oscillating molecular turnstile. *Dalton Trans.* **2011**, *40*, 5244-5248.
- (76) Guenet, A.; Graf, E.; Kyritsakas, N.; Hosseini, M. W. Porphyrin-based switchable molecular turnstiles. *Chem. Eur. J.* **2011**, *17*, 6443-6452.
- (77) Lang, T.; Graf, E.; Kyritsakas, N.; Hosseini, M. W. Strapped-porphyrin-based molecular turnstiles. *Chem. Eur. J.* **2012**, *18*, 10419-10426.
- (78) Lang, T.; Graf, E.; Kyritsakas, N.; Hosseini, M. W. Zinc- and palladium-porphyrin based turnstiles. *New J. Chem.* **2013**, *37*, 112-118.
- (79) Zigon, N.; Guenet, A.; Graf, E.; Kyritsakas, N.; Hosseini, M. W. A platinum turnstile with a palladium lock. *Dalton Trans.* **2013**, *42*, 9740-9745.

- (80) Zigon, N.; Larpent, P.; Jouaiti, A.; Kyritsakas, N.; Hosseini, M. W. Optical reading of the open and closed states of a molecular turnstile. *Chem. Commun.* **2014**, *50*, 5040-5042.
- (81) Zigon, N.; Larpent, P.; Jouaiti, A.; Kyritsakas, N.; Hosseini, M. W. A luminescent molecular turnstile. *Dalton Trans.* **2014**, *43*, 15779-15784.
- (82) Zigon, N.; Kyritsakas, N.; Hosseini, M. W. Organometallic turnstiles: acid and base locking and unlocking. *Dalton Trans.* **2014**, *43*, 152-157.
- (83) Zigon, N.; Hosseini, M. W. A bi-stable Pt(II) based molecular turnstile. *Chem. Commun.* **2015**, *51*, 12486-12489.
- (84) Meshkov, I. N.; Bulach, V.; Gorbunova, Y. G.; Kyritsakas, N.; Grigoriev, M. S.; Tsivadze, A. Y.; Hosseini, M. W. Phosphorus(V) porphyrin-based molecular turnstiles. *Inorg. Chem.* **2016**, *55*, 10774-10782.
- (85) Godde, B.; Jouaiti, A.; Fluck, A.; Kyritsakas, N.; Mauro, M.; Hosseini, M. W. Symmetrical or non-symmetrical luminescent turnstiles based on hydroquinone stators and rotors bearing pyridyl or *p*-dimethylaminopyridyl coordinating units. *Dalton Trans.* **2017**, *46*, 14897-14906.
- (86) Godde, B.; Ritaine, D.; Jouaiti, A.; Mauro, M.; Hosseini, M. W. A pyridyl-benzimidazole based molecular luminescent turnstile. *New J. Chem.* **2018**, *42*, 7810-7815.
- (87) Ng, P. L.; Lambert, J. N. Synthesis of macrocyclic inclusion complexes using olefin metathesis. *Synlett* **1999**, *1999*, 1749-1750.

(88) Zeits, P. D.; Rachiero, G. P.; Hampel, F.; Reibenspies, J. H.; Gladysz, J. A. Gyroscope-like platinum and palladium complexes with *trans*-spanning bis(pyridine) ligands. *Organometallics* **2012**, *31*, 2854-2877.

(89) Rochon, F. D.; Beauchamp, A. L.; Bensimon, C. Multinuclear NMR spectra of $[\text{Pt}(\text{L})\text{Cl}_3]^-$ (L = pyridine derivatives) complexes and crystal structure of *trans*-Pt(2,6-di(hydroxymethyl)pyridine) $_2\text{Cl}_2\cdot\text{H}_2\text{O}$. *Can. J. Chem.* **1996**, *74*, 2121-2130.

(90) Tessier, C.; Rochon, F. D. Multinuclear NMR study and crystal structures of complexes of the types *cis*- and *trans*-Pt(Ypy) $_2\text{X}_2$, where Ypy = pyridine derivative and X = Cl and I. *Inorganica Chim. Acta*, **1999**, *295*, 25-38.

(91) Shima, T.; Bauer, E. B.; Hampel, F.; Gladysz, J. A. Alkene metatheses in transition metal coordination spheres: dimacrocyclizations that join *trans* positions of square-planar platinum complexes to give topologically novel diphosphine ligands. *Dalton Trans.* **2004**, 1012-1028.

(92) Steigleder, E.; Shima, T.; Lang, G. M.; Ehnbohm, A.; Hampel, F.; Gladysz, J. A. Partially shielded $\text{Fe}(\text{CO})_3$ rotors: syntheses, structures, and dynamic properties of complexes with doubly *trans* spanning diphosphines, $\text{trans-}\overline{\text{Fe}(\text{CO})_3(\text{PhP}((\text{CH}_2)_n)_2\text{PPh})}$. *Organometallics* **2017**, *36*, 2891-2901.

(93) Joshi, H.; Kharel, S.; Bhuvanesh, N.; Gladysz, J. A. Synthesis, structure, and reactivity of doubly *trans*-spanning bis(dialkyl selenide) complexes; a new route to diselenamacrocycles via alkene metathesis in metal coordination spheres. *J. Organomet. Chem.* **2018**, *875*, 80-87.

(94) Stollenz, M.; Joshi, H.; Ehnbohm, A.; Fiedler, T.; Kharel, S.; Reibenspies, J. H.; Bhuvanesh, N.; Hall, M. B.; Gladysz, J. A. Platinum complexes containing or derived from olefinic phosphines $P(X)((CH_2)_6CH=CH_2)_2$ ($X = OH, Ph, (CH_2)_6CH=CH_2$); ring closing metatheses, structures, and *trans/cis* isomerizations. *Polyhedron* **2019**, *158*, 325-333.

(95) Setaka, W.; Sato, K.; Ohkubo, A.; Kabuto, C.; Kira, M. Phenylene-bridged polysilaalkane macrocycles as framed molecular rotor. *Chem. Lett.* **2006**, *35*, 596-597.

(96) Phan, S. T.; Setaka, W.; Kira, M. Ring-closing metathesis for the synthesis of phenylene-bridged silamacrocycles. *Chem. Lett.* **2007**, *36*, 1180-1181.

(97) Shima, T.; Hampel, F.; Gladysz, J. A. Molecular gyroscopes: $\{Fe(CO)_3\}$ and $\{Fe(CO)_2(NO)\}^+$ rotators encased in three-spoke stators; facile assembly by alkene metatheses. *Angew. Chem. Int. Ed.* **2004**, *43*, 5537-5540; molekulare gyroskope: $\{Fe(CO)_3\}$ - und $\{Fe(CO)_2(NO)\}^+$ -rotatoren in einem dreispeichigen stator; einfache synthese durch alkenmetathese, *Angew. Chem.* **2004**, *116*, 5653-5656.

(98) Nawara, A. J.; Shima, T.; Hampel, F.; Gladysz, J. A. Gyroscope-like molecules consisting of PdX_2/PtX_2 rotators encased in three-spoke stators: Synthesis via alkene metathesis, and facile substitution and demetalation. *J. Am. Chem. Soc.* **2006**, *128*, 4962-4963.

(99) Wang, L.; Hampel, F.; Gladysz, J. A. 'Giant' gyroscope-like molecules consisting of dipolar $Cl-Rh-CO$ rotators encased in three-spoke stators that define 25-27-membered macrocycles. *Angew. Chem. Int. Ed.* **2006**, *45*, 4372-4375; 'Gyroskop-

Giganten': Dipolare Cl–Rh–CO-rotatoren, umgeben von statoren aus drei speichen 25- bis 27-gliedriger makrocyclen, *Angew. Chem.* **2006**, *118*, 4479-4482.

(100) Wang, L.; Shima, T.; Hampel, F.; Gladysz, J. A. Gyroscope-like molecules consisting of three-spoke stators that enclose "switchable" neutral dipolar rhodium rotators; reversible cycling between faster and slower rotating Rh(CO)I and Rh(CO)₂I species. *Chem. Commun.* **2006**, 4075-4077.

(101) Hess, G. D.; Hampel, F.; Gladysz, J. A. Octahedral gyroscope-like molecules with M(CO)₃(X) rotators encased in three-spoked diphosphine stators: Syntheses by alkene metathesis/hydrogenation sequences, structures, dynamic properties, and reactivities. *Organometallics* **2007**, *26*, 5129-5131.

(102) Skopek, K.; Gladysz, J. A. Syntheses of gyroscope-like molecules via three-fold ring closing metatheses of bis(phosphine) complexes *trans*-L_yM(P((CH₂)_nCH=CH₂)₃)₂, and extensions to bis(phosphite) complexes *trans*-Fe(CO)₃(P(O(CH₂)_nCH=CH₂)₃)₂. *J. Organomet. Chem.* **2008**, *693*, 857-866.

(103) Nawara-Hultzsch, A. J.; Skopek, K.; Shima, T.; Barbasiewicz, M.; Hess, G. D.; Skaper, D.; Gladysz, J. A. Syntheses and palladium, platinum, and borane adducts of symmetrical trialkylphosphines with three terminal vinyl groups, P((CH₂)_mCH=CH₂)₃. *Z. Naturforsch. B.* **2010**, *65b*, 414-424.

(104) Nawara-Hultzsch, A. J.; Stollenz, M.; Barbasiewicz, M.; Szafert, S.; Lis, T.; Hampel, F.; Bhuvanesh, N.; Gladysz, J. A. Gyroscope-like molecules consisting of PdX₂/PtX₂ rotators within three-spoke dibridgehead diphosphine stators: Syntheses,

substitution reactions, structures, and dynamic properties. *Chem. Eur. J.* **2014**, *20*, 4617-4637.

(105) Estrada, A. L.; Jia, T.; Bhuvanesh, N.; Blümel, J.; Gladysz, J. A. Substitution and catalytic chemistry of gyroscope-like complexes derived from Cl–Rh–CO rotators and triply *trans* spanning di(trialkylphosphine) ligands. *Eur. J. Inorg. Chem.* **2015**, *2015*, 5318-5321.

(106) Lang, G. M.; Shima, T.; Wang, L.; Cluff, K. J.; Skopek, K.; Hampel, F.; Blümel, J.; Gladysz, J. A. Gyroscope-like complexes based on dibridgehead diphosphine cages that are accessed by three-fold intramolecular ring closing metatheses and encase $\text{Fe}(\text{CO})_3$, $\text{Fe}(\text{CO})_2(\text{NO})^+$, and $\text{Fe}(\text{CO})_3(\text{H})^+$ rotators. *J. Am. Chem. Soc.* **2016**, *138*, 7649-7663.

(107) Lang, G. M.; Bhuvanesh, N.; Reibenspies, J. H.; Gladysz, J. A. Syntheses, reactivity, structures, and dynamic properties of gyroscope-like iron carbonyl complexes based on dibridgehead diarsine cages. *Organometallics* **2016**, *35*, 2873-2889.

(108) Lang, G. M.; Skaper, D.; Hampel, F.; Gladysz, J. A. Synthesis, reactivity, structures, and dynamic properties of gyroscope like iron complexes with dibridgehead diphosphine cages: Pre- vs. post-metathesis substitutions as routes to adducts with neutral dipolar $\text{Fe}(\text{CO})(\text{NO})(\text{X})$ rotors. *Dalton Trans.* **2016**, *45*, 16190-16204.

(109) Taher, D.; Nawara-Hultsch, A. J.; Bhuvanesh, N.; Hampel, F.; Gladysz, J. A. Mono- and disubstitution reactions of gyroscope like complexes derived from Cl–Pt–Cl rotators within cage like dibridgehead diphosphine ligands. *J. Organomet. Chem.* **2016**, *821*, 136-141.

(110) Fiedler, T.; Bhuvanesh, N.; Hampel, F.; Reibenspies, J. H.; Gladysz, J. A. Gyroscope like molecules consisting of trigonal or square planar osmium rotators within three-spoked dibridgehead diphosphine stators: Syntheses, substitution reactions, structures, and dynamic properties. *Dalton Trans.* **2016**, *45*, 7131-7147.

(111) Hess, G. D.; Fiedler, T.; Hampel, F.; Gladysz, J. A. Octahedral gyroscope-like molecules consisting of rhenium rotators within cage-like dibridgehead diphosphine stators: Syntheses, substitution reactions, structures, and dynamic Properties. *Inorg. Chem.* **2017**, *56*, 7454-7469.

(112) Kharel, S.; Joshi, H.; Bhuvanesh, N.; Gladysz, J. A. Syntheses, structures, and thermal properties of gyroscope-like complexes consisting of PtCl₂ rotators encased in macrocyclic dibridgehead diphosphines P((CH₂)_n)₃P with extended methylene chains (*n* = 20/22/30) and isomers thereof. *Organometallics* **2018**, *37*, 2991-3000.

(113) Joshi, H.; Kharel, S.; Ehnbohm, A.; Skopek, K.; Hess, G. D.; Fiedler, T.; Hampel, F.; Bhuvanesh, N.; Gladysz, J. A. Three-fold intramolecular ring closing alkene metatheses of square planar complexes with *cis* phosphorus donor ligands P(X(CH₂)_mCH=CH₂)₃ (X = –, *m* = 5-10; X = O, *m* = 3-5): Syntheses, structures, and thermal properties of macrocyclic dibridgehead diphosphorus complexes. *J. Am. Chem. Soc.* **2018**, *140*, 8463-8478.

(114) Ruwwe, J.; Martín-Alvarez, J. M.; Horn, C. R.; Bauer, E. B.; Szafert, S.; Lis, T.; Hampel, F.; Cagle, P. C.; Gladysz, J. A. Olefin metatheses in metal coordination spheres: Versatile new strategies for the construction of novel monohapto or polyhapto

cyclic, macrocyclic, polymacrocyclic, and bridging ligands. *Chem. Eur. J.* **2001**, *7*, 3931-3950.

(115) Stahl, J.; Bohling, J. C.; Bauer, E. B.; Peters, T. B.; Mohr, W.; Martín-Alvarez, J. M.; Hampel, F.; Gladysz, J. A. *sp* carbon chains surrounded by *sp*³ carbon double helices: A class of molecules that are accessible by self-assembly and models for "insulated" molecular-scale devices. *Angew. Chem. Int. Ed.* **2002**, *41*, 1871-1876; Von *sp*³-kohlenstoff-helices umgebene *sp*-kohlenstoffketten: Eine klasse von molekülen, die durch selbstorganisation zugänglich und modell-verbindungen für 'isolierte' molekulare bauelemente sind, *Angew. Chem.* **2002**, *114*, 1951-1957.

(116) Horn, C. R.; Martín-Alvarez, J. M.; Gladysz, J. A. Olefin metatheses in metal coordination spheres: A new approach to steric shielding in dirhenium *sp* carbon chain complexes of the formula (η^5 -C₅Me₅)Re(NO)(PR₃)(C≡CC≡CC≡CC≡C)-(R₃P)(ON)Re(η^5 -C₅Me₅). *Organometallics* **2002**, *21*, 5386-5393.

(117) Bauer, E. B.; Hampel, F.; Gladysz, J. A. Alkene metatheses in transition metal coordination spheres: Effect of ring size and substitution on the efficiencies of macrocyclizations that join *trans* positions of square-planar platinum complexes. *Organometallics* **2003**, *22*, 5567-5580.

(118) Lewanzik, N.; Oeser, T.; Blümel, J.; Gladysz, J. A. Generation of *trans*-spanning diphosphine ligands via alkene metathesis: Synthesis, structure, and dynamic behavior of a missing link in a series of square-planar platinum complexes. *J. Mol. Catal. A. Chem.* **2006**, *254*, 20-28.

(119) Han, J.; Deng, C.; Fang, R.; Zhao, D.; Wang, L.; Gladysz, J. A. Square-planar palladium complexes with *trans* di- and tribenzylphosphine ligands bearing O(CH₂)₄CH=CH₂ substituents; two- and three-fold intramolecular ring-closing metatheses. *Organometallics* **2010**, *29*, 3231-3234.

(120) For a representative example of the additional content, see Kharel, S.; Joshi, H.; Bierschenk, S.; Stollenz, M.; Taher, D.; Bhuvanesh, N.; Gladysz, J. A. Homeomorphic isomerization as a design element in container molecules; binding, displacement, and selective transport of MCl₂ species (M = Pt, Pd, Ni). *J. Am. Chem. Soc.* **2017**, *139*, 2172-2175.

(121) T. Fiedler, J. A. Gladysz, Multifold ring closing olefin metatheses in syntheses of organometallic molecules with unusual connectivities, in *Olefin metathesis – theory and practice*, Grela, K. Ed.; John Wiley & Sons, New Jersey; **2014**, pp. 311-328.

(122) Review: Setaka, W.; Inagaki, Y.; Yamaguchi, K. Chemistry of macrocage molecules with a bridged π -electron system as crystalline molecular gyrotops. *J. Syn. Org. Chem. Jpn.* **2019**, *77*, 813-822.

(123) Setaka, W.; Yamaguchi, K. Thermal modulation of birefringence observed in a crystalline molecular gyrotop. *Proc. Natl. Acad. Sci. U.S.A.* **2012**, *109*, 9271-9275.

(124) Setaka, W.; Yamaguchi, K. Order–disorder transition of dipolar rotor in a crystalline molecular gyrotop and its optical change. *J. Am. Chem. Soc.* **2013**, *135*, 14560-14563.

- (125) Setaka, W.; Yamaguchi, K. A molecular balloon: Expansion of a molecular gyrotop cage due to rotation of the phenylene rotor. *J. Am. Chem. Soc.* **2012**, *134*, 12458-12461.
- (126) Setaka, W.; Koyama, A.; Yamaguchi, K. Cage size effects on the rotation of molecular gyrotops with 1,4-naphthalenediyl rotor in solution. *Org. Lett.* **2013**, *15*, 5092-5095.
- (127) Setaka, W.; Higa, S.; Yamaguchi, K. Ring-closing metathesis for the synthesis of a molecular gyrotop. *Org. Biomol. Chem.* **2014**, *12*, 3354-3357.
- (128) Inagaki, Y.; Yamaguchi, K.; Setaka, W. A crystalline molecular gyrotop with germanium junctions between a phenylene rotor and alkyl spokes. *RSC Adv.* **2014**, *4*, 58624-58630.
- (129) Setaka, W.; Inoue, K.; Higa, S.; Yoshigai, S.; Kono, H.; Yamaguchi, K. Synthesis of crystalline molecular gyrotops and phenylene rotation inside the cage. *J. Org. Chem.* **2014**, *79*, 8288-8295.
- (130) Shionari, H.; Inagaki, Y.; Yamaguchi, K.; Setaka, W. A pyrene-bridged macrocage showing no excimer fluorescence. *Org. Biomol. Chem.* **2015**, *13*, 10511-10516.
- (131) Nishiyama, Y.; Inagaki, Y.; Yamaguchi, K.; Setaka, W. 1,4-naphthalenediyl-bridged molecular gyrotops: Rotation of the rotor and fluorescence in solution. *J. Org. Chem.* **2015**, *80*, 9959-9966.
- (132) Masuda, T.; Arase, J.; Inagaki, Y.; Kawahata, M.; Yamaguchi, K.; Ohhara, T.; Nakao, A.; Momma, H.; Kwon, E.; Setaka, W. Molecular gyrotops with a five-

membered heteroaromatic ring: Synthesis, temperature-dependent orientation of dipolar rotors inside the crystal, and its birefringence change. *Cryst. Growth Des.* **2016**, *16*, 4392-4401.

(133) Fujiwara, A.; Inagaki, Y.; Momma, H.; Kwon, E.; Yamaguchi, K.; Kanno, M.; Kono, H.; Setaka, W. A crystalline molecular gyrotop with a biphenylene dirotor and its temperature-dependent birefringence. *CrystEngComm* **2017**, *19*, 6049-6056.

(134) Takashima, H.; Inagaki, Y.; Momma, H.; Kwon, E.; Yamaguchi, K.; Setaka, W. Ferrocene-diyl bridged macrocages: Steric effects of the cage on the redox properties of ferrocene moiety. *Organometallics* **2018**, *37*, 1501-1506.

(135) Tsurunaga, M.; Inagaki, Y.; Momma, H.; Kwon, E.; Yamaguchi, K.; Yoza, K.; Setaka, W. Dielectric relaxation of powdered molecular gyrotops having a thiophene dioxide-diyl as a dipolar rotor. *Org. Lett.* **2018**, *20*, 6934-6937.

(136) Hashimoto, H.; Inagaki, Y.; Momma, H.; Kwon, E.; Setaka, W. Kinetic stabilization of carbazole nitroxides by inclusion in a macrocage and their electron spin resonance characterization. *J. Org. Chem.* **2019**, *84*, 11783-11789.

(137) Hashimoto, H.; Inagaki, Y.; Momma, H.; Kwon, E.; Yamaguchi, K.; Setaka, W. Polarized fluorescence of a crystal having uniaxially oriented molecules by a carbazole-diyl-bridged macrocage. *CrystEngComm* **2019**, *21*, 3910-3914.

(138) Inagaki, Y.; Ueda, S.; Yamaguchi, K.; Setaka, W. A furan-2,5-diyl bridged macrocage as a highly distorted molecular gyrotop. *Chem. Lett.* **2020**, *49*, 1291-1293.

- (139) Setaka, W.; Ohmizu, S.; Kabuto, C.; Kira, M. A molecular gyroscope having phenylene rotator encased in three-spoke silicon-based stator. *Chem. Lett.* **2007**, *36*, 1076-1077.
- (140) Setaka, W.; Ohmizu, S.; Kira, M. Molecular gyroscope having a halogen-substituted *p*-phenylene rotator and silaalkane chain stators. *Chem. Lett.* **2010**, *39*, 468-469.
- (141) Setaka, W.; Ohmizu, S.; Kira, M. Kinetic stabilization against the oxidation reaction induced by a silaalkane cage in a thiophene-bridged molecular gyroscope. *Chem. Commun.* **2014**, *50*, 1098-1100.
- (142) For crystallographically characterized examples, see reference [143](#) and Dixon, F. M.; Eisenberg, A. H.; Farrell, J. R.; Mirkin, C. A.; Liabe-Sands, L. M.; Rheingold, A. L. Neutral macrocycles via halide-induced ring opening of binuclear condensed intermediates. *Inorg. Chem.* **2000**, *39*, 3432-3433.
- (143) Koshevoy, I. O.; Sizova, O. V.; Tunik, S. P.; Lough, A.; Poë, A. J. A novel five-coordinate rhodium(I) complex. *Eur. J. Inorg. Chem.* **2005**, *2005*, 4516-4520.
- (144) E. V. Anslyn, D. A. Dougherty, *Modern physical organic chemistry*. University Science Books, Sausalito, California; **2006**, pp. 97-98.
- (145) E. N. Eliel, S. H. Wilen, *Stereochemistry of organic compounds*. John Wiley & Sons, New York; **1994**, pp. 624-629 and 1142-1155.
- (146) The dipoles approximately bisect the OC–Fe–NO angles, with the negative ends extending between the two oxygen atoms. See endnote 34 of reference 108.

- (147) Horansky, R. D.; Clarke, L. I.; Price, J. C.; Khuong, T.-A. V.; Jarowski, P. D.; Garcia-Garibay, M. A. Dielectric response of a dipolar molecular rotor crystal. *Phys. Rev. B* **2005**, *72*, 014302.
- (148) Horansky, R. D.; Clarke, L. I.; Winston, E. B.; Price, J. C.; Karlen, S. D.; Jarowski, P. D.; Santillan, R.; Garcia-Garibay, M. A. Dipolar rotor-rotor interactions in a difluorobenzene molecular rotor crystal. *Phys. Rev. B* **2006**, *74*, 054306.
- (149) Pickardt, J.; Rösch, L.; Schumann, H. Die kristallstruktur von tetracarbonyl(tri-*t*-butylphosphin) eisen. *J. Organomet. Chem.* **1976**, *107*, 241-248.
- (150) Rheingold, A. L.; Fountain, M. E. Tetracarbonyl(tri-*tert*-butylstibine)iron, $[\text{Fe}(\text{CO})_4\{\text{Sb}(\text{C}_4\text{H}_9)_3\}]$. *Acta Cryst.* **1985**, *C41*, 1162-1164.
- (151) Breunig, H. J.; Borrmann, T.; Lork, E.; Moldovan, O.; Rat, C. I.; Wagner, R. P. Syntheses, crystal structures and DFT studies of $[\text{Me}_3\text{EM}(\text{CO})_5]$ (E = Sb, Bi; M = Cr, W), *cis*- $[(\text{Me}_3\text{Sb})_2\text{Mo}(\text{CO})_4]$, and $[t\text{-Bu}_3\text{BiFe}(\text{CO})_4]$. *J. Organomet. Chem.* **2009**, *694*, 427-432.
- (152) Bauer, E. B.; Hampel, F.; Gladysz, J. A. Alkyne metatheses in transition metal coordination spheres: Convenient tungsten- and molybdenum-catalyzed syntheses of novel metallamacrocycles. *Adv. Synth. Catal.* **2004**, *346*, 812-822.
- (153) Prack, E.; O'Keefe, C. A.; Moore, J. K.; Lai, A.; Lough, A. J.; Macdonald, P. M.; Conradi, M. S.; Schurko, R. W.; Fekl, U. A Molecular rotor possessing an H–M–H "spoke" on a P–M–P "axle": A platinum(II) *trans*-dihydride spins rapidly even at 75 K. *J. Am. Chem. Soc.* **2015**, *137*, 13464-13467.

- (154) Yogendra, S.; Hennersdorf, F.; Bauzá, A.; Frontera, A.; Fischer, R.; Weigand, J. J. Carbodiphosphorane mediated synthesis of a triflyloxyphosphonium dication and its reactivity towards nucleophiles. *Chem. Commun.* **2017**, *53*, 2954-2957.
- (155) Marahatta, A. B.; Kanno, M.; Hoki, K.; Setaka, W.; Irle, S. Theoretical investigation of the structures and dynamics of crystalline molecular gyroscopes. *J. Phys. Chem. C.* **2012**, *116*, 24845-24854.
- (156) Dominguez, Z.; Dang, H.; Strouse, M. J.; Garcia-Garibay, M. A. Molecular "compasses" and "gyroscopes". I. Expedient synthesis and solid state dynamics of an open rotor with a bis(triarylmethyl) frame. *J. Am. Chem. Soc.* **2002**, *124*, 2398-2399.
- (157) Godinez, C. E.; Zepeda, G.; Garcia-Garibay, M. A. Molecular compasses and gyroscopes. II. Synthesis and characterization of molecular rotors with axially substituted bis[2-(9-triptycyl)ethynyl]arenes. *J. Am. Chem. Soc.* **2002**, *124*, 4701-4707.
- (158) Dominguez, Z.; Dang, H.; Strouse, M. J.; Garcia-Garibay, M. A. Molecular 'compasses' and 'gyroscopes.' III. Dynamics of a phenylene rotor and clathrated benzene in a slipping-gear crystal lattice. *J. Am. Chem. Soc.* **2002**, *124*, 7719-7727.
- (159) Dominguez, Z.; Khuong, A.-T. V.; Dang, H.; Sanrame, C. N.; Nuñez, J. E.; Garcia-Garibay, M. A. Molecular compasses and gyroscopes with polar rotors: Synthesis and characterization of crystalline forms. *J. Am. Chem. Soc.* **2003**, *125*, 8827-8837.
- (160) Khuong, T.-A. V.; Zepeda, G.; Ruiz, R.; Khan, S. I. Garcia-Garibay, M. A. Molecular compasses and gyroscopes: Engineering molecular crystals with fast internal rotation. *Cryst. Growth Des.* **2004**, *4*, 15-18.

(161) Czajkowska-Szczykowska, D.; Aguilar-Granda, A.; Maj, J.; Wilczewska, A. Z.; Witkowski, S.; Santillan, R.; Garcia-Garibay, M. A.; Morzycki, J. W.; Rodríguez-Molina, B. Solid state characterization of bridged steroidal molecular rotors: Effect of the rotator fluorination on their crystallization. *Cryst. Growth Des.* **2016**, *16*, 1599-1605.

(162) Rodríguez-Molina, B.; Farfán, N.; Romero, M.; Méndez-Stivalet, J. M.; Santillan, R.; Garcia-Garibay, M. A. Anisochronous dynamics in a crystalline array of steroidal molecular rotors: Evidence of correlated motion within 1D helical domains. *J. Am. Chem. Soc.* **2011**, *133*, 7280-7283.

(163) Rodríguez-Molina, B.; Pérez-Estrada, S.; Garcia-Garibay, M. A. Amphidynamic crystals of a steroidal bicyclo[2.2.2]octane rotor: A high symmetry group that rotates faster than smaller methyl and methoxy groups. *J. Am. Chem. Soc.* **2013**, *135*, 10388-10395.

(164) Rodríguez-Molina, B.; Ochoa, M. E.; Romero, M.; Khan, S. I.; Farfán, N.; Santillan, R.; Garcia-Garibay, M. A. Conformational polymorphism and isomorphism of molecular rotors with fluoroaromatic rotators and mestranol stators. *Cryst. Growth Des.* **2013**, *13*, 5107-5115.

(165) Czajkowska-Szczykowska, D.; Rodríguez-Molina, B.; Magaña-Vergara, N. E.; Santillan, R.; Morzycki, J. W.; Garcia-Garibay, M. A. Macrocyclic molecular rotors with bridged steroidal frameworks. *J. Org. Chem.* **2012**, *77*, 9970-9978.

(166) Pérez-Estrada, S.; Rodríguez-Molina, B.; Xiao, L.; Santillan, R.; Jiménez-Osés, G.; Houk, K. N.; Garcia-Garibay, M. A. Thermodynamic evaluation of aromatic

CH/ π interactions and rotational entropy in a molecular rotor. *J. Am. Chem. Soc.* **2015**, *137*, 2175-2178.

(167) Pérez-Estrada, S.; Rodríguez-Molina, B.; Maverick, E. F.; Khan, S. I.; Garcia-Garibay, M. A. Throwing in a monkey wrench to test and determine geared motion in the dynamics of a crystalline one-dimensional (1D) columnar rotor array. *J. Am. Chem. Soc.* **2019**, *141*, 2413-2420.

(168) Khuong, T.-A. V.; Zepeda, G.; Sanrame, C. N.; Dang, H.; Bartberger, M. D.; Houk, K. N.; Garcia-Garibay, M. A. Crankshaft motion in a highly congested bis(triarylmethyl)peroxide. *J. Am. Chem. Soc.* **2004**, *126*, 14778-14786.

(169) Stopin, A.; Garcia-Garibay, M. A. Crystals and aggregates of a molecular tetra-rotor with multiple trityl embraces derived from tetraphenyladamantane. *Cryst. Growth Des.* **2012**, *12*, 3792-3798.

(170) Torres-Huerta, A.; Rodríguez-Molina, B.; Höpfl, H.; Garcia-Garibay, M. A. Synthesis and solid-state characterization of self-assembled macrocyclic molecular rotors of bis(dithiocarbamate) ligands with diorganotin(IV). *Organometallics* **2014**, *33*, 354-362.

(171) Scudder, M.; Dance, I. Dimorphic intra- and intermolecular aryl motifs in symmetrical hexafaceted molecules $(Ar_nX)_3Y-Z-Y(XAr_n)_3$. *Chem. Eur. J.* **2002**, *8*, 5456-5468.

(172) Dance, I.; Scudder, M. Crystal supramolecularity: Elaborate six-, eight- and twelve-fold concerted phenyl embraces in compounds $[M(PPh_3)_3]_z$ and $[M(PPh_3)_4]_z$. *New J. Chem.* **1998**, *22*, 481-492.

(173) Gavezzotti, A. The calculation of molecular volumes and the use of volume analysis in the investigation of structured media and of solid-state organic reactivity. *J. Am. Chem. Soc.* **1983**, *105*, 5220-5225.

(174) Nangia, A. Pseudopolymorph: Retain this widely accepted term. *Cryst. Growth Des.* **2006**, *6*, 2-4.

(175) Commins, P.; Nuñez, J. E.; Garcia-Garibay, M. A. Synthesis of bridged molecular gyroscopes with closed topologies: Triple one-pot macrocyclization. *J. Org. Chem.* **2011**, *76*, 8355-8363.

(176) Nuñez, J. E.; Natarajan, A.; Khan, S. I.; Garcia-Garibay, M. A. Synthesis of a triply-bridged molecular gyroscope by a directed meridional cyclization strategy. *Org. Lett.* **2007**, *9*, 3559-3561.

(177) O'Brien, Z. J.; Karlen, S. D.; Khan, S.; Garcia-Garibay, M. A. Solid-state molecular rotors with perdeuterated stators: Mechanistic insights from biphenylene rotational dynamics in ordered and disordered crystal forms. *J. Org. Chem.* **2010**, *75*, 2482-2491.

(178) Karlen, S. D.; Garcia-Garibay, M. A. Highlighting gyroscopic motion in crystals in ^{13}C CPMAS spectra by specific isotopic substitution and restricted cross polarization. *Chem. Commun.* **2005**, 189-191.

(179) Gardinier, J. R.; Pellechia, P. J.; Smith, M. D. Ionic rotors. Preparation, structure, and dynamic solid-state ^2D NMR study of the 1,4-diethynylbenzenebis(triphenylborate) dianion. *J. Am. Chem. Soc.* **2005**, *127*, 12448-12449.

(180) Santillán, R.; Karlen, S. D.; Dang, H.; Garcia-Garibay, M. A. Synthesis and characterization of natural abundance and isotopically labeled 1,4-bis(3,3,3-triphenylpropynyl)-2,3-difluorobenzene. A molecular gyroscope with a polar rotator. *J. Mex. Chem. Soc.* **2008**, *52*, 125-129.

(181) Rodriguez-Molina, B.; Ochoa, M. E.; Farfán, N.; Santillan, R.; Garcia-Garibay, M. A. Synthesis, characterization, and rotational dynamics of crystalline molecular compasses with *N*-heterocyclic rotators. *J. Org. Chem.* **2009**, *74*, 8554-8565.

(182) Karlen, S. D.; Reyes, H.; Taylor, R. E.; Khan, S. I.; Hawthorne, M. F.; Garcia-Garibay, M. A. Symmetry and dynamics of molecular rotors in amphidynamic molecular crystals. *Proc. Natl. Acad. Sci. U.S.A.* **2010**, *107*, 14973-14977.

(183) Colvin, E. W. *Silicon in Organic Synthesis*. Butterworth, London, **1981**, Table 2.1. ISBN 0-408-1083102.

(184) Akimov, A. V.; Kolomeisky, A. B. Molecular dynamics study of crystalline molecular gyroscopes. *J. Phys. Chem. C*, **2011**, *115*, 13584-13591.

(185) Jin, M.; Chung, T. S.; Seki, T.; Ito, H.; Garcia-Garibay, M. A. Phosphorescence control mediated by molecular rotation and aurophilic interactions in amphidynamic crystals of 1,4-bis[tri-(*p*-fluorophenyl)phosphane-gold(I)-ethynyl]benzene. *J. Am. Chem. Soc.* **2017**, *139*, 18115-18121.

(186) Jin, M.; Yamamoto, S.; Seki, T.; Ito, H.; Garcia-Garibay, M. A. Anisotropic thermal expansion as the source of macroscopic and molecular scale motion in phosphorescent amphidynamic crystals. *Angew. Chem. Int. Ed.* **2019**, *58*, 18003-18010; *Angew. Chem.* **2019**, *131*, 18171-18178.

(187) Karlen, S. D.; Ortiz, R.; Chapman, O. L.; Garcia-Garibay, M. A. Effects of rotational symmetry order on the solid state dynamics of phenylene and diamantane rotators. *J. Am. Chem. Soc.* **2005**, *127*, 6554-6555.

(188) Arcos-Ramos, R.; Rodriguez-Molina, B.; Gonzalez-Rodriguez, E.; Ramirez-Montes, P. I.; Ochoa, M. E.; Santillan, R.; Farfán, N.; Garcia-Garibay, M. A. Crystalline arrays of molecular rotors with TIPS-trityl and phenolic-trityl stators using phenylene, 1,2-difluorophenylene and pyridine rotators. *RSC Adv.* **2015**, *5*, 55201-55208.

(189) Nuñez, J. E.; Khuong, T.-A. V.; Campos, L. M.; Farfán, N.; Dang, H.; Karlen, S. D.; Garcia-Garibay, M. A. Crystal phases and phase transitions in a highly polymorphogenic solid-state molecular gyroscope with *meta*-methoxytrityl frames. *Cryst. Growth Des.* **2006**, *6*, 866-873.

(190) Arcos-Ramos, R.; Rodríguez-Molina, B.; Romero, M.; Méndez-Stivalet, J. M.; Ochoa, M. E.; Ramírez-Montes, P. I.; Santillan, R.; Garcia-Garibay, M. A.; Farfán, N. Synthesis and evaluation of molecular rotors with large and bulky *tert*-butyldiphenylsilyloxy-substituted trityl stators. *J. Org. Chem.* **2012**, *77*, 6887-6894.

(191) Jiang, X.; O'Brien, Z. J.; Yang, S.; Lai, L. H.; Buenaflor, J.; Tan, C.; Khan, S.; Houk, K. N.; Garcia-Garibay, M. A. Crystal fluidity reflected by fast rotational motion at the core, branches, and peripheral aromatic groups of a dendrimeric molecular rotor. *J. Am. Chem. Soc.* **2016**, *138*, 4650-4656.

(192) Khuong, T.-A. V.; Dang, H.; Jarowski, P. D.; Maverick, E. F.; Garcia-Garibay, M. A. Rotational dynamics in a crystalline molecular gyroscope by variable-

temperature ^{13}C NMR, ^2H NMR, X-ray diffraction, and force field calculations. *J. Am. Chem. Soc.* **2007**, *129*, 839-845.

(193) The E_a value quoted for the rotation of the *p*-phenylene unit of **140** in Figure 15 of reference **37**, a perspective article (4.4 kcal/mol), is a typographical error (see Table 2.5 of this review for correct values from earlier papers).

(194) O'Brien, Z. J.; Natarajan, A.; Khan, S.; Garcia-Garibay, M. A. Synthesis and solid-state rotational dynamics of molecular gyroscopes with a robust and low density structure built with a phenylene rotator and a tri(*meta*-terphenyl)methyl stator. *Cryst. Growth Des.* **2011**, *11*, 2654-2659.

(195) Garcia-Garibay, M. A.; Godinez, C. E. Engineering crystal packing and internal dynamics in molecular gyroscopes by refining their components. Fast exchange of a phenylene rotator by ^2H NMR. *Cryst. Growth Des.* **2009**, *9*, 3124-3128.

(196) Godinez, C. E.; Zepeda, G.; Mortko, C. J.; Dang, H.; Garcia-Garibay, M. A. Molecular crystals with moving parts: Synthesis, characterization, and crystal packing of molecular gyroscopes with methyl-substituted triptycyl frames. *J. Org. Chem.* **2004**, *69*, 1652-1662.

(197) Karlen, S. D.; Godinez, C. E.; Garcia-Garibay, M. A. Improved physical properties and rotational dynamics in a molecular gyroscope with an asymmetric stator structure. *Org. Lett.* **2006**, *8*, 3417-3420.

(198) Escalante-Sánchez, E.; Rodríguez-Molina, B.; Garcia-Garibay, M. A. Toward crystalline molecular rotors with linearly conjugated diethynyl-phenylene rotators and pentiptycene stators. *J. Org. Chem.* **2012**, *77*, 7428-7434.

- (199) Hughs, M.; Jimenez, M.; Khan, S.; Garcia-Garibay, M. A. Synthesis, rotational dynamics, and photophysical characterization of a crystalline linearly conjugated phenyleneethynylene molecular dirotor. *J. Org. Chem.* **2013**, *78*, 5293-5302.
- (200) Jiang, X.; Rodríguez-Molina, B.; Nazarian, N.; Garcia-Garibay, M. A. Rotation of a bulky triptycene in the solid state: Toward engineered nanoscale artificial molecular machines. *J. Am. Chem. Soc.* **2014**, *136*, 8871-8874.
- (201) Alameddine, B.; Baig, N.; Shetty, S.; Al-Sagheer, F.; Al-Mousawi, S. Microwave-assisted [4+2] Diels–Alder cycloaddition of 1,4-Diethynyl triptycene with various cyclopentadienone derivatives: Promising building blocks for polymer networks. *Asian. J. Org. Chem.* **2018**, *7*, 378-382.
- (202) Howe, M. E.; Garcia-Garibay, M. A. Fluorescence and rotational dynamics of a crystalline molecular rotor featuring an aggregation-induced emission fluorophore. *J. Org. Chem.* **2019**, *84*, 9570-9576.
- (203) Colin-Molina, A.; Karothu, D. P.; Jellen, M. J.; Toscano, R. A.; Garcia-Garibay, M. A.; Naumov, P.; Rodríguez-Molina, B. Thermosalient amphidynamic molecular machines: Motion at the molecular and macroscopic scales. *Matter* **2019**, *1*, 1033-1046.
- (204) Lemouchi, C.; Vogelsberg, C. S.; Zorina, L.; Simonov, S.; Batail, P.; Brown, S.; Garcia-Garibay, M. A. Ultra-fast rotors for molecular machines and functional materials via halogen bonding: Crystals of 1,4-bis(iodoethynyl)bicyclo[2.2.2]octane with distinct gigahertz rotation at two sites. *J. Am. Chem. Soc.* **2011**, *133*, 6371-6379.

(205) Catalano, L.; Pérez-Estrada, S.; Terraneo, G.; Pilati, T.; Resnati, G.; Metrangolo, P.; Garcia-Garibay, M. A. Dynamic characterization of crystalline supramolecular rotors assembled through halogen bonding. *J. Am. Chem. Soc.* **2015**, *137*, 15386-15389.

(206) Catalano, L.; Perez-Estrada, S.; Wang, H.-H.; Ayitou, A. J.-L.; Khan, S. I.; Terraneo, G.; Metrangolo, P.; Brown, S.; Garcia-Garibay, M. A. Rotational dynamics of diazabicyclo[2.2.2]octane in isomorphous halogen-bonded co-crystals: Entropic and enthalpic effects. *J. Am. Chem. Soc.* **2017**, *139*, 843-848.

(207) Simonov, S.; Zorina, L.; Wzietek, P.; Rodríguez-Forteza, A.; Canadell, E.; Mézière, C.; Bastien, G.; Lemouchi, C.; Garcia-Garibay, M. A.; Batail, P. Static modulation wave of arrays of halogen interactions transduced to a hierarchy of nanoscale change stimuli of crystalline rotors dynamics. *Nano Lett.* **2018**, *18*, 3780-3784.

(208) Lemouchi, C.; Mézière, C.; Zorina, L.; Simonov, S.; Rodríguez-Forteza, A.; Canadell, E.; Wzietek, P.; Auban-Senzier, P.; Pasquier, C.; Giamarchi, T. Garcia-Garibay, M. A.; Batail, P. Design and evaluation of a crystalline hybrid of molecular conductors and molecular rotors. *J. Am. Chem. Soc.* **2012**, *134*, 7880-7891.

(209) Jiang, X.; Duan, H.-B.; Jellen, M. J.; Chen, Y.; Chung, T. S.; Liang, Y.; Garcia-Garibay, M. A. Thermally activated transient dipoles and rotational dynamics of hydrogen-bonded and charge-transferred diazabicyclo[2.2.2]octane molecular rotors. *J. Am. Chem. Soc.* **2019**, *141*, 16802-16809.

(210) Gould, S. L.; Tranchemontagne, D.; Yaghi, O. M.; Garcia-Garibay, M. A. Amphidynamic character of crystalline MOF-5: Rotational dynamics of terephthalate phenylenes in a free-volume, sterically unhindered environment. *J. Am. Chem. Soc.* **2008**, *130*, 3246-3247.

(211) Morris, W.; Taylor, R. E.; Dybowski, C.; Yaghi, O. M.; Garcia-Garibay, M. A. Framework mobility in the metal-organic framework crystal IRMOF-3: Evidence for aromatic ring and amine rotation. *J. Mol. Struct.* **2011**, *1004*, 94-101.

(212) Winston, E. B.; Lowell, P. J.; Vacek, J.; Chocholoušová, J.; Michl, J.; Price, J. C. Dipolar molecular rotors in the metal-organic framework crystal IRMOF-2. *Phys. Chem. Chem. Phys.* **2008**, *10*, 5188-5191.

(213) Jiang, X.; Duan, H.-B.; Khan, S. I.; Garcia-Garibay, M. A. Diffusion-controlled rotation of triptycene in a metal-organic framework (MOF) sheds light on the viscosity of MOF-confined solvent. *ACS Cent. Sci.* **2016**, *2*, 608-613.

(214) Vogelsberg, C. S.; Uribe-Romo, F. J.; Lipton, A. S.; Yang, S.; Houk, K. N.; Brown, S.; Garcia-Garibay, M. A. Ultrafast rotation in an amphidynamic crystalline metal organic framework. *Proc. Natl. Acad. Sci. U.S.A.* **2017**, *114*, 13613-13618.

(215) Liepuoniute, I.; Huynh, C. M.; Perez-Estrada, S.; Wang, Y.; Khan, S.; Houk, K. N.; Garcia-Garibay, M. A. Enhanced rotation by ground state destabilization in amphidynamic crystals of a dipolar 2,3-difluorophenylene rotator as established by solid state ^2H NMR and dielectric spectroscopy. *J. Phys. Chem. C*, **2020**, *124*, 15391-15398.

(216) Khudozhitkov, A. E.; Kolokolov, D. I.; Stepanov, A. G.; Bolotov, V. A.; Dybtsev, D. N. Metal-cation-independent dynamics of phenylene ring in microporous MOFs: A ^2H solid-state NMR study. *J. Phys. Chem. C* **2015**, *119*, 28038-28045.

(217) Yang, J.-S.; Swager, T. M. Fluorescent porous polymer films as TNT chemosensors: Electronic and structural effects. *J. Am. Chem. Soc.* **1998**, *120*, 11864-11873.

(218) Martin, J. R.; Hastings, S. D.; Freeman, J. L.; Gray, G. M. Synthesis, characterization and the thermal isomerization mechanism of a series of *trans*-tetra-carbonyl-bis(phosphinite)molybdenum(0) complexes and an evaluation of their potential to form heterobimetallic compounds. *J. Organomet. Chem.* **2014**, *751*, 695-702.

(219) Huang, F.; Wang, G.; Ma, L.; Wang, Y.; Chen, X.; Che, Y.; Jiang, H. Molecular spur gears based on a switchable quinquepyridine foldamer acting as a stator. *J. Org. Chem.* **2017**, *82*, 12106-12111.

(220) Inukai, M.; Fukushima, T.; Hijikata, Y.; Ogiwara, N.; Horike, S.; Kitagawa, S. Control of molecular rotor rotational frequencies in porous coordination polymers using a solid-solution approach. *J. Am. Chem. Soc.* **2015**, *137*, 12183-12186.

(221) Khan, N. S.; Perez-Aguilar, J. M.; Kaufmann, T.; Hill, P. A.; Taratula, O.; Lee, O.-S.; Carroll, P. J.; Saven, J. G.; Dmochowski, I. J. Multiple hindered rotators in a gyroscope-inspired tribenzylamine hemicryptophane. *J. Org. Chem.* **2011**, *76*, 1418-1424.

(222) Sugino, H.; Kawai, H.; Fujiwara, K.; Suzuki, T. Molecular gyroscope with a *trans*-cyclohexane-1,4-diimine rotor unit: Isolation and characterization of a geometric isomer as a formal intermediate of hindered rotation. *Chem. Lett.* **2012**, *41*, 79-81.

(223) Conn, M. M.; Rebek, J. Jr. Self-assembling capsules. *Chem. Rev.* **1997**, *97*, 1647-1668.

(224) Kitagawa, H.; Kobori, Y.; Yamanaka, M.; Yoza, K.; Kobayashi, K. Encapsulated-guest rotation in a self-assembled heterocapsule directed toward a supramolecular gyroscope. *Proc. Natl. Acad. Sci. U.S.A.* **2009**, *106*, 10444-10448. The authors thank Prof. Kobayashi for a personal communication clarifying some of the yield data Figure 2.66.

(225) See also Kobayashi, K.; Ishii, K.; Yamanaka, M. Orientational isomerism and binding ability of nonsymmetrical guests encapsulated in a self-assembling heterodimeric capsule. *Chem. Eur. J.* **2005**, *11*, 4725-4734.

(226) Li, W.; He, C.-T.; Zeng, Y.; Ji, C.-M.; Du, Z.-Y.; Zhang, W.-X.; Chen, X.-M. Crystalline supramolecular gyroscope with a water molecule as an ultra small polar rotator modulated by charge-assisted hydrogen bonds. *J. Am. Chem. Soc.* **2017**, *139*, 8086-8089.

(227) Jose, D.; Datta, A. Molecular rotor inside a phosphonate cavitand: Role of supramolecular interactions. *J. Phys. Chem. Lett.* **2010**, *1*, 1363-1366. In their concluding paragraph, these authors speculated the structural modifications of their system could lead to (thermal) unidirectional rotation of the rotator.

- (228) Huang, R.-K.; Xiao, Z.-F.; Liu, D.-X.; Zhang, W.-X.; Chen, X.-M. Unprecedented water-controlled rotator-stator conversion of supramolecular rotors in crystals. *Chem. Commun.* **2019**, *55*, 7159-7162.
- (229) Krause, M.; Hulman, M.; Kuzmany, H.; Dubay, O.; Kresse, G.; Vietze, K.; Seifert, G.; Wang, C.; Shinohara, H. Fullerene quantum gyroscope. *Phys. Rev. Lett.* **2004**, *93*, 137403.
- (230) Comotti, A.; Bracco, S.; Sozzani, P. Molecular rotors built in porous materials. *Acc. Chem. Res.* **2016**, *49*, 1701-1710.
- (231) Zhao, K.; Dron, P. I.; Kaleta, J.; Rogers, C. T.; Michl, J. Arrays of dipolar molecular rotors in tris(*o*-phenylenedioxy)cyclotriphosphazene. *Top. Curr. Chem.* **2014**, 163-212.
- (232) Kobr, L.; Zhao, K.; Shen, Y.; Comotti, A.; Bracco, S.; Shoemaker, R. K.; Sozzani, P.; Clark, N. A.; Price, J. C.; Rogers, C. T.; Michl, J. Inclusion compound based approach to arrays of artificial dipolar molecular rotors. A surface inclusion. *J. Am. Chem. Soc.* **2012**, *134*, 10122-10131.
- (233) Kobr, L.; Zhao, K.; Shen, Y.; Polívková, K.; Shoemaker, R. K.; Clark, N. A.; Price, J. C.; Rogers, C. T.; Michl, J. Inclusion compound based approach to arrays of artificial dipolar molecular rotors: Bulk inclusions. *J. Org. Chem.* **2013**, *78*, 1768-1777.
- (234) Kobr, L.; Zhao, K.; Shen, Y.; Shoemaker, R. K.; Rogers, C. T.; Michl, J. Tris-*o*-phenylenedioxy cyclotriphosphazene (TPP) inclusion compounds containing a dipolar molecular rotor. *Cryst. Growth Des.* **2014**, *14*, 559-568.

(235) Kaleta, J.; Dron, P. I.; Zhao, K.; Shen, Y.; Císařová, I.; Rogers, C. T.; Michl, J. Arrays of molecular rotors with triptycene stoppers: Surface inclusion in hexagonal tris(*o*-phenylenedioxy)cyclotriphosphazene. *J. Org. Chem.* **2015**, *80*, 6173-6192.

(236) Dron, P. I.; Zhao, K.; Kaleta, J.; Shen, Y.; Wen, J.; Shoemaker, R. K.; Rogers, C. T.; Michl, J. Bulk Inclusions of pyridazine-based molecular rotors in tris(*o*-phenylenedioxy)cyclotriphosphazene (TPP). *Adv. Funct. Mater.* **2016**, *26*, 5718-5732.

(237) Michl, J. Farewell editorial. *Chem. Rev.* **2015**, *115*, 1-2.

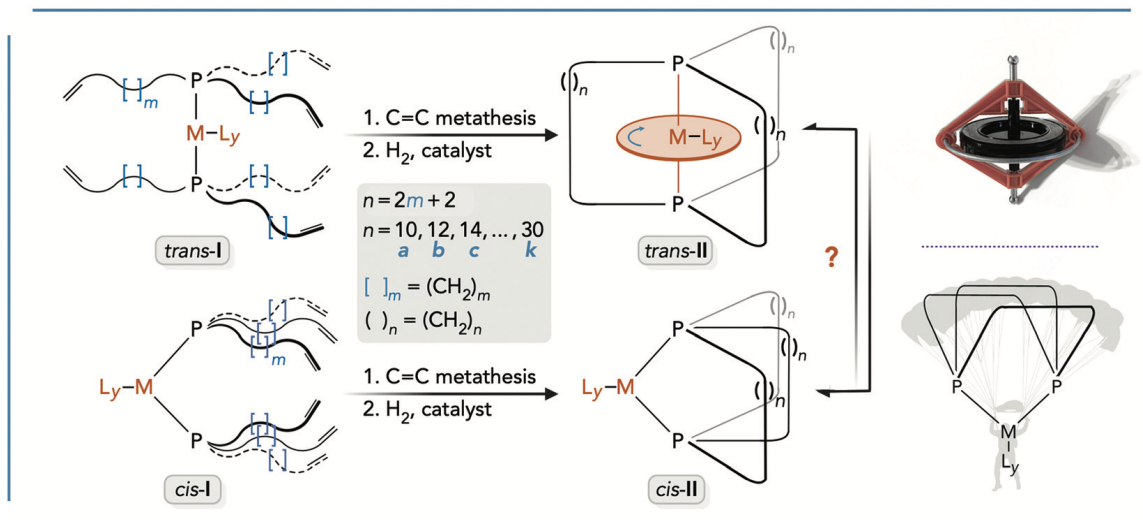
3. PLATINUM(II) ALKYL COMPLEXES OF CHELATING DIBRIDGEHEAD
DIPHOSPHINES $P((CH_2)_n)_3P$ ($n = 14, 18, 22$); FACILE *cis/trans* ISOMERIZATIONS
INTERCONVERTING GYROSCOPE AND PARACHUTE LIKE ADDUCTS[†]

3.1. Introduction

The broad field of molecular rotors is highly relevant to several types of molecular machines, and *in lieu* of an extensive list of primary research articles, readers are referred to three expansive reviews.¹⁻³ We have had an ongoing interest in the subnanoscale miniaturization of various macroscopic devices, and this has driven the synthesis and intensive study of two classes of metal complexes in our group. The first, exemplified by *trans*-**II** in Scheme 3.1, has been termed "gyroscope like" due to the obvious geometric resemblance.³ Such species can be accessed via three-fold ring closing metathesis/hydrogenation sequences involving complexes with *trans* phosphine ligands of the formula $P((CH_2)_mCH=CH_2)_3$ (*trans*-**I**).³⁻⁷ This affords adducts of cage like dibridgehead diphosphines with three connecting $(CH_2)_n$ bridges ($n = 2m + 2$). Depending upon the lengths of the methylene segments and the sizes of the ligands, the ML_y rotators may be capable of rotation, exchanging the positions of the ligands or (equivalently) the $(CH_2)_n$ bridges.

[†] Reproduced from Zhu, Y.; Ehnbohm, A.; Fiedler, T.; Shu, Y.; Bhuvanesh, N.; Hall, M. B.; Gladysz, J. A. Platinum(II) Alkyl Complexes of Chelating Dibridgehead Diphosphines $P((CH_2)_n)_3P$ ($n = 14, 18, 22$); Facile *cis/trans* Isomerizations Interconverting Gyroscope and Parachute like Adducts *Dalton Trans.* **2021**, *50*, 12457-12477, with permission from the Royal Society of Chemistry.

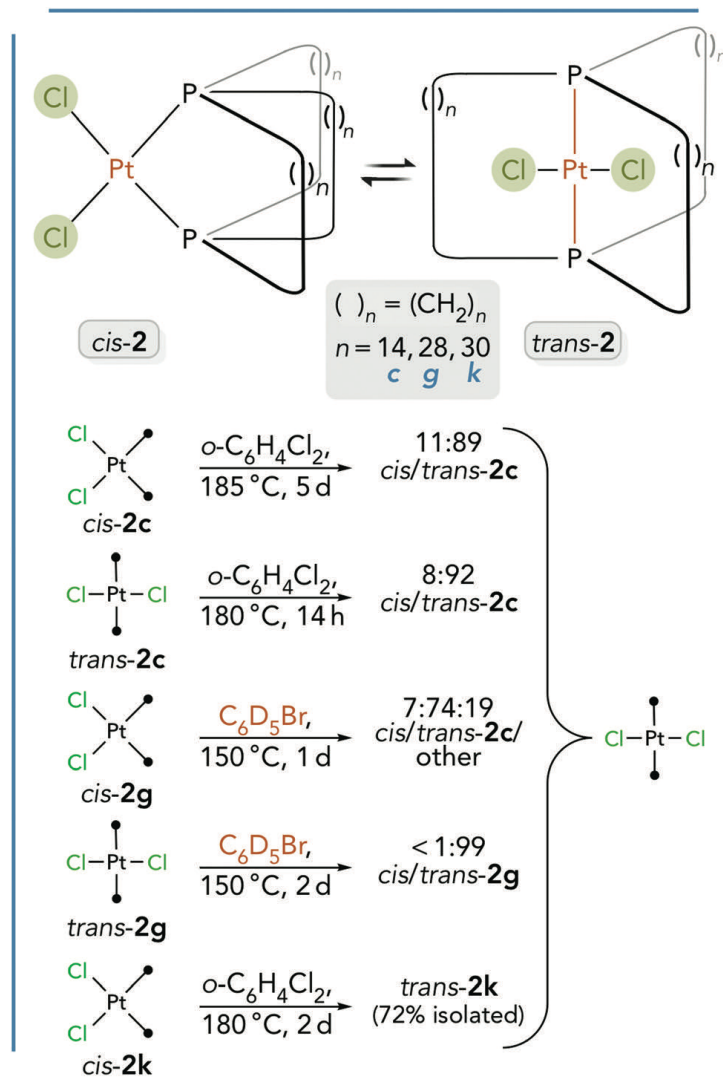
When such sequences are carried out with analogous *cis* complexes (e.g. *cis-I*, Scheme 3.1), the same diphosphine ligands can be generated, but now with the donor atoms connecting *cis* positions.⁸ When accessed in square planar geometries, one $(\text{CH}_2)_n$ bridge can be visualized as lying in the coordination plane, the second above, and the third below. Depending upon the lengths of the methylene segments and the sizes of the ligands, the bridges may be capable of "jump rope" dynamic processes that exchange their positions. When square planar versions of *cis-II* are viewed from appropriate perspectives, there is some resemblance to a parachutist, so they are often termed "parachute like".



Scheme 3.1 Generalized syntheses of gyroscope like (*trans-II*) and parachute like (*cis-II*) metal complexes.

In analyzing the dynamic behavior of both classes of complexes, it has been important to exclude alternative mechanisms for exchanging the positions of ligands or $(\text{CH}_2)_n$ bridges.⁹ Specifically, any facile *trans/cis* isomerization could open up new pathways. In one embodiment, gyroscope like *trans-II* might first undergo a hypothetically endergonic isomerization to parachute like *cis-II*, where $(\text{CH}_2)_n$ exchange might be more rapid than in *trans-II* ("jump rope" rate > ML_y rotation). Alternatively, one can play the Devil's advocate in the opposite direction. Thus, we have sought to probe the relative stabilities of *cis/trans-II* and their thermal interconversion both experimentally and computationally.

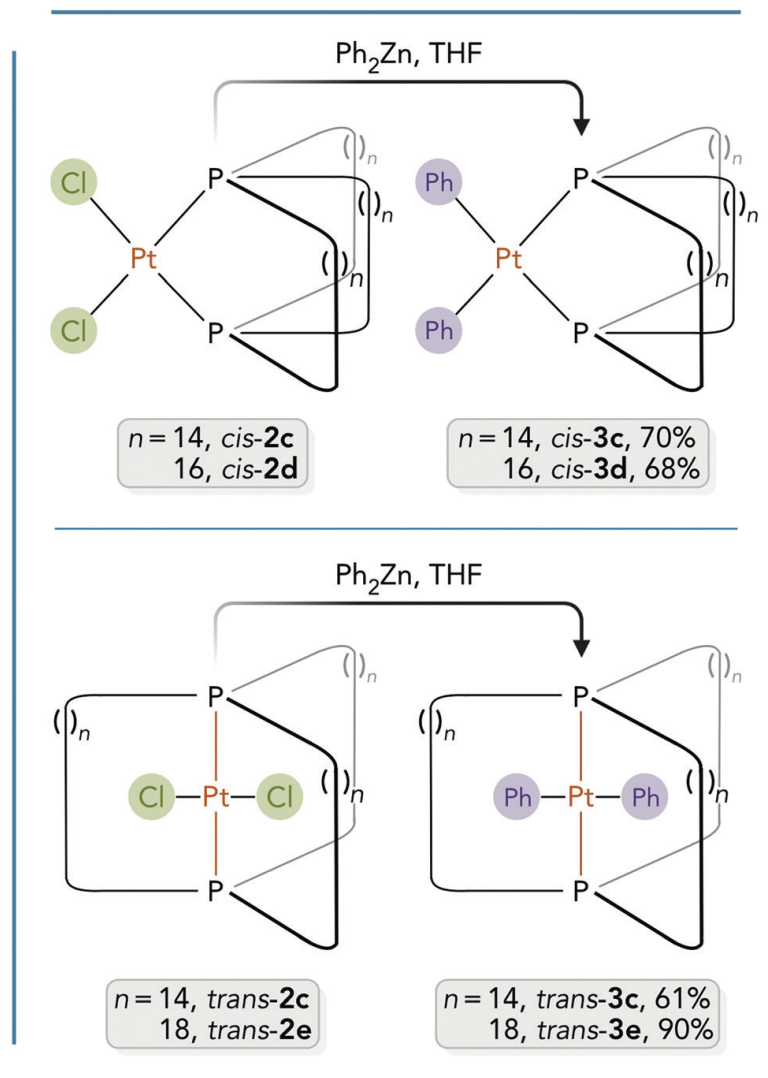
In earlier studies, we examined these issues with a series of platinum dichloride complexes, *cis*- and *trans*- $\text{Pt}(\text{Cl})_2(\overline{\text{P}((\text{CH}_2)_n)_3})$ (*cis*- and *trans-2*).^{4c,8} As shown in Scheme 3.2, temperatures of 150-185 °C were required to effect equilibrations on reasonable time scales from either direction. In all cases, the gyroscope like *trans* isomers were favored. To facilitate comparisons with other chapters and papers, the same letter indices have been employed for *n* (*n* = 10, **a**; 12, **b**; 14, **c**; etc.). Computationally, as one goes from $(\text{CH}_2)_{10}$ (**2a**) to $(\text{CH}_2)_{22}$ (**2g**), or 13- to 25-membered macrocycles, the gyroscope like *trans-2* ranges from 5.1 to 9.2 kcal mol⁻¹ more stable than the parachute like *cis-2*.^{8,10}



Scheme 3.2 Previously studied isomerizations of parachute and gyroscope like complexes.

The acyclic precursor complexes *cis*- and *trans*-Pt(Cl)₂(P((CH₂)_mCH=CH₂)₃)₂ (*cis*- and *trans*-**1**) could also be thermally equilibrated.^{4c} Here, in line with literature precedent,^{11,12} there is a significant effect of solvent polarity that tracks the dipole moments (*cis* > *trans*; more polar CH₂Cl₂: appreciable amounts of both isomers; less polar toluene: >95% *trans*).¹³ Other reactivity data are relevant. As shown in Scheme 3.3, the dichloride complexes **2** and Ph₂Zn react at room temperature to give the diphenyl complexes $\overline{\text{Pt}(\text{Ph})_2(\text{P}((\text{CH}_2)_n)_3\text{P})}$ (**3**).⁴ Since *cis*-**2c,d** and *trans*-**2c,e** afford *cis*-**3c,d** and *trans*-**3c,e**, respectively, these fit the textbook definition of stereospecific reactions.¹⁴ Furthermore, the stereospecificity excludes *cis/trans* isomerization at any stage of the reaction coordinates.

In this paper, we report the surprising observation of much lower energy pathways for the interconversion of *trans*-**II** and *cis*-**II** when the chloride ligands in **2** are replaced by one or more alkyl groups. Since these isomerizations impinge upon a number of mechanistic questions, even beyond those expressed above, it was imperative to bring definition to the phenomena. Accordingly, a variety of synthetic, structural, thermolytic, and computational experiments have been carried out, as detailed in the narrative below.



Scheme 3.3 Stereospecific substitution of chloride ligands by phenyl ligands in *trans* and *cis* platinum complexes.

3.2. Results Part I: Experimental [major contribution: Mr. Y. Zhu]

3.2.1. Syntheses and NMR characterization

As shown in Scheme 3.4, the gyroscope like platinum dichloride complexes *trans*-**2c,e,g**^{4a} were treated with diethyl ether solutions of MeLi (2.1-2.3 equiv.). Workups gave the new parachute like dimethyl complexes *cis*-Pt(Me)₂(P((CH₂)_n)₃P) (*cis*-**4c,e,g**) in 70-94% yields as air stable white solids. When the first such reaction was conducted, the *trans/cis* isomerization was considered surprising. Thus, the neutral alumina columns used in initial experiments were omitted. However, identical results were obtained.

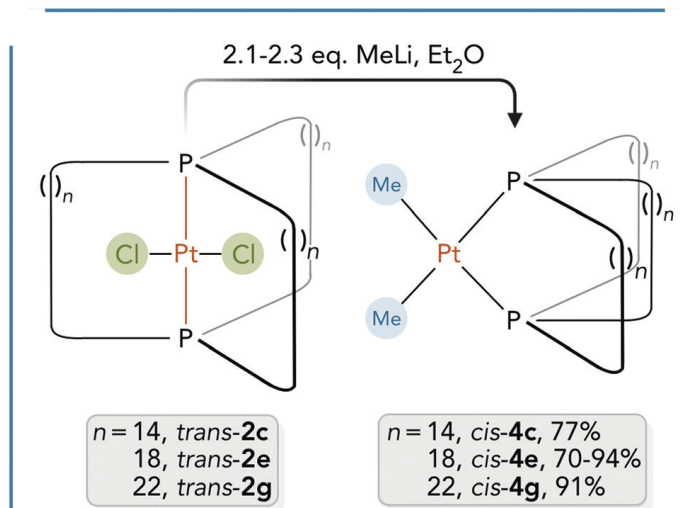
These and all other new complexes below were characterized by NMR spectroscopy (¹H, ¹³C{¹H}, ³¹P{¹H}) and microanalyses, as summarized in the Experimental section 3.6. The *cis* stereochemistry was evidenced by a number of features, such as the lower ¹J_{PPt} values (1853-1886 Hz vs. 2389-2398 Hz for *trans*-**2c,e,g**).¹⁵ Each ¹³C{¹H} NMR spectrum showed a doublet of doublets for the methyl groups (²J_{CP(*trans*)} = 101.7-101.1 Hz, ²J_{CP(*cis*)} = 9.9-10.0 Hz). Each ¹H NMR spectrum also showed a doublet of doublets (³J_{HP(*trans*)} = 7.3-6.7 Hz, ³J_{HP(*cis*)} = 6.1-5.7 Hz), and platinum satellites were usually visible (²J_{HPt} = 66-65 Hz). The ¹H and ³¹P NMR properties were very similar to those reported for the related acyclic complexes *cis*-Pt(Me)₂(PR₃)₂.^{16,17}

A reaction of *trans*-**2c** and only 1.1 equiv. of MeLi was similarly conducted. A ³¹P{¹H} NMR spectrum of the crude reaction mixture showed 40-50% conversion to the

dimethyl complex *cis-4c*. The only other signal detected was that of the starting material *trans-2c*. Thus, it was not possible to interrogate the stereochemistry of the presumed intermediate, the methyl chloride complex $\overline{\text{Pt}(\text{Cl})(\text{Me})(\text{P}((\text{CH}_2)_{14})_3\text{P})}$ (**5c**). When the reaction of *trans-2c* and 2.2 equiv. of MeLi (Scheme 3.4) was repeated at 0 °C, the result was the same as at room temperature.

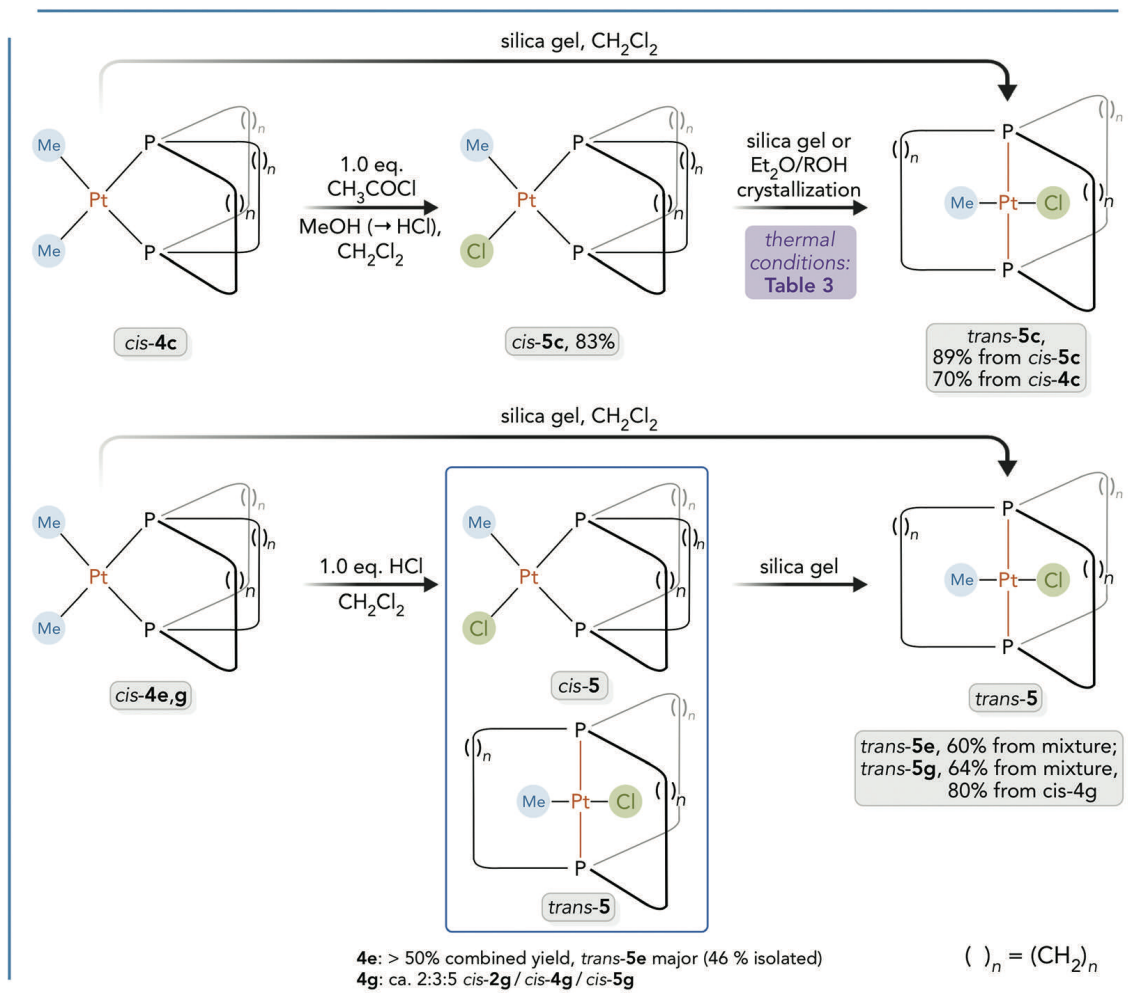
As shown in Scheme 3.5, CH₂Cl₂ solutions of *cis-4c,e,g* were treated with 1.0 equiv. of HCl. In some cases the HCl was generated in situ from acetyl chloride (1.0 equiv.) and excess methanol, and in other cases 2.0 M Et₂O solutions were used. With *cis-4c*, a chromatographic workup (neutral alumina) gave parachute like *cis-* $\overline{\text{Pt}(\text{Cl})(\text{Me})(\text{P}((\text{CH}_2)_{14})_3\text{P})}$ (*cis-5c*) in 83% yield. The lower symmetry was evidenced by doubled ³¹P NMR signals, and $\overline{\text{PtCH}_3}$ ¹H and ¹³C NMR signals that were now doublets of doublets. Analogous patterns have been noted for the related complexes *cis-* $\overline{\text{Pt}(\text{Cl})(\text{Me})(\text{PR}_3)_2}$.^{17,18}

The stereochemical homogeneity of *cis-5c* was quickly found to be tied to a hair trigger. Either exposure to silica gel (in the form of a column or slurry) or crystallization (Et₂O/methanol or Et₂O/ethanol) afforded gyroscope like *trans-5c* (≥89%). Even CH₂Cl₂ solutions of the dimethyl complex *cis-4c*, when slurried with silica gel, gave *trans-5c* (70%). The NMR properties of *trans-5c* were similar to those of the dichloride complex *trans-2c*, with the ¹H and ¹³C NMR spectra showing triplets for the $\overline{\text{PtCH}_3}$ group.



Scheme 3.4 Substitution of the chloride ligands in *trans-2c,e,g* by methyl ligands with isomerization.

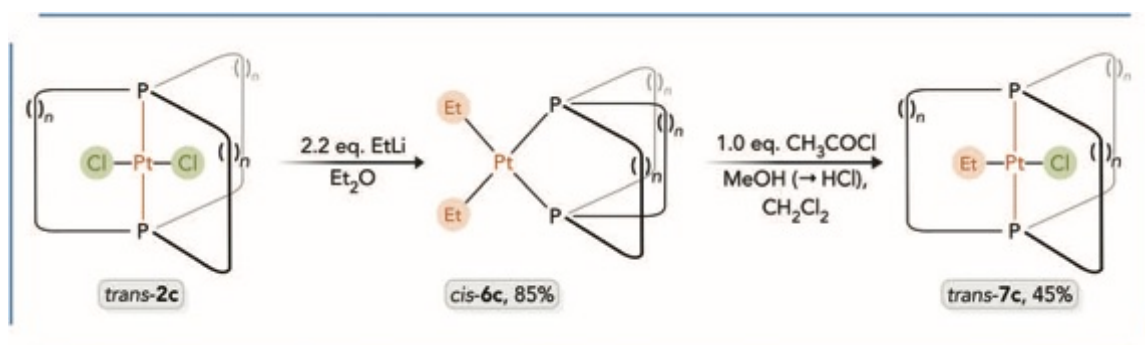
With *cis-4e,g*, the analogous methyl chloride complexes *cis-5e,g* could be detected "on the fly", but isolated samples always contained significant amounts of *trans-5e,g*. These mixtures were further slurried with silica gel to give pure *trans-5e,g* (60-64%). Additional details can be found in the Experimental section 3.6. The NMR properties were similar to those of *trans-5c*, and all three complexes exhibited $^1J_{\text{PPt}}$ values (2824-2796 Hz) that were diagnostic of the *trans* stereochemistry.¹⁵ Given the modest dependence of the chemistry in Scheme 3.3, Scheme 3.4, and Scheme 3.5 upon the lengths of the (CH₂)_n bridges, subsequent experiments were confined to (CH₂)₁₄ systems ("c series").



Scheme 3.5 Introduction of halide ligands and attendant isomerization.

As depicted in Scheme 3.6, a parallel sequence was carried out with *trans-2c* and EtLi in place of MeLi. The parachute like diethyl complex $\text{cis-Pt}(\text{Et})_2(\text{P}(\text{CH}_2)_{14})_3\text{P}$ (*cis-6c*) was isolated in 85% yield. NMR spectra showed a $^1J_{\text{PPt}}$ value of 1746 Hz, and PtCH_2CH_3 ^1H signal patterns similar to those of related acyclic complexes $\text{cis-Pt}(\text{Et})_2(\text{PR}_3)_2$.¹⁶ Next, *cis-6c* was treated with HCl analogously to the dimethyl complex *cis-4c* in Scheme 3.5. However, the same chromatographic workup (neutral alumina) afforded

only gyroscope like *trans-7c* (45%). Accordingly, the NMR spectra now showed a $^1J_{\text{PPt}}$ value of 3002 Hz, and PtCH_2CH_3 ^1H signal patterns similar to those of other complexes of the type *trans*-Pt(Cl)(Et)(PR₃)₂.¹⁹ No significant amounts of byproducts were noted when crude reaction mixtures were assayed by ^{31}P NMR.



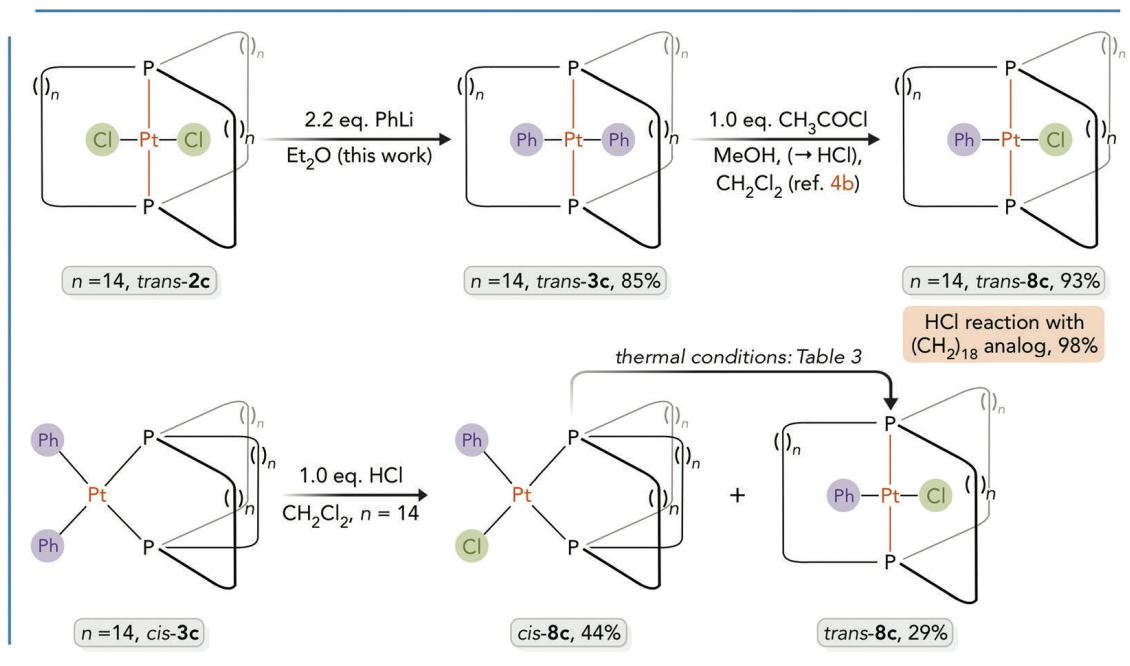
Scheme 3.6 Substitution and isomerization reactions involving ethyl ligands.

The main difference between the substitution reactions of the gyroscope like dichloride complex *trans-2c* in Scheme 3.4 and Scheme 3.6 and that in Scheme 3.3 is the use of alkyl lithium versus aryl zinc nucleophiles. Thus, as shown in Scheme 3.7 (top), *trans-2c* was treated with PhLi in a procedure analogous to that in Scheme 3.6. Workup gave the gyroscope like diphenyl complex *trans-3c* in 85% yield. All of the syntheses in this chapter have been reproduced several times, often by different coworkers. However, in one case this same reaction gave, under essentially identical conditions, *trans-3c* and *cis-3c* in 50% and 29% isolated yields, respectively. Regardless, the chloride/phenyl

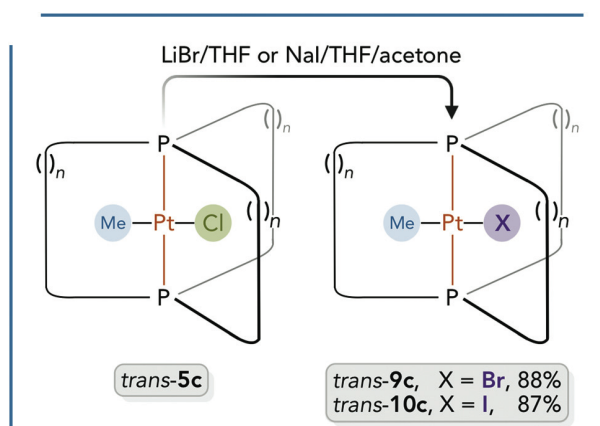
ligand substitution is not accompanied by the same degree of isomerization as chloride/alkyl ligand substitution.

In previous work, the gyroscope like diphenyl complexes $\overline{\text{Pt}(\text{Ph})_2(\text{P}((\text{CH}_2)_n)_3\text{P})}$ (*trans*-**3c,e**) had been shown to react with 1.0 equiv. of HCl to give the gyroscope like phenyl chloride complexes $\overline{\text{Pt}(\text{Cl})(\text{Ph})(\text{P}((\text{CH}_2)_n)_3\text{P})}$ (*trans*-**8c,e**) in 93-98% yields after workup. This is exemplified with *trans*-**3c** in Scheme 3.7 (top). However, analogous substitution reactions with parachute like *cis*-**3** had not been investigated. Thus, *cis*-**3c** and HCl were similarly combined (Scheme 3.7, bottom). A chromatographic workup (neutral alumina) gave the easily separated products *cis*-**8c** (44%) and *trans*-**8c** (29%). The structure of the former, a new compound, followed readily from the types of NMR properties detailed above.

In connection with thermolyses described below, authentic samples of platinum bromide and iodide complexes became of interest. Thus, as shown in Scheme 3.8, the gyroscope like chloride complex *trans*-**5c** was treated (in separate reactions) with LiBr or NaI. Workups gave the gyroscope like halide complexes $\overline{\text{Pt}(\text{X})(\text{Me})(\text{P}((\text{CH}_2)_{14})_3\text{P})}$ (X = Br, *trans*-**9c**; Cl, *trans*-**10c**) in 87-88% yields. The structure and stereochemistry followed readily from the NMR properties, as well as a crystal structure in the following section.



Scheme 3.7 Substitution and isomerization reactions involving phenyl ligands.



Scheme 3.8 Halide substitution reactions.

3.2.2. Crystallographic characterization

Due to the varied stereochemical issues involving the preceding complexes, crystal structures were sought wherever possible. Single crystals of *cis-4c*, *trans-5c*, *trans-7c*, and *trans-10c* could be obtained, and the X-ray structures were determined as described in the Experimental section 3.6 and Table 3.1. Key metrical parameters are summarized in Table 3.2. Thermal ellipsoid plots are depicted in Figure 3.1, Figure 3.2, Figure 3.3, and Figure 3.4. All of the structures exhibited disorder that could easily be modeled (Me/X positions in *trans-5c* and *trans-10c*; certain (CH₂)_n segments in *cis-4c*, *trans-5c*, and *trans-7c*). Data are given only for the dominant conformation.

As shown in Figure 3.1, the dimethyl complex *cis-4c* exhibits, as with other parachute like adducts structurally characterized earlier,⁸ one macrocycle in which the proximal CH₂ groups lie close to the coordination plane, and two in which the proximal CH₂ groups lie in roughly perpendicular planes. With the gyroscope like ethyl chloride complex *trans-7c*, three independent molecules were found in the unit cell. Since these involved rather minor conformational differences, only one is depicted in Figure 3.3, but all are illustrated in Appendix A (Figure 11.1).

The views of the iodide complex *trans-10c* in Figure 3.4 and the analogous chloride complex *trans-5c* in Figure 3.2 have been arranged as closely as possible. While these adducts clearly pass the "eye test" as isostructural, the space groups are not identical (*Pbca* vs. *P12₁/n1*) and the crystal lattices differ.

Table 3.1 Summary of crystallographic data.

crystallographic parameters	<i>cis-4c</i>	<i>trans-5c</i>	<i>trans-7c</i>	<i>trans-10c</i>
empirical formula	C ₄₄ H ₉₀ P ₂ Pt	C ₄₃ H ₈₇ ClP ₂ Pt	C ₄₄ H ₈₉ ClP ₂ Pt	C ₄₃ H ₈₇ IP ₂ Pt
formula weight	876.18	896.60	910.63	988.05
temperature [K]	110(2)	110(2)	110(2)	110(2)
diffractometer	Quest	Quest	APEX II	APEX II
wavelength [Å]	0.71073	0.71073	0.71073	0.71073
crystal system	monoclinic	monoclinic	monoclinic	orthorhombic
space group	<i>P</i> 12 ₁ / <i>c</i> 1	<i>P</i> 12 ₁ / <i>n</i> 1	<i>P</i> 12 ₁ / <i>c</i> 1	<i>Pbca</i>
<i>unit cell dimensions:</i>				
<i>a</i> [Å]	10.3514(4)	16.2658(9)	38.540(7)	20.481(6)
<i>b</i> [Å]	15.4895(6)	13.6513(8)	14.255(3)	13.685(4)
<i>c</i> [Å]	28.4607(12)	19.9653(11)	25.681(4)	33.232(10)
α [°]	90	90	90	90
β [°]	95.7670(10)	90.909(2)	91.995(2)	90
γ [°]	90	90	90	90
<i>V</i> [Å ³]	4540.2(3)	4432.7(4)	14100(4)	9314(5)
<i>Z</i>	4	4	12	8
ρ_{calc} [Mg m ⁻³]	1.282	1.344	1.287	1.409
μ [mm ⁻¹]	3.188	3.325	3.137	3.770
<i>F</i> (000)	1848	1880	5736	4048
crystal size [mm ³]	0.441 × 0.207 × 0.182	0.493 × 0.475 × 0.292	0.10 × 0.10 × 0.10	0.56 × 0.16 × 0.12
Θ limit [°]	1.949 to 24.999	1.948 to 27.496	1.66 to 27.50	2.336 to 27.497
index range (<i>h, k, l</i>)	-12, 12; -18, 18; -33, 33	-21, 21; -17, 17; -25, 25	-50, 50; -18, 18; -133, 33	-26, 26; -17, 17; -43, 43
reflections collected	102005	173120	154056	97076
independent reflections	7997	10146	32379	10629
<i>R</i> (int)	0.0451	0.0537	0.0930	0.0463
completeness to Θ	99.9	99.8	99.9	99.6
max./min. transmission	0.4291/0.1274	0.2616/0.0906	0.7457/0.4356	0.7456/0.4890
data/restraints/parameters	7997/801/566	10 146/123/459	32 379/1956/1676	10 629/3/426
goodness-of-fit on <i>F</i> ²	1.073	1.056	1.056	1.076
<i>R</i> indices (final) [<i>I</i> > 2 σ (<i>I</i>)]				
<i>R</i> ₁	0.0331	0.0183	0.0585	0.0353
w <i>R</i> ₁	0.0695	0.0387	0.1194	0.0837
<i>R</i> indices (all data)				
<i>R</i> ₂	0.0378	0.0226	0.0934	0.0493
w <i>R</i> ₂	0.0732	0.402	0.1364	0.0918
largest diff. peak and hole [e Å ⁻³]	2.107 and -2.309	0.683 and -0.795	1.927 and -1.925	2.037 and -1.132

Table 3.2 Key crystallographic bond lengths [\AA] and angles [$^\circ$].

	<i>cis-4c</i>	<i>trans-5c</i> ^a	<i>trans-7c(1)</i> ^b	<i>trans-7c(2)</i> ^b	<i>trans-7c(3)</i> ^b	<i>trans-10c</i> ^a
Pt–P	2.2844(11) 2.2818(11)	2.2810(5) 2.2920(5)	2.2887(16) 2.3089(16)	2.2848(19) 2.3037(19)	2.284(2) 2.285(2)	2.2946(12) 2.3032(13)
Pt–C	2.105(4) 2.106(5)	2.074(7)	2.102(6)	2.093(8)	2.104(8)	2.179(5)
Pt–Cl <i>or</i> I	—	2.4020(6)	2.4052(16)	2.401(2)	2.408(2)	2.6864(8)
P–Pt–P	104.15(4)	176.055(17)	172.37(6)	177.07(7)	172.97(9)	175.55(4)
P–Pt–C	86.76(16) 167.83(15) 87.06(17) 167.78(17)	88.0(3) 90.7(3)	87.77(17) 90.75(17)	88.1(2) 91.6(2)	91.5(2) 87.1(2)	87.66(16) 90.56(16)
C–Pt–C	82.6(2)	—	—	—	—	—
P–Pt–Cl <i>or</i> I	—	92.74(2) 88.70(2)	91.60(6) 90.31(6)	92.29(7) 88.21(7)	90.03(9) 91.85(8)	93.77(3) 88.46(3)
C–Pt–Cl <i>or</i> I	—	177.7(3)	176.6(2)	176.6(3)	176.0(3)	173.42(16)

^a Values for the dominant X–Pt–CH₃ orientation. ^b Values for the three independent molecules in the unit cell.

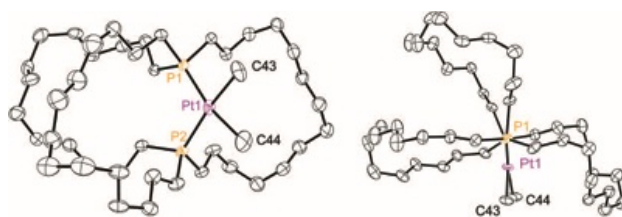


Figure 3.1 Thermal ellipsoid plots of the molecular structure of *cis-4c* (50% probability level, dominant conformation).

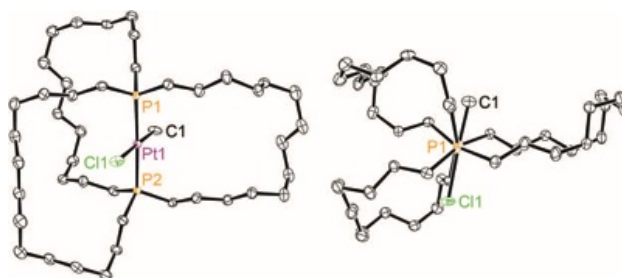


Figure 3.2 Thermal ellipsoid plots of the molecular structure of *trans-5c* (50% probability level, dominant conformation).

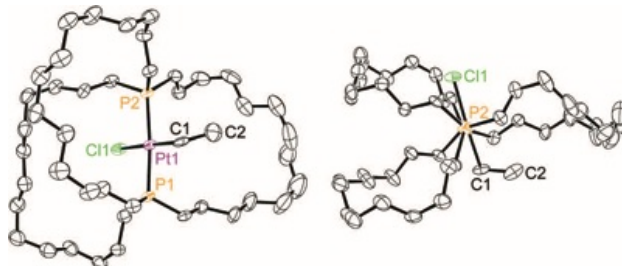


Figure 3.3 Thermal ellipsoid plots of the molecular structure of *trans-7c* (50% probability level, one of three independent molecules).



Figure 3.4 Thermal ellipsoid plots of the molecular structure of *trans-10c* (50% probability level, dominant conformation).

3.2.3. Additional characterization of equilibria

Attention was turned to addressing certain gaps in the preceding preparative data. Although the reactions in Scheme 3.5 convincingly show that for the methyl chloride complexes **5c,e,g**, the *trans*/gyroscope isomers are more stable than the *cis*/parachute isomers, purely thermal conversions of purified samples were lacking. Accordingly, when *o*-C₆H₄Cl₂ or C₆D₅Br solutions of *cis*-**5c** were kept at 100-110 °C for 3-7 h, or toluene solutions kept at 80 °C for 72 h, or mesitylene solutions kept at 140 °C for 0.5 h, >99% conversions to *trans*-**5c** were observed, as assayed by ³¹P{¹H} NMR. These data are from entries 9-13 of Table 3.3.

The previously reported thermolyses in Scheme 3.2 unambiguously show that the gyroscope like dichloride complexes *trans*-**2** are more stable than the parachute like *cis*-**2**. Since the procedures for isolating the latter did not involve silica gel (found to promote *cis/trans* isomerization in Scheme 3.5), it was of interest to see if conversion to *trans*-**2c** might be effected in slurries. However, no reaction occurred when *cis*-**2c** was combined with silica gel for 24 h at room temperature in toluene-*d*₈ or CDCl₃ (entry 1, Table 3.3).

The workups for isolating the analogous diphenyl complexes *cis*-**3c,d** (Scheme 3.3) did involve silica gel.⁸ Nonetheless, *cis*-**3c** was slurried with the same batch used in Scheme 3.5. No reaction was observed after 5 h at room temperature or 24 h at 80 °C (entry 4, Table 3.3). When a mesitylene solution of *cis*-**3c** was kept at 140 °C for 30 h (entry 3, Table 3.3), ³¹P{¹H} NMR spectra showed the gradual conversion to two new species, neither of which was *trans*-**3c** (δ /ppm 7.4 (s, 84%) and 4.3 (s, 16%)).²⁰

When a toluene-*d*₈ solution of the parachute like dimethyl complex *cis-4c* was kept at 80 °C for 10 h (entry 5, Table 3.3) or slurried at room temperature with silica gel for 24 h (entry 7, Table 3.3), no reaction was observed. However, when slurried at 80 °C for 24 h (entry 8, Table 3.3), complete conversion to two unknown species occurred (δ /ppm 11.4 (s, 76%) and 6.2 (s, 24%)).²⁰ When a mesitylene solution of *cis-4c* was kept at 140 °C for 30 h, there was ca. 16% conversion to an unknown new species.

When a mesitylene solution of the gyroscope like methyl chloride complex *trans-5c* was kept at 140 °C for 30 h (entry 14, Table 3.3), most of the *trans-5c* remained, with 13% conversion to an unknown species (7.3 ppm; no detectable *cis-5c*). However, an analogous experiment with the corresponding ethyl chloride complex *trans-7c* (entry 15, Table 3.3) showed the gradual conversion to an unknown product (³¹P{¹H} NMR: 7.4 ppm, s, ¹J_{PPt} = 2447 Hz),²⁰ with one main intermediate (18.3 ppm), the NMR properties of which (Experimental section 3.6) indicated a platinum hydride complex (¹H NMR: -16.78 ppm, t, ²J_{HP} = 13.8 Hz).

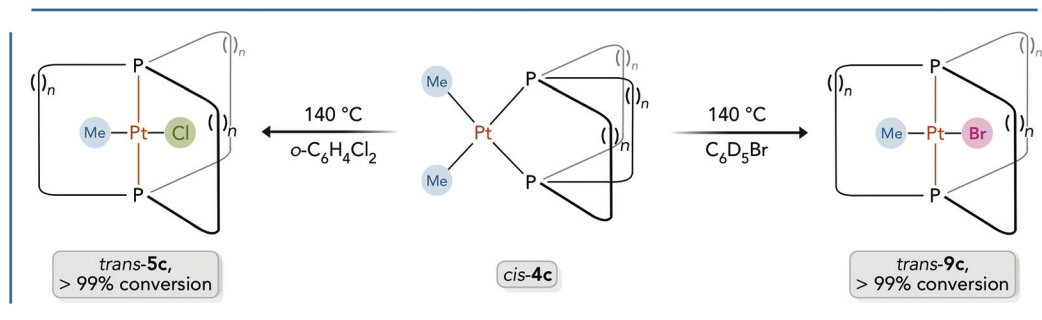
Next, *o*-C₆H₄Cl₂ solutions of the new parachute like phenyl chloride complex *cis-8c* (Scheme 3.7) were kept at 100 °C for 6 h or 140 °C for 0.5 h (entries 16 and 17, Table 3.3). In both cases, >99% conversion to gyroscope like *trans-8c* was observed. Thus, the relative thermodynamic stabilities of the phenyl chloride complexes are analogous to those of the alkyl chloride complexes.

Some attempted thermal equilibrations gave well-defined alternative reactions. As shown in Scheme 3.9, a C₆D₅Br solution of the parachute like dimethyl complex *cis-4c* was kept at 110 °C for 7 h (little change) and then 140 °C for 6 h. The higher temperature gave complete conversion to the gyroscope like methyl bromide complex *trans-9c*, as confirmed by ³¹P and ¹H NMR. Toluene-*d*₅ was also detected. An analogous reaction of the diethyl complex *cis-6c* (140 °C) initially gave what was assigned as the ethyl bromide complex *trans*-Pt(Br)(Et)(P((CH₂)₁₄)₃P) based upon the similar ¹J_{Pt} value (2771 vs. 2806 Hz). With time, this further converted to the previously isolated dibromide complex *trans*-Pt(Br)₂(P((CH₂)₁₄)₃P) (¹J_{Pt} 2347 vs. 2344^{4a} Hz). In another example, an *o*-C₆H₄Cl₂ solution of *cis-4c* was kept at 140 °C for 12 h. Complete conversion to the gyroscope like methyl chloride complex *trans-5c* occurred. In this case, an unknown intermediate could be seen by ³¹P NMR (8.9 ppm, s).

Table 3.3 Summary of thermolysis experiments.

entry	starting material	solvent	temperature (°C)	time (h)	result ^a	entry
1		<i>cis-2c</i>	toluene- <i>d</i> ₈ or CDCl ₃ /silica gel	25	24	>99:1 <i>cis/trans-2c</i>
2		<i>cis-3c</i>	toluene- <i>d</i> ₈	80	10	>99:1 <i>cis/trans-3c</i>
3			mesitylene	140	30	>99% conv. unknown species ^b
4			toluene- <i>d</i> ₈ /silica gel	25, then 80	5, then 24	>99:1 <i>cis/trans</i>
5		<i>cis-4c</i>	toluene- <i>d</i> ₈	80	10	>99:1 <i>cis/trans-4c</i>
6			mesitylene	140	30	16% conv. unknown species ^b
7			toluene- <i>d</i> ₈ /silica gel	25	24	>99:1 <i>cis/trans</i>
8			toluene- <i>d</i> ₈ /silica gel	25, then 80	5, then 24	>99% conv. unknown species ^b
9		<i>cis-5c</i>	toluene- <i>d</i> ₈	80	10	86:14 <i>cis/trans-5c</i>
10			<i>o</i> -C ₆ H ₄ Cl ₂	100	3	<1:99 <i>cis/trans-5c</i>
11			<i>o</i> -C ₆ H ₄ Cl ₂	140	0.5	<1:99 <i>cis/trans-5c</i>
12			C ₆ D ₅ Br	110	7	<1:99 <i>cis/trans-5c</i>
13		<i>trans-5c</i>	mesitylene	140	30	13% conv. unknown species ^b
14		<i>trans-7c</i>	mesitylene	140	30	>99% conv. unknown species ^b
15		<i>cis-8c</i>	<i>o</i> -C ₆ H ₄ Cl ₂	100	6	<1:99 <i>cis/trans-8c</i>
16			<i>o</i> -C ₆ H ₄ Cl ₂	140	0.5	<1:99 <i>cis/trans-8c</i>
17		<i>trans-8c</i>	mesitylene	140	30	<1:99 <i>cis/trans-8c</i>

^a Assayed by ³¹P NMR as detailed in the Experimental section 3.6. ^b Chemical shifts are provided in the Experimental section; when only 13-16% conversion is noted, the remaining material is the educt. ^b A platinum hydride intermediate can be observed by ¹H NMR; see text and Experimental section 3.6.



Scheme 3.9 Thermolyses that afford well defined complex/solvent reactions.

3.3. Results Part II: Computational Data [major contribution: Mr. A. Ehnbohm]

In order to better interpret the preceding isomerizations, molecular dynamics simulations followed by DFT optimizations were carried out for all complexes with $(\text{CH}_2)_{14}$ bridges ("c series") along the lines reported earlier.⁸ The molecular dynamics annealing simulations were run to maximize the likelihood of correctly identifying the lowest energy conformer.²¹ The ten lowest conformations from each trajectory were extracted and "cleaned up" using a semi-empirical method (PM7) followed by DFT optimizations (in the gas phase at 25 °C or 298 K).²² The computed relative energies of these species are shown in Figure 3.5. It was critical to incorporate dispersion corrections in order to obtain appropriately folded $(\text{CH}_2)_{14}$ bridges. Subsequently, single point corrections were performed using an implicit solvation model for two typical solvents from Table 3.3 (*o*- $\text{C}_6\text{H}_4\text{Cl}_2$, toluene).²³ Frequency calculations were also performed to confirm that minimum structures were obtained and further to afford temperature corrections to the Gibbs energy at a representative temperature from Table 3.3 (140 °C or 414 K).

It was also sought to compare the relative energies of acyclic model complexes, which would not be subject to possible ring strain effects derived from the dibridgehead diphosphine ligands. For this purpose, PEt_3 as opposed to PMe_3 was selected for the phosphine ligands, as the former better mimics the electronic effect exerted by the three $(\text{CH}_2)_{14}$ bridges.²⁴ These species are designated with double primes; for example *trans-2''* represents *trans*-Pt(Cl)₂(PEt₃)₂, the analog of the gyroscope like dichloride complex *trans-2c*.

In Figure 3.5 and Figure 3.6, the energies of the *trans* isomers are displayed relative to those of the *cis* isomers symbolized in the columns at the far left. In Figure 3.5, most of the gyroscope isomers are 11.5-19.2 kcal mol⁻¹ more stable than the parachute isomers in the gas phase. However, the energies of the two dialkyl complexes *cis/trans-4c* and *cis/trans-6c* are closer, with the *trans* isomers 6.7-7.4 kcal mol⁻¹ more stable. Figure 3.5 also shows the energy differences for the dichloride complexes *cis/trans-2c*. This system was also examined by DFT earlier,⁸ with the important result that the *trans* isomers were more stable for all the $(\text{CH}_2)_n$ bridge lengths examined ($n = 10, 12, 14, 16, 18, 20, 22$).¹⁰ All bond lengths and angles about platinum nicely model those determined crystallographically (Table 3.2 and earlier papers for *trans-2c*,^{4a} *cis-2c*,⁸ *trans-3c*,^{4a} *cis-3c*,⁸ and *trans-8c*^{4b}), and some are depicted in the graphics below.

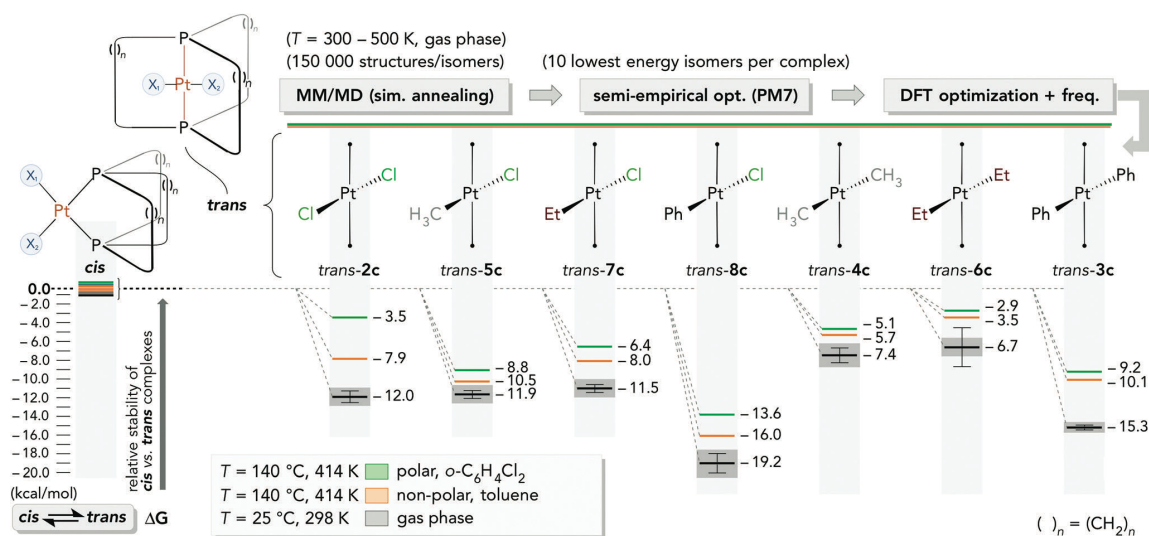


Figure 3.5 Relative energies (ΔG , kcal mol⁻¹) of isomeric *cis*/parachute and *trans*/gyroscope platinum complexes as computed by DFT (gas phase or toluene or *o*-C₆H₄Cl₂ solutions) preceded by molecular dynamics and semi-empirical (PM7) computations.

In Figure 3.6, the results for the PEt₃ substituted acyclic model compounds are presented. Here, the gas phase energy differences closely (albeit not perfectly) follow the pattern in Figure 3.5, but average 6.6 kcal mol⁻¹ lower. This suggests that the *cis*/parachute isomers in Figure 3.5 are ca. 6.6 kcal mol⁻¹ destabilized relative to the *trans*/gyroscope isomers (and/or that the latter are in some manner stabilized). In any case, the *cis* and *trans* dialkyl complexes Pt(R)₂(PEt₃)₂ are rendered approximately equal in energy.

In response to a reviewer inquiry regarding the origin of the 6.6 kcal mol⁻¹ difference, the PtX₂ or PtXX' fragments were excised from the structures of all *cis*/parachute and *trans*/gyroscope complexes in Figure 3.5, in each case taking the most favorable of the ten conformations analyzed. Single point calculations were carried out on the remaining dibridgehead diphosphines, a process that freezes the phosphorus–

phosphorus distances (3.4-3.5 vs. 4.5-4.6 Å) and all other atoms. In all cases, the gas phase energies of the gyroscope-derived diphosphines were lower (2.8-7.3 kcal mol⁻¹). Next, the diprimary and dissecondary diphosphines H₂P(CH₂)₁₄PH₂ and HP((CH₂)₁₄)₂PH, derived by deleting two and one (CH₂)₁₄ bridges, respectively, were similarly examined. A detailed analysis of the results (see highlights in Appendix A; Figure 11.9) suggests that bridge/bridge interactions provide stabilization in the *trans*/gyroscope systems. Torsional interactions and angle strain (e.g. at phosphorus) seemingly have subordinate roles in the energy differences. Further analysis is provided below and in Appendix A.

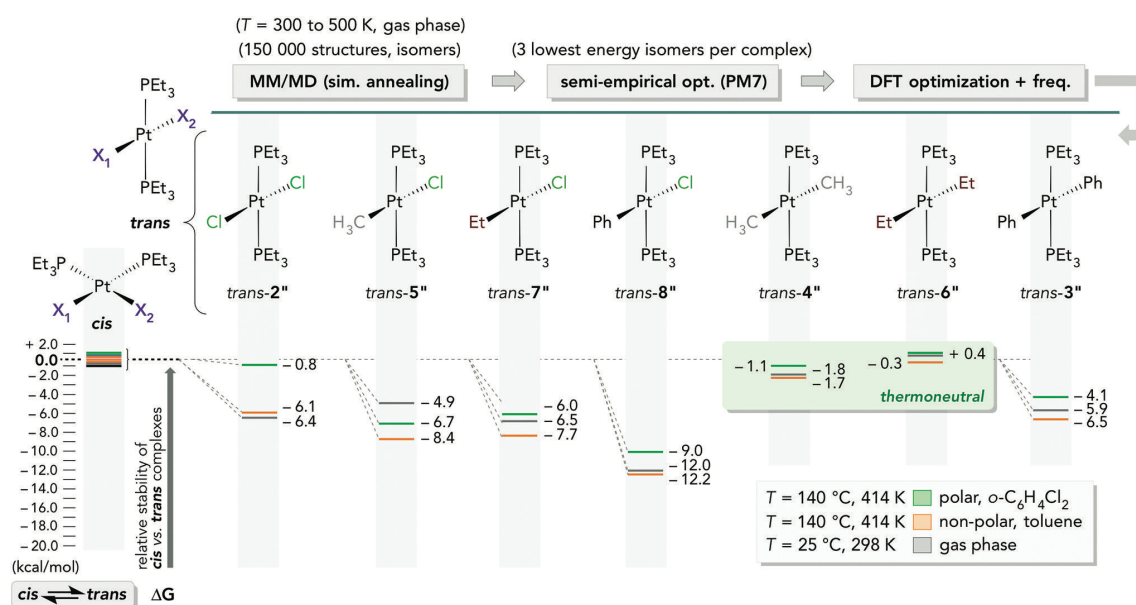


Figure 3.6 Relative energies (ΔG , kcal mol⁻¹) of isomeric *cis* and *trans* platinum complexes with acyclic triethylphosphine ligands as computed by DFT (gas phase or toluene or *o*-C₆H₄Cl₂ solutions) preceded by molecular dynamics and semi-empirical (PM7) computations.

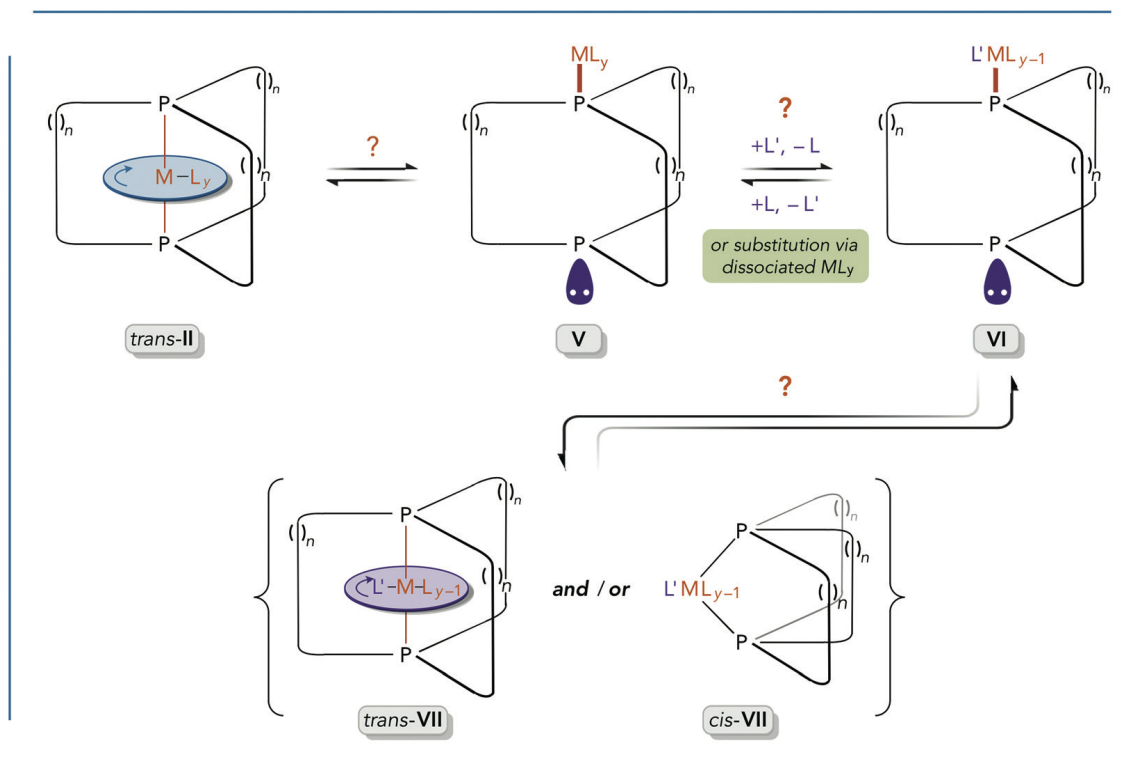
3.4. Discussion

3.4.1. Preliminary remarks

Scheme 3.3 to Scheme 3.8 diagram a number of substitution reactions involving gyroscope and parachute like complexes. Although this study is concerned with general isomerization rates and equilibria as opposed to mechanism, it should be noted that substitution mechanisms of square planar platinum(II) complexes have been extensively studied, going back more than 60 years.^{25,26} However, the gyroscope like complexes may have pathways available that lack counterparts in classical complexes. For example, equilibria exist that allow the ML_y rotators to "escape" from their cages.^{4a,5c,27,28} A possible initial step is shown in Scheme 3.10 (*trans*-**II** \rightarrow **V**). This entails the cleavage of one metal–phosphorus bond and isomerization of the dibridgehead diphosphine ligand from an "*in/in*" to an "*out/out*" geometry.²⁹ Such isomerizations are facile with the free diphosphines.²⁸

Thus, there exists the possibility that substitution occurs external to the cage, perhaps involving **V** directly, or another transient species. Furthermore, as shown in Scheme 3.10, either gyroscope (*trans*-**VII**) or parachute (*cis*-**VII**) products could be preferred kinetically. Also, per studies of related acyclic platinum(II) complexes, mechanisms would be expected to differ depending upon the attacking group, especially for nucleophilic or organometallic agents such as RLi versus electrophilic agents such as HCl.¹⁷ Finally, although purely thermal *cis/trans* isomerizations of platinum(II) complexes have been established, a wide variety of catalysts have been documented.^{11,30-32} To sum, this digression conveys the diversity of phenomena that

might play roles in Scheme 3.3-Scheme 3.8, but are beyond the scope of the present investigation.



Scheme 3.10 Potential equilibria that may play a role in substitution reactions.

3.4.2. Coordination geometries: *trans*/gyroscope versus *cis*/parachute

One starting point for analysis involves the gyroscope and parachute like dichloride complexes *trans*-**2** and *cis*-**2** (Scheme 3.2). As reported earlier,⁸ both DFT and thermolysis data (Scheme 3.2) show the former to be more stable, at least for (CH₂)_{*n*} bridges with *n* ≥ 10. In syntheses where the educts cannot bias the stereochemical outcome — for example,²⁷ PtCl₂ and the dibridgehead diphosphine P((CH₂)₁₄)₃P — *trans*-**2** is always the exclusive product. The new computational data in Figure 3.5 and Figure 3.6 establish an intrinsic energetic preference for the gyroscope like isomers (ca. 6.6 kcal mol⁻¹ with (CH₂)₁₄ bridges). The single point calculations with P((CH₂)₁₄)₃P localize the principal origin of the energy differences within the diphosphine ligands. The additional calculations with HP((CH₂)₁₄)₂PH and H₂P((CH₂)₁₄)PH₂ point to non-covalent chain/chain interactions, and any attendant dispersion forces, as stabilizing factors in the gyroscope systems. Efforts to identify destabilizing steric features unique to the parachute systems have so far not been successful.

Computations have previously been carried out with related phosphite complexes, for which only parachute like *cis* isomers have been synthetically accessed.⁸ Here the DFT data show the *cis* isomers to be considerably more stable. Since phosphite ligands are stronger π-acceptors than phosphine ligands,^{33,34} geometries in which the π-donor chloride ligands³⁵ are *trans* to the phosphorus donor atoms become preferred. In other words, this favorable electronic interaction dominates over any steric factors that may prefer gyroscope like dibridgehead diphosphite complexes.

Alkyl ligands are considered to be strong σ -donors — indeed, the strongest among the ligands in this study³⁴ — and in the context of the *trans* influence (*vide infra*), *trans* geometries are considered to be particularly unfavorable. From this perspective, the formation of the parachute like dialkyl complexes *cis-4c,e,g* and *cis-6c* in Scheme 3.4 and Scheme 3.6 is less surprising. However, we were unable to access any of the corresponding *trans* isomers, precluding an experimental confirmation of the relative stabilities. Thus, two scenarios remain in play: (a) *cis-4c,e,g* and *cis-6c* represent kinetically but not thermodynamically favored substitution products and conditions for isomerizations to *trans-4c,e,g* and *trans-6c* remain to be developed, or (b) *cis-4c,e,g* and *cis-6c* represent thermodynamically favored substitution products, either produced directly (kinetic products) or via transient *trans* isomers.

In our opinion, the computational data fit best with the latter. Although parachute like *cis-4c* and *cis-6c* remain 7.4-6.7 kcal mol⁻¹ less stable than gyroscope like *trans-4c* and *trans-6c* in the gas phase (Figure 3.5), these differences narrow to 5.7-2.9 kcal mol⁻¹ in toluene or *o*-C₆H₄Cl₂, with the diminution always more pronounced in the more polar dichlorinated solvent. For the acyclic model compounds **4''** and **6''** (Figure 3.6), the *cis* and *trans* isomers have essentially equal energies. In addition, ethyl is a stronger σ -donor than methyl,³⁶ further destabilizing the *trans* isomers. In any case, Figure 3.5 reproduces the relative trends in our data, although *trans-4c* and *trans-6c* appear overstabilized compared to their *cis* isomers.³⁷

Consider next the diphenyl complexes **3** introduced in Scheme 3.3. The computations in Figure 3.5 indicate much greater stabilities for the *trans*/gyroscope versus *cis*/parachute isomers as compared to the dialkyl analogs. The same trend is seen with the acyclic analogs in Figure 3.6. The ligating sp^2 carbon atom of a phenyl ligand constitutes a weaker σ -donor than the sp^3 carbon atom of an alkyl ligand,³⁶ attenuating the electronic mismatch in the *trans* isomers.³⁸ However, numerous experimental attempts to establish equilibria (Table 3.3) have been unsuccessful. Regardless, it can be concluded that the reaction of *cis*-**2c** and Ph_2Zn to give *cis*-**3c** (Scheme 3.3) is under kinetic control.

The remaining equilibrium issues in Scheme 3.3-Scheme 3.8 are quite clear-cut. In all cases, it can be shown experimentally that the *trans*/gyroscope methyl or phenyl chloride complexes **5c,e,g** and **8c** are much more stable than the *cis*/parachute analogs (Scheme 3.5 and Scheme 3.7), and the same can be presumed for the ethyl chloride complex **7c** (Scheme 3.6). These trends are fully supported by the computations. In all cases the weak σ -donor chloride ligand is preferentially directed opposite to the stronger alkyl or phenyl σ -donor.³⁴

There still remain various open questions. For example, a reviewer inquired regarding the mechanism of the *cis/trans* isomerizations that take place over silica gel in Scheme 3.5. Silica gel promotes or catalyzes quite a broad spectrum of organic reactions,³⁹ but to the authors' knowledge has not been previously observed to effect geometric isomerizations of metal complexes. Nonetheless, given the plethora of *cis/trans* equilibration mechanisms established for square planar platinum(II)

complexes,^{11,30-32} many possible roles are easily envisioned. Since isomerization also occurs upon attempted Et₂O/ROH crystallization, perhaps the hydroxyl groups associated with silica are involved.

3.4.3. Further electronic and structural considerations

The preceding analysis made little reference to the "trans influence", which is considered the thermodynamic counterpart of the "trans effect".^{25,26,40,41} There have been extensive studies of these phenomena in platinum(II) chemistry. For the ligands of interest in this paper, the trans influence increases in the order Cl⁻ < I⁻ < Ph⁻ < PR₃ < Me⁻ < Et⁻.^{36,41c} However, these concepts are often applied rather simplistically, although even in early studies it was appreciated that the trends represent a complex mash-up of σ - and π -donor/acceptor effects, the relative importance of which can vary from substrate to substrate.⁴² Accordingly, correlations with the equilibria established above are not attempted. Much work involving the trans influence has been focused upon structural trends — specifically, the effect of a series of *trans* ligands upon a metal–ligand bond distance. A longer bond *trans* to the ligand of interest is taken as evidence of destabilization, and a shorter bond is taken as evidence for stabilization.^{36,40,41} One question is whether our computed structures, excerpted in Figure 3.7, conform to these expectations.

For example, with the chloride-substituted gyroscope like complexes *trans-7c*, *trans-5c*, *trans-8c*, and *trans-2c*, the platinum–chlorine bond lengths (2.47, 2.46, 2.44, 2.35 Å) contract as the trans influences of the ethyl, methyl, phenyl, and chloride ligands

decrease. The same trend holds for the platinum–carbon bond lengths in the diethyl, dimethyl, and diphenyl complexes *trans-6c*, *trans-4c*, and *trans-3c* (2.16, 2.15, 2.09 Å). With the *cis*/parachute complexes, the platinum–phosphorus bond lengths do not change as much as the *trans* ligand is varied, except in the case of the dichloride complex *cis-2c* (2.28 Å vs. 2.38–2.39 Å for *trans* ethyl, methyl, and phenyl ligands). However, the platinum–carbon bond lengths follow the same trends as in the *trans* complexes. They are (as compared to *trans* complexes) uniformly longer in *cis-5c*, *cis-7c*, and *cis-8c* (all bonds *cis* to chloride), and shorter in *cis-4c*, *cis-6c*, and *cis-3c* (all bonds *cis* to alkyl).

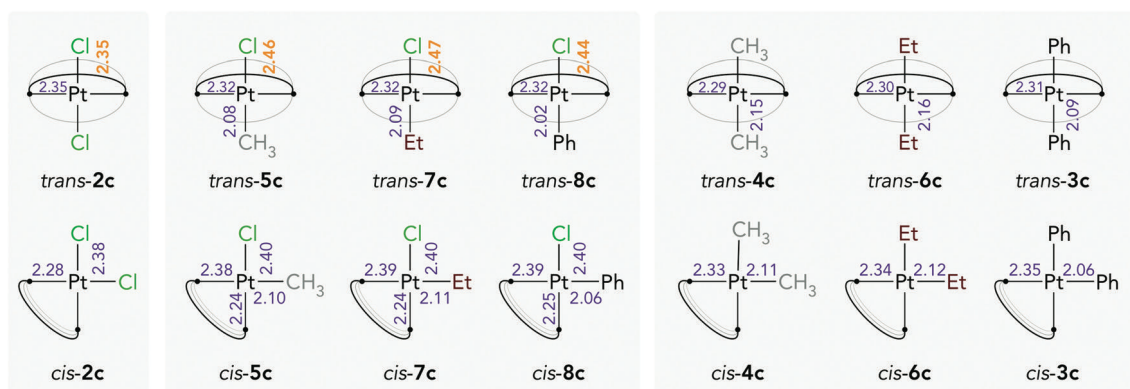


Figure 3.7 Platinum–ligand bond lengths (Å) for computed *trans*/gyroscope and *cis*/parachute complexes.

The experimental structural data for *cis-4c*, *trans-5c*, and *trans-7c* (Table 3.2) are in excellent agreement with the bond lengths in Figure 3.7 and other computed metrical parameters. All values are in the normal ranges for square planar platinum(II) complexes.⁴³⁻⁴⁵ The analogous methyl and ethyl chloride complexes *trans-5c* and *trans-7c* exhibit bond lengths and angles about platinum that are within experimental error. In the methyl chloride and iodide complexes *trans-5c* and *trans-10c*, the platinum–carbon

bonds lengthen from 2.074(7) Å to 2.179 (5) Å. This can be attributed to the greater trans influence of the iodide ligand noted above.^{25,41c}

3.4.4. Additional properties of new complexes

Although this study is not concerned with the dynamic properties of the complexes in Scheme 3.3-Scheme 3.8, certain features are apparent from the ¹³C NMR spectra. Specifically, all of the *trans*/gyroscope complexes in the "c series" exhibit only seven signals. This indicates that rapid ML_y rotation (or (CH₂)₁₄ bridge exchange) takes place on the NMR time scale at room temperature (with the number of signals, 14/2, reflecting the formal horizontal mirror plane). Similar behavior has been observed with other methyl substituted rotors,^{5c,7} but *trans-7c* represents the first case with a larger ethyl ligand. The analogs with longer (CH₂)_n bridges, *trans-4e.g*, also gave the minimum number of ¹³C NMR signals. These processes have been analyzed in depth in a recent review (previous chapter) that collects all available activation parameters.³ A key consideration involves the van der Waals radii of the ML_y rotors versus the clearance allowed by the (CH₂)_n bridges.

In contrast, the parachute like complex *cis-3c* exhibits eleven CH₂ ¹³C NMR signals, indicating that the "jump rope" process is slow on the NMR time scale at room temperature. In theory, two sets of seven signals with a ca. 2:1 intensity ratio should be observable, but sufficient resolution was not available at 126 MHz. As reported earlier, the corresponding dichloride complex *cis-2c* exhibits twelve signals.⁸ The higher

homologs *cis-3e.g* give the minimum number of signals (nine and eleven), indicative of rapid jump rope processes.

The thermolyses in Scheme 3.9 convert the parachute like dimethyl complex *cis-4c* to the gyroscope like methyl halide complexes *trans-5c* and *trans-9c*. This suggests an initial oxidative addition of the high boiling haloarene solvent to give a platinum(IV) species, a type of reaction with significant precedent.⁴⁶ Indeed, toluene-*d*₅ can be identified as a product in the reaction with bromobenzene-*d*₅. Evidence has also been obtained from related reactions for the formation of species with new platinum–carbon bonds. Another fascinating lead only briefly mentioned above is the apparent formation of a platinum bis(phosphine) hydride intermediate upon attempted isomerization of the ethyl chloride complex *trans-5c*. All of these transformations and the mesitylene-derived products in Table 3.3 remain under active investigation.

3.5. Conclusions

With respect to the gyroscope like dichloride complexes *trans-2c,e,g*, this study has established that isomerization normally accompanies reactions with alkyl lithium reagents to give the dialkyl complexes *cis-4c,e,g* and *cis-6c* (Scheme 3.4 and Scheme 3.6). In contrast, phenyl nucleophiles normally afford *trans* diphenyl complexes, although lesser amounts of *cis* adducts are sometimes observed in reactions with PhLi. Subsequent reactions of *cis-4c,e,g* and HCl (1.0 equiv.) give detectable quantities of *cis* alkyl chloride complexes that easily convert (over silica gel or at ~100 °C) to the gyroscope like isomers *trans-5c,e,g*. The *cis* phenyl chloride complex *cis-8c* undergoes an analogous thermal isomerization to *trans-8c*. DFT calculations indicate that the

trans/gyroscope complexes always have lower energies than the *cis*/parachute complexes in the gas phase. However, isomeric dimethyl and diethyl complexes have nearly the same energies in *o*-C₆H₄Cl₂.³⁷ With acyclic model compounds the energy differences are much less, and the isomeric dimethyl and diethyl complexes exhibit essentially equal energies.

Overall, this work has brought several concepts from traditional platinum(II) coordination chemistry into the modern context of the chelating and potentially *trans* spanning dibridgehead diphosphine ligands P((CH₂)_n)₃P. These data greatly enhance the confidence with which the NMR data associated with various dynamic processes can be interpreted. These include ML_y rotation in the gyroscope like complexes and the "jump rope" (CH₂)_n exchange in the parachute like complexes, both of which will be topics of future reports.

3.6. Experimental [major contribution: Mr. Y. Zhu]

3.6.1. General

Reactions were conducted under nitrogen atmospheres unless noted. Materials were utilized as follows: CH₂Cl₂ purified by a Glass Contour system; hexanes (98.5%, Sigma-Aldrich), EtOAc (99.5%, Sigma-Aldrich), methanol (99.8%, Sigma-Aldrich), CDCl₃, HCl (2.0 M in Et₂O, Alfa-Aesar), Et₃N (99%, Alfa-Aesar), silica gel (40-63 μm, 230-400 mesh, Silicycle), and neutral alumina (Brockmann I, for chromatography, 40-300 μm, 60A, Acros), used as received.

NMR spectra were recorded on standard 500 MHz FT spectrometers at ambient probe temperatures and referenced as follows (δ , ppm): ^1H : residual internal CHCl_3 (7.26); $^{13}\text{C}\{^1\text{H}\}$: internal CDCl_3 (77.16); $^{31}\text{P}\{^1\text{H}\}$: external 85% H_3PO_4 (0.00).

3.6.1.1. Representative syntheses: $\overline{\text{cis-Pt}(\text{Cl})(\text{Me})(\text{P}((\text{CH}_2)_{18})_3\text{P})}$ (*cis-5e*) and *trans-5e*.

Procedure A. Under air, a round bottom flask was charged with *cis-4e* (0.0838 g, 0.0802 mmol), CH_2Cl_2 (8 mL), and methanol (0.4 mL). Then HCl (2.0 M in Et_2O , 0.040 mL, 0.080 mmol) was added with stirring. After 0.5 h, the solvent was removed by rotary evaporation. The white solid was chromatographed on neutral alumina (first 3:1:0.02 v/v/v hexanes/ CH_2Cl_2 / Et_3N , then 25:1:0.2 v/v/v hexanes/ EtOAc / Et_3N). The solvent was removed from the product containing fractions (TLC monitoring) by rotary evaporation. This gave *trans-5e* (0.0389 g, 0.0365 mmol, 46%), with subsequent fractions affording *trans-5e/cis-5e* mixtures.

Procedure B. A vial was charged with a *trans-5e/cis-5e* mixture (0.0274 g, 0.0257 mmol; obtained from a different run of procedure A, ca. 1:2 by ^{31}P NMR), silica gel (1.2375 g) and CH_2Cl_2 (10 mL). The mixture was stirred (rt). After 12 h, the sample was filtered and the silica gel further washed with CH_2Cl_2 (40 mL). The solvent was removed from the filtrate to give *trans-5e* (0.0165 g, 0.0155 mmol, 60%) as a beige oil. Data for *cis-5e*: NMR (CDCl_3 , δ /ppm): $^{31}\text{P}\{^1\text{H}\}$ (202 MHz) 10.3 (d, $^2J_{\text{PP}} = 12.3$ Hz, $^1J_{\text{PPt}} = 1750$ Hz, *trans* to CH_3), 3.56 (d, $^2J_{\text{PP}} = 12.1$ Hz, $^1J_{\text{PPt}} = 4362$ Hz, *cis* to CH_3).

Data for *trans-5e*: NMR (CDCl_3 , δ /ppm): ^1H (500 MHz) 1.88-1.75 (br m, 12H, PCH_2), 1.65-1.50 (br m, 12H, PCH_2CH_2), 1.46-1.38 (br m, 12H, $\text{PCH}_2\text{CH}_2\text{CH}_2$), 1.38-

1.23 (br m, 72H, remaining $\underline{\text{CH}}_2$), 0.31 (t, 3H, $^3J_{\text{HP}} = 6.2$ Hz, $^2J_{\text{HPt}} = 83$ Hz, ⁴⁸ Pt $\underline{\text{CH}}_3$);
 $^{13}\text{C}\{^1\text{H}\}$ (126 MHz) 30.8 (virtual t, ⁴⁹ $J_{\text{CP}} = 6.4$ Hz, P $\underline{\text{CH}}_2\text{CH}_2\underline{\text{CH}}_2$), 28.6 (s, $\underline{\text{CH}}_2$),
28.48 (s, $\underline{\text{CH}}_2$), 28.47 (s, $\underline{\text{CH}}_2$), 28.4 (s, $\underline{\text{CH}}_2$), 28.0 (s, $\underline{\text{CH}}_2$), 27.8 (s, $\underline{\text{CH}}_2$), 23.9 (s,
P $\underline{\text{CH}}_2\underline{\text{CH}}_2$), 21.5 (virtual t, ⁴⁹ $J_{\text{CP}} = 15.9$ Hz, P $\underline{\text{CH}}_2$), -23.4 (t, $J_{\text{CP}} = 6.5$ Hz, Pt $\underline{\text{CH}}_3$);
 $^{31}\text{P}\{^1\text{H}\}$ (202 MHz) 8.8 (s, $^1J_{\text{PPt}} = 2824$ Hz).⁴⁸

3.6.2. Thermolyses (Table 3.3 and Scheme 3.9)

NMR tubes were charged with the following materials and kept at the indicated temperature except for brief intervals when spectra (δ /ppm) were recorded.

3.6.2.1. Entry 1

cis-2c (0.0086 g, 0.0094 mmol or 0.0096 g, 0.0104 mmol), silica gel (0.0925 g), toluene-*d*₈ or CDCl₃ (0.6 mL), 25 °C, 24 h. ³¹P{¹H} NMR 4.5 or 4.8 (s, ¹J_{Pt} = 3498 or 3548 Hz, ⁴⁸ *cis-2c*, >99%).

3.6.2.2. Entry 2

cis-3c (0.0070 g, 0.0070 mmol), toluene-*d*₈ (0.7 mL), 80 °C, 10 h. ³¹P{¹H} NMR 4.9 (s, ¹J_{Pt} = 1762 Hz, ⁴⁸ *cis-3c*, >99%).

3.6.2.3. Entry 3

cis-3c (0.0090 g, 0.0090 mmol), mesitylene (0.6 mL), 140 °C, 30 h. ³¹P{¹H} NMR 7.4 (s, unknown, 84%), 4.3 (s, unknown, 16%).²⁰ Spectra taken after 1.5-12 h showed additional minor signals.

3.6.2.4. Entry 4

cis-3c (0.0059 g, 0.0059 mmol), silica gel (0.0927 g), toluene-*d*₈ (0.6 mL), 25 °C, 5 h and then 80 °C, 24 h. ³¹P{¹H} NMR 0.5 (s, ¹J_{Pt} = 1760 Hz, ⁴⁸ *cis-3c*, >99%).

3.6.2.5. Entry 5

cis-4c (0.0062 g, 0.0068 mmol), toluene-*d*₈ (0.7 mL), 80 °C, 10 h. ³¹P{¹H} NMR 7.3 (s, ¹J_{Pt} = 1868 Hz, ⁴⁸ *cis-4c*, >99%).

3.6.2.6. Entry 6

cis-4c (0.0081 g, 0.0092 mmol), mesitylene (0.6 mL), 140 °C, 30 h. $^{31}\text{P}\{^1\text{H}\}$ NMR 13.6 (s, unknown, 8%), 10.8 (unknown, 2%), 9.3 (s, unknown, 6%), 7.3 (s, $^1J_{\text{PPt}} = 1865$ Hz, ⁴⁸ *cis-4c*, 84%).

3.6.2.7. Entry 7

cis-4c (0.0071 g, 0.0081 mmol), silica gel (0.1096 g), toluene-*d*₈ (0.6 mL), 25 °C, 24 h. $^{31}\text{P}\{^1\text{H}\}$ NMR 7.3 (s, $^1J_{\text{PPt}} = 1870$ Hz, ⁴⁸ *cis-4c*, >99%).

3.6.2.8. Entry 8

cis-4c (0.0072 g, 0.0082 mmol), silica gel (0.0927 g), toluene-*d*₈ (0.6 mL), 25 °C, 5 h (little conversion) and then 80 °C, 24 h. $^{31}\text{P}\{^1\text{H}\}$ NMR 11.4 (s, unknown, 76%), 6.2 (s, unknown, 24%).²⁰

3.6.2.9. Entry 9

cis-5c (0.0061 g, 0.0068 mmol), toluene-*d*₈ (0.7 mL), 80 °C, 10 h. $^{31}\text{P}\{^1\text{H}\}$ NMR 11.3 and 5.0 (2 d, $^2J_{\text{PP}} = 11.5$ Hz/ $^1J_{\text{PPt}} = 1736$ Hz⁴⁸ and $^2J_{\text{PP}} = 11.5$ Hz/ $^1J_{\text{PPt}} = 4167$ Hz, ⁴⁸ *cis-5c*, 86%), 11.1 (s, *trans-5c*, 14%). The 72 h experiment was similarly carried out in toluene-*d*₀.

3.6.2.10. Entry 10

cis-5c (0.0143 g, 0.0159 mmol), *o*-C₆H₄Cl₂ (0.6 mL), 100 °C, 3 h. $^{31}\text{P}\{^1\text{H}\}$ NMR 10.8 (s, $^1J_{\text{PPt}} = 2834$ Hz, ⁴⁸ *trans-5c*, >99%).

3.6.2.11. Entry 11

cis-5c (0.0064 g, 0.0071 mmol), *o*-C₆H₄Cl₂ (0.7 mL), 140 °C, 0.5 h. ³¹P{¹H} NMR 10.8 (s, ¹J_{PPt} = 2834 Hz,⁴⁸ *trans-5c*, >99%).

3.6.2.12. Entry 12

cis-5c (0.0091 g, 0.0100 mmol), C₆D₅Br (0.6 mL), 110 °C, 7 h. ³¹P{¹H} NMR 11.1 (s, ¹J_{PPt} = 2828 Hz,⁴⁸ *trans-5c*, >99%). ¹H NMR 2.00-1.84 (m, 12H, PCH₂), 1.84-1.69 (m, 12H, PCH₂CH₂), 1.61-1.49 (m, 12H, PCH₂CH₂CH₂), 1.49-1.32 (m, 48H, remaining CH₂), 0.54 (t, 3H, ³J_{HP} = 5.5 Hz, ²J_{HPt} = 80 Hz,⁴⁸ PtCH₃).

3.6.2.13. Entry 13

cis-5c (0.0059 g, 0.0066 mmol), mesitylene (0.6 mL), 140 °C, 0.5 h. ³¹P{¹H} NMR 10.4 (s, ¹J_{PPt} = 2841 Hz,⁴⁸ *trans-5c*, >99%).

3.6.2.14. Entry 14

trans-5c (0.0072 g, 0.0080 mmol), mesitylene (0.6 mL), 140 °C, 30 h. ³¹P {¹H} NMR 10.8 (s, ¹J_{PPt} = 2844 Hz,⁴⁸ *trans-5c*, 87%), 7.3 (s, unknown, 13%).

3.6.2.15. Entry 15

trans-7c (0.0089 g, 0.0098 mmol), mesitylene (0.6 mL), 140 °C, 30 h. ³¹P {¹H} NMR 7.4 (s, ¹J_{PPt} = 2447 Hz,⁴⁸ unknown, >99%).²⁰ Spectra taken after 1.5-18 h showed one main intermediate: ³¹P{¹H} NMR 18.3 (s, ¹J_{PPt} = 2756 Hz 48); ³¹P NMR (undecoupled): 18.3 (br s, *w*_{1/2} = 27 Hz, ¹J_{PPt} = 2754 Hz⁴⁸); ¹H NMR -16.78 (t, ²J_{HP} = 13.8 Hz, ¹J_{HPt} = 1254 Hz,⁴⁸ referenced to C₆H₃(CH₃)₃ at δ 6.78 ppm).

3.6.2.16. Entry 16

cis-8c (0.0075 g, 0.0078 mmol), *o*-C₆H₄Cl₂ (0.6 mL), 100 °C, 6 h. ³¹P{¹H}

NMR 7.7 (s, ¹J_{PPt} = 2806 Hz, ⁴⁸ *trans-8c*, >99%).

3.6.2.17. Entry 17

cis-8c (0.0053 g, 0.0055 mmol), *o*-C₆H₄Cl₂ (0.6 mL), 140 °C, 0.5 h. ³¹P{¹H}

NMR 7.7 (s, ¹J_{PPt} = 2806 Hz, ⁴⁸ *trans-8c*, >99%).

3.6.2.18. Entry 18

trans-8c (0.0098 g, 0.0100 mmol), mesitylene (0.6 mL), 140 °C, 30 h. ³¹P {¹H}

NMR 7.7 (s, ¹J_{PPt} = 2806 Hz, ⁴⁸ *trans-8c*, >99%).

3.6.2.19. Scheme 3.9 (right)

cis-4c (0.0134 g, 0.0153 mmol), C₆D₅Br (0.6 mL), 110 °C, 7 h and then 140 °C, 6 h. ³¹P{¹H} NMR 8.9 (s, ¹J_{PPt} = 2806 Hz, *trans-9c*, >99%). ¹H NMR 2.28 (s, 1H, C₆D₅CH₃), ⁵⁰ 2.03-1.92 (m, 12H, PCH₂), 1.79-1.68 (m, 12H, PCH₂CH₂), 1.59-1.49 (m, 12H, PCH₂CH₂CH₂), 1.49-1.37 (m, 48H, remaining CH₂), 0.61 (t, 3H, ³J_{HP} = 6.0 Hz, ²J_{HPt} = 80 Hz, ⁴⁸ PtCH₃).

3.6.2.20. Scheme 3.9 (left)

cis-4c (0.0062 g, 0.0071 mmol), *o*-C₆H₄Cl₂ (0.6 mL), 140 °C, 12 h. ³¹P{¹H}

NMR 10.8 (s, ¹J_{PPt} = 2834 Hz, ⁴⁸ *trans-5c*, >99%). A spectrum taken after 1 h showed an additional minor signal at 8.9 (s, unknown).

3.6.3. Crystallography

A. Methanol was slowly added dropwise to an Et₂O solution of *cis*-**4c**. After each drop, the mixture was shaken to redissolve the white precipitate formed. When the precipitate persisted, Et₂O was added to regenerate a homogeneous solution, which was kept at 4 °C. After 3 d, colorless crystals were obtained, and data were collected as outlined in Table 3.1. Cell parameters were obtained from 45 frames using a 1° scan and refined with 102,005 reflections. Integrated intensity information for each reflection was obtained by reduction of the data frames with the program APEX3.⁵¹ Lorentz and polarization corrections were applied. Data were scaled, and absorption correction were applied using the program SADABS.⁵² The space group was determined from systematic reflection conditions and statistical tests. The structure was solved using XT/XS in APEX3.^{51,53} The structure was refined (weighted least squares refinement on F^2) to convergence.^{53,54} All non-hydrogen atoms were refined with anisotropic thermal parameters. Hydrogen atoms were placed in idealized positions using a riding model. The atoms C29 through C42 and C23 to C24 exhibited elongated thermal ellipsoids and/or nearby residual electron density peaks. These were successfully modeled by disorder between two positions, with occupancy ratios of 0.64:0.36, and 0.81:0.19 respectively. Appropriate restraints and/or constraints were applied to keep the bond distances, angles, and thermal ellipsoids meaningful. The absence of additional symmetry and voids were confirmed using PLATON (ADDSYM).⁵⁵

B. Colorless crystals of *trans*-**5c** were obtained in a procedure analogous to that for *cis*-**4c**, but starting from the isomer *cis*-**5c**. Either methanol or ethanol could be used.

Data were collected on a crystal from each solvent system and both gave the same structure, which was solved as in method A. Two pairs of atoms, C11/C1 and C39/C40 exhibited abnormal thermal ellipsoids. These were successfully modeled by disorder between two positions, with occupancy ratios of 0.89:0.11 and 0.88:0.12 respectively.

C. An Et₂O solution of *trans-10c* was layered with methanol. After 7 d, data were collected on the yellow blocks as outlined in Table 3.1. The structure was solved and refined in a manner parallel to that in method A. The iodide and methyl ligands (I1, C1) were disordered, but this could be modeled and refined to an 86:14 occupancy ratio (I1 and I1a as well as C1 and C1a were constrained to have the same thermal ellipsoids).

D. Colorless crystals of *trans-7c* were obtained in a procedure analogous to that for *cis-4c*. Data were collected and the structure was solved in a manner parallel to that in method A. Three independent molecules were found in the asymmetric unit. For one, the carbon atoms of the methylene chains exhibited elongated thermal ellipsoids (C91-C132), suggesting disorder. This could be modeled between two positions with an occupancy ratio of 0.33:0.67. Appropriate restraints were used to keep bond distances, angles, and thermal ellipsoids meaningful. However, some thermal ellipsoids associated with the modeled positions remained elongated, suggesting further disorder.

3.7. References

- (1) Kottas, G. S.; Clarke, L. I.; Horinek, D.; Michl, J. Artificial Molecular Rotors. *Chem. Rev.* **2005**, *105*, 1281-1376.
- (2) Dattler, D.; Fuks, G.; Heiser, J.; Moulin, E.; Perrot, A.; Yao, X.; Giuseppone, N. Design of collective motions from synthetic molecular switches, rotors, and motors. *Chem. Rev.* **2020**, *120*, 310-433.
- (3) Ehnbohm, A.; Gladysz, J. A. Gyroscopes and the Chemical Literature, 2002-2020: Approaches to a Nascent Family of Molecular Devices. *Chem. Rev.* **2021**, *121*, 3701-3750.
- (4) (a) Nawara-Hultsch, A. J.; Stollenz, M.; Barbasiewicz, M.; Szafert, S.; Lis, T.; Hampel, F.; Bhuvanesh, N.; Gladysz, J. A. Gyroscope-Like Molecules Consisting of PdX₂/PtX₂ Rotators within Three-Spoke Dibrigehead Diphosphine Stators: Syntheses, Substitution Reactions, Structures, and Dynamic Properties. *Chem. Eur. J.* **2014**, *20*, 4617-4637. (b) Taher, D.; Nawara-Hultsch, A. J.; Bhuvanesh, N.; Hampel, F.; Gladysz, J. A. Mono- and Disubstitution Reactions of Gyroscope Like Complexes Derived from Cl-Pt-Cl Rotators within Cage Like Dibrigehead Diphosphine Ligands. *J. Organomet. Chem.* **2016**, *821*, 136-141. (c) Kharel, S.; Joshi, H.; Bhuvanesh, N.; Gladysz, J. A. Syntheses, Structures, and Thermal Properties of Gyroscope-like Complexes Consisting of PtCl₂ Rotators Encased in Macrocyclic Dibrigehead Diphosphines P((CH₂)_n)₃P with Extended Methylene Chains (*n* = 20/22/30) and Isomers Thereof. *Organometallics* **2018**, *37*, 2991-3000.

(5) Wang, L.; Hampel, F.; Gladysz, J. A. "Giant" Gyroscope-Like Molecules Consisting of Dipolar Cl–Rh–CO Rotators Encased in Three-Spoke Stators That Define 25-27-Membered Macrocycles. *Angew. Chem. Int. Ed.* **2006**, *45*, 4372-4375; "Gyroskop-Giganten": Dipolare Cl–Rh–CO Rotatoren, umgeben von Statoren aus drei Speichen 25-bis 27-gliedriger Makrocyclen. *Angew. Chem.* **2006**, *118*, 4479-4482. (b) Wang, L.; Shima, T.; Hampel, F.; Gladysz, J. A. Gyroscope-like molecules consisting of three-spoke stators that enclose "switchable" neutral dipolar rhodium rotators; reversible cycling between faster and slower rotating Rh(CO)I and Rh(CO)₂I species. *Chem. Commun.* **2006**, 4075-4077. (c) Estrada, A. L.; Jia, T.; Bhuvanesh, N.; Blümel, J.; Gladysz, J. A. Substitution and Catalytic Chemistry of Gyroscope-Like Complexes Derived from Cl–Rh–CO Rotators and Triply *trans* Spanning Di(trialkylphosphine) Ligands. *Eur. J. Inorg. Chem.* **2015**, *2015*, 5318-5321.

(6) (a) Lang, G. M.; Shima, T.; Wang, L.; Cluff, K. J.; Skopek, K.; Hampel, F.; Blümel, J.; Gladysz, J. A. Gyroscope-Like Complexes Based on Dibridgehead Diphosphine Cages That Are Accessed by Three-Fold Intramolecular Ring Closing Metatheses and Encase Fe(CO)₃, Fe(CO)₂(NO)⁺, and Fe(CO)₃(H)⁺ Rotators. *J. Am. Chem. Soc.* **2016**, *138*, 7649-7663. (b) Lang, G. M.; Bhuvanesh, N.; Reibenspies, J. H.; Gladysz, J. A. Syntheses, Reactivity, Structures, and Dynamic Properties of Gyroscope-like Iron Carbonyl Complexes Based on Dibridgehead Diarsine Cages. *Organometallics* **2016**, *35*, 2873-2889. (c) Lang, G. M.; Skaper, D.; Hampel, F.; Gladysz, J. A. Synthesis, reactivity, structures, and dynamic properties of gyroscope like iron complexes with dibridgehead diphosphine cages: pre- vs. post-metathesis substitutions as routes to

adducts with neutral dipolar Fe(CO)(NO)(X) rotors. *Dalton Trans.* **2016**, *45*, 16190-16204.

(7) (a) Fiedler, T.; Bhuvanesh, N.; Hampel, F.; Reibenspies, J. H.; Gladysz, J. A. Gyroscope like molecules consisting of trigonal or square planar osmium rotators within three-spoked dibridgehead diphosphine stators: syntheses, substitution reactions, structures, and dynamic properties. *Dalton Trans.* **2016**, *45*, 7131-7147. (b) Hess, G. D.; Fiedler, T.; Hampel, F.; Gladysz, J. A. Octahedral Gyroscope-like Molecules Consisting of Rhenium Rotators within Cage-like Dibridgehead Diphosphine Stators: Syntheses, Substitution Reactions, Structures, and Dynamic Properties. *Inorg. Chem.* **2017**, *56*, 7454-7469.

(8) Joshi, H.; Kharel, S.; Ehnbohm, A.; Skopek, K.; Hess, G. D.; Fiedler, T.; Hampel, F.; Bhuvanesh, N.; Gladysz, J. A. Three-Fold Intramolecular Ring Closing Alkene Metatheses of Square Planar Complexes with *cis* Phosphorus Donor Ligands P(X(CH₂)_mCH=CH₂)₃ (X = —, *m* = 5-10; X = O, *m* = 3-5): Syntheses, Structures, and Thermal Properties of Macrocyclic Dibridgehead Diphosphorus Complexes. *J. Am. Chem. Soc.* **2018**, *140*, 8463-8478.

(9) For example, a variety of data exclude initial ligand (L) dissociation from *trans-II*,³ including square planar,^{4a,c,5b,c} trigonal bipyramidal,⁶ and octahedral⁷ coordination geometries.

(10) Interestingly, the energy differences do not vary monotonically. Rather, there is an apparent even/odd alternation with respect to *n/2* (odd, *trans-2* 9.2-8.5 kcal/mol more stable; even, *trans-2* 5.8-5.1 kcal/mol more stable).⁸

(11) G Anderson, G. K.; Cross, R. J. Isomerisation Mechanisms of Square-Planar Complexes. *Chem. Soc. Rev.* **1980**, *9*, 185-215.

(12) Redfield, D. A.; Nelson, J. H. Equilibrium Energetics of Cis-Trans Isomerization for two Square-Planar Palladium(II)-Phosphine Complexes *Inorg. Chem.* **1973**, *12*, 15-19.

(13) Quantitative solvatochromic polarity values are available for all solvents employed in this study ($\text{CH}_2\text{Cl}_2 > \text{CHCl}_3 > o\text{-C}_6\text{H}_4\text{Cl}_2 > \text{C}_6\text{H}_5\text{Cl} > \text{C}_6\text{H}_5\text{Br} > \text{toluene} > \text{mesitylene}$): C. Reichardt and T. Welton, *Solvents and Solvent Effects in Organic Chemistry*. 4th Ed; Wiley: Weinheim, 2011; pp. 455-456.

(14) (a) E. L. Eliel, S. H. Wilen, *Stereochemistry of Organic Compounds*; Wiley: New York, 1994; pp. 837-838 and 1208. (b) Ward, R. S. *Selectivity versus specificity*. *Chemistry in Britain*, 1991, 803-804.

(15) Grim, S. O.; Keiter, R. L.; McFarlane, W. A Phosphorus-31 Nuclear Magnetic Resonance Study of Tertiary Phosphine Complexes of Platinum(II). *Inorg. Chem.* **1967**, *6*, 1133-1137.

(16) Romeo, R.; D'Amico, G.; Sicilia, E.; Russo, N.; Rizzato, S. β -Hydrogen Kinetic Effect. *J. Am. Chem. Soc.* **2007**, *129*, 5744-5755 (see the supporting information therein).

(17) Romeo, R. D'Amico, G. Mechanistic Insight into the Protonolysis of the Pt–C Bond as a Model for C–H Bond Activation by Platinum(II) Complexes. *Organometallics* **2006**, *25*, 3435-3446 (see the supporting information therein).

(18) Otto, S. Structure and solution behavior of cyclooctadiene complexes of platinum(II). *Inorg. Chim. Acta*, **2010**, *363*, 3316-3320.

(19) (a) Brainard, R. L.; Whitesides, G. M. The Mechanism of Thermal Decomposition of *trans*-Chloroethylbis(triethylphosphine)platinum(II). *Organometallics* **1985**, *4*, 1550-1557. (b) Holtcamp, M. W.; Labinger, J. A.; Bercaw, J. E. Ligand effects on the rates of protonolysis and isotopic exchange for platinum(II) alkyls. *Inorg. Chim. Acta*, **1997**, *265*, 117-125.

(20) The identities of the unknown thermolysis products are being further investigated, but are beyond the scope of the present study.

(21) Dassault Systèmes BIOVIA, Materials Studio 6.0, San Diego: Dassault Systèmes, 2017.

(22) (a) Christensen, A. S.; Kubař, T.; Cui, Q.; Elstner, M. Semiempirical Quantum Mechanical Methods for Noncovalent Interactions for Chemical and Biochemical Applications. *Chem. Rev.* **2016**, *116*, 5301-5337. (b) Stewart, J. J. P. Optimization of parameters for semiempirical methods VI: more modifications to the NDDO approximations and re-optimization of parameters. *J. Mol. Model.* **2013**, *19*, 1-32.

(23) Marenich, A. V.; Cramer, C. J.; Truhlar, D. G. Universal Solvation Model Based on Solute Electron Density and on a Continuum Model of the Solvent Defined by the Bulk Dielectric Constant and Atomic Surface Tensions. *J. Phys. Chem. B.* **2009**, *113*, 6378-6396.

(24) (a) Romeo, R.; Arena, G.; Scolaro, L. M. Steric and Electronic Factors Influencing the Reactivity of Tertiary Phosphines toward Platinum(II) Complexes. *Inorg. Chem.* **1992**, *31*, 4879-4884. (b) Suresh, C. H.; Koga, N. Quantifying the Electronic Effect of Substituted Phosphine Ligands via Molecular Electrostatic Potential. *Inorg. Chem.* **2002**, *41*, 1573-1578.

(25) Basolo, F.; Pearson, R. G. *Mechanisms of Inorganic Reactions*. John Wiley & Sons, New York, 2nd edn, 1967.

(26) Langford, C. H.; Gray, H. B. *Ligand Substitution Processes*. W. A. Benjamin, Reading, Massachusetts, 1966.

(27) Kharel, S.; Joshi, H.; Bierschenk, S.; Stollenz, M.; Taher, D.; Bhuvanesh, N.; Gladysz, J. A. Homeomorphic Isomerization as a Design Element in Container Molecules; Binding, Displacement, and Selective Transport of MCl_2 Species (M = Pt, Pd, Ni). *J. Am. Chem. Soc.* **2017**, *139*, 2172-2175.

(28) Stollenz, M.; Barbasiewicz, M.; Nawara-Hultsch, A. J.; Fiedler, T.; Laddusaw, R. M.; Bhuvanesh, N.; Gladysz, J. A. Dibrigehead Diphosphines that Turn Themselves Inside Out. *Angew. Chem. Int. Ed.* **2011**, *50*, 6647-6651; Dreifach-verbrückte Diphosphane mit von innen nach außen invertierender Konfiguration. *Angew. Chem.* **2011**, *123*, 6777-6781.

(29) Alder, R. W.; East, S. P. In/Out Isomerism. *Chem. Rev.* **1996**, *96*, 2097-2111.

(30) Louw, W. J. Preparative and Kinetic Study on the Mechanisms of Isomerization of Square-Planar Complexes. Kinetic Evidence for Pseudorotation of a Five-Coordinate Intermediate. *Inorg. Chem.* **1977**, *16*, 2147-2160.

(31) Cooper, M. K.; Downes, J. M. Chelate Complexes of Phosphorus–Nitrogen Ligands. 1. Deprotonation, Cis-Trans Isomerism, and Anion-Catalyzed Isomerization in Platinum(II) Complexes of (*o*-Aminophenyl)diphenylphosphine. *Inorg. Chem.* **1978**, *17*, 880-884.

(32) M Holt, M. S.; Nelson, J. H. Platinum(II) complexes of (cyanoethyl)phosphines. *Inorg. Chem.* **1986**, *25*, 1316-1320.

(33) (a) Leysens, T.; Peeters, D.; Orpen, A. G.; Harvey, J. N. How Important Is Metal-Ligand Back-Bonding toward YX_3 Ligands ($Y = N, P, C, Si$)? An NBO Analysis. *Organometallics* **2007**, *26*, 2637-2645. (b) Pérez, H. F.; Etayo, P.; Panossian, A.; Vidal-Ferran, A. Phosphine-Phosphinite and Phosphine-Phosphite Ligands: Preparation and Applications in Asymmetric Catalysis. *Chem. Rev.* **2011**, *111*, 2119-2176.

(34) The relative σ donor and π acceptor properties of a variety of ligands are treated in this review: Coe, B. J.; Glenwright, S. J. Trans-effects in octahedral transition metal complexes. *Coord. Chem. Rev.* **2000**, *203*, 5-80.

(35) (a) Fagnou, K.; Lautens, M. Halide Effects in Transition Metal Catalysis. *Angew. Chem. Int. Ed.* **2002**, *41*, 26-47; Der Einfluss von Halogenidionen in der Übergangsmetallkatalyse. *Angew. Chem.* **2002**, *114*, 26-49. (b) Lichtenberger, D. L.; Rai-Chaudhuri, A. R.; Seidel, M. J.; Gladysz, J. A.; Agbossou, S. K.; Igau, A.; Winter, C. H. Delocalized Electronic Interactions in Chiral Cyclopentadienylrhenium Halide

Complexes. Valence Photoelectron Spectra of CpRe(NO)(L)X (Cp = η^5 -C₅H₅, η^5 -C₅(CH₃)₅; L = CO, P(C₆H₅)₃; X = Cl, Br, I). *Organometallics* **1991**, *10*, 1355-1364.

(36) Zhu, J.; Lin, Z.; Marder, T. B. Trans Influence of Boryl Ligands and Comparison with C, Si, and Sn Ligands. *Inorg. Chem.* **2005**, *44*, 9384-9390.

(37) (a) Importantly, the *trans* isomers essentially lack dipole moments, and only solvent corrected gas phase optimized structures were computed. The *cis* isomers, with their much larger dipole moments, would be expected to further optimize their gas phase geometries in the more polar solvents (versus a much lesser extent with the *trans* isomers), resulting in additional stabilization (b) It is also worth noting that out of the equilibria in Figure 3.5 and Figure 3.6, the largest *cis/trans* energy differences in toluene (less polar) as compared to *o*-C₆H₄Cl₂ (more polar)¹³ are for the dichloride complexes **2c** and **2''** ($\Delta\Delta G = 4.4$ (7.9 vs. 3.5) and 5.3 (6.1 vs. 0.8) kcal mol⁻¹, respectively). This follows from the higher dipole moments of the *cis* dichloride complexes versus the other *cis* complexes.

(38) Given that *trans-3c* and *cis-3c* exhibit the second highest gas phase energy difference in Figure 3.5, we speculate that additional steric or electronic factors are in play.

(39) For a lead reference with many relevant citations, see Jones, E. V.; Chen, D.; Wright, S. W.; Trujillo, J. I.; France, S. Elucidation of a Sequential Iminium Ion Cascade Reaction Triggered by a Silica Gel-Promoted Aza-Peterson Reaction. *J. Org. Chem.* **2020**, *85*, 15660-15666.

(40) Appleton, T. G.; Clark, H. C.; Manzer, L. E. The trans-Influence: Its Measurement and Significance. *Coord. Chem. Rev.* **1973**, *10*, 335-422.

(41) (a) Mitoraj, M. P.; Zhu, H.; Michalak, A.; Ziegler, T. On the Origin of the Trans-Influence in Square Planar d^8 -Complexes: A Theoretical Study. *Int. J. Quantum Chem.* **2009**, *109*, 3379-3386. (b) Pinter, B.; Van Speybroeck, V.; Waroquier, M.; Geerlings, P.; De Proft, F. *trans* effect and *trans* influence: importance of metal mediated ligand-ligand repulsion. *Phys. Chem. Chem. Phys.* **2013**, *15*, 17354-17365. (c) Tsipis, A. C. *Trans-Philicity (trans-Influence/trans-Effect) Ladders for Square Planar Platinum(II) Complexes Constructed by ^{35}Cl NMR Probe.* *J. Comput. Chem.* **2019**, *40*, 2550-2562.

(42) See for example Table 5.7 of ref. [25](#).

(43) For crystal structures of five complexes of the formula $\text{cis-Pt}(\text{Me})_2(\text{PR}_2\text{R}')_2$ (R, R' = alkyl or aryl), see Haar, C. M.; Nolan, S. P.; Marshall, W. J.; Moloy, K. G.; Prock, A.; Giering, W. P. Synthetic, Structural, and Solution Thermochemical Studies in the Dimethylbis(phosphine)platinum(II) System. Dichotomy between Structural and Thermodynamic Trends. *Organometallics* **1999**, *18*, 474-479.

(44) Crystal structure of $\text{trans-Pt}(\text{Cl})(\text{Me})(\text{PMePh}_2)_2$: Bennett, M. A.; Chee, H.-K.; Robertson, G. B. Comparison of σ -Alkyl and σ -Perfluoroalkyl Groups as Ligands. 1. Crystal and Molecular Structures of the Methyl-, (Trifluoromethyl)-, and (Pentafluoroethyl)platinum(II) Complexes $\text{trans-PtClR}(\text{PMePh}_2)_2$ (R = CH_3 , CF_3 , C_2F_5). *Inorg. Chem.* **1979**, *18*, 1061-1070.

(45) Crystal structure of *trans*-Pt(Cl)(Me)(PPh₃)₂: Bardi, R.; Piazzesi, A. M. Crystal and Molecular Structure of Trans-(Methyl)chlorobis(triphenylphosphine)-platinum(II). *Inorg. Chim. Acta* **1981**, *47*, 249-254.

(46) Altus, K. M.; Bowes, E. G.; Beattie, D. D.; Love, J. A. Intermolecular Oxidative Addition of Aryl Halides to Platinum(II) Alkyl Complexes. *Organometallics* **2019**, *38*, 2273-2277.

(47) The ¹H and ¹³C NMR signals of the dibridgehead diphosphine ligands were assigned by analogy to those in ref. 4 (*trans* complexes) and ref. 8 (*cis* complexes), which were in turn established by 2D NMR experiments.

(48) This coupling represents a satellite (d, ¹⁹⁵Pt = 33.8%) and is not reflected in the peak multiplicity given.

(49) Hersh, W. H. False AA'X Spin-Spin Coupling Systems in ¹³C NMR: Examples Involving Phosphorus and a 20-Year-Old Mystery in Off-Resonance Decoupling. *J. Chem. Educ.* **1997**, *74*, 1485-1488. The *J* values represent the distance between adjacent peaks in the apparent triplet.

(50) Based upon integration, the yield of toluene-*d*₅ is about 33%.

(51) *APEX3*, Bruker AXS Inc. Madison, WI, USA, 2012.

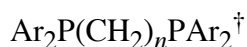
(52) Sheldrick, G. M. *SADABS*, Bruker AXS Inc. Madison, WI, USA, 2001.

(53) (a) Sheldrick, G. M. A short history of *SHELX*. *Acta Cryst.* **2008**, *A64*, 112-122. (b) Sheldrick, G. M. *SHELXT* – Integrated space-group and crystal-structure determination. *Acta Cryst.* **2015**, *A71*, 3-8.

(54) O Dolomanov, O. V.; Bourhis, L. J.; Gildea, R. J. Howard, J. A. K.; Puschmann, H. *OLEX2: A Complete Structure Solution, Refinement and Analysis Program. J. Appl. Crystallogr.* **2009**, *42*, 339-341.

(55) Spek, A. L. Single-crystal structure validation with the program *PLATON*. *J. Appl. Crystallogr.* **2003**, *36*, 7-13.

"4. TOWARD FRAMEWORKS WITH MULTIPLE ALIGNED AND INTERACTIVE
Fe(CO)₃ ROTATORS: SYNTHESSES AND STRUCTURES OF DIIRON
COMPLEXES LINKED BY TWO *trans*-DIAXIAL α,ω -DIPHOSPHINE LIGANDS



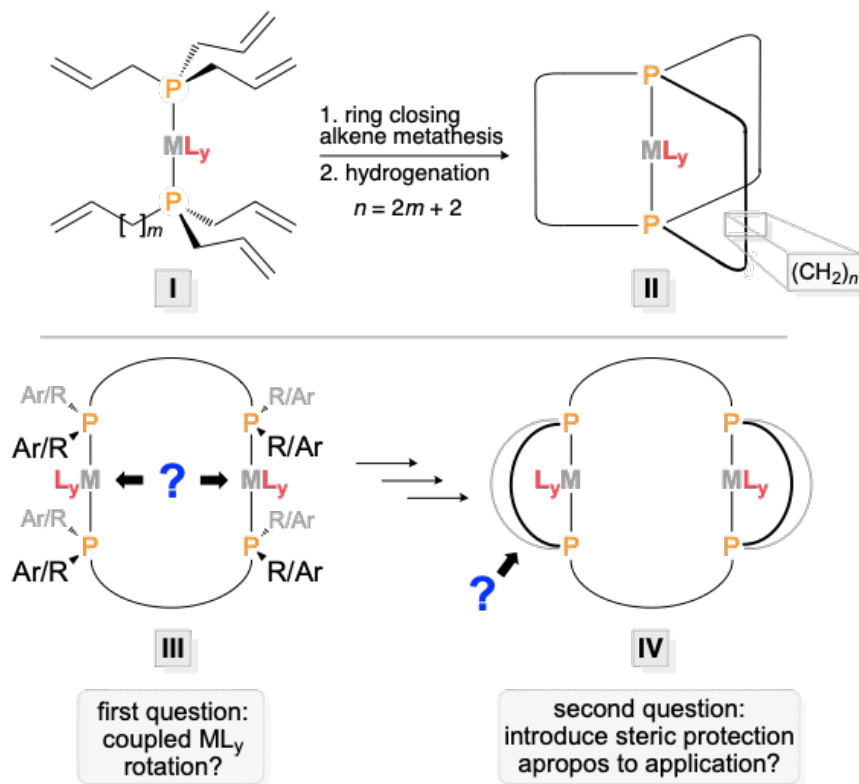
4.1. Introduction

There has been much recent interest in molecular rotors, a broad class of compounds that can be dissected into two components, rotators and stators.¹ In particular, assemblies with multiple rotators that are capable of coupled interactions hold promise for various types of molecular machines.²⁻⁴ Such phenomena have been most intensively studied in the context of sterically driven gearing.^{2,3} Purely electronic rotor/rotor interactions have also received attention.⁴

We have been engaged in the synthesis of what we term gyroscope like transition metal complexes.⁵⁻⁸ These are most commonly accessed as shown in Scheme 4.1 (top). Complexes with two *trans*-trialkylphosphine ligands of the formula P((CH₂)_mCH=CH₂)₃ (**I**) are first prepared. Then three-fold intramolecular ring closing alkene metatheses are carried out. Subsequent hydrogenations afford target complexes **II** with triply *trans*-spanning dibridgehead diphosphine ligands in surprisingly high overall

[†] Reprinted with permission from Zarcone, S. R.; Chu, G. M.; Ehnbohm, A.; Cardenal, A.; Fiedler, T.; Bhuvanesh, N.; Hall, M. B.; Gladysz, J. A. Toward Frameworks with Multiple Aligned and Interactive Fe(CO)₃ Rotators: Syntheses and Structures of Diiron Complexes Linked by Two *trans*-Diaxial α,ω -Diphosphine Ligands Ar₂P(CH₂)_nPAr₂. *Inorg. Chem.* **2021**, *60*, 3714-3330. Copyright 2021 American Chemical Society.

yields. Depending upon the sizes of the ligands on the metal (L_y) and the lengths of the $(CH_2)_n$ segments ($n = 2m + 2$), the ML_y moieties in **II** may (or may not) be able to rotate within the cage like diphosphine.⁵⁻⁸

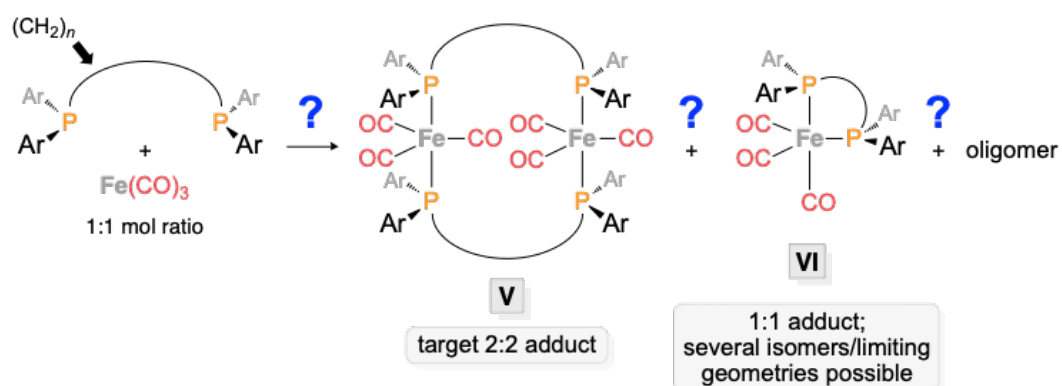


Scheme 4.1 Syntheses of gyroscope-like complexes (**II**) and new targets with two ML_y rotators with parallel axes (**III** and **IV**).

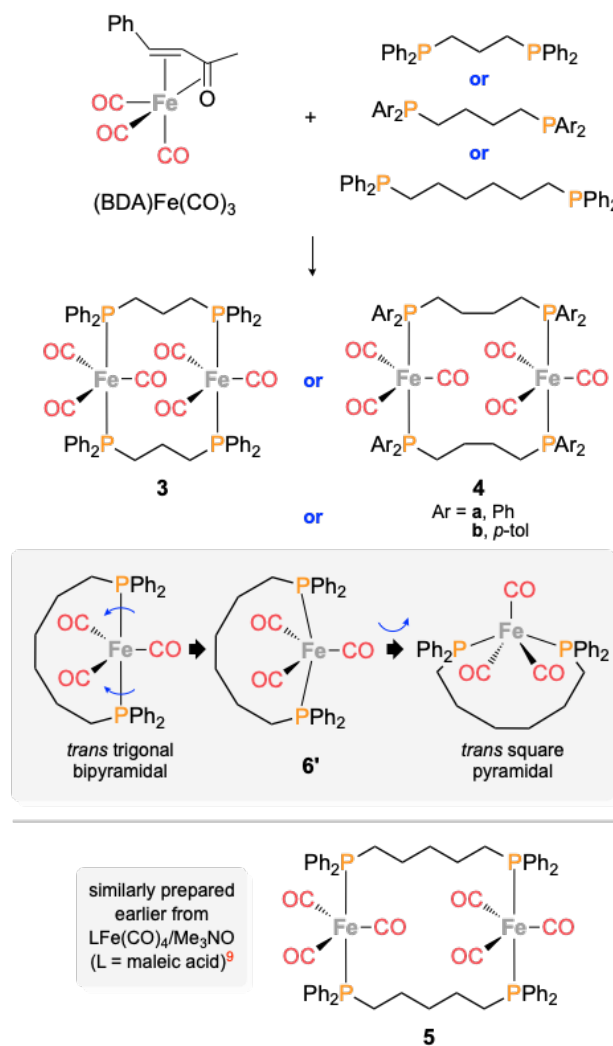
As sketched in Scheme 4.1 (bottom), we sought to extend this effort to related bimetallic complexes with sterically coupled ML_y rotators, both with (**IV**) and without (**III**) protective *trans*-spanning polyphosphine ligands. A significant portion of our results with **II** have involved trigonal bipyramidal iron complexes with the rotators $Fe(CO)_3$, $Fe(CO)_2(NO)^+$, and $Fe(CO)(NO)(X)$ ($X = Cl, Br, I, \text{ and } CN$).⁷ Hence, for

initial exploratory studies, a minimalist approach involving reactions of α,ω -diphosphines $\text{Ar}_2\text{P}(\text{CH}_2)_n\text{PAr}_2$ and $\text{Fe}(\text{CO})_3$ sources was selected, as outlined in Scheme 4.2. We were particularly interested in accessing diiron tetraphosphorus species **V** with $n = 3$ and 4. For these systems, molecular models suggested sterically interactive rotators. Indeed, as described below, this simple strategy does afford the target complexes.

During the later stages of this work, we became aware of a similar synthesis of species **V** with $n/\text{Ar} = 5/\text{Ph}$ by Liu and Gau.⁹ Furthermore, as shown in Scheme 4.2, reactions of diphosphines $\text{Ar}_2\text{P}(\text{CH}_2)_n\text{PAr}_2$ and $\text{Fe}(\text{CO})_3$ sources are also capable, in principle, of giving monoiron diphosphorus species such as **VI**, as well as oligomers or other adducts. Indeed, there are several previous reports of **VI** ($\text{Ar} = \text{Ph}$) with n ranging from 1 to 5.¹⁰⁻¹⁴ As outlined below, these can exhibit different limiting geometries,¹¹ and as a collateral result of this study, a rare type of isomer has been isolated in the case of $n = 6$. To provide additional support for the structural assignments made herein and in earlier reports,⁹⁻¹⁴ as well as a road map to guide future research, the IR $\nu_{\text{C}\equiv\text{O}}$ patterns are computed by DFT methods and compared to those found experimentally. These calculations furthermore yield free energies that show the equilibria $2\text{VI} \rightleftharpoons \text{V}$ to be exergonic.



Scheme 4.2 Some possible products derived from equimolar amounts of $\text{Fe}(\text{CO})_3$ sources and α,ω -diphosphines $\text{Ar}_2\text{P}(\text{CH}_2)_n\text{PAr}_2$ (**V** and **VI**).



Scheme 4.3 Syntheses of new diiron and monoiron complexes.

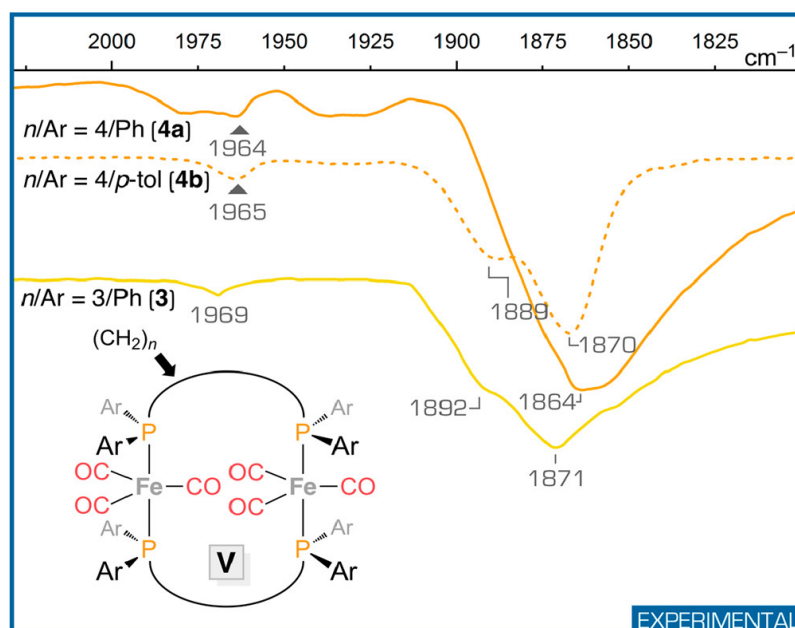


Figure 4.1 IR spectra (ATR/powder film, $\nu_{\text{C}\equiv\text{O}}$ region) of the new diiron complexes **V** with principal features highlighted.

4.2. Results

4.2.1. Syntheses of Title Complexes [major contribution: Mr. S. Zarcone, Dr. G. Zhu]

The η^4 -benzylideneacetone complex $(\text{BDA})\text{Fe}(\text{CO})_3$ ¹⁵ has seen extensive use as a functional equivalent of the $\text{Fe}(\text{CO})_3$ fragment.^{7a,15,16} The phenyl substituted α,ω -diphosphines $\text{Ph}_2\text{P}(\text{CH}_2)_n\text{PPh}_2$ ($n = 3, 4,$ and 6) were obtained from commercial sources, and the *p*-tolyl analog $(p\text{-tol})_2\text{P}(\text{CH}_2)_4\text{P}(p\text{-tol})_2$ was isolated in 47% yield from the reaction of the phosphido anion $(p\text{-tol})_2\text{P}^- \text{Li}^+$ and the corresponding α,ω -dibromide. This 1,4-diphosphine had been previously synthesized from $\text{Cl}_2\text{P}(\text{CH}_2)_4\text{PCl}_2$ and the Grignard reagent *p*-tolMgBr.¹⁷ Accordingly, $(\text{BDA})\text{Fe}(\text{CO})_3$ was treated with 1.2 equiv

of $\text{Ph}_2\text{P}(\text{CH}_2)_3\text{PPh}_2$ (1,3-bis(diphenylphosphino)propane) or $\text{Ph}_2\text{P}(\text{CH}_2)_4\text{PPh}_2$ (1,4-bis(diphenylphosphino)butane) in THF. After 48 h, the solvent was removed. As shown in Scheme 4.3, workups gave the target complexes *trans,trans*- $(\text{CO})_3\text{Fe}[\text{Ph}_2\text{P}(\text{CH}_2)_n\text{PPh}_2]_2\text{Fe}(\text{CO})_3$ [$n = 3$ (**3**) and 4 (**4a**)] as air-sensitive yellow or pale yellow solids in 44 and 19% yields, respectively. These and all other new complexes below were characterized by microanalyses, IR spectroscopy (ATR and powder film) and NMR spectroscopy (^1H , $^{13}\text{C}\{^1\text{H}\}$, and $^{31}\text{P}\{^1\text{H}\}$). The IR $\nu_{\text{C}\equiv\text{O}}$ bands are depicted in Figure 4.1 and summarized in Table 4.1. The remaining data are given in the Experimental section 4.5. Both **3** and **4a** were soluble in toluene, THF, and DMSO and insoluble in hexane. Although **3** was insoluble in CH_2Cl_2 , **4a** was soluble in both CH_2Cl_2 and CDCl_3 .

The spectroscopic properties of **3** and **4a** were consistent with the proposed structures. In particular, the IR spectra showed one strong $\nu_{\text{C}\equiv\text{O}}$ band (1871 or 1864 cm^{-1}), and a second much weaker band at higher frequency (1969 or 1964 cm^{-1}). As can be derived from group theory,¹⁸ this pattern is characteristic of axially disubstituted trigonal bipyramidal complexes of the formula *trans*- $\text{Fe}(\text{CO})_3\text{L}_2$. However, there are many literature reports (L = phosphine) in which the weaker band is missing or has possibly been overlooked.^{7a,16b} This includes the higher homolog derived from 1,5-bis(diphenylphosphino)pentane, *trans,trans*- $(\text{CO})_3\text{Fe}[\text{Ph}_2\text{P}(\text{CH}_2)_5\text{PPh}_2]_2\text{Fe}(\text{CO})_3$ (**5**; 1877 cm^{-1}),⁹ which is depicted in Scheme 4.3 (bottom; see the introduction section 4.1).¹⁹

Of course, the diiron complexes **3** and **4a** and the trigonal bipyramidal monoiron complexes *trans*-Fe(CO)₃L₂ have different molecular symmetries, and this will affect the vibrational spectra. Also, a shoulder was evident on the strong $\nu_{\text{C}\equiv\text{O}}$ band of **3** (1892 cm⁻¹; Figure 1). Thus, the IR $\nu_{\text{C}\equiv\text{O}}$ bands of all iron carbonyl complexes prepared or discussed in this paper have been computed using DFT, as summarized in Table 1 and described and analyzed below.

The NMR spectra also supported the structures of **3** and **4a**. With **3**, two CO ¹³C{¹H} signals could be observed (214.7 and 212.4 ppm, both apparent m), consistent with sterically restricted Fe(CO)₃ rotators. To our knowledge, all monoiron diphosphorus adducts **VI** (Scheme 4.2) examined to date afford a single CO signal at ambient probe temperatures. In the case of **4a**, only a very weak CO signal (214.0 ppm) could be tentatively assigned. The ³¹P{¹H} NMR chemical shifts of **3** and **4a** (75.12 and 73.96 ppm in DMSO-*d*₆) were also quite close to that of the analogous Ph₂P(CH₂)₅PPh₂ adduct **5** (75.53 ppm in CDCl₃).⁹ The signal of the corresponding monoiron adduct *cis*-(CO)₃Fe[$\overline{\text{Ph}_2\text{P}(\text{CH}_2)_5\text{PPh}_2}$] (**5'**)²⁰ is much further upfield (55.46 ppm).

The preceding reactions were extended in two ways. First, with the idea of procuring more soluble complexes with additional NMR "handles", (BDA)Fe(CO)₃ was similarly combined with the *p*-tolyl substituted diphosphine (*p*-tol)₂P(CH₂)₄P(*p*-tol)₂ (0.8 equiv; Scheme 4.3). Workup gave the target complex *trans,trans*-(CO)₃Fe[(*p*-tol)₂P(CH₂)₄P(*p*-tol)₂]₂Fe(CO)₃ (**4b**) in 56% yield, which was soluble in the same solvents as **4a** and partially soluble in hexane. The IR spectrum showed two main $\nu_{\text{C}\equiv\text{O}}$

bands analogous to those of **3** and **4a** (1870 s and 1965 w cm^{-1}), and a shoulder as noted with **3** (1889 cm^{-1} ; Figure 4.1 and Table 4.1). A high-resolution mass spectrum (ESI) gave an envelope of intense ions with the masses and isotope distribution expected for **4b** + H. The $^{13}\text{C}\{^1\text{H}\}$ NMR spectrum also showed a single CO signal that was coupled to phosphorus (220.7 ppm, t, $J_{\text{CP}} = 8.7$ Hz), consistent with rapid $\text{Fe}(\text{CO})_3$ rotation on the NMR time scale. Although ^1H NMR spectra suggested a purity of ca. 90%, a crystalline sample was easily obtained as described below.

Second, $(\text{BDA})\text{Fe}(\text{CO})_3$ was similarly combined with the hexamethylene diphosphine $\text{Ph}_2\text{P}(\text{CH}_2)_6\text{PPh}_2$ (1.2 equiv) in THF (Scheme 4.3). A chromatographic workup of the red solution gave a yellow solid (31%) that was initially thought to be the diiron complex *trans,trans*- $(\text{CO})_3\text{Fe}[\text{Ph}_2\text{P}(\text{CH}_2)_6\text{PPh}_2]_2\text{Fe}(\text{CO})_3$ (**6**). However, a high-resolution mass spectrum (ESI) suggested a monoiron diphosphorus species. The IR spectrum showed a strong $\nu_{\text{C}\equiv\text{O}}$ band at 1863 cm^{-1} and a second weak one at 1965 cm^{-1} . Also, the $^{13}\text{C}\{^1\text{H}\}$ NMR spectrum exhibited two CO signals (ca. 2:1). These data were best reconciled with the structural assignment *trans*- $(\text{CO})_3\text{Fe}[\overline{\text{Ph}_2\text{P}(\text{CH}_2)_6\text{PPh}_2}]$ (**6'**),²⁰ as further supported in the following section.

Table 4.1 Experimental and computed IR $\nu_{\text{C}\equiv\text{O}}$ bands for monoiron (**1'**-**6'**) and diiron (**3**, **4a,b**, **5**, and **6**) complexes.

complex	<i>n</i>	geometry ^a	$\nu_{\text{C}\equiv\text{O}}$ (cm ⁻¹) experimental	medium	$\nu_{\text{C}\equiv\text{O}}$ (cm ⁻¹) computed ^b
1' ^c	1	sq pyr <i>cis</i> ^d	1984 s, 1911 m, 1901 s	CH ₂ Cl ₂	1968 s, 1915 s, 1911 s
2' ^e	2	sq pyr <i>cis</i> ^d	1982 s, 1913 m, 1892 s	CH ₂ Cl ₂	1970 s, 1919 m, 1901 s
3' ^f	3	tbp <i>cis</i>	1982 s, 1909 m, 1881 s	CH ₂ Cl ₂	1969 s, 1910 m, 1890 s
4'a ^g	4	tbp <i>cis</i>	1981 s, 1908 m, 1879 s	CH ₂ Cl ₂	1966 s, 1907 m, 1882 s
4'b ^h	4	tbp <i>cis</i>	—	—	1964 s, 1904 m, 1880 s
5' ⁱ	5	tbp <i>cis</i>	1983 s, 1912 s, 1883 s	CH ₂ Cl ₂	1964 s, 1906 m, 1882 s
6' ^j	6	sq pyr <i>trans</i>	1965 w, 1863 s	powder film	1941 w ^k , 1892 m, 1865 s
3 ^j	3	tbp <i>trans</i>	1969 w, 1892 sh, 1871 s	powder film	1939 w ^k , 1889 sh, 1876 s
4a ^j	4	tbp <i>trans</i>	1964 w, 1864 s	powder film	1933 w ^k , 1871 sh, 1867 s
4b ^j	4	tbp <i>trans</i>	1965 w, 1889 sh, 1870 s	powder film	1930 w ^k , 1871 sh, 1862 s
5 ⁱ	5	tbp <i>trans</i>	1877 s	CH ₂ Cl ₂	1935 w ^k , 1873 sh, 1865 s
6 ^h	6	tbp <i>trans</i>	—	—	1960 w ^k , 1897 s, 1893 s

^a These correspond to the crystal structures for **1'**-**3'**, **5'**, **6'**, **3**, **4a,b**, and **5** and are replicated by the computed structures in all cases. ^b Determined by DFT as described in the text. ^c The experimental values are from ref **14b**; similar data have been reported in refs **14a** (1989 s, 1919 ms, 1909 s; CHCl₃) and **14c** (1989, 1913, 1907; THF, no intensity information). ^d These complexes exhibit intermediate sq pyr/tbp geometries but are considered predominantly sq pyr; see refs **10-12**. ^e The experimental values are from ref **14b**; similar data have been reported in ref **14c** (1984, 1914, 1888; THF, no intensity information). ^f The experimental values are from ref **14b**; similar data have been reported in refs **13** (1983 s, 1908 ms, 1882 s; CH₂Cl₂/0.1 M Bu₄NPF₆), **14c** (1984, 1914, 1888; THF, no intensity information), and **14d** (1986 s, 1914 ms, 1984 vs; CH₂Cl₂ or 1980 s, 1908 s, 1885 vs; Nujol). ^g The experimental values are from ref **14b**; similar data have been reported in ref **14c** (1983, 1912, 1886; THF, no intensity information). This complex has not yet been crystallographically characterized. ^h This complex has not yet been synthesized. ⁱ The experimental values are from ref **9**. ^j This work. ^k These absorptions are predicted to be very weak or undetectable.

The isolation of **6'** prompted us to check whether related monoiron species (**3'**, **4'a**, and **4'b**) might have been generated under the conditions used to access **3** and **4a,b**. As further detailed in the Experimental section 4.5, species with plausible $^{31}\text{P}\{^1\text{H}\}$ NMR chemical shifts for such adducts were sometimes observed in the crude reaction mixtures but were removed upon the prescribed workup. When concentrations were varied, these sometimes became the major products.

4.2.2. Structural Data [major contribution: Mr. A. Ehnbom, Mr. S. Zarcone]

Crystals of solvates of **3**, **4a**, **4b**, and **6'** could be grown, and the X-ray structures were determined as outlined in Table 4.2 and the Experimental section 4.5. Thermal ellipsoid plots are depicted in Figure 4.2 and Figure 4.3. Key metrical parameters are listed in Table 4.3 and Table 4.4. The latter emphasizes features relevant to nonbonded interactions in the diiron complexes, and includes the previously published structure for **59** and DFT results for **6** described below. These two structures are depicted in Figure 4.4. For all complexes, the atoms have been renumbered from those in the CCDC files to achieve a uniform pattern that facilitates data comparison.

Table 4.2 General crystallographic data.

crystallographic parameters	3 ·(CH ₂ Cl ₂) ₄	4a ·(toluene) ₆	4b ^a	6' ·(toluene) _{0.5}
empirical formula	C ₆₄ H ₆₀ Cl ₈ Fe ₂ O ₆ P ₄	C ₁₀₄ H ₁₀₄ Fe ₂ O ₆ P ₄	C ₇₀ H ₇₂ Fe ₂ O ₆ P ₄	C _{36.5} H ₃₆ FeO ₃ P ₂
formula weight	1444.30	1685.45	1244.86	640.44
temperature [K]	110(2)	110(2)	110(2)	120(2)
diffractometer	Bruker GADDS	Bruker GADDS	Bruker QUEST	Bruker QUEST
wavelength [Å]	1.5418	1.5418	0.71073	0.71073
crystal system	triclinic	triclinic	monoclinic	monoclinic
space group	<i>P</i> -1	<i>P</i> -1	<i>P</i> 2 ₁ / <i>c</i>	<i>P</i> 2 ₁ / <i>n</i>
<i>unit cell dimensions:</i>				
<i>a</i> [Å]	12.5070(5)	11.2478(5)	12.2470(16)	10.1433(5)
<i>b</i> [Å]	12.5333(5)	15.2495(6)	15.299(2)	29.2030(14)
<i>c</i> [Å]	22.0792(8)	26.8362(12)	22.763(3)	10.7720(5)
α [°]	88.807(3)	106.296(3)	90	90
β [°]	73.868(2)	99.572(3)	94.774(2)	92.699(10)
γ [°]	77.784(2)	94.533(3)	90	90
<i>V</i> [Å ³]	3246.8(2)	3246.8(2)	4250.2(10)	3187.3(3)
<i>Z</i>	4	2	2	4
ρ_{calc} [Mg m ⁻³]	1.477	1.296	0.973	1.335
μ [mm ⁻¹]	7.950	3.833	0.455	0.609
<i>F</i> (000)	1480	1776	1304	1340
crystal size [mm ³]	0.11 × 0.07 × 0.04	0.05 × 0.04 × 0.02	0.10 × 0.08 × 0.05	0.20 × 0.18 × 0.11
Θ limit [°]	2.08 to 60.00	1.749 to 60.968	2.261 to 22.545	2.790 to 28.428
index range (<i>h</i> , <i>k</i> , <i>l</i>)	-13, 14; -4, 14; -24, 24	-12, 12; -17, 17; -30, 30	-13, 13; -16, 16; -24, 24	-13, 13; -39, 38; -14, 14
reflections collected	76986	92070	60697	43668
independent reflections	9463	12925	5547	7998
<i>R</i> (int)	0.0701	0.0701	0.0488	0.0372
max./min. transmission	0.7416/0.4751	0.7227/0.5462	0.4267/0.3776	0.4311/0.3852
data/restraints/parameters	9463/3/765	12925/346/976	5547/0/374	7998/456/481
goodness-of-fit on <i>F</i> ²	1.031	1.106	1.074	1.120
<i>R</i> indices (final) [<i>I</i> > 2 σ (<i>I</i>)]				
<i>R</i> ₁	0.0606	0.0945	0.0998	0.0331
w <i>R</i> ₁	0.1508	0.1772	0.2644	0.0674
<i>R</i> indices (all data)				
<i>R</i> ₂	0.0691	0.1262	0.1055	0.0470
w <i>R</i> ₂	0.1563	0.1937	0.2683	0.0766
largest diff. peak and hole [e Å ⁻³]	1.881 and -1.073	0.707 and -0.675	1.025 and -0.661	0.397 and -0.342

^a The crystal contained disordered solvent molecules, which were treated as described in the Experimental section 4.5. As a result, the density is underestimated.

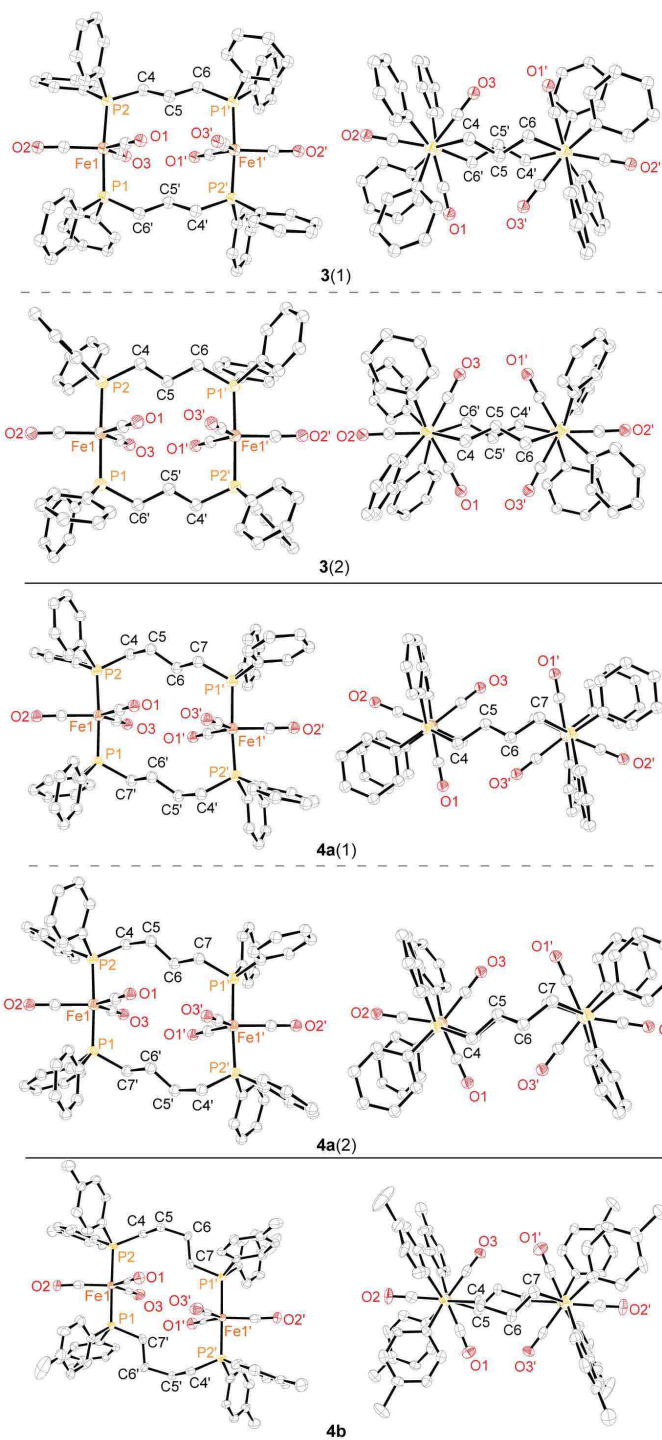


Figure 4.2 Thermal ellipsoid plots (50% probability) of the molecular structures of **3** (two independent molecules (**1** and **2**)), **4a** (two independent molecules (**1** and **2**)), and **4b**. Solvent molecules in the lattices have been omitted.

For both **3** and **4a**, two independent molecules were found in the unit cell, each with an inversion center. These are denoted as **3**(1), **3**(2), **4a**(1), and **4a**(2) in the graphics and tables. The structure of **4b** also exhibits an inversion center, and **5** features a C_2 axis that is perpendicular to the Fe_2P_4 plane. The radii of the $Fe(CO)_3$ rotators fall into a narrow range centered at 4.45 Å (Table 4.4), as computed by taking the average iron–oxygen distance and adding the van der Waals radius of an oxygen atom (1.52 Å).²¹ Unsurprisingly, these closely agree with values found earlier.^{7a}

Measures of the relationships between the two P–Fe–P axes of the diiron complexes were sought. Three nearly collinear points, each with independent experimental error, do not very accurately define a plane. Thus, least-squares planes derived from each P–Fe–P axis and the distal iron atom were calculated (P–Fe–P/Fe'). As summarized in Table 4.4, the complexes with inversion centers (**3** and **4a,b**) gave plane/plane angles of 0°, indicating rigorously parallel axes. The others (**5** and **6**) gave plane/plane angles of 7.6–12.0°. The relationships between the axes are also reflected by the four P–Fe–Fe'–P torsion angles, which as noted in Table 4.4 are always close to 0° or ±180°.

Measures of the relationships between the planes of the rotators were also sought. For this purpose, the four-atom least-squares $Fe(C)_3$ planes were used (as opposed to the seven-atom $Fe(CO)_3$ planes). The inversion centers in **3** and **4a,b** render the two $Fe(C)_3$ planes as parallel, so it is a simple matter to measure the offsets. In both independent molecules of **3**, the two planes are nearly coplanar (miniscule offsets of 0.087 and 0.029 Å). In the two independent molecules of **4a**, the separations increase significantly and

are more highly differentiated (0.985 and 1.217 Å). In **4b**, the offset further increases (1.677 Å). These relationships are illustrated in Figure 4.5.

In **5** and **6**, the Fe(C)₃ planes are no longer parallel; therefore, the rotators do not have a uniform separation. We have not been able to devise a meaningful geometric parameter that quantifies the offset. However, as can be "eyeballed" in Figure 4.5, the rotators are more closely spaced than those in **4a,b**. The situation with the two P–Fe–P axes is similar, for as noted above these are rigorously parallel for **3** and **4a,b** but not **5** and **6**. Accordingly, fixed distances can be assigned with the former group but not the latter.

As illustrated in Figure 4.5, the iron–iron distances in **3** are 5.894(9)-5.782(1) Å (independent molecules 1 and 2), whereas those in **4a,b** (6.466(1)-6.403(1) Å), **5** (7.601(3) Å), and **6** (8.517 Å) are progressively longer, reflecting the increasing (CH₂)_n tether lengths. However, it should be emphasized that due to the offset of the Fe(C)₃ planes, the distances between the P–Fe–P axes are shorter. For complexes **3** and **4a,b** where this can be quantified, the trend is not monotonic. Rather, **3** (*n* = 3) and **4b** (*n* = 4) give essentially identical values (≈5.8 Å). All of these factors bear on the potential for Fe(CO)₃/Fe(CO)₃ interactions, which are further analyzed in the Discussion section 4.3.

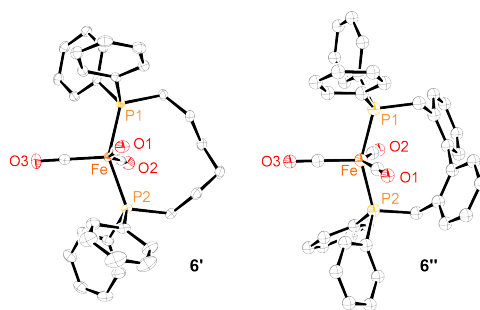


Figure 4.3 Thermal ellipsoid plots (50% probability) of the molecular structure of **6'** (left) and a relevant complex from the literature, **6''** (right; see the Discussion section 4.3). Solvent molecules in the lattices have been omitted.

The IR spectrum of crystalline monoiron complex **6'** was identical with that isolated from Scheme 4.3. The P–Fe–P bond angle, $147.4(2)^\circ$ (Table 4.3 and Figure 4.3), represents a dramatic reduction from the 180° expected for an idealized trigonal bipyramid with *trans*-diaxial phosphine ligands, and the values found for **3** and **4a,b** ($172.8(1)$ - $178.4(1)^\circ$). Thus, **6'** is best regarded as *trans* square pyramidal, with the carbonyl ligand that extends to the left in Figure 4.3 representing the apical position. These relationships are sketched in Scheme 4.3. Accordingly, the OC–Fe–CO bond angles are no longer ca. 120° as in the other complexes, but rather $151.8(1)^\circ$ (for the two basal CO ligands) or $104.7(1)$ - $103.5(1)^\circ$ (for the apical CO ligand). The same conclusions are reached using other geometric features.¹¹

In **6'**, the iron–carbon distances for the two CH₂ carbon atoms closest to the plane of the Fe(CO)₃ rotator (see Figure 4.3) are 3.939 and 4.518 Å. When the van der Waals radius of an *sp*³ carbon atom²¹ is subtracted, "clearances" of 2.24-2.82 Å are obtained. Since these values are well within the radius of the Fe(CO)₃ rotator (4.45 Å), a 360° rotation should be impossible (although oscillations of a few degrees may take place).

4.2.3. DFT Computations [major contribution: Mr. A. Ehnbohm]

Given the established relationship between IR $\nu_{\text{C}\equiv\text{O}}$ band patterns and structure,¹⁸ and the various ways in which experimental data might be misleading (impurities, mixtures of isomers, crystal versus solution structures, etc.), DFT was utilized to calculate the absorptions for all of the preceding diiron and monoiron complexes. Techniques and functionals that have proved reliable in past studies were employed,^{13,22} as detailed further in the Experimental section 4.5 and Appendix B. In all cases, initial energy minimizations afforded structures very close to those obtained crystallographically, as illustrated in Appendix B; Figure 12.5 and Figure 12.6. The IR results are summarized in Table 4.1 and Figure 4.6. The IR spectrum of **3'** has been similarly computed in an earlier study.¹³

As shown in Figure 4.6 (bottom), the title complexes **3**, **4a,b**, **5**,⁹ and **6** (only characterized computationally given the isolation of **6'**) are predicted to exhibit three vibrational modes (**a-c**), each with the $\text{Fe}(\text{CO})_3$ units strongly coupled. The lowest frequency band (corresponding to **c**) is always the most intense, and shifts randomly within a 26 cm^{-1} range as n increases from 3 to 6 ($1876, 1867/1862, 1865, 1893\text{ cm}^{-1}$).

These bands are furthermore predicted to exhibit shoulders at slightly higher frequencies ($4\text{-}13\text{ cm}^{-1}$, corresponding to **b**). However, in computations the peaks can be narrowed or broadened per the line width selected, as illustrated in Figure 4.6 (compare the inset with 8 cm^{-1} line widths to the other spectra with 4 cm^{-1} line widths). Thus, these shoulders may or may not be visible experimentally (they are seen for **3** and **4b**).

There is no dipole moment change associated with the third highest frequency vibrational mode (**a**). Hence, these are formally IR-inactive. Nonetheless, weak absorptions are observed experimentally for **3** and **4a,b** (1964-1969 cm^{-1}).

Next, we focus on the spectra of monoiron complexes **3'**, **4'a**, **5'**, and **6'** depicted in Figure 4.6 (top). These feature different coordination geometries as summarized in Table 4.1 and represented in Figure 4.6 as **VI'** (tbp *cis*), **VI''** (sq pyr *cis*), and **VI'''** (sq pyr *trans*). Complex **6'**, new to this study and possessing the rare geometry **VI'''**, is predicted to exhibit three IR $\nu_{\text{C}\equiv\text{O}}$ bands. However, the two lowest frequency bands (1865 s, 1892 m cm^{-1}) apparently merge into a single band experimentally (1863 cm^{-1}). In any case, the weak highest frequency band is reproduced (1941 vs. 1965 cm^{-1}),

The IR $\nu_{\text{C}\equiv\text{O}}$ bands computed for the remaining monoiron complexes are in excellent agreement with those found experimentally. Furthermore, coordination modes **VI'** and **VI''** give quite similar patterns, with three bands of strong to medium intensities. However, the most important conclusion is that an impurity of this type should be apparent in the IR spectrum of a diiron complex. For example, the highest frequency bands are intense in the monoiron complexes (1984-1981 cm^{-1}) but very weak in the diiron complexes (1969-1965 cm^{-1}).

Table 4.3 Key interatomic distances (Å) and bond angles (°) for crystallographically characterized complexes.

	3 ·(CH ₂ Cl ₂) ₄ ^{a,b}	4a ·(toluene) ₆ ^{a,b}	4b ^{a,c}	6 ·(toluene) _{0.5}
Fe1–P1	2.211(1)/2.200(1)	2.213(2)/2.214(2)	2.209(2)	2.214(1)
Fe1–P2	2.211(2)/2.212(1)	2.209(2)/2.207(2)	2.208(2)	2.217(1)
Fe1–C1	1.772(5)/1.778(6)	1.781(8)/1.760(8)	1.784(9)	1.769(2)
Fe1–C2	1.773(4)/1.763(6)	1.752(8)/1.781(7)	1.765(9)	1.775(2)
Fe1–C3	1.776(4)/1.774(4)	1.767(7)/1.765(6)	1.784(9)	1.769(2)
C1–O1	1.160(6)/1.148(7)	1.156(8)/1.170(9)	1.195(1)	1.155(2)
C2–O2	1.160(5)/1.164(7)	1.166(8)/1.163(8)	1.162(1)	1.156(2)
C3–O3	1.157(5)/1.157(5)	1.163(7)/1.162(7)	1.144(1)	1.152(2)
Fe1–O1	2.931(4)/2.926(4)	2.938(6)/2.930(5)	2.928(6)	2.933(1)
Fe1–O2	2.933(3)/2.926(5)	2.919(6)/2.944(5)	2.926(7)	2.931(1)
Fe1–O3	2.933(3)/2.931(3)	2.931(4)/2.927(4)	2.933(6)	2.921(1)
C1–Fe1–C2	115.7(2)/118.7(2)	122.3(3)/122.0(3)	122.2(4)	151.8(1)
C1–Fe1–C3	125.0(2)/122.1(2)	118.3(3)/117.7(3)	120.1(4)	103.5(1)
C2–Fe1–C3	119.3(2)/119.2(2)	119.4(3)/120.3(3)	117.7(4)	104.7(1)
P1–Fe1–P2	174.6(1)/178.4(1)	172.8(1)/174.3(1)	176.8(1)	147.4(2)

^a The diiron complexes feature inversion centers that exchange primed and unprimed atoms (see Figure 4.2). ^b Values are given for each of the two independent molecules (1,2) in the unit cell. ^c See Experimental section 4.5 for information on solvent in the lattice.

Table 4.4 Additional structural features of crystallographically or computationally characterized diiron complexes.^a

complex (method)	3 ·(CH ₂ Cl ₂) ₄ ^{a,b}	4a ·(toluene) ₆ ^{a,b}	4b ^{a,c}	6' ·(toluene) _{0.5}	3 ·(CH ₂ Cl ₂) ₄ ^{a,b}
radius Fe(CO) ₃ rotator ^f	4.45/4.45	4.45/4.45	4.45	4.45	4.47
Fe1···Fe1' ^g	5.894(9)/5.782(1)	6.403(1)/6.466(1)	6.151(2)	7.601(3)	8.517
P1···P2 ^g	4.417(2)/4.412(2)	4.414(2)/4.416(2)	4.415(3)	4.422(3)	4.455
P1···P2' ^g	5.703(1)/5.722(2)	6.597(2)/6.599(2)	6.128(3)	7.539(4)	8.452
O1···O3' ^g	3.308(5)/3.007(5)	3.677(8)/3.610(7)	3.432(1)	6.723(1) ^h	5.531
O3···O3' ^g	5.284(5)/5.954(5)	4.546(7)/5.285(7)	6.531(9)	6.913(1) ^h	7.738
P1–Fe1–P2/Fe1' vs. P1'–Fe1'–P2'/Fe1' ⁱ	0.00/0.00	0.00/0.00	0.00	7.67	12.00
P2–Fe1–Fe1'–P1' ^j	2.1/–0.2	5.3/4.7	–3.3	–7.7	–10.8
P2–Fe1–Fe1'–P2' ^j	180.0/–180.0	–180.0/180.0	180.0	171.0	167.8
P1–Fe1–Fe1'–P2' ^j	–2.1/0.2	–5.3/–4.7	3.3	–7.7	–13.3
P1'–Fe1'–Fe1–P1' ^j	–180.0/180.0	–180.0/180.0	–180.0	173.7	168.2
Fe1–P2–C4–C5 ^j	57.4/–42.3	–70.3/–70.0	80.1	60.3	63.4/68.6
P2–C4–C5–C6 ^j	–177.6/166.3	111.9/104.8	–136.2	173.9	159.2/–169.7
C4–C5–C6–C7 ^j	—	178.3/–179.7	74.1	66.3	65.2/67.5
C5–C6–C7–C8 ^j	—	—	—	164.5	76.0/170.5
C6–C7–C8–C9 ^j	—	—	—	—	63.2/–63.0
C _{ω-2} –C _{ω-1} –C _ω –P1' ^{j,k}	162.8/–175.3	–174.6/–167.1	163.1	–174.9	155.31/–137.2
C _{ω-1} –C _ω –P1'–Fe1' ^{j,l}	–46.2/50.9	–70.5/–71.6	–175.1	54.5	64.42/74.05
P1–Fe1–P2 / P1'–Fe1'–P2' axis/axis distance ^m	5.884/5.780	6.166/6.400	5.853	— ⁿ	— ⁿ
offset of rotators Fe1(C) ₃ / Fe1'(C') ₃ ^m	0.087/0.029	0.980/1.209	1.665	— ⁿ	— ⁿ

^a Quantities not available from the crystallographic output were calculated using standard programs such as Mercury. ^b These complexes feature inversion centers that exchange primed and unprimed atoms (see Figure 4.2). ^c Values are given for each of the two independent molecules (1, 2) in the unit cell. ^d See the Experimental section 4.5 for information on solvent in the lattice. ^e From ref 9. ^f Calculated by averaging the Fe–O distances and adding the van der Waals radius of oxygen (1.52 Å). ^g Nonbonded distance (Å). ^h

These values are for O1···O1' and O3···O1', respectively (the crystallographic C₂ symmetry of this compound necessitates minor changes in atom numbering). ⁱ Angle between two four-atom least-squares planes (°). ^j Torsion angle (°). ^k This torsion angle is the counterpart to P2–C4–C5–C6; ω = 6, 7, 7, 8, and 9 for the respective entries. ^l This torsion angle is the counterpart to Fe1–P2–C4–C5; ω = 6, 7, 7, 8, and 9 for the respective entries. ^m Due to the inversion centers in **3**·(CH₂Cl₂)₄, **4a**·(toluene)₆, and **4b**, the two axes or planes are parallel with a constant intervening distance (Å). ⁿ Due to the absence of inversion centers in **5** and **6**, the P–Fe–P axes and Fe(C)₃ planes are not parallel, and unique separations cannot be assigned. Figure 4.5 allows visual estimates.

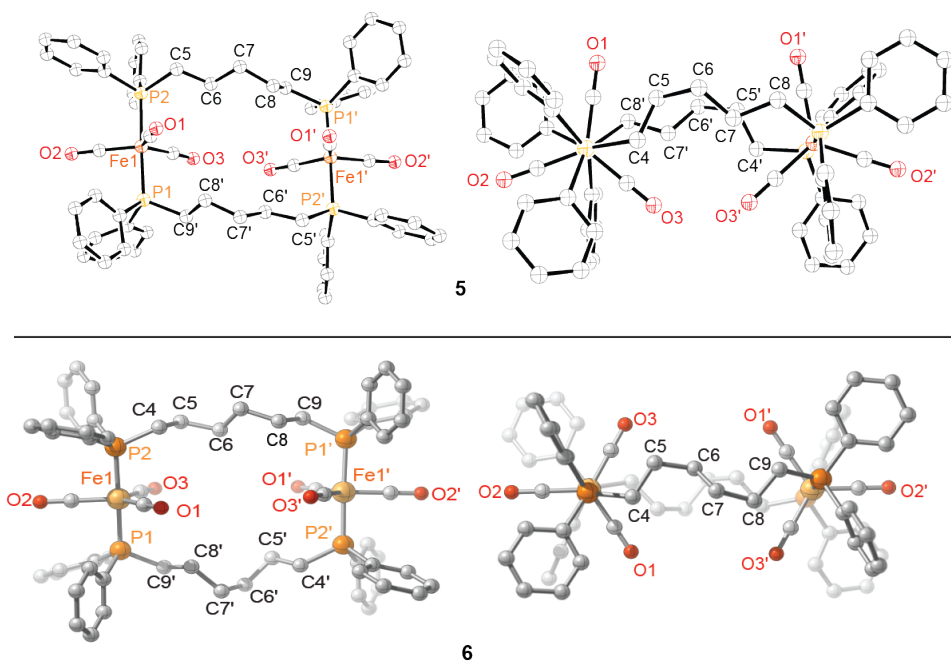


Figure 4.4 Thermal ellipsoid plots (50% probability) of the previously reported molecular structure of **5** (top)⁹ and a plot of the computed structure for the yet unknown higher homolog **6** (bottom). The primed atoms in the latter (employed for uniformity with the other structures) are misleading, as there are no symmetry elements.

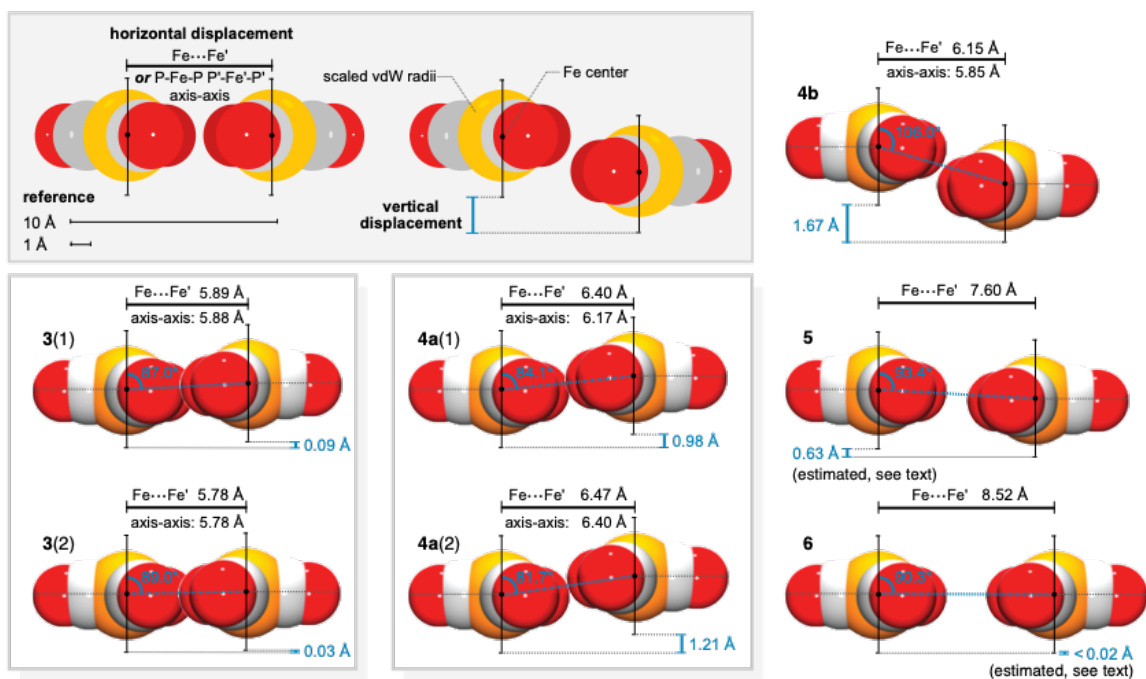


Figure 4.5 Space-filling side views of the $\text{Fe}(\text{CO})_3$ rotators in **3** (two independent molecules (1 and 2)), **4a** (two independent molecules (1 and 2)), and **4b**, **5**, and **6** (computed structure) illustrating the offset between the two $\text{Fe}(\text{CO})_3$ planes and iron–iron and (when constant) P–Fe–P axis–axis distances.

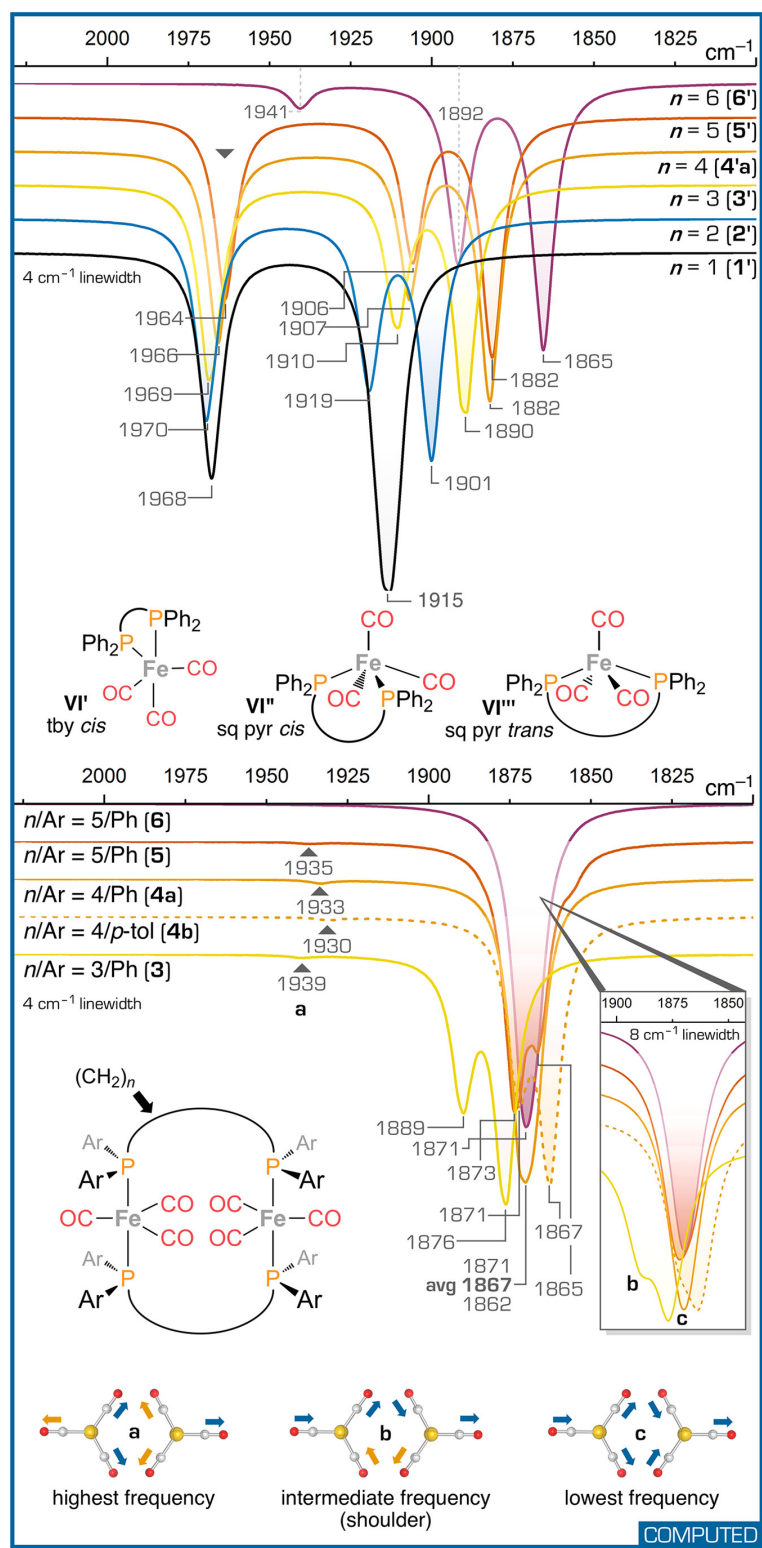


Figure 4.6 Computed IR $\nu_{\text{C}\equiv\text{O}}$ bands for monoiron and diiron carbonyl complexes.

In the course of computing the IR spectra, total energies corresponding to the most stable form of each iron complex were obtained (both gas and solution phase). These allow the free energies for the monoiron/diiron complex equilibria shown in Scheme 4.4 to be calculated. Interestingly, the diiron complexes are always the more stable, at least for the range of n examined.

4.3. Discussion

4.3.1. Syntheses [major contribution: Mr. S. Zarcone, Dr. G. Zhu]

The preceding results, together with literature data, indicate that the $\text{Fe}(\text{CO})_3$ source and conditions associated with Scheme 4.2 have a profound influence upon the type of product obtained. In our first cycle of experiments with the diphosphines $\text{Ar}_2\text{P}(\text{CH}_2)_n\text{PAr}_2$, only the target diiron tetraphosphorus complexes (**V**) were detected. However, as these reactions were investigated by additional co-workers, with the usual minor variances in conditions, it became apparent that monoiron diphosphorus complexes **VI** could also form. From a different direction, several other groups have reported reactions of $\text{Fe}(\text{CO})_3$ sources and the diphosphine $\text{Ph}_2\text{P}(\text{CH}_2)_3\text{PPh}_2$.^{13,14b-d} In contrast to our results, only the monoiron complex **3'** was isolated.

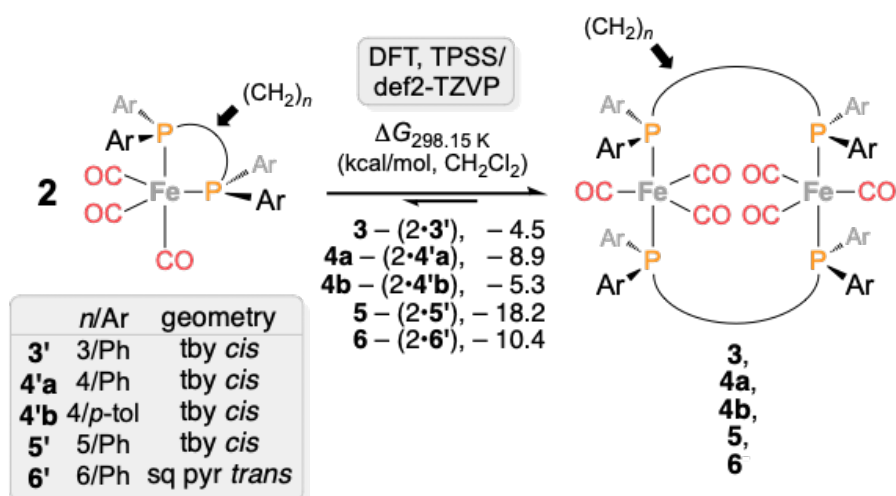
So far, only Liu and Goh, in their studies with $\text{Ph}_2\text{P}(\text{CH}_2)_5\text{PPh}_2$, have been able to optimize conditions for either type of product.⁹ In refluxing THF, the maleic acid (MA) adduct $(\text{MA})\text{Fe}(\text{CO})_4$ and the amine oxide $\text{Me}_3\text{N}^+\text{O}^-$ afford the diiron complex **5** in 45% yield, as depicted in Scheme 4.3 (bottom). In contrast, the cyclooctene (COE) adduct $(\text{COE})_2\text{Fe}(\text{CO})_3$ gives the monoiron product **5'** in 93% yield ($-60\text{ }^\circ\text{C}$ to RT,

THF). There is presently no rationale for this dichotomy. The higher temperature reaction affords the more stable product, **5**, according to the computational data in Scheme 4.4. However, **5'** is recovered unchanged after two days when subjected to these conditions.⁹

4.3.2. Steric Interactions Diiron Complexes [major contribution: Mr. A. Ehnbom, Mr. S. Zarcone]

With regard to the main objectives of this study, the most important structural features are those that affect correlated $\text{Fe}(\text{CO})_3/\text{Fe}(\text{CO})_3$ rotation or gearing. Thus, it is encouraging to see parallel or nearly parallel P–Fe–P axes maintained throughout the series **3**, **4a,b**, **5**, and **6** in Figure 4.2 and Figure 4.4. However, as the lengths of the $(\text{CH}_2)_n$ tethers increase, potential structural motifs multiply.

For example, conformations with nonparallel axes or twisted endgroups are likely to become increasingly accessible. Alternatively, the planes of the $\text{Fe}(\text{CO})_3$ rotators can become increasingly offset, such that they no longer efficiently engage. In this study, the maximum separation is found with **4b** (1.67 Å; Table 4.4 and Figure 4.5), which is comparable to the van der Waals radii of carbon and oxygen atoms (1.70 Å, 1.52 Å). When the offset reaches the van der Waals *diameters* of the CO ligands, the two rotators can no longer sterically engage.



Scheme 4.4 Computed ΔG values for the hypothetical equilibrium between monoiron and diiron complexes classical.

The offsets have their origins in the conformations of the $\text{FeP}(\text{CH}_2)_n\text{PFe}$ segments. In both independent molecules of **3**, the two FePCC units have *gauche* conformations (torsion angles ± 42 - 57° ; see Table 4.4), and the two PCCC units have *anti* conformations (torsion angles ± 178 - 166°), as easily visualized in Figure 4.2. Alternative *gauche/anti* patterns are highly unlikely. However, the longer $\text{FeP}(\text{CH}_2)_4\text{PFe}$ segments in **4a,b** allow two different motifs. In both molecules of **4a**, the two FePCC units remain *gauche* (torsion angles -70° to -72°). The CCCC units and one PCCC unit are *anti* (± 167 - 180°), whereas the other PCCC unit adopts an intermediate conformation (105 - 112°). In contrast, with **4b**, one FePCC unit becomes *anti* (-175°), while the other remains *gauche* (80°). The former catapults a methylene group much further from the rotator plane (Figure 4.2, bottom), rendering a greater offset more likely. The adjacent PCCC unit is approximately *anti* (-136°), and to close the ring the CCCC unit must adopt a *gauche* conformation (74°).

In summary, the *anti* FePCC unit in **4b** can be viewed as introducing a "stair step" that increases the likelihood of significantly offset Fe(CO)₃ rotators. In solution, one could logically expect **4a** and **4b** to sample both types of conformations as well as others. The FeP(CH₂)_nPFe conformations of **5** and **6** are not analyzed in similar detail, but a casual inspection of Figure 4.4 shows increasingly complex torsion angle patterns that at some value of *n* would promote P–Fe–P axes that are distinctly nonparallel.

With regard to steric interactions between the Fe(CO)₃ rotators in **3**, **4a,b**, **5**, and **6**, the starting point for analysis is the van der Waals radii of the rotators (4.45 Å; Table 4.4). In order to ensure that two parallel and coplanar rotators never sterically interact, the P–Fe–P axes must be spaced by twice this amount, or 8.90 Å. Of all of the diiron complexes considered in this study, only **6**, with an iron–iron distance of 8.517 Å, approaches this limit.

Top views of the Fe(CO)₃ rotators in **3** and **4a,b** are given in Figure 4.7. Interestingly, only in one case are there van der Waals contacts. In viewing such projections, it should be kept in mind that per Figure 4.5, none of the neighboring Fe(CO)₃ units are strictly coplanar with respect to each other. Thus, as noted above, the distances between the parallel P–Fe–P axes are shorter than the iron–iron distances.

Next, we consider the arbitrary Fe(CO)₃/Fe(CO)₃ orientation in panel **A** of Figure 4.8, which has no crystallographic counterpart in Figure 4.7. This can be viewed as a head-to-tail arrangement of two rotators with respect to two Fe–CO vectors. In these analyses, the Fe(CO)₃ units are constrained to be coplanar, so the iron–iron and P–Fe–P

axis separations are identical. These distances are reduced until there is van der Waals contact between the two rotators, which occurs at an iron–iron separation of 6.67 Å. Interestingly, the approach is limited not by the van der Waals radii of the iron atom or carbonyl oxygen, but rather the carbonyl carbon (see inset).

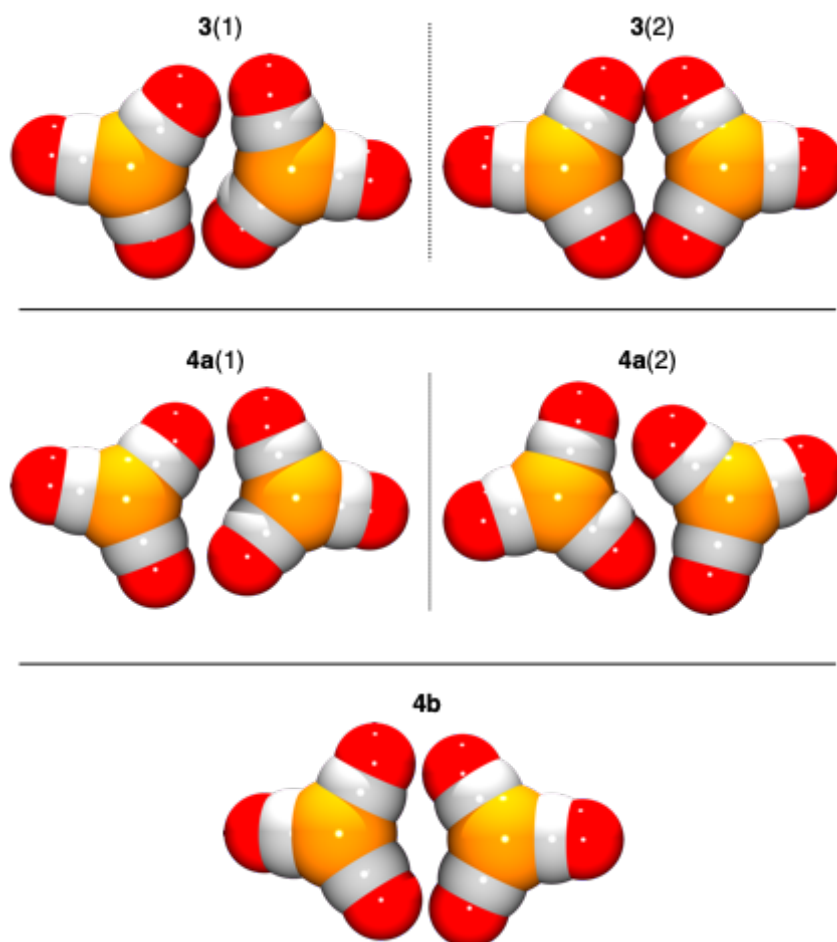


Figure 4.7 Space-filling "top" views of the $\text{Fe}(\text{CO})_3$ rotators of **3** (top, both independent molecules), **4a** (middle, both independent molecules), and **4b** (bottom) at van der Waals radii.

In panel **B** of Figure 4.8, the iron–iron distance in panel **A** is maintained, but the $\text{Fe}(\text{CO})_3$ rotator on the left is rotated by 180° to give a tail-to-tail orientation of the two $\text{Fe}-\text{CO}$ vectors, as seen in the crystal structures of **3(2)** and **4b**. This opens up some void space between the rotators, which at the narrowest is 0.64 \AA ($\text{CO}\cdots\text{OC}$). As shown in panel **C**, a variant is then considered in which both rotators have been rotated clockwise by 25° , approximating other orientations in Figure 4.7 (**3(1)**, **4a(1)**, and **4a(2)**). Now the void space narrows to 0.73 \AA ($\text{CO}\cdots\text{OC}$) and 0.65 \AA ($\text{CO}\cdots\text{C}$).

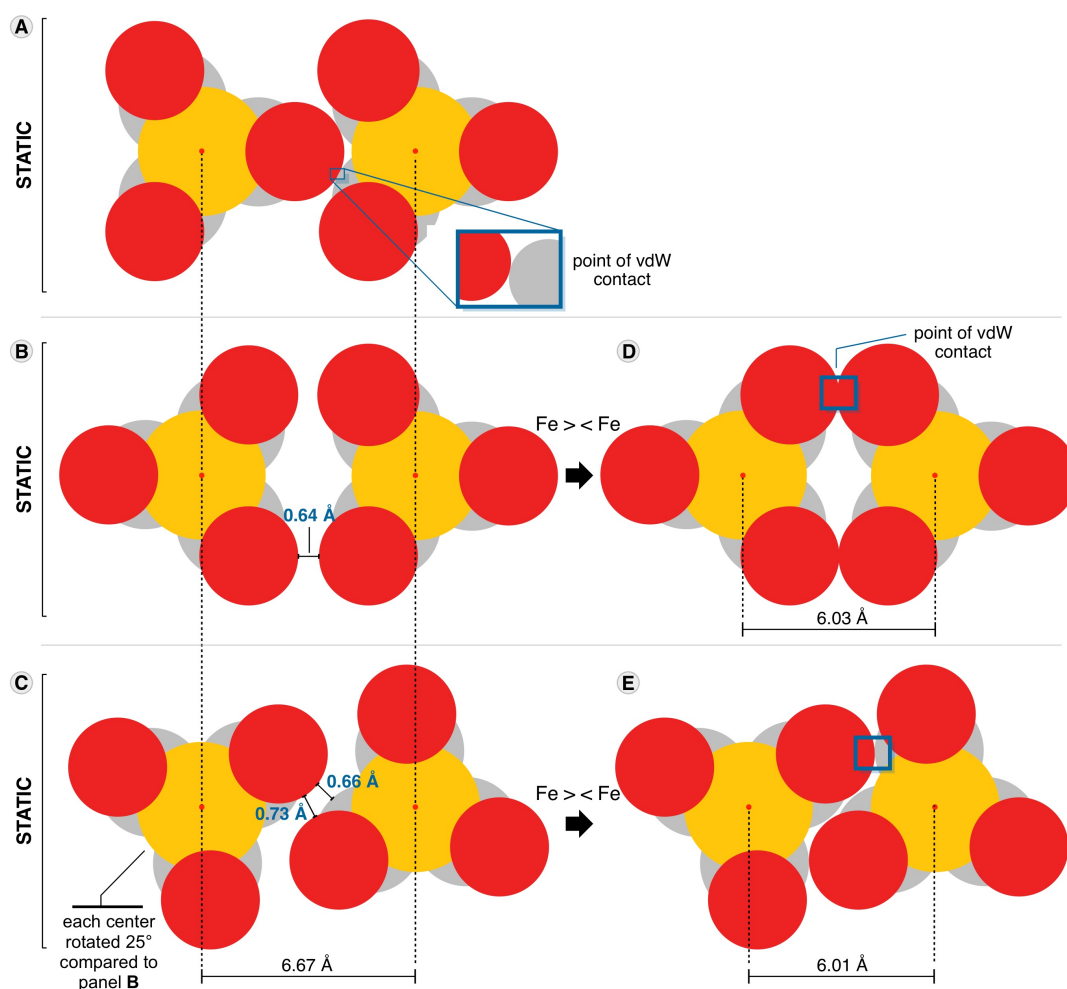


Figure 4.8 Analyses of interactions in hypothetical conformations of complexes with two coplanar $\text{Fe}(\text{CO})_3$ rotators (see text).

Next, the $\text{Fe}(\text{CO})_3$ conformations in panels **B** and **C** were maintained but the iron–iron distances were compressed until the onset of van der Waals contacts. As shown in panels **D** and **E**, separations of 6.03–6.01 Å could be realized. We suggest that these represent realistic "minimum contacts" for coplanar $\text{Fe}(\text{CO})_3$ rotators. Of course, at such distances gearing would likely be frozen. It is more challenging to define an iron–iron distance at which gearing would be optimal.

One approach is to define additional limiting values. For example, what is the minimum iron–iron distance at which one $\text{Fe}(\text{CO})_3$ rotator can experience sterically barrierless rotation (i.e. no van der Waals contacts) with respect to the other? This is addressed in Figure 4.9, where the $\text{Fe}(\text{CO})_3$ on the right (Fe2) is kept static, with the CO ligands as far removed from the $\text{Fe}(\text{CO})_3$ on the left (Fe1) as possible. For example, rotating Fe2 slightly clockwise or counterclockwise from the orientation depicted would force one of the two CO oxygen atoms directed toward Fe1 still closer to Fe1.

Accordingly, Fe1 and the proximal CO oxygen atom from Fe2 must have a steric clearance that matches the sum of the radius of the $\text{Fe}(\text{CO})_3$ rotator and the van der Waals radius of the CO oxygen atom, 5.97 Å (4.45 + 1.52 Å). Applying standard trigonometric relationships, this corresponds to a Fe1–Fe2 separation of 6.79 Å. Said differently, this is the closest iron–iron approach for which one $\text{Fe}(\text{CO})_3$ can rotate independently of the other (although van der Waals contacts will ensue with any other Fe2 conformation). One take-home message from Figure 4.8 and Figure 4.9 is that the "sweet spot" for gearing involves a narrow range of iron–iron distances, perhaps on the

order of 6.70-6.50 Å. Other approaches to defining optimal spacings for gears derived from trigonal rotators have been described by Baldrige and Siegal, who have introduced concepts such as gearing fidelity.^{3a} They also emphasize issues with treating atoms as "hard spheres", possible roles of dispersion forces, and a host of other factors.

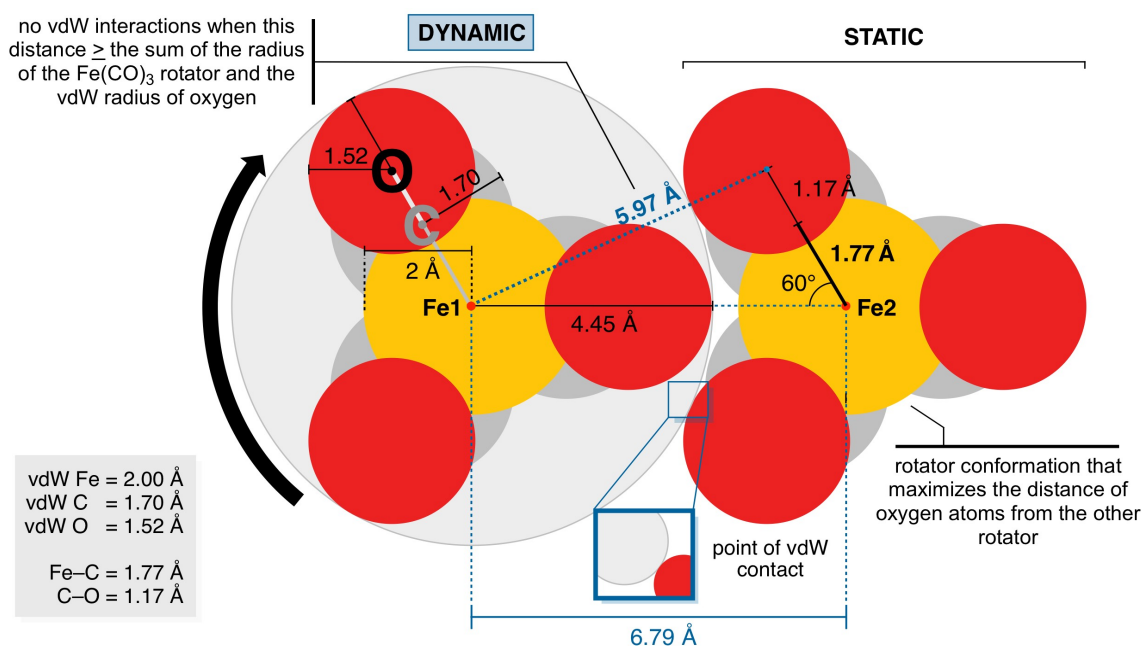


Figure 4.9 Minimum iron/iron spacing required (6.79 Å) for rotation of a $\text{Fe}(\text{CO})_3$ rotator with no van der Waals (vdW) interactions with a neighboring $\text{Fe}(\text{CO})_3$ rotator.

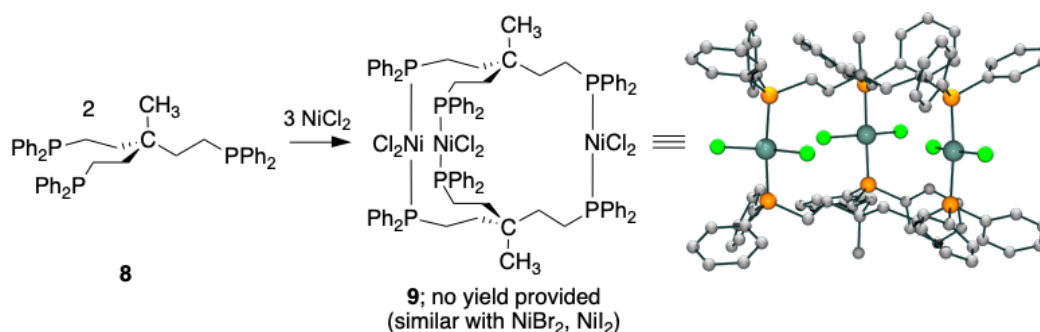
4.3.3. Related Complexes and Directions

Several attributes of new square pyramidal monoiron complex **6'** also merit note. First, it features the shortest methylene chain capable of bridging two *trans* phosphorus donor atoms for any coordination geometry.^{23,24} Interestingly, a similar complex, **6''**, with a diphosphine derived from 2,2'-dimethylbiphenyl has been reported by Casey, the crystal structure of which is shown in Figure 4.3 (right).²⁵ As with **6'**, six carbon atoms tether the *trans* phosphorus donor atoms, but most are sp^2 hybridized.

The P–Fe–P and basal CO–Fe–CO bond angles in **6''** (152.0(1) and 141.8(4)°), are close to those of **6'** (147.4(2) and 151.8(1)°). As with **6'**, the IR spectrum shows one strong $\nu_{C\equiv O}$ band (1882 cm^{-1}) and a second weaker band at a higher frequency (1970 cm^{-1}).²⁵ However, with **6''** only a single CO $^{13}\text{C}\{^1\text{H}\}$ NMR signal is observed at -80°C , in contrast to the two found at ambient probe temperature for **6'**.²⁵ As noted above, the close $\text{Fe}\cdots(\text{CH}_2)$ contacts in **6'** seemingly block $\text{Fe}(\text{CO})_3$ rotation, and the crystallographic data for **6''** deliver an analogous prediction. Other mechanisms for ^{13}C NMR signal coalescence would include rapid and reversible CO dissociation.

With regard to bimetallic complexes with sterically coupled rotors, as embodied by **III** in Scheme 4.1, the synthetic strategy applied in Scheme 4.2 is not limited to $\text{Fe}(\text{CO})_3$ sources or trigonal bipyramidal adducts. Indeed, α,ω -diphosphines $\text{Ph}_2\text{P}(\text{CH}_2)_n\text{PPh}_2$ have also been used to template the synthesis of analogous square planar adducts *trans,trans*- $\text{L}'\text{LM}[\text{Ar}_2\text{P}(\text{CH}_2)_n\text{PAr}_2]_2\text{MLL}'$, for example, with $\text{M}/n = \text{Rh}/1-4$.²⁶

There is also a ground for cautious optimism with regard to extending this synthetic strategy to arrays with increased numbers of rotators. As shown in Scheme 4.5, combination of the triphosphine $\text{CH}_3\text{C}(\text{CH}_2\text{CH}_2\text{PPh}_2)_3$ (**8**) with NiCl_2 affords the 2:3 trinickel hexaphosphorus adduct **9**, with three roughly parallel P–Ni–P axes.²⁷ Here the phosphorus atoms are connected by five-carbon bridges. In principle, the degree of steric communication between the rotators could be fine-tuned by adjusting this spacing or varying the chloride ligands.



Scheme 4.5 A triphosphine that templates the synthesis of trinickel complexes with three approximately parallel rotators.

However, as detailed in the preceding analyses, the conformational flexibility of these types of diphosphine or triphosphine ligands present challenges with regard to precisely controlling rotator/rotator interactions. As illustrated by **4a** and **4b** in Figure 4.2 and **5**, even when the $(\text{CH}_2)_n$ tethers are of equal lengths, the iron–iron distances, P–Fe–P axis separations, and distances between the planes of the two rotators can vary considerably. A second-generation approach would involve more rigid diphosphines with fewer degrees of freedom, as might be realized with a cyclohexane containing ligand with two 1,3-diaxial PAR_2 moieties. Such building blocks would seemingly enforce coplanar $\text{Fe}(\text{CO})_3$ rotors and parallel P–Fe–P axes.

4.4. Conclusion

This study has shown that it is possible to access diiron tetraphosphorus systems of the type **V** directly from $\text{Fe}(\text{CO})_3$ sources and diphosphines $\text{Ar}_2\text{P}(\text{CH}_2)_n\text{PAr}_2$ with $n = 3$ and 4 (Scheme 4.2 and Scheme 4.3). These results augment an earlier report of an adduct with $n/\text{Ar} = 5/\text{Ph}$.⁹ The short $\text{Fe}(\text{CO})_3/\text{Fe}(\text{CO})_3$ distances in these systems lead to steric interactions. The current NMR data suggest very high rotational barriers in **3** and lower barriers likely involving correlated rotation in **4a,b**. However, preliminary experiments show that a rigorous interrogation of these processes is best approached with ^{13}C O labeled substrates or perhaps via lower symmetry isosteric systems that feature one or more CO/NO^+ substitutions.⁷ Thus, no additional data regarding dynamic properties are presented at this time. Additionally, as noted in the preceding section, other types of diphosphines with fewer degrees of conformational freedom may afford adducts with more efficient rotator/rotator coupling.

The computational data further show that the diiron tetraphosphorus complexes **V** are thermodynamically more stable than all of the possible coordination geometries of the monoiron diphosphorus complexes **VI**. They also establish diagnostic IR $\nu_{\text{C}\equiv\text{O}}$ band patterns for the diiron complexes that allow structures to be verified for crystalline and noncrystalline samples as well as in solution where dynamic NMR properties may be probed. Although other potential applications for the new diiron and monoiron carbonyl compounds should not be overlooked,²⁸ this work has provided a detailed foundation for further studies of interactive $\text{Fe}(\text{CO})_3/\text{Fe}(\text{CO})_3$ rotators. Finally, extensions of these

themes to triiron, tetrairon, and higher systems are easily envisioned, where there are intriguing possibilities for "water wheels" and other types of molecular machines.

4.5. Experimental [major contribution: Mr. S. Zarcone, Dr. G. Zhu]

4.5.1. General

All reactions and workups were conducted under inert atmospheres using oven-dried glassware. Solvents were purified using a Glass Contour system; CDCl_3 and $\text{DMSO-}d_6$ (2 × Cambridge Isotopes) were freeze-pump-thaw degassed. The diphosphines $\text{Ph}_2\text{P}(\text{CH}_2)_n\text{PPh}_2$ ($n = 3$, TCI; $n = 4$, Alfa-Aesar), and silica (Silicycle, 40-63 μm , 230-400 mesh), were used as received. $(\text{BDA})\text{Fe}(\text{CO})_3$ was prepared by a literature procedure.¹⁵

NMR spectra were recorded on standard FT instruments at ambient probe temperatures and referenced as follows (δ , ppm): ^1H , residual internal CHCl_3 (7.27) or $\text{DMSO-}d_5$ (2.50); $^{13}\text{C}\{^1\text{H}\}$, internal CDCl_3 (77.00) or $\text{DMSO-}d_6$ (39.52); $^{31}\text{P}\{^1\text{H}\}$, external 85% H_3PO_4 (0.00). IR spectra were recorded using a Shimadzu IRAffinity-1 spectrometer with a Pike MIRacle ATR system (diamond/ZnSe crystal). Microanalyses were conducted by Atlantic Microlab. Electrospray ionization mass spectrometry (ESI-MS) was carried out with a Thermo Scientific Q Exactive Focus instrument.

4.5.1.1. Representative syntheses: *trans,trans*-(CO)₃Fe[Ph₂P(CH₂)₃PPh₂]₂Fe(CO)₃ (**3**)

A Schlenk flask was charged with (BDA)Fe(CO)₃ (0.200 g, 0.699 mmol), Ph₂P(CH₂)₃PPh₂ (0.236 g, 0.573 mmol), and THF (7.4 mL) with stirring and covered with aluminum foil. A yellow precipitate formed. After 48 h, the solvent was removed by oil-pump vacuum, and cold THF was added. The mixture was filtered through a pad of silica (3 × 5 cm) that was rinsed first with cold THF and then with toluene. The solvent was removed from the yellow toluene rinses by oil-pump vacuum to give **3** as a pale yellow solid (0.139 g, 0.126 mmol, 44% of theory (0.573/2 mmol)) that decomposed to a black solid at >153 °C. Anal. Calcd (%) for C₆₀H₅₂Fe₂O₆P₄ (1048.21): C, 65.24; H, 4.75. Found: C, 65.86; H, 4.73. NMR (DMSO-*d*₆, δ in ppm): ¹H (500 MHz) 7.71-7.65 (br m, 16H, C₆H₅), 7.52-7.44 (m, 24H, C₆H₅), 2.75-2.65 (br m, 8H, PCH₂), 2.39-2.28 (br m, 4H, PCH₂CH₂). ¹³C{¹H} (125 MHz, cryoprobe)²⁹ 214.7 (apparent m, CO), 212.4 (apparent m, CO), 136.7 (apparent m, *i* to P), 131.2 (br s, w_{1/2} 37 Hz, *o* to P), 129.9 (s, *p* to P), 128.4 (br s, w_{1/2} 34 Hz, *m* to P), 33.8 (apparent m, PCH₂), 21.5 (s, PCH₂CH₂). ³¹P{¹H} (202 MHz) 75.12 (s). IR (powder film, cm⁻¹): 3068 (w), 2959 (w), 1969 (w, ν_{C=O}), 1892 (sh, ν_{C=O}), 1871 (s, ν_{C=O}), 1433 (m), 1092 (m), 957 (m), 795 (m), 745 (m), 692 (s), 633 (s). HRMS (ESI, *m/z*): calcd for C₆₀H₅₂Fe₂O₆P₄ [M + H]⁺: 1105.1441. Found: 1105.1449.

4.5.1.2. Representative syntheses: *trans,trans*-(CO)₃Fe[Ph₂P(CH₂)₄PPh₂]₂Fe(CO)₃ (**4a**)

(BDA)Fe(CO)₃ (0.500 g, 1.75 mmol), Ph₂P(CH₂)₄PPh₂ (0.611 g, 1.43 mmol), and THF (19 mL) were combined in a procedure analogous to that for **3**. An identical workup gave **4a** as a yellow solid (0.153 g, 0.135 mmol, 19% of theory (1.43/2 mmol)) that decomposed to a black solid at ≥118 °C. Anal. Calcd (%) for C₆₂H₅₆Fe₂O₆P₄ (1076.24): C, 65.74; H, 4.98. Found: C, 65.14; H, 5.20.³⁰ NMR (CDCl₃, δ in ppm): ¹H (500 MHz) 7.69-7.52 (br m, 16H, C₆H₅), 7.46-7.30 (br m, 24H, C₆H₅), 2.67 (br apparent s, 8H, PCH₂), 1.81 (br apparent s, 8H, PCH₂CH₂). ¹³C{¹H} (125 MHz)^{29,31} 214.0 (very weak s, tentative CO), 137.5-137.1 (apparent m, *i* to P), 131.9 (virtual t, ²J_{CP} = 4.8 Hz, *o* to P), 129.4 (s, *p* to P), 128.0 (virtual t, ³J_{CP} = 4.6 Hz, *m* to P), 29.5 (apparent m, PCH₂), 25.6 (apparent m, PCH₂CH₂). ³¹P{¹H} (202 MHz) 73.96 (s). IR (powder film, cm⁻¹): 3054 (w), 2965 (w), 1964 (w, ν_{C≡O}), 1864 (s, ν_{C≡O}), 1434 (m), 1093 (m), 1014 (m), 794 (m), 743 (m), 694 (s), 633 (s). HRMS (ESI, *m/z*): calcd for C₆₂H₅₆Fe₂O₆P₄ [M + H]⁺, 1133.1754. Found, 1133.1775.

4.5.2. Crystallography

A. A CH₂Cl₂ solution of **3** was kept at -40 °C. After 4 days, colorless blocks were collected, and data were obtained as outlined in Table 4.2. Cell parameters were obtained from 180 data frames taken at widths of 0.5° and refined with 9463 reflections. The unit cell was determined using the program Cell Now.³² Integrated intensity information for each reflection was obtained by reduction of the data frames with APEX2.³³ Data were corrected for Lorentz and polarization factors, crystal decay effects, and absorption effects (using SADABS).³⁴ The structure was solved using SHELXTL.³⁵ Hydrogen atoms were placed in idealized positions and refined using a riding model. All non-hydrogen atoms were refined with anisotropic thermal parameters. Two independent molecules were found in the unit cell, each with an inversion center. Four molecules of CH₂Cl₂ were present for every molecule of **3**. Two were disordered but could be modeled successfully. However, the irregular thermal ellipsoids and residual electron density close to the chlorine atoms suggested further disorder.

B. A toluene solution of **4a** was kept at -40 °C. After 2 weeks, colorless blocks were collected, and data were obtained as outlined in Table 4.2. The structure was solved as in procedure A (180 frames, 0.5° scan, 12 925 reflections). Two independent molecules were found in the unit cell, each with an inversion center. Six toluene molecules were present for every molecule of **4a**. Residual electron densities close to four toluene molecules indicated disorder, and each was modeled between two positions. Some of the carbon atoms exhibited irregular thermal ellipsoids, and restraints were used to keep them reasonable.

C. CHCl₃ vapor was allowed to slowly diffuse into a toluene solution of **4b** at 0 °C. After two days, yellow blocks were collected, and data were obtained as outlined in Table 4.2. Cell parameters were obtained from 45 data frames taken at widths of 1°. Integrated intensity information for each reflection was obtained by reduction of the data frames with APEX3.³⁵ All data were corrected for Lorentz and polarization factors, crystal decay effects, and (using SADABS)³⁴ absorption effects. The structure was solved using XT/XS in APEX3.^{33,35} Solvent molecules were found. However, they were disordered, and/or the sites were partially occupied, and could not be modeled successfully. Hydrogen atoms were placed in idealized positions and refined using a riding model. All non-hydrogen atoms were refined with anisotropic thermal parameters. The solvent molecules were MASKed using OLEX2³⁶ during the final least squares refinement cycles. The absence of additional symmetry and voids was confirmed using PLATON (ADDYSM).³⁷ The structure was refined (weighted least-squares refinement on F^2) to convergence.^{35,36}

D. Pentane vapor was allowed to slowly diffuse into a toluene solution of **6'** at 0 °C. After two days, yellow blocks were collected, and data were obtained as outlined in Table 4.2. The structure was solved as in procedure A (45 frames, 1° scan, 7998 reflections). A half molecule of toluene was present for every molecule of **6'**; the elongated ellipsoids suggested disorder, which was successfully modeled between two positions with a 0.66:0.34 occupancy ratio.

4.5.3. DFT Computations

An all-electron triple- ζ -quality basis set was used on all atoms including iron (def2-TZVP).³⁸ Thus, no pseudopotential was used on heavier elements. This basis set was paired with the TPSS³⁹ functional, which has been shown to reproduce experimental IR spectra of iron carbonyl complexes.^{13,22} All computations were performed using the Gaussian program suite, employing an ultrafine grid (99,590) to enhance accuracy.⁴⁰ First, all species were optimized and then subjected to frequency calculations to perform a vibrational analysis. The IR spectra were computed for all mono- and diiron species. These calculations were separated from the optimizations, and additional memory (150 GB) was necessary to reach convergence. The vibrational frequencies were inspected and all structures were deemed to be local minima. The scaling factor (0.9863) was close to values that proved optimal in earlier studies.⁴¹

4.6. References

(1) Kottas, G. S.; Clarke, L. I.; Horinek, D.; Michl, J. Artificial Molecular Rotors. *Chem. Rev.* **2005**, *105*, 1281-1376.

(2) Reviews of this extensive literature: (a) Iwamura, H.; Mislow, K. Stereochemical Consequences of Dynamic Gearing. *Acc. Chem. Res.* **1988**, *21*, 175-182.

(b) Goswami, A.; Saha, S.; Biswas, P. K.; Schmittel, M. (Nano)mechanical Motion Triggered by Metal Coordination: from Functional Devices to Networked Multicomponent Catalytic Machinery. *Chem. Rev.* **2020**, *120*, 125-199. (see especially section 2.2).

(c) Dattler, D.; Fuks, G.; Heiser, J.; Moulin, E.; Perrot, A.; Yao, X.; Giuseppone, N. Design of Collective Motions from Synthetic Molecular Switches, Rotors, and Motors. *Chem. Rev.* **2020**, *120*, 310-433. (see especially section 4.2). (d) Liepuoniute, I.; Jellen, M. J.; Garcia-Garibay, M. A. Correlated motion and mechanical gearing in amphidynamic crystalline molecular machines. *Chem. Sci.* **2020**, *11*, 12994-13007.

(3) Some representative primary literature: (a) Frantz, D. K.; Linden, A.; Baldrige, K. K.; Siegel, J. S. Molecular Spur Gears Comprising Triptycene Rotators and Bibenzimidazole-Based Stators. *J. Am. Chem. Soc.* **2012**, *134*, 1528-1535. (b)

Lemouchi, C.; Iliopoulos, K.; Zorina, L.; Simonov, S.; Wzietek, P.; Cauchy, T.; Rodríguez-Fortea, A.; Canadell, E.; Kaleta, J.; Michl, J.; Gindre, D.; Chrysos, M.; Batail, P. Crystalline Arrays of Pairs of Molecular Rotors: Correlated Motion, Rotational Barriers, and Space-Inversion Symmetry Breaking Due to Conformational Mutations. *J. Am. Chem. Soc.* **2013**, *135*, 9366-9376. (c) Pérez-Estrada, S.; Rodríguez-Molina, B.;

Maverick, E. F.; Khan, S. I.; Garcia-Garibay, M. A. Throwing in a Monkey Wrench to Test and Determine Geared Motion in the Dynamics of a Crystalline One-Dimensional (1D) Columnar Rotor Array. *J. Am. Chem. Soc.* **2019**, *141*, 2413-2420.

(4) (a) de Jonge, J. J.; Ratner, M. A.; de Leeuw, S. W. Local Field Controlled Switching in a One-Dimensional Dipolar Array. *J. Phys. Chem. C*, **2007**, *111*, 3770-3777. (b) Zhao, K.; Dron, P. I.; Kaleta, J.; Rogers, C. T.; Michl, J. Arrays of Dipolar Molecular Rotors in Tris(*o*-phenylenedioxy) cyclotriphosphazene. *Top. Curr. Chem.* **2014**, *354*, 163-211. (c) Sharma, K.; Friedrich, B. Pair-eigenstates and mutual alignment of coupled molecular rotors in a magnetic field. *Phys. Chem. Chem. Phys.* **2016**, *18*, 13467-13477. (d) Abolins, B. P.; Zillich, R. E.; Whaley, K. B. Quantum phases of dipolar rotors on two-dimensional lattices. *J. Chem. Phys.* **2018**, *148*, 102338.

(5) Ehnbohm, A.; Gladysz, J. A. Gyroscopes and the Chemical Literature, 2002-2020: Approaches to a Nascent Family of Molecular Devices. *Chem. Rev.* **2021**, *121*, 3701-3750.

(6) Lead references, square planar complexes: (a) Nawara-Hultsch, A. J.; Stollenz, M.; Barbasiewicz, M.; Szafert, S.; Lis, T.; Hampel, F.; Bhuvanesh, N.; Gladysz, J. A. Gyroscope-Like Molecules Consisting of PdX₂/PtX₂ Rotators within Three-Spoke Dibrigehead Diphosphine Stators: Syntheses, Substitution Reactions, Structures, and Dynamic Properties. *Chem. - Eur. J.* **2014**, *20*, 4617-4637. (b) Kharel, S.; Joshi, H.; Bhuvanesh, N.; Gladysz, J. A. Syntheses, Structures, and Thermal Properties of Gyroscope-like Complexes Consisting of PtCl₂ Rotators Encased in Macrocyclic Dibrigehead Diphosphines P((CH₂)_n)₃P with Extended Methylene Chains (*n* =

20/22/30) and Isomers Thereof. *Organometallics* **2018**, *37*, 2991-3000. (c) Estrada, A. L.; Jia, T.; Bhuvanesh, N.; Blümel, J.; Gladysz, J. A. Substitution and Catalytic Chemistry of Gyroscope-Like Complexes Derived from Cl–Rh–CO Rotators and Triply *trans* Spanning Di-(trialkylphosphine) Ligands. *Eur. J. Inorg. Chem.* **2015**, *2015*, 5318-5321.

(7) Lead references, trigonal bipyramidal complexes: (a) Lang, G. M.; Shima, T.; Wang, L.; Cluff, K. J.; Skopek, K.; Hampel, F.; Blümel, J.; Gladysz, J. A. Gyroscope-Like Complexes Based on Dibridgehead Diphosphine Cages That Are Accessed by Three-Fold Intramolecular Ring Closing Metatheses and Encase Fe(CO)₃, Fe(CO)₂(NO)⁺, and Fe(CO)₃(H)⁺ Rotators. *J. Am. Chem. Soc.* **2016**, *138*, 7649-7663.

(b) Lang, G. M.; Skaper, D.; Hampel, F.; Gladysz, J. A. Synthesis, reactivity, structures, and dynamic properties of gyroscope like iron complexes with dibridgehead diphosphine cages: pre- vs. post-metathesis substitutions as routes to adducts with neutral dipolar Fe(CO)(NO)(X) rotors. *Dalton Trans.* **2016**, *45*, 16190-16204.

(8) Lead references, octahedral complexes: (a) Fiedler, T.; Bhuvanesh, N.; Hampel, F.; Reibenspies, J. H.; Gladysz, J. A. Gyroscope like molecules consisting of trigonal or square planar osmium rotators within three-spoked dibridgehead diphosphine stators: syntheses, substitution reactions, structures, and dynamic properties. *Dalton Trans.* **2016**, *45*, 7131-7147. (b) Hess, G. D.; Fiedler, T.; Hampel, F.; Gladysz, J. A. Octahedral Gyroscope-like Molecules Consisting of Rhenium Rotators within Cage-like Dibridgehead Diphosphine Stators: Syntheses, Substitution Reactions, Structures, and Dynamic Properties. *Inorg. Chem.* **2017**, *56*, 7454-7469.

(9) Syntheses and crystal structures of $cis\text{-}(\text{CO})_3\text{Fe}[\overline{\text{Ph}_2\text{P}(\text{CH}_2)_5\text{PPh}_2}]$ (**5'**) and $trans,trans\text{-}(\text{CO})_3\text{Fe}[\text{Ph}_2\text{P}(\text{CH}_2)_5\text{PPh}_2]_2\text{Fe}(\text{CO})_3$ (**5**): Liu, L.-K.; Luh, L.-S.; Gau, H.-M. Preparation and Structure Studies of Monomeric and Dimeric [Bis(diphenylphosphino)pentane]tricarbonyliron(0). *Inorg. Chem.* **1992**, *31*, 3434-3437.

(10) Crystal structure of $cis\text{-}(\text{CO})_3\text{Fe}[\overline{\text{Ph}_2\text{PCH}_2\text{PPh}_2}]$ (**1'**): Cotton, F. A.; Hardcastle, K. I.; Rusholme, G. A. AN X-RAY STRUCTURAL STUDY OF THE FLUXIONAL MOLECULE [BIS(DIPHENYLPHOSPHINO)METHANE]TRICARBONYLIRON. *J. Coord. Chem.* **1973**, *2*, 217-223.

(11) The energies of trigonal bipyramidal and square planar isomers can be quite close, with modest intervening barriers, and intermediate structures are sometimes found.^{10,12} To help differentiate borderline cases, a "tau" parameter has been devised: Crans, D. C.; Tarlton, M. L.; McLauchlan, C. C. Trigonal Bipyramidal or Square Pyramidal Coordination Geometry? Investigating the Most Potent Geometry for Vanadium Phosphatase Inhibitors. *Eur. J. Inorg. Chem.* **2014**, *2014*, 4450-4468. and earlier papers cited therein; 1 = tbp, 0 = sq pyr. Those associated with **1'**, **2'**, **3'**, **5'**, and **6'** are 0.76, 0.33, 0.93, 0.74, and 0.10, respectively. Those for the diiron complexes range from 0.92 to 0.84.

(12) Syntheses and crystal structures of $cis\text{-}(\text{CO})_3\text{Fe}[\overline{\text{Ph}_2\text{P}(\text{CH}_2)_2\text{PPh}_2}]$ (**2'**): Battaglia, L. P.; Delledonne, D.; Nardelli, M.; Pelizzi, C.; Predieri, G.; Chiusoli, G. P. The crystal and molecular structure of [bis(diphenylphosphino) ethane] tricarbonyliron(0). *J. Organomet. Chem.* **1987**, *330*, 101-113.

(13) Syntheses and crystal structures of $cis\text{-(CO)}_3\text{Fe}[\overline{\text{Ph}_2\text{P}(\text{CH}_2)_3\text{PPh}_2}]$ (**3'**): Ringenberg, M. R.; Wittkamp, F.; Apfel, U.-P.; Kaim, W. Redox Induced Configurational Isomerization of Bisphosphine-Tricarbonyliron(I) Complexes and the Difference a Ferrocene Makes. *Inorg. Chem.* **2017**, *56*, 7501-7511.

(14) Other works reporting syntheses of $cis\text{-(CO)}_3\text{Fe}[\overline{\text{Ph}_2\text{P}(\text{CH}_2)_n\text{PPh}_2}]$: (a) $n = 1$ (**1'**): Wegner, P. A.; Evans, L. F.; Haddock, J. Bimetallic Iron Carbonyl Derivatives of Bidentate Phosphine Ligands. *Inorg. Chem.* **1975**, *14*, 192-194. (b) $n = 1-4$ (**1'-4'**): Sowa, J. R. Jr.; Zanotti, V.; Facchin, G.; Angelici, R. J. Calorimetric Studies of the Heats of Protonation of the Metal in $\text{Fe}(\text{CO})_3$ (bidentate phosphine, arsine) Complexes: Effects of Chelate Ligands on Metal Basicity. *J. Am. Chem. Soc.* **1992**, *114*, 160-165. (c) $n = 1-4$ (**1'-4'**): Luo, L.; Nolan, S. P. Enthalpies of Reaction of (Diene)- and (Enone)iron Tricarbonyl Complexes with Monodentate and Bidentate Ligands. Solution Thermochemical Study of Ligand Substitution in the $\text{L}_2\text{Fe}(\text{CO})_3$ Complexes. *Inorg. Chem.* **1993**, *32*, 2410-2415. (d) $n = 3$ (**3'**): Langford, G. R.; Akhtar, M.; Ellis, P. D.; MacDiarmid, A. G.; Odom, J. D. Synthesis and Multinuclear Magnetic Resonance Study of Stereochemically Nonrigid Derivatives of Iron Pentacarbonyl Containing Bidentate Ligands. *Inorg. Chem.* **1975**, *14*, 2937-2941.

(15) (a) Howell, J. A. S.; Johnson, B. F. G.; Josty, P. L.; Lewis, J. Synthesis and reactions of tetracarbonyl- and tricarbonyliron complexes of α,β -unsaturated ketones. *J. Organomet. Chem.* **1972**, *39*, 329-333. (b) Brookhart, M.; Nelson, G. O. The reaction of benzylideneacetoneiron tricarbonyl with dienes; measurement of relative reactivities using competition experiments. *J. Organomet. Chem.* **1979**, *164*, 193-202.

(16) (a) Skopek, K.; Gladysz, J. A. Syntheses of gyroscope-like molecules via three-fold ring closing metatheses of bis(phosphine) complexes *trans*- $L_yM(P((CH_2)_nCH=CH_2)_3)_2$, and extensions to bis(phosphite) complexes *trans*- $Fe(CO)_3(P(O(CH_2)_nCH=CH_2)_3)_2$. *J. Organomet. Chem.* **2008**, *693*, 857-866. (b) Lang, G. M.; Skaper, D.; Shima, T.; Otto, M.; Wang, L.; Gladysz, J. A. Syntheses of Iron(0) Complexes of Symmetrical Trialkylphosphines with Three Terminal Vinyl Groups, $P((CH_2)_mCH=CH_2)_3$. *Aust. J. Chem.* **2015**, *68*, 1342-1351. (c) Steigleder, E.; Shima, T.; Lang, G. M.; Ehnbohm, A.; Hampel, F.; Gladysz, J. A. Partially Shielded $Fe(CO)_3$ Rotors: Syntheses, Structures, and Dynamic Properties of Complexes with Doubly *trans* Spanning Diphosphines, $trans\text{-}\overline{Fe(CO)_3(PhP((CH_2)_n)_2PPh)}$. *Organometallics* **2017**, *36*, 2891-2901.

(17) Leitner, W.; Bühl, M.; Fornika, R.; Six, C.; Baumann, W.; Dinjus, E.; Kessler, M.; Krüger, C.; Ruffńska, A. ^{103}Rh Chemical Shifts in Complexes Bearing Chelating Bidentate Phosphine Ligands. *Organometallics* **1999**, *18*, 1196-1206.

(18) Adams, D. M. *Metal-Ligand and Related Vibrations*. St. Martin's Press: New York, 1968; Chapter 3.4.

(19) The IR spectrum of **4a** (Figure 4.1) exhibits some weak features that do not have counterparts in the spectra of **3** or **4b**. These do not arise from any **4'a** contaminant.

(20) Throughout this manuscript, primed compound numbers indicate monoiron complexes $(CO)_3\overline{Fe[Ph_2P(CH_2)_nPPh_2]}$ regardless of coordination geometry or stereochemistry. All trigonal bipyramidal complexes presented have *cis* phosphorus

donor atoms (**3'**, **4'a**, **5'**; axial/equatorial), but square pyramidal complexes can be either *cis* (**1'**, **2'**) or *trans* (**6'**, **6''**; basal/basal in all cases).

(21) (a) Bondi, A. van der Waals Volumes and Radii. *J. Phys. Chem.* **1964**, *68*, 441-451. (b) Mantina, M.; Chamberlin, A. C.; Valero, R.; Cramer, C. J.; Truhlar, D. G. Consistent van der Waals Radii for the Whole Main Group. *J. Phys. Chem. A*, **2009**, *113*, 5806-5812.

(22) Representative studies validating the use of the TPSS functional and/or def2-TZVP basis set for IR calculations in related systems: (a) Brothers, S. M.; Darensbourg, M. Y.; Hall, M. B. Modeling Structures and Vibrational Frequencies for Dinitrosyl Iron Complexes (DNICs) with Density Functional Theory. *Inorg. Chem.* **2011**, *50*, 8532-8540. (b) Meng, L.; Liu, S.; Qin, Q.; Zeng, B.; Chi, C. Infrared Photodissociation Spectroscopy of Heteronuclear Arsenic-Iron Carbonyl Cluster Anions. *J. Phys. Chem. A*, **2020**, *124*, 1158-1166. (c) Speelman, A. L.; Zhang, B.; Silakov, A.; Skodje, K. M.; Alp, E. E.; Zhao, J.; Hu, M. Y.; Kim, E.; Krebs, C.; Lehnert, N. Unusual Synthetic Pathway for an $\{\text{Fe}(\text{NO})_2\}^9$ Dinitrosyl Iron Complex (DNIC) and Insight into DNIC Electronic Structure via Nuclear Resonance Vibrational Spectroscopy. *Inorg. Chem.* **2016**, *55*, 5485-5501. (d) Pan, S.; Zhao, L.; Dias, H. V. R.; Frenking, G. Bonding in Binuclear Carbonyl Complexes $\text{M}_2(\text{CO})_9$ (M = Fe, Ru, Os). *Inorg. Chem.* **2018**, *57*, 7780-7791. (e) Kerpál, C.; Harding, D. J.; Rayner, D. M.; Fielicke, A. Small Platinum Cluster Hydrides in the Gas Phase. *J. Phys. Chem. A*, **2013**, *117*, 8230-8237.

(23) Bessel, C. A.; Aggarwal, P.; Marschilok, A. C.; Takeuchi, K. J. Transition-Metal Complexes Containing *trans*-Spanning Diphosphine Ligands. *Chem. Rev.* **2001**, *101*, 1031-1066.

(24) A report of a square planar nickel complex with a *trans*-spanning pentamethylene diphosphine $\text{Cy}_2\text{P}(\text{CH}_2)_5\text{PCy}_2$ has been questioned:²³ Issleib, V. K.; Hohlfeld, G. Beiträge zur Komplexchemie der Phosphine und Phosphinoxyde. X. Schwermetallkomplexe ditertiärer Phosphine. *Z. Anorg. Allg. Chem.* **1961**, *312*, 169-179.

(25) Casey, C. P.; Whiteker, G. T.; Campana, C. F.; Powell, D. R. Pentacoordinate $\text{Fe}(\text{CO})_3$ Complexes of Diphosphine Ligands with Bite Angles Greater Than 120° . *Inorg. Chem.* **1990**, *29*, 3376-3381.

(26) See the following lead references, and earlier work cited therein: (a) Balch, A. L.; Tulyathan, B. Interactions between rhodium(I) centers in dimeric complexes. *Inorg. Chem.* **1977**, *16*, 2840-2845. (b) Cowie, M.; Dwight, S. K. Unusual structural and chemical trends within a series of binuclear rhodium carbonyl halide complexes and the structure of one member of this series, *trans*- $[\text{Rh}_2\text{Cl}_2(\text{CO})_2((\text{C}_6\text{H}_5)_2\text{PCH}_2\text{P}-(\text{C}_6\text{H}_5)_2)_2]$. *Inorg. Chem.* **1980**, *19*, 2500-2507.

(27) Cecconi, F.; Midollini, S.; Orlandini, A.; Sacconi, L. Trimeric nickel(II) complexes with bridging triphosphine ligand 1,1,1-tris-(diphenylphosphinoethyl)ethane (etp_3). X-ray structure of the complex $[\text{Ni}_3\text{Cl}_6(\text{etp}_3)_2]\cdot 0.7\text{CHCl}_3$. *Inorg. Chim. Acta* **1980**, *42*, 59-63.

(28) Jiang, X.; Xiao, Z.; Zhong, W.; Liu, X. Brief survey of diiron and monoiron carbonyl complexes and their potentials as CO-releasing molecules (CORMs). *Coord. Chem. Rev.* **2021**, *429*, No. 213634.

(29) Of the phenyl $^{13}\text{C}\{^1\text{H}\}$ NMR signals, that with the chemical shift closest to benzene (128.4 ppm) is attributed to the *meta* carbon atom, and the other signal of comparable intensity (and phosphorus coupling) is attributed to the *ortho* carbon atom. See Mann, B. E. The Carbon-13 and Phosphorus-31 Nuclear Magnetic Resonance Spectra of Some Tertiary Phosphines. *J. Chem. Soc. Perkin Trans. 2*, **1972**, 30-34.

(30) The $^{31}\text{P}\{^1\text{H}\}$ NMR spectra of the crude reaction mixture suggest that some **4'a**^{14b} may be formed. However, this species is removed upon workup.

(31) For virtual triplets, the $^xJ_{\text{CP}}$ values represent *apparent* couplings between adjacent peaks that take place through a minimum of x bonds. Hersh, W. H. False AA'X Spin-Spin Coupling Systems in ^{13}C NMR: Examples Involving Phosphorus and a 20-Year-Old Mystery in Off-Resonance Decoupling. *J. Chem. Educ.* **1997**, *74*, 1485-1488.

(32) Sheldrick, G. M. *Cell_Now*: Program for Obtaining Unit Cell Constants from Single Crystal Data, version 2008/1; University of Göttingen, 2007.

(33) *APEX2/3*; Bruker AXS Inc.: Madison, WI, 2016.

(34) Sheldrick, G. M. *SADABS*; Bruker AXS Inc.: Madison, WI, 2001.

(35) (a) Sheldrick, G. M. A short history of *SHELX*. *Acta Crystallogr. Sect. A: Found. Crystallogr.* **2008**, *A64*, 112-122. (b) Sheldrick, G. M. *SHELXT* — Integrated space-group and crystal structure determination. *Acta Crystallogr. Sect. A: Found. Adv.* **2015**, *71*, 3-8. (c) Sheldrick, G. M. Crystal structure refinement with *SHELXL*. *Acta*

Crystallogr. Sect. C: Struct. Chem. **2015**, *C71*, 3-8. (d) XT, XS; Bruker AXS Inc.: Madison, WI, 2016.

(36) Dolomanov, O. V.; Bourhis, L. J.; Gildea, R. J.; Howard, J. A. K.; Puschmann, H. *OLEX2: A Complete Structure Solution, Refinement and Analysis Program. J. Appl. Crystallogr.* **2009**, *42*, 339-341.

(37) Spek, A. L. Single-crystal structure validation with the program. *J. Appl. Crystallogr.* **2003**, *36*, 7-13.

(38) Weigend, F.; Ahlrichs, R. Balanced basis sets of split valence, triple zeta valence and quadruple zeta valence quality for H to Rn: Design and assessment of accuracy. *Phys. Chem. Chem. Phys.* **2005**, *7*, 3297-3305.

(39) Tao, J.; Perdew, J. P.; Staroverov, V. N.; Scuseria, G. E. Climbing the Density Functional Ladder: Nonempirical Meta-Generalized Gradient Approximation Designed for Molecules and Solids. *Phys. Rev. Lett.* **2003**, *91*, 146401.

(40) Frisch, M. J.; Trucks, G. W.; Schlegel, H. B.; Scuseria, G. E.; Robb, M. A.; Cheeseman, J. R.; Scalmani, G.; Barone, V.; Mennucci, B.; Petersson, G. A.; Nakatsuji, H.; Caricato, M.; Li, X.; Hratchian, H. P.; Izmaylov, A. F.; Bloino, J.; Zheng, G.; Sonnenberg, J. L.; Hada, M.; Ehara, M.; Toyota, K.; Fukuda, R.; Hasegawa, J.; Ishida, M.; Nakajima, T.; Honda, Y.; Kitao, O.; Nakai, H.; Vreven, T.; Montgomery, J. A. Jr.; Peralta, J. E.; Ogliaro, F.; Bearpark, M.; Heyd, J. J.; Brothers, E.; Kudin, K. N.; Staroverov, V. N.; Kobayashi, R.; Normand, J.; Raghavachari, K.; Rendell, A.; Burant, J. C.; Iyengar, S. S.; Tomasi, J.; Cossi, M.; Rega, N.; Millam, J. M.; Klene, M.; Knox, J. E.; Cross, J. B.; Bakken, V.; Adamo, C.; Jaramillo, J.; Gomperts, R.; Stratmann, R. E.;

Yazyev, O.; Austin, A. J.; Cammi, R.; Pomelli, C.; Ochterski, J. W.; Martin, R. L.; Morokuma, K.; Zakrzewski, V. G.; Voth, G. A.; Salvador, P.; Dannenberg, J. J.; Dapprich, S.; Daniels, A. D.; Farkas, O.; Foresman, J. B.; Ortiz, J. V.; Cioslowski, J.; Fox, D. J. *Gaussian 09*, revision D.01; Gaussian, Inc.: Wallingford, CT, 2009.

(41) (a) Kesharwani, M. K.; Brauer, B.; Martin, J. M. L. Frequency and Zero-Point Vibrational Energy Scale Factors for Double-Hybrid Density Functionals (and Other Selected Methods): Can Anharmonic Force Fields Be Avoided? *J. Phys. Chem. A* **2015**, *119*, 1701-1714. (b) Assefa, M. K.; Devera, J. L.; Brathwaite, A. D.; Mosley, J. D.; Duncan, M. A. Vibrational scaling factors for transition metal carbonyls. *Chem. Phys. Lett.* **2015**, *640*, 175-179.

5. "A COMPUTATIONAL INVESTIGATION OF STRUCTURE, ENERGETICS,
HOMEOMORPHIC AND CONFIGURATIONAL ISOMERIZATION, AND NMR
PROPERTIES OF MACROCYCLIC ALIPHATIC DIBRIDGEHEAD DIPHOSPHINES
EXHIBITING *IN/OUT* ISOMERISM

5.1. Introduction

The broad field of stereoisomerism features several prominent intersections with that of topology. For example, the Hückel and Möbius isomers of conjugated cycloalkenes (CH)_n (cyclobutadiene, benzene, etc.) were recognized in the 1960s and their electronic properties correlated to the preferred transition states of a variety of pericyclic reactions.¹ Since that time, a number of macrocyclic molecules with Möbius topologies and varying degrees of unsaturation have been isolated.²

Bicyclic compounds, which have played a central role in the development of organic chemistry,³ also present a fertile topological playground. They are characterized by two bridgehead atoms, which may be heteroatomic. A familiar example would be DABCO (**I**), a dibridgehead diamine comprised of six membered rings (Figure 5.1A). Cryptands such as **II** would be commonly encountered macrocyclic counterparts.⁴

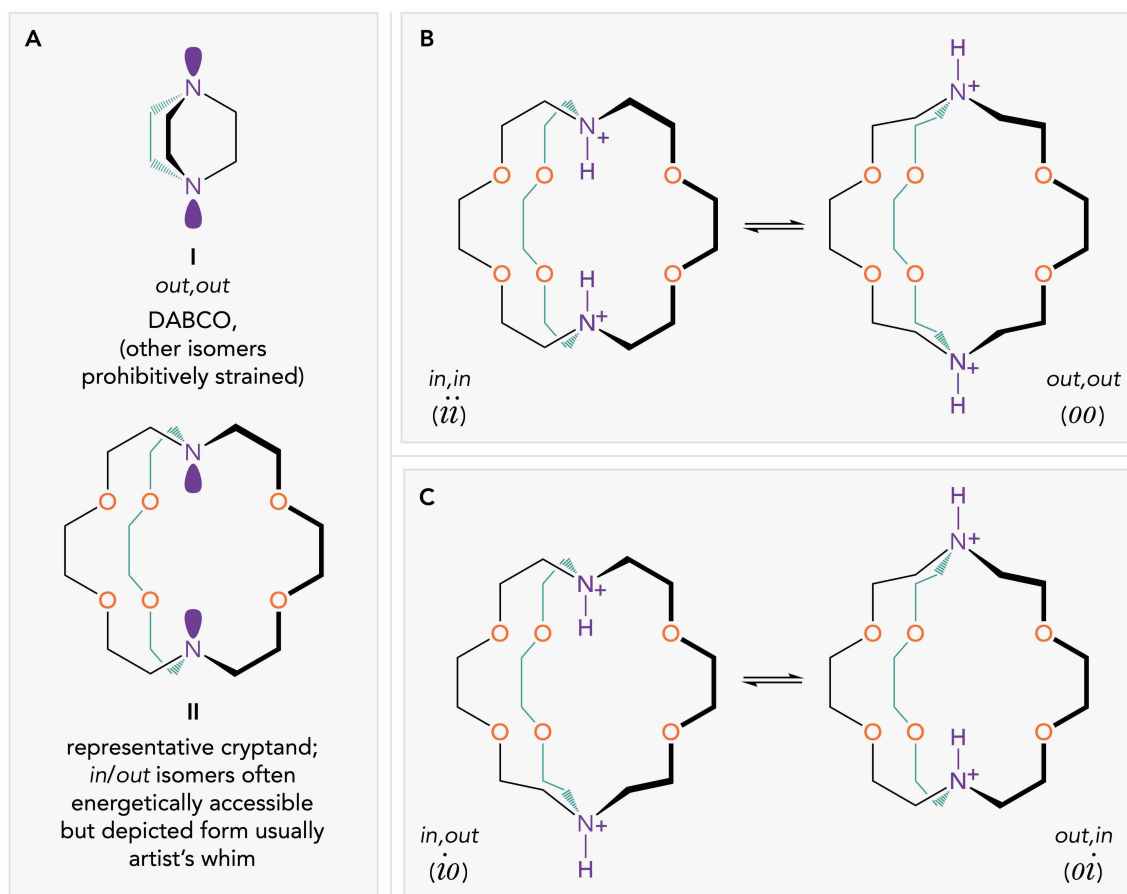


Figure 5.1 Representative dibridgehead diamines **I** and **II** (A), and principal diprotonated forms of **II** (B,C).

When the bridges connecting the bridgehead atoms become sufficiently long, *in,out* stereoisomerism becomes possible.⁵ For example, both nitrogen lone pairs in DABCO point out, and any other arrangement would be regarded as unreasonable. However, as subjects of investigation, *in,out* and *in,in* variants are no more sterically preposterous than Möbius benzene. In contrast, all lone pair orientations in **II** would seem energetically accessible, with the *in,in* isomer required for cryptate formation.

The principal limiting isomers are illustrated in Figure 5.1B,C using diprotonated **II**, thereby fixing the nitrogen stereochemistry. The first two represent *in,in* and *out,out*

isomers, and the next two *in,out* and *out,in* isomers. In order to connect the *in,in/out,out* and *in,out* manifolds, a bridgehead atom must invert. As introduced in Figure 5.1B,C, these isomers will henceforth be abbreviated *ii*, *oo*, *io*, and *oi*, respectively.

Of course, the bridgehead N–H groups can be replaced by any number of E–X moieties and the (CH₂)₂O(CH₂)₂O(CH₂)₂ bridges by any number of linkers. The (CH₂)_{*n*} linkers of interest in this study will be represented by curved lines as defined in Figure 5.2A, and abbreviations such as *ii* and *oo* further denoted *ii_n* and *oo_n*. Note that in the idealized *io* and *oi* isomers, there is no horizontal mirror plane, so in the absence of other phenomena separate NMR signals for the two E–X groups would be expected. Although these isomers are degenerate, this is lifted when the northern and southern hemispheres are not identical.

Ambiguities can arise in non-idealized conformations and topological subcategories introduced below.⁶ Accordingly, one can define a given E–X bridgehead as *in* or *out* based upon the angle of the E–E–X vector, as illustrated in Figure 5.2B.⁷ However, even this intuitive protocol is of questionable applicability to certain complex conformations of systems with longer linkers that resemble knotted "furballs".

With sufficiently long bridges, unusual and not very widely recognized dynamic behavior becomes possible, as implied by the equilibrium arrows in Figure 5.1B,C. Such molecules can literally be turned "inside out" — a process termed *homeomorphic isomerization*⁸ — by threading one bridge through the other two. This leads to apparent inversions of the bridgehead atoms, when in fact no significant geometric distortions are required.

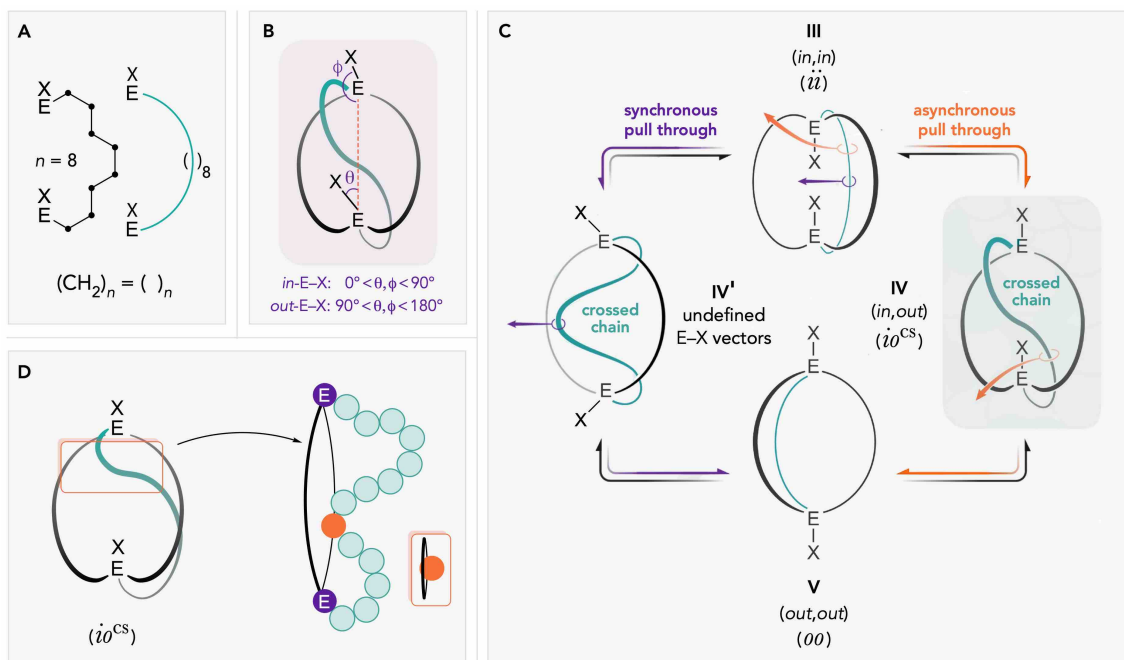


Figure 5.2 Conventions for representing methylene linkers $(\text{CH}_2)_n$ (**A**), criteria for assigning *in/out* orientations to E–X bridgeheads (**B**), homeomorphic isomerization illustrated for *ii* and *oo* isomers including the two limiting "crossed-chain" (*cs*) intermediates **IV** and **IV'** (**C**), and the onset of what would be classified as a crossed-chain species in analyses below (**D**; the "peekaboo" limit).

The threading process introduces additional topological features.⁷ As shown in Figure 5.2C for the *ii* isomer **III**, "grasping" the rear bridge near the top and "pulling through" the macrocycle defined by the other two bridges "flips" the upper E–X moiety, giving the *io* species **IV**. This has been termed a "crossed-chain" or "intertwined chain" isomer, and the former is henceforth abbreviated "*cs*". When the unique bridge or chain is now grasped near the bottom and pulled through, the lower E–X flips and the *oo* isomer **V** is realized. Alternatively, as shown in **III'**, this same bridge may be simultaneously grasped near both the top and bottom, such that pulling gives **V** without

the intermediacy of the io^{cs} species **IV**. These will be referred to as "asynchronous" and "synchronous" homeomorphic isomerizations, respectively.

The homeomorphic interconversion of io and oi isomers also requires cross-chained species, as illustrated later in this text. But despite all this attention to definition, in the course of examining thousands of conformations derived from calculations below, it became apparent that there are large numbers that are not so easily classified. For example, sometimes one bridge protrudes slightly through the macrocycle defined by the other two, without a large change in the relative orientations of the E–X vectors, as illustrated in Figure 5.2D. Thus, for certain statistical analyses, any such species is counted as a cs isomer.

Although a number of compounds could logically be assumed to be capable of homeomorphic isomerization, there have only been a handful of explicit demonstrations.⁹⁻¹¹ These can be divided into two categories: (1) the direct observation of both ii and oo forms and demonstration of an equilibrium,^{9d,10,11b} or (2) the observation of separate NMR signals for the E–X moieties of io isomers at lower temperatures, and their coalescence at higher temperatures.^{9a,b,e,10} The Habicher and Bauer groups have studied a number of fascinating macrocyclic dibridgehead diphosphorus compounds, and invoked the preceding types of processes to rationalize many NMR properties, but without realizing the limits (1) or (2).⁷ A parallel situation has recently been reported by Setaka with dibridgehead disilanes with $(CH_2)_{14}$ bridges.¹²

Our interest in this subject began with the unexpected conversion of the platinum complex *trans*-**1** shown in Figure 5.3 to the dibridgehead diphosphine $\text{P}((\text{CH}_2)_{14})_3\text{P}$ (*14-2*),^{8,13} in which each bridge consists of fourteen methylene groups. Due to the much higher pyramidal inversion barriers for phosphorus as opposed to nitrogen, it proved possible to isolate (after additional manipulations) pure samples of *io*₁₄-**2**, which underwent rapid homeomorphic isomerization as established by ³¹P NMR (ΔG^\ddagger (200 K) 8.5 kcal/mol, CH₂Cl₂). Similarly, the isomers *ii*₁₄-**2** and *oo*₁₄-**2** could be isolated in a rapidly interconverting 97:3 equilibrium mixture of *cis/trans*-**1** (ΔG^\ddagger (193 K) 10.4 kcal/mol, *oo*₁₄ → *ii*₁₄, toluene).

Later, homologs with longer bridges were synthesized,¹⁴ but studies of their dynamic properties remain in progress. Curiously, no compounds of the formula $\text{P}((\text{CH}_2)_n)_3\text{P}$ had been previously reported in which *n* exceeds four for any of the bridges. Furthermore, these diphosphines proved to be incredibly flexible as ligands, with **2** capable of adapting to both *trans* and *cis* positions, per *trans*-**1** (an *ii*_{*n*} adduct) and *cis*-**1** (an *oo*_{*n*} adduct) in Figure 5.3.¹⁵ As a result of this topological adaptability, they were furthermore effective as "container molecules" for transporting precious metal payloads from one aqueous phase to another.¹⁴

Surprisingly, there have been few modern computational investigations of *in/out* and/or homeomorphic isomerization in macrocyclic bicyclic compounds. From a historical standpoint, molecular mechanics and other early calculations can be noted.^{9b-e,16} Some recent studies have involved somewhat more specialized questions involving a

tetrathio dibridgehead diimine (Figure 5.4A).¹⁷ Others have involved systems with close relationships to the dibridgehead diphosphines in Figure 5.3, but involving (1) dibridgehead diorthoesters in which all three *in/out* orientations of the HC(OR)₃ units can be observed (Figure 5.4B),¹¹ or (2) dibridgehead disilanes where the computations were only intended as a preliminary screen of isomer energies (Figure 5.4C).¹²

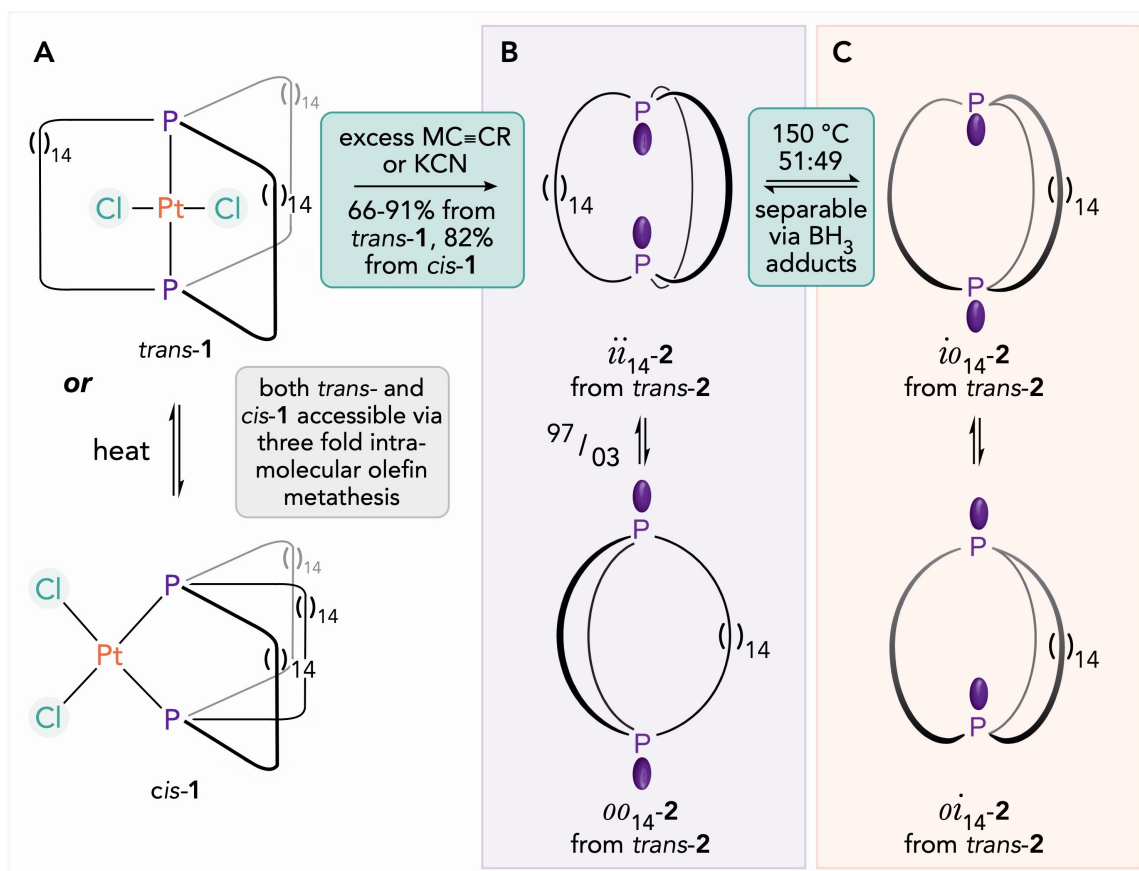


Figure 5.3 The first macrocyclic aliphatic dibridgehead diphosphines.

In view of the many general issues noted above that apply to dibridgehead diphosphines such as **2** and are difficult to address experimentally, especially in view of the degrees of conformational freedom. A detailed computational study has been undertaken that is singular in its breadth and depth. The questions addressed below include (1) what are the most stable conformations associated with each type of isomer? (2) what governs the energetic difference between isomers (structural, dispersive/steric, electronic effects, etc.)? (3) what are the most likely pathways for homeomorphic isomerization (synchronous or asynchronous)? (4) for which cage sizes is homeomorphic isomerism possible? (5) what is the nature of any competing pyramidal inversion process? (6) can spectroscopic properties of the isomers be computed to aid assignments? Parallel computations have been carried with several series of related compounds (dibridgehead diphosphine dioxides, dibridgehead diarsines, etc.) and these more specialized second-generation studies will be described separately.¹⁸

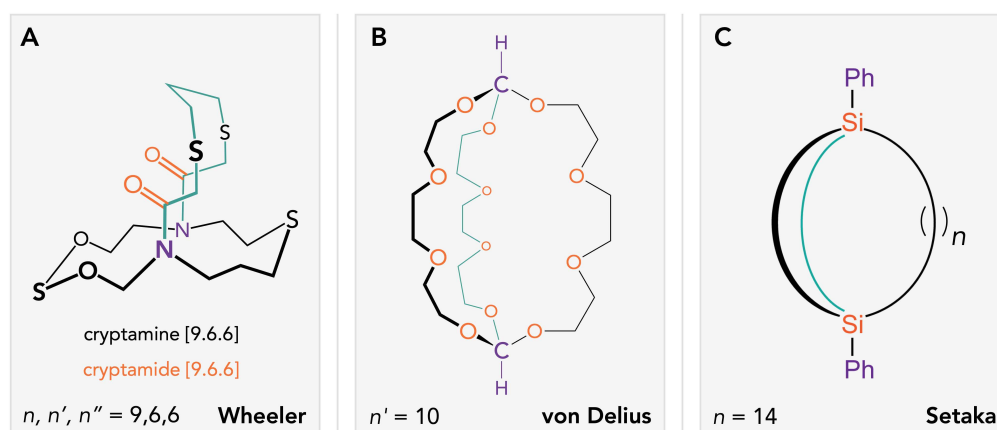


Figure 5.4 Related systems studied by the Wheeler (A), von Delius (B), and Setaka groups (C).

5.2. Results and Discussion

5.2.1. Preliminary comments

To facilitate analysis, the terms "small", "medium", and "large" will be refer to values of n of 4-6, 7-13, and 14-20, respectively. As is well appreciated from earlier studies of macrocyclic hydrocarbons,^{9c-d} DFT optimizations would not be ideal for searching for the lowest energy conformations, as the conformational landscape is too large, and it would be prohibitively expensive to run such long simulations.¹⁹ Any optimized structure would be biased by the trial structure provided, and objectives 1-3 enumerated above would be virtually impossible to answer by static computational techniques. Importantly, a protocol termed simulated annealing allows for the sampling of the conformational space.²⁰ Recall that for large molecules, such as proteins, conformational changes often require extended time scales (as slow as millisecond, 10^{-3} s), whereas small molecules, such as our macrocyclic species, change conformations on the nano to pico second time scale (10^{-9} to 10^{-12} s).²¹ It is essential to apply an appropriate time and temperature scale in probing the homeomorphic isomerization with simulated annealing (objective 3).

The computational workflow is summarized in Figure 5.5 (follow panels **A** through **J**). In brief, each ii_n and oo_n species was subjected to temperature oscillations (in intervals) while sampling the conformational space through simulated annealing (**A**). This resulted in 1500 sampled structures (**B**) per species. However, in the case of $n = 4-5$, many of these structures are not unique due to the small conformational space.²² The energies were minimized using force-field methods (**C**), and for each compound the 150

lowest energy conformations were extracted and analyzed. Following sorting **(D)** of these data, each could be classified as " ii_n ", " io_n ", " oo_n ", or " io_n^{CS} ". Further computational details are provided in Appendix C. In all Figures, these are given the symbols " I ", " \blacklozenge ", " O ", and " \times ", respectively. Selected species were then subjected to DFT computations with NMR analysis **(F)**, and/or compared to experimentally determined crystal structures **(G)**. Finally, components of the energies were analyzed and van der Waals forces and surface areas **(H)** were computed for a selection of species to investigate the structural aspects of the data. Dispersion interactions are important for these system, which should not come as a surprise since the stability of a simple n -alkane heavily depends on van der Waals forces, with the most stable conformation of n -pentane in the gas phase being a completely folded species.²³

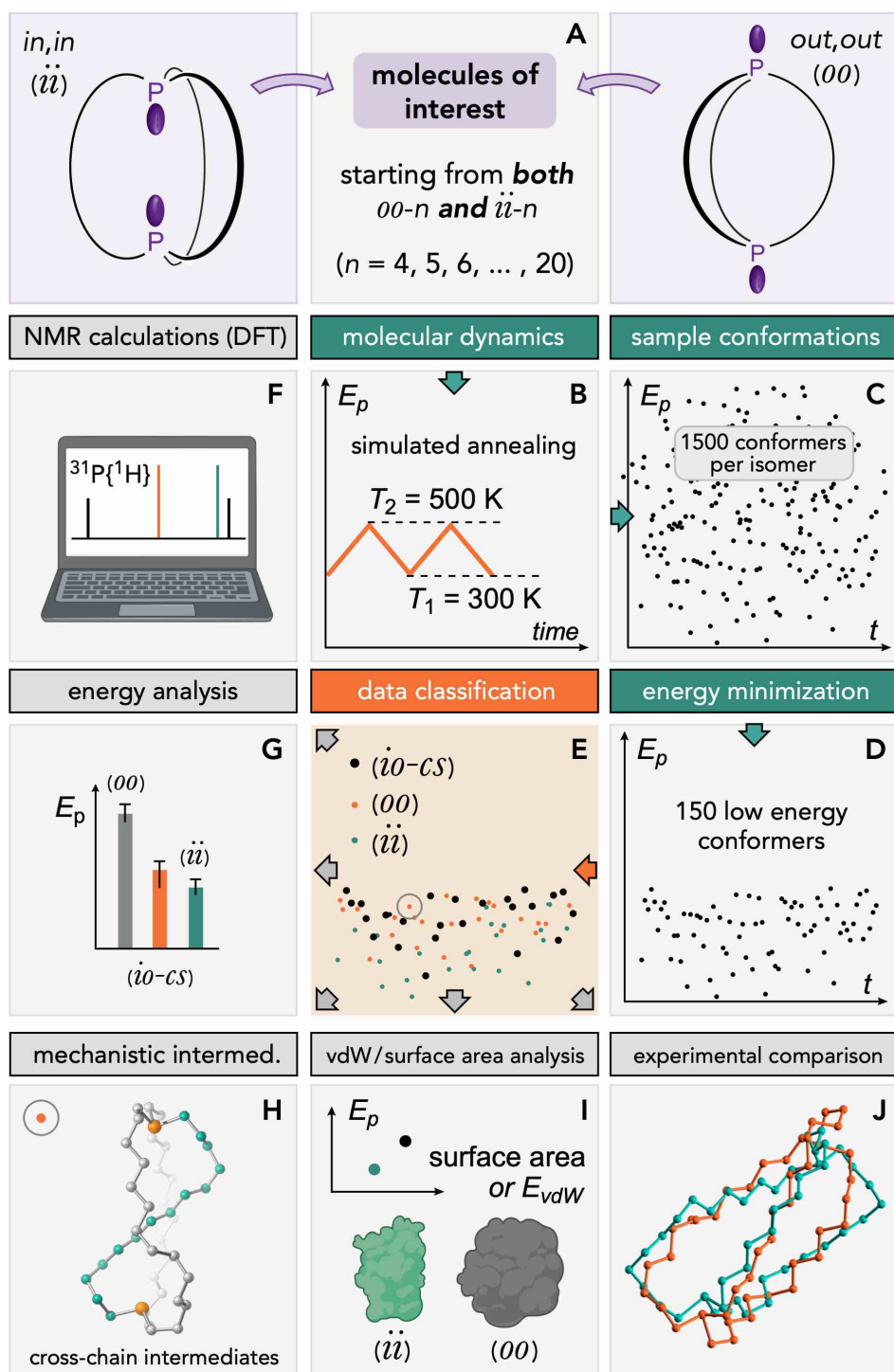


Figure 5.5 A pictorial overview of the calculation pipeline and workflow of this study.

5.2.2. Conformational stability of different dibridgehead diphosphine isomers

Simulated annealing computations^{20,22} were used to probe the relative stabilities of the isomers depicted in Figure 5.2 (**III-V**; i.e. ii_n , oo_n , io_n^{cs}) as a function of methylene chain length n ((CH₂)₄ through (CH₂)₂₀). Pursuant to a point of microscopic reversibility in the mechanistic section 5.2.7, it was important that these be carried out with both ii_n and oo_n species. Various aspects of the data are presented in Figure 5.6 to Figure 5.8 and Table 5.1. The cages with $n = 14$ are of special interest due to the availability of experimental data.¹⁰

The energies of the global minima for each of the ii_n and oo_n species ($n = 4-20$) are summarized in Table 5.1 and plotted in Figure 5.6A. The average energies of the entire ensembles (the 150 conformers) of ii_n and oo_n are depicted in Figure 5.6B, including "error" bars that correspond to one standard deviation of the mean data.²⁴ In addition, Boltzmann weighted energies of ii_n/oo_n species ($n = 5-20$) were computed at $T = 298.15$ K (Appendix C, Table 13.3). These data mimic those reported in Figure 5.6A. A lower energy indicates that the species is more stable. In general, the data show that the ii_n isomers are more stable than oo_n for all values of $n > 12$, as well as some lower values. In general, differences of under 2 kcal/mol would be considered less meaningful.

Importantly, the computations yielded thousands of local energy minima, each derived from thermal annealing over a period of time, the result of which is termed a frame (f). A given minimum is thereby designated $frame_{zzz}$. All of these had to be carefully examined. In favorable cases the energies were close to those of the global minima and are therefore important determinants of the relative isomer populations. To convey this complexity, Figure 5.7 plots the average energies of all 150 local minima for each isomer, as well as the standard deviations.

Table 5.1 Relative energies of ii_n vs. oo_n ($n = 5-20$) for the lowest energy structures.

cage size (n)	absolute energy of ii_n (E_p) (kcal/mol)	absolute energy of oo_n (E_p) (kcal/mol)	energy difference (kcal/mol)
4	N/A	—	—
5	70.7	96.8	26.1
6	40.4	60.2	19.8
7	30.1	42.8	12.7
8	32.3	31.5	-0.8
9	31.0	34.1	3.1
10	34.1	32.1	-2.0
11	33.7	37.5	3.8
12	35.0	35.5	0.5
13	32.5	38.4	5.9
14	34.6	40.2	5.6
15	32.9	43.8	10.9
16	33.1	42.6	9.5
17	34.5	46.9	12.4
18	34.2	46.0	11.8
19	32.9	48.5	15.6
20	36.3	44.8	8.5

The latter are generally quite small, indicating numerous structures clustered around a given energy. The basis for this energetic difference is explored in the next sections (5.2.3 to 5.2.6) but is foreshadowed in Figure 5.6 with the purple and orange boxes. With the smallest cage $(\text{CH}_2)_4$ no energetic minima could be detected for ii_4 . These immediately underwent pyramidal inversion to form oo_4 or io_4 . Additional structural features associated with these small cages will be discussed in section 5.2.4.

Applying Figure 5.5D, the molecular mechanics optimizations of the various sampled structures yield the total energy (E_{tot}) for each isomer. This energy represents the sum of the potential (E_{p}) and kinetic energy (E_{k}), with the former being the focus of this study. The potential energies are the sum of several energetic terms, for example E_{ang} (angular energy), E_{bond} (bond energy), E_{tors} (torsion energy), E_{inv} (inversion energy), and E_{vdW} (van der Waals energy).^{20,25}

One of the most obvious features of Figure 5.6B is that ii_n isomers are predicted to be more stable than oo_n isomers for $n > 13$. The origin of this preference is believed to be dispersion forces. Although the trend is not monotonic, as n increases above 13 the energetic preference for ii_n isomers increases. As the macrocycle size decreases, $n = 12$ is the first where the energies are comparable. The reason for the stability differences is discussed further in sections 5.2.3 to 5.2.6.

A complementary plot of the energetic data for ii_n and oo_n ($n = 6-20$) is given in Figure 5.7. Due to sheer amount of computational data generated by thermal annealing, statistical analyses are essential. Accordingly, each colored box in Figure 5.7 represents

50% of the data points, and specifically those in the middle 25-75% of the energy distributions, with the diamonds indicating the average energies. The technical expression for such boxes is the interquartile range (IQR).^{26,27} The black lines (whiskers) indicate the range at which the outliers are present.

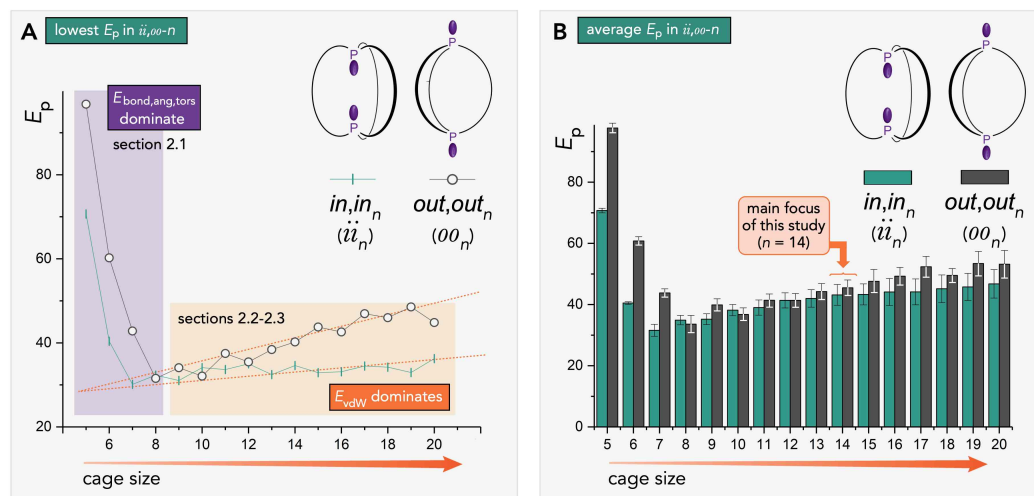


Figure 5.6 The relative energy (stability, potential energy, E_p) of the lowest energy species (panel A) for each cage size of ii_n vs. oo_n ($n = 4-20$). The average energy (potential energy, E_p) of all species of the ii_n and oo_n ($n = 4-20$) type from the annealing data set (panel B). Only energies of structures with the same n are directly comparable.

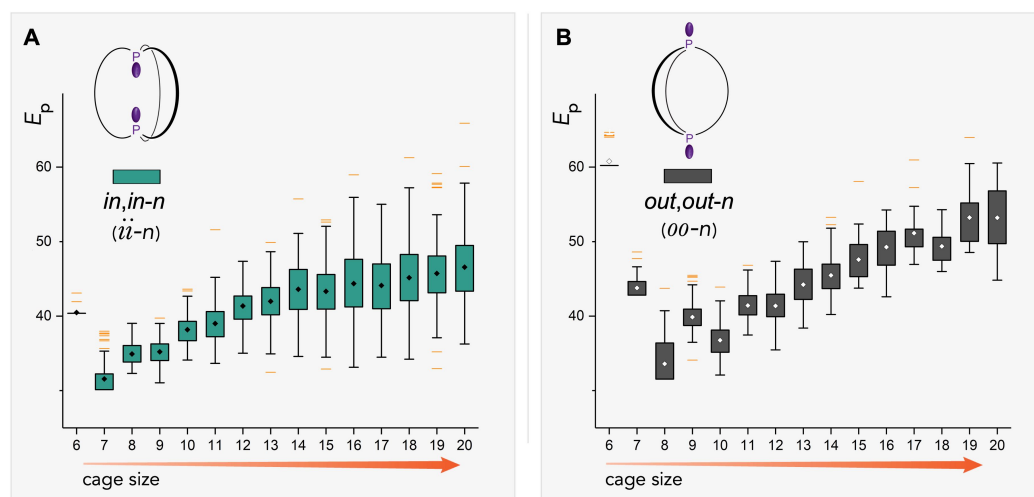


Figure 5.7 Whisker plots of the ii_n (A) and oo_n (B) for the $n = 6-20$ data sets showing the 25-75% energetic range as the average represented. The diamond symbol represents the average energy of each n data set. The horizontal solid black lines (whiskers) indicate the range of outliers (one standard deviation) and the horizontal orange lines indicate extreme values. Only energies of structures with the same n are directly comparable.

Plots in Figure 5.7 represent the data itself correctly. However, the threshold of what is qualified as an outlier and extreme value can be changed. Said differently, any data point within a factor of 1.5 of the IQR is termed an outlier, and if it exceeds this factor it is classified as an extreme point, and these are represented with horizontal orange lines.

In general, the statistically determined averaged energies are wider in the ii_n species than the oo_n species including the extreme values. Approximately the same number of extreme outliers is observed in both data sets.

An alternative approach to analyze the data is to count the frequency of different isomers in each trajectory, denoted $[ii_n]$ and $[oo_n]$. An equilibrium constant (K) for $ii_n \rightleftharpoons oo_n$ where $K = [oo_n]/[ii_n]$ can be estimated. The equilibrium constant is directly related to Gibbs energy (G) using the formula $\Delta G^\circ = -RT \cdot \ln K$. The general trend for $T = 298.15$ K yields $K < 1$ because $[ii_n] > [oo_n]$. Upon examination of the data using different ranges of n , several values of G can be computed. For $n = 4-20$, $G \approx 0.3$ kcal/mol as $K = 0.6$; $n = 12-20$, $G \approx 0.7$ kcal/mol, $K = 0.32$; $n = 14-20$, $G \approx 0.95$ kcal/mol, $K = 0.2$; $n = 14$, $G \approx 0.1$ kcal/mol, $K = 0.91$. Thus, the ii_n isomer is favored irrespective of n .

A more holistic view of the energetic data is provided in Figure 5.8C "which sums" all the individually sorted and energy minimized species. Figure 5.8A represents only the ii_n data whereas Figure 5.8B contains oo_n . These data contain two important lessons: (1) the conformational space of the macrobicyclic cages dramatically increases from the "smaller" cages ($n = 4-6$) to the "larger" ones ($n = 14-20$), as indicated by the

energetic spread in the data. This result is perhaps intuitive, but it is still necessary to determine as it provides a gauge for when a computational user should use static (e.g. DFT) vs. dynamic methods.²⁸ It was envisioned that the medium sized cages ($n = 7-12$) would exhibit a significant energetic "spread" along the z -axes of Figure 5.8A-C, but this was not observed. (2) For the small cages ($n = 4-6$) the conformational space is finite, and although the data have been collected running simulations starting from both ii and oo_n species, there is an abundance of ii_n isomers from $n = 14$ and beyond. The increased frequency of ii_{14-20} over oo_{14-20} isomers suggests that the ii_{14-20} isomer is energetically more stable than the oo_{14-20} isomer. The next sections (5.2.3 to 5.2.6) will outline the underlying basis for this latter observation. Figure 5.8C shows all the computed data for the dibridgehead diphosphines of $n = 4-20$ and has a new isomer, intermediate " io_n^{cs} ". These are depicted with an orange cross (×).

With respect to each structure generated by simulated annealing, the stereochemistry (ii_n , oo_n , io_n , etc.) was assigned by manual inspection. The directionality of the phosphorus lone pairs was considered first as summarized in Figure 5.8B. Chain crossing (cs) was assigned when one carbon atom (or even part of a carbon atom) from one $(CH_2)_n$ linker entered the circle spanned by the two remaining linkers, which represents a topologically relaxed criterion from that implied in Figure 5.2D. When n became very large (> 17), intricate and convoluted conformations could be observed. Sometimes these became essentially impossible to classify. Frame 95 of the trajectory

for ii_{20} is shown in Figure 5.8D, which serves to illustrate a topologically convoluted species, with strong resemblance to a hairball.

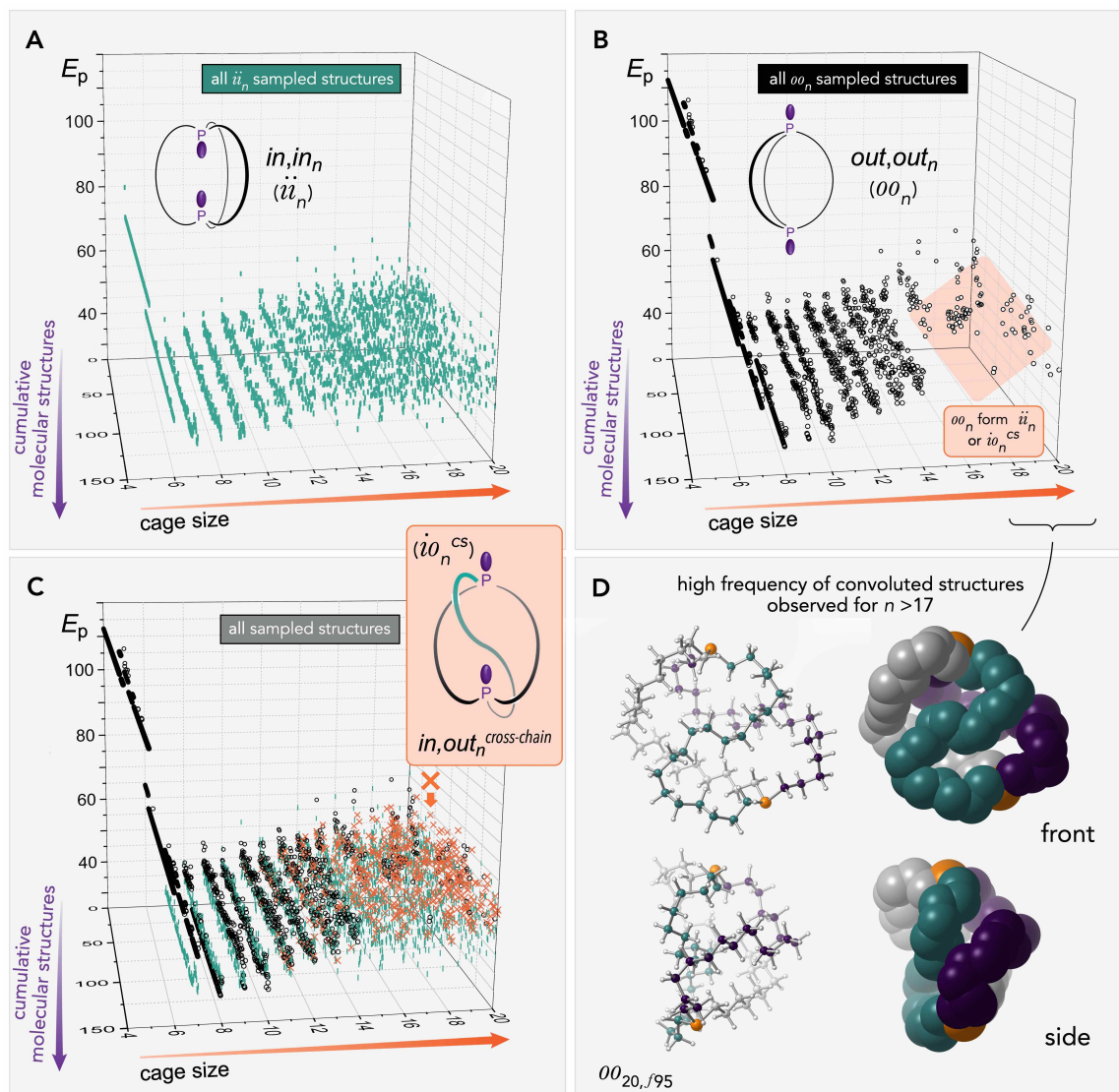


Figure 5.8 All data frames of ii_n ($n = 6-20$) and oo_n ($n = 4-20$). This three dimensional plot has the potential energy given on the y-axis, the annealing cycles (frames in ns) given on the z-axis and the cage size (n) on the x-axis. Only energies of structures with the same n are directly comparable.

5.2.3. Justification for the energetic differences between the *ii* and *oo* isomers.

As shown in the previous section, the computational data suggest that the *ii_n* ($n \geq 14$) isomers are more stable than the *oo_n* ($n \geq 14$) isomers. However, no analysis of the underlying reasons were provided. Experimental data supports that the *ii₁₄* isomer is more stable than *oo₁₄* through preliminary DFT calculations and ³¹P NMR spectra.¹⁰ Two distinct ³¹P NMR peaks were observed, as detailed in section 5.2.8. A ³¹P EXSY NMR experiment established that the species responsible for the two signals were in equilibrium ($\Delta G_{193K} = 1.33$ kcal/mol).

However, related species crystallized in the *oo₁₄* (or mixed *oo_{14,8}*) form as depicted in Figure 5.9C-F.^{10,29-31} The latter observation does not preclude *ii₁₄* species being the more stable species in solution as packing effects, which can impact the energetic profile, often accompany solid-state data. This is of particular relevance to this study considering the relatively small energetic differences computed for all involved species. The study herein considers only gas phase computed data and no guest-host assemblies have been examined. Guests can readily enter the *oo_n* species and is observed for several macrobicyclic cage types (Figure 5.9C,D,E).^{4,10,29-31}

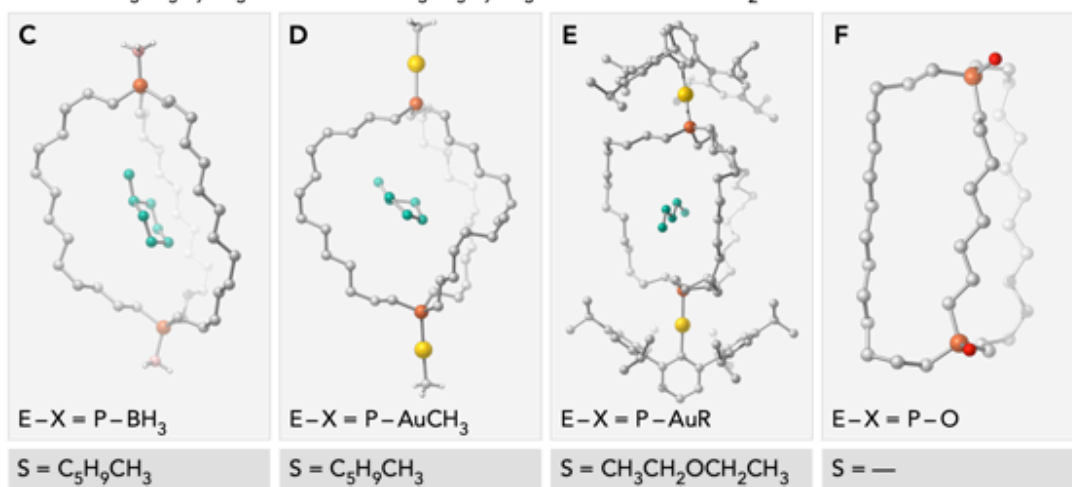
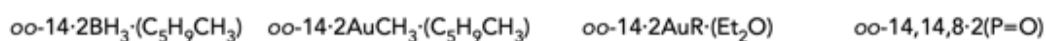
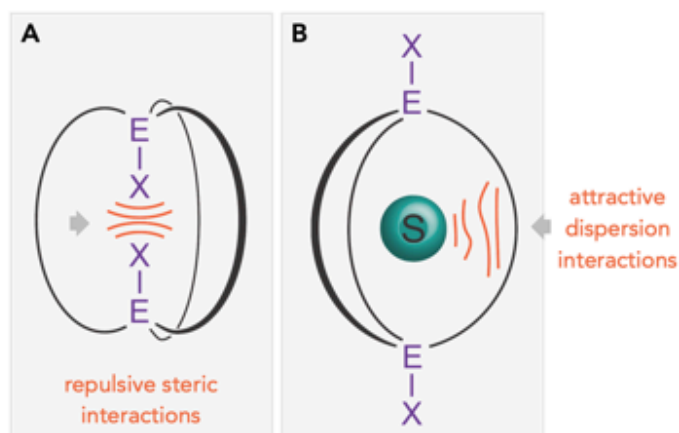


Figure 5.9 An illustration of the repulsive part (steric interactions) of the E_{vdW} term between two E-X groups of a ii_n species (**A**) whereas **B** shows the attractive dispersion forces between a solvent molecule (S) and a tether. Experimentally observed single crystal structures of macrobicyclic cages (**C-F**). All species crystallize in oo_n and several structures contain guest molecules in the assembly.^{10,29-31}

Another reason, which would favor the oo species in the experimentally observed crystal structures, is the steric bulk, which the endgroups introduce (Figure 5.9A). The computed phosphine in this study only bears lone pairs on the phosphine bridgeheads. The dibridgehead diphosphine dioxides shown in Figure 5.9F contain oxo endgroups (X-E = P-O) at each bridgehead. This imposes an increased steric "bulk" at each bridgehead in the ii_n isomer and any potential steric repulsion between the two

bridgeheads E-groups would be relieved in the *oo* conformation.³¹ A related system with a comparable steric footprint ($E = \text{BH}_3$) also crystallizes in the *oo* form.¹⁰ The largest steric demand among the species represented in Figure 5.9E belongs to a gold adduct which carries large aromatic mesitylene like endgroups at each bridgehead. Unsurprisingly, this crystallizes in the *oo* form.³⁰ A related system with AuCH_3 endgroups also crystallized in the *oo* form (Figure 5.8D).²⁹

A more detailed understanding of the relative energetic difference between the ii_n and oo_n isomers was sought. The energetic data of the semi-empirically optimized ii_{14} and oo_{14} structures were analyzed in greater detail with particular attention to the van der Waals (vdW) terms. As can already be inferred from the guest molecules that entered the macrobicyclic cage complexes in Figure 5.9, attractive dispersion forces are of great importance.^{10,29,31} The electronic structure of ii_n and oo_n are nearly identical when considering both have a near zero dipole moment. This is in stark contrast to for example the *in,out_n* "*io_n*" species that will be introduced fully in the next section (5.2.4). Thus, the relative stability difference must stem from purely vdW interactions or structural effects. Because vdW interactions increase in magnitude with large methylene tethers (within the chains) we will begin to examine any structural effects in small cages where the vdW forces would be minimal.

5.2.4. Structural effects.

Selected frames from the computational data related to ii_4 , oo_4 , and io_4 are shown in Figure 5.10. As noted earlier in the energetic section and in Figure 5.8A (see the x -axis in the "lane" for $n = 4$), oo_4 isomers (Figure 5.8B) but none of ii_4 were reported. An interesting phenomenon occurred for the smallest macrobicyclic cage compounds, which were examined in this study. When subjecting the oo_4 species to simulated annealing they remained in the oo_4 form (Figure 5.10, bottom). However, when repeating the procedure for ii_4 , these species immediately converted to new io_4 species, none of which contained crossed chains. This new isomer is depicted in the top right panel of Figure 5.10. The process of interconverting ii_4 (or oo_4) to io_4 is *pyramidal inversion*. There is no feasible pathway known to the authors that can transform ii_n (or oo_n) to io_n through a crossing chain intermediate. Said differently, the homeomorphic isomerization process cannot convert ii_n or oo_n into io_n . The pyramidal inversion mechanism vs. the homeomorphic isomerization pathway will be addressed in the mechanistic section 5.2.7.

The io_4 isomer has a computed P...P distance of 3.127 Å which is larger than the input geometry of ii_4 (2.678 Å), and the annealed oo_4 species measures 4.942 Å. There are dipolar interactions between the two phosphorous groups, which are directed towards each other in the ii_4 isomer. More importantly, basic metrics (r_{vdW}) account for why ii_4 would not be an unfeasible structure. The phosphorous r_{vdW} is 1.8 Å which results in narrow fit in io_4 , and the ii_4 species would be even more strained.³² Although

experimental data for white phosphorous (P_4) shows interatomic P–P distances of 2.1994(3) Å as determined by gas phase electron diffractometry,³³ the phosphorous atoms r_{vdW} of 1.8 Å leaves no "clearance".³² The largest energetic contributors to the high E_p include the angular (E_{ang}), torsion (E_{tors}), and bond (E_{bond}) energy terms in these small cage compounds.

When analyzing the different energy terms from the molecular mechanics optimizations of the different frames, it becomes apparent that the E_{ang} , E_{tors} , and E_{inv} in these small systems are what contributes in most to E_p , and thus these terms are critical in determining the stability of these small species. The van der Waals terms are essentially constant and these vary less than 0.7 kcal/mol for oo_4 and less than 2.2 kcal/mol for ii_4 (which becomes io_4). As a comparison, the difference of the highest and lowest E_{vdW} term for oo_{14} is 18.14 kcal/mol, and 19.13 kcal/mol for ii_{14} . In contrast, the bond energy E_{bond} , E_{ang} , and E_{tors} energy differences of the highest and lowest term are 1.4, 3.5, 2.3 kcal/mol for ii_4 , and 1.7, 3.5, 2.4 kcal/mol for oo_4 . Thus, the bond angle term and the torsion term dominate in both ii_4 and oo_4 , indicating a high degree of angular and torsional strain. For both ii_{14} and oo_{14} the E_{vdW} is the term with the greatest difference and these differences are > 8.0 kcal/mol larger than any other term.

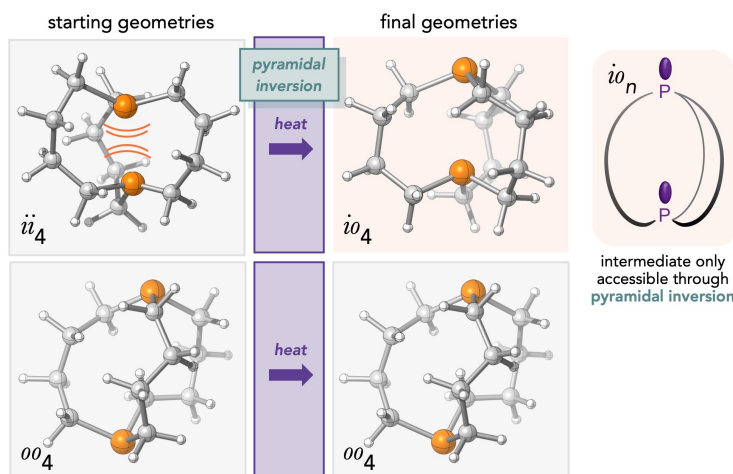


Figure 5.10 A selection of topologically different computed structures.

The energy differences of ii_n vs. oo_n as shown in Figure 5.8 for $n = 5, 6,$ and 7 were investigated further. Selected lower dibridgehead phosphine homologs have been reported in the literature including [3.3.3], [4.3.3], and [4.4.3].⁵ The structural terms ($E_{\text{bond}}, E_{\text{ang}}, E_{\text{tors}}$) and their percent contribution for selected cage sizes are presented in Table 5.2. The angular and torsional terms differ substantially in $n = 5$ and 6 , and are 6% larger in the ii_7 (red text, Table 5.2). On the contrary, in longer cages ($n = 14$) the difference in percent contribution of the structural terms are minute (blue text, Table 5.2). A negative value indicates that the energetic term is more favorable in the ii_n species than in the corresponding oo_n . Thus, from the data in Table 5.2, it can be concluded that for $n = 5$ and 6 , a torsional strain in the ii_n species is present, however, this is relieved for $n = 7$. The angular energy term is strongly negative for $n = 6$ which suggests that there is a stronger "angular strain" in oo than ii . The angular trend reverses for $n = 7$. The bonding term is comparatively small for all the species in Table 5.2.

Table 5.2 Percent difference in the contribution of individual terms of E_p for ii_n vs. oo_n of $n = 5-7$ and 14.
 A positive value indicates that the value for ii_n is greater than oo_n .

cage size (n)	E_{bond} (% of E_p)	E_{ang} (% of E_p)	E_{tors} (% of E_p)
5	-2	-2	+10
6	-1	-19	+18
7	-1	+6	-1
14	0	0	3

5.2.5. Qualitative analysis of the van der Waals effects (dispersion and sterics)

The van der Waals forces within each cage increase with larger n . Recall that simple alkanes will fold upon themselves, including the short chain in n -pentane. This folding process occurs in order to increase the attractive dispersion interactions.^{22,34} The key to understand why ii_{14} vs. oo_{14} is more stable is revealed by analyzing the E_{vdW} of the different species (of the entire ensemble), and by computing the surface areas (abbreviated "A2"), which the different conformations render. As noted in section 5.2.4, the E_{vdW} term dominates in larger systems, and fluctuates the most between conformers in both ii_{14} and the oo_{14} data set. This suggests that this term is the key to understanding stability differences between the ii_n and oo_n isomers.

A smaller void space in the center of the cage will result in a smaller surface area of any given structure. The smaller void will increase the dispersive (attractive) van der Waals interactions between each methylene linker within the given isomer. The overall E_{vdW} is positive because the atoms bonded to each other are inside their vdW radii. (Figure 5.11B). However, any two (or three) chains that approach each other will contribute attractive dispersion forces if the distance is appropriate. This can lower the E_{vdW} term, and even make it negative. Figure 5.11B shows the relationship of the attractive vdW interactions through the dispersion and the repulsive part. This structure energy relationship is illustrated clearly in the Figure 5.11A. Note that any discussed frame number from a given trajectory is abbreviated " f_{zzz} ", for example f_{12} for frame 12. Two different frames from the same trajectory of ii_{14} are shown in Figure 5.11. The top

frame (f_{12}) is one of the highest energy (E_p) isomers (with a large and positive E_{vdW}) in this trajectory whereas the frame shown in the bottom (f_{86}) has one of the lowest E_p (with a smaller, less positive E_{vdW}). Clearly, a qualitative analysis of these structures can be made by inspecting Figure 5.11. The larger computed A2 in f_{12} is created because the Connolly surface probe sphere³⁵ can enter the inner core, which is impossible in f_{86} . The void space in the center of f_{12} is apparent, as is the lack of one in f_{86} . The computed E_{vdW} is -0.2 kcal/mol for f_{86} and 14.7 for f_{12} , illustrating a stark contrast between the two. The computed solvent-accessible surface area, using a probe with a 4.0 Å radius, yields 560 Å² for f_{86} whereas f_{12} is 727 Å². A deeper analysis of the computed A2 is given in the next paragraph (shown in Figure 5.12) featuring all isomers (frames) in the ii_{14} and oo_{14} trajectories. Thus, a quantitative analysis of the data including a statistical treatment is used to verify whether the qualitative observations above still hold true, and is given in section 5.2.5.

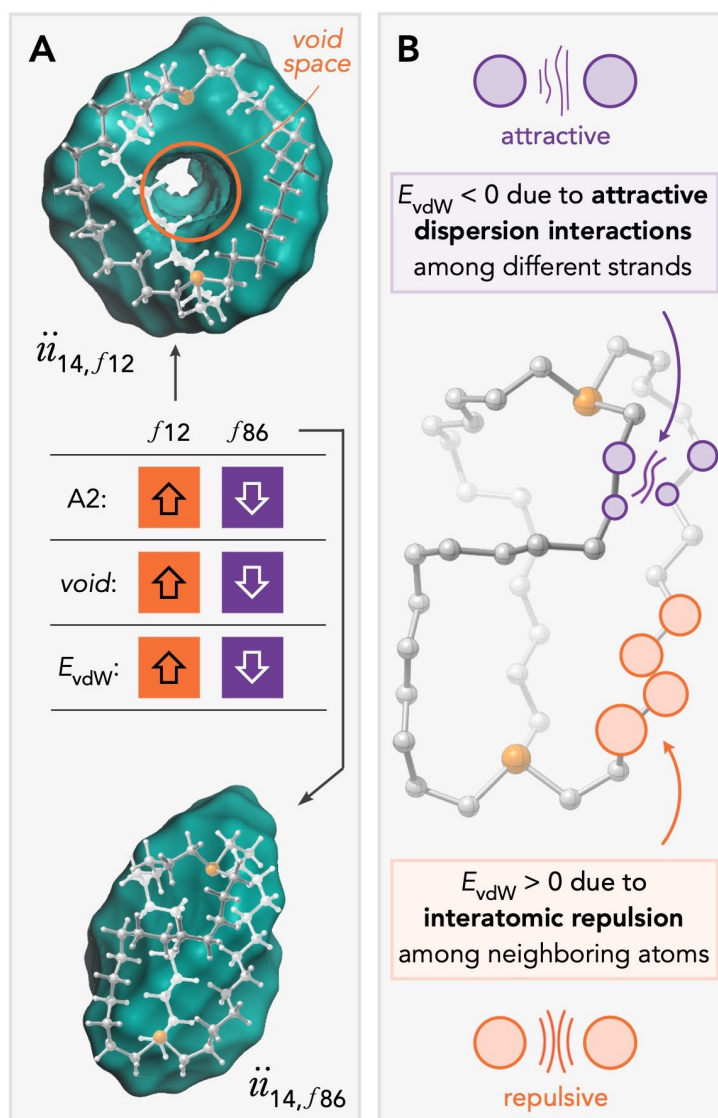


Figure 5.11 Correlation between surface area, void space, and dispersion interactions (part of E_{vdW}) for a topologically relevant $ii_{14,f12}$ (top) and $ii_{14,f86}$ (bottom).

Before further analyzing the computed surfaces areas for all the frames of ii_{14} and oo_{14} in the preceding sections, a pictorial description is provided of how the solvent-accessible surfaces areas are computed. The Connolly molecular surface, also termed solvent excluded surface, is a contact surface^{35b} that is created when a spherical probe

with a defined probe radius representing the solvent, is rolled over the entire molecular structure. Connolly surface areas were computed for each ii_{14} and oo_{14} conformation with a Connolly probe radius of 4.0 Å.³⁵ The choice of Connolly probe sphere diameter was made to approximate a small solvent molecule. The kinetic diameter of dichloromethane is 3.3 Å and the Lennard-Jones molecular diameter is 4.7 Å.³⁶ Thus, an average of 4.0 Å was chosen. A depiction of this concept is provided in Figure 5.12. A larger surface area implies larger void space (empty volume within the cage), which in turn implies less dispersion interactions because each "strand" of the diphosphine cage will lose the ability to attractively interact with another due to the increased distance between each strand. For any two isomers a larger Connolly surface implies a larger void space because the probe sphere can only enter the inside of the cages if there is enough void space.

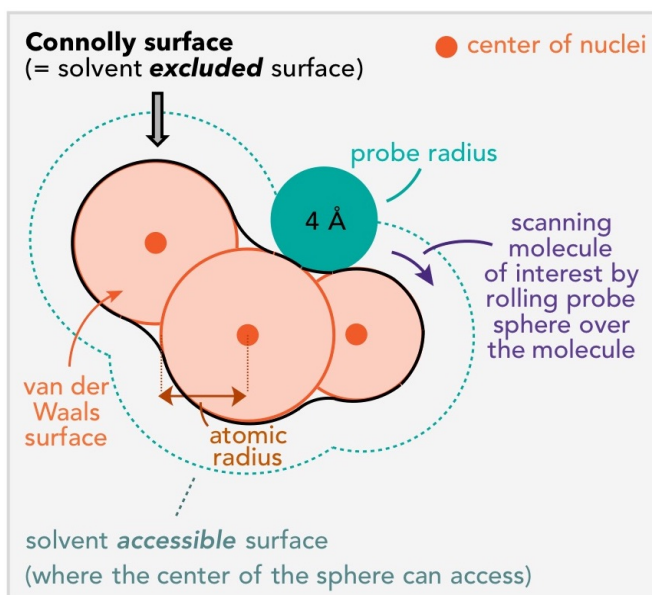


Figure 5.12 A rendition of a Connolly surface onto an arbitrary three-atom molecule.

5.2.6. Quantitative analysis of the van der Waals effects (dispersion and sterics)

Moving from the qualitative model provided in section 5.2.5 to an analysis including statistical treatments of all ii_{14} and oo_{14} data allows for the precise understanding of the surface-area-to- E_{vdW} energy relationship (Figure 5.13A,B).

A strong correlation as shown in Figure 5.13C,D is apparent after analyzing all of the frames from the oo_{14} and ii_{14} trajectories. The solvent-accessible surface areas were computed for each frame and were then plotted as a histogram (Figure 5.13A). These data show that the largest frequency of ii_{14} species have an A2 slightly below 600 \AA^2 whereas oo_{14} is ca. 660 \AA^2 . The two curves in the histogram and the computed mean average shown in Figure 5.13B suggest that ii_{14} species have a statistically smaller A2 compared to oo_{14} , with an average volume of 620.2 \AA^2 vs. 650.7 \AA^2 . Furthermore, it is apparent that there are more oo_{14} isomers with higher A2 (black circles) compared to the frequency of ii_{14} (green vertical lines) by inspecting Figure 5.13B.

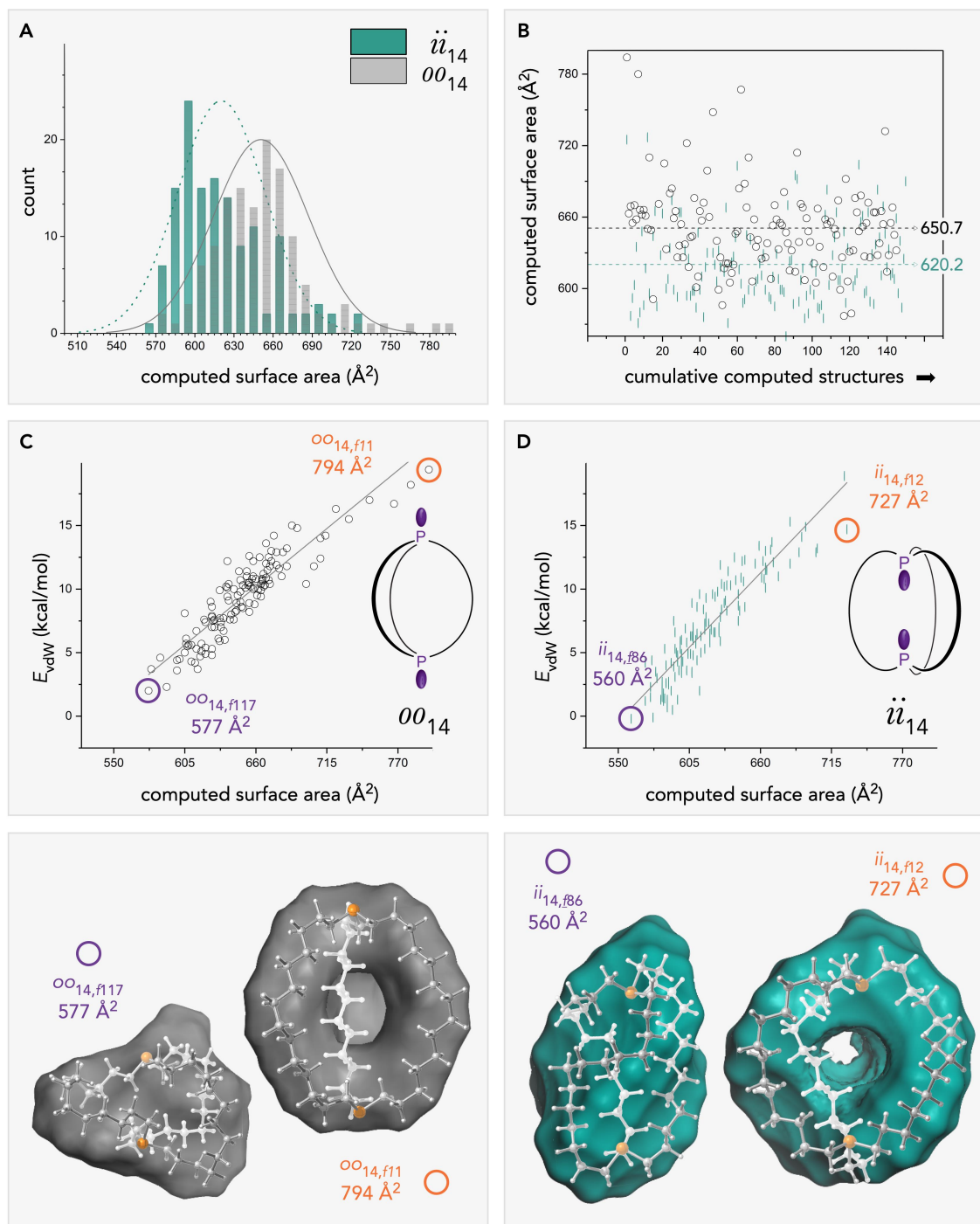


Figure 5.13 The distribution of computed solvent-accessible surface areas (A²) of ii_{14} and oo_{14} (A), and all ii_{14}/oo_{14} species as a function of the computed A² (B). The computed A² as a function of E_{vdW} for all ii_{14} and oo_{14} species (C, D) with linear regression analysis.

Next, the correlation between the A2 vs. E_{vdW} term was investigated and the best fit was rendered through a linear model Figure 5.13C-D. The equation $y = 0.083x - 44.7$ defines the line for oo_{14} isomers in Figure 5.13C whereas the one line for ii_{14} isomers in Figure 5.13D is described by $y = 0.106x - 59.8$. Both equations had an adjusted R^2 of 83% indicating a strong correlation.

Two selected structures with diametrically different A2 and E_{vdW} are displayed. Much like the species in section 5.2.5, which are hollow and have a larger "inflated" cage structure, this generates a large surface area which reduces the attractive (negative) contribution of the E_{vdW} term, which in turn increases this value, and raises E_p . This is true for both the ii_{14} and oo_{14} samples. The opposite also holds true, a compact cage structure with a small void space minimizes A2, which increases the attractive dispersion interactions between the tethers. This lowers the overall E_{vdW} term and ultimately E_p .

Other types of correlations were investigated, for example, the E_{vdW} vs. E_p . However, these relationships were more complex and no linear correlation could be established. The reason for this low correlation is likely due to the fact that the potential energy is a sum of the multiple energetic terms. Although the E_{vdW} term is dominant in the larger cages, the contribution from the remaining terms precludes a linear relationship being established between E_{vdW} and E_p . Because molecular volumes are also rendered during a Connolly surface calculation, attempted correlations of the molecular volume (A3) and E_{vdW} for ii_{14} and oo_{14} were made. However, no strong linear correlation was found between A3 and E_{vdW} of either species as indicated by

small R^2 values of 0.75 (ii_{14}) and 0.42 (oo_{14}), respectively. Thus, the surface area has the strongest linear correlation compared to any other metric and as such A3 will not be further addressed.

After analyzing the larger body of data it becomes apparent that there is a strong surface-area-to- E_{vdW} relationship, and with statistical metrics to support this fact. However, it is still interesting to study the potential energy of the ii_{14} and oo_{14} trajectories ($= E_p$ on the y-axis), and select frames that have extreme E_p values to see if additional conclusions can be made after inspecting the topology of these structures. When inspecting the highest E_p frames in each data set, common patterns emerged (Figure 5.14A,B). Upon analysis of the E_{vdW} , high energy species often contained a void space associated with a larger A2 (for instance $ii_{14,f1}$ with 725 \AA^2 , and $oo_{14,f59}$ with 646 \AA^2). In contrast, the lowest energy E_p frames only have $ii_{14,f146}$ 596 \AA^2 , and $oo_{14,f55}$ with 621 \AA^2 , a difference of 129 and 25 \AA^2 , respectively. Structurally this is manifested in the lack of void space in the low energy frames as well as a much more compressed structure. This result leads to the lowering of the E_{vdW} terms due to the attractive dispersive interactions between the strands within the low energy cages. For example, the lowest energy E_p frames only have E_{vdW} terms of 1.3 kcal/mol ($ii_{14,f146}$) and 5.4 kcal/mol ($oo_{14,f55}$), whereas the high-energy frames have much higher E_{vdW} terms, 18.9 kcal/mol ($ii_{14,f1}$) and 9.5 kcal/mol ($oo_{14,f59}$), respectively. This represents differences of 17.6 and 4.5 kcal/mol for the respective set.

The last item to notice in Figure 5.14 are the red crosses (×) which denote the *in,out* intermediate for the homeomorphic isomerization process. This *in,out* intermediate contains a cross-chain (io_n^{CS}) and is thus distinct from the other *in,out* species (io_n) which lacked the crossing chain. For example, io_4 as shown in the top right panel of Figure 5.10, an intermediate that is attained only after a pyramidal inversion event. The cross-chain intermediates will be discussed in further detail in the mechanistic section 5.2.7.

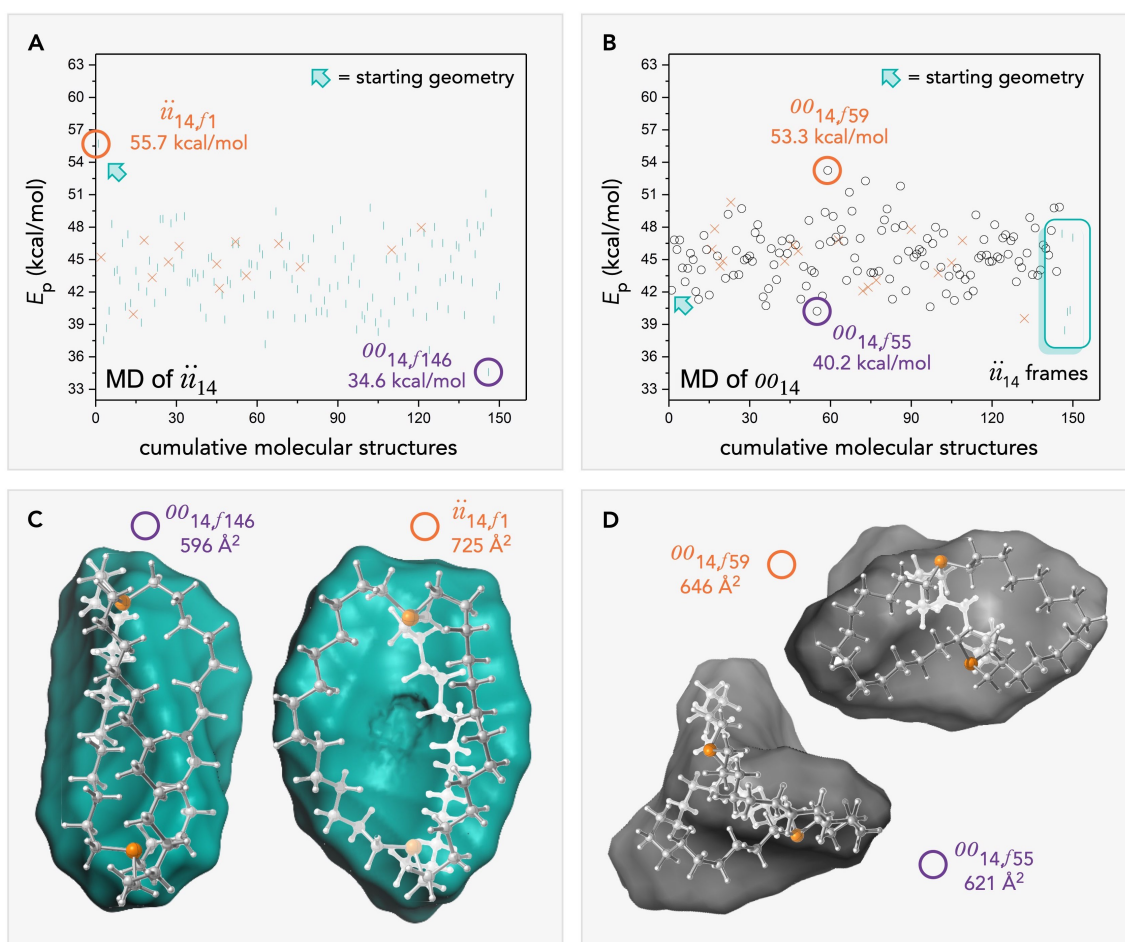


Figure 5.14 The two trajectories of ii_{14} and oo_{14} a function of potential energy (E_p) with selected frames depicted.

5.2.7. Mechanistic considerations (pathway, intermediates)

Up to this point the ii_n and oo_n isomers have been our main focus, however, there are additional isomers.

After simulated annealing of a small ii_4 cage the io_4 (\blacklozenge) isomer was rendered. This species was introduced in section 5.2.4 and depicted in Figure 5.10 and lacked a crossing chain. This type of intermediate can only be obtained through pyramidal inversion at one bridgehead. The computed inversion barrier for acyclic phosphines is large, ca. 30 kcal/mol.³⁷

A transition state calculation (DFT, QST3 algorithm) was nevertheless run in order to probe whether a strained cage with $n = 7$ could influence the barrier. It had very little effect on the inversion barrier. Indeed, as shown in Figure 5.15A, the computed barriers were 42.0 kcal/mol (**TS2**) for an acyclic model compound, trimethyl phosphine. A modestly lower barrier (**TS1**) of 38.5 kcal/mol was rendered when converting ii_7 into io_7 via **TS2**. Note that only one bridgehead atom is inverted (the top phosphorous atom of ii_7 in Figure 5.15) and that the phosphorus atoms in both the computed species are sp^2 hybridized. A cage size of $n = 7$ was chosen in order to avoid inducing too much angular or torsional strain into the system. Furthermore this smaller model is more computationally cost effective than an $n = 14$ analogue. This data is an important part in our mechanistic understanding of the interconversion process shown in Figure 5.2. Thus, if the ii_n (**III**) or oo_n (**V**) species are equilibrating the io_n isomer cannot be accessed unless pyramidal inversion occurs, which would require high temperatures.

Figure 5.15B simply details that both ii_n and oo_n can be converted to io_n with one of the bridgeheads inverting. However, it must not be forgotten that **VII** (same type as produced in the process depicted in Figure 5.15A upon simulated annealing) can undergo the homeomorphic isomerization itself (if n is sufficiently large). This results in a somewhat inverted relationship with regards to which species feature cross-chains, as illustrated in Figure 5.2B. When **VII** undergoes simulated annealing, two new isomers (**VI**, **VIII**) are formed, and both contain cross-chains.

These two new isomers have both of the lone pairs either pointing outwards (oo_n^{cs}) or inwards (ii_n^{cs}). A more in-depth analysis of ii_n^{cs} (**VI**) and oo_n^{cs} (**VIII**) is omitted because ii_n (**III**) or oo_n (**V**) needs to first undergo pyramidal inversion to access **VIII**. Thus, **VI** and **VIII** are not the primary focus of this study. However, all io_n structures for $n = 4, 5, 6, 7, \dots, 20$ were subjected to the same simulated annealing heating conditions as shown in Figure 5.8 for the ii_n and oo_n species. Interestingly, isomers of the type **VI** and **VIII** both formed. However, in contrast to the earlier computed data in Figure 5.8 where the order of relative stability was $ii_n > io_n^{cs} > oo_n$, the oo_n^{cs} are now more stable than ii_n^{cs} , which can have E–X groups in close proximity, and occur more frequently in the data set. The reason for the smaller frequency of **VI** is probably due to increased sterics within the cage, analogous to Figure 5.9A but with the addition of a crossing chain.

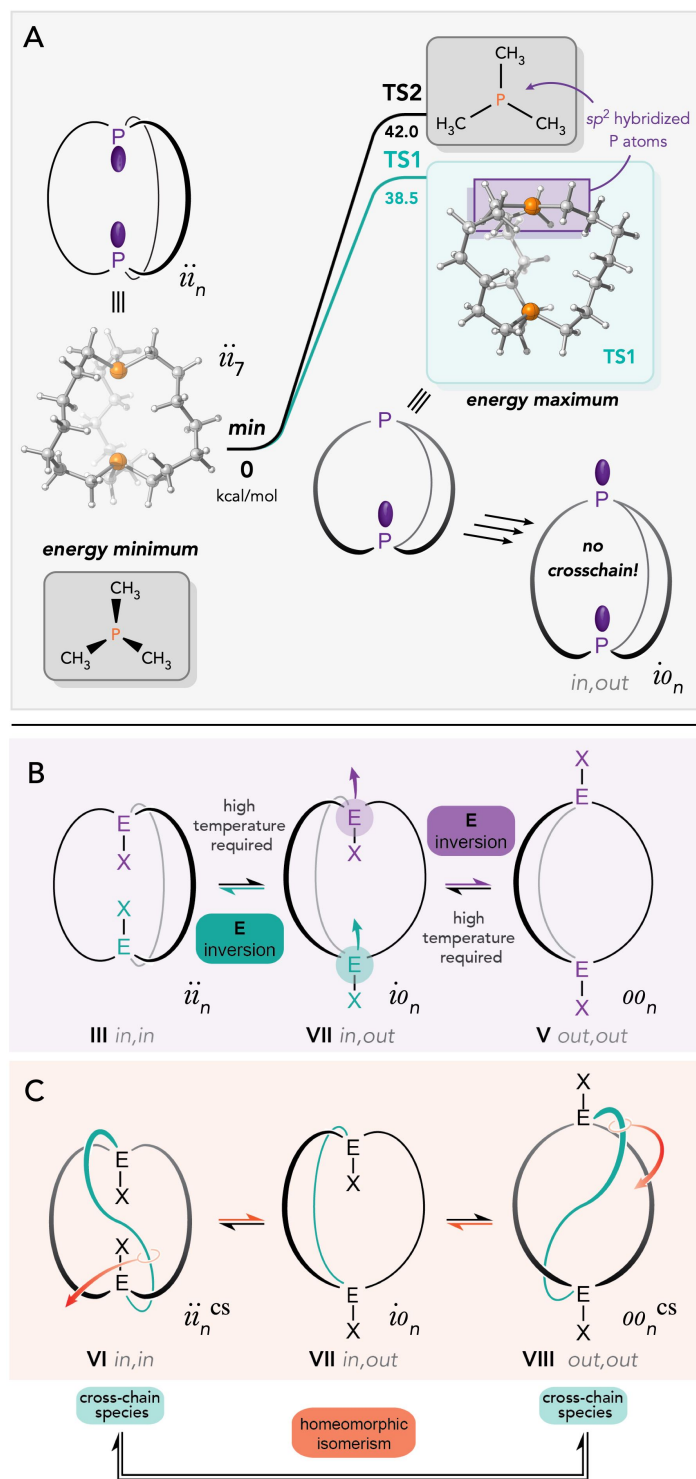


Figure 5.15 Probing the inversion barrier of a macrobicyclic phosphine ($n = 7$) from ii_7 vs. an acyclic trimethyl phosphine model compound (A). The io_n can undergo inversion to form ii_n or oo_n (B). The io_n species can have a chain threading through to form two new species with crossing chains (ii_n^{cs} and oo_n^{cs}) (C).

The intermediate that characterizes the homeomorphic mechanism will be examined in detail. Let us return to the isomer species **IV** presented in Figure 5.2 which contains a crossing-chain and with both E–X groups (lone pairs) aligned. **IV** is a reasonable intermediate if a sample of phosphines oo_{14} or ii_{14} are prepared.

IV represents one of the three possible cross-chain "cs" intermediates in our data. The other two were discussed in a preceding section (**VI**, **VIII**) and will not be treated in further detail because a pyramidal inversion process is necessitated, assuming that the origin is a real sample of oo_{14} or ii_{14} . Intermediates **VI** and **VIII** arise from two different pathways, and irrespective of whether the basis is ii_n or oo_n a pyramidal inversion of one bridgehead atom must always occur. Both of these scenarios are depicted in the bottom panel of Figure 5.15, which summarizes all plausible intermediates in one panel, except **IV**.

A perhaps fine yet important detail is that the homeomorphic process is the complete inversion of *both* lone pairs or E–X groups, and nothing "half" thereof. Thus, it is the process of interconverting $V \rightleftharpoons III$ but neither of $V \rightleftharpoons IV$ or $III \rightleftharpoons IV$.

Now returning to **IV**, note that one of the macrocycles of **III** in Figure 5.2 was "pulled through" which "turned" one bridgehead "inside out". It is equally possible to turn the other bridgehead of **V** "outside in", which reverses the process. Both these scenarios lead to **IV** as the mechanistic intermediate and **IV** has an *in,out* or "io" configuration of the lone pairs.

If one allows a bridgehead of the regular ii_n or oo_n species to invert (via a high barrier pyramidal inversion) a non-threaded io_n isomer (**VII**) can form. This intermediate

was observed in our data when heating a small ii_4 cage in the simulated annealing. If one of the non-threaded io_n species **VII** has one strand pulled through the ring spanned by the remaining two tethers, **VI** or **VIII** can be formed. We will not attempt to distinguish the " oo_n^{CS} " or " ii_n^{CS} " form (**VI**, **VIII**) of the cross-chain isomer family from one with " io_n^{CS} " when classifying the data, i.e. these are all classified as a "cross-chain" species. This is done because the focus of interest in this study is the io_n^{CS} intermediate **IV** shown in Figure 5.16. Furthermore, the population of oo_n^{CS} and ii_n^{CS} is never mixed or observed in the same data set as io_n^{CS} .

Two possible pathways were envisioned, one being synchronous (Figure 5.16-**III**, follow purple arrows) and the other asynchronous (Figure 5.16-**IV**, follow orange arrows). Intermediate **IV** has a crossing chain that is pulled halfway through in an *asynchronous* manner and all the generated data in this manuscript, irrespective of cage size, supports **IV**. No structures with topology similar to that of **III** were ever observed. Attempts to model this specific motion were made and a "hand made" model was constructed. As shown in Figure 5.17**D** a steric "knot" is formed in the center, which is presumed to be the reason this pathway is not *followed*. Perhaps for much greater values of n this intermediate can be observed. The asynchronous pathway allows for less steric interactions (Figure 5.17**C**) in the crossing event as compared to the synchronous pathway. Experimentally, the asynchronous structure is also observed as shown in Figure 5.17**E-F**. All computationally harvested structures are of the same kind, and one computed structure is illustrated in Figure 5.17**C**.

The energetic data of **IV** (io_n^{CS}) is shown in Figure 5.17**B**, and the average potential energy of io_n^{CS} lies between that of ii_n and oo_n where $n = 5-20$ for ii_n/oo_n and 11-20 for io_n^{CS} . This represents the overall average of all E_p data, however, $n = 4$ is excluded as to not skew the data. As can be noted from Figure 5.17**A** (see the gray arrow), this type of intermediate only becomes observable in cage sizes of $n = 12$ or above. Most of the cross-chained species for $n = 12$ and 13 are only what was referred to in the earlier section as "peekaboo" cross-chain structure. All analyzed cross-chain intermediates were of the type shown in Figure 5.17**C**, i.e. either partly crossed through or halfway through, consistent with the crystallized structures depicted in Figure 5.17**E,F**. The fully threaded cross-chain intermediates are observable from $n = 14$ and up.

Lastly, in order to probe for which cage sizes (n) the homeomorphic pathway is feasible, additional trajectories were performed (e.g. Figure 5.17**A,B**). Cross-chain structures for $n = 12$ were observed but none of them had the chain halfway through and none of them resulted in a full conversion (i.e. $ii_{12} \rightleftharpoons oo_{12}$) when starting from ii_{12} or oo_{12} . Therefore, extended trajectories for $n = 13$ did not result in fully threaded io_n^{CS} , only for $n \geq 14$ (one depicted in Figure 5.17**A**, f88). Only partially "crossed" chains were observed, and none of the type shown in Figure 5.17**B**. Further, no isomer change was observed from ii_{13} to oo_{13} , or vice versa (Figure 5.17**A,B**, respectively). However, consistent with other cage types, the frequency of io_n^{CS} species in the oo_{13} trajectory is increased compared to ii_{13} , presumably because they are closer in potential energy.

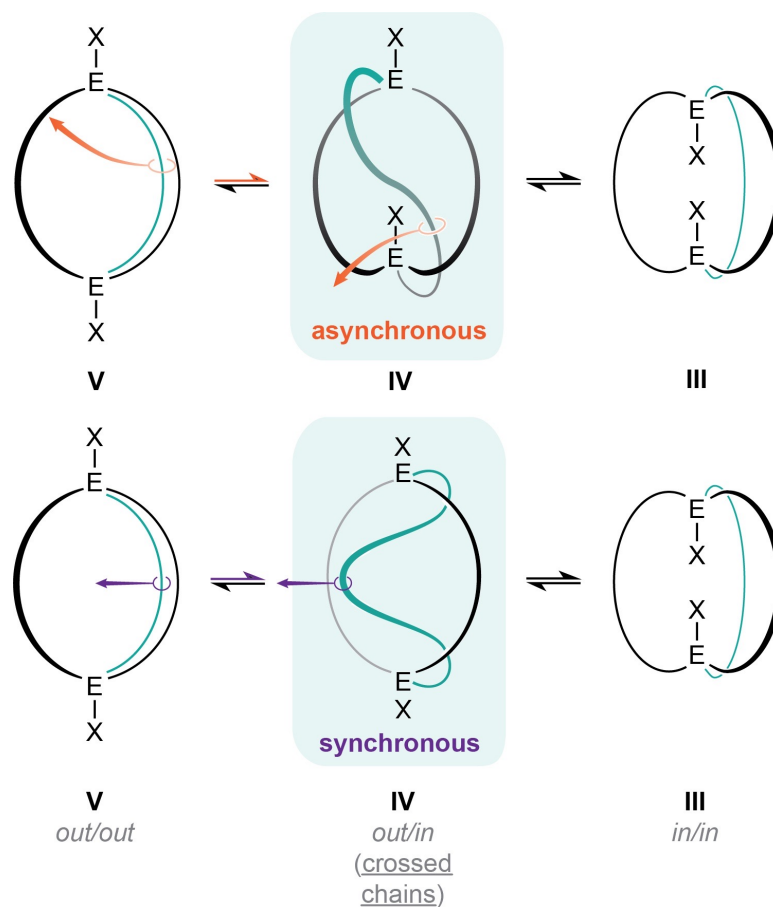


Figure 5.16 Synchronicity of the homeomorphic pathway. Note that the E-X bond in the left center panel showing **IV** have been omitted as both bridgehead groups would need to have a directionality facing the reader, which is difficult to depict.

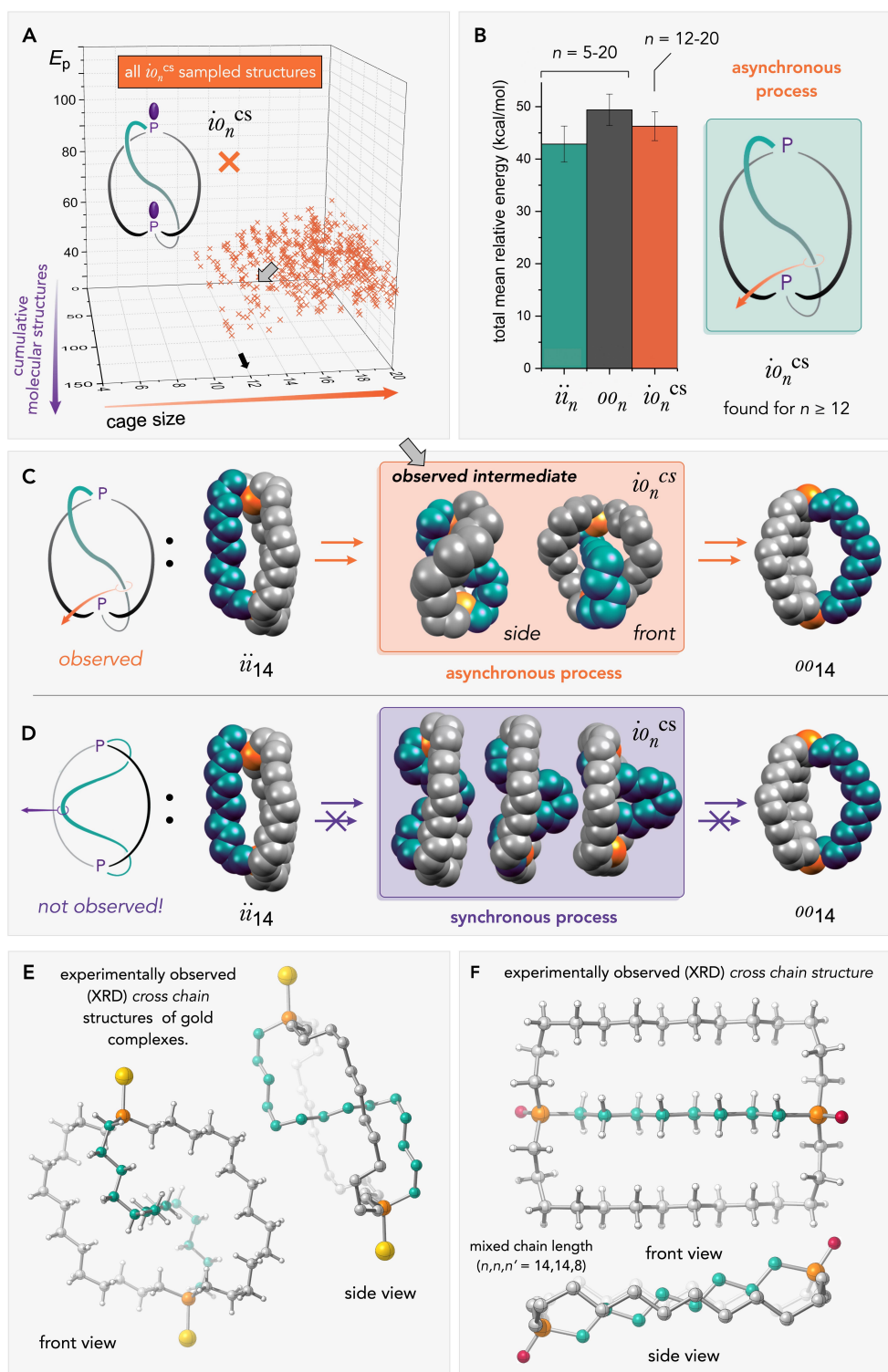


Figure 5.17 Cross-chain intermediates as a function of cage size (A), and the average energies of the ii_n , oo_n , and $i0_n^{CS}$ isomers. The two hypothesized pathways with different synchronicity for interconverting ii_{14} and oo_{14} (C and D). Experimentally characterized cross-chain species (E,F).

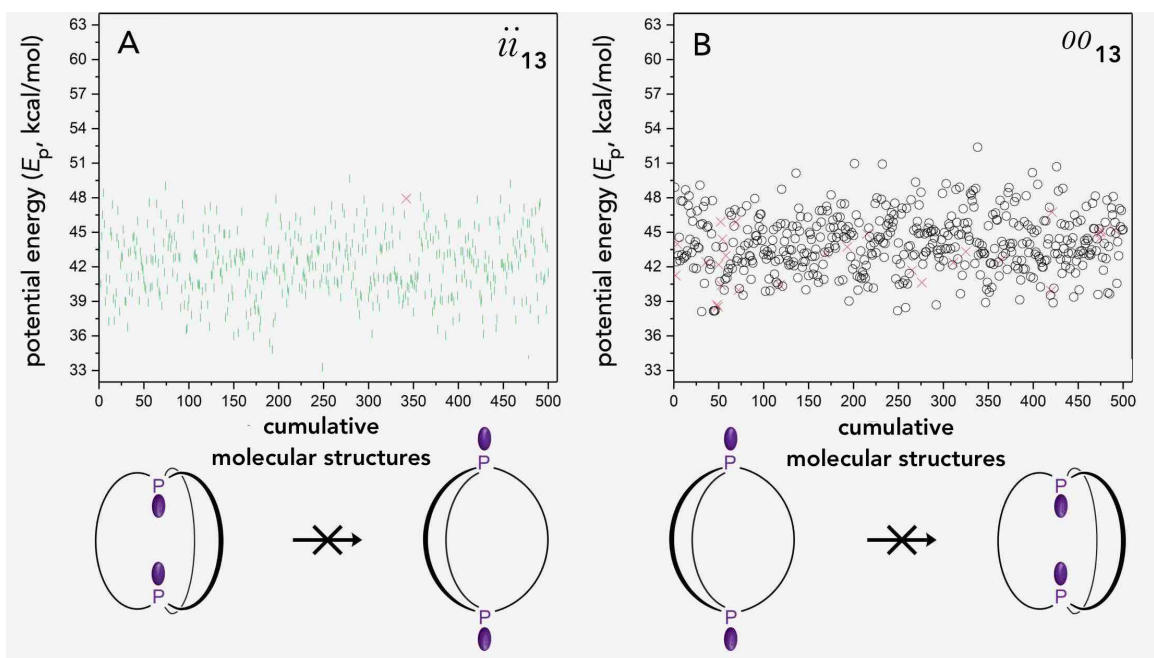


Figure 5.18 Probing the cutoff for homeomorphic isomerism by performing extended trajectories for ii_{13} and oo_{13} .

5.2.8. ^{31}P NMR chemical shifts of selected diphosphines

The ^{31}P NMR chemical shifts of selected diphosphines were computed using the gauge independent atomic orbitals method (DFT) of a single structure.³⁸ The results are shown in Figure 5.19 side by side with experimental values. The agreement is excellent.

The computed data clearly show the ^{31}P NMR chemical shift of ii_{14} (33.5 ppm) to be 3.3 ppm downfield of oo_{14} (36.8 ppm). The experimental chemical shift difference of these species is ca. 4.0 ppm with oo_{14} (37.5 ppm) and ii_{14} (33.5 ppm) carrying the same relative order. Therefore, it is not surprising that the ^{31}P NMR spectra of io_{14} exhibits two signals, one at 32.5 ppm for the "in" phosphorus atom (P_{in}) and another at 38.0 ppm for the "out" phosphorus atom (P_{out}). The separation in chemical shift between these two signals are 5.5 ppm. The computed chemical shift difference for the same pair is 7.8 ppm, and have the same relative ordering as in the experimental data. Since these two signals have equal intensities in experimental spectra, there are no obvious alternative approach to making this assignment. Thus, based on the computations for io_{14} vs. ii_{14}/oo_{14} , the downfield signal is assigned to the P_{in} .

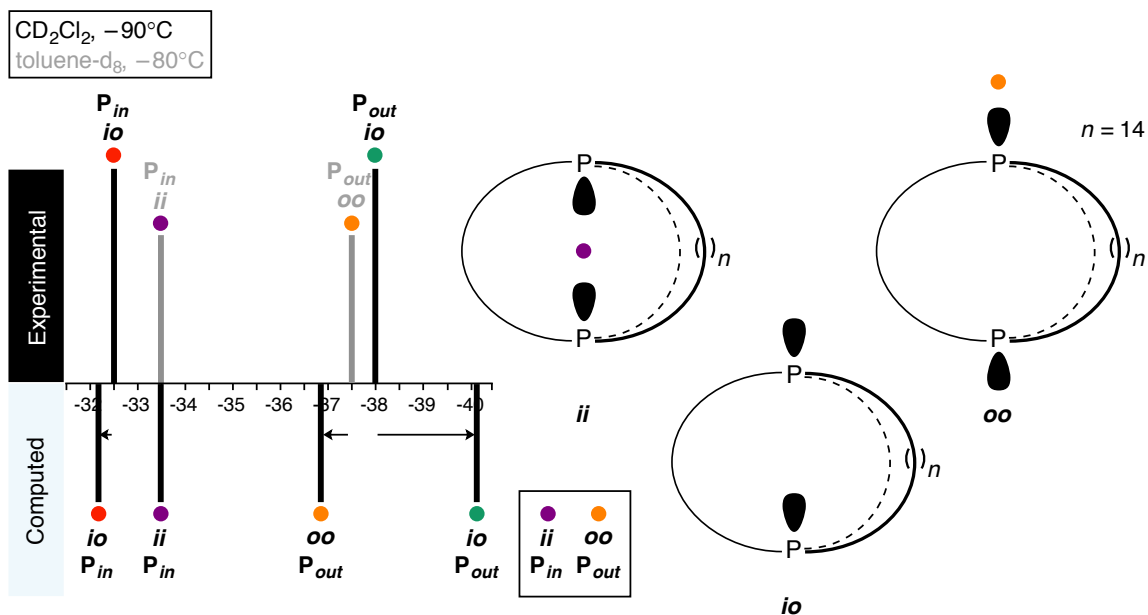


Figure 5.19 Experimental and computed ³¹P NMR chemical shifts for *ii*₁₄, *io*₁₄, and *oo*₁₄.

5.3. Conclusions

The relative stability difference of P((CH₂)_n)₃P for *ii*₁₄ and *oo*₁₄ were computed to be 5.6 kcal/mol, favoring the *ii*₁₄ isomer. Previous experimental ³¹P NMR data is presented in Figure 5.19 (top) illustrating the chemical shift region containing two peaks of an equilibrating mixture of *ii*₁₄ and *oo*₁₄. However, the signal intensity is not depicted. The experimental signal ratio of ca. 97:3 (-80 °C, toluene-*d*₈) was based on the computations herein, the high intensity peak is proposed to correspond to *ii*₁₄. Computed ³¹P NMR data together with the relative stabilities of *ii*₁₄ and *oo*₁₄ both support this conclusion.

The io_n^{cs} intermediate in the homeomorphic isomerization process is observed computationally, and is a topological match to crystallized species although the experimental structures feature bulky bridgehead substituents that prevent the in,in manifold. Thus, subjecting oo_n ($n > 13$) to simulated annealing results in the formation of ii_n isomers via io_n^{cs} . Further, two specific type of pathways were examined but only the *asynchronous* process was observed. While "peekaboo" type cross-chain intermediates were observed for $n = 12$ and 13 , these species were not observed in the given simulation time to fully converted to the ii_n isomer (or oo_n , if starting from ii_n). Thus, the homeomorphic pathway is therefore suggested to be active for $n < 14$ as a full conversion per definition is required, i.e. it is not enough to simply observe "peekaboo" type cross chain intermediates. The $n = 14$ is the first cage size where $P((CH_2)_n)_3P$ fully threads through interconverting oo_n to ii_n , and proceeding via io_n^{cs} .

A justification for the energetic stability difference which favors the ii_{14} isomer was sought. After inspecting all the computed species it became clear that topology had profound impact on the energetics. In an effort to quantify this notion molecular surface areas were computed for all ii_{14} and oo_{14} structures. A strong linear correlation between E_{vdW} and surface area was detected. Upon further inspection of the lowest energy species, irrespective of isomer type (ii_n vs. oo_n), they were found to feature the smallest void space and largest tether-to-tether contact, maximizing dispersion interactions. The ii_n species exhibited stronger dispersion interaction and thus lower E_{vdW} terms. The

energetic differences of ii_n vs. oo_n are largely attributed to E_{vdW} terms for large cages whereas structural terms dominate in smaller cages.

The barrier for the alternative mechanism, pyramidal inversion, is too large to proceed at room temperature; however, it is accessible at higher temperatures. The cage in the dibridgehead phosphines does not significantly change the height of the pyramidal inversion barrier. If one begins the simulated annealing from io_n instead of ii_n/oo_n both of the hypothesized intermediates (ii_n^{CS} and oo_n^{CS}) are observed. The latter is more frequently observed, in agreement with experimental data where structures with large E–X groups tend to crystallize in oo_n^{CS} . A summary of all the observed (and hypothesized) intermediates is shown in Figure 5.20.

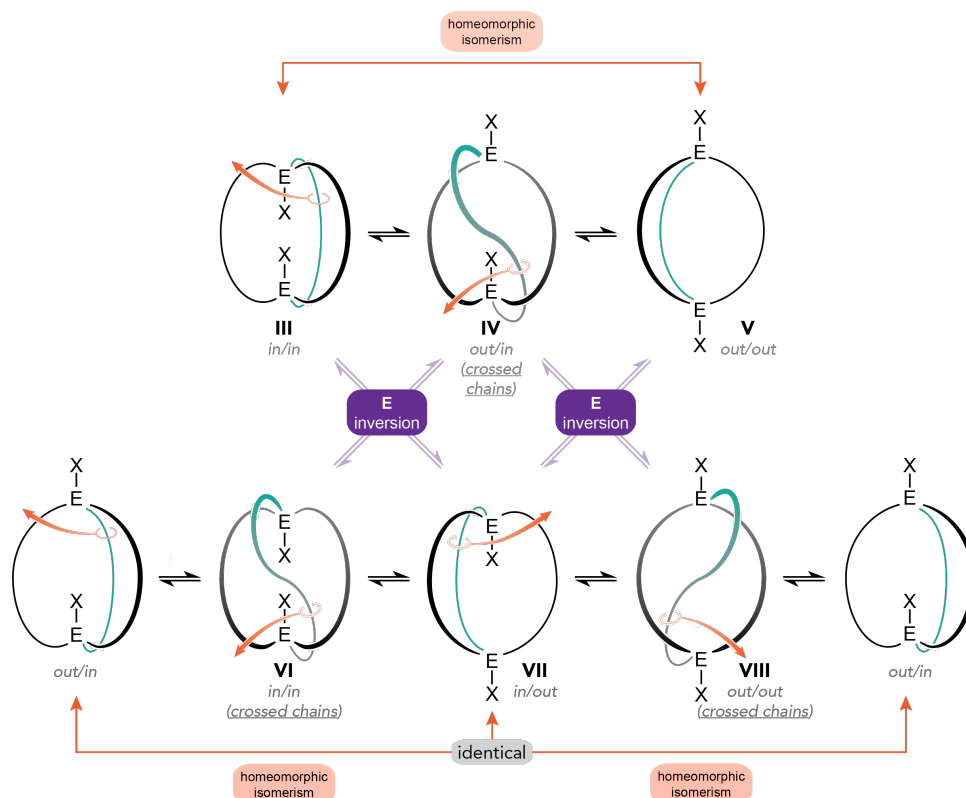


Figure 5.20 A summary of all intermediates including hypothesized species.

5.4. References

(1) (a) H. E. Zimmerman, *Quantum Mechanics for Organic Chemists*. Academic Press, Inc. New York, 1975, pp. 1-215. (b) H. E. Zimmerman, The Möbius-Hückel Concept in Organic Chemistry. Application to Organic Molecules and Reactions. *Acc. Chem. Res.* **1971**, *4*, 272-280.

(2) (a) Herges, R. Topology in Chemistry: Designing Möbius Molecules. *Chem. Rev.* **2006**, *106*, 4820-4842. (b) Rzepa, H. S. Möbius Aromaticity and Delocalization. *Chem. Rev.* **2005**, *105*, 3697-3715.

(3) E. L. Eliel, S. H. Wilen, and L. N. Mander, *Stereochemistry of Organic Compounds*, Wiley, New York, 1994, pp. 696-697.

(4) Kang, S. O.; Llinares, J. M.; Day, V. W.; Bowman-James, K. Cryptand-like anion receptors. *Chem. Soc. Rev.* **2010**, *39*, 3980-4003.

(5) Alder, R. W.; Butts, C. P.; Orpen, A. G.; Read, D.; Oliva, J. M. Superbasic bridgehead diphosphines: the effects of strain and intrabridgehead P...P bonding on phosphine basicity. *J. Chem. Soc. Perkin Trans. 2*, **2001**, 282-287, and references therein.

(6) Alder, R. W.; East, S. P. In/Out Isomerism. *Chem. Rev.* **1996**, *96*, 2097-2011.

(7) Bauer, I.; Habicher, W. D. IN,OUT-ISOMERISM OF PHOSPHORUS BRIDGEHEAD CAGE COMPOUNDS. A REVIEW. *Collect. Czech. Chem. Commun.* **2004**, *69*, 1195-1230.

(8) Park, C. H.; Simmons, H. E. Macrobicyclic Amines. II. *out-out* \rightleftharpoons *in-in* Prototropy in 1,(*k* + 2)-Diazabicyclo[*k.l.m*]alkaneammonium Ions. *J. Am. Chem. Soc.*

1968, 90, 2429-2431. See also the immediately preceding and following communications.

(9) (a) Haines, A. H.; Karntiang, P. Synthesis of Some *out,in*- and *out,out*-Macrobicyclic Polyethers derived from Glycerol. *Out,in-in,out* Isomerism. *J. Chem. Soc. Perkin Trans. 1*, **1979**, 2577-2587. (b) Wareham, R. S.; Kilburn, J. D.; Turner, D. L.; Rees, N. H.; Holmes, D. S. Homeomorphic Isomerism in a Peptidic Macrobicycle. *Angew. Chem. Int. Ed. Engl.* **1995**, 34, 2660-2662; Homöomorphe Isomerie in einem Peptid-Makrobicyclus. *Angew. Chem.* **1995**, 107, 2902-2904. (c) Saunders, M. Stochastic Search for the Conformations of Bicyclic Hydrocarbons. *J. Comput. Chem.* **1989**, 10, 203-208. (d) Saunders, M.; Krause, N. The Use of Stochastic Search in Looking for Homeomorphic Isomerism: Synthesis and Properties of Bicyclo[6.5.1]tetradecane. *J. Am. Chem. Soc.* **1990**, 112, 1791-1795. (e) Alder, R. W.; Heilbronner, E.; Honegger, E.; McEwan, A. B.; Moss, R. E.; Olefirowicz, E.; Petillo, P. A.; Sessions, R. B.; Weisman, G. R.; White, J. M.; Yang, Z.-Z. The *out,out* to *out,in* Transition for 1,(n+2)-Diazabicyclo[n.3.1]alkanes. *J. Am. Chem. Soc.* **1993**, 115, 6580-6591.

(10) Stollenz, M.; Barbasiewicz, M.; Nawara-Hultsch, A. J.; Fiedler, T.; Laddusaw, R. M.; Bhuvanesh, N.; Gladysz, J. A. Dibridgehead Diphosphines that Turn Themselves Inside Out. *Angew. Chem. Int. Ed.* **2011**, 50, 6647-6651; Dreifach-verbrückte Diphosphane mit von innen nach außen invertierender Konfiguration. *Angew. Chem.* **2011**, 123, 6777-6781.

(11) (a) Wang, X.; Shyshov, O.; Hanževački, M.; Jäger, C. M.; von Delius, M. Ammonium Complexes of Orthoester Cryptands Are Inherently Dynamic and Adaptive. *J. Am. Chem. Soc.* **2019**, *141*, 8868-8876. (b) Löw, H.; Mena-Osteritz, E.; Mullen, K. M.; Jäger, C. M.; von Delius, M. Self-Assembly, Adaptive Response, and *in,out*-Stereoisomerism of Large Orthoformate Cryptands. *ChemPlusChem* **2020**, *85*, 1008-1012.

(12) Ikeda, Y.; Inagaki, Y.; Setaka, W. Simultaneous synthesis and characterization of *in/out*-isomers of disilabicyclo[14.14.14]alkanes. *Chem. Commun.* **2021**, *57*, 7838-7841.

(13) (a) Nawara-Hultsch, A. J.; Stollenz, M.; Barbasiewicz, M.; Szafert, S.; Lis, T.; Hampel, F.; Bhuvanesh, N.; Gladysz, J. A. Gyroscope-Like Molecules Consisting of PdX₂/PtX₂ Rotators within Three-Spoke Dibrigehead Diphosphine Stators: Syntheses, Substitution Reactions, Structures, and Dynamic Properties. *Chem. Eur. J.* **2014**, *20*, 4617-4637. (b) Nawara, A. J.; Shima, T.; Hampel, F.; Gladysz, J. A. Gyroscope-like Molecules Consisting of PdX₂/PtX₂ Rotators Encased in Three-Spoke Stators: Synthesis via Alkene Metathesis, and Facile Substitution and Demetalation. *J. Am. Chem. Soc.* **2006**, *128*, 4962-4963.

(14) Kharel, S.; Joshi, H.; Bierschenk, S.; Stollenz, M.; Taher, D.; Bhuvanesh, N.; Gladysz, J. A. Homeomorphic Isomerization as a Design Element in Container Molecules; Binding, Displacement, and Selective Transport of MCl₂ Species (M = Pt, Pd, Ni). *J. Am. Chem. Soc.* **2017**, *139*, 2172-2175.

(15) Zhu, Y.; Ehnbom, A.; Fiedler, T.; Shu, Y.; Bhuvanesh, N.; Hall, M. B.; Gladysz, J. A. Platinum(II) alkyl complexes of chelating dibridgehead diphosphines $P((CH_2)_n)_3P$ ($n = 14, 18, 22$); facile *cis/trans* isomerizations interconverting gyroscope and parachute like adducts. *Dalton Trans.* **2021**, *50*, 12457-12477.

(16) Jones, I. W.; Lynn, M. A.; Mash, E. A. Conformational analysis of bridgehead-substituted bicyclo[*m.m.m*]alkanes and bicyclo[8.8.*n*]alkanes. *Tetrahedron*, **2009**, *65*, 10317-10322.

(17) (a) Walker, T. L.; Taschner, I. S.; Chandra, S. M.; Taschner, M. J.; Engle, J. T.; Schrage, B. R.; Ziegler, C. J.; Gao, X.; Wheeler, S. E. Lone-Pair-Induced Topicity Observed in Macrobicyclic Tetra-thia Lactams and Cryptands: Synthesis, Spectral Identification, and Computational Assessment. *J. Org. Chem.* **2018**, *83*, 10025-10036.

(b) Taschner, I. S.; Walker, T. L.; Chandra, S. M.; Schrage, B. R.; Ziegler, C. J.; Gao, X.; Wheeler, S. E. Topomeric aza/thia cryptands: synthesis and theoretical aspects of *in/out* isomerism using *n*-alkyl bridging. *Org. Chem. Front.* **2020**, *7*, 1164-1176.

(18) Ehnbom, A.; Kuszynski, J. E.; M.; Hall, M. B.; Gladysz, J. A. Homeomorphic Isomerism for *out,out* and *in,in* Macrocycles of $X[(CH_2)_n]_3X$ ($X = N, PO, PBH_3, As, Sb, Bi, n = 4-20$) Observed Using Simulated Annealing. *manuscript in preparation*.

(19) (a) Hawkins, P. C. D. Conformation Generation: The State of the Art. *J. Chem. Inf. Model.* **2017**, *57*, 1747-1756. (b) Bursch, M.; Hansen, A.; Pracht, P.; Kohn, J. T.; Grimme, S. Theoretical study on conformational energies of transition metal complexes. *Phys. Chem. Chem. Phys.* **2021**, *23*, 287-299.

(20) (a) Kirkpatrick, S.; Gelatt, C. D.; Vecchi, M. P. Jr. Optimization by Simulated Annealing. *Science* **1983**, *220*, 671-680. (b) Wilson, S. R.; Cui, W.; Moskowitz, J. W.; Schmidt, K. E. Applications of Simulated Annealing to the Conformational Analysis of Flexible Molecules. *J. Comput. Chem.* **1991**, *12*, 342-349. (c) Leli, F.; Crimaldi, P.; Cristinziano, P. L. Conformational Energy Minimization by Simulated Annealing Using Molecular Dynamics: Some Improvements to the Monitoring Procedure. *Biopolymers*, **1991**, *31*, 663-670.

(21) (a) Benkovic, S. J.; Hammes-Schiffer, S. A Perspective on Enzyme Catalysis. *Science* **2003**, *301*, 1196-1202. (b) Eisenmesser, E. Z.; Bosco, D. A.; Akke, M.; Kern, D. Enzyme Dynamics During Catalysis. *Science* **2002**, *295*, 1520-1523. (c) Kamerlin, S. C. L.; Warshel, A. At the dawn of the 21st century: Is dynamics the missing link for understanding enzyme catalysis? *Proteins* **2009**, 1339-1375. (d) Lindorff-Larsen, K.; Maragakis, P.; Piana, S.; Shaw, D. E. Picosecond to Millisecond Structural Dynamics in Human Ubiquitin. *J. Phys. Chem. B.* **2016**, *120*, 8313-8320.

(22) The simulated annealing cycle was set up using 150 anneal cycles with an initial temperature of 300 K and mid-cycle temperature of 500 K. The heating ramps per cycle is five and the dynamic steps per ramp is 20,000. This leads to the total number of 30,000,000 steps per trajectory, generating 1,500 conformations. These conformations are not necessarily unique. This set of structures is then geometry optimized using molecular mechanics calculations and the universal force-field (UFF) with a fine quality.

(23) (a) Ashbaugh, H. S.; Garde, S.; Kaler, E. W.; Paulaitis, M. E. Conformational Equilibria of Alkanes in Aqueous Solution: Relationship to Water

Structure Near Hydrophobic Solutes. *Biophys. J.* **1999**, *77*, 645-654. (b) Salam, A.; Deleuze, M. S. High-level theoretical study of the conformational equilibrium of n-pentane. *J. Chem. Phys.* **2002**, *116*, 1296-1302.

(24) A conventional standard deviation has been calculated for the data using the equation $\sigma = \sqrt{\sum(x_i - \bar{x})^2 / N}$, where \bar{x} is the mean value of all energetic data and N is the sample size, and x_i is the value from the population.

(25) The kinetic energy term (E_k) is related to the thermal energy of the system and its temperature (T), and is less relevant to this study.

(26) G. Upton, I. Cook. *Understanding Statistics*. Oxford University Press. 1996, p. 55.

(27) These classifications can be changed from their standard usage, however, the conventional factor of 1.5 for IQR was applied. The whiskers thus represent the statistical outliers in the data set with a "coefficient" or factor of 1.5. This suggest that outliers have a range and any data points that fall within this energetic range be outside the 25-75% average of the IQR.

(28) Initially symmetrized models were constructed of the ii_n and oo_n species and both the energetic landscape and the computed spectroscopic data became completely different and in disagreement with experimental data. The resultant structures were also significantly higher in energy than the "MD-processed" data that the symmetrized structures were later subjected to. However, the smallest cages behaved similarly to the MD-models due to their small conformational space.

(29) Stollenz, M.; Bhuvanesh, N.; Reibenspies, J. H.; Gladysz, J. A. Syntheses and Structures of Digold Complexes of Macrobicyclic Dibridgehead Diphosphines That Can Turn Themselves Inside Out. *Organometallics* **2011**, *30*, 6510-6513.

(30) Stollenz, M.; Taher, D.; Bhuvanesh, N.; Reibenspies, J. H.; Baranová, Z.; Gladysz, J. A. Steric control of the *in/out* sense of bridgehead substituents in macrobicyclic compounds: isolation of new "crossed chain" variants of *in/out* isomers. *Chem. Commun.* **2015**, *51*, 16053-16056.

(31) Kharel, S.; Jia, T.; Bhuvanesh, N.; Reibenspies, J. H.; Blümel, J.; Gladysz, J. A. A Nontemplated Route to Macrocyclic Dibridgehead Diphosphorus Compounds: Crystallographic Characterization of a "Crossed-Chain" Variant of *in/out* Stereoisomers. *Chem. Asian J.* **2018**, *13*, 2632-2640.

(32) Bondi, A. van der Waals Volumes and Radii. *J. Phys. Chem.* **1964**, *68*, 441-451.

(33) Cossairt, B. M.; Cummins, C. C.; Head, A. R.; Lichtenberger, D. L.; Berger, R. J. F.; Hayes, S. A.; Mitzel, N. W.; Wu, G. On the Molecular and Electronic Structures of AsP₃ and P₄. *J. Am. Chem. Soc.* **2010**, *132*, 8459-8465.

(34) S. Grimme, Chapter 16. Dispersion Interaction and Chemical Bonding, *The Chemical Bond: Chemical Bonding Across the Periodic Table*, First ed. Frenking, G.; Shaik, S., Eds. Wiley-VCH, Weinheim, 2014, pp. 477-499.

(35) (a) Connolly, M. L. Solvent-accessible surfaces of proteins and nucleic-acids. *Science* **1983**, *221*, 709-713. (b) The Connolly surface was computed with a fine grid resolution for each annealed *ii*₁₄ and *oo*₁₄ structure. A grid interval of 0.25 Å was

used. The solvent radius is 0.0 Å and the Connolly radius is 1.0 Å. The Connolly radius was increased until the surface area is constant. The same radius is then used for all the different conformations. The occupied volume vs. A_2 vs. E_p and E_{vdw} , was then computed.

(36) (a) Silvestre-Albero, J.; Wahby, A.; Sepúlveda-Escribano, A.; Martínez-Escandell, M.; Kanekob, K.; Rodríguez-Reinosoa, F. Ultrahigh CO₂ adsorption capacity on carbon molecular sieves at room temperature. *Chem. Commun.* **2011**, *47*, 6840-6842.

(b) Borkar, C.; Tomar, D.; Gumma, S. Adsorption of Dichloromethane on Activated Carbon. *J. Chem. Eng. Data.* **2010**, *55*, 1640-1644.

(37) Kölmel, C.; Ochsenfeld, C.; Ahlrichs, R. An *ab initio* investigation of structure and inversion barrier of triisopropylamine and related amines and phosphines. *Theor. Chim. Acta.* **1991**, *82*, 271-284.

(38) Gaussian 16, *Revision C.01*, Frisch, M. J.; Trucks, G. W.; Schlegel, H. B.; Scuseria, G. E.; Robb, M. A.; Cheeseman, J. R.; Scalmani, G.; Barone, V.; Petersson, G. A.; Nakatsuji, H.; Li, X.; Caricato, M.; Marenich, A. V.; Bloino, J.; Janesko, B. G.; Gomperts, R.; Mennucci, B.; Hratchian, H. P.; Ortiz, J. V.; Izmaylov, A. F.; Sonnenberg, J. L.; Williams-Young, D.; Ding, F.; Lipparini, F.; Egidi, F.; Goings, J.; Peng, B.; Petrone, A.; Henderson, T.; Ranasinghe, D.; Zakrzewski, V. G.; Gao, J.; Rega, N.; Zheng, G.; Liang, W.; Hada, M.; Ehara, M.; Toyota, K.; Fukuda, R.; Hasegawa, J.; Ishida, M.; Nakajima, T.; Honda, Y.; Kitao, O.; Nakai, H.; Vreven, T.; Throssell, K.; Montgomery, J. A. Jr.; Peralta, J. E.; Ogliaro, F.; Bearpark, M. J.; Heyd, J. J.; Brothers, E. N.; Kudin, K. N.; Staroverov, V. N.; Keith, T. A.; Kobayashi, R.; Normand, J.;

Raghavachari, K.; Rendell, A. P.; Burant, J. C.; Iyengar, S. S.; Tomasi, J.; Cossi, M.;
Millam, J. M.; Klene, M.; Adamo, C.; Cammi, R.; Ochterski, J. W.; Martin, R. L.;
Morokuma, K.; Farkas, O.; Foresman, J. B.; Fox, D. J. Gaussian, Inc. Wallingford CT,
2016.

6. ORIGIN OF SHIELDING AND DESHIELDING EFFECTS IN NMR SPECTRA OF CONJUGATED POLYYNES[†]

6.1. Introduction

In previous generations, chemists were taught that "ring currents" were largely responsible for NMR shielding and deshielding phenomena associated with benzene, ethyne (acetylene), and derivatives thereof.^{1,2} The models traditionally employed are depicted in Figure 6.1. They offered intuitively plausible rationales for the deshielding of benzene protons (**I**) and the shielding of ethyne protons (**II**), as well as effects in certain types of derivatives. For example, two of the sp^3 protons of [7]paracyclophane (**1**), in which the methylene chain must closely hug the π -face of the *p*-phenylene moiety, exhibit markedly upfield ¹H NMR signals at -0.3 to -0.9 ppm (δ , CCl₄).³ These models also gained currency in their apparent applicability to non-benzenoid aromatic systems, such as 9,10-dihydropyrenes.⁴ They also begged the question as to possible cumulative effects in one-dimensional arrays, such as [*n,n*]paracyclophanes and conjugated polyynes.

[†] Reprinted with permission from (1) Ehnbohm, A.; Hall, M. B.; Gladysz, J. A. Origin of Shielding and Deshielding Effects in NMR Spectra of Organic Conjugated Polyynes. *Org. Lett.* **2019**, *21*, 753-757; and (2) Weisbach, N.; Kuhn, H.; Amini, H.; Ehnbohm, A.; Hampel, F.; Reibenspies, J.; Hall, M. B.; Gladysz, J. A. Triisopropylsilyl (TIPS) Alkynes as Building Blocks for Syntheses of Platinum Triisopropylsilylpolyynyl and Diplatinum Polyynediyl Complexes. *Organometallics* **2019**, *38*, 3294-3310. Copyright 2019 American Chemical Society.

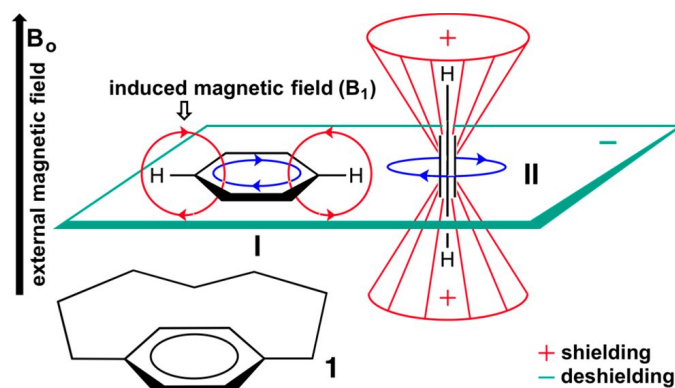


Figure 6.1 Classical ring-current-based shielding/deshielding models for benzene (I) and ethyne (II).^{1,2}

However, subsequent computational studies have shown models I and II to be erroneous.⁵ These feature calculations and analyses of "nucleus independent chemical shifts" or "NICS" associated with the three-dimensional space surrounding benzene and ethyne. The resulting chemical shift "maps" or grid plots, depicted in Figure 6.2, show pronounced shielding regions (red spheres) (1) within and above the benzene ring and (2) within the HC≡CH linkage or along immediately adjacent vectors. The deshielding regions (green spheres) are comparatively modest, occurring at significant radial extensions from the benzene ring and HC≡CH axis. The patterns are clearly inconsistent with ring current models.⁶

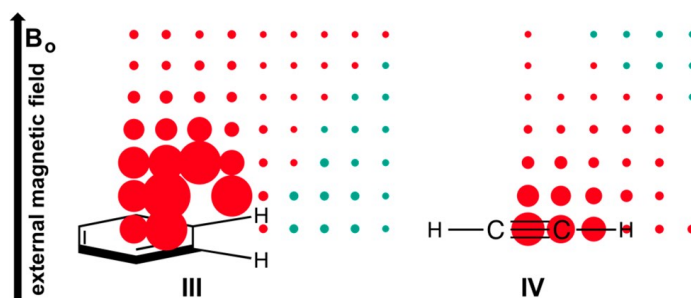


Figure 6.2 Computed NICS about benzene (III) and ethyne (IV), with red and green spheres indicating shielding and deshielding, respectively. The data are from ref 5, which can be consulted for the scales represented by the spheres.

We have had a longstanding interest in the physical and chemical properties of extended polyynes that are capped on one or both termini by transition metal fragments.⁷⁻⁹ These have the general formula $L_yM(C\equiv C)_nZ$ ($Z = SiR_3, H$) and $L_yM(C\equiv C)_nML_y$. A typical example of the latter is given in Figure 6.3 (2).^{8b} These have more recently been expanded to include rotaxanes such as **3**.⁹ The interpretation of the NMR properties of such assemblies — which also have been of interest in several other research groups¹⁰⁻¹³ — requires that the shielding and deshielding regions, and their attendant magnitudes, of organic polyynes be precisely defined.

Surprisingly, to our knowledge there have been no NICS studies of simple acyclic 1,3-diyne, 1,3,5-triynes, or any higher homologs.¹⁴ In this chapter, this conspicuous gap is addressed for the doubly terminal organic polyynes $H(C\equiv C)_nH$ ($n = 2-10$), and selected aryl derivatives. To validate the methods, they are extended to newly synthesized platinum containing complexes, superbly reproducing the experimental spectra and enabling assignments that would have heretofore been impossible.

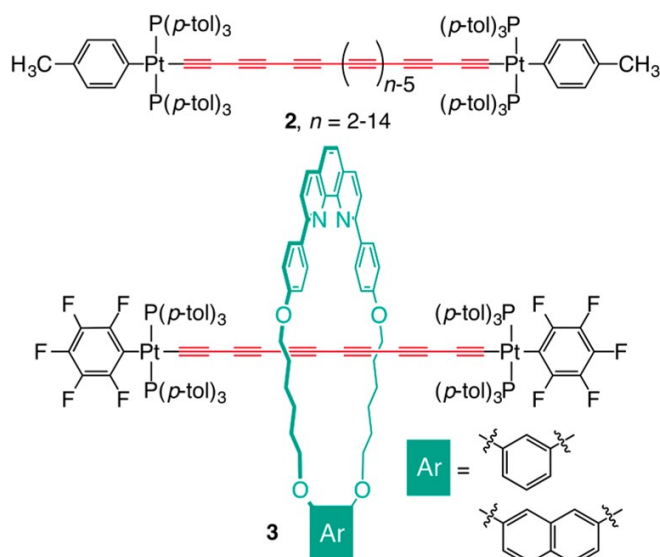


Figure 6.3 Representative diplatinum polyynediyl complexes.

6.2. Experimental [major contribution: A. Ehnbom]

The NICS values for the polyynes $Z(\text{C}\equiv\text{C})_nZ$ ($Z = \text{H}, \text{Ar}, \text{Ar}'\text{L}_2\text{Pt}$) were computed using standard protocols.¹⁵ The full results and details are presented in Appendix D.

6.3. Results and Discussion (part 1) [major contribution: A. Ehnbom]

Data for three representative substrates are depicted in Figure 6.4. As is easily seen, there is marked shielding (1) within and (2) proximal to the sp carbon chain or $(\text{C}\equiv\text{C})_n$ segment. This tails off with the radial distance and eventually a very slightly deshielded region is reached (2.5-3.0 Å). The most important conclusion is that the magnitude of the shielding at any distance is essentially independent of the sp carbon chain length and the position along the chain. In other words, one encounters nearly the same NICS value regardless of the number of triple bonds or exact location along the $(\text{C}\equiv\text{C})_n$ segment. There are no additive or multiplicative effects.

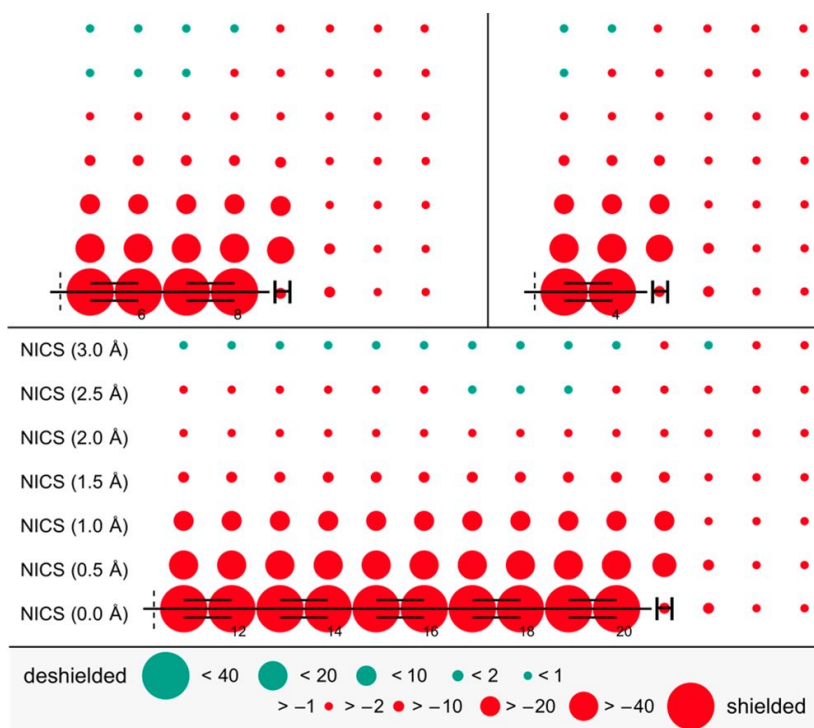


Figure 6.4 Representative NICS grid plots for ethyne and the dimeric polyynes $\text{H}(\text{C}\equiv\text{C})_n\text{H}$ ($n = 2-10$). The distances are not to scale. The grid points on the y -axis represent increments of 0.50 \AA , and those on the x -axis represent increments of $1.19-1.21$ or $1.35-1.37 \text{ \AA}$ (for $\text{C}=\text{C}$ and $\equiv\text{C}-\text{C}\equiv$ linkages, respectively) or $1.06-1.11 \text{ \AA}$ (for $\text{C}-\text{H}$ linkages and points extending further out from the carbon chain).

The same holds as the one-dimensional vectors defined by or parallel to the sp carbon chains are extended. As shown in Figure 6.4, the shielding found at the hydrogen atoms is markedly attenuated. However, at radial extensions of $0.5-2.0 \text{ \AA}$, the diminution is not as pronounced. When grid points further out on the $\text{H}(\text{C}\equiv\text{C})_n\text{H}$ axes are sampled, the degree of shielding gradually decreases. This same trend is found when the grid is radially extended.

These results indicate that in rotaxanes derived from organic polyynes, the ^1H and ^{13}C NMR chemical shifts of the mechanically linked macrocycles are not directly affected by the sp carbon chain lengths. However, these chemical shifts will be

influenced by the distances of the macrocycle nuclei from the endgroups, which will in turn be affected by the *sp* carbon chain length. This will be the principal origin of any chemical shift trends as the *sp* carbon chain lengths are varied.

In the course of calculating the NICS grids for the diterminal polyynes $\text{H}(\text{C}\equiv\text{C})_n\text{H}$, chemical shifts for the hydrogen and carbon atoms were also obtained. Although such compounds become unstable at moderate chain lengths, some experimental data are available,¹⁶⁻¹⁹ and are presented in Figure 6.5 and Figure 6.6. For the calculated values, there is a monotonic downfield shift from δ 1.245 to 1.360 as *n* is extended from **2** (1,3-butadiyne) to **10** (1,3,5,7,9,11,13,15,17,19-eicosadecayne). From the slope in Figure 6.6, the value for eicosadecayne (δ 1.360) appears to be close to an asymptotic limit, such that there would be little change in still longer polyynes. For the experimental values (*n* = 2-6), there is a general downfield trend, but — perhaps due to the different solvents employed¹⁶⁻¹⁹ and experimental error — the shifts are very close for *n* = 3-6 (δ 2.12 to 2.16).

As can readily be seen in Figure 6.6, the ^1H chemical shift computed for ethyne is downfield from that of 1,3-butadiyne, as opposed to the upfield value that would have been extrapolated from the other data points. This discontinuity is not necessarily surprising as ethyne (with *n* = 1) is not a polyyne. There is a hydrogen atom on the opposite end of the triple bond from the $\text{HC}\equiv$ group, as opposed to an *sp* carbon atom in the higher homologs. However, the experimental ^1H NMR chemical shift of ethyne (δ 1.91 ppm in CDCl_3 in two studies)¹⁶ is upfield of those of 1,3-butadiyne and 1,3,5-

hexatriyne. In the absence of any experimental artifact, it must be concluded that the computations fail to model this one datum.²⁰ Nonetheless, a variety of benchmarking computations are provided in Appendix D that validates the methodology.

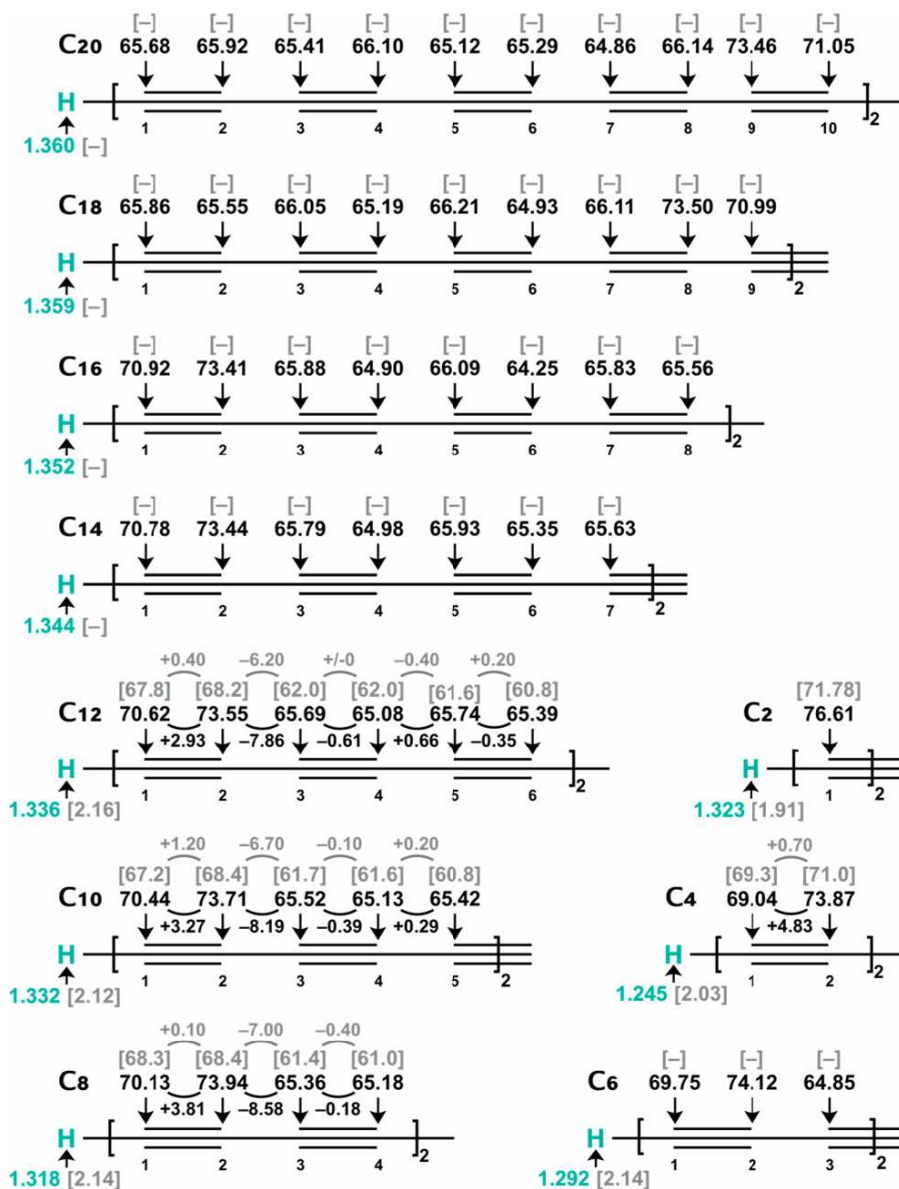


Figure 6.5 Computed ^1H and ^{13}C NMR chemical shifts of ethyne and the diterminal polyynes $\text{H}(\text{C}\equiv\text{C})_n\text{H}$ vs. TMS and (when available) experimental values [in brackets].

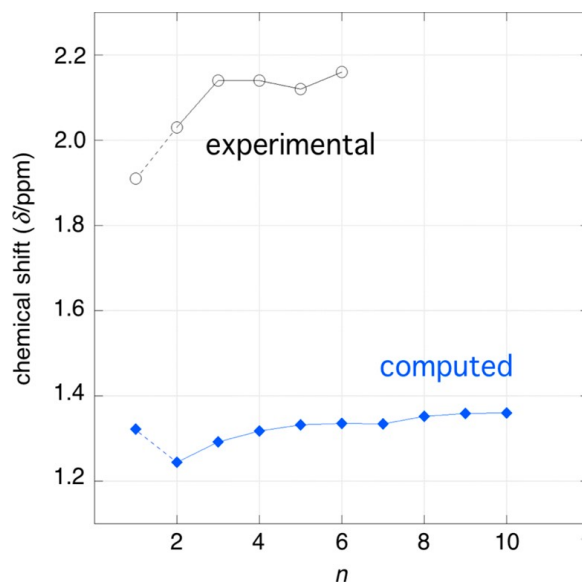


Figure 6.6 Computed ^1H NMR chemical shifts for ethyne and the diterminal polyynes $\text{H}(\text{C}\equiv\text{C})_n\text{H}$ vs. TMS (blue rhomb) and experimental values (open circle).

We were curious as to whether the preceding ^1H NMR chemical shift trends might be manifested in monoterminally conjugated polyynes $\text{R}(\text{C}\equiv\text{C})_n\text{H}$, which also become less stable at higher chain lengths.²¹ The most extensive series of data that could be located was for the series $\text{Tr}^*(\text{C}\equiv\text{C})_n\text{H}$ (**4**), where Tr^* denotes a hexakis(*t*-butyl)-substituted trityl group as shown in Figure 6.7.^{11b} Tykwinski could obtain ^1H NMR spectra for $n = 1-7$. However, more than one solvent was employed, complicating comparisons (n , δ (ppm)/solvent: **1**, 2.59/ CDCl_3 ; **2**, 2.10/ CDCl_3 ; **3**, 2.07/ CDCl_3 ; **4**, 2.07/ CDCl_3 ; **5**, 2.26/ CD_2Cl_2 ; **6**, 2.11/ CDCl_3 ; **7**, 2.23/ CD_2Cl_2). A less extensive series of aryl substituted terminal polyynes (**5**, Figure 6.7) exhibited a nicely monotonic upfield trend as n increased from **1** to **4** (δ (ppm)/ CDCl_3 3.20, 2.54, 2.31, 2.23).²¹

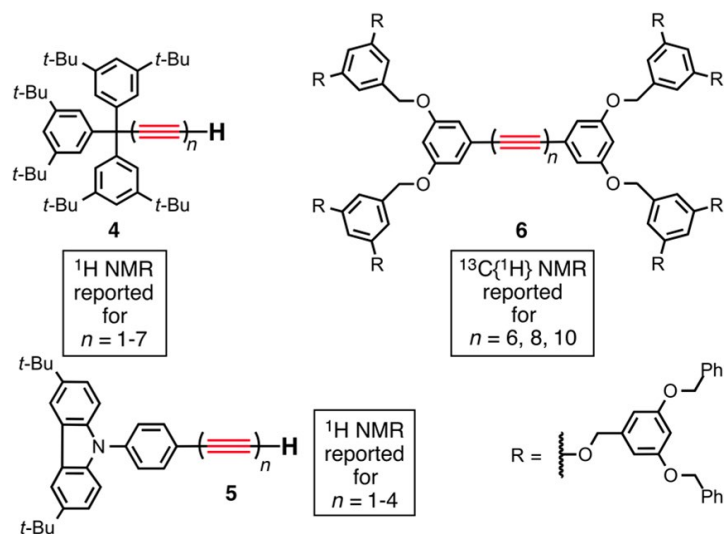


Figure 6.7 Organic conjugated polyynes used for chemical shift comparisons. ^{11a,b,21}

The ^{13}C NMR chemical shifts computed for $\text{H}(\text{C}\equiv\text{C})_n\text{H}$ are plotted in Figure 6.8. As n is extended from 2 to 10, the chemical shifts of the terminal carbon atoms (C1) shift monotonically to lower fields. As was seen with the computed ^1H NMR chemical shifts, ethyne ($n = 1$) presents an exception to the monotonic trend exhibited by the higher homologs. The shift computed for C2 of 1,3-butadiyne also slightly deviates from an analogous monotonic trend. Interestingly, the chemical shifts of the "odd numbered carbon atoms" (C1, C3, C5, etc.) move downfield with increasing chain length, but those of the "even numbered carbon atoms" (C2, C4, etc.) move upfield. Overall, the chemical shift trends are in general but not perfect agreement with those found experimentally for 1,3-butadiyne, 1,3,5,7-octatetrayne, 1,3,5,7,9-decapentayne, and 1,3,5,7,9,11-dodecahexayne ($n = 2, 4, 5, 6$; Figure 6.5).

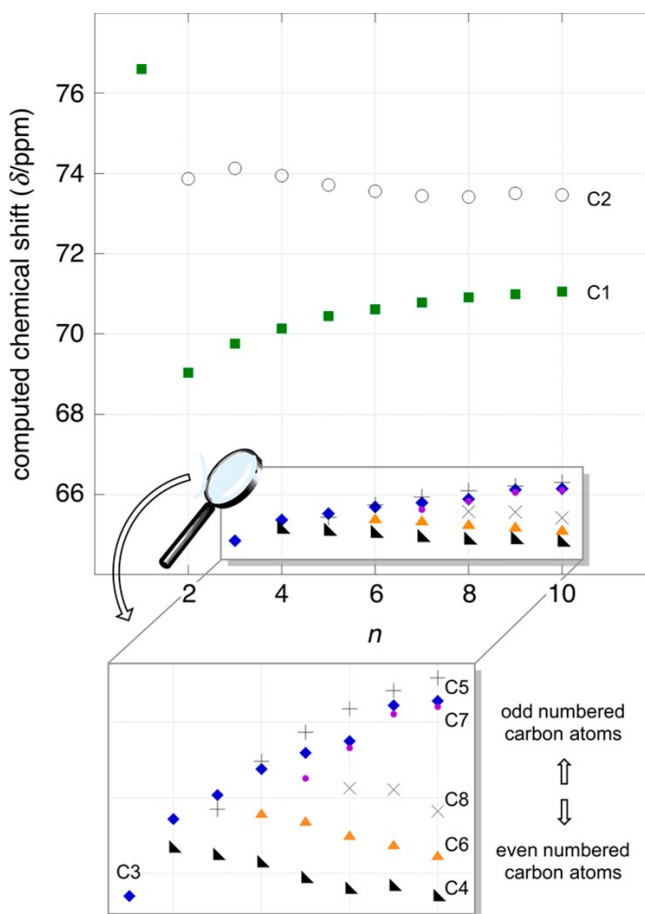


Figure 6.8 Computed ^{13}C NMR chemical shifts for ethyne and the diterminal polyynes $\text{H}(\text{C}\equiv\text{C})_n\text{H}$ ($\text{HC1}\equiv\text{C2}-\text{C3}\equiv\text{C4}\dots$) vs. TMS as a function of n (green square = C1; open circle = C2; blue rhomb = C3; black triangle = C4; black plus sign = C5; orange triangle = C6; purple filled circle = C7; black cross = C8).

We were also curious as to whether the preceding ^{13}C NMR chemical shift trends might be manifested in non-terminal organic conjugated polyynes. Hirsch has characterized a series of polyynes $\text{Ar}^*(\text{C}\equiv\text{C})_n\text{Ar}^*$ ($6; n = 6, 8, 10$) in which Ar^* denotes a dendrimer like aryl endgroup (Figure 6.7).^{11a} As summarized in Figure 6.9, his experimental data (recorded in acetone- d_6) strikingly mirror the computed trends, providing further validation of the methodology. Tykwinski also studied an extensive series of polyynes $\text{Tr}^*(\text{C}\equiv\text{C})_n\text{Tr}^*$ derived from the oxidative coupling of **4**,^{11b} and

conducted ^{13}C labeling studies with other substrates to secure NMR assignments.²² However, the correlations with his ^{13}C NMR spectra ($n = 4, 6, 8, 10$; recorded in CDCl_3) are weaker. In this context, it should be noted that the ^{13}C NMR signals of long polyynes can be challenging to observe for a number of well understood reasons, including decreased solubility with chain length, rendering the chemical shifts subject to greater experimental error. Also, as noted by a reviewer, the non-hydrogen endgroups introduce electronic interactions with the sp carbon chain that are not represented in our calculations.

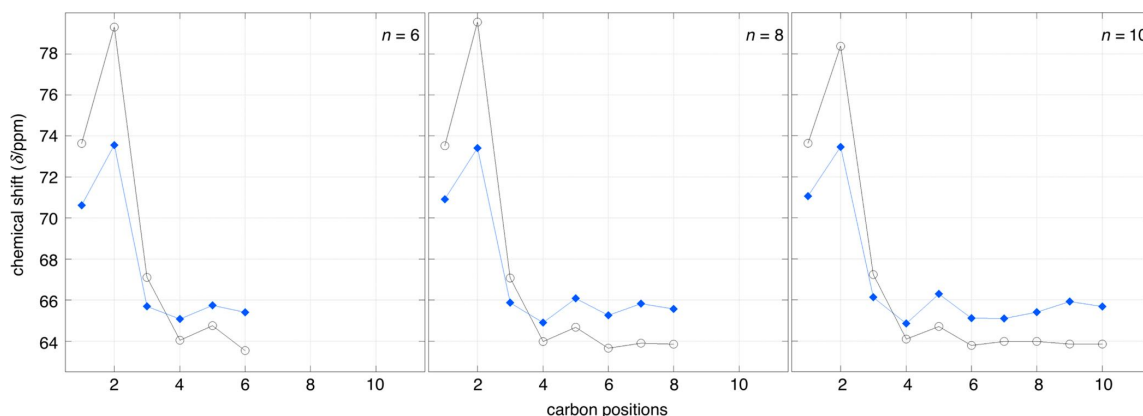


Figure 6.9 Correlation of ^{13}C NMR chemical shifts trends computed for $\text{H}(\text{C}\equiv\text{C})_n\text{H}$ (blue diamond) vs. those observed experimentally for $\text{Ar}^*(\text{C}\equiv\text{C})_n\text{Ar}^*$ (**6**; open circle; acetone- d_6). The C7/C8 and C9/C10 signals of $\text{Ar}^*(\text{C}\equiv\text{C})_{10}\text{Ar}^*$ were reported as overlapping singlets at δ 63.97 and 63.84 ppm, respectively.

6.4. Results and Discussion (part 2) [major contribution: A. Ehnbohm, Dr. H. Amini]

Given the projected need for ^{13}C NMR assignments for higher homologs of various complexes in this or other recent studies (e.g. **2** in Figure 6.3),²³ it was sought to benchmark the methodology versus data for the platinum and platinum and trialkylsilyl adducts in Table 6.1 – particularly the signal rich species with unsymmetrically substituted *sp* carbon chains for which assignments were most problematic. In these *trans* complexes, **Pt^T** denotes (*p*-tol)(*p*-tol₃P)₂Pt, **Pt^F** denotes (C₆F₅)(*p*-tol₃P)Pt, and **Pt** denotes (*p*-tol₃P)₂Pt. Note that ^{31}P , ^{195}Pt , and ^{29}Si all have nuclear spin (*I*) of $\frac{1}{2}$, but their natural abundance decreases from 100% to 33.8% to 4.67%. Thus, ^{195}Pt and ^{29}Si will give rise to satellites that may be difficult to detect.

Prior to probing the ^{13}C NMR properties of the title complexes by DFT computations, it is appropriate to describe the partial signal assignments that were already possible. Based upon all previous studies of platinum polyynyl complexes, the PtC \equiv C resonance is always the farthest downfield, although as illustrated in Table 6.1 the nature of the *trans* ligand significantly impacts the chemical shift (103.1-125.2 ppm). These signals shift downfield when the *sp* carbon chain is lengthened, which is one of the criteria that allow the **PtC₄TIPS** segments to be differentiated from the **PtC₈TIPS** or **PtC₁₂TIPS** segments in certain complexes (Table 6.1).

Table 6.1 Experimental $^{13}\text{C}\{^1\text{H}\}$ and computed [brackets]^a ^{13}C NMR chemical shifts (δ /ppm; CDCl_3 , referenced to TMS).

complex	$\text{Pt}\overline{\text{C}}\equiv\text{C}$ $\{^2J_{\text{CP}}\}$	$\text{Pt}\overline{\text{C}}\equiv\overline{\text{C}}$ $\{^3J_{\text{CP}}\}$	$\overline{\text{C}}\equiv\overline{\text{C}}\text{Si}$ $\{^4J_{\text{CP}}\}$	$\text{C}\equiv\overline{\text{C}}\text{Si}$ $\{^5J_{\text{CP}}\}$	$\text{Pt}\overline{\text{C}}\equiv\overline{\text{C}}\overline{\text{C}}$ thru $\overline{\text{C}}\overline{\text{C}}\equiv\overline{\text{C}}\text{Si}$ or $\overline{\text{C}}\overline{\text{C}}\equiv\text{C}\text{Pt}$
Pt^TC₈TIPS	120.1 [125.5] {14.9}	95.7 [103.7]	91.2 [98.4]	81.3 [79.7]	66.9 [64.3], 58.7 [62.2], 64.3 [66.8], 55.1 [60.6]
Pt^TC₁₂TIPS	123.7 ^b [132.8]	95.3 [98.2]	90.1 [95.6]	85.0 [84.4]	61.1 [62.5], 62.4 [63.2], 65.9 [64.5], 64.3 [64.1], 67.4 [65.7], 58.9 [62.6], 60.2 [66.4], 55.3 [59.1]
Pt^TC₁₆TIPS	125.2 [128.3] {14.4}	95.1 [100.4]	89.6 [97.0]	86.6 [83.2]	63.8 [61.4], 65.0 [62.1], 66.6 [63.6], 67.8 [63.9], 62.3 [63.9], 61.6 [63.1], 63.0 [64.5], 60.1 [62.3], 62.0 [65.5], 55.4 [61.1], 61.2 [65.9], 58.8 [57.9]
Pt^FC₆TIPS	103.3 [120.7]	95.5 [104.7]	91.9 [99.4]	79.4 [80.4]	66.5 [65.2], 56.2 [61.7]
Pt^FC₈TIPS	106.1 [121.1]	95.2 [103.6]	90.9 [98.1]	82.2 [81.3]	63.7 [63.7], 59.6 [63.6], 66.6 [66.4], 56.3 [61.5]
Pt^FC₁₀TIPS	107.8 [121.3]	95.0 [102.7]	90.3 [97.6]	84.0 [82.2]	62.7 [62.3], 64.7 [64.1], 66.5 [65.4], 59.5 [63.9], 60.4 [66.2], 56.5 [60.0]
Pt^FC₁₂TIPS	— ^b [122.0]	94.8 [102.0]	90.0 [97.3]	85.4 [82.9]	61.4 [61.5], 62.1 [63.8], 63.8 [64.1], 63.2 [64.3], 65.2 [65.3], 59.6 [62.6], 60.7 [66.0], 56.5 [59.1]
TIPSC₄Pt C₄TIPS	104.2 [122.0] {15.0}	95.9 [102.4] {2.3}	94.4 [99.9] {2.3}	72.9 [76.3] {1.1}	—
TIPSC₄Pt C₈TIPS	110.6 ^c [119.5] {15.1}	96.3 ^c [100.8] {2.0}	90.9 ^c [98.1]	82.1 ^c [80.5]	63.8 [63.8], 59.3 [62.6], 66.2 [66.3], 56.3 [60.5]
	103.5 ^d [125.9] {14.3}	94.3 ^d [99.7] {2.3}	94.0 ^d [99.3]	73.8 ^d [77.2]	—
TIPSC₄Pt C₁₂TIPS	113.6 ^{b,c} [124.1] {15.1}	96.7 ^c [96.7] {2.8}	89.9 ^c [98.0] {2.7}	85.3 ^c [81.4] {1.3}	60.6 [62.2], 59.5 [61.4], 63.9 [64.3], 62.1 [62.3], 65.2 [65.5], 61.4 [60.9], 66.7 [66.3], 56.4 [57.7]

Table 6.1 *continued*.

complex	PtC≡C { ² J _{CP} }	PtC≡C { ³ J _{CP} }	C≡CSi { ⁴ J _{CP} }	C≡CSi { ⁵ J _{CP} }	PtC≡CC thru CC≡CSi or CC≡Cpt ^a
Pt ^F C ₁₂ Pt ^{Fe}	103.1 ^d [118.9]	93.93 ^d [102.1]	93.88 ^d [99.5]	74.1 ^d [78.6]	57.1 [61.3], 65.7 [65.7], 61.0 [64.1], 63.0 [65.8] ^f
Pt ^F C ₁₆ Pt ^{Fe}	106.5 [118.4]	95.5 [105.1]	—	—	56.8 [60.1], 64.9 [64.8], 60.1 [62.6], 66.7 [65.6], 61.5 [63.5], 63.1 [64.4] ^f
Pt ^F C ₂₀ Pt ^F	109.1 [119.7]	95.0 [103.2]	—	—	56.5 [59.7], 65.7 [63.6], 59.7 [61.8], 67.2 [64.6], 60.8 [62.3], 64.2 [63.9], 62.0 [62.8], 63.1 [63.3] ^f
Pt ^F C ₂₄ Pt ^F	— ^b [119.3]	94.7 [100.3]	—	—	56.5 [59.7], 66.1 [63.2], 59.5 [61.6], 67.5 [64.4], 60.6 [62.0], 64.8 [63.8], 61.6 [62.3], 63.9 [63.4], 62.4 [62.7], 63.1 [63.0] ^f

^a The signal assignments represent the best fit to the computations as discussed in the text. The "T" and "F" in the compound names represent *p*-tol and *p*-C₆F₅ ligands, respectively; other abbreviations are defined in the text. ^b This signal was very weak or not observed. ^c For the C₈TIPS or C₁₂TIPS chain. ^d For the C₄TIPS chain. ^e From reference 8a. ^f This sequence of chemical shifts should be repeated in reverse to reach that for the CC≡Cpt carbon atom.

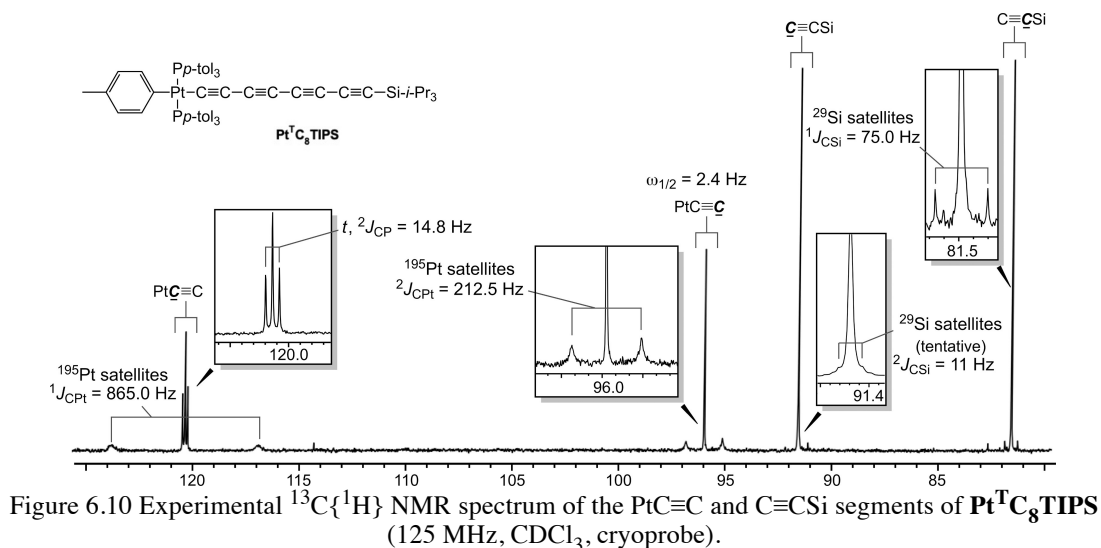
The $\text{Pt}\underline{\text{C}}\equiv\text{C}$ signals are furthermore coupled to ^{31}P (giving a triplet) and ^{195}Pt (giving a doublet of satellites). As shown in Table 6.1, the $^2J_{\text{CP}}$ values range from 14.3 to 15.1 Hz, but are not always detected or resolved. Similarly, platinum couplings can be difficult to observe in the absence of special measures, such as taken in Figure 6.10 below. Nonetheless, $^1J_{\text{CPt}}$ and $^2J_{\text{CPt}}$ values of 650-875 Hz and 212-238 Hz have been observed for the related complexes $\text{Pt}^{\text{T}}\text{C}_4\text{H}$, $\text{Pt}^{\text{T}}\text{C}_6\text{H}$, $\text{Pt}^{\text{T}}\text{C}_6\text{TES}$, and $\text{Pt}^{\text{T}}\text{C}_{12}\text{Pt}^{\text{T}}$.^{8c,24} The *sp* carbon atoms that are remote from the metal endgroups are at most very weakly coupled to phosphorus and platinum, so they give narrower and more intense signals.

As shown in Table 6.1, the $\text{Pt}\underline{\text{C}}\equiv\text{C}$ signals fall into a narrower range (93.9-96.7 ppm) and shift very slightly upfield with increasing chain length. In optimal cases, small phosphorus couplings can be detected ($^3J_{\text{CP}}$ 2.0-2.8 Hz), but the signal/noise ratio is compromised by the platinum couplings as noted above. As found with all extended polyynes in Table 6.1, the signals for the *sp* carbon atoms that are more than two atoms removed from an endgroup fall into a relatively narrow upfield range (55.3-67.8 ppm).

For all complexes with PtC_xSi linkages ($x > 6$) that have been characterized, there are two additional resonances that are (1) upfield of the $\text{Pt}\underline{\text{C}}\equiv\text{C}$ signals and (2) downfield of the signals of the carbon atoms that are more than two atoms removed from an endgroup. These are clearly associated with the $\underline{\text{C}}\equiv\text{CSi}$ moiety. With very well resolved spectra of the triethylsilylpolyyne complexes $\text{Pt}^{\text{F}}\text{C}_x\text{TES}$ ($x = 8, 10, 12$), the upfield signals exhibit $^1J_{\text{CSi}}$ values of 73.0-75.9 Hz,²⁵ in accord with the 75.0 Hz found for $\text{Pt}^{\text{T}}\text{C}_8\text{TIPS}$ in Figure 6.10 below. Hence, these are assigned to the $\underline{\text{C}}\equiv\text{CSi}$ carbon atoms,

in agreement with similar $^1J_{\text{CSi}}$ values of organic analogs.²⁶ In some silylated polyynes, satellites can be detected for the more downfield $\text{C}\equiv\text{CSi}$ signals, but the $^2J_{\text{CSi}}$ values are much lower (10.8-16.1 Hz).^{25,26}

In order to establish a baseline reference for the preceding diverse types of couplings, a $^{13}\text{C}\{^1\text{H}\}$ NMR spectrum of $\text{Pt}^{\text{T}}\text{C}_8\text{TIPS}$ was recorded for an extended period in a cryoprobe. As shown in Figure 6.10, phosphorus coupling was observed for the $\text{PtC}\equiv\text{C}$ signal ($^2J_{\text{CP}}$ 14.8 Hz), but not the $\text{PtC}\equiv\text{C}$ signal, which had a width at half-height (2.4 Hz) similar to the $^3J_{\text{CP}}$ values exhibited by several of the complexes in Table 6.1 (2.0-2.8 Hz). Large platinum couplings were easily detected for the $\text{PtC}\equiv\text{C}$ signals ($^1J_{\text{CPt}}$ 865.0 Hz; $^2J_{\text{CPt}}$ 212.5 Hz). Silicon coupling was observed for the $\text{C}\equiv\text{CSi}$ signal ($^1J_{\text{CSi}}$ 75.0 Hz), and the $\text{C}\equiv\text{CSi}$ signal appeared to exhibit a smaller less distinct coupling ($^2J_{\text{CSi}}$ 11 Hz; tentative assignment). Similar $^nJ_{\text{CSi}}$ values have been found with silylated butadiynes.²⁶



In any case, ^{13}C NMR chemical shifts were computed as done for the organic polyynes in section 6.2 in order to (1) confirm the preceding assignments and (2) nail down the nuclei responsible for the remaining signals. These computations and the preceding experimental data verify that the assignments of $\underline{\text{C}}\equiv\underline{\text{C}}\text{Si}$ signals have been reversed in two previous full papers.⁸ Also, Tykwinski has synthesized bis(silylated) polyynes in which selected carbon atoms have been ^{13}C labeled.²⁷ The coupling constant patterns in a mixture of $\text{TIPSC}\equiv\text{C}^{13}\underline{\text{C}}\equiv\text{C}-\text{C}\equiv\text{CTMS}$ and $\text{TIPSC}\equiv\text{CC}\equiv^{13}\underline{\text{C}}\equiv\text{CTMS}$ similarly confirm the downfield/upfield relationship of the $\underline{\text{C}}\equiv\underline{\text{C}}\text{Si}$ signals.

The computational results are depicted graphically in Table 6.2. The agreement with experimental signals is striking, although some deviation is apparent with the $\text{Pt}\underline{\text{C}}\equiv\text{C}$ signals, where the heavy-atom effect causes large distortions.²⁸ Furthermore, it must be kept in mind that there are error bars on both the experimental and computational sides.²⁸ Thus, pairwise swaps involving closely spaced experimental peaks remain possible, e.g. signals assigned to C3 and C4 or C3 and C8 in $\text{TIPSC}_4\text{PtC}_{12}\text{TIPS}$ in Table 6.2. But in any case, this computational approach clearly brings a heretofore unattainable level of rigor to signal assignments in metal polyynyl species.

Table 6.2 Correlation of ^{13}C NMR chemical shifts computed for the compounds in Table 6.1 (blue diamonds) versus those observed experimentally (open circles).

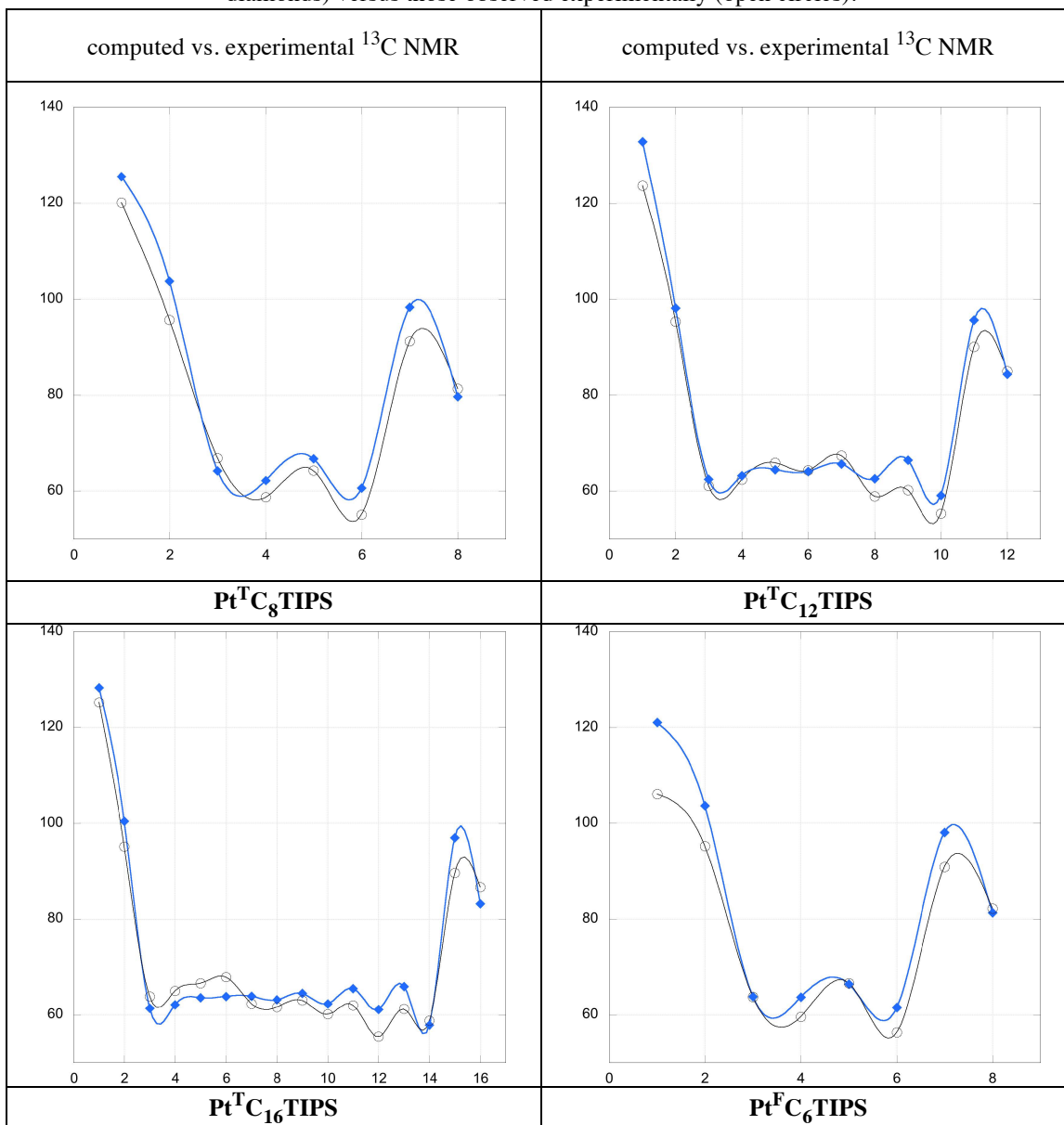


Table 6.2 continued.

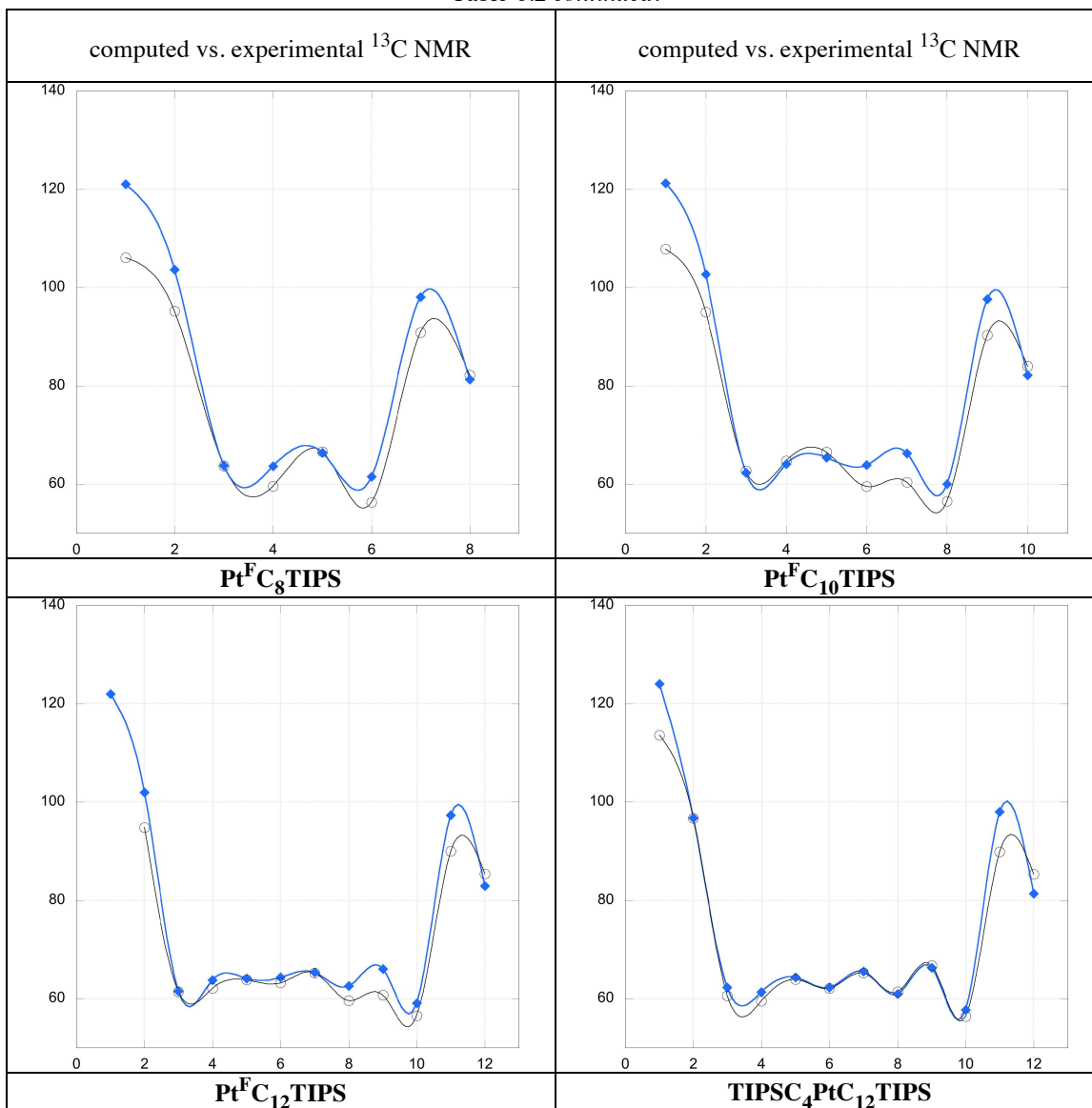


Table 6.2 continued.

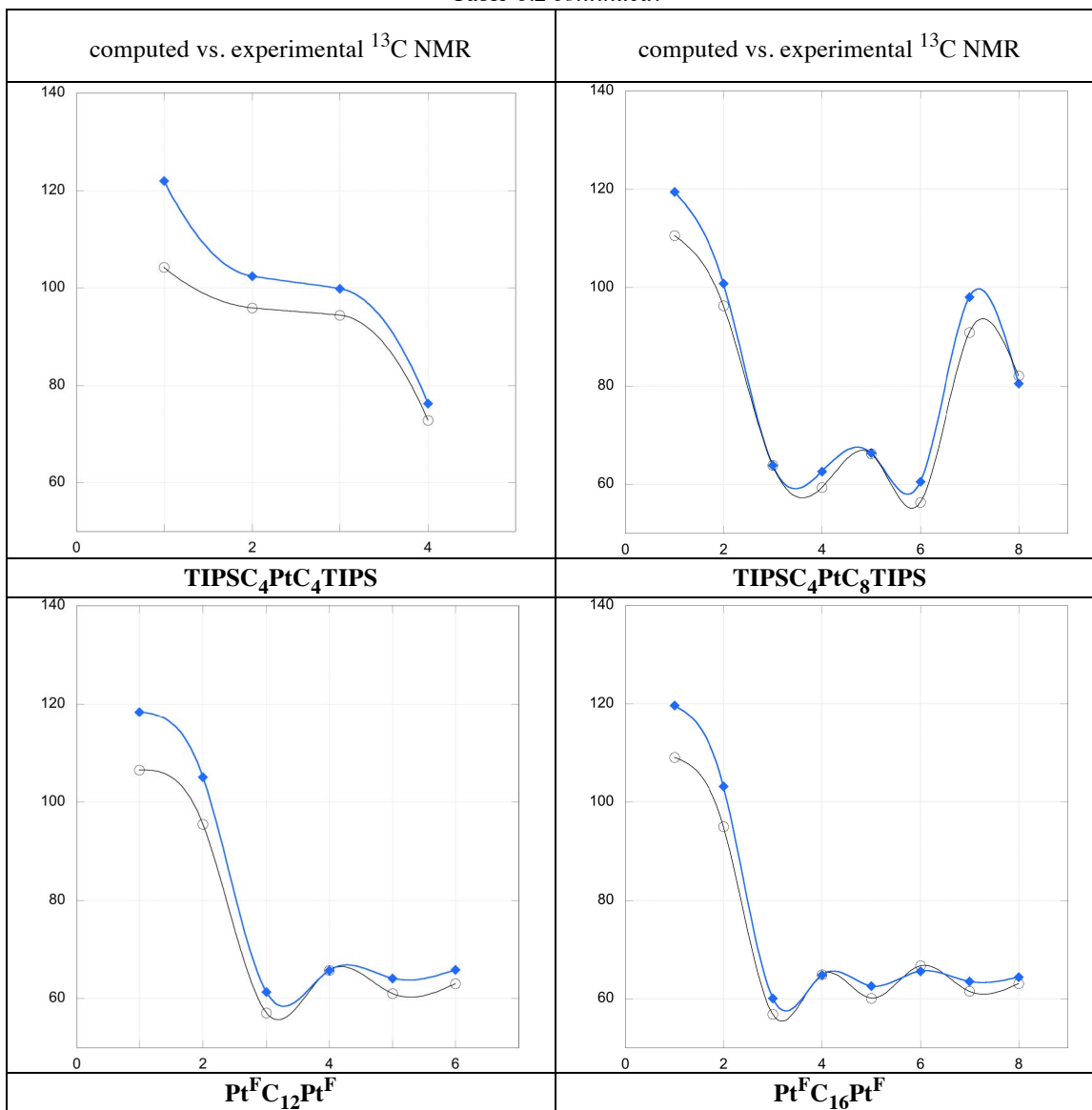
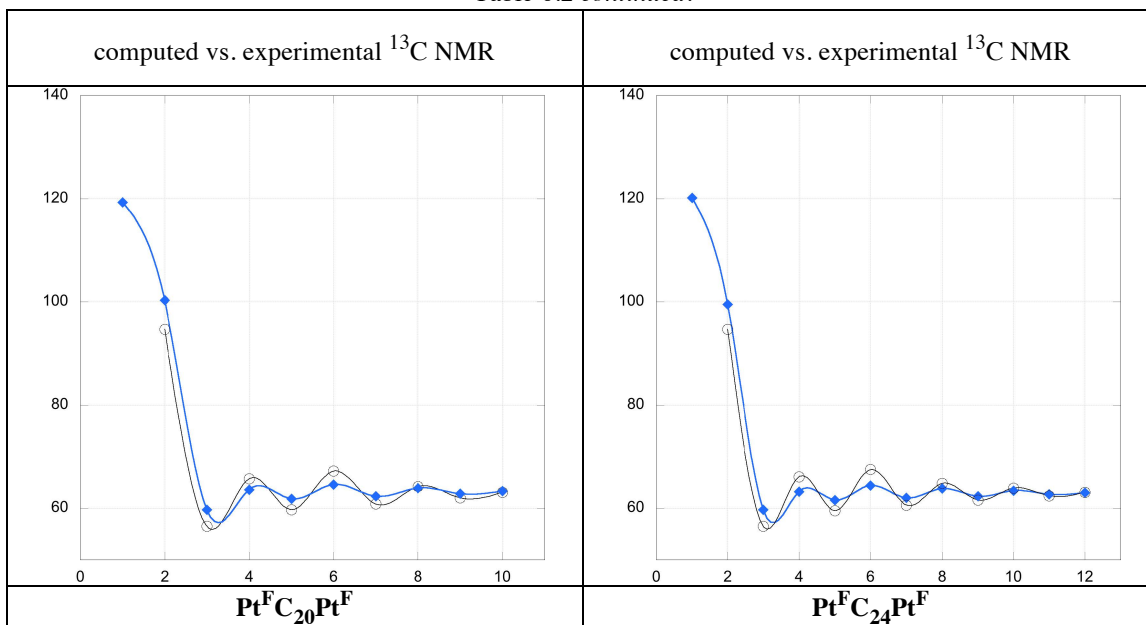


Table 6.2 continued.



6.5. Conclusions

In conclusion, the nucleus independent chemical shift grids associated with the doubly terminal conjugated polyynes $\text{H}(\text{C}\equiv\text{C})_n\text{H}$ do not exhibit any special additive or multiplicative effects, or vestiges of the old ring current model (Figure 6.1). In other words, the degrees of shielding or deshielding encountered in a radial direction perpendicular to the $(\text{C}\equiv\text{C})_n$ linkages are essentially identical, irrespective of the number of the triple bonds and the position or location along the $(\text{C}\equiv\text{C})_n$ linkages. This has significant implications for interpreting the NMR data of conjugated polyynes that engage in mechanical bonding, such as rotaxanes. Finally, it has been shown that the data from these and attendant DFT calculations can also be useful in assigning the C_{sp} ^{13}C NMR signals of conjugated polyynes. These include unsymmetrically substituted systems with trialkylsilyl or platinum(II) endgroups, where except for the $\text{Pt}\underline{\text{C}}\equiv\underline{\text{C}}$ and $\text{Si}\underline{\text{C}}\equiv\underline{\text{C}}$ units the situation is hopeless experimentally.

6.6. References

(1) Johnson, C. E. Jr.; Bovey, F. A. Calculation of Nuclear Magnetic Resonance Spectra of Aromatic Hydrocarbons. *J. Chem. Phys.* **1958**, *29*, 1012-1014.

(2) du Vernet, R.; Boekelheide, V. Nuclear Magnetic Resonance Spectroscopy. Ring-Current Effects on Carbon-13 Chemical Shifts. *Proc. Nat. Acad. Sci. USA* **1974**, *71*, 2961-2964.

(3) Wolf, A. D.; Kane, V. V.; Levin, R. H.; Jones, M. Jr. [7]Paracyclophane. *J. Am. Chem. Soc.* **1973**, *95*, 1680-1680.

(4) Mitchell, R. H.; Chen, Y.; Khalifa, N; Zhou, P. The Synthesis, Aromaticity, and NMR Properties of [14]Annulene Fused Organometallics. Determination of the Effective Bond Localizing Ability ("Relative Aromaticity") and Diamagnetic Anisotropy of Several Organometallic Moieties. *J. Am. Chem. Soc.* **1998**, *120*, 1785-1794 and earlier work cited therein.

(5) Wannere, C. S.; Schleyer, P. v. R. How Do Ring Currents Affect ¹H NMR Chemical Shifts? *Org. Lett.* **2003**, *5*, 603-608, and earlier work by others cited therein.

(6) Nonetheless, contributions from classical ring currents continue to be considered in various contexts: Pelloni, S.; Lazzeretti, P. Ring current models for acetylene and ethylene molecules. *Chemical Physics* **2009**, *356*, 153163.

(7) Dembinski, R.; Bartik, T.; Bartik, B.; Jaeger, M.; Gladysz, J. A. Toward Metal-Capped One-Dimensional Carbon Allotropes: Wirelike C₆-C₂₀ Polyynediyl Chains that Span Two Redox-Active (η^5 -C₅Me₅)Re(NO)(PPh₃) Endgroups. *J. Am. Chem. Soc.* **2000**, *122*, 810-822 and earlier work cited therein.

(8) (a) Mohr, W.; Stahl, J.; Hampel, F.; Gladysz, J. A. Synthesis, Structure, and Reactivity of *sp* Carbon Chains with Bis(phosphine) Pentafluorophenylplatinum Endgroups: Butadiynediyl (C₄) through Hexadecaoctaynediyl (C₁₆) Bridges, and Beyond. *Chem. Eur. J.* **2003**, *9*, 3324-3340. (b) Zheng, Q.; Bohling, J. C.; Peters, T. B.; Frisch, A. C.; Hampel, F.; Gladysz, J. A. A Synthetic Breakthrough into an Unanticipated Stability Regime: A Series of Isolable Complexes in which C₆, C₈, C₁₀, C₁₂, C₁₆, C₂₀, C₂₄, and C₂₈ Polyynediyl Chains Span Two Platinum Atoms. *Chem. Eur. J.* **2006**, *12*, 6486-6505.

(9) (a) Weisbach, N.; Baranová, Z.; Gauthier, S.; Reibenspies, J. H.; Gladysz, J. A. A new type of insulated molecular wire: a rotaxane derived from a metal-capped conjugated tetrayne. *Chem. Commun.* **2012**, *48*, 7562-7564. (b) Baranová, Z.; Amini, H.; Bhuvanesh, N.; Gladysz, J. A. Rotaxanes Derived from Dimetallic Polyynediyl Complexes: Extended Axles and Expanded Macrocycles. *Organometallics* **2014**, *33*, 6746-6749. (c) Amini, H.; Baranová, Z.; Weisbach, N.; Gauthier, S.; Bhuvanesh, N.; Reibenspies, J. H.; Gladysz, J. A. Syntheses, Structures, and Spectroscopic Properties of 1,10-Phenanthroline-Based Macrocycles Threaded by PtC₈Pt, PtC₁₂Pt, and PtC₁₆Pt Axles: Metal-Capped Rotaxanes as Insulated Molecular Wires. *Chem. Eur. J.* **2019**, *25*, 15896-15914.

(10) See also: Bruce, M. I.; Zaitseva, N. N.; Nicholson, B. K.; Skelton, B. W.; White, A. H. Syntheses and molecular structures of some compounds containing many-atom chains end-capped by tricobalt carbonyl clusters. *J. Organomet. Chem.* **2008**, *693*, 2887.

(11) Contemporary research groups active with organic conjugated polyynes: (a) Gibtner, T.; Hampel, F.; Gisselbrecht, J.-P.; Hirsch, A. End-Cap Stabilized Oligoynes: Model Compounds for the Linear *sp* Carbon Allotrope Carbyne. *Chem. Eur. J.* **2002**, *8*, 408-432 and earlier work cited therein. (b) Chalifoux, W. A.; Tykwinski, R. R. Synthesis of polyynes to model the *sp*-carbon allotrope carbyne. *Nature Chem.* **2010**, *2*, 967-971 and earlier work cited therein. (c) Kohn, D. R.; Gawel, P.; Xiong, Y.; Christensen, K. E.; Anderson, H. L. Synthesis of Polyynes Using Dicobalt Masking Groups. *J. Org. Chem.* **2018**, *83*, 2077-2086.

(12) Other studies of rotaxanes based upon conjugated polyynes: (a) Saito, S.; Takahashi, E.; Nakazono, K. Synthesis of [2]Rotaxanes by the Catalytic Reactions of a Macrocyclic Copper Complex. *Org. Lett.* **2006**, *8*, 5133-5136. (b) Movsisyan, L. D.; Franz, M.; Hampel, F.; Thompson, A. L.; Tykwinski, R. R.; Anderson, H. L. Polyynone Rotaxanes: Stabilization by Encapsulation. *J. Am. Chem. Soc.* **2016**, *138*, 1366-1376 and earlier work cited therein.

(13) Catenanes that contain conjugated polyynes: (a) Dietrich-Buchecker, C. O.; Khemiss, A.; Sauvage, J.-P. High-yield Synthesis of Multiring Copper(I) Catenates by Acetylenic Oxidative Coupling. *J. Chem. Soc. Chem. Commun.* **1986**, 1376-1378. (b) Dietrich-Buchecker, C. O.; Hemmert, C.; Khémiss, A.-K.; Sauvage, J.-P. Synthesis of Dicopper [3]-Catenates and [3]-Catenands by Acetylenic Oxidative Coupling. Preparation and Study of Corresponding Homodimetallic [3]-Catenates (Ag^+ , Zn^{2+} , Co^{2+} , and Ni^{2+}). *J. Am. Chem. Soc.* **1990**, *112*, 8002-8008. (c) Hamilton, D. G.; Sanders, J. K. M.; Davies, J. E.; Clegg, W.; Teat, S. J. Neutral [2]catenanes from oxidative

coupling of π -stacked components. *Chem. Commun.* **1997**, 897-898. (d) Hamilton, D. G.; Feeder, N.; Prodi, L.; Teat, S. J.; Clegg, W.; Sanders, J. K. M. Tandem Hetero-Catenation: Templating and Self-Assembly in the Mutual Closure of Two Different Interlocking Rings. *J. Am. Chem. Soc.* **1998**, *120*, 1096-1097. (e) Hamilton, D. G.; Prodi, L.; Feeder, N.; Sanders, J. K. M. Synthesis of macrocycles and an unusually asymmetric [2]catenane via templated acetylenic couplings. *J. Chem. Soc. Perkin Trans. 1*, **1999**, 1057-1065. (f) Duda, S.; Godt, A. The Effect of Ring Size on Catenane Synthesis. *Eur. J. Org. Chem.* **2003**, 3412-3420. (g) Gunter, M. J.; Farquhar, S. M. Neutral π -associated porphyrin [2]catenanes. *Org. Biomol. Chem.* **2003**, *1*, 3450-3457. (h) Miljanić, O. Š.; Dichtel, W. R.; Mortezaei, S.; Stoddart, J. F. Cyclobis(paraquat-*p*-phenylene)-Based [2]Catenanes Prepared by Kinetically Controlled Reactions Involving Alkynes. *Org. Lett.* **2006**, *8*, 4835-4838. (i) Miljanić, O. Š.; Dichtel, W. R.; Khan, S. I.; Mortezaei, S.; Heath, J. R.; Stoddart, J. F. Structural and Co-conformational Effects of Alkyne-Derived Subunits in Charged Donor-Acceptor [2]Catenanes. *J. Am. Chem. Soc.* **2007**, *129*, 8236-8246. (j) Sato, Y.; Yamasaki, R.; Saito, S. Synthesis of [2]Catenanes by Oxidative Intramolecular Diyne Coupling Mediated by Macrocyclic Copper(I) Complexes. *Angew. Chem. Int. Ed.* **2009**, *48*, 504-507; *Angew. Chem.* **2009**, *121*, 512-515.

(14) However, the NICS associated with a currently unknown class of molecules, fully conjugated cyclic polyynes of the formulae C_6 , C_{10} , C_{14} , C_{18} , C_{22} , C_{26} , and C_{30} ($(C\equiv C)_n^-$), have been reported: Remya, K.; Suresh, C. H. Carbon rings: a DFT study on geometry, aromaticity, intermolecular carbon-carbon interactions and stability. *RSC Adv.* **2016**, *6*, 44261-44271.

(15) See the Appendix D for all the computational details including validations of the methodology employed.

(16) ^1H and ^{13}C NMR spectra of $\text{HC}\equiv\text{CH}$ (in CDCl_3): (a) Zuschneid, T.; Fischer, H.; Handel, T.; Albert, K.; Häfelinger, G. Experimental Gas Phase ^1H NMR Spectra and Basis Set Dependence of *ab initio* GIAO MO Calculations of ^1H and ^{13}C NMR Absolute Shieldings and Chemical Shifts of Small Hydrocarbons. *Z. Naturforsch.* **2004**, *59b*, 1153-1176 (see Table 2). (b) Abraham, R. J.; Reid, M. Proton chemical shifts in NMR. Part 16. Proton chemical shifts in acetylenes and the anisotropic and steric effects of the acetylene group. *J. Chem. Soc. Perkin Trans. 2*, **2001**, 1195-1204.

(17) ^1H NMR spectra of $\text{H}(\text{C}\equiv\text{C})_n\text{H}$ ($n = 2, 3$; in CDCl_3): Preparation of Pure Triacetylene, Tetraacetylene, and Pentaacetylene and Investigation of Their Electronic Spectra, Kloster-Jensen, E. *Angew. Chem. Int. Ed.* **1972**, *11*, 438-439; Reindarstellung und Elektronenspektrum des Triacetylen, Tetraacetylen und Pentaacetylen, *Angew. Chem.* **1972**, *84*, 483-485.

(18) ^1H and ^{13}C NMR spectra of $\text{H}(\text{C}\equiv\text{C})_n\text{H}$ ($n = 4, 5, 6$; in $\text{C}_2\text{D}_2\text{Cl}_4$): Wakabayashi, T.; Tabata, H.; Doi, T.; Nagayama, H.; Okuda, K.; Umeda, R.; Hisaki, I.; Sonoda, M.; Tobe, Y.; Minematsu, T.; Hashimoto, K.; Hayashi, S. Resonance Raman spectra of polyynes C_{10}H_2 and C_{12}H_2 in solution. *Chem. Phys. Lett.* **2007**, *433*, 296-300.

(19) ^{13}C NMR spectrum of $\text{H}(\text{C}\equiv\text{C})_2\text{H}$: Kurosu, H.; Webb, G. A.; Ando, I. *Ab initio* ^{13}C Nuclear Shielding Calculations for Some Hydrocarbons using the GIAO Procedure. *Magn. Reson. Chem.* **1992**, *30*, 1122-1124.

(20) The use of implicit solvent models often gives little improvement. However, explicit solvent models may potentially be more helpful, and promising new computational methodologies are becoming available. See for example: Stoychev, G. L.; Auer, A. A.; Neese, F. Efficient and Accurate Prediction of Nuclear Magnetic Resonance Shielding Tensors with Double-Hybrid Density Functional Theory. *J. Chem. Theory Comput.* **2018**, *14*, 4756-4771.

(21) Wang, C.; Batsanov, A. S.; West, K.; Bryce, M. R. Synthesis and Crystal Structures of Isolable Terminal Aryl Hexatriyne and Octatetrayne Derivatives: $\text{Ar}(\text{C}\equiv\text{C})_n\text{H}$ ($n = 3, 4$). *Org. Lett.* **2008**, *10*, 3069-3072.

(22) Tykwinski, R. R.; Luu, T. Synthesis and ^{13}C NMR Spectroscopy of ^{13}C -Labeled α,ω -Diphenylpolyynes. *Synthesis* **2012**, *44*, 1915-1922. Subtle "oscillations" in chemical shift trends noted by these authors are also manifested in our computational data.

(23) Amini, H.; Weisbach, N.; Gauthier, S.; Kuhn, H.; Bhuvanesh, N.; Hampel, F.; Reibenspies, J. H.; Gladysz, J. A. Trapping of Terminal Platinapolyynes by Copper(I) Catalyzed Click Cycloadditions; Probes of Labile Intermediates in Syntheses of Complexes with Extended *sp* Carbon Chains, and Crystallographic Studies. *Chem. Eur. J.* **2021**, *27*, 12619-12634.

(24) Peters, T. B.; Bohling, J. C.; Arif, A. M.; Gladysz, J. A. C₈ and C₁₂ *sp* Carbon Chains that Span Two Platinum Atoms; The First Structurally Characterized 1,3,5,7,9,11-hexayne. *Organometallics* **1999**, *18*, 3261-3263 and the supporting information.

(25) Weisbach, N. Mono-, di-, and trinuclear *cis* and *trans* Platinum Polyynyl and Polyynediyl Complexes with up to 40 *sp* Carbon Atoms. Doctoral Thesis, Friedrich-Alexander-Universität Erlangen-Nürnberg, Erlangen, Germany, 2011.

(26) The $\text{Si}\underline{\text{C}}\equiv\underline{\text{C}}$ ¹³C NMR signals of the trimethylsilyl butadiynes Me₃SiC≡CC≡CEMe₃ (E = Si, Sn) exhibit ¹J_{CSi} values of 77.0-79.0 Hz and ²J_{CSi} values of 10.8-13.6 Hz: Wrackmeyer, B. NMR-UNTERSUCHUNGEN AN ALKYL-STANNANEN. *J. Organomet. Chem.* **1979**, *166*, 353-363. Comparable data for Et₃SiC≡CC≡CSiEt₃ (**TESC₄TES**) can be found in reference [25](#).

(27) Eisler, S.; Slepko, A. D.; Elliot, E.; Luu, T.; McDonald, R.; Hegmann, F. A.; Tykwinski, R. R. Polyynes as a Model for Carbyne: Synthesis, Physical Properties, and Nonlinear Optical Response. *J. Am. Chem. Soc.* **2005**, *127*, 2666-2676.

(28) (a) A reviewer has inquired about the magnitudes of the error bars. Experimentally, this is difficult to rigorously address in the absence of replicate measurements. The resolution on the y-axis in Table 6.2 is ca. 1 ppm, and in accord with general practices on reporting significant digits of ¹³C NMR chemical shifts, signals with good signal/noise should not be off by more than 0.2 ppm. Computationally, errors are very dependent upon the level of theory, as treated in depth in a review.^{[28b](#)} The

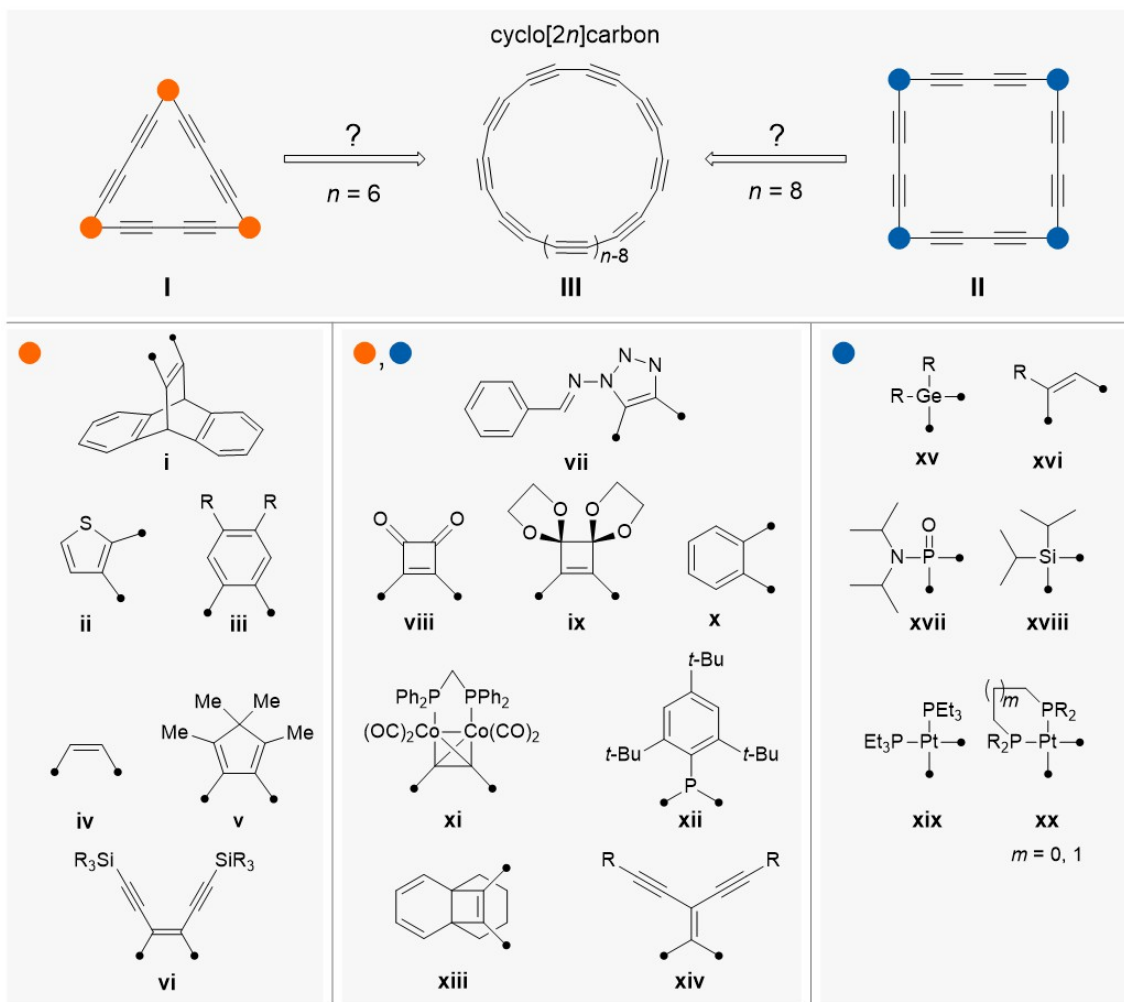
average difference between measured and computed chemical shifts over all of our data (Table 6.1) is 2.4%. The $\text{Pt}\underline{\text{C}}\equiv$ signals are subject to higher average errors due to the heavy atom effect.^{28b} (b) Lodewyk, M. W.; Siebert, M. R.; Tantillo, D. J. Computational Prediction of ^1H and ^{13}C Chemical Shifts: A Useful Tool for Natural Product, Mechanistic, and Synthetic Organic Chemistry. *Chem. Rev.* **2012**, *112*, 1839-1862.

"7. MACROCYCLIC COMPLEXES DERIVED FROM FOUR *cis*-L₂Pt CORNERS
AND FOUR BUTADIYNE-DIYL LINKERS; SYNTHESSES, ELECTRONIC
STRUCTURES, AND SQUARE VERSUS SKEW RHOMBUS GEOMETRIES[†]

7.1. Introduction

Macrocycles that approximate the shapes of polygons¹ have been at the forefront of many lines of research over the last 25 years. Of particular interest have been adducts in which the polygon edges are polyynediyl moieties, $-(C\equiv C)_n-$, such as in the "triangle" **I** and "square" **II** in Scheme 7.1.²⁻⁶ Although there are many reasons to pursue such species, one of the more obvious would be to attempt the extrusion of the corners, or appropriate subunits thereof, to afford a molecule often called "cyclocarbon" (**III**).⁷ This consists of a circle of *sp* hybridized carbon atoms, and the polyene valence isomer shown in Scheme 7.1 is widely viewed as more stable than the cumulated form, except at smaller ring sizes.⁷ The compound with $n = 9$, cyclo[18]carbon or C₁₈, has recently been generated on a NaCl/Cu(111) surface by CO extrusion from a "triangle" with cyclobutenedione corners (**I-ix**).⁸

[†] Reproduced in part with permission from Collins, B. K.; Clough-Mastry, M.; Ehnbohm, A.; Bhuvanesh, N.; Hall, M. B.; Gladysz, J. A. Macrocyclic Complexes Derived from Four *cis*-L₂Pt Corners and Four Butadiynediyl Linkers; Syntheses, Electronic Structures, and Square versus Skew Rhombus Geometries. *Chem. Eur. J.* **2021**, *27*, 10021-10039. Copyright 2021 Wiley-VCH GmbH.



Scheme 7.1 Some previously characterized polygon shaped molecules with butadiynediyl or $-(C\equiv C)_2-$ edges.⁶

Some corner units that have been incorporated into **I** and **II** are illustrated in Scheme 7.1 (**i-xxi**). These include several platinum(II) fragments (**xx-xxi**) that have been applied in "square" systems **II**.⁵ These complexes, which were reported some time ago by Youngs, Bruce, and Anderson, are separately depicted in Scheme 7.2 (**IV-i'** through **IV-iv'**). However, the transcript has since remained silent with regard to higher homologs⁹ or follow-up studies.

We have had an ongoing interest in platinum alkynyl complexes, including diplatinum polyynediyl species $\text{Pt}(\text{C}\equiv\text{C})_n\text{Pt}$ where n is as high as 14.¹⁰⁻¹³ Thus, it was natural that the preceding topics should eventually capture our attention. Given the number of reactions that effect efficient reductive eliminations of sp^2 or sp hybridized hydrocarbyl groups from platinum(II),¹⁴ species of the type **IV** constitute attractive precursors to cyclocarbons **III**. Furthermore, longer $-(\text{C}\equiv\text{C})_n-$ segments would afford cyclocarbons with diminished ring strain. That derived via extrusion of the corner units of **II** or **IV**, C_{16} , was viewed as likely to be quite reactive and problematic to isolate.

However, our initial efforts at synthesizing higher homologs of the Pt_4C_{16} complexes **IV** unearthed a number of complications, one being solubility. In an effort to regroup, we decided to revisit the syntheses of cyclic tetraplatinum complexes with C_4 edges, but with building blocks that would be better platforms for extended systems. Furthermore, the electronic structure and redox properties of **IV** had never been investigated, outside of one early computational effort.^{5b} Accordingly, we report below the syntheses of six new Pt_4C_{16} adducts, their detailed physical characterization, and DFT data that provide insight into various conformational, electronic, and spectroscopic properties, as well as potential equilibria.

7.2. Results Part I: Experimental [major contribution: Ms. B. K. Collins, Dr. Clough Mastry]

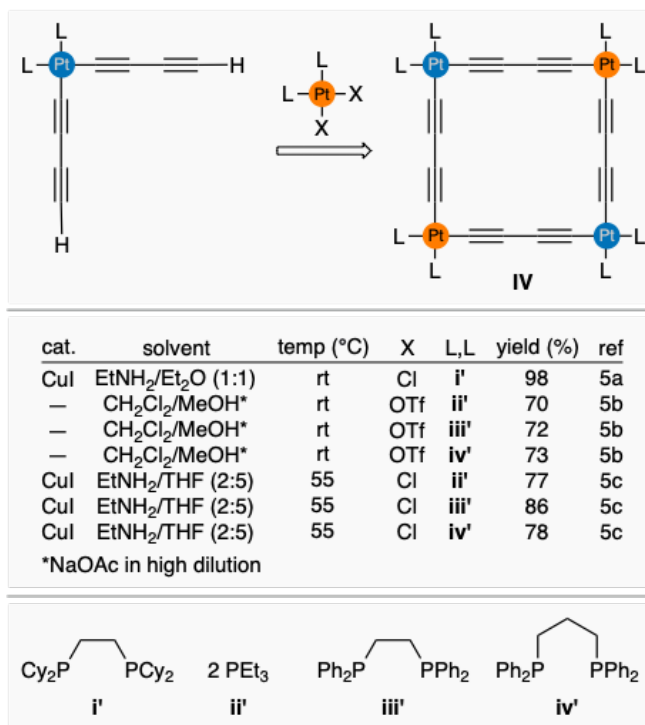
7.3. Diphosphine syntheses

It was thought that geminally disubstituted bis(diphenylphosphino)-propane chelate ligands would likely enhance the lipophilicities and solubilities of the preceding Pt₄C₁₆ systems or homologs with longer $-(C\equiv C)_n-$ segments. As summarized in Scheme 7.3, those studied included the previously reported 1,3-diphosphines Me₂C(CH₂PPh₂)₂ (**1a**),¹⁵ Et₂C(CH₂PPh₂)₂ (**1b**),¹⁵ and Bn₂C(CH₂PPh₂)₂ (**1e**),¹⁶ and the new diphosphines *n*-Bu₂C(CH₂PPh₂)₂ (**1c**), *n*-Dec₂C(CH₂PPh₂)₂ (**1d**), and (*p*-tolCH₂)₂C(CH₂PPh₂)₂ (**1f**).

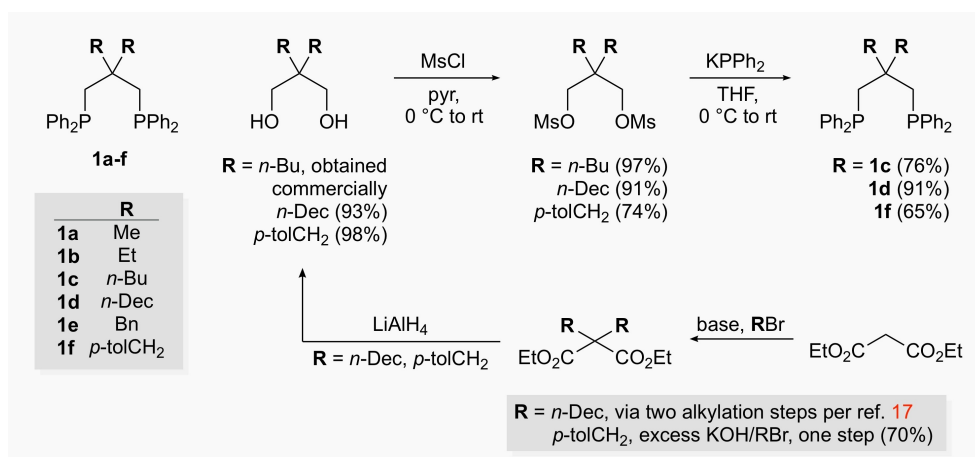
The new ligands were synthesized as depicted in Scheme 7.3. In the case of **1c**, the corresponding 1,3-diol was commercially available. A mesylation/substitution sequence gave **1c** in 76% overall yield. For **1d** and **1f**, it was necessary to start from diethyl malonate.¹⁷ The requisite dialkylated malonates were obtained by standard protocols and reduced to the 1,3-diols (93-98%). Procedures analogous to those used for **1c** then delivered **1d** and **1f** (83-48%). The literature syntheses of the previously reported diphosphines were conceptually similar.^{16,18}

All diphosphines were air stable white solids although **1c,d** had tendencies to oil. They readily oxidized in solution. All new compounds in Scheme 7.3 were characterized by NMR and IR spectroscopy, mass spectrometry, and microanalyses, as summarized in the Experimental section 7.14. The ³¹P{¹H} NMR chemical shifts of the diphosphines are collected in Table 7.1. The PCH₂C ¹³C{¹H} NMR signals were components of non-

first-order spin systems and coupling constants were assigned by simulations as described elsewhere.¹⁹



Scheme 7.2 Previously reported Pt₄C₁₆ complexes with four like corners.

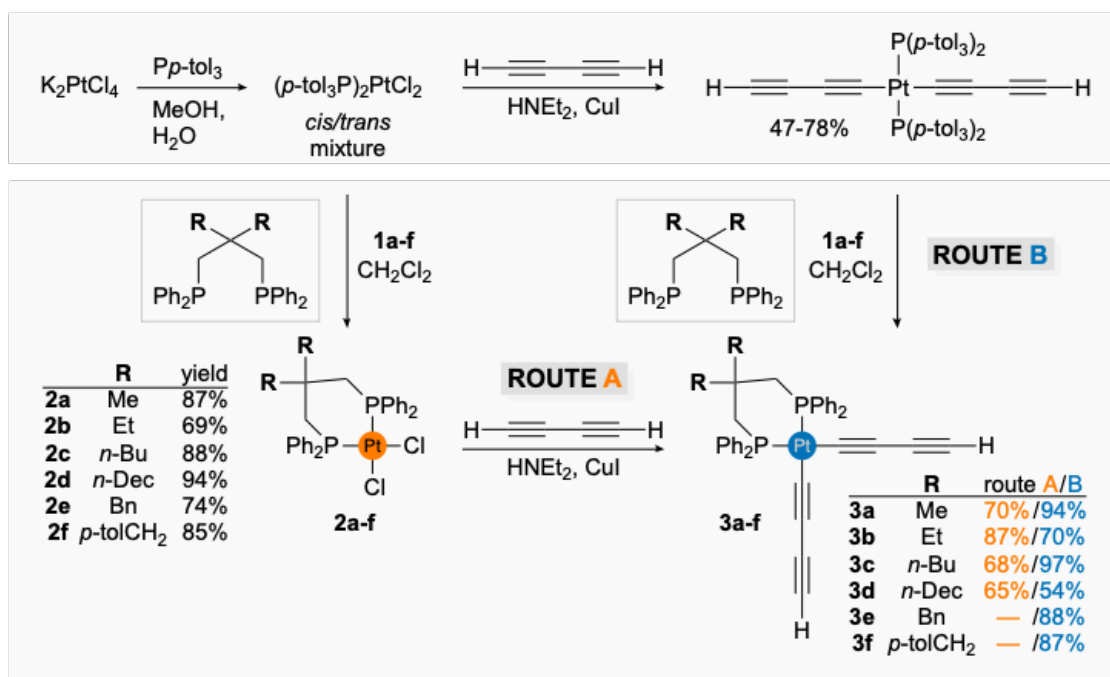


Scheme 7.3 The 1,3-diphosphine ligands used in this study, and syntheses of those not previously reported (**1c,d,f**).

7.4. Monoplatinum complexes

Attention was turned to the preparation of suitable platinum precursors for accessing the target molecules. Per the earlier syntheses in Scheme 7.2, the dichloride complexes *cis*-(R₂C(CH₂PPh₂)₂)PtCl₂ (**2**) and bis(butadiynyl) complexes *cis*-(R₂C(CH₂PPh₂)₂)Pt((C≡C)₂H)₂ (**3**) were sought. As shown in Scheme 7.4, the former could be isolated in 69-94% yields (average 83%) from reactions of the 1,3-diphosphines **1a-f** with *cis/trans* mixtures of (*p*-tol₃P)₂PtCl₂²⁰ in CH₂Cl₂. Complexes **2a-f** were air stable white solids of generally modest solubilities. Nonetheless, NMR spectra (¹H, ¹³C{¹H}, ³¹P{¹H}) could be recorded without difficulty in CDCl₃ or CD₂Cl₂. The NMR, IR, and microanalytical data are summarized in the Experimental section 7.14 and Table 7.1.

Two routes to the bis(1,3-butadiynyl) complexes **3a-f** were investigated (**A**, **B**). In route **A**, the dichloride complexes **2a-d** were treated with excess 1,3-butadiyne in the presence of CuI (catalyst) and HNEt₂ (cosolvent and base for the HCl generated). These represent the standard Sonogashira/Hagihara conditions²¹ that have often been used to construct platinum–alkynyl bonds, as also applied in Scheme 7.2 above. As shown in Scheme 7.4, chromatographic workups gave **3a-d** as air stable tan or light yellow solids in 65-87% yields (average 73%).



Scheme 7.4 Syntheses of monoplatinum complexes.

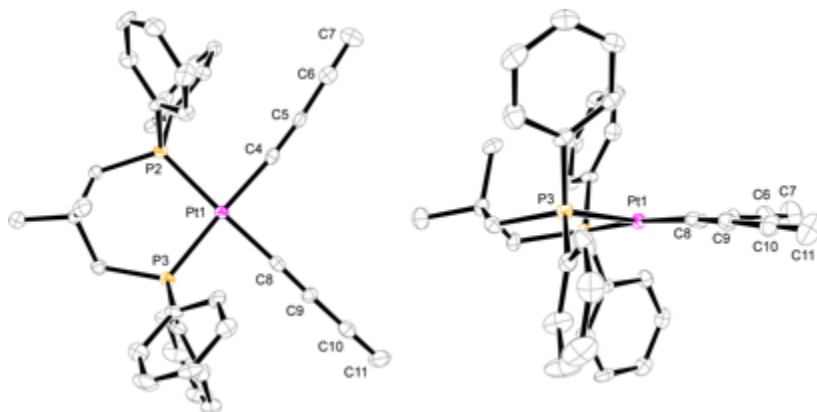


Figure 7.1 Thermal ellipsoid plots (50% probability level) of the crystal structure of **3a**·CH₂Cl₂ with the solvate molecule omitted. Bond lengths (Å) and angles (°) associated with platinum or the butadiynyl ligands: Pt1–C4 1.998(4), Pt1–C8 2.004(4), Pt–P2 2.2912(10), Pt–P3 2.2870(9), C4≡C5 1.212(5), C5–C6 1.387(5), C6≡C7 1.178(5), C8≡C9 1.211(5), C9–C10 1.376(6), C10≡C11 1.188(5), P2–Pt1–P3 96.06(3), Pt1–C4–C5 174.2(3), Pt1–C8–C9 175.6(3), C4–C5–C6 175.1(4), C5–C6–C7 179.8(6), C8–C9–C10 178.2(4), C9–C10–C11 178.9(4).

Table 7.1 $^{31}\text{P}\{^1\text{H}\}$ NMR data for **1a-1f**, **2a-2f**, **3a-3f**, and **4a-4f**.

complex	$^{31}\text{P}\{^1\text{H}\}$ NMR { $^1J_{\text{Ppt}}$ (Hz)}
1a	-26.2
1b	-26.2
1c	-25.8
1d	-25.8
1e	-26.3
1f	-26.1
<hr/>	
2a	-1.3 (3431)
2b	-2.5 (3429)
2c	-2.6 (3419)
2d	-2.6 (3417)
2e	-2.0 (3376)
2f	-2.0 (3386)
<hr/>	
3a^a	-4.9 (2224)
3b	-5.6 (2257)
3c	-6.4 (2225)
3d	-6.6 (2221)
3e	-4.8 (2192)
3f	-3.3 (2196)
<hr/>	
4a^b	-6.1 (2219)
4b^b	-7.7 (2243)
4c^b	-8.5 (2247)
4d	-8.6 (2240)
4e	-4.8 (2192)
4f	-4.6 (2172)

^a Data for *trans*-(*p*-tol₃P)₂Pt((C≡C)₂H)₂: ^{12b} 17.0 ppm, $^1J_{\text{Ppt}}$ 2527 Hz.

^b Data in CD₂Cl₂: **4a**, -5.5 to -5.7 (2200-2195); **4b**, -7.0 to -7.4 (2230-2196); **4c**, -7.7 (2254).

Alternatively, (*p*-tol₃P)₂PtCl₂ was similarly treated with 1,3-butadiyne (route **B**). Following published procedures, the bis (butadiynyl) complex *trans*-(*p*-tol₃P)₂Pt((C≡C)₂H)₂ was isolated in 47-78% yields.^{12b,19} This adduct was combined with the 1,3-diphosphines **1a-f** to give the target complexes **3a-f** in 54-97% (average 82%) yields. Overall, the two routes were judged comparable in terms of ease and yields.

Complexes **3a-f** were characterized analogously to the dichlorides **2a-f**. They were more soluble in common solvents such as CH₂Cl₂ or CHCl₃. However, solutions (non-degassed) generally showed significant decomposition after several days. The ¹J_{Pt} values (2200-2300 Hz; Table 7.1) were much smaller than those of **2a-f** (3300-3400 Hz).

The ¹³C{¹H} NMR signals of the *sp* hybridized carbon atoms are summarized in Table 7.2. The chemical shift trends follow those of related platinum mono(butadiynyl) complexes reported earlier.^{10a,b} However, the PtC≡ signals are now doublets of doublets due to coupling to inequivalent *cis* and *trans* phosphorus atoms (²J_{CP}). For reference, the PtC≡ signal of the precursor *trans*-(*p*-tol₃P)₂Pt((C≡C)₂H)₂ is a triplet due to coupling to two homotopic *cis* phosphorus atoms (CDCl₃, 102.7 ppm, ²J_{CP} = 15.3 Hz).²² The ²J_{CP} value is similar to the smaller ²J_{CP} values in Table 7.2 (18.2-22.1 Hz), which are thereby assigned to the *cis* phosphorus atoms. The much larger ²J_{CP} values (145.6-149.0 Hz) must therefore be associated with the *trans* phosphorus atoms. For the PtC≡C signals, only one coupling is resolved (³J_{CP} = 17.8-18.4 Hz), and assigned to the *trans* phosphorus atom.

Single crystals of the solvate **3a**·CH₂Cl₂ could be grown. X-ray data were collected and the structure refined as summarized in Table 7.3 and the experimental section 7.14.2. Thermal ellipsoid plots are shown in Figure 7.1. The metrical parameters are very similar to those of the analogous compound lacking the geminal dimethyl groups (Scheme 7.2),^{5b} and a comparative table is provided in Appendix E.

7.5. Syntheses of tetraplatinum complexes

Next, the Pt₄C₁₆ complexes $[(R_2C(CH_2PPh_2)_2)[Pt(C\equiv C)_2]_4$ (**4**) were sought. As depicted in Scheme 7.5, equimolar quantities of **2** and **3** were reacted under Sonogashira/Hagihara coupling conditions.²¹ In contrast to the similar platinum–carbon bond forming reactions involving 1,3-butadiyne in Scheme 7.4, those in Scheme 7.5 required elevated temperatures (55 °C) and extended time periods (48-72 h) to go to completion.

The Pt₄C₁₆ complexes **4a-f** were isolated as air stable and usually tan solids in 89-14% yields. Although these species could be "completely characterized", including three crystal structures, analytically pure samples could not be obtained. As detailed in the Experimental section 7.14, all complexes were admixed with 1-2 equiv. of an ammonium salt, as established by ¹H and ¹³C{¹H} NMR. In many cases, this was [H₂NEt₂]⁺ Cl⁻, the standard coproduct of the Sonogashira/Hagihara conditions.²¹ In other cases, this was the protonated tertiary amine [HNEt₃]⁺ Cl⁻, as samples remained at the origin in silica gel thin layer chromatography unless HNEt₂ or NEt₃ was added to the

eluting solvent (e. g. 5% in CH₂Cl₂). All attempts to remove these materials by washings²³ or heating under vacuum were unsuccessful.

These observations were reproduced by several coworkers over the course of several years. Microanalyses showed appropriate levels of chlorine, but the presence of lesser amounts of iodine (from the CuI catalyst) was not excluded. The formula weight of the ammonium salt was factored into all yield calculations. Typical NMR spectra, which show minor impurities, are included in Appendix E. Similar observations were reported by Bruce and Anderson with their Pt₄C₁₆ complexes in Scheme 7.2.^{5b,c} Insight regarding this phenomenon is provided by DFT calculations below.

Mass spectrometry represents another probe of composition, and the ESI⁺ traces of **4a,b** showed strong ions corresponding to [**4**+HNEt₂]⁺ (40-25%). MALDI⁺ experiments involving various matrices never showed amine derived adducts. However, ions of the composition [**4**+H]⁺, [**4**+K]⁺ or [**4**+Cu]⁺ could be detected. Since copper was not present in the matrices employed, the last ion must originate from the CuI. In no case were ions diagnostic of other macrocycle cores observed (Pt₃C₁₂, Pt₅C₂₀, Pt₆C₂₄, etc.).

Table 7.2 $^{13}\text{C}\{^1\text{H}\}$ NMR data for **3a-3f** and **4a-4f** (δ , ppm; CDCl_3 unless noted).

complex	PtC \equiv C ($^2J_{\text{CP}}$ (Hz) ^a)	PtC \equiv C (J (Hz)) ^b	C \equiv C	\equiv CH
3a	95.4 (146.6, 18.2)	91.9 (18.4)	71.7	61.6
3b	95.7 (149.0, 20.0)	91.7 (17.8)	71.8	61.3
3c	96.1 (148.0, 19.2)	91.6 (18.2)	72.0	61.2
3d	95.8 (147.2, 19.0)	91.5 (17.9)	71.8	61.1
3e	96.1 (145.6, 22.1)	92.8 (18.1)	71.8	61.9
3f	96.3 (146.4, 19.4)	92.7 (18.4)	71.9	61.9
4a	91.8 (141.1, 21.1)	96.9 (16.9)	—	—
—	91.8 (148.2, 10.6) ^c	96.7 (18.9) ^c	—	—
4b	91.4 (144.9, 19.9)	96.8 (21.0)	—	—
—	93.2 (137.3, 29.6) ^c	96.7 (23.2) ^c	—	—
4c	92.3 (135.6, 16.8) ^c	96.5 (17.3) ^c	—	—
4d	91.3 (146.1, 20.1)	96.5 (15.1)	—	—
4e	92.5 (149.0, 19.1)	97.6 (19.9)	—	—
4f	88.4 (149.6, 18.1)	97.5 (16.9)	—	—

^a The smaller value is derived from the *cis* phosphorus atom, as established in the text. ^b Multiplet, including triplet with apparent J value indicated. For more detailed analyses of NMR spectra of complexes related to **3a-f**, including simulations. ^c These data are from a spectrum recorded in CD_2Cl_2 .

Table 7.3 General crystallographic data.

crystallographic parameters	3a ·CH ₂ Cl ₂	4a ^a	4b ·2CH ₂ Cl ₂ ^a	4b ·3.44DMSO ^b
empirical formula	C ₃₈ H ₃₄ Cl ₂ P ₂ Pt	C ₁₃₂ H ₁₁₁ P ₈ Pt ₄	C ₁₄₂ H ₁₄₀ Cl ₄ P ₈ Pt ₄	C _{164.9} H _{210.6} O _{12.4} P ₈ Pt ₄ S _{12.4}
formula weight	818.58	2725.33	3016.45	3818.51
temperature [K]	110(2)	110(2)	110(2)	110.0
diffractometer	Bruker GADDS	Bruker GADDS	Bruker GADDS	Bruker QUEST
wavelength [Å]	1.54178	1.54178	1.54178	0.71073
crystal system	orthorhombic	triclinic	triclinic	triclinic
space group	<i>Pbca</i>	<i>P</i> -1	<i>P</i> -1	<i>P</i> -1
<i>unit cell dimensions:</i>				
<i>a</i> [Å]	17.3247(11)	13.9731(6)	21.4521(12)	19.9523(10)
<i>b</i> [Å]	16.4634(11)	19.3822(8)	22.7781(15)	20.5839(10)
<i>c</i> [Å]	24.0781(16)	32.3857(13)	25.5864(15)	24.8550(12)
α [°]	90	90.232(2)	101.570(3)	113.118(2)
β [°]	90	100.137(2)	106.404(3)	107.319(2)
γ [°]	90	94.743(2)	111.935(3)	93.375(2)
<i>V</i> [Å ³]	6867.6(8)	8603.0(6)	10446.6(11)	8781.1(8)
<i>Z</i>	8	2	2	2
ρ_{calc} [Mg m ⁻³]	1.583	1.052	0.959	1.444
μ [mm ⁻¹]	10.144	6.895	6.173	3.451
<i>F</i> (000)	3232	2670	2984	3861
crystal size [mm ³]	0.08 × 0.07 × 0.02	0.10 × 0.09 × 0.04	0.04 × 0.03 × 0.03	0.162 × 0.149 × 0.024
θ limit [°]	3.67 to 60.00	2.29 to 60.00	1.917 to 60.50	1.80 to 24.73
index range (<i>h, k, l</i>)	-18, 19; -18, 18; -27, 27	-15, 14; -21, 21; -36, 36	-24, 24; -26, 26; -29, 29	-23, 23; -24, 24; -29, 29
reflections collected	96875	73407	146971	229989
independent reflections	5095	24343	31113	29975
<i>R</i> (int)	0.0911	0.0486	0.0765	0.0580
max./min. transmission	0.4623/0.2365	0.7519/0.6310	0.4623/0.3237	0.3306/0.2328
data/restraints/parameters	5095/0/390	24343/0/1297	31113/434/1431	29975/121/1540
goodness-of-fit on <i>F</i> ²	0.969	0.960	1.069	1.027
<i>R</i> indices (final) [<i>I</i> > 2 σ (<i>I</i>)]				
<i>R</i> ₁	0.0232	0.0396	0.0716	0.0417
w <i>R</i> ₁	0.0493	0.0996	0.1895	0.0983
<i>R</i> indices (all data)				
<i>R</i> ₂	0.0320	0.0505	0.1083	0.0503
w <i>R</i> ₂	0.0503	0.1030	0.2153	0.1027
largest diff. peak and hole [e Å ⁻³]	0.674 and -0.843	2.538 and -1.109	6.546 and -2.016	3.812 and -1.941

^a Some or all of the solvent molecules associated with these structures were removed using protocols described in the Experimental section 7.14.2. Hence, the formula weight and density are underestimated. ^b The empirical formula includes nine DMSO molecules that were masked; see Experimental section 7.14.2.

Table 7.4 Key crystallographic distances [Å] and angles [°] for new Pt₄C₁₆ complexes.

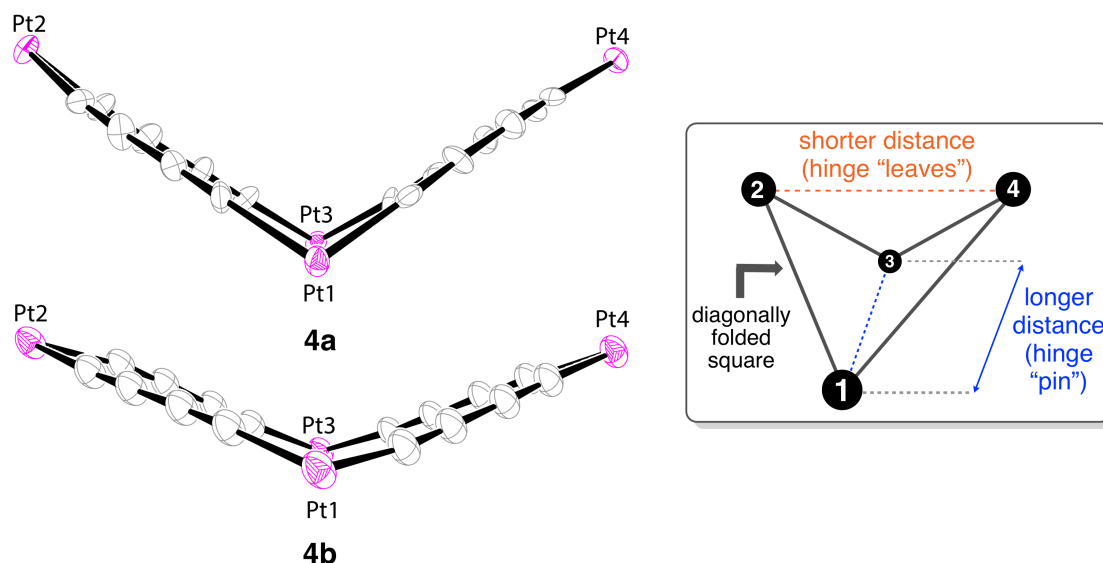
	4a	4b ·2CH ₂ Cl ₂ ^b	4b ·3.44DMSO ^b
Pt1–C1	2.006(6)	2.019(11)	2.006(6)
Pt1–C16	1.998(7)	2.044(12)	2.005(6)
Pt2–C4	2.001(6)	2.007(10)	1.986(5)
Pt2–C5	2.010(6)	2.009(14)	2.012(5)
Pt3–C8	2.008(6)	2.051(13)	2.018(6)
Pt3–C9	2.009(6)	2.005(10)	1.992(6)
Pt4–C12	2.022(6)	2.011(10)	2.026(7)
Pt4–C13	1.998(6)	2.003(11)	2.017(6)
avg. Pt–C	2.007(8) ^b	2.019(18) ^b	2.008(13) ^b
Pt1–P1	2.2825(15)	2.284(3)	2.2837(15)
Pt1–P2	2.2819(14)	2.266(3)	2.2727(14)
Pt2–P3	2.2810(15)	2.268(3)	2.2811(13)
Pt2–P4	2.2809(16)	2.279(3)	2.2839(14)
Pt3–P5	2.2771(15)	2.292(3)	2.2713(15)
Pt3–P6	2.2812(15)	2.267(4)	2.2873(14)
Pt4–P7	2.2770(14)	2.274(3)	2.2669(16)
Pt4–P8	2.2787(15)	2.276(3)	2.2603(18)
avg. Pt–P	2.2800(2) ^b	2.276(9) ^b	2.276(9) ^b
C1≡C2	1.231(9)	1.203(14)	1.209(8)
C2–C3	1.377(9)	1.383(15)	1.384(8)
C3≡C4	1.212(9)	1.199(14)	1.210(8)
C5≡C6	1.192(8)	1.151(16)	1.205(8)
C6–C7	1.408(9)	1.383(17)	1.383(8)
C7≡C8	1.187(8)	1.216(15)	1.203(8)
C9≡C10	1.208(8)	1.218(14)	1.200(9)
C10–C11	1.376(9)	1.347(15)	1.388(10)
C11≡C12	1.180(8)	1.237(14)	1.180(9)
C13≡C14	1.218(8)	1.195(15)	1.192(8)
C14–C15	1.372(9)	1.402(17)	1.386(9)
C15≡C16	1.220(9)	1.167(15)	1.191(8)
avg. C≡C	1.206(17) ^b	1.198(17) ^b	1.199(10) ^b
C16–Pt1–C1	86.1(2)	88.2(4)	86.2(2)
C4–Pt2–C5	88.6(2)	88.1(4)	87.5(2)
C8–Pt3–C9	86.5(2)	87.8(4)	86.6(2)
C12–Pt4–C13	88.3(2)	87.1(4)	89.87(17)
avg. C–Pt–C	87.4(12) ^b	87.8(5) ^b	87.5(16) ^b

Table 7.4 continued.

	4a	4b ·2CH ₂ Cl ₂ ^b	4b ·3.44DMSO ^b
Pt1–C1–C2	176.5(5)	174.7(10)	176.3(5)
C1–C2–C3	177.4(7)	179.2(16)	176.8(7)
C2–C3–C4	177.9(6)	175.3(15)	179.7(6)
C3–C4–Pt2	176.6(5)	177.4(10)	179.6(5)
Pt2–C5–C6	179.4(6)	172.2(11)	178.6(5)
C5–C6–C7	177.9(7)	176.3(13)	178.3(7)
C6–C7–C8	177.0(8)	173.9(11)	178.0(7)
C7–C8–Pt3	173.6(5)	172.9(9)	177.1(6)
Pt3–C9–C10	174.7(5)	178.2(10)	175.2(6)
C9–C10–C11	177.7(7)	178.3(12)	175.7(8)
C10–C11–C12	179.6(8)	178.1(13)	179.2(8)
C11–C12–Pt4	174.1(5)	175.6(9)	176.9(7)
Pt4–C13–C14	176.9(5)	175.7(11)	175.8(6)
C13–C14–C15	177.9(7)	175.9(14)	177.9(8)
C14–C15–C16	177.6(7)	177.7(13)	179.2(8)
C15–C16–Pt1	177.0(5)	170.2(11)	175.5(6)
Pt1–Pt2–Pt3 vs. Pt1–Pt4–Pt3 ^c	111	138	135
Pt1–Pt2	7.812	7.798	7.790
Pt1–Pt4	7.789	7.786	7.784
Pt2–Pt3	7.785	7.813	7.817
Pt3–Pt4	7.772	7.790	7.773
Pt1–Pt3	10.144	10.710	10.745
Pt2–Pt4	9.735	10.582	10.434

^a The atom numbers for **4b**·2CH₂Cl₂ and **4b**·3.44DMSO have been changed from those in the CIF files to facilitate comparisons with **4a**. ^b This represents the standard deviation of the averaged values. ^c A plane/plane angle.

Table 7.5 Views of the puckered hinge like Pt₄C₁₆ cores of **4a** (middle) and **4b** (bottom), and plane/plane angles (°) and platinum-platinum distances (Å) in these and related complexes.



complex	Pt1–Pt2–Pt3 vs. Pt1–Pt4–Pt3 (°)	Pt1–Pt2	Pt1–Pt4	Pt2–Pt3	Pt3–Pt4	Pt1–Pt3	Pt2–Pt4
4a ^a	111	7.812	7.789	7.785	7.772	10.144	9.735
4b ·2CH ₂ Cl ₂ ^a	138	7.798	7.786	7.813	7.790	10.710	10.582
4b ·3.44DMSO ^a	135	7.790	7.784	7.817	7.773	10.745	10.434
IV-iii ^b	180	7.811	7.829	7.829	7.811	11.502	10.597
IV-iii ^b	176	7.779	7.789	7.726	7.782	11.265	10.703
IV-iv ^c	125	7.775	7.776	7.776	7.775	10.726	9.972

^a These complexes contain additional solvent molecules that could not be refined; see text. ^b These data are for two different solvates of **IV-iii**. ^{5b} ^c These data correspond to a solvate. ^{5b}

7.6. Physical characterization of tetraplatinum complexes

The NMR properties of **4a-f** generally paralleled those of **3a-f**. As summarized in Table 7.1, the $^{31}\text{P}\{^1\text{H}\}$ NMR chemical shifts and $^1J_{\text{PPt}}$ values were quite similar. However, the $^{13}\text{C}\{^1\text{H}\}$ NMR chemical shifts of the $\text{Pt}\underline{\text{C}}\equiv\underline{\text{C}}$ signals (Table 7.2) flip-flopped, with C_α downfield of C_β , as could be unambiguously inferred from the $^nJ_{\text{CP}}$ values. The IR spectra exhibited a single $\nu_{\text{C}\equiv\text{C}}$ band (2150-2191 cm^{-1}), always within 8 cm^{-1} of that found for **3a-f**.

To our knowledge, no UV-visible or cyclic voltammetry data for the previously synthesized Pt_4C_{16} systems in Scheme 7.2 have been reported. Accordingly, UV-visible spectra of **4a,b** were recorded in CH_2Cl_2 . These are depicted in Figure 7.2, together with spectra of the precursor *cis* bis(butadiynyl) complexes **3a,b** and the diplatinum butadiynediyl or PtC_4Pt complex *trans,trans*-(C_6F_5)(*p*-tol₃P)₂Pt(C≡C)₂Pt(*Pp*-tol₃)₂(C_6F_5) (**5**). The Pt_4C_{16} systems exhibit much more intense and red-shifted absorptions, indicating chromophoric units fundamentally different from those in related $\text{Pt}((\text{C}\equiv\text{C})_2\text{H})_2$ or $\text{Pt}(\text{C}\equiv\text{C})_2\text{Pt}$ species. This is further treated computationally below.

Cyclic voltammograms of the PtC_4Pt complex **5** in CH_2Cl_2 under standard conditions exhibit a partially reversible one electron oxidation.^{10a,13b} However, parallel experiments with **4a,b** show multistage oxidations (0.8-1.2V) that are essentially irreversible.

After some effort, single crystals of a solvate of **4a** were obtained from DMSO/EtOAc. X-ray data were collected and the structure refined as summarized in Table 7.3 and the experimental section 7.14.2. Numerous DMSO molecules were present, most of which were disordered. In a standard protocol they were removed using the programs SQUEEZE and PLATON. Further details are provided in the experimental section 3.6.3. The molecular structure of **4a** is depicted in Figure 7.3 (top), and key metrical parameters are summarized in Table 7.4.

Crystals of **4b** could be grown from CH₂Cl₂/(toluene/Et₂O). X-ray data were similarly collected and treated. Of the many solvent molecules present, two (both CH₂Cl₂) could be refined, and the rest were removed via SQUEEZE and PLATON. The molecular structure of **4b**·2CH₂Cl₂ is also shown in Figure 7.3 (bottom). Interestingly, another solvate of **4b** could be crystallized from DMSO/EtOAc. Of the numerous DMSO molecules, 3.44 could be successfully modeled, and the rest were "masked". Since the structure of the Pt₄C₁₆ core was quite similar to that in the previous structure, it is not depicted, but metrical parameters are included in tables and graphics below.²⁴

The perspectives in Figure 7.3 obscure an important structural feature. Namely, the Pt₄C₁₆ units are not planar, but rather puckered, reminiscent of cyclobutane. This trait is highlighted in the hinge like partial structures in Table 7.5. Two platinum atoms with a 1,3 relationship define the pivot pin of a hinge (Pt1, Pt3), and the other two the distal termini of the leaves of a hinge (Pt2, Pt4).

As further illustrated in the inset in Table 7.5, the distance between the former pair is always greater than that of **4b**·3.44DMSO vs. **4a** indicates a lower degree of

puckering. between the latter (**4a**, 10.144 Å vs. 9.735 Å; **4b**·2CH₂Cl₂, 10.710 Å vs. 10.582 Å; **4b**·3.44DMSO 10.745 Å vs. 10.434 Å). The greater distance between Pt2 and Pt4 in **4b**·2CH₂Cl₂.

Puckering is most simply quantified by the angle defined by the planes of the two leaves. The planes were approximated by those of the three component platinum atoms. As summarized in Table 7.5, the angles in **4a**, **4b**·2CH₂Cl₂, and **4b**·3.44DMSO range from 111° to 138°. In contrast, crystal structures of the previously reported complex **IV-iii'** (two different solvates) exhibit nearly planar Pt₄C₁₆ cores, as reflected by plane/plane angles of 180-176°. Although this is consistent with essentially square geometries, the Pt1–Pt3 and Pt2–Pt4 distances involving opposite corners differ by 9-5% ($\Delta\text{\AA}$ 0.905 and 0.562).

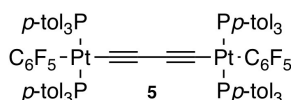
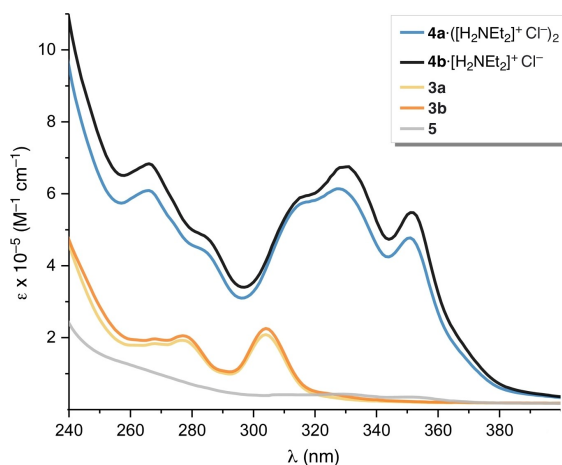
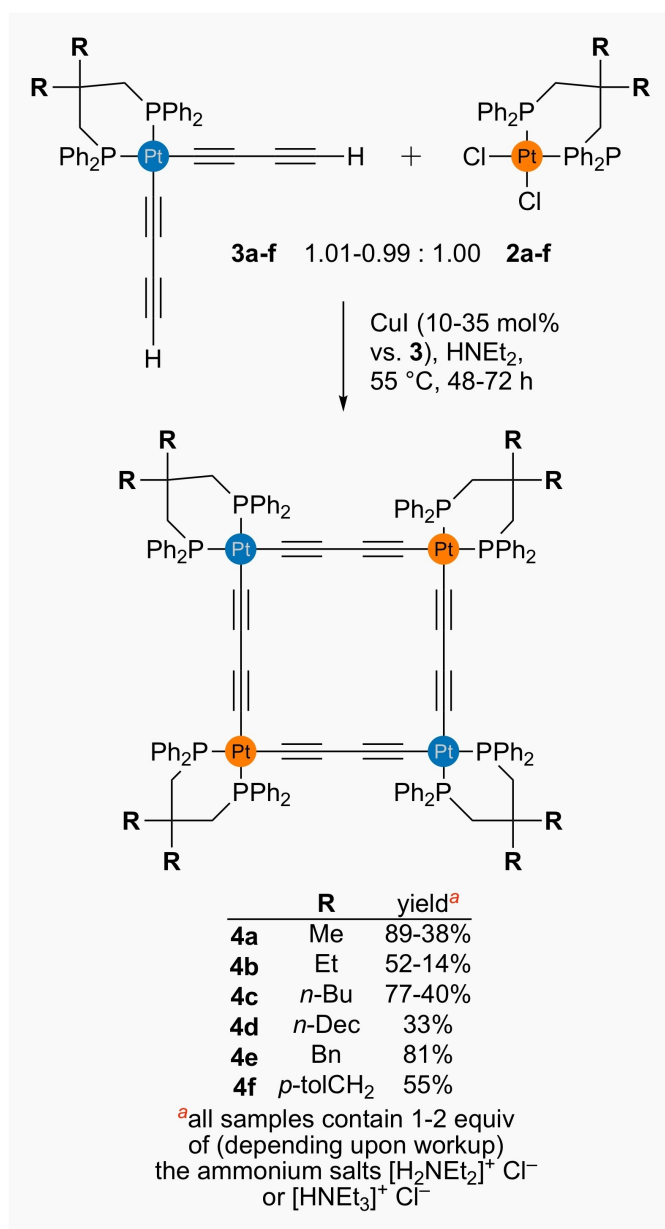


Figure 7.2 UV-visible spectra of the Pt₄C₁₆ complexes **4a,b**·([H₂NEt₂)⁺ Cl⁻)_n, the precursor Pt(C₄H₉)₂ species **3a,b**, and the PtC₄Pt species **5** (3.0 × 10⁻⁵ M in CH₂Cl₂). λ_{max} (nm) [ε (M⁻¹ cm⁻¹): **4a**, 266 [564,000], 327 [602,000], 350 [454,000]; **4b**, 266 [639,000], 330 [635,000], 351 [525,000]; **3a**, 268 [130,000], 277 [138,000], 304 [166,000]; **3b**, 268 [128,000], 277 [136,000], 304 [165,000]; **5**, 330 [17,500], 350 [13,600]. The ε values for **4a,b** are calculated including the formula weight of the [H₂NEt₂)⁺ Cl⁻ present (see text and experimental section 7.6 and 7.14).



Scheme 7.5 Syntheses of Pt₄C₁₆ complexes that are admixed with 1-2 equiv. of ammonium salts (see text).

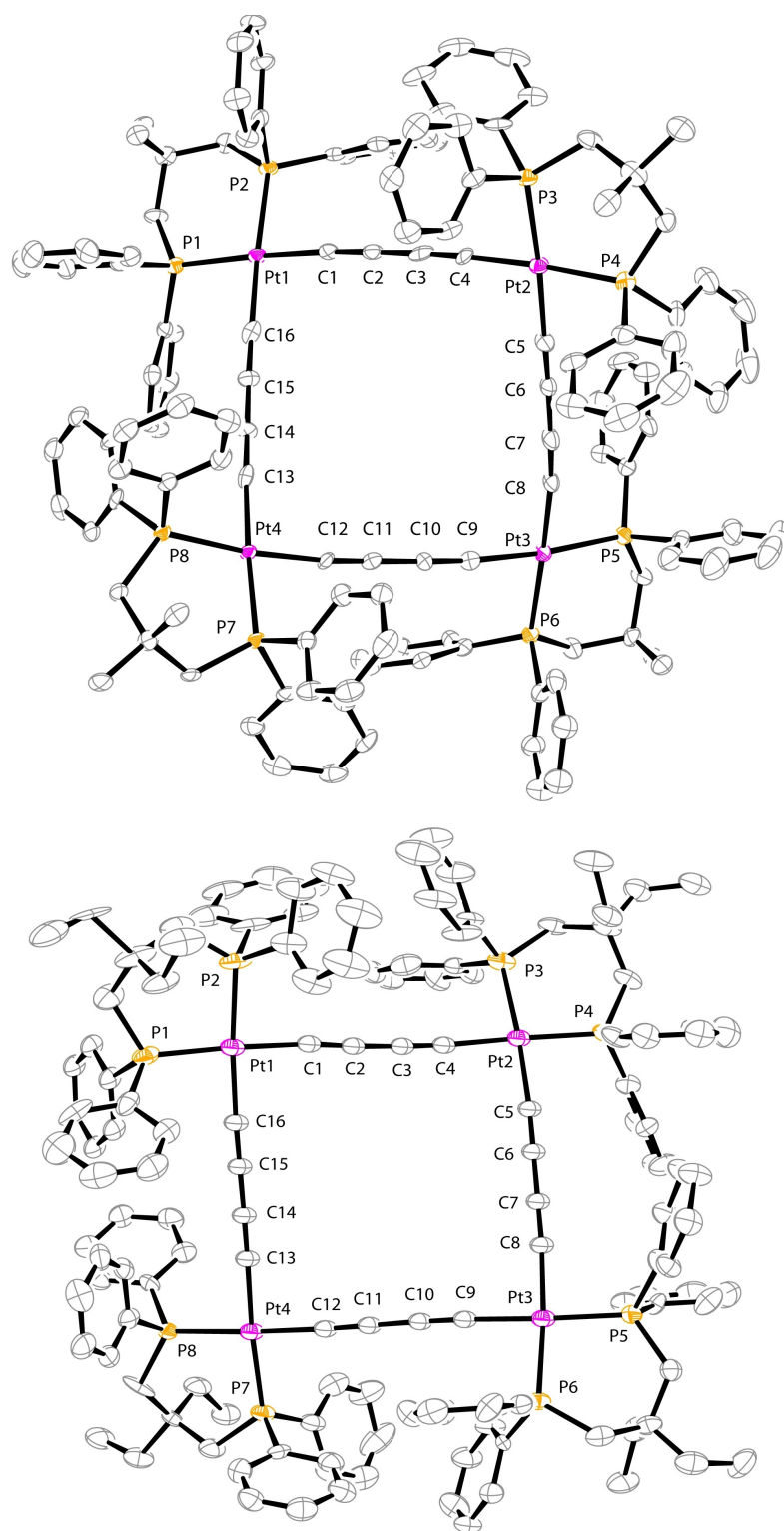


Figure 7.3 Thermal ellipsoid plots (50% probability) of the molecular structures of the Pt₄C₁₆ complexes **4a**. Solvate molecules have been omitted.

In a quest for further insight, a ^{195}Pt NMR spectrum of **4a** was recorded. Only a single signal was observed (-3339 ppm, CD_2Cl_2), coupled to ^{31}P (t, $^1J_{\text{PtP}} = 2215$ Hz) with nearly the same J value as measured from the ^{31}P NMR spectrum (2200 Hz). Thus, there must be a low energy pathway by which the platinum corners in puckered conformations can exchange, or a planar ground state conformation in solution. These issues helped prompt the computational investigation in the following section.

7.7. Results Part II: Computations [major contribution: Mr. A. Ehnbohm]

7.8. Computations: Conformational and constitutional equilibria

Insight was sought regarding a number of properties of the Pt_4C_{16} complexes. The first concerned structure. Earlier computational investigations have nicely modeled features associated with linear $\text{Pt}(\text{C}\equiv\text{C})_n\text{Pt}$ segments,²⁵ so the edge units were not of particular concern. However, a rationale for the variable planar (\sim square) and puckered (skew rhombus) Pt_4C_{16} conformations exhibited by the six structures in Table 7.5 was desired.

Although the authors have considerable computational resources available that have sufficed for many types of large molecules,²⁶ due to the four platinum atoms in **4a** it proved necessary to study a model compound in which the PPh groups were replaced by PMe groups (denoted **4'a**). Accordingly, a number of DFT conditions (functional, basis sets, solvents, etc.) were applied to the planar and puckered forms of **4'a** from their fully optimized structures in the CAM-B3LYP/6-311G(d) level of theory in the gas phase. Subsequent frequency analyses confirmed that both were local minima. The angle

between the "hinge leaves" of the latter was 142° (Pt1–Pt3 10.370 Å, Pt2–Pt4 10.339 Å). However, as shown in Figure 7.4 (bottom), comparable energy ranges were found, viewed over all of the theoretical models employed.

This suggests that crystal packing forces may also play roles in the structures in Table 7.5, as further supported in the Discussion section 7.10. Transition states were also probed, but in order to realize a converged structure, it was necessary to replace all phosphine ligands by PH_3 (**4''**). This exhibited the intuitively expected intermediate geometry with the imaginary vibration displacing two diagonal corners upwards, with the other two moving downwards (Figure 7.4, top). For this stripped down model, the puckered conformation was very slightly more stable, but the value (-0.3 kcal/mol) was well within the range viewed as "experimental error" for DFT calculations. The modest barrier calculated (ca. 14 kcal/mol) is consistent with the ^{195}Pt NMR data for **4a**.

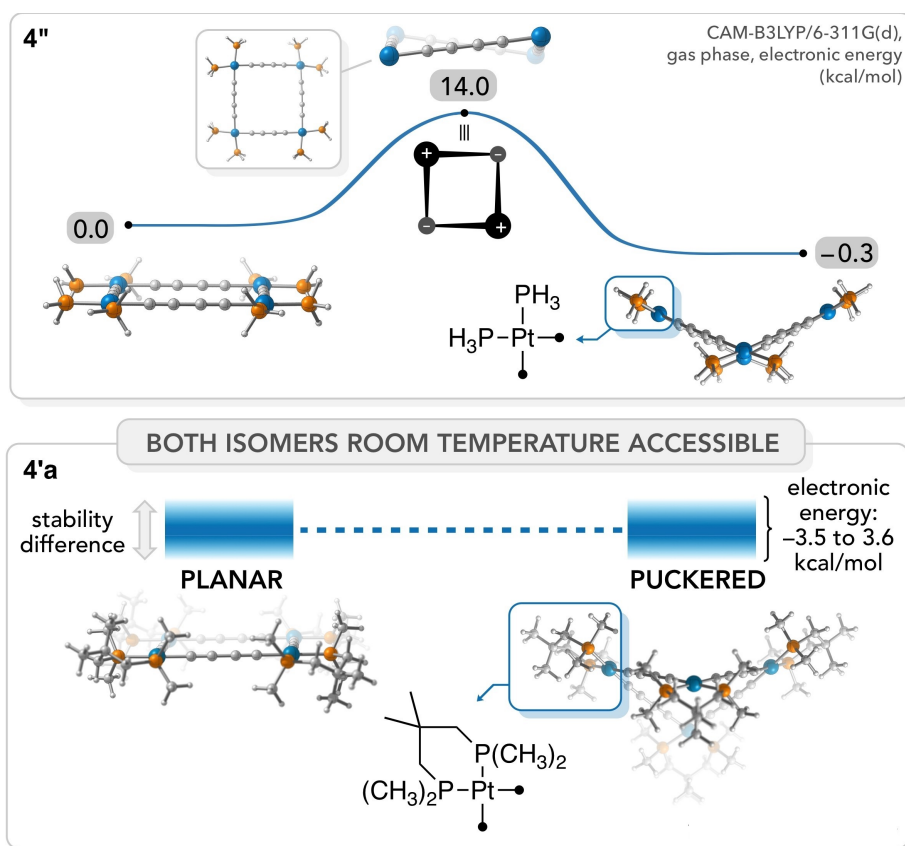


Figure 7.4 Limiting geometries of the model compounds **4'a** (PMe in place of PPh of **4a**) and **4''** (2PH₃ in place of each diphosphine of **4a**), and the intervening transition state for the latter.

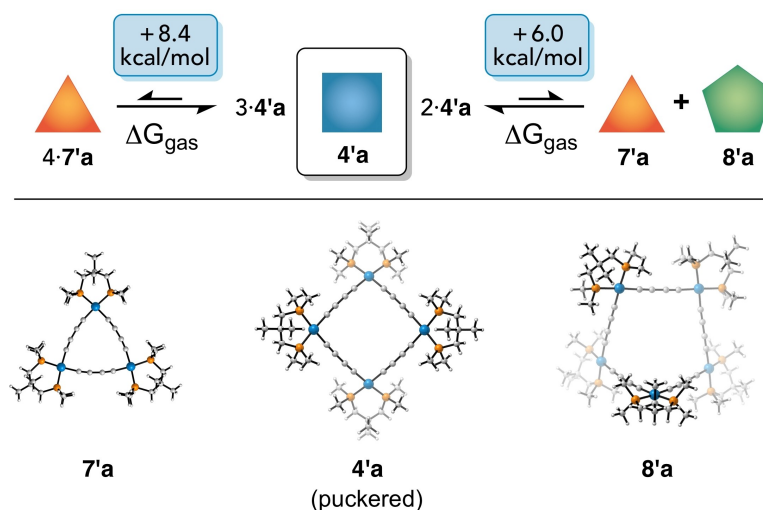


Figure 7.5 ΔG_{gas} values, computed at the CAM-B3LYP/6-311G(d) level of theory, associated with hypothetical isodesmic equilibria involving **4'a**, **7'a**, and **8'a** (top), and the corresponding structures (bottom).

Two types of byproducts can be conceptualized from Scheme 7.2 and Scheme 7.5. For one, the pairwise Sonogashira/Hagihara condensations would be allowed to further propagate prior to ring closure. This leads to higher homologs such as Pt₆C₂₄ or Pt₈C₃₂ species, all with even numbers of platinum atoms. For the other, there would be a redistribution mechanism that enables macrocycles with both even and odd numbers of platinum atoms to form. In supramolecular and self-assembly phenomena, equilibria between three- and four-sided polygon-like species are quite common.²⁷

Accordingly, analogous DFT techniques were applied to obtain the structures and energies of the corresponding Pt₃C₁₂ (**7'a**) and Pt₅C₂₀ (**8'a**) complexes, further properties of which were sought for various purposes below. Unsurprisingly, these were found to exhibit triangular and half chair geometries, as shown in Figure 7.5 (bottom) or (in a larger format) in Appendix E; Figure 15.1. The latter featured four approximately coplanar platinum atoms (average/maximum deviation from the least squares plane: 0.565/0.650 Å), with the fifth "headrest" atom significantly displaced from the plane (5.681 Å). It was then a simple matter to calculate the energies associated with the isodesmic equilibria depicted in Figure 7.5 (top).

That on the left shows the conversion of 3·**4'a** to 4·**7'a** to be endergonic, with a ΔG_{gas} of 8.4 kcal/mol. Such equilibria are favored entropically, and in some cases the rigidity of the edge units and/or ring strain in the smaller macrocycle play important roles.^{27d} Alternatively, the disproportionation of 2·**4'a** to a 1:1 mixture of **7'a** and **8'a**

can be considered. Apropos to the presumably reduced strain in **8'a** vs. **7'a**, this equilibrium is less endergonic, with a ΔG_{gas} of 6.0 kcal/mol.

7.9. Computations: Electronic and electrostatic properties

Special electronic properties are associated with a host of fully conjugated cyclic unsaturated compounds, and often analogs in which the conjugation is seemingly interrupted. Thus, simulated UV-visible data were sought. Towards this end, TD-DFT calculations were set up for **4'a** and the corresponding monoplatinum bis(butadiynyl) complex **3'a**. The computed spectra are shown in Figure 7.6 (middle) and a full list of electronic transitions is provided in Table 15.2. Figure 7.6 is clearly in good qualitative agreement with the experimental spectra in Figure 7.2.²⁸ Note the marked red shifts and enhanced intensities for **4'a** as compared to **3'a**.

The Pt₄C₁₆ complex **4'a** exhibits three particularly strong absorptions at $\lambda > 300$ nm, one of which (320 nm) presents itself as a shoulder of a band at 310 nm. For the absorption at 348 nm, there are two underlying transitions with very close energies. The longest wavelength band at 378 nm is not visible under normal experimental conditions due to its low intensity. All of these are predominantly ligand-to-metal charge transfer (LMCT) absorptions; with electron density transferred from the butadiyne segments to platinum based 6*p*-type orbitals. The principal orbitals contributing to one of the transitions represented in the 348 nm band are depicted in Figure 7.7. The 378 nm transition has mainly HOMO/LUMO character. These orbitals are illustrated in Figure 7.7, and others are collected in Appendix E; Figure 15.5.

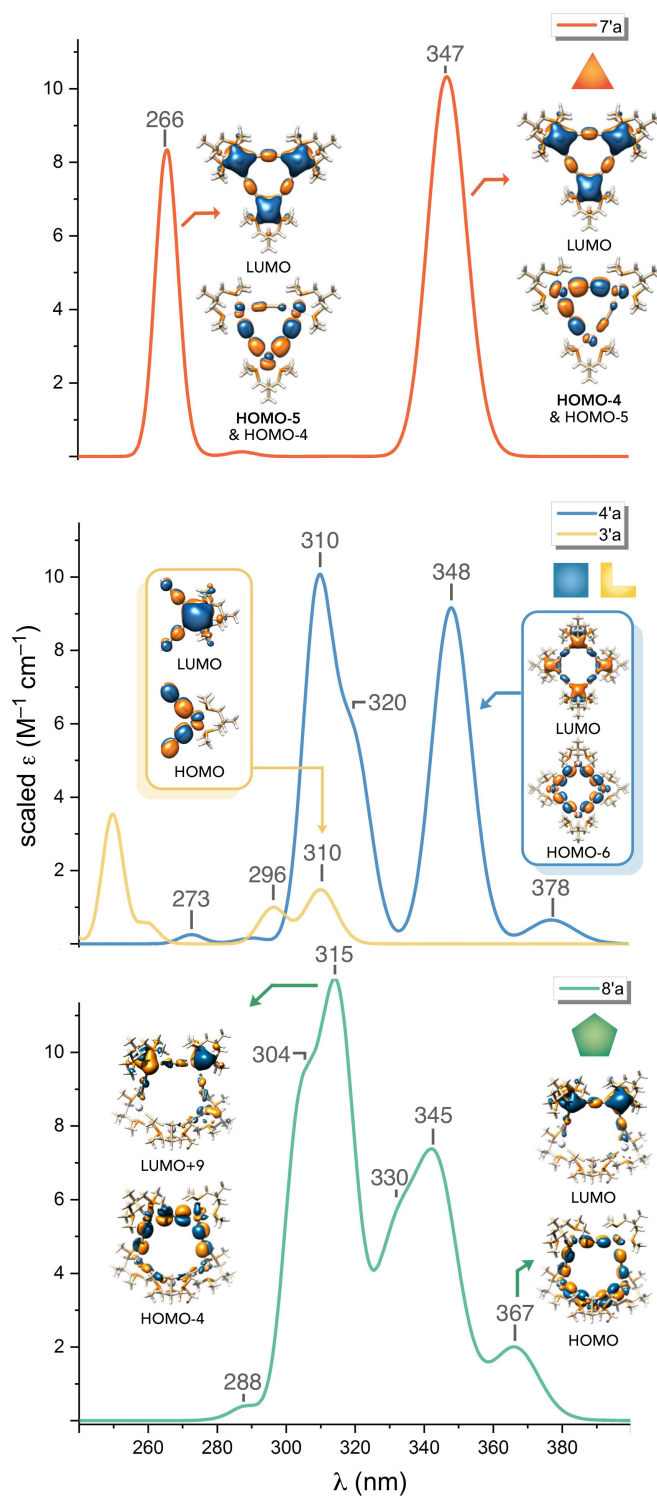


Figure 7.6 Computed UV-visible spectra (top, **7'a**; middle, **3'a** and **4'a** bottom **8'a**) and orbitals that are dominant contributors to selected transitions.

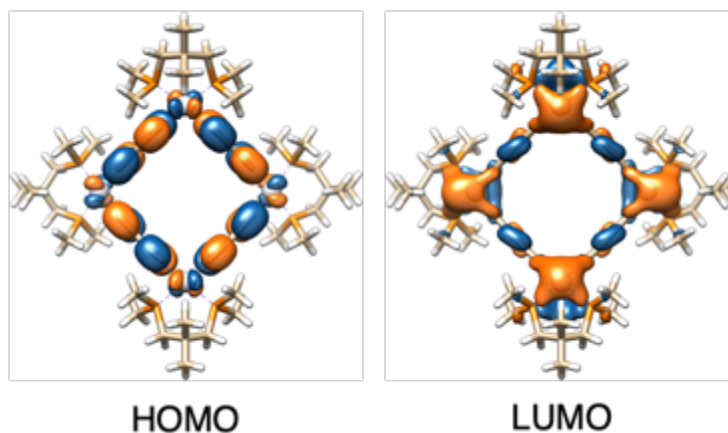


Figure 7.7 The HOMO and LUMO of **4'a**.

In order to support certain generalizations (below), the TD-DFT calculations were extended to the Pt₃C₁₂ and Pt₅C₂₀ complexes **7'a** and **8'a** (Figure 7.5). As can be gleaned from Figure 7.6, the triplatinum complex **7'a** exhibits fewer intense bands than **4'a**, with one of them markedly blue shifted to 266 nm. Two transitions contribute to each. In contrast, the pentaplatinum complex **8'a** exhibits slightly more bands than **4'a** in the 300-380 nm region, generally of somewhat greater intensities. However, the difference between **8'a** and **4'a** is not as dramatic as that between **4'a** and **7'a**, suggesting that geometric constraints may be beginning to limit the extent of conjugation. For both **7'a** and **8'a**, the principal orbitals involved for representative transitions are depicted in Figure 7.6, and more extensive sets are provided in Appendix E; Figure 15.4 and Figure 15.6.

Finally, electrostatic potential surface maps were computed for **4'a**, **7'a**, and **8'a**, as illustrated in Figure 7.8. Importantly, these revealed a significant negative surface charge surrounding the Pt_nC_{4n} cores. This would naturally support the binding of positively charged species near the centers of the macrocycles. Indeed, the ammonium cations $[\text{H}_2\text{NEt}_2]^+$ and $[\text{HNEt}_3]^+$ have pronounced positive surface potentials, thus creating a "perfect storm" for adduct formation. In accord with the ease of purification of **3a-f** from the byproduct $[\text{H}_2\text{NEt}_2]^+ \text{Cl}^-$, no pronounced negative surface potential is found for **3'a**.

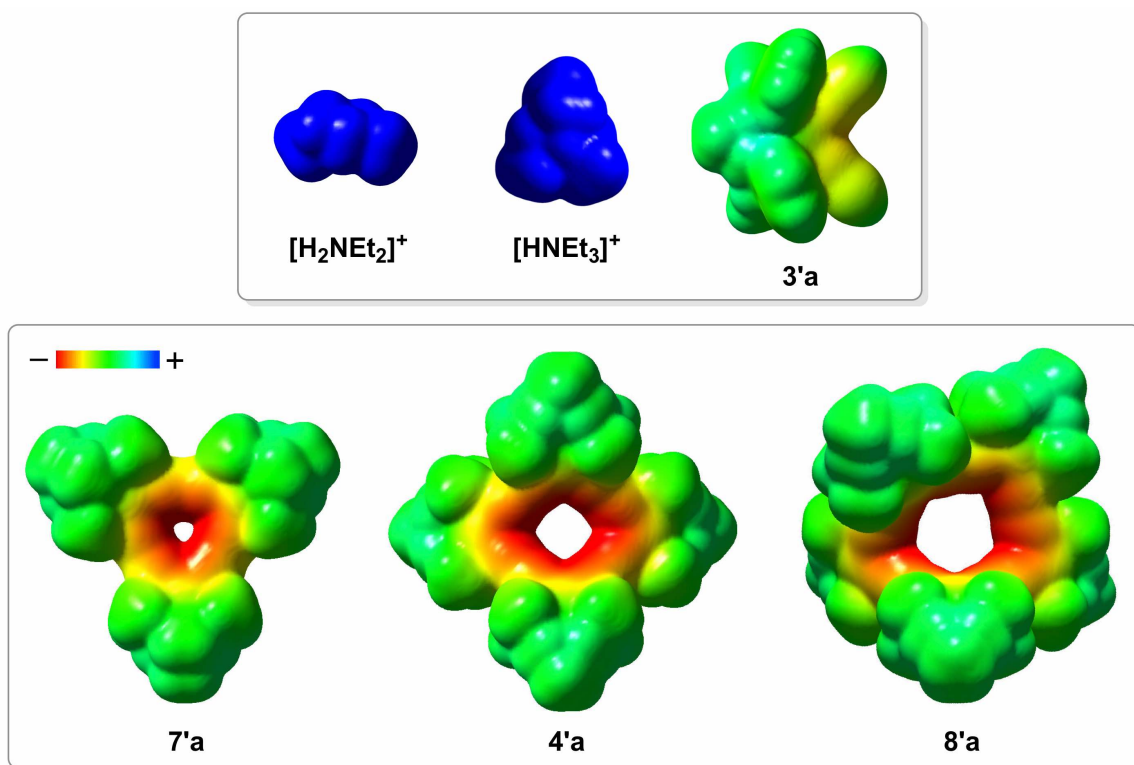


Figure 7.8 Electrostatic potential surface maps of **7'a**, **4'a**, **8'a**, and other relevant species.

7.10. Discussion

7.11. Syntheses and adducts of title complexes

This work has significantly expanded the availability of macrocyclic polygon like Pt_4C_{16} complexes that feature identical platinum(II) corners and butadiynediyl edges, and established comparable energies for skew rhombus¹ and "square" geometries. To our knowledge, such species are unknown with other metals or polyynediyl linkers. However, some mixed $\text{Pt}_2\text{Pt}'_2\text{C}_{16}$ complexes with unlike platinum corners have been reported.^{5b,c} Otherwise the closest relatives would be the tetragermanium or tetrasilicon adducts **II-xvi** or **II-xix** in Scheme 7.1.^{3a,d} Of course, platinum corners are ubiquitous in a host of fascinating polygon like structures that stem from self-assembly processes.^{29,30}

The isolation of the title complexes **4a-f** is severely complicated by their high affinities for ammonium cation byproducts derived from the Sonogashira/Hagihara coupling reactions employed. Challenging crystallizations aside,²⁴ we were unable to develop practical purification protocols that removed these species. Our experiences parallel those of other research groups. Bruce could isolate 1:1 adducts of **IV-ii'**, **IV-iii'**, or **IV-iv'** (Scheme 7.2) and $[\text{H}_2\text{NEt}_2]^+ \text{TfO}^-$, as evidenced by NMR and IR spectroscopy, ions of the composition $\text{IV}\cdot[\text{H}_2\text{NEt}_2]^+$ in ESI mass spectra, and microanalyses.^{5b} When HNCy_2 or $\text{HN}(i\text{-Pr})_2$ were used in place of HNEt_2 with **IV-ii'**, mass spectra of the partially characterized products gave analogous ions. Anderson reported comparable data for **IV-iv'** and $[\text{H}_2\text{NEt}_2]^+ \text{Cl}^-$.^{5c} However, efforts to remove the ammonium ions were largely unsuccessful. As noted in Scheme 7.2, Bruce worked

around this problem by switching to platinum bis(triflate) building blocks that could condense with bis(butadiynyl) complexes using nonnitrogenous anionic bases.^{5b}

The electrostatic potential surface maps in Figure 7.8 provide insight regarding these purification issues. We had not anticipated such a pronounced concentration of negative charge around the Pt_4C_{16} core, although it was discovered later that Nakamura had reported similar computational results for the "triangle" **I-iv** (Scheme 7.1; R = OCH_3) and the higher tris(octatetraynediyl) homolog.^{2g} There is no significant charge concentration in complexes that model the corner environments, i.e. the bis(butadiynyl) complex **3'a** in Figure 7.8, or in diplatinum complexes with $\text{Pt}(\text{C}\equiv\text{C})_n\text{Pt}$ units. These have frequently been synthesized by Sonogashira/Hagihara methodologies without any subsequent purification difficulties. In any case, the nature of the supramolecular bonding interactions between the Pt_4C_{16} complexes and the ammonium cations awaits further study, for which crystal structures would be helpful.

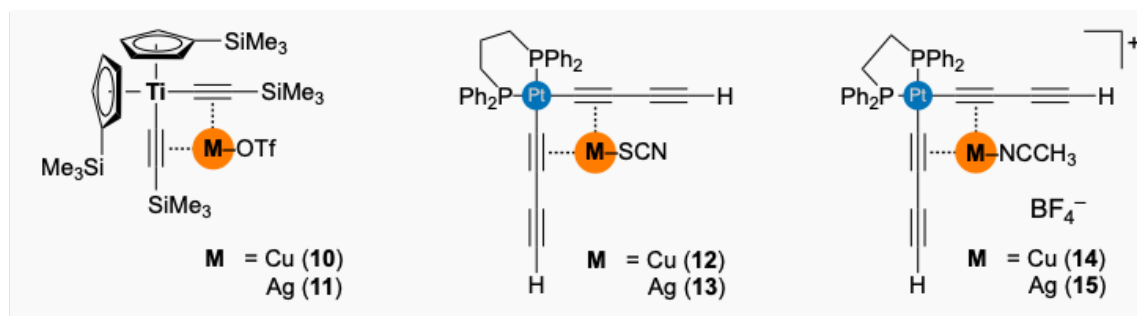


Figure 7.9 Previously reported "tweezer" complexes.

In phenomena that may be conceptually related, Lang³¹ has demonstrated that a variety of *cis* bis(alkynyl) or bis (polyynyl) complexes can chelate to coinage metal fragments. This affords "tweezer" complexes with two $\pi\text{-C}\equiv\text{C}$ linkages, as exemplified by the titanium and platinum complexes **10-13** in Figure 7.9. Similar species, such as the platinum complexes **14** and **15**, have been characterized by Bruce.^{5b} Bruce has also obtained excellent evidence for adducts of **IV-iii'** (Scheme 7.2) with $[\text{Cu}(\text{NCMe})_2]^+ \text{BF}_4^-$ (two equiv/**IV-iii'**) and $[\text{Ag}(\text{NCMe})_2]^+ \text{BF}_4^-$ (four equiv/**IV-iii'**). These remain to be structurally characterized.

7.12. Additional structural and electronic features

In all four new crystal structures herein, the six membered diphosphine chelate rings are not planar, but adopt half chair conformations. This is most easily visualized for **3a**·CH₂Cl₂ in Figure 7.1, which has only one such chelate. The five-atom $\underline{\text{C}}\underline{\text{H}}_2\text{-}\underline{\text{P}}\text{-}\underline{\text{Pt}}\text{-}\underline{\text{P}}\text{-}\underline{\text{C}}\underline{\text{H}}_2$ moiety is essentially planar, with the maximum/average deviation from the least squares plane being 0.096/0.060 Å. In contrast, the quaternary C(CH₃)₂ or "headrest" carbon atom sits 0.689 Å above this plane.

The same analysis can be applied to **4a**, **4b**·2CH₂Cl₂, and **4b**·3.44DMSO. The average deviations from the $\underline{\text{C}}\underline{\text{H}}_2\text{-}\underline{\text{P}}\text{-}\underline{\text{Pt}}\text{-}\underline{\text{P}}\text{-}\underline{\text{C}}\underline{\text{H}}_2$ least squares plane (taken over four chelate rings) are 0.101 Å, 0.028 Å, and 0.033 Å, respectively. The distances of the four quaternary carbon atoms in **4a** from this plane (0.594-0.640 Å) are comparable to that in **3a**. However, the corresponding distances in **4b**·2CH₂Cl₂, and **4b**·3.44DMSO, which

feature larger geminal diethyl groups, are somewhat greater (0.716-0.816 Å and 0.787-0.813 Å).

Interestingly, one other series of "squares" in Scheme 7.1, the carbocycles **II-xvii**, have also been observed to exist in both puckered (R = H, CH₂OAc) and planar (R = CH₂OH) conformations in the crystalline state.^{3c} This could be correlated with slight differences in solid-state UV-visible spectra, and was attributed to crystal packing forces associated with hydrogen bonding interactions. DFT calculations (R = CH₂OH) indicated an energy difference (ΔG , gas phase) of 1.92 kcal/mol favoring the puckered form. Contrasting puckered vs. planar geometries have also been found for two related macrocyclic tetraplatinum alkynyl species, one of which was accessed via self-assembly.³⁰ For each adduct, the equilibrium has been studied by DFT, and analyzed in terms of electronic, mechanical, and electronic strain.^{30b}

A wealth of data involving the electronic transitions responsible for the bands in Figure 7.2 and Figure 7.6 can be found in Appendix E (Table 15.2 and Figure 15.3, Figure 15.4, and Figure 15.5). We are not aware of other TD-DFT studies for any of the compounds represented in Scheme 7.1. However, in some cases the UV-visible data alone are instructive. For example, the tetragermanium species **II-xvi** as well as each higher homolog through the octagermanium species [Ph₂Ge(C≡C)₂]₈ has been characterized.^{3d} All of these compounds exhibit λ_{max} near 248, 262, 270 (sh), 278 nm, and 295 nm. There are no additional or shifted bands as the number of (C≡C)₂ edges are varied. Rather, only the molar extinction coefficients increase, as would be expected

from an increasing number of non-interacting $\text{Ge}(\text{C}\equiv\text{C})_2\text{Ge}$ units. A parallel situation is found with the related silicon compound **II-xix** and higher homologs.^{3a}

Hence, the platinum corners in the title compounds provide unique vectors for conjugation, creating an extended chromophore with no counterpart in Scheme 7.1. The TD-DFT computations suggest that that Pt_3C_{12} and Pt_5C_{20} analogs behave similarly. However, this should be extrapolated to higher homologs with caution, as progressively greater deviations from planarity would be expected, interfering with conjugation. The only other transition metal containing species in Scheme 7.1 are **I-xii** and **II-xii**, which are technically carbocyclic but feature dicobalt substituents at each corner.^{4b} Here only a slight red shift in the lowest energy band is apparent (370 vs. 381 nm) with increased macrocycle size, as well as with trailing shoulders (445/546 vs. 453/560 nm).

7.13. Conclusion

This study has added to the platinum building blocks that can be used to prepare macrocycles comprised of four platinum corners and butadiynediyl edges. The new Pt_4C_{16} systems crystallize with puckered or skew rhombus conformations,¹ but DFT calculations and other data suggest that planar or puckered geometries are local minima differing only slightly in energy. Thus, packing forces become important determinants of solid-state conformation.

These adducts are challenging to isolate in pure form. This is attributed to the highly negative electrostatic potentials surrounding the macrocycle cores, providing binding sites for cationic byproducts (ammonium cations, Cu^+). The Pt_4C_{16} systems feature highly delocalized electronic structures, as reflected by intense UV-visible bands that have no counterparts in monoplatinum or diplatinum model compounds, and further characterized by time dependent DFT calculations that define the underlying transitions and orbitals involved. The longer wavelength absorptions have dominant LMCT character. The same holds for related Pt_3C_{12} and Pt_5C_{20} complexes, as assayed by DFT. Equilibria involving conversions of Pt_4C_{16} systems to Pt_3C_{12} analogs or a 1:1 $\text{Pt}_3\text{C}_{12}/\text{Pt}_5\text{C}_{20}$ mixture are endergonic.

This work provides a much improved foundation for the pursuit of higher homologs with longer polyynediyl segments (e. g. Pt_4C_{24} or Pt_4C_{32} species).⁹ Efforts directed at these targets, as well as other novel carbon rich platinum complexes, will be reported in due course.

7.14. Experimental [major contribution: Ms. B. K. Collins, Dr. Clough Mastry]

7.14.1. General

The synthetic procedures for selected monoplatinum "corners" and a tetraplatinum "square" are reported below.

7.14.1.1. Representative syntheses: $(Me_2C(CH_2PPh_2)_2)PtCl_2$ (**2a**)

A Schlenk flask was charged with *cis/trans*-(*p*-tol₃P)₂PtCl₂ (1.003 g, 1.15 mmol),²⁰ Me₂C(CH₂PPh₂)₂ (**1a**;¹⁵ 0.615 g, 1.40 mmol), and CH₂Cl₂ (20 mL) with stirring. After 24 h, the solvent was removed by rotary evaporation. The residue was washed with Et₂O (100 mL), EtOH (100 mL), and hexanes (100 mL), and dried by oil pump vacuum to give **2a** as a white solid (0.705 g, 0.998 mmol, 87%), which slightly darkened at 250 °C and blackened at 375 °C. Anal. Calcd. for C₂₉H₃₀Cl₂P₂Pt (706.08): C, 49.30; H, 4.28; Found: C, 47.84; H, 4.34.³² NMR (δ (ppm), CD₂Cl₂): ¹H 7.92-7.79 (m, 8H, *o* to P), 7.50-7.37 (m, 12H, *m* and *p* to P), 2.31 (d, ²J_{HP} = 9.7 Hz, 4H, PCH₂), 0.55 (s, 6H, CH₃); ¹³C{¹H} 134.7 (virtual t, ³³ ²J_{CP} = 5.6 Hz, *o* to P), 131.9 (s, *p* to P), 129.3 (m, *J* = 73.7 Hz, *J* = 7.0 Hz, *i* to P),³⁴ 129.0 (virtual t, ³³ ³J_{CP} = 5.6 Hz, *m* to P), 35.4 (s, C(CH₃)₂), 32.3 (t, ¹J_{CP} = 8.7 Hz, PCH₂),³⁵ 30.0 (s, CH₃); ³¹P{¹H} -1.3 (s, ¹J_{PPt} = 3431 Hz).³⁶ IR (cm⁻¹, powder film): 2954 (w), 1481 (m), 1435 (s), 1103 (s), 840 (s), 802 (s), 748 (s), 694 (s). MS:[37] MALDI⁺ (matrix DCTB), 670 ([**2a**-Cl]⁺, 60%).

7.14.1.2. Representative syntheses: $[(Me_2C(CH_2PPh_2)_2)[Pt(\overline{C\equiv C})_2]_4$ (**4a**)

Schlenk flask was charged with **2a** (0.481 g, 0.692 mmol), **3a** (0.503 g, 0.686 mmol), THF (300 mL), HNEt₂ (120 mL), and CuI (0.0259 g, 0.136 mmol) with stirring and heated to 55 °C. After 3 d, the precipitate was isolated by filtration, washed with Et₂O (300 mL) and hexanes (300 mL), and dried by oil pump vacuum (rt, 20 h) to give **4a** admixed with 2.0 equiv. of [H₂NEt₂]⁺ Cl⁻ as a green solid (0.833 g, 0.282 mmol, 82% based upon the formula weight of **4a**·([H₂NEt₂]⁺ Cl⁻)₂). The sample was kept under vacuum at 90 °C (20 h), but was recovered unchanged. The ¹H and ¹³C{¹H} NMR spectra showed minor impurities. Anal. Calcd. for C₁₄₀H₁₄₄Cl₂N₂P₈Pt₄ (2953.73): C, 56.93; H, 4.91; N, 0.95; Cl, 2.40; Found: C, 53.31; H, 4.82; N, 0.96; Cl, 2.53.³² NMR (δ (ppm), CD₂Cl₂): ¹H 7.72-7.56 (m, 32H, *m* to P), 7.28 (t, ³J_{HH} = 7.3 Hz, 16H, *p* to P), 7.16 (t, ³J_{HH} = 7.1 Hz, 32H, *o* to P), 3.21 (q, ³J_{HH} = 7.4 Hz, 8H, [H₂N(CH₂CH₃)₂]⁺), 2.32-2.21 (m, 16H, PCH₂), 1.35 (t, ³J_{HH} = 7.2 Hz, 12H, [H₂N(CH₂CH₃)₂]⁺), 0.65 (s, 24H, CH₃); ¹³C{¹H} 134.2 (virtual t, ³³ ²J_{CP} = 5.2 Hz, *o* to P), 132.7 (m, *J* = 68.8 Hz, *J* = 8.4 Hz, *i* to P), 130.7 (s, *p* to P), 128.4 (virtual t, ³³ ³J_{CP} = 5.3 Hz, *m* to P), 96.7 (m, *J* = 18.9 Hz, PtC≡C), 91.8 (dd, ²J_{CP} = 148.2 Hz, ²J_{CP} = 10.6 Hz, PtC≡C), 43.9 (s, [H₂N(CH₂CH₃)₂]⁺), 37.5 (t, ²J_{CP} = 16.6 Hz, C(CH₂)₄), 36.2 (s, CH₃), 32.9 (t, ¹J_{CP} = 7.3 Hz, PCH₂), 12.0 (s, [H₂N(CH₂CH₃)₂]⁺); ³¹P{¹H} -5.5 (s, ¹J_{PPt} = 2200 Hz);³⁶ ¹⁹⁵Pt -3339 (t, ¹J_{PtP} = 2215 Hz). MS:³⁷ ESI⁺, 2807.7068

([**4a**+H₂NEt₂]⁺ (calc. 2807.6860), 40%), 1376.3172 ([**4a**+H+NH₄]²⁺ (calc. 1376.3154), 100%); MALDI⁺ (matrix DCTB), 2797 ([**4a**+Cu]⁺, 100%), 2733 ([**4a**+H]⁺, 90%).

7.14.2. Crystallography

A. A CH₂Cl₂ solution of **3a** was stored at 3 °C. After 3 d, green plates were obtained. Data were collected as outlined in Table 7.3. Cell parameters were obtained from 180 data frames taken at widths of 0.5°. Integrated intensity information for each reflection was obtained by reduction of the data frames with the program APEX2.³⁸ Data were corrected for Lorentz and polarization factors, and using SADABS³⁹ for absorption and crystal decay effects. The structure was solved by direct methods using SHELXTL (SHELXS).⁴⁰ All non-hydrogen atoms were refined with anisotropic thermal parameters. The hydrogen atoms were placed in idealized positions, and refined using a riding model. The parameters were refined by weighted least squares refinement on F^2 to convergence.⁴⁰

B. A DMSO solution of **4a** was layered with EtOAc at 3 °C.²⁴ After 7 d, yellow-brown crystals were obtained. Data were collected as outlined in Table 7.3. Data were treated as in procedure A (with integrated intensity information via the program SAINTplus).⁴¹ Approximately 14-16 DMSO molecules per asymmetric unit were found from the Fourier difference map. Most of these were disordered, and all were SQUEEZE'd using PLATON.⁴² The absence of additional symmetry and twin components were verified using PLATON. The hydrogen atoms were placed in idealized

positions, and refined using a riding model. The parameters were refined by weighted least squares refinement on F^2 to convergence.³⁹

C. A CH_2Cl_2 solution of **4b** was layered with toluene and Et_2O and stored at 3 °C.²⁴ After 8 d, colorless multifaceted crystals were obtained. Data were collected as outlined in Table 7.3. Several molecules of CH_2Cl_2 and other possible solvents were found, amounting to 1606 electrons per asymmetric unit. Two CH_2Cl_2 molecules were modeled successfully, and the remaining disordered molecules were removed using the same procedure as in procedure B. The structure solution and refinement were carried out analogously.

D. EtOAc vapor was allowed to slowly diffuse into a DMSO solution of **4b**.²⁴ After ca. one month, brown blocks were obtained. Data were collected as outlined in Table 7.3. The structure was solved and refined along the lines of procedures B and C. Several DMSO molecules were located and could be modeled successfully, refining to a total occupancy of 3.44. Nine additional DMSO molecules could not be modeled, and were MASKed using OLEX2.⁴³

7.15. References

(1) The term polygon is applied more liberally by chemists than mathematicians, who would require equilateral and equiangular geometries, and frown upon bow-shaped edges. In Euclidian geometry, this term as well as rhombus or the more encompassing designations quadrilateral or tetragon are reserved for planar structures. The term "skew", incorporated in the title of this article, is used to denote non-planar variants. See Sunday, J. G. Regular Polygons in Affine Spaces. *Proc. London Math. Soc.* **1973**, *30*, 301-329.

(2) Previous reports, species of the type **I**: (a) Okamura, W. H.; Sondheimer, F. 1,3,7,9,13,15-Hexadehydro[18]annulene. *J. Am. Chem. Soc.* **1967**, *23*, 5991-5992. (b) Anthony, J.; Knobler, C. B.; Diederich, F. Stable [12]- and [18]Annulenes Derived from Tetraethynylethene. *Angew. Chem. Int. Ed. Engl.* **1993**, *32*, 406-409; Stabile, von Tetraethynylethen abgeleitete [12]- und [18]Annulene. *Angew. Chem.* **1993**, *105*, 437-440. (c) Sarkar, A.; Haley, M. M. Synthesis and characterization of dehydrothieno[18]annulenes. *Chem. Comm.* **2000**, 1733-1734. (d) Bhaskar, A.; Guda, R.; Haley, M. M.; Goodson, T. Building Symmetric Two-Dimensional Two-Photon Materials. *J. Am. Chem. Soc.* **2006**, *128*, 13972-13973. (e) Kivala, M.; Mitzel, F.; Boudon, C.; Gisselbrecht, J.-P.; Seiler, P.; Gross, M.; Diederich, F. Two-Dimensional Acetylenic Scaffolding: Extended Donor-Substituted Perethynylated Dehydroannulenes. *Chem. Asian J.* **2006**, *1*, 479-489. (f) Tahara, K.; Johnson, C. A.; Fujita, T.; Sonoda, M.; De Schryver, F. C.; De Feyter, S.; Haley, M. M.; Tobe, Y. Synthesis of Dehydrobenzo[18]annulene Derivatives and Formation of Self-Assembled Monolayers:

Implications of Core Size on Alkyl Chain Interdigitation. *Langmuir*, **2007**, *23*, 10190-10197. (g) Kato, S.; Takahashi, N.; Nakamura, Y. J. Hexadecadehydrodibenzo[20]-, Tetracosadehydrotribenzo[30]-, and Dotriacontadehydrotetrabenzo[40]annulenes: Syntheses, Characterizations, Electronic Properties, and Self-Associations. *Org. Chem.* **2013**, *78*, 7658-7663. (h) Crowe, J. W.; Baldwin, L. A.; McGrier, P. L. Luminescent Covalent Organic Frameworks Containing a Homogenous and Heterogeneous Distribution of Dehydrobenzoannulene Vertex Units. *J. Am. Chem. Soc.* **2016**, *138*, 10120-10123. (i) Dai, H.; Wang, S.; Hisaki, I.; Nakagawa, S.; Ikenaka, N.; Deng, K.; Xiao, X.; Zeng, Q. On-Surface Self-Assembly of a C_3 -Symmetric π -Conjugated Molecule Family Studied by STM: Two-Dimensional Nanoporous Frameworks. *Chem. Asian J.* **2017**, *12*, 2558-2564. (j) Takahashi, N.; Kato, S.; Yamaji, M.; Ueno, M.; Iwabuchi, R.; Shimizu, Y.; Nitani, M.; Ie, Y.; Aso, Y.; Yamanobe, T.; Uehara, H.; Nakamura, Y. J. Tetraalkoxyphenanthrene-Fused Hexadecadehydro[20]- and Tetracosadehydro[30]annulenes: Syntheses, Aromaticity/Antiaromaticity, Electronic Properties, and Self-Assembly. *Org. Chem.* **2017**, *82*, 8882-8896. (k) Sowden, M. J.; Ward, J. S.; Sherburn, M. S. Synthesis and Properties of 2,3-Diethynyl-1,3-Butadienes. *Angew. Chem. Int. Ed.* **2020**, *59*, 4145-4153; *Angew. Chem.* **2020**, *132*, 4174-4182.

(3) Previous reports, species of the type **II**: (a) Unno, M.; Negishi, K.; Matsumoto, H. Extended Silapericyclines. *Chem. Lett.* **2001**, 340-341. (b) van Assema, S. G. A.; Bas de Jong, G.; Ehlers, A. W.; de Kanter, F. J. J.; Schakel, M.; Spek, A. L.; Lutz, M.; Lammertsma, K. Acetylene-Substituted Phosphane Oxides: Building Blocks for Macrocycles. *Eur. J. Org. Chem.* **2007**, 2405-2412. (c) Suzuki, M.; Comito, A.;

Khan, S. I.; Rubin, Y. Nanochannel Array within a Multilayered Network of a Planarized Dehydro[24]annulene. *Org. Lett.* **2010**, *12*, 2346-2349. (d) Tanimoto, H.; Fujiwara, T.; Mori, J.; Nagao, T.; Nishiyama, Y.; Morimoto, T.; Ito, S.; Tanaka, K.; Chujo, Y.; Kakiuchi, K. Extended germa[*N*]pericyclines: synthesis and characterization. *Dalton Trans.* **2017**, *46*, 2281-2288.

(4) Previous reports, homologous species of the types **I** and **II**: (a) Rubin, Y.; Kahr, M.; Knobler, C. B.; Diederich, F.; Wilkins, C. L. The Higher Oxides of Carbon $C_{8n}O_{2n}$ ($n = 3-5$): Synthesis, Characterization, and X-ray Crystal Structure. Formation of Cyclo[*n*]carbon Ions C_n^+ ($n = 18, 24$), C_n^- ($n = 18, 24, 30$), and Higher Carbon Ions Including C_{60}^+ in Laser Desorption Fourier Transform Mass Spectrometric Experiments. *J. Am. Chem. Soc.* **1991**, *113*, 495-500. (b) Diederich, F.; Rubin, Y.; Chapman, O. L.; Goroff, N. S. Synthetic Routes to the Cyclo[*n*]carbons. *Helv. Chim. Acta* **1994**, *77*, 1441-1457. (c) Adamson, G. A.; Rees, C. W. Towards the total synthesis of cyclo[*n*]carbons and the generation of cyclo[6]carbon. *J. Chem. Soc. Perkin Trans. 1*, **1996**, 1535-1543. (d) Haley, M. M.; Bell, M. L.; English, J. J.; Johnson, C. A.; Weakley, T. J. R. Versatile Synthetic Route to and DSC Analysis of Dehydrobenzoannulenes: Crystal Structure of a Heretofore Inaccessible [20]Annulene Derivative. *J. Am. Chem. Soc.* **1997**, *119*, 2956-2957. (e) Tobe, Y.; Fujii, T.; Matsumoto, H.; Tsumuraya, K.; Noguchi, D.; Nakagawa, N.; Sonoda, M.; Naemura, K.; Achiba, Y.; Wakabayashi, T. [2 + 2] Cycloreversion of [4.3.2]Propella-1,3,11-trienes: An Approach to Cyclo[*n*]carbons from Propellane-Annulated Dehydro[*n*]annulenes. *J. Am. Chem. Soc.* **2000**, *122*, 1762-1775. (f) Märkl, G.; Zollitsch, T.; Kreitmeier, P.; Prinzhorn, M.; Reithinger, S.; Eibler, E.

Polyphospha[*m*]cyclo[*n*]carbons ($m + n = 15, 20, 25, 30, 40$). *Chem. Eur. J.* **2000**, *6*, 3806-3820. (g) Diederich, F. Carbon-rich acetylenic scaffolding: rods, rings, and switches. *Chem Comm.* **2001**, 219-227 and two earlier papers cited therein.

(5) Previous reports, Pt₄C₁₆ species **II**: (a) ALQaisi, S. M.; Galat, K. J.; Chai, M.; Ray, D. G.; Rinaldi, P. L.; Tessier, C. A.; Youngs, W. J. Synthesis of Neutral Tetranuclear and Octanuclear Macrocyclic Platinum–Butadiyne Heterocyclines. *J. Am. Chem. Soc.* **1998**, *120*, 12149-12150. (b) Bruce, M. I.; Costuas, K.; Halet, J.-F.; Hall, B. C.; Low, P. J.; Nicholson, B. K.; Skelton, B. W.; White, A. H. Preparation of buta-1,3-diyne complexes of platinum(II) and their use in the construction of neutral molecular squares: synthesis, structural and theoretical characterization of *cyclo*-{Pt(μ -C \equiv C-C \equiv C)(dppe)}₄ and related chemistry. *J. Chem. Soc. Dalton Trans.* **2002**, 383-398. (c) Janka, M.; Anderson, G. K.; Rath, N. P. Synthesis of Neutral Molecular Squares Composed of Bis(phosphine)platinum Corner Units and Dialkynyl Linkers. Solid-State Characterization of [Pt(μ -C \equiv CC \equiv C)(dppp)]₄. *Organometallics* **2004**, *23*, 4382-4390.

(6) Some macrocycles comprised of butadiynyl linkers and five,^{4a,b,c,g} six,^{4f,g} and eight^{4f,g} identical vertices have also been reported.

(7) Anderson, H. L.; Patrick, C. W.; Scriven, L. M.; Woltering, S. L. A Short History of Cyclocarbons. *Bull. Chem. Soc. Jpn.* **2021**, *94*, 798-811.

(8) Kaiser, K.; Scriven, L. M.; Schulz, F.; Gawel, P.; Gross, L.; Anderson, H. L. An *sp*-hybridized molecular carbon allotrope, cyclo[18]carbon. *Science* **2019**, *365*, 1299-1301.

(9) A few higher homologs of **I** and **II** with octatetraynediyl linkers have been reported.^{2e,g,k} See also Anderson, H. L.; Walter, C. J.; Vidal-Ferran, A.; Hay, R. A.; Lowden, P. A.; Sanders, J. K. M. Octatetryne-linked porphyrins: 'stretched' cyclic dimers and trimers with very spacious cavities. *J. Chem. Soc. Perkin Trans. 1*, **1995**, 2275-2279.

(10) (a) Mohr, W.; Stahl, J.; Hampel, F.; Gladysz, J. A. Synthesis, Structure, and Reactivity of *sp* Carbon Chains with Bis(phosphine) Pentafluorophenylplatinum Endgroups: Butadiynediyl (C₄) through Hexadecaoctaynediyl (C₁₆) Bridges, and Beyond. *Chem. Eur. J.* **2003**, 9, 3324-3340. (b) Zheng, Q.; Bohling, J. C.; Peters, T. B.; Frisch, A. C.; Hampel, F.; Gladysz, J. A. A Synthetic Breakthrough into an Unanticipated Stability Regime: A Series of Isolable Complexes in which C₆, C₈, C₁₀, C₁₂, C₁₆, C₂₀, C₂₄, and C₂₈ Polyynediyl Chains Span Two Platinum Atoms. *Chem. Eur. J.* **2006**, 12, 6486-6505. (c) Weisbach, N.; Kuhn, H.; Amini, H.; Ehnbohm, A.; Hampel, F.; Reibenspies, J. H.; Hall, M. B.; Gladysz, J. A. Triisopropylsilyl (TIPS) Alkynes as Building Blocks for Syntheses of Platinum Triisopropylsilylpolyynyl and Diplatinum Polyynediyl Complexes. *Organometallics* **2019**, 38, 3294-3310.

(11) (a) Stahl, J.; Mohr, W.; de Quadras, L.; Peters, T. B.; Bohling, J. C.; Martín-Alvarez, J. M.; Owen, G. R.; Hampel, F.; Gladysz, J. A. *sp* Carbon Chains Surrounded by *sp*³ Carbon Double Helices: Coordination-Driven Self-Assembly of Wirelike Pt(C≡C)_nPt Moieties That Are Spanned by Two P(CH₂)_mP Linkages. *J. Am. Chem. Soc.* **2007**, 129, 8282-8295. (b) de Quadras, L.; Bauer, E. B.; Mohr, W.; Bohling, J. C.; Peters, T. B.; Martín-Alvarez, J. M.; Hampel, F.; Gladysz, J. A. *sp* Carbon Chains

Surrounded by sp^3 Carbon Double Helices: Directed Syntheses of Wirelike $Pt(C\equiv C)_nPt$ Moieties That are Spanned by Two $P(CH_2)_mP$ Linkages via Alkene Metathesis. *J. Am. Chem. Soc.* **2007**, *129*, 8296-8309. (c) de Quadras, L.; Bauer, E. B.; Stahl, J.; Zhuravlev, F.; Hampel, F.; Gladysz, J. A. sp Carbon Chains Surrounded by sp^3 Carbon Double Helices: Wire-Like $Pt(C\equiv C)_nPt$ Moieties that are Spanned by two α,ω -Diphosphines that Bear Heteroatoms or Alkyl Substituents. *New. J. Chem.* **2007**, *31*, 1594-1604. (d) Owen, G. R.; Stahl, J.; Hampel, F.; Gladysz, J. A. Coordination-Driven Self-Assembly, Structures, and Dynamic Properties of Diplatinum Hexatriynediyl and Butadiynediyl Complexes in which the sp Carbon Chains are Shielded by sp^3 Carbon Chains: Towards Endgroup-Endgroup Interactions. *Chem. Eur. J.* **2008**, *14*, 73-87.

(12) (a) Owen, G. R.; Gauthier, S.; Weisbach, N.; Hampel, F.; Bhuvanesh, N.; Gladysz, J. A. Towards Multistranded Molecular Wires: Syntheses, Structures, and Reactivities of Tetraplatinum bis(Polyynediyl) Complexes with $\overline{Pt-C_x-Pt-(P(CH_2)_3P)_2-Pt-C_x-Pt-(P(CH_2)_3P)_2}$ Cores ($x = 4, 6, 8$). *Dalton Trans.* **2010**, *39*, 5260-5271. (b) Zheng, Q.; Schneider, J. F.; Amini, H.; Hampel, F.; Gladysz, J. A. Wire Like Diplatinum, Triplatinum, and Tetraplatinum Complexes Featuring $X[PtC\equiv C-C\equiv CC\equiv CC\equiv C]_mPtX$ Segments; Iterative Syntheses and Functionalization for Measurements of Single Molecule Properties. *Dalton Trans.* **2019**, *48*, 5800-5816.

(13) (a) Clough, M. C.; Fiedler, T.; Bhuvanesh, N.; Gladysz, J. A. A Phase Based Approach to Insulated Molecular Wires: Diplatinum Octatetraynediyl Complexes Bearing Fluorous Trialkylphosphine Ligands. *J. Organomet. Chem.* **2016**, *812*, 34-42.

(b) Amini, H.; Baranová, Z.; Weisbach, N.; Gauthier, S.; Bhuvanesh, N.; Reibenspies, J. H.; Gladysz, J. A. Syntheses, Structures, and Spectroscopic Properties of 1,10-Phenanthroline-Based Macrocycles Threaded by PtC₈Pt, PtC₁₂Pt, and PtC₁₆Pt Axles: Metal-Capped Rotaxanes as Insulated Molecular Wires. *Chem. Eur. J.* **2019**, *25*, 15896-15914.

(14) (a) Yamago, S.; Watanabe, Y.; Iwamoto, T. Synthesis of [8]Cycloparaphenylene from a Square-Shaped Tetranuclear Platinum Complex. *Angew. Chem. Int. Ed.* **2010**, *49*, 757-759; *Angew. Chem.* **2010**, *122*, 769-771. (b) Dewhurst, R. D.; Hill, A. F.; Willis, A. C. The Interplay of Bis(tricarbido) and Dimetallaooctatetrayne Complexes of Platinum. *Organometallics* **2009**, *28*, 4735-4740. (c) Ammann, M.; Rang, A.; Schalley, C. A.; Bäuerle, P. A Synthetic Approach Towards Interlocked π -Conjugated Macrocycles. *Eur. J. Org. Chem.* **2006**, 1940-1948.

(15) van Rijn, J. A.; Siegler, M. A.; Spek, A. L.; Bouwman, E.; Drent, E. Ruthenium-Diphosphine-Catalyzed Allylation of Phenols: A *gem*-Dialkyl-Type Effect Induces High Selectivity toward *O*-Allylation. *Organometallics* **2009**, *28*, 7006-7014.

(16) Bianchini, C.; Lee, H. M.; Meli, A.; Moneti, S.; Vizza, F.; Fontani, M.; Zanello, P. Copolymerization of Carbon Monoxide with Ethene Catalyzed by Palladium (II) Complexes of 1,3-Bis(diphenylphosphino)propane Ligands Bearing Different Substituents on the Carbon Backbone. *Macromolecules* **1999**, *32*, 4183-4193.

(17) Buwalda, R. T.; Wagenaar, A.; Engberts, J. B. F. N. Synthesis and Aggregation Behavior of Cyclic Single- and Double-Tailed Phosphate Amphiphiles: A Novel Class of Phosphate Surfactants — Comparison with the Aggregation Behavior of Sodium Di-*n*-alkyl Phosphates. *Liebigs Ann. Recl.* **1997**, 1745-1753.

(18) Kraihanzel, C. S.; Ressler, J. M.; Gray, G. M. A Multinuclear Nuclear Magnetic Resonance Study of Metal Complexes of the Ligands $\text{Ph}_2\text{ECH}_2\text{CMe}_2\text{CH}_2\text{EPh}_2$ (E = P, As). *Inorg. Chem.* **1982**, *21*, 879-887.

(19) Weisbach, N. Mono-, di-, and trinuclear *cis* and *trans* Platinum Polyynyl and Polyynediyl Complexes with up to 40 *sp* Carbon Atoms. Doctoral Thesis, Friedrich-Alexander-Universität Erlangen-Nürnberg, Erlangen, Germany, 2011.

(20) (a) Matern, E.; Pikies, J.; Fritz, G. Komplexchemie P-reicher Phosphane und Silylphosphane. XXI. Zum Einfluß der PR_3 -Liganden auf Bildung und Eigenschaften der Phosphinophosphiniden-Komplexe $[\{\eta^2\text{-}^t\text{Bu}_2\text{P-P}\}\text{Pt}(\text{PR}_3)_2]$ und $[\{\eta^2\text{-}^t\text{Bu}_2\text{P}^1\text{P}^2\}\text{Pt}(\text{P}^3\text{R}_3)(\text{P}^4\text{R}'_3)]$. *Z. Anorg. Allg. Chem.* **2000**, *626*, 2136-2142. (b) The *cis* and *trans* isomers of $(p\text{-tol}_3\text{P})_2\text{PtCl}_2$ are easily distinguished by $^{31}\text{P}\{^1\text{H}\}$ NMR (δ (ppm), C_6D_6): *cis*, 14.1 ($^1J_{\text{PPt}} = 3627$ Hz); *trans*, 19.7 ($^1J_{\text{PPt}} = 2650$ Hz). The former is the kinetic product and dominates.

(21) (a) Chinchilla, R.; Nájera, C. Recent advances in Sonogashira reactions. *Chem. Soc. Rev.* **2011**, *40*, 5084-5121. (b) Sonogashira, K.; Yatake, T.; Tohda, Y.; Takahashi, S.; Hagihara, N. Novel Preparation of σ -Alkynyl Complexes of Transition Metals by Copper(I) Iodide-catalysed Dehydrohalogenation. *J. Chem. Soc. Chem. Commun.* **1977**, 291-292. (c) Sonogashira, K.; Takahashi, S.; Hagihara, N. New Extended Chain Polymer. Poly[*trans*-bis(tri-*n*-butylphosphine)platinum 1,4-butadienydiyl]. *Macromolecules* **1977**, *10*, 879-880.

(22) Zheng, Q.; Hampel, F.; Gladysz, J. A. Longitudinally Extended Molecular Wires based upon $\text{PtC}\equiv\text{CC}\equiv\text{CC}\equiv\text{CC}\equiv\text{C}$ Repeat Units: Iterative Syntheses of Functionalized Linear PtC_8Pt , $\text{PtC}_8\text{PtC}_8\text{Pt}$, and $\text{PtC}_8\text{PtC}_8\text{PtC}_8\text{Pt}$ Assemblies. *Organometallics* **2004**, *23*, 5896-5899.

(23) The complexes **4a-f** or their ammonium salt adducts were soluble in CHCl_3 , CH_2Cl_2 , and DMSO, but insoluble in hexane. Those with shorter geminal substituents were insoluble in diethyl ether (**4a-c**), but those with more lipophilic substituents were soluble (**4d-f**). Complex **4c** was soluble in ethyl acetate and slightly soluble in toluene, but **4a,b** were not.

(24) The crystals used for the three structure determinations of **4a,b** took periods of one week to one month to grow from samples that contained $[\text{H}_2\text{NEt}_2]^+$, and were not obtained in preparatively useful quantities. Rather, data were collected on the most promising looking crystals fished out of a bulk sample of rather mediocre appearance. Bruce and Anderson report similar experiences with their crystallizations of Pt_4C_{16} complexes (Table 5).^{5b,c} With **4a,b**, there were no obvious signs of any $[\text{H}_2\text{NEt}_2]^+$ in the residual electron density peaks.

(25) (a) Zhuravlev, F.; Gladysz, J. A. Electronic Structure and Chain-Length Effects in Diplatinum Polyynediyl Complexes *trans,trans*- $[(\text{X})(\text{R}_3\text{P})_2\text{Pt}(\text{C}\equiv\text{C})_n\text{Pt}(\text{PR}_3)_2(\text{X})]$: A Computational Investigation. *Chem. Eur. J.* **2004**, *10*, 6510-6522. (b) Samoc, M.; Dalton, G. T.; Gladysz, J. A.; Zheng, Q.; Velkov, Y.; Ågren, H.; Norman, P.; Humphrey, M. G. Cubic Nonlinear Optical Properties of Platinum-Terminated

Polyynediyl Chains. *Inorg. Chem.* **2008**, *47*, 9946-9957. (c) Sahnoune, H.; Baranová, Z.; Bhuvanesh, N.; Gladysz, J. A.; Halet, J.-F. A Metal-Capped Conjugated Polyynene Threaded through a Phenanthroline-Based Macrocyclic. Probing beyond the Mechanical Bond to Interactions in Interlocked Molecular Architectures. *Organometallics* **2013**, *32*, 6360-6367. (d) Li, Y.; Winkel, R. W.; Weisbach, N.; Gladysz, J. A.; Schanze, K. S. Photophysics of Platinum Tetrayne Oligomers: Delocalization of Triplet Exciton. *J. Phys. Chem. A* **2014**, *118*, 10333-10339. (e) Gauthier, S.; Porter, A.; Achelle, S.; Roisnel, T.; Dorcet, V.; Barsella, A.; Le Poul, N.; Level, P. G.; Jacquemin, D.; Robin-Le Guen, F. Mono- and Diplatinum Polyynediyl Complexes as Potential Push-Pull Chromophores: Synthesis, Characterization, TD-DFT Modeling, and Photophysical and NLO Properties. *Organometallics* **2018**, *37*, 2232-2244.

(26) Wititsuwannakul, T.; Hall, M. B.; Gladysz, J. A. A Computational Study of Hydrogen Bonding Motifs in Halide, Tetrafluoroborate, Hexafluorophosphate, and Tetraarylborate Salts of Chiral Cationic Ruthenium and Cobalt Guanidinobenzimidazole Hydrogen Bond Donor Catalysts; Acceptor Properties of the 'BARf' Anion. *Polyhedron* **2020**, *187*, 114618.

(27) (a) Fujita, M.; Sasaki, O.; Mitsuhashi, T.; Fujita, T.; Yazaki, J.; Yamaguchi, K.; Ogura, K. On the structure of transition-metal-linked molecular squares. *Chem. Commun.* **1996**, 1535-1536. (b) Sautter, A.; Schmid, D. G.; Jung, G.; Würthner, F. A Triangle-Square Equilibrium of Metallosupramolecular Assemblies Based on Pd(II) and Pt(II) Corners and Diazadibenzoperylene Bridging Ligands. *J. Am. Chem. Soc.* **2001**, *123*, 5424-5430. (c) Schweiger, M.; Seidel, S. R.; Arif, A. M.; Stang, P. J. Solution and

Solid State Studies of a Triangle-Square Equilibrium: Anion-Induced Selective Crystallization in Supramolecular Self-Assembly. *Inorg. Chem.* **2002**, *41*, 2556-2559. (d) Weilandt, T.; Troff, R. W.; Saxell, H.; Rissanen, K.; Schalley, C. A. Metallo-Supramolecular Self-Assembly: the Case of Triangle-Square Equilibria. *Inorg. Chem.* **2008**, *47*, 7588-7598. (e) Cotton, F. A.; Murillo, C. A.; Yu, R. Dynamic equilibrium between cyclic oligomers. Thermodynamic and structural characterization of a square and a triangle. *Dalton Trans.* **2006**, 3900-3905. (f) Holló-Sitkei, E.; Tárkányi, G.; Párkányi, L.; Megyes, T.; Besenyei, G. Steric Effects in the Self-Assembly of Palladium Complexes with Chelating Diamine Ligands. *Eur. J. Inorg. Chem.* **2008**, 1573-1583.

(28) The experimental UV-visible spectrum of **3b** exhibits absorptions in the 260-280 nm range that lack counterparts in the spectrum computed for **3'b**. These represent transitions associated with the phenyl rings.

(29) Sun, Y; Chen, C.; Liu, J.; Stang, P. J. Recent developments in the construction and applications of platinum-based metallacycles and metallocages *via* coordination. *Chem. Soc. Rev.* **2020**, *49*, 3889-3919, and extensive earlier literature cited therein.

(30) (a) Plutnar, J.; Givelet, C.; Lemouchi, C.; Dytrtová, J. J.; Cisařová, I.; Teat, S. J.; Michl, J. Mechanical vs Electronic Strain: Oval-Shaped Alkynyl-Pt(II)-Phosphine Macrocycles. *Organometallics* **2019**, *38*, 4633-4644. (b) Buchanan, E. A.; Michl, J. Mechanical vs Electronic Strain: Calculated Configurations of Alkynyl-Pt(II)-Phosphine Macrocycles. *Organometallics* **2020**, *39*, 1195-1201.

(31) Lang, H.; George, D. S. A.; Rheinwald, G. Bis(alkynyl) transition metal complexes, $R^1C\equiv C-M-C\equiv CR^2$, as organometallic chelating ligands; formation of $\mu,\eta^{1(2)}$ -alkynyl-bridged binuclear and oligonuclear complexes. *Coord. Chem. Rev.* **2000**, *206*, 101-197.

(32) (a) This sample cannot be represented as analytically pure, but the microanalytical data are nonetheless presented to illustrate the best results obtained to date. (b) Gabbaï, F. P.; Chirik, P. J.; Fogg, D. E.; Meyer, K.; Mindiola, D. J.; Schafer, L. L.; You, S.-L. An Editorial About Elemental Analysis. *Organometallics* **2016**, *35*, 3255-3256.

(33) The J values given for virtual triplets represent the apparent couplings between adjacent peaks and not the mathematically rigorous coupling constants. See Hersh, W. H. False AA'X Spin-Spin Coupling Systems in ^{13}C NMR: Examples Involving Phosphorous and a 20-Year-Old Mystery in Off-Resonance Decoupling. *J. Chem. Educ.* **1997**, *74*, 1485-1488.

(34) This signal is part of a complex spin system and the coupling constants were assigned by a simulation.¹⁹

(35) This signal is part of a complex spin system and appears as a triplet superimposed upon a broad hump. The coupling constant was assigned by a simulation.¹⁹

(36) This coupling represents a satellite (d, $^{195}Pt = 33.8\%$), and is not reflected in the peak multiplicity given.

(37) m/z , most intense peak of isotope envelope (relative intensity).

(38) *APEX2*, Program for Data Collection on Area Detectors. BRUKER AXS Inc. 5465 East Cheryl Parkway, Madison, WI 53711-5373 USA.

(39) G Sheldrick, G. M. *SADABS*, Program for Absorption Correction of Area Detector Frames, University of Göttingen, 2008.

(40) Sheldrick, G. M. A short history of *SHELX*. *Acta Cryst.* **2008**, *A64*, 112-122.

(41) *SAINT* (Version 7). Program for Data Integration from Area Detector Frames, Bruker–Nonius Inc. 5465 East Cheryl Parkway, Madison, WI 53711-5373 USA.

(42) Spek, A. L. Single-crystal structure validation with the program *PLATON*. *J. Appl. Cryst.* **2003**, *36*, 7-13.

(43) Dolomanov, O. V.; Bourhis, L. J.; Gildea, R. J.; Howard, J. A. K.; Puschmann, H. *OLEX2*: A Complete Structure Solution, Refinement and Analysis Program, *J. Appl. Cryst.* **2009**, *42*, 339-341.

"8. OCTAHEDRAL WERNER COMPLEXES WITH SUBSTITUTED
ETHYLENEDIAMINE LIGANDS: A STEREOCHEMICAL PRIMER FOR A
HISTORIC SERIES OF COMPOUNDS NOW EMERGING AS A MODERN FAMILY
OF CATALYSTS[†]

8.1. Conspectus

As reported by Alfred Werner in 1911-1912, salts of the formally D_3 symmetric $[\text{Co}(\text{en})_3]^{3+}$ (en = ethylenediamine) trication were among the first chiral inorganic compounds to be resolved into enantiomers, the absolute configurations of which are denoted Λ (left-handed helix) or Δ (right-handed helix). After a 100 year dormant period during which few useful reactions of these substitution inert complexes were described, carbon substituted derivatives have recently been found to be potent catalysts for enantioselective organic synthesis. This review systematically outlines the fascinating range of stereoisomers that can arise, such as conformers associated with the five membered chelate rings (λ/δ), alignment modes of the C–C bonds with the C_3 symmetry axis (*lellob*), geometric isomers (*fac/mer*), and configurational diastereomers (*R/S*) arising from carbon stereocenters. These analyses demonstrate a profound stereochemical diversity that can be applied in catalyst optimization. Efforts are made to

[†] Reproduced from Ehnbohm, A.; Ghosh, S. K.; Lewis, K. G.; Gladysz, J. A. Octahedral Werner complexes with substituted ethylenediamine ligands: a stereochemical primer for a historic series of compounds now emerging as a modern family of catalysts. *Chem. Soc. Rev.* **2016**, *45*, 6799-6811, with permission from the Royal Society of Chemistry.

bridge the often orthogonal nomenclature systems inorganic and organic chemists employ to describe these phenomena.

Key Learning Points: (1) Representations, symmetry, absolute configuration of the chiral octahedral trication $[\text{Co}(\text{en})_3]^{3+}$. (2) Conformations of the en ligands in $[\text{Co}(\text{en})_3]^{3+}$, and *lellob* orientations. (3) Stereoisomers of analogs with 1,2-propylenediamine ligands. (4) Stereoisomers of analogs with vicinally disubstituted ethylenediamine ligands. (5) Diastereomer stabilities and catalysis.

8.2. Introduction

Werner complexes with chelating 1,2-diamines have played prominent roles in the development of inorganic and coordination chemistry, particularly with regard to structure and stereochemistry.^{1,2} For example, octahedral cobalt(III) adducts — the most widespread family of Werner diamine complexes — were the first chiral inorganic compounds to be isolated in enantiomerically pure form.² However, until recently they have had few, if any, applications in synthetic organic chemistry, either as reagents or catalysts. One reason is that cobalt(III) complexes are, by virtue of their low spin d^6 electronic configurations, substitution inert,³ thereby preventing the coordination and activation of organic substrates at reasonable temperatures.

Recently, there have been conceptual and practical breakthroughs that have enabled chiral Werner complexes to serve as highly effective catalysts for enantioselective organic reactions.⁴⁻⁶ One has been the realization that the N–H bonds associated with coordinated amines are capable of functioning as hydrogen bond donors

to Lewis basic organic substrates.^{4,7} Over the last 20 years, a number of chiral organic hydrogen bond donors have been found to be effective catalysts for a multitude of enantioselective transformations.⁸ Not surprisingly, coordination compounds can function similarly, and frequently offer architectures and binding site arrays that have no counterparts in organic systems. Another has been the development of lipophilic⁴ and/or fluorophilic⁹ Werner complexes, such that catalysis can be conducted in the absence of water, which would otherwise saturate (or compete with substrate access to) the hydrogen bond donor sites.

Given this new interest in chiral Werner complexes, the authors thought it would be helpful to review the many hierarchal levels of stereochemistry that can be embodied in octahedral cobalt(III) complexes of chelating 1,2-diamines, for which ethylenediamine (*en*) is the archetype. This has already seen extensive analysis,¹⁰ but the literature is fragmented, and many studies present crystal structures or CD spectra with little accompanying insight. A potential entry-level stumbling block is that organic and inorganic chemists often favor different vocabularies in analyzing the same phenomena. Hence, efforts are made to employ both syntaxes side by side throughout this review.

Several conspicuous omissions deserve note at the outset. First, some cobalt *N,N,N',N'*-tetramethyl ethylenediamine (TMEDA) complexes have been reported.¹¹ However, there are questions regarding the existence of the cobalt(III)tris(chelate).¹² Dissecondary diamine chelates, which feature NHRR' donor groups, are easily accessed,¹³ but introduce additional stereocenters. The "asymmetric nitrogen atoms"

rapidly invert in the free ligands, but become fixed upon coordination. This leads to a further level of stereoisomerism, which can be subject to either kinetic or thermodynamic control. Outside of efforts by Searle,^{13b-d} there have been no systematic studies of such coordination environments, and it is left to motivated readers to derive the extensive families of stereoisomers that can result.

8.3. The chiral $[\text{Co}(\text{en})_3]^{3+}$ trication: cobalt stereocenter

All octahedral tris(chelate) complexes are chiral, and the enantiomers of the $[\text{Co}(\text{en})_3]^{3+}$ trication can be rendered in the "Star of David" motifs shown in Figure 8.1a. These non-superimposable mirror images differ in whether the connections between the "front triangle" and "rear triangle" run in counter clockwise or clockwise directions. This constitutes an example of helical chirality, with the first motif being left-handed and the second right. As detailed in many inorganic textbooks, the former is designated Λ and the latter Δ .¹⁴ In the organic literature, enantiomers that can be viewed as left or right-handed helices are often designated M and P . Other common representations of the enantiomers of $[\text{Co}(\text{en})_3]^{3+}$ are given in Figure 8.1b and c. Such compounds are sometimes referred to — together with non-planar complexes of formula $\text{M}(\text{A})(\text{B})(\text{C})(\text{D})$ — as "*chiral at metal*". Note also that the two NH_2 protons, and the two CH_2 protons, are diastereotopic and can give different ^1H NMR signals.

In 1912, Werner reported that the enantiomers of $[\text{Co}(\text{en})_3]^{3+}$ can be separated by fractional crystallization of the diastereomeric tartrate salts.^{2e} Chloride anion exchange then afforded the resolved enantiomers, Λ - and Δ - $[\text{Co}(\text{en})_3]^{3+} 3\text{Cl}^-$ In the

preceding year, Werner described analogous resolutions of cations of the formulae $[\text{Co}(\text{en})_2(\text{A})(\text{B})]^{n+}$ and $[\text{Co}(\text{en})_2(\text{A})_2]^{n+}$. As is evident from Figure 8.1d, two chelating ligands are sufficient to render an octahedral complex chiral. Tricationic tris(ethylenediamine) adducts of other metals ($[\text{M}(\text{en})_3]^{3+}$, $\text{M} = \text{Cr}$,^{15,16} Rh ,^{16,17} Ir ¹⁸) and the tetracation¹⁹ $[\text{Pt}(\text{en})_3]^{4+}$ were similarly resolved via salts of various chiral anions.

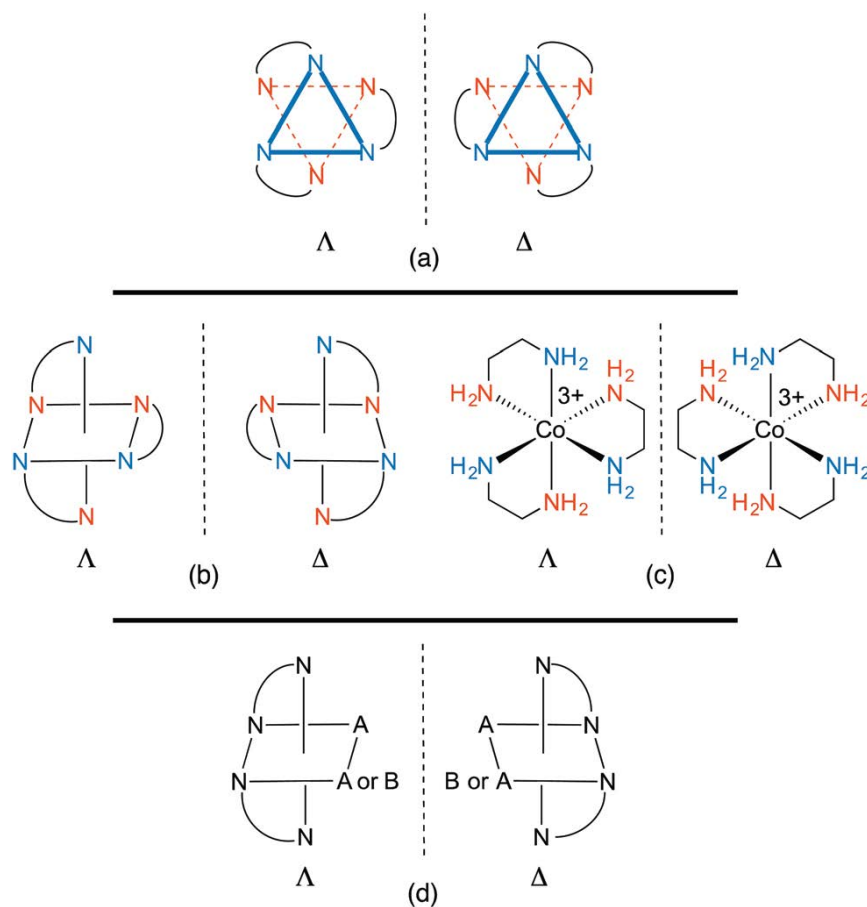


Figure 8.1 Representations of the enantiomeric Λ and Δ - $[\text{Co}(\text{en})_3]^{3+}$ trications (a-c) and the related bis(chelates) $[\text{Co}(\text{en})_2(\text{A})_2]^{3+}$ and $[\text{Co}(\text{en})_2(\text{A})(\text{B})]^{n+}$ (d).

Despite being chiral, the $[\text{Co}(\text{en})_3]^{3+}$ trication possesses several symmetry elements. However, for reasons that become obvious in section 8.3, this initial analysis approximates the chelate backbones as planar, or having identical conformations. With this proviso, there is a principal C_3 axis that runs perpendicular to the plane of the paper in Figure 8.1a and exchanges each blue nitrogen atom (and each vermilion nitrogen atom). There are furthermore three C_2 axes in a perpendicular plane (the plane of the paper) that exchange blue and vermilion nitrogen atoms. This corresponds to the chiral point group D_3 . However, the authors are not aware of any crystal structures where the trication exhibits this idealized symmetry,⁷ as the counter anions (and/or solvate molecules) hydrogen bond to the NH groups in motifs that lower the symmetry.

The enantiomers of $[\text{Co}(\text{en})_3]^{3+}$ are extremely stable with respect to ligand dissociation or racemization under ambient conditions. The half-lives for the hydrolysis and racemization of $[\text{Co}(\text{en})_3]^{3+} 3\text{Cl}^-$ in 0.10 M aqueous NaOH at 25 °C have been estimated as 3.2 years (38 kcal mol^{-1}) and >3.2 years, respectively.^{3b} Other reports confirm that no racemization of $[\text{Co}(\text{en})_3]^{3+} 3\text{Cl}^-$ occurs in aqueous solution during (a) 3 months at room temperature, (b) 75 minutes at 85 °C in the presence of 100 equiv. of NaNO_2 , or (c) 15 hours at reflux in the presence of HCl.²⁰ However, when activated charcoal is added, racemization takes place within two minutes at 90 °C.²¹ The charcoal is believed to function as a redox catalyst, allowing the generation of small amounts of substitution labile cobalt(II). Naturally, the enantiomers give mirror image CD spectra with opposite signs for $\Delta\epsilon$ or $[\theta]$.²² When additional ligand based stereocenters are

introduced, such that diastereomers result, the shapes of the CD spectra remain largely a function of the cobalt configuration.^{5b,23} Hence, cobalt configurations can be reliably assigned from the sign of the Cotton effect.

8.4. The chiral $[\text{Co}(\text{en})_3]^{3+}$ trication: ligand conformations

In the previous section, the conformations of the ethylenediamine chelate rings were not considered. With respect to the CH_2CH_2 backbone, a gauche orientation of the two NH_2 groups (torsion angle *ca.* 60°) would be expected to be much more stable than an eclipsed orientation (torsion angle *ca.* 0°). Thus, as illustrated by **A** and **B** in Figure 8.3, non-planar rings would be anticipated. For each $\text{Co}(\text{en})$ fragment, two non-superimposable mirror images are possible. These are commonly designated with the lower case Greek letters Λ and Δ and correspond to left-handed and right-handed helices, respectively (the counterclockwise and clockwise senses are illustrated with green arrows in Figure 8.2). Each NH_2 and CH_2 group features one hydrogen atom that is pseudoaxial, and one that is pseudoequatorial.

The axial and equatorial hydrogen atoms of cyclohexane rapidly exchange *via* a "ring flip", and the same holds for the hydrogen atoms of the ethylenediamine chelate rings. Thus, the Λ and Δ conformers will readily equilibrate (see Figure 8.2, bottom). However, in the absence of disorder, each chelate will crystallize in one conformation or the other.

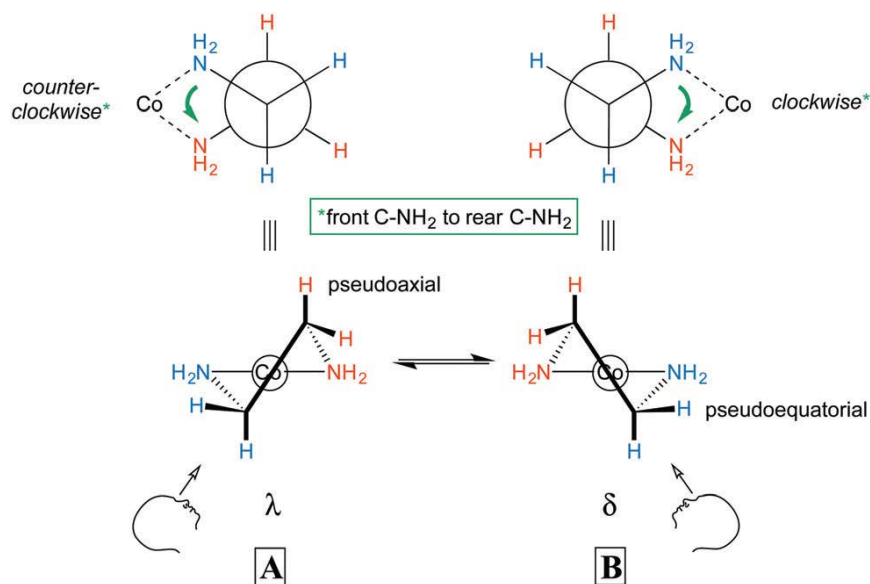


Figure 8.2 Chelate conformations of ethylenediamine.

Importantly, the conformation of the chelate affects the relative orientations of the $\text{CH}_2\text{-CH}_2$ bonds and the symmetry of the $[\text{Co}(\text{en})_3]^{3+}$ trication. First, consider the "docking" of three λ ethylenediamine units to give a trication with a Δ configuration at cobalt. The initial step is shown in Figure 8.3A, and when all three chelates are in place, the structure represented as $\Delta\text{-}\lambda\lambda\lambda$ results. Next, consider the docking of three δ ethylenediamine units to give a trication with the same Δ configuration at cobalt (i.e. an identical spatial orientation of chelating cobalt-nitrogen bonds). The initial step is shown in Figure 8.3B. In order for the cobalt-nitrogen bond locations to "match up", the δ ethylenediamine must first be rotated by 90° . When all three chelates have been similarly put in place, the structure represented as $\Delta\text{-}\lambda\lambda\lambda$ results.

In the first structure ($\Delta\text{-}\lambda\lambda\lambda$; Figure 8.3A), the λ chelates are said to adopt *lel* orientations, so named because the three $\text{CH}_2\text{-CH}_2$ bonds are parallel to the C_3

symmetry axis.²⁴ These linkages are often incorporated into Newman type projections, as indicated by hollow circles. In the second structure (Δ - $\delta\delta\delta$; Figure 8.3B), the δ chelates are said to adopt *ob* orientations, so named because the three CH_2 - CH_2 bonds are oblique to the C_3 axis. The designations Δ - $\lambda\lambda\lambda$ and Δ -*lel*₃ (Figure 8.3A) are both found in the literature, and can be used interchangeably, but with one important caveat that soon follows below. The same holds for Δ - $\delta\delta\delta$ and Δ -*ob*₃.

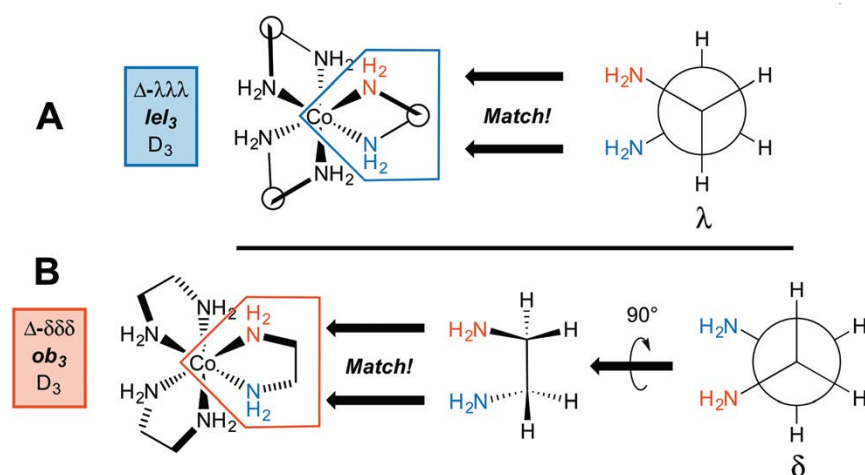


Figure 8.3 Accommodation of ethylenediamine ligands with three λ or three δ conformations in the coordination sphere of an octahedral cobalt atom with a Δ configuration.

When the $[\text{Co}(\text{en})_3]^{3+}$ trication has a Λ configuration at cobalt, these relationships are reversed. A λ chelate leads to an *ob* orientation while a δ chelate results in a *lel* orientation. Furthermore, each of the three ethylenediamine ligands can independently adopt either an *ob* or *lel* orientation. Therefore, for a complex with a given cobalt configuration, four diastereomers exist.

All possibilities are depicted in Figure 8.4. Note that the complexes analyzed in Figure 8.3, and their mirror images, have D_3 symmetry. However, the new diastereomers introduced in Figure 8.4, with mixed *lel* and *ob* orientations, have C_2 symmetry.

Figure 8.4 also illustrates a "trap" or potential error in identifying enantiomers. Just like the descriptors R/S always identify enantiomers of compounds with a single tetrahedral carbon stereocenter, so will the family of descriptors consisting of upper/lower case delta/lambda identify mirror image components of the $[\text{Co}(\text{en})_3]^{3+}$ trication. In other words, the stereoisomer $\Delta\text{-}\lambda\lambda\lambda$ can automatically be regarded as the enantiomer of $\Delta\text{-}\delta\delta\delta$.

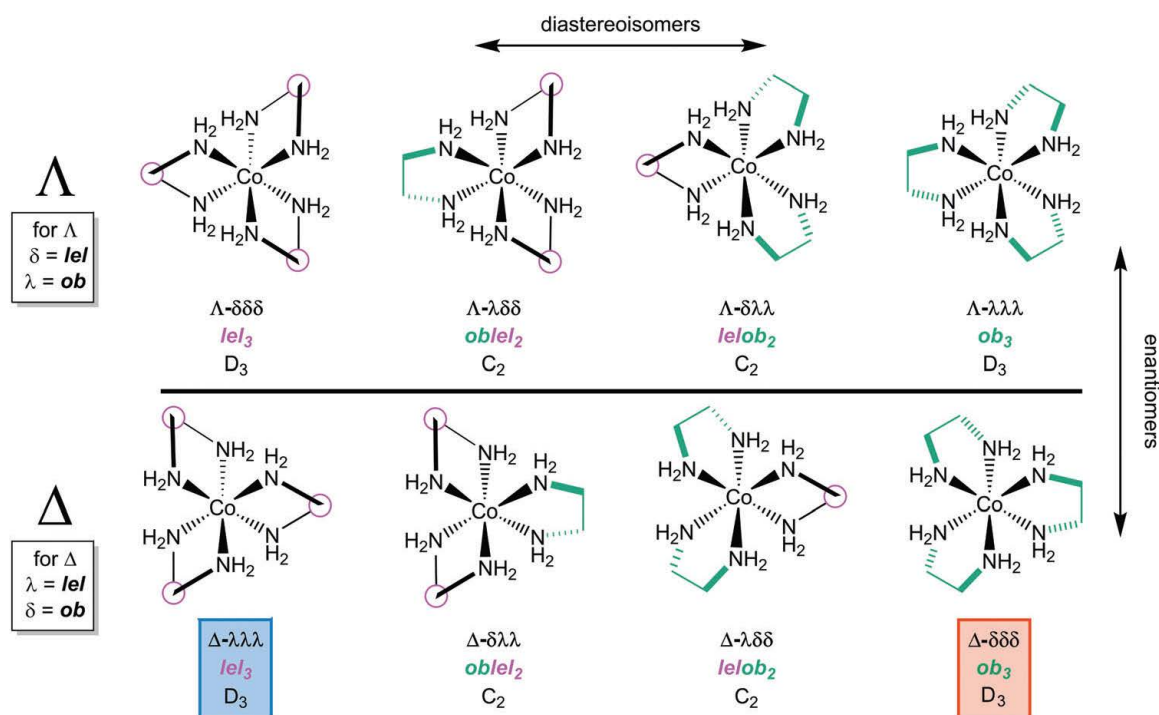


Figure 8.4 All possible stereoisomers of the $[\text{Co}(\text{en})_3]^{3+}$ trication.

However, this is not the case with *lel/ob*. Instead, Δ -*lel*₃ and Δ -*ob*₃ are diastereomers, as is easily seen in the upper left and lower right structures in Figure 8.4. Rather, it is Δ -*lel*₃ and Δ -*lel*₃ that are enantiomers. Another way to look at this is as follows: if the C_3 axis is perpendicular to the plane of the paper, and one enantiomer is reflected in the plane of the paper to give the other, a "parallel" (*lel*) orientation of the CH₂-CH₂ bond with respect to the C_3 axis must be preserved. For these reasons, the authors generally refer to *lel/ob* as "orientations" or "perspectives".

In practice, the conformations of the ethylenediamine chelate rings rapidly interconvert and do not have to be considered when analyzing the complexes in Figure 8.1. In other words, the four diastereomers with Λ configurations in Figure 8.4, as well as the four diastereomers with Δ configurations, will not normally be distinguishable in solution. However, all of these motifs can be observed in crystal structures.⁷ They also become important with certain types of substituted ethylenediamine ligands as described below.

Tris(chelate) complexes with larger rings, such as derived from 1,3-diaminopropane²⁵ and 1,4-diaminobutane²⁶ ligands, have also been reported. These similarly yield Λ and Δ enantiomers, but the additional CH₂ units give rise to larger numbers of chelate conformations. These have not yet been analyzed in comparable detail. However, parallels between chair, boat, and twist-boat cyclohexane and 1,3-diaminopropane chelate conformations have been noted.²

8.5. Octahedral Werner complexes with monosubstituted ethylenediamine ligands

The simplest monoalkylated diamine ligand is 1,2-propylenediamine (*pn*).²⁷ Whereas ethylenediamine is limited to two conformational enantiomers (see Figure 8.2), this ligand allows for two configurational enantiomers: (*R*)-1,2-propylenediamine ((*R*)-*pn*) and (*S*)-1,2-propylenediamine ((*S*)-*pn*). In the following analysis, cobalt(III) tris(chelate) complexes with homochiral ligands (i.e. all *R* or all *S*) are treated first.

8.5.1. Stereoisomerism at the cobalt center

As with ethylenediamine (Figure 8.1), three *pn* ligands can chelate to give either a Λ or Δ cobalt configuration. However, the methyl group lowers the chelate symmetry from an "A–A" to an "A–B" motif. This in turn leads to *facial* (*fac*) and *meridional* (*mer*) stereoisomers, which can be viewed as counterparts to geometric isomers in organic compounds. Figure 8.5 illustrates the four possible adducts of cobalt(III) and (*R*)-*pn* that can result (ignoring the chelate conformations). Four additional adducts can be generated with (*S*)-*pn*.

8.5.2. Chelate conformation

The conformation of the five membered chelate ring plays a more involved role with substituted ethylenediamine complexes than with the parent ligand. For 1,2-propylenediamine, the chelate will logically prefer conformations that place the methyl group in pseudoequatorial positions over pseudoaxial positions. Figure 8.6 illustrates the pseudoequatorial and pseudoaxial versions of both (*R*)-*pn* and (*S*)-*pn* ligands.

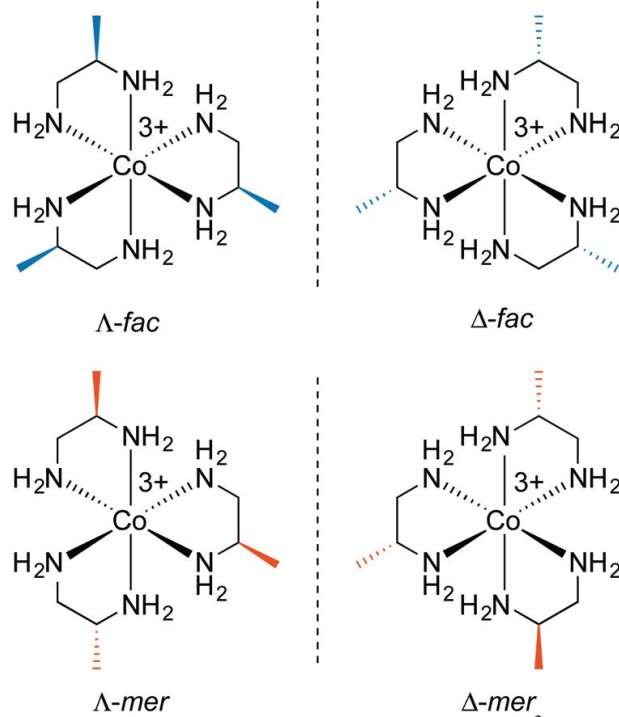


Figure 8.5 The *fac/mer* isomers of the $[\text{Co}(\text{R-pn})_3]^{3+}$ trication.

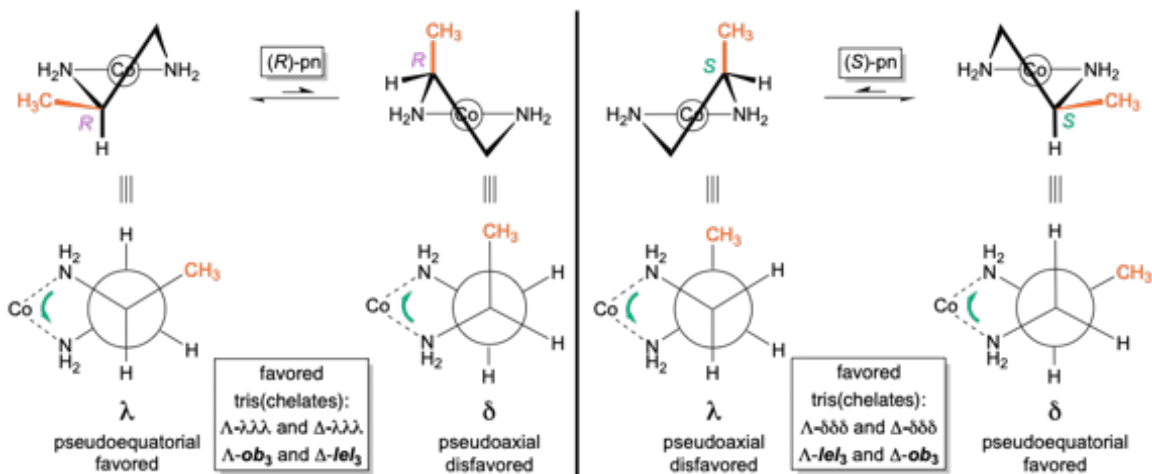


Figure 8.6 Chelate conformations of *(R)*-pn and *(S)*-pn.

For (*R*)-*pn*, the λ conformation of the chelate directs the methyl group into a pseudoequatorial position. A "ring flip" to the δ conformation is unfavorable because the methyl group must occupy a pseudoaxial position. It then follows that the tris(chelate) $[\text{Co}((R)\text{-}pn)_3]^{3+}$ should, irrespective of *mer/fac* geometry, preferentially exist as either Λ - $\lambda\lambda\lambda$ or Δ - $\lambda\lambda\lambda$ stereoisomers. With reference to the analyses of *ob/lel* orientations of unsubstituted ethylenediamine (Figure 8.3 and Figure 8.4), this means that in the Λ complex, the chelate $\text{CH}_2\text{-CHCH}_3$ linkages will all be oblique to the C_3 axis (Λ -*ob*₃). Similarly, in the Δ complex the chelate $\text{CH}_2\text{-CHCH}_3$ linkages will align parallel to the C_3 axis (Δ -*lel*₃).

In contrast, the (*S*)-*pn* ligand will be more stable in the δ conformation (Figure 8.6, right). Thus, $[\text{Co}((S)\text{-}pn)_3]^{3+}$ should preferentially exist as either Λ - $\delta\delta\delta$ or Δ - $\delta\delta\delta$ stereoisomers, which correspond to Λ -*lel*₃ and Δ -*ob*₃. In any event, Figure 8.7 summarizes the four preferred stereoisomers of $[\text{Co}((R)\text{-}pn)_3]^{3+}$, considering all possible combinations of metal configurations, chelate conformations, and *fac/mer* geometries. As a side comment on nomenclature, one could ask whether the first example, labeled Λ -*fac*- $\delta\delta\delta$, might equally well be represented as Λ -*fac*-*RRR*. The authors would discourage this practice, as the absolute configurations of the carbon stereocenters are already specified in the formula $[\text{Co}((R)\text{-}pn)_3]^{3+}$, and the absence of the $\lambda\lambda\lambda$ designation leaves open the possibility that one of the chelate rings might display an alternative δ conformation as, for example, a consequence of crystallization.

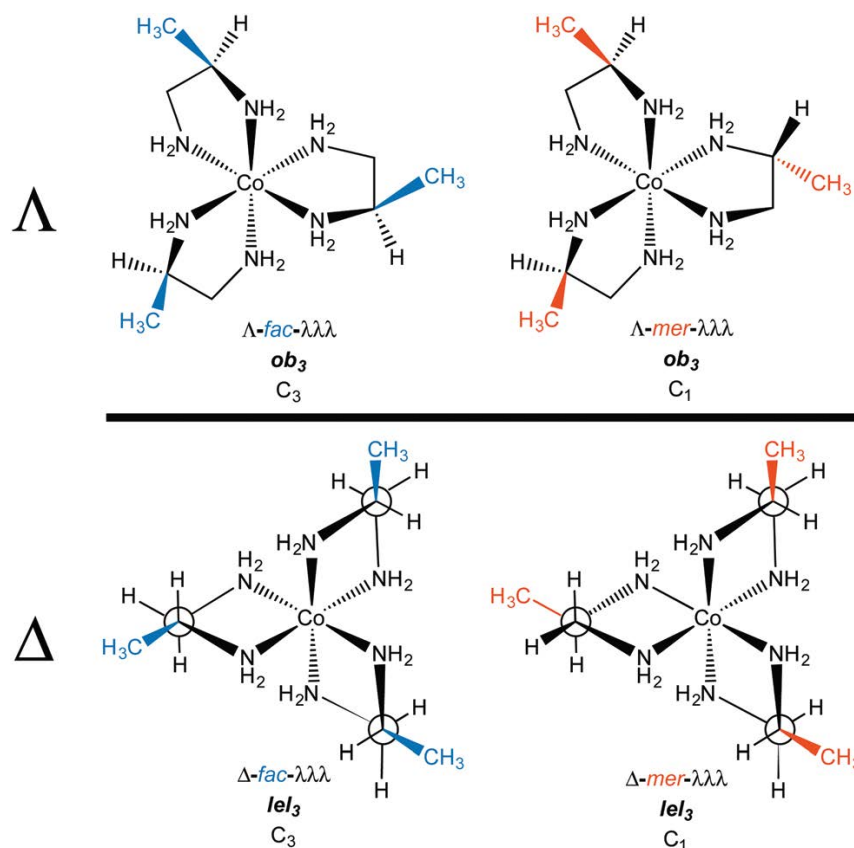


Figure 8.7 Principal stereoisomers of the $[\text{Co}((R)\text{-pn})_3]^{3+}$ trication.

Alert readers will note that upon going from Figure 8.1a-c to Figure 8.4 to Figure 8.7, structures of progressively lower symmetries are encountered (D_3 , C_3 , C_2 , C_1). Thus, it is essential to define a common reference point. Accordingly, this is taken as the "formal" or "pseudo" C_3 axis that is perpendicular to the two "Star of David" triangles (Figure 8.1a), each comprised of one NH_2 group from each of the three chelate rings. This corresponds to a true C_3 axis for structures with D_3 or C_3 symmetry, and is always depicted perpendicular to the plane of the paper.

8.5.3. A Stereoisomers allowing all possible combinations of ligand configurations

Cobalt(III) complexes of racemic pn are also chiral. This leads to a series of stereoisomers consisting of 2:1 or 1:2 (heterochiral) mixtures of (R)- pn and (S)- pn ligands, in addition to those enumerated above. Table 8.1 summarizes these various isomers, which were originally enumerated by Harnung.²⁷ However, drawing the new structures is left as an exercise for the reader — one that would be very appropriate for a graduate student take-home exam. The answers are supplied in Appendix F; Figure 16.2.

8.6. Octahedral Werner complexes with symmetrically disubstituted ethylenediamine ligands

Many Werner complexes have been prepared from ethylenediamine ligands with two identical vicinal substituents. Examples include 2,3-butanediamine(1,2-dimethylethylenediamine),²⁸ 1,2-cyclohexanediamine ($chxn$),^{29,30} and 1,2-diphenylethylenediamine ($dpen$).^{23,31,32} In all cases, three ligand stereoisomers are possible, as depicted for $chxn$ in Figure 8.8. The first two are chiral and constitute the familiar " rac " pair, whereas the last is the achiral *meso* diastereomer.

Due to the metal centered chirality, *meso* ligands can yield chiral adducts, and enantiopure complexes have in fact been isolated.^{28a,30a} Since $chxn$ complexes have received the most attention in the literature, these are treated first.

Table 8.1 Stereoisomers of $[\text{Co}(pn)_3]^{3+}$ trications comprised of all combinations of (*R*)-*pn* and (*S*)-*pn* ligands (rows in bold are for tris(*R*)-*pn*) adducts as analyzed in Figure 8.7).

cobalt configuration	ligand configuration	preferred chelate conformation	perspective down the C_3 axis ^a	geometric type isomers	number of stereoisomers
Λ	<i>SSS</i>	$\delta\delta\delta$	<i>lel</i> ₃	<i>fac</i> (1), <i>mer</i> (1)	2
Δ	<i>RRR</i>	$\lambda\lambda\lambda$		<i>fac</i> (1), <i>mer</i>(1)	2
Λ	<i>RSS</i>	$\lambda\delta\delta$	<i>oblel</i> ₂	<i>fac</i> (1), <i>mer</i> (3)	4
Δ	<i>SRR</i>	$\delta\lambda\lambda$		<i>fac</i> (1), <i>mer</i> (3)	4
Λ	<i>SRR</i>	$\delta\lambda\lambda$	<i>lelob</i> ₂	<i>fac</i> (1), <i>mer</i> (3)	4
Δ	<i>RSS</i>	$\lambda\delta\delta$		<i>fac</i> (1), <i>mer</i> (3)	4
Λ	<i>RRR</i>	$\lambda\lambda\lambda$	<i>ob</i> ₃	<i>fac</i> (1), <i>mer</i>(1)	2
Δ	<i>SSS</i>	$\delta\delta\delta$		<i>fac</i> (1), <i>mer</i> (1)	2
number of stereoisomers					24^b

^a Or an equivalent axis as defined in the text. ^b This increases if chelate conformations that have pseudoaxial methyl groups are allowed (see Figure 8.6).

8.6.1. Stereoisomerism at the cobalt center

Consider first the chelation of three identical ligands of any of the preceding types to cobalt. As with the other cases above, either Λ or Δ configurations can result. As a general rule, disubstituted ethylenediamine ligands that have C_2 symmetry, such as *trans-chxn* or (*S,S*)- or (*R,R*)-*dpen*, do not lead to *fac/mer* isomers. For *cis* or *meso* (*R,S*)-*chxn* or (*R,S*)-*dpen*, which are not C_2 symmetric, *fac/mer* isomers result. In a *fac* isomer, the three Co–NH₂ bonds that connect to carbon atoms with *R* configurations would all have bond angles of ca. 90°. In a *mer* isomer, one of these angles would be ca. 180°.

8.6.2. Ligand conformation: *trans*-1,2-cyclohexanediamine (*trans-chxn*)²⁹

As shown in Figure 8.9, the chelation of *trans-chxn* requires that both NH₂ groups occupy equatorial positions (a single atom cannot span axial substituents that have 1,2 relationships). With (*R,R*)-*chxn* (top left), this in turn requires a λ chelate conformation. Thus, for the tris(chelate) [Co((*R,R*)-*chxn*)₃]³⁺, only Λ - $\lambda\lambda\lambda$ (Λ -*ob*₃) and Δ - $\lambda\lambda\lambda$ (Δ -*lel*₃) stereoisomers are possible (bottom left). In contrast, (*S,S*)-*chxn* requires a δ chelate conformation (Figure 8.9, top right). For the tris(chelate) [Co((*S,S*)-*chxn*)₃]³⁺, only Λ - $\delta\delta\delta$ (Λ -*lel*₃) and Δ - $\delta\delta\delta$ (Δ -*ob*₃) stereoisomers are possible (bottom right), each enantiomeric with one of the isomers of [Co((*R,R*)-*chxn*)₃]³⁺. There are no other stereoisomers for tris(chelates) in which the *trans-chxn* ligands are homochiral.

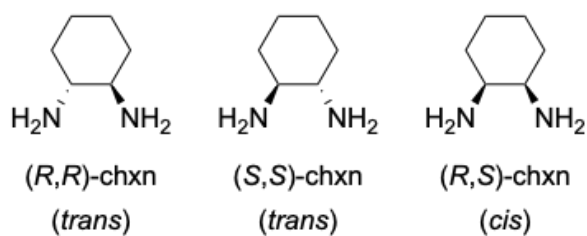


Figure 8.8 Configurational stereoisomers of 1,2-cyclohexanediamine.

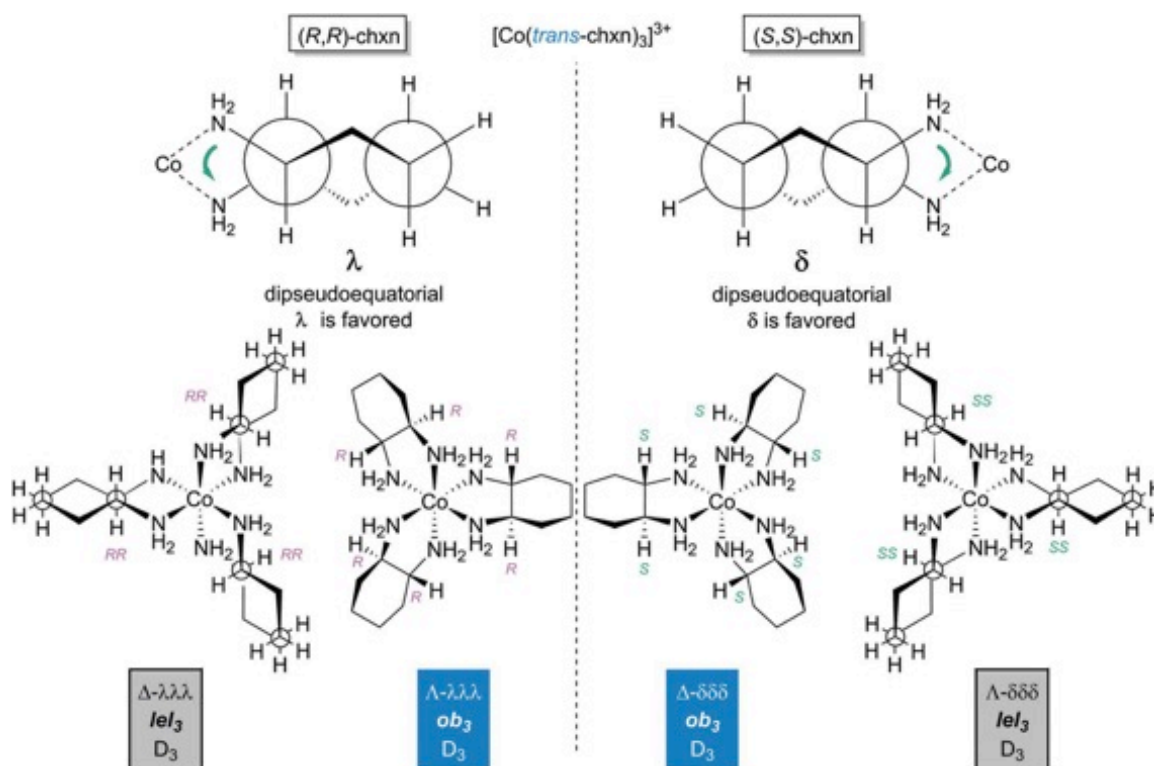


Figure 8.9 Diamine chelate conformations and principal stereoisomers of the $[\text{Co}(\textit{trans}\text{-chxn})_3]^{3+}$ trication with homochiral (all *S,S* or all *R,R*) ligands.

Next, consider the complexes possible when the *trans-chxn* ligands are no longer restricted to be homochiral (as with syntheses carried out with racemic diamine).²⁹ This is reminiscent of the scenario entertained for *pn* in Table 8.1, but more tractable due to the higher ligand symmetry and constraints imposed by the cyclohexane ring. The eight possible stereoisomers are depicted in Figure 8.10, four with a Λ cobalt configuration (top), and four with a Δ configuration (bottom). Each set of four contains a complex derived from (i) three (*R,R*)-*chxn* ligands (depicted in fuller form in Figure 8.9), (ii) two (*R,R*)-*chxn* ligands and one (*S,S*)-*chxn* ligand, (iii) one (*R,R*)-*chxn* ligand and two (*S,S*)-*chxn* ligands, and (iv) three (*S,S*)-*chxn* ligands (depicted in Figure 8.9).

Enantiomeric relationships are color coded in Figure 8.10. Here, designations such as Λ - $\lambda\lambda\lambda$ and Λ -*RR/RR/RR* would be fully equivalent, given the inability of *trans-chxn* to chelate when the amino groups occupy axial positions. The latter expression may be more intuitive for organic chemists.

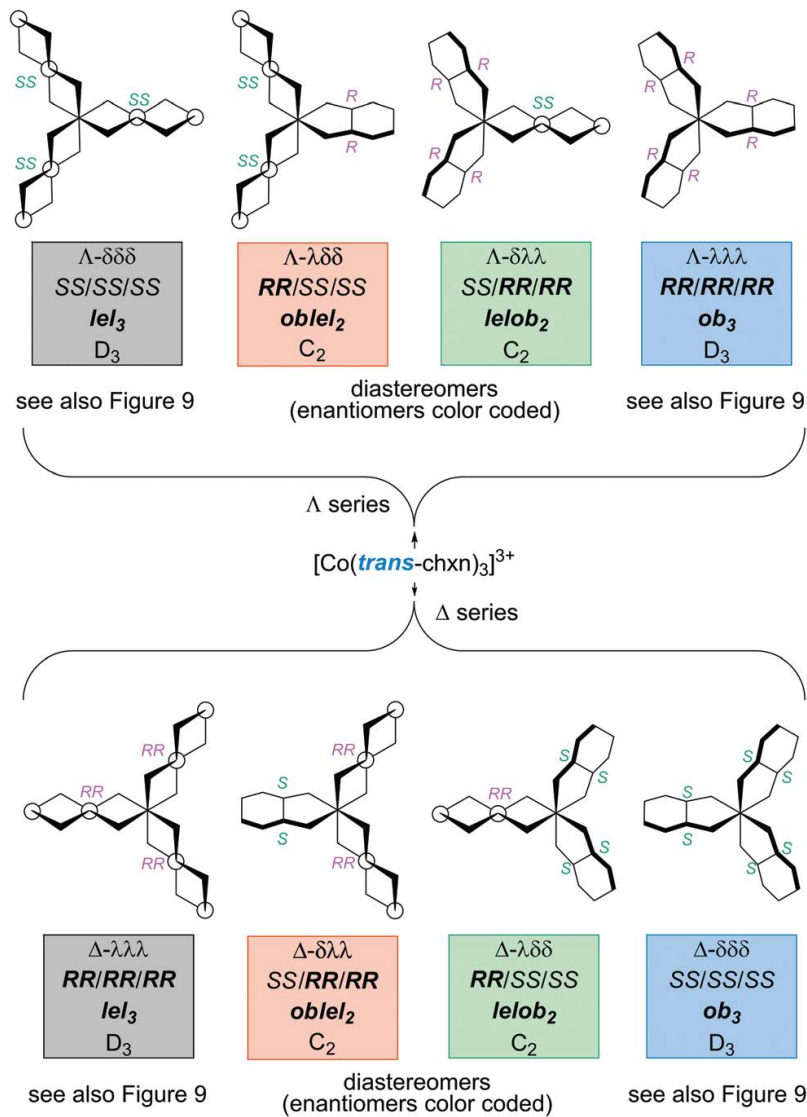


Figure 8.10 Stereoisomers of the $[\text{Co}(\text{trans-chxn})_3]^{3+}$ trication with all possible combinations of (*R,R*)-*chxn* and (*S,S*)-*chxn* ligands.

8.6.3. Ligand conformation: *cis*-1,2-cyclohexanediamine (*cis*-*chxn*)

As illustrated in Figure 8.11, the chelation of the *meso* ligand, *cis*- or (*R,S*)-*chxn*, requires that one amino group occupy an equatorial position on the cyclohexane ring, and the other an axial position. With respect to the five membered chelate ring, one CCH₂ substituent must occupy a pseudoequatorial position, and the other a pseudoaxial position. The partial structures in Figure 8.11 (top) can be interconverted by a cyclohexane "ring flip", analogous to those of related bicyclic molecules such as *cis*-perhydroindane and *cis*-decalin.³⁰

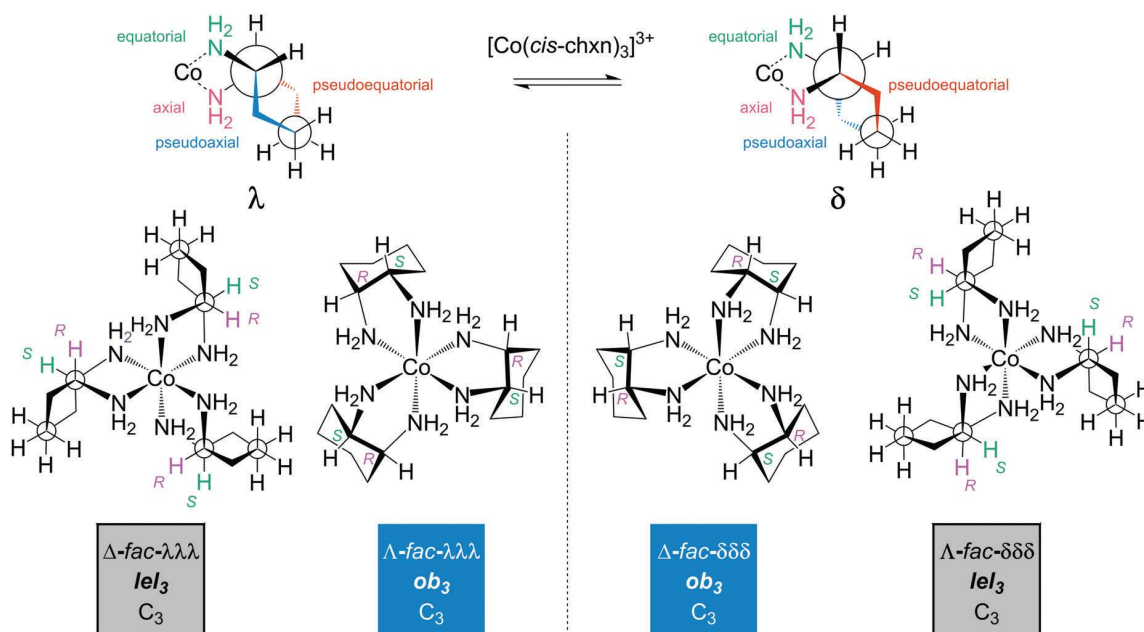


Figure 8.11 Diamine chelate conformations and representative stereoisomers of the $[\text{Co}(\textit{cis}\text{-chxn})_3]^{3+}$ trication; axial and equatorial are used to designate C–N bond positions on the cyclohexane ring, and pseudoaxial and pseudoequatorial are used to designate C–CH₂ bond positions on the chelate ring.

Four representative stereoisomeric cobalt tris(chelates) are shown in Figure 8.11 (bottom). These have cobalt and chelate configurations as well as *lel/ob* orientations and enantiomeric relationships analogous to those of $[\text{Co}(\textit{trans-chxn})_3]^{3+}$ in Figure 8.9. However, additional *fac/mer* descriptors are required; all of those illustrated are *fac* isomers (as is easily derived from the *R/S* labels). As one generates all possible permutations of cobalt and chelate configurations and *fac/mer* arrays, a plethora of stereoisomers proves possible. Only by simultaneously building molecular models of each (to ensure no duplicates and optimally test for mirror images) were the authors able to convince themselves of the existence of 24 stereoisomers (12 pairs of enantiomers). Given this somewhat overwhelming set of data, the structures are depicted in Appendix F (Figure 16.4) and summarized in Table 16.1. However, many of them can be interconverted by a cyclohexane "ring flip", and when this is applied to all three chelates only four distinct families of isomers remain. These consist of Λ -*fac* and Δ -*fac* groupings (enantiomeric, four members each), and Λ -*mer* and Δ -*mer* groupings (enantiomeric, eight members each).

Interestingly, although all four types of stereoisomers have been isolated in enantiopure form, they have not been extensively analyzed.³⁰ Given the low barriers for most cyclohexane "ring flips", these likely exist as mixtures of conformers in solution. In any case, Figure 16.4 (Appendix F) testifies as to the incredible stereochemical diversity associated with the title compounds.

8.6.4. Ligand conformation: (*S,S*)- and (*R,R*)-1,2-diphenylethylenediamine (*dpen*)

As illustrated in Figure 8.12, the chelation of either enantiomer of *dpen* requires that both phenyl groups occupy either pseudoequatorial or pseudoaxial positions. Naturally the former will be greatly favored. This results in a λ chelate conformation for (*R,R*)-*dpen* and a δ conformation for (*S,S*)-*dpen*. It then follows that for the tris(chelate) $[\text{Co}((\textit{R,R})\text{-dpen})_3]^{3+}$, the stereoisomers $\Lambda\text{-}\lambda\lambda\lambda$ ($\Lambda\text{-ob}_3$) and $\Delta\text{-}\lambda\lambda\lambda$ ($\Delta\text{-lel}_3$) should be the more stable (Figure 8.12, bottom left). Similarly, for $[\text{Co}((\textit{S,S})\text{-dpen})_3]^{3+}$, the stereoisomers $\Lambda\text{-}\lambda\lambda\lambda$ ($\Lambda\text{-lel}_3$) or $\Delta\text{-}\delta\delta\delta$ ($\Delta\text{-ob}_3$) will be the more stable (Figure 8.12, bottom right; mirror images of the bottom left structures). All of these are analogous to the isomers given for *trans*- or (*S,S*)- and (*R,R*)-*chxn* in Figure 8.9 (in which the CCH_2 substituents on the chelate ring are constrained to occupy pseudoequatorial positions).

As was analyzed for other chiral chelate ligands above, tris(chelate) complexes of *dpen* can be generated from a racemate. As shown in Figure 8.13, eight stereoisomers are possible, four with a Λ configuration at cobalt and four with a Δ configuration. Half of these feature combinations of heterochiral (*R,R*)-*chxn* and (*S,S*)-*chxn* ligands. The situation is closely related to that for $[\text{Co}(\textit{trans}\text{-chxn})_3]^{3+}$ in Figure 8.10.

A similar analysis for the *meso* ligand (*R,S*)-*dpen* leads to a set of isomers analogous to those of $[\text{Co}(\textit{cis}\text{-chxn})_3]^{3+}$ in Figure 8.11 and Figure 16.4 (Appendix F). However, reports to date indicate that such adducts are labile, presumably due to steric interactions resulting from the phenyl group that must occupy a pseudoaxial position on

the chelate ring.³² Several isomeric tris(chelate) cobalt(III) complexes of the meso ligand (*R,S*)-2,3-butanediamine have been isolated.^{28a,b}

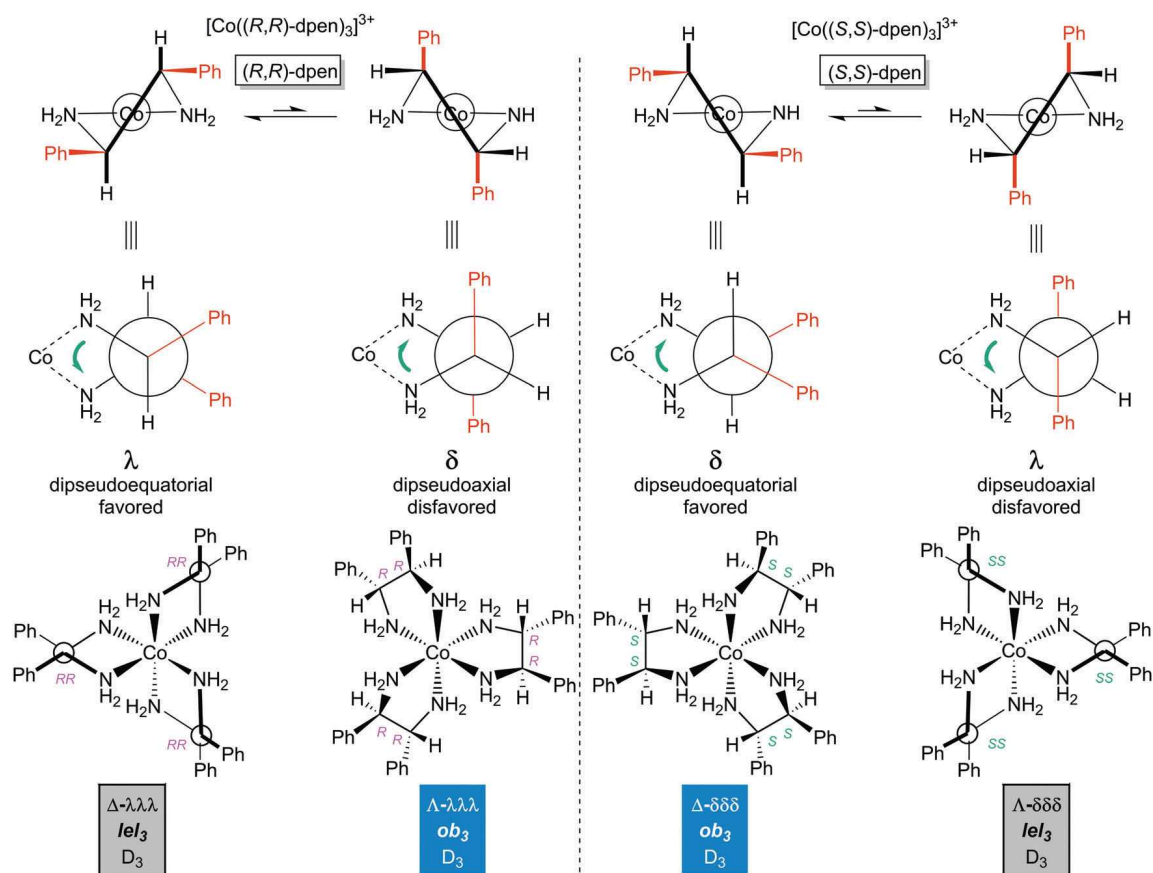


Figure 8.12 Diamine chelate conformations and principal configurational stereoisomers of the $[\text{Co}(\text{dpen})_3]^{3+}$ trication with homochiral (all *S,S* or all *R,R*) ligands.

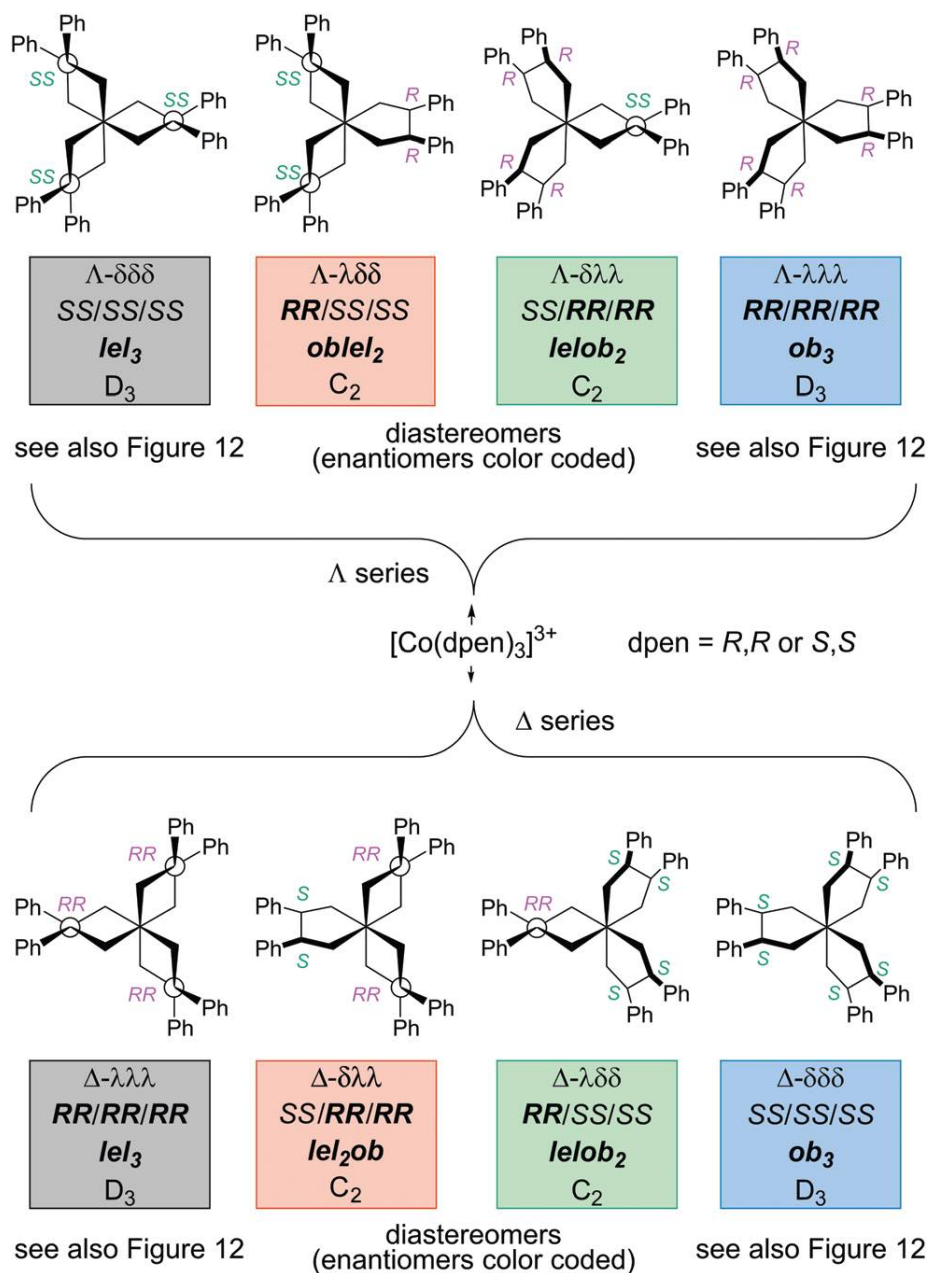


Figure 8.13 Stereoisomers of the $[\text{Co}(\text{dpen})_3]^{3+}$ trication with all possible combinations of (R,R) - dpen and (S,S) - dpen ligands.

8.7. Diastereomer stabilities

A detailed discussion or analysis of the relative stabilities of the preceding types of diastereomers would be beyond the scope of this review. Indeed, there is strong evidence that interactions with anions can affect stability orders in solution,^{5a,26b} and this issue is currently being probed. In their seminal study of the $[\text{Co}(\text{en})_3]^{3+}$ trication, Corey and Bailar estimated Δ - $\lambda\lambda\lambda$ - $[\text{Co}(\text{en})_3]^{3+}$ (which has a lel_3 orientation per Figure 8.3) to be more stable than Δ - $\delta\delta\delta$ - $[\text{Co}(\text{en})_3]^{3+}$ (which has an ob_3 orientation) by 1.8 kcal mol⁻¹.²⁴ This was based upon intramolecular carbon–hydrogen and hydrogen–hydrogen interactions; a treatment the authors admitted was a rough approximation. Isomers with $oblel_2$ and $lelob_2$ orientations were thought to have intermediate stabilities. More recent DFT results suggest that Δ - $\lambda\lambda\lambda$ - $[\text{Co}(\text{en})_3]^{3+}$ is 1.5 kcal mol⁻¹ more stable than Δ - $\delta\delta\delta$ - $[\text{Co}(\text{en})_3]^{3+}$ in water.^{22a}

In another study, Harnung was able to equilibrate diastereomers of the trichloride salt $[\text{Co}(\text{trans-}chxn)_3]^{3+} 3\text{Cl}^-$.²⁹ As shown in Figure 8.14, an aqueous solution of the racemate, both enantiomers of which have lel_3 orientations (Figure 8.10), was refluxed over charcoal²¹ in the presence of added racemic *trans-}chxn*. All of the stereoisomers depicted in Figure 8.10 were generated, and the ratios (determined after chromatographic separation) showed a distinct trend. Namely, the original stereoisomers with lel_3 orientations dominated, and quantities monotonically decreased as the proportion of *ob* orientations increased.

In a follow up experiment shown in Figure 8.15,²⁷ an aqueous solution of enantiopure Δ -[Co((*R,R*)-*chxn*)₃]³⁺ 3Cl⁻ (which has a *lel*₃ orientation) was refluxed over charcoal in the presence of enantiopure (*R,R*)-*chxn*. After the same time, only 7% of a new stereoisomer had been generated, Λ -[Co((*R,R*)-*chxn*)₃]³⁺ 3Cl⁻ (which per Figure 8.10 has an *ob*₃ orientation).

An experiment analogous to that in Figure 8.14 was conducted with the salt [Co(*pn*)₃]³⁺ 3Cl⁻ that had been generated from racemic *pn* and an achiral cobalt(II) precursor.²⁷ The many possible isomers of this trication were analyzed in Table 8.1. Chromatography gave separate fractions for the *lel*₃, *oblel*₂, *lelob*₂, and *ob*₃ structures (each fraction a mixture of stereoisomers) in a 35.0:41.1:18.0:4.0 ratio with excellent mass balance. Additional background regarding the often surprisingly efficient chromatographic separation of isomeric (even enantiomeric) tris(diamine) cobalt(III) complexes is provided elsewhere.³³ A version of this experiment with non racemic [Co(*pn*)₃]³⁺ 3X⁻ has also been reported.³⁴ An equilibration similar to that in Figure 8.14 but with the *meso* or *cis chxn* adduct [Co((*R,S*)-*chxn*)₃]³⁺ 3X⁻ has been mentioned, but the isomer ratios were not given.^{30a}

Thus, a clear bias for isomers with *lel* rich orientations is observed in the preceding experiments. However, it should be noted that in Figure 8.14 and Figure 8.15, reactants already possessing *lel*₃ orientations were employed. Also, the authors did not definitively establish that equilibrium had been attained. Perhaps longer reaction times would have resulted in greater proportions of products with *ob*-rich orientations.

Furthermore, the counter anion, chloride, is a strong hydrogen bond acceptor and may influence equilibrium ratios. Nonetheless, the aggregate data strongly suggest a trend, which is furthermore consistent with preliminary DFT computational results obtained by the authors.

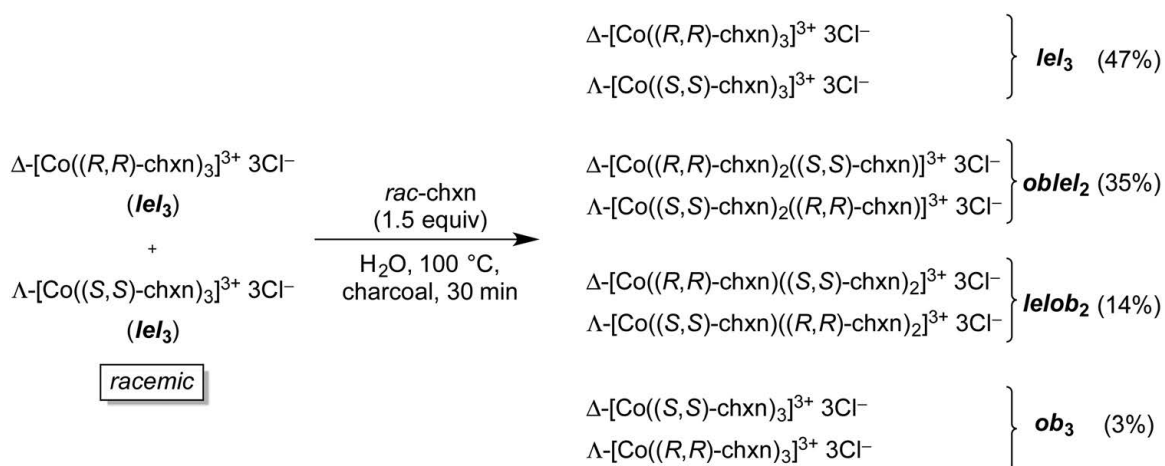


Figure 8.14 Thermal equilibration of racemic $[\text{Co}(\text{trans-chxn})_3]^{3+} 3\text{Cl}^-$ in the presence of excess ligand.

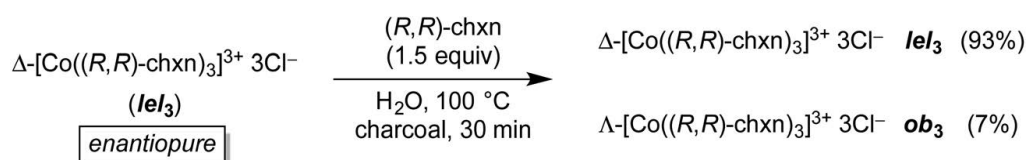


Figure 8.15 Thermal equilibration of enantiopure $\Delta\text{-[Co}((R,R)\text{-dpen})_3]^{3+} 3\text{Cl}^-$ in the presence of excess ligand.

8.8. Catalysis

A detailed treatment of the catalytic properties of the preceding types of complexes will be deferred until additional results from the authors' laboratory are published. However, applications reported to date are summarized in Figure 8.16.⁴⁻⁶ These include Michael additions of malonate esters to α,β -unsaturated nitro compounds (top) and ketones, additions of 1,3-dicarbonyl compounds to di(*t*-butyl)azodicarboxylate, yielding amino acid precursors (middle), and ring opening polymerizations of lactide (bottom).

With the first reaction, a bifunctional catalyst that incorporates a tertiary amine proves somewhat more effective than a monofunctional catalyst with *dpen* ligands that is used in conjunction with Et₃N. With the last reaction, another type of chelating nitrogen donor ligand, in which the activating NH groups are found in the chelate backbone, proves to be especially effective (see Figure 8.16C). Although the polymerizations have yet to be conducted with an enantiopure catalyst, the other reactions have and under optimum conditions deliver products of >90% ee. Many mechanistic questions surrounding these processes remain extant.

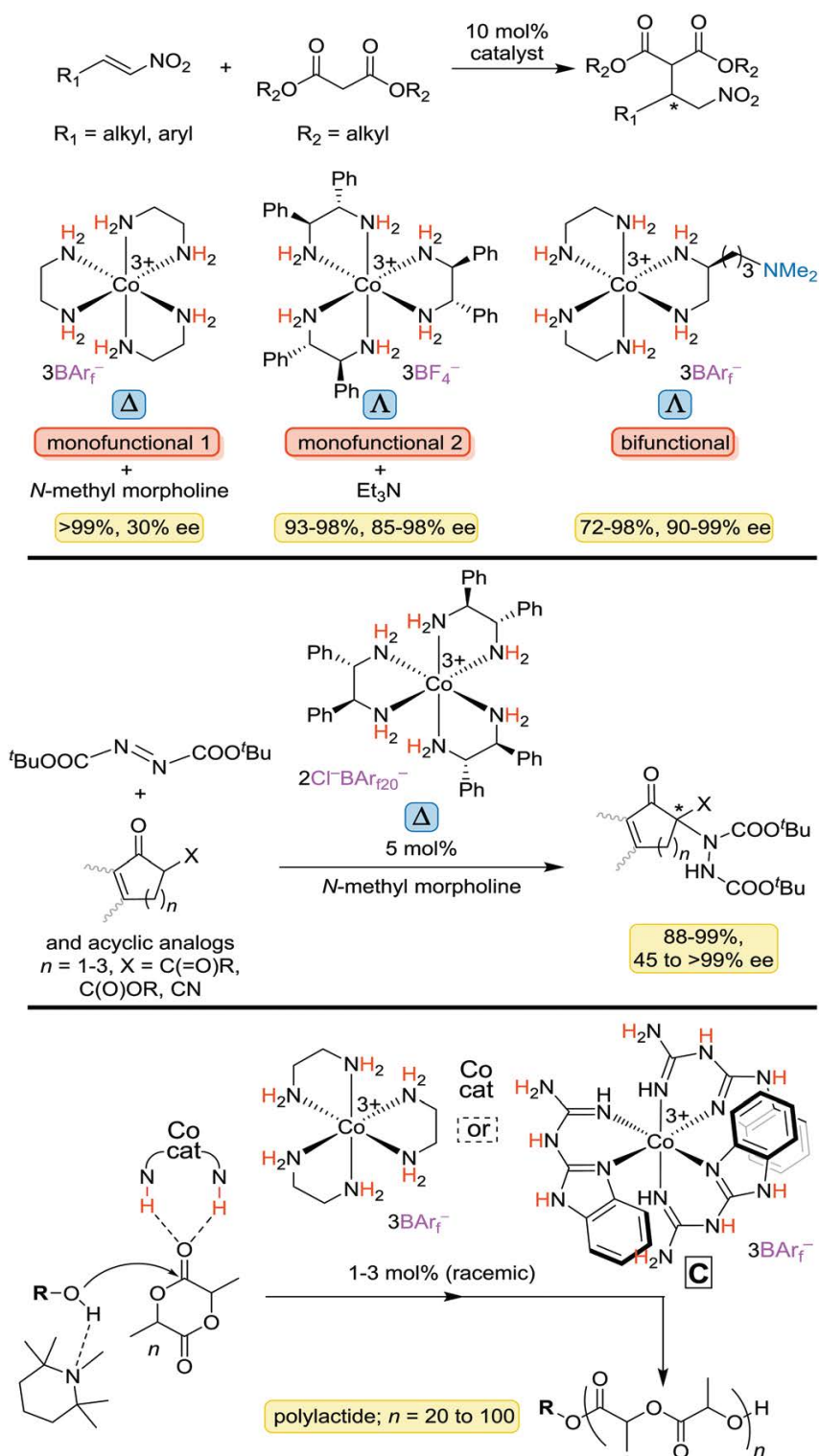


Figure 8.16 Organic transformations that can be catalyzed by cobalt(III) complexes with ethylenediamine or substituted ethylenediamine ligands ($BAR_f^- = B(3,5-C_6H_3(CF_3)_2)_4^-$; $BAR_{f20}^- = B(C_6F_5)_4^-$).

8.9. Summary and recommendations

Although all of the examples cited in this survey involve cobalt, the principles and conclusions can clearly be extrapolated to all octahedral tris(chelate) metal complexes of ethylenediamines. Also, most types of carbon substituted ethylenediamine ligands should be closely modeled by one of the examples analyzed. For instance, *pn* can be viewed as representative of all monosubstituted diamines. For geminally disubstituted analogs such as $\text{H}_2\text{NCRR}'\text{CH}_2\text{NH}_2$, the larger R/R' group would prefer a pseudoequatorial position in the chelate ring, leading to stereoisomers analogous to those of *pn*. The *chxn* and *dpen* complexes define the stereoisomer space for ethylenediamines with identical vicinal substituents. In cases where the substituents are rendered unequal (e.g. $\text{H}_2\text{NCHRCHR}'\text{NH}_2$), what were formerly *rac* type ligands will now have an added layer of *fac/mer* isomerism. However, such cobalt tris(chelate) complexes remain, to the authors' knowledge, unknown.

Underneath the many structures given above can be found a variety of types of "names". In the authors' view, the most appropriate one will be situational. If one wishes to specify a reactant or product, representations of the type in Figure 8.14 and Figure 8.15 are sufficient. If one wishes to denote a specific three-dimensional structure, all of the descriptors Λ/Δ , *R/S*, λ/δ , and (for diamines without C_2 symmetry) *fac/mer* will generally be necessary. With certain conformationally restricted diamines (e.g. *chxn*), the *R/S* and λ/δ designations may be formally redundant, but both are recommended nonetheless. The authors consider it a disservice to the reader to replace the configuration of a ligand, such as (*R,R*)-*chxn* in Figure 8.14 and Figure 8.15, with the

sign of the optical rotation, such as $(-)$ -*chxn*. However, the sign of the optical rotation of the complex may be added at the front of the name if desired.

In the authors' opinion, the descriptors *lel* and *ob* do not represent primary stereochemical phenomena but rather chelate orientations or perspectives that are enforced by fundamental stereochemical variables. Hence, these designations are given separately. However, they are clearly valuable for purposes of geometric classification. Furthermore, as noted in the previous section, this feature appears to be a major determinant with respect to chromatographic retention times and thermodynamic stabilities. Efforts to drill down deeper on this relationship are underway.

These are exciting times for Werner complexes. They have always been a classroom favorite, but most often for illustrating tried and true physical principles established long ago. Now they have contemporary applications in enantioselective catalysis,^{4-6,35,36} and the literature and new analyses summarized above should help to better understand the underlying phenomena and more methodically mine this emerging field.

8.10. References

(1) General treatments of inorganic stereochemistry that include introductions to Werner complexes of 1,2-diamines: (a) von Zelewsky, A. *Stereochemistry of Coordination Compounds*, John Wiley & Sons, Chichester, 1996. (b) Amouri, H.; Gruselle, M. *Chirality in Transition Metal Chemistry*, John Wiley & Sons, Chichester, 2008. (c) Hawkins, C. J. *Absolute Configuration of Metal Complexes*, Wiley-Interscience, New York, 1971. (d) See also Kauffman, G. B. Alfred Werner's research on optically active coordination compounds. *Coord. Chem. Rev.* **1974**, *12*, 105-149.

(2) (a) Werner, A. Zur Kenntnis des asymmetrischen Kobaltatoms. I. *Chem. Ber.* **1911**, *44*, 1887-1898. V. L. King is listed as an author for the experimental section. (b) Werner, A. Zur Kenntnis des asymmetrischen Kobaltatoms. II. *Chem. Ber.* **1911**, *44*, 2445-2455. (c) Werner, A. Zur Kenntnis des asymmetrischen Kobaltatoms. III. *Chem. Ber.* **1911**, *44*, 3272-3278. (d) Werner, A. Zur Kenntnis des asymmetrischen Kobaltatoms. IV. *Chem. Ber.* **1911**, *44*, 3279-3284. (e) Werner, A. Zur Kenntnis des asymmetrischen Kobaltatoms. V. *Chem. Ber.* **1912**, *45*, 121-130.

(3) (a) Taube, H. Rates and Mechanisms of Substitution in Inorganic Complexes in Solution. *Chem. Rev.* **1952**, *50*, 69-126. (b) Data for $[\text{Co}(\text{en})_3]^{3+}$: Friend J. A.; Nunn, E. K. Substitution reactions in the trisethylenediaminecobalt(III) ion. *J. Chem. Soc.* **1958**, 1567-1571. (c) For an entry level rationale, see Malik, W. U.; Tuli, G. D.; Madan, R. D. *Selected Topics in Inorganic Chemistry*, S. Chand & Company, New Delhi, 2002, chapter 14.

(4) Ganzmann, C.; Gladysz, J. A. Phase Transfer of Enantiopure Werner Cations into Organic Solvents: An Overlooked Family of Chiral Hydrogen Bond Donors for Enantioselective Catalysis. *Chem. Eur. J.* **2008**, *14*, 5397-5400.

(5) (a) Lewis, K. G.; Ghosh, S. K.; Bhuvanesh, N.; Gladysz, J. A. Cobalt(III) Werner Complexes with 1,2-Diphenylethylenediamine Ligands: Readily Available, Inexpensive, and Modular Chiral Hydrogen Bond Donor Catalysts for Enantioselective Organic Synthesis. *ACS Cent. Sci.* **2015**, *1*, 50-56. (b) Ghosh, S. K.; Ganzmann, C.; Bhuvanesh, N.; Gladysz, J. A. Werner Complexes with ω -Dimethylaminoalkyl Substituted Ethylenediamine Ligands: Bifunctional Hydrogen-Bond-Donor Catalysts for Highly Enantioselective Michael Additions. *Angew. Chem. Int. Ed.* **2016**, *55*, 4356-4360; Werner-Komplexe mit ω -Dimethylaminoalkyl-substituierten Ethylendiaminliganden: bifunktionale H-Brückendonor-Katalysatoren für hoch enantioselektive Michael-Additionen. *Angew. Chem.* **2016**, *128*, 4429-4433. (c) Kumar, A.; Ghosh, S. K.; Gladysz, J. A. Tris(1,2-diphenylethylenediamine)cobalt(III) Complexes: Chiral Hydrogen Bond Donor Catalysts for Enantioselective α -Aminations of 1,3-Dicarbonyl Compounds. *Org. Lett.* **2016**, *18*, 760-763.

(6) See also (a) Thomas, C.; Gladysz, J. A. Highly Active Families of Catalysts for the Ring-Opening Polymerization of Lactide: Metal Templated Organic Hydrogen Bond Donors Derived from 2-Guanidinobenzimidazole. *ACS Catalysis*, **2014**, *4*, 1134-1138. (b) Luu, Q.; Gladysz, J. A. An Air- and Water-Stable Hydrogen-Bond-Donor Catalyst for the Enantioselective Generation of Quaternary Carbon Stereocenters by

Additions of Substituted Cyanoacetate Esters to Acetylenic Esters. *Chem. Eur. J.* **2020**, *26*, 10230-10239.

(7) Ghosh, S. K.; Ehnbohm, A.; Lewis, K. G.; Gladysz, J. A. Hydrogen bonding motifs in structurally characterized salts of the tris(ethylenediamine) cobalt trication, $[\text{Co}(\text{en})_3]^{3+}$; An interpretive review, including implications for catalysis. *Coord. Chem. Rev.* **2017**, *350*, 30-48.

(8) Taylor, M. S.; Jacobsen, E. N. Asymmetric Catalysis by Chiral Hydrogen-Bond Donors. *Angew. Chem. Int. Ed.* **2006**, *45*, 1520-1543; Asymmetrische Katalyse durch chirale Wasserstoffbrückendonoren. *Angew. Chem.* **2006**, *118*, 1550-1573. (b) Doyle, A. G.; Jacobsen, E. N. Small-Molecule H-Bond Donors in Asymmetric Catalysis. *Chem. Rev.* **2007**, *107*, 5713-5743. (c) Yu, X.; Wang, W. Hydrogen-Bond-Mediated Asymmetric Catalysis. *Chem. Asian J.* **2008**, *3*, 516-532.

(9) Ghosh, S. K.; Ojeda, A. S.; Guerrero-Leal, J.; Bhuvanesh, N.; Gladysz, and J. A. New Media for Classical Coordination Chemistry: Phase Transfer of Werner and Related Polycations into Highly Nonpolar Fluorous Solvents. *Inorg. Chem.* **2013**, *52*, 9369-9378.

(10) (a) A recent review that is complementary to this one: Liu, Y.; Liu, Y.; Drew, M. G. B. The handedness structure of octahedral metal complexes with chelating ligands. *Coord. Chem. Rev.* **2014**, *260*, 37-64. (b) Y. Saito, in *Topics in Stereochemistry*, ed. E. L. Eliel, N. L. Alinger, 1978, vol. 10, pp. 95-174.

(11) (a) Comuzzi, C.; Melchior, A.; Polese, P.; Portanova, R.; Tolazzi, M. Cobalt(II) Complexes with Nitrogen Donors and Their Dioxygen Affinity in Dimethyl

Sulfoxide. *Eur. J. Inorg. Chem.* **2002**, 2194-2201 (b) Johansson, A.; Wingstrand, E.; Håkansson, M. Towards absolute asymmetric synthesis. Synthesis and crystal structure of stereochemically labile MCl_2 ($M = Co, Ni, Cu, Zn$) complexes with diamine ligands. *Inorg. Chim. Acta*, **2005**, 358, 3293-3302.

(12) (a) Hendry, P.; Ludi, A. A pentuply-bridging carbonyl group: crystal and molecular structure of a salt of the 1-oxo-2-phenyl-1,2-dicarbododecaborate(12) anion, $[LH]^+[O(Ph)C_2B_{10}H_{10}]^-$ ($L = 1,8-N,N,N',N'$ -tetramethylnaphthalenediamine). *J. Chem. Soc. Chem. Commun.* **1987**, 891-892. (b) When a SciFinder search was conducted for the tris(TMEDA) trication $[Co(Me_2NCH_2CH_2NMe_2)_3]^{3+}$, the previous reference was obtained. However, there are no structural or line formulae given in this article, and a key phrase "producing 2,3-methyl-2,3-diaminobutane or tetramethylethylenediamine (*tmen*)" can be construed to mean two separate compounds or the same compound (the title and abstract of the article are ambiguous). As can be inferred from subsequent papers in this series involving other metals, the authors must intend *tmen* to be 2,3-methyl-2,3-diaminobutane, meaning that instead salts of $[Co(NH_2CMe_2CMe_2NH_2)_3]^{3+}$ have been synthesized: Brönnimann, S.; Zilian, A.; Güdel, H. U.; Ludi, A. Absorption and emission spectra of tris(2,3-diamino-2,3-dimethylbutane) Chromium(III). *Inorg. Chim. Acta*, **1990**, 173, 159-162. (c) A SciFinder search for $[Co(NH_2CMe_2CMe_2NH_2)_3]^{3+}$ does not afford ref. [12a](#). However, it does yield a corresponding full paper: Hendry, P.; Ludi, A. Steric Crowding in Coordination

Compounds: Electron-transfer kinetics of the $[\text{Co}(\text{tmen})_3]^{3+/2+}$ couple ($\text{tmen} = 2,3$ -dimethylbutane-2,3-diamine). *Helv. Chim. Acta*, **1988**, *71*, 1966-1970.

(13) (a) Hearson, J. A.; Mason, S. F.; Seal, R. H. Influence of *N*-alkyl substituents in a diamine chelate ring on the optical activity of the $[\text{Co}^{\text{III}}\text{N}_6]$ chromophore. *J. Chem. Soc. Dalton Trans.* **1977**, *10*, 1026-1034. (b) Searle, G. H.; Keene, F. R. Cobalt(III) complexes with *N*-methylethane-1,2-diamine (*meen*). Synthesis and characterization of the isomers of $[\text{Co}(\text{meen})_3]^{3+}$, $[\text{Co}(\text{meen})_2(\text{en})]^{3+}$ and $[\text{Co}(\text{meen})(\text{en})_2]^{3+}$. *Inorg. Chim. Acta* **1989**, *155*, 125-138. (c) Searle, G. H.; Tiekink, E. R. T. Cobalt(III) complexes with *N*-methylethane-1,2-diamine (*meen*). Crystal structures of the stable isomers of $[\text{Co}(\text{meen})_3]^{3+}$ and $[\text{Co}(\text{meen})_2(\text{en})]^{3+}$. *Inorg. Chim. Acta*, **1989**, *156*, 57-63. (d) Atkinson, I. M.; Keene, F. R.; Searle, G. H. Conformational analyses of the isomers of the systems $[\text{Co}(\text{men})_n(\text{en})_{3-n}]^{3+}$ ($\text{men} = N$ -methylethane-1,2-diamine, $\text{en} = \text{ethane-1,2-diamine}$; $n = 1-3$). *J. Chem. Soc. Dalton Trans.* **1991**, *1*, 45-51.

(14) Piper, T. S. PARTIAL CHROMATOGRAPHIC RESOLUTION, ROTATORY DISPERSION, AND ABSOLUTE CONFIGURATION OF OCTAHEDRAL COMPLEXES CONTAINING THREE IDENTICAL BIDENTATE LIGANDS. *J. Am. Chem. Soc.* **1961**, *83*, 3908-3909.

(15) Werner, A. Über Spiegelbildisomerie bei Chromverbindungen. II. *Ber. Dtsch. Chem. Ges.* **1912**, *45*, 865-869.

(16) F. Galsbøl. in *Inorganic Syntheses*, Ed. R. W. Parry, McGraw-Hill, New York, 1970, pp. 269-280.

(17) Werner, A. Über Spiegelbildisomerie bei Rhodium-Verbindungen. I. *Chem. Ber.* **1912**, *45*, 1228-1236.

(18) (a) Werner, A.; Smirnof, A. P. Über optisch-aktive Iridiumverbindungen. *Helv. Chim. Acta*, **1920**, *3*, 472-486. (b) Galsbøl, F.; Rasmussen, B. S. The Preparation, Resolution, and Characterization of Tris(1,2-ethanediamine)iridium(III) Complexes. *Acta Chem. Scand.* **1982**, *A36*, 83-87.

(19) Werner, A. Über Spiegelbildisomerie bei Platinverbindungen I. *Vierteljahresschr. Naturforsch. Ges. Zürich*, **1917**, *62*, 553-564.

(20) Gehman, W. G.; Fernelius, W. C. The mechanism of racemization of the tris(ethylenediamine)cobalt(III) cation. *J. Inorg. Nucl. Chem.* **1957**, *9*, 71-81.

(21) (a) Douglas, B. D. Racemization of Tris-(ethylenediamine)-cobalt(III) Ion in the Presence of Decolorizing Carbon. *J. Am. Chem. Soc.* **1954**, *76*, 1020-1021. (b) For interesting observations regarding differences between types of charcoals and their catalyst lifetimes, see the final paragraph of the Experimental section of ref. [27](#).

(22) (a) Jorge, F. E.; Autschbach, J.; Ziegler, T. On the Origin of Optical Activity in Tris-diamine Complexes of Co(III) and Rh(III): A Simple Model Based on Time-Dependent Density Function Theory. *J. Am. Chem. Soc.* **2005**, *127*, 975-985. (b) Bell, C. F. *Syntheses and Physical Studies of Inorganic Compounds*, Pergamon, New York, 1972, chapter. 22.

(23) Bosnich, B.; Harrowfield MacB. J. Regional rule for the optical activity of conformational isomers of octahedral transition metal complexes. *J. Am. Chem. Soc.* **1972**, *94*, 3425-3437.

(24) Corey, E. J.; Bailer, J. C. Jr. The Stereochemistry of Complex Inorganic Compounds. XXII. Stereospecific Effects in Complex Ions. *J. Am. Chem. Soc.* **1959**, *81*, 2620-2628.

(25) (a) Nomura, T.; Marumo, F.; Saito, Y. The Crystal Structure of (-)-D-Tris(trimethylenediamine)cobalt(III) Bromide Monohydrate. *Bull. Chem. Soc. Jpn.* **1969**, *42*, 1016-1020. (b) Sunatsuki, Y.; Miyahara, S.; Suzuki, T.; Kojima, M.; Nakashima, T.; Matsumoto, N.; Galsbøl, F. Homochiral column structure of *rac*- and Λ -[M^{III}(tn)₃]P₃O₉ (M = Co, Cr; tn = 1,3-diaminopropane; P₃O₉ = cyclotriphosphate(3-)) produced by multiple hydrogen bonds. *New J. Chem.* **2010**, *34*, 2777-2784.

(26) (a) Fujita, J.; Ogino, H. THE ALKYLATION OF 1,3,5-TRITHIANES. *Chem. Lett.* **1974**, *1*, 57-58. (b) Sato, S.; Saito, Y.; Fujita, J.; Ogino, H. The absolute configuration of (+)₅₈₉-tris(1,4-diaminobutane)-cobalt(III) ion, (+)₅₈₉-[Co(tmd)₃]³⁺. *Inorg. Nucl. Chem. Lett.* **1974**, *10*, 669-673.

(27) Harnung, S. E.; Kallesøe, S.; Sargeson, A. M.; Schäffer, C. E. The Tris[(±)-1,2-propanediamine]cobalt(III) System. *Acta Chem. Scand.* **1974**, *A28*, 385-398.

(28) (a) Kojima, M.; Funaki, H.; Yoshikawa, Y.; Yamasaki, K. Isomerism of the Metal Complexes Containing Multidentate Ligands. VI. Geometric and Optical Isomers of the Tris(*meso*-2,3-butanediamine)-cobalt(III) Complex. *Bull. Chem. Soc. Jpn.* **1975**, *48*, 2801-2804. (b) Hilleary, C. J.; Them, T. F.; Tapscott, R. E. Stereochemical Studies on Diastereomers of Tris(2,3-butanediamine)cobalt(III). *Inorg. Chem.* **1980**, *19*, 102-107. (c) Gargallo, M. F.; Lechuga, L.; Puerta, M. C.; González-Vílchez, F.; Vilaplana, R.

Stereoisomerism in coordination chemistry: A laboratory experiment for undergraduate students. *J. Chem. Educ.* **1988**, *65*, 1018-1019.

(29) Harnung, S. E.; Sørensen, B. S.; Creaser, I.; Maegaard, H.; Pfenninger, U.; Schäffer, C. E. The Tris[(±)-*trans*-1,2-cyclohexanediamine]cobalt(III) System. *Inorg. Chem.* **1976**, *15*, 2123-2126.

(30) (a) Toftlund, H.; Laier, T. Geometric and Optical Isomerism in Cobalt(III) and Chromium(III) Tris Complexes of *cis*-1,2-Cyclohexanediamine. *Acta. Chem. Scand.* **1977**, *31*, 651-656. (b) Mizuta, T.; Toshitani, K.; Miyoshi, K. Structural Study of Optical Resolution. XV. Chiral Discrimination of the Facial Isomer of the Tris((*R,S*)-1,2-cyclohexanediamine)cobalt(III) Cation with (*R,R*)-Tartrate Anion. *Bull. Chem. Soc. Jpn.* **1991**, *64*, 1183-1191.

(31) Kuroda, R.; Mason, S. F. Crystal structure and absolute configuration of (+)-tris[(-)-1,2-diphenylethylenediamine]cobalt(III) nitrate monohydrate. *J. Chem. Soc. Dalton Trans.* **1977**, *10*, 1016-1020.

(32) For the isolation of racemic $[\text{Co}((R,S)\text{-dpen})_3]^{3+} 3\text{Cl}^-$, which slowly decomposes in solution, see Kojima, M.; Ishiguro, M.; Fujita, J. Preparation and Properties of Cobalt(III) Complexes Containing *meso*-1,2-Diphenyl-1,2-ethanediamine. *Bull. Chem. Soc. Jpn.* **1978**, *51*, 3651-3652.

(33) Yoshikawa, Y.; Yamasaki, K. Chromatographic resolution of metal complexes on sephadex ion exchangers. *Coord. Chem. Rev.* **1979**, *28*, 205-229. See in particular sections F-v and F-vi.

(34) Dwyer, F. P.; Garvan, F. L.; Shulman, A. Stereospecific Influences in Metal Complexes Containing Optically Active Ligands. Part I. Some of the Optical Isomers of Tris-(propylenediamine)-cobalt(III) Ion. *J. Am. Chem. Soc.* **1959**, *81*, 290-294.

(35) See also (a) Gong, L.; Chen, L.-A.; Meggers, E. Asymmetric Catalysis Mediated by the Ligand Sphere of Octahedral Chiral-at-Metal Complexes. *Angew. Chem. Int. Ed.* **2014**, *53*, 10868-10874; Asymmetrische Katalyse über die Ligandensphäre von oktaedrischen Komplexen mit chiralem Metallzentrum. *Angew. Chem.* **2014**, *126*, 11046-11053. (b) Ma, J.; Ding, X.; Hu, Y.; Huang, Y.; Gong, L.; Meggers, E. Metal-templated chiral Brønsted base organocatalysis. *Nat. Commun.* **2014**, *5*, 4531. (c) Huo, H.; Fu, C.; Wang, C.; Harms, K.; Meggers, E. Metal-templated enantioselective enamine/H-bonding dual activation catalysis. *Chem. Commun.* **2014**, *50*, 10409-10411. (d) Liu, J.; Gong, L.; Meggers, E. Asymmetric Friedel-Crafts alkylation of indoles with 2-nitro-3-arylacrylates catalyzed by a metal-templated hydrogen bonding catalyst. *Tetrahedron Lett.* **2015**, *56*, 4653-4656. (e) Hu, Y.; Zhou, Z.; Gong, L.; Meggers, E. Asymmetric aza-Henry reaction to provide oxindoles with quaternary carbon stereocenter catalyzed by a metal-templated chiral Brønsted base. *Org. Chem. Front.* **2015**, *2*, 968-972.

(36) Maleev, V. I.; North, M.; Larionov, V. A.; Fedyanin, I. V.; Savel'yeva, T. F.; Moscalenko, M. A.; Smolyakov, A. F.; Belokon, Y. N. Chiral Octahedral Complexes of Cobalt(III) as "Organic Catalysts in Disguise" for the Asymmetric Addition of a Glycine Schiff Base Ester to Activated Olefins. *Adv. Synth. Catal.* **2014**, *356*, 1803-1810.

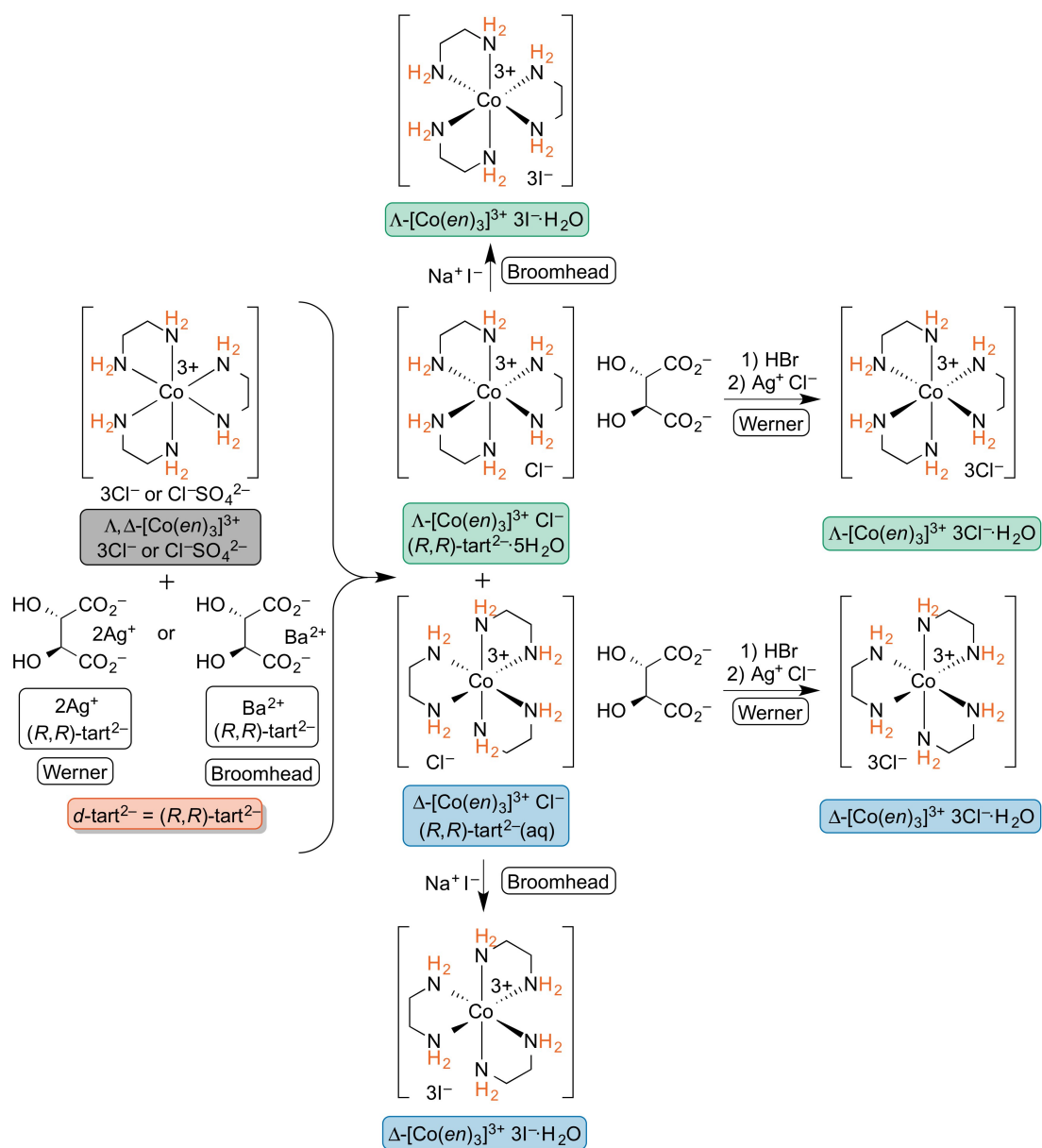
'9. HYDROGEN BONDING MOTIFS IN STRUCTURALLY CHARACTERIZED
SALTS OF THE TRIS (ETHYLENEDIAMINE) COBALT TRICATION, $[\text{Co}(\text{en})_3]^{3+}$;
AN INTERPRETIVE REVIEW, INCLUDING IMPLICATIONS FOR CATALYSIS[†]

9.1. Introduction

The title complexes, Werner salts of the trication $[\text{Co}(\text{en})_3]^{3+}$ (en = ethylenediamine), have always been a classroom favorite.^{1,2} However, until recently the emphasis has been on illustrating well-understood physical phenomena that were established long ago. For example, the trication is chiral, as can easily be appreciated when the non-superimposable mirror images are represented in a "Star of David" motif as shown in Figure 9.1A.³ The descriptors Λ and Δ are used to specify the cobalt configuration. The former indicates a left-handed helix, consistent with the counterclockwise direction that the chelates must take in connecting the front and rear triangles in the left structure (Figure 9.1A). The latter indicates a right-handed helix, with the chelates taking a clockwise direction when connecting the front and rear triangles (right structure). The hydrogen atoms on each NH_2 group are diastereotopic, and are sometimes distinguished as NHH' .

[†] Reprinted from: Hydrogen bonding motifs in structurally characterized salts of the tris(ethylenediamine) cobalt trication, $[\text{Co}(\text{en})_3]^{3+}$; An interpretive review, including implications for catalysis. *Coord. Chem. Rev.* **2017**, 350, 30-48. Copyright 2017, with permission from Elsevier.

Salts of the types $[\text{Co}(\text{en})_3]^{3+} y\text{X}^{z-}$, $[\text{Co}(\text{en})_2(\text{A-A})]^{n+} y\text{X}^{z-}$, and $[\text{Co}(\text{en})_2(\text{A-B})]^{n+} y\text{X}^{z-}$ were the first inorganic compounds to be resolved into enantiomers, as detailed by Werner in a series of five papers in 1911-1912.³ Several recipes have been applied to the trication $[\text{Co}(\text{en})_3]^{3+}$.^{3e,4} The original procedure of Werner began with an aqueous solution of silver (*R,R*)-tartrate ($2\text{Ag}^+ (\text{R,R})\text{-tart}^{2-}$), as shown in Scheme 9.1.^{3e} This led to the diastereomeric mixed chloride/tartrate salts Λ - and Δ - $[\text{Co}(\text{en})_3]^{3+} \text{Cl}^- (\text{R,R})\text{-tart}^{2-}$. The former crystallized as a pentahydrate, and the latter remained in solution. Chloride ion exchange then provided the resolved enantiomers Λ - and Δ - $[\text{Co}(\text{en})_3]^{3+} 3\text{Cl}^-$. Later, Broomhead replaced silver (*R,R*)-tartrate with the less expensive and more stable barium salt ($\text{Ba}^{2+} (\text{R,R})\text{-tart}^{2-}$).^{4a} He also treated the intermediate chloride/tartrate salts with iodide ion, leading to Λ - and Δ - $[\text{Co}(\text{en})_3]^{3+} 3\text{I}^-$. Additional variants, such as with antimony tartrate, have also been described.^{4b} These procedures are so simple and forgiving that they are often used as undergraduate laboratory experiments.



Scheme 9.1 Resolution of the enantiomeric Λ and Δ -[Co(en)₃]³⁺ trications.^{3e,4a}

Despite the chirality of the trication $[\text{Co}(\text{en})_3]^{3+}$, symmetry elements are present. For example, there is a principal C_3 axis that runs perpendicular to the plane of the paper and through the centers of the triangles in Figure 9.1A. This axis is also easily visualized in the wire-frame representations in Figure 9.1C, or the space filling analogs in Figure 9.1D. There are furthermore three C_2 axes in a perpendicular plane, parallel to that of the paper. One C_2 axis is redirected perpendicular to the plane of the paper in Figure 9.1E and Figure 9.1F. Together, the C_3 and three C_2 axes code for the chiral point group D_3 . Importantly, this symmetry requires that the three chelates either (1) be planar (which is not the case for ethylenediamine, but would be applicable to bipy, 1,10-phenanthroline, and related ligands), or (2) have identical non-planar conformations. These issues are parsed in more detail elsewhere,⁵ and the non-planar conformations are analyzed further below. Several recent developments have prompted renewed interest in salts of the trication $[\text{Co}(\text{en})_3]^{3+}$ and related complexes. One has been the realization that the NH bonds associated with coordinated amines are capable of functioning as hydrogen bond donors towards Lewis basic organic substrates.^{6,7} Over the last 20 years, a number of chiral organic hydrogen bond donors have been found to be effective catalysts for a multitude of enantioselective transformations.⁸ The same is proving to be true for Werner complexes and related species.^{7,9-11}

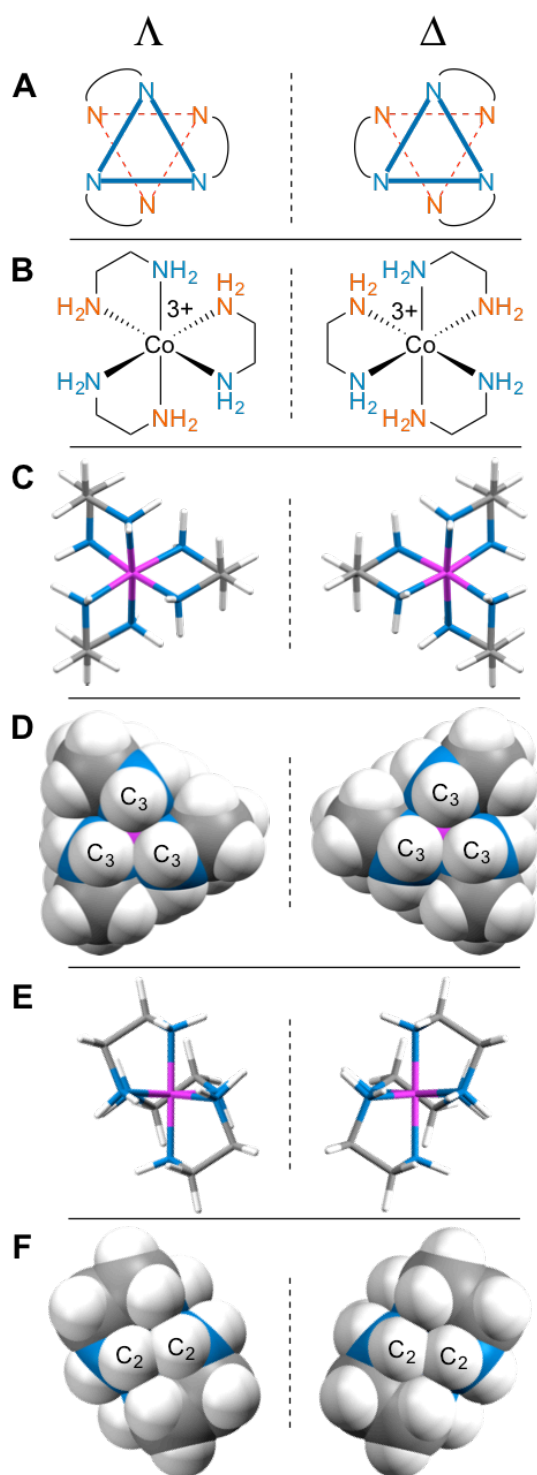


Figure 9.1 Representations of the enantiomeric Λ - and Δ -[Co(en)₃]³⁺ trications.

These results were to some extent foreshadowed by the resolution of enantiomers in Scheme 9.1. It is thought that the relative solubilities of the diastereomeric salts are primarily controlled by the strengths of the trication/tartrate hydrogen bonding interactions (stronger interaction = lower aqueous solubility). Thus, the resolution reflects the thermodynamic binding preference of a given cobalt configuration for a specific tartrate configuration. It has been established crystallographically that for diastereomeric tartrate salts of the tris(*trans*-1,2-cyclohexanediamine) cobalt trication, Λ - and Δ -[Co(*S,S*-*chxn*)₃]³⁺ Cl⁻ (*R,R*)-tart²⁻·2H₂O, the more soluble diastereomer exhibits longer NH···O contacts and a less favorable tartrate conformation.^{12,13}

These investigators also conclude, in line with earlier analyses,¹⁴ that a similar scenario applies with tartrate salts of the tris(ethylenediamine) trication [Co(*en*)₃]³⁺, where there is much crystallographic data.¹⁵ However, here comparisons must be made between diastereomers with different hydration levels and/or counteranions that accompany tartrate, per the mixed chloride and iodide salts in Scheme 9.1 (as well as crystals that contain more than one independent trication).^{15e} Furthermore, some of these analyses involve crystal structures that have never been deposited in publically accessible databases (apparently not an editorial requirement for early papers in *Chem. Lett.*).¹⁶ Hence, certain published conclusions are difficult to independently assess.

Given the increasing numbers of enantioselective reactions catalyzed by tris(1,2-diamine) cobalt(III) species,⁷ we sought to better understand the nature of hydrogen bonding to the [Co(*en*)₃]³⁺ trication. In contrast to the many organic hydrogen bond

donors applied in catalysis, which commonly feature one or two binding sites, $[\text{Co}(\text{en})_3]^{3+}$ contains twelve NH groups. As can be inferred from Figure 9.1, at least three of these, and more likely four or five, can be simultaneously accessed in transition state assemblies. As one approach to systematizing the possibilities, we decided to examine hydrogen bonding in crystalline salts of the formula $[\text{Co}(\text{en})_3]^{3+} y\text{X}^{z-}$ ($y/z = 3/1, 1/3, 1.5/2$), and analogous species with mixed anions. We wondered whether there might be recurring or "conserved" motifs — or rare and presumably disfavored motifs — that could provide guidance.

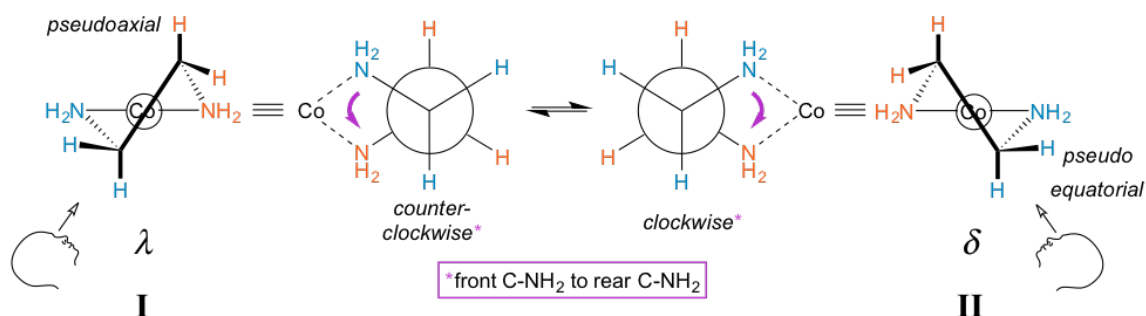


Figure 9.2 Chelate conformations of ethylenediamine.

Indeed, over one hundred fifty crystal structures of such salts have been reported in the literature, and every one, including those with anions that are poor hydrogen bond acceptors, show extensive hydrogen bonding in the solid state. An exhaustive list of structures with references is provided in Table 17.3 in Appendix G and several dozen representative complexes are examined in detail in sections 9.5.2 to 9.5.8 below. Nomenclature for classifying the various modes of hydrogen bonding is formulated. This

effort follows in the conceptual footsteps of Etter, who sought to formulate generalizations involving hydrogen bond patterns in organic molecules and supramolecular assemblies derived therefrom.¹⁷

9.2. Ethylenediamine ligand conformations

In order to thoroughly analyze the hydrogen bonding motifs, certain stereochemical features of ethylenediamine ligands must be briefly reviewed.⁵ With respect to the CH₂CH₂ backbone, a gauche orientation of the two NH₂ groups (torsion angle 60°) would be expected to be much more stable than an eclipsed orientation (torsion angle ca. 0°). Thus, as illustrated by **I** and **II** in Figure 9.2, non-planar chelate rings would be anticipated.

For each Co(en) moiety, two non-superimposable mirror images are possible. These are commonly designated with the lower case Greek letters λ and δ , and correspond to left-handed and right-handed helices, respectively.^{5,18} The counterclockwise and clockwise senses are illustrated with purple arrows in Figure 9.2. Each NH₂ and CH₂ group features one hydrogen atom that is pseudoaxial, and one that is pseudoequatorial. The axial and equatorial atoms rapidly exchange via "ring flips". Thus, the λ and δ conformers will readily equilibrate. However, in the absence of disorder, each chelate will crystallize in one conformation or the other.

Importantly, the conformation of the chelate affects the relative orientations of the CH₂–CH₂ bonds and the symmetry of the [Co(en)₃]³⁺ trication. First, consider the "docking" of three λ ethylenediamine units to give a trication with a Δ configuration at

cobalt. The initial step is shown in Figure 9.3A, and when all three chelates are in place, the structure represented as $\Delta\text{-}\lambda\lambda\lambda$ results. Next, consider the docking of three δ ethylenediamine units to give a trication with the same Δ configuration at cobalt (i.e. an identical spatial orientation of chelating cobalt–nitrogen bonds). The initial step is shown in Figure 9.3B. In order for the cobalt–nitrogen bond locations to "match up", the δ ethylenediamine must first be rotated by 90° . When all three chelates have been similarly put in place, a $\Delta\text{-}\delta\delta\delta$ structure results.

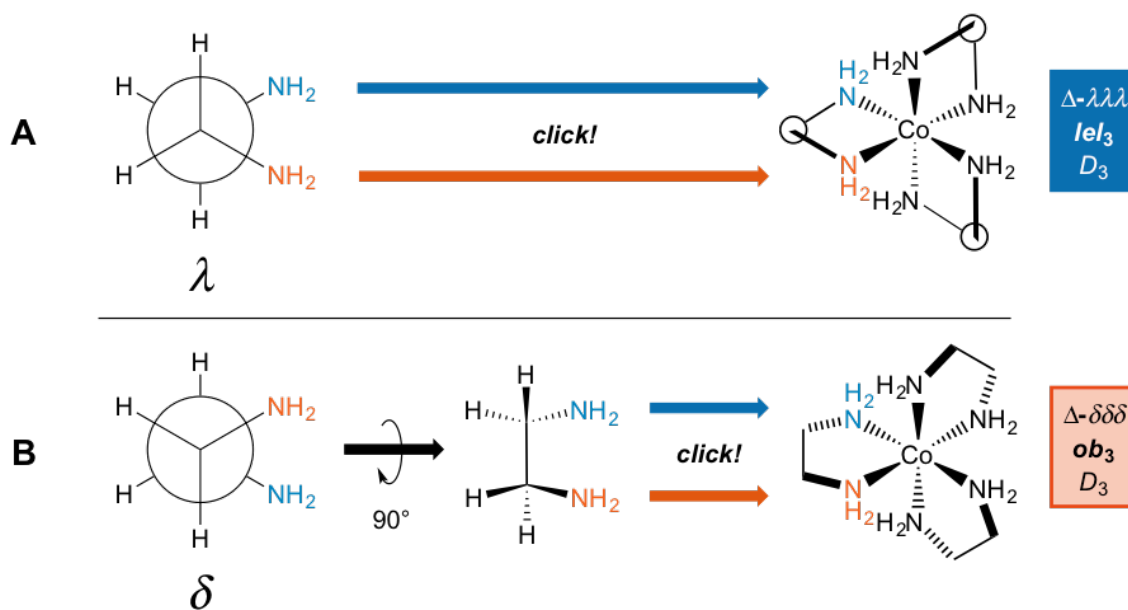


Figure 9.3 Accommodation of ethylenediamine ligands with three λ or three δ conformations in the coordination sphere of an octahedral cobalt atom with a Δ configuration.

In the first or Δ - $\lambda\lambda\lambda$ structure (Figure 9.3A), the λ chelates are said to adopt *lel* orientations, so named because the three CH_2 - CH_2 bonds are parallel to the C_3 symmetry axis.^{5,18} These linkages are often incorporated into Newman type projections, as indicated by hollow circles. In the second or Δ - $\delta\delta\delta$ structure (Figure 9.3B), the δ chelates are said to adopt *ob* orientations, so named because the three CH_2 - CH_2 bonds are oblique to the C_3 axis. The designations Δ - $\lambda\lambda\lambda$ and Δ -*lel*₃ (Figure 9.3A) are both found in the literature, and can be used interchangeably. The same holds for Δ - $\delta\delta\delta$ and Δ -*ob*₃. However, an important caveat follows below.

When the $[\text{Co}(\text{en})_3]^{3+}$ trication has a Δ configuration at cobalt, these relationships are reversed. A λ chelate leads to an *ob* orientation while a δ chelate results in a *lel* orientation. Furthermore, each of the three ethylenediamine ligands can independently adopt either an *ob* or *lel* orientation. Therefore, for a complex with a given cobalt configuration, four diastereomers exist. All possibilities are depicted in Figure 9.4. In contrast, in Figure 9.1 only the *lel*₃ orientations of Λ - and Δ - $[\text{Co}(\text{en})_3]^{3+}$ were depicted. One motivation was to keep the number of structural variables to a minimum in the introduction; another was that, as will be seen below, *lel* chelate orientations dominate in the crystal structures. Indeed, a number of studies point to the *lel*₃ form of each enantiomer being more stable than the *ob*₃ form.^{18,19}

Figure 9.4 also illustrates a "trap" or potential error in identifying enantiomers. Just like the descriptors *R/S* always identify enantiomers of compounds with a single tetrahedral carbon stereocenter, so will the family of descriptors consisting of upper/lower case delta/lambda identify mirror image components of the $[\text{Co}(\text{en})_3]^{3+}$ trication. In other words, Λ - $\lambda\lambda\lambda$ and Δ - $\delta\delta\delta$ stereoisomers can automatically be regarded as *enantiomers*.

However, this is not the case with *lel/ob*. Instead, Λ -*lel*₃ and Δ -*ob*₃ stereoisomers are *diastereomers*, as is easily seen in the upper left and lower right structures in Figure 9.4. Rather, Λ -*lel*₃ and Δ -*lel*₃ would designate enantiomers. Another way to view this is as follows: if the C₃ axis is perpendicular to the plane of the paper, and one enantiomer is reflected in the plane of the paper to give the other, a "parallel" (*lel*) orientation of the CH₂-CH₂ bond with respect to the C₃ axis must be preserved. For these reasons, we generally refer to *lel/ob* as "orientations" or "perspectives".

In practice, the conformations of the ethylenediamine chelate rings rapidly interconvert in solution, and therefore the diastereomeric trications in Figure 9.4 will usually not be distinguishable. However, crystal structures will normally exhibit fixed motifs. It is important to note that the mixed *lel/ob* stereoisomers in Figure 9.4 have C₂ symmetry. Thus, they lack a formal C₃ axis. Nonetheless, a pseudo C₃ axis can be defined. This runs perpendicular to the two unique Star of David triangles that are comprised of one NH₂ group from each of the three chelate rings, and constitutes a useful point of reference in analyses below.

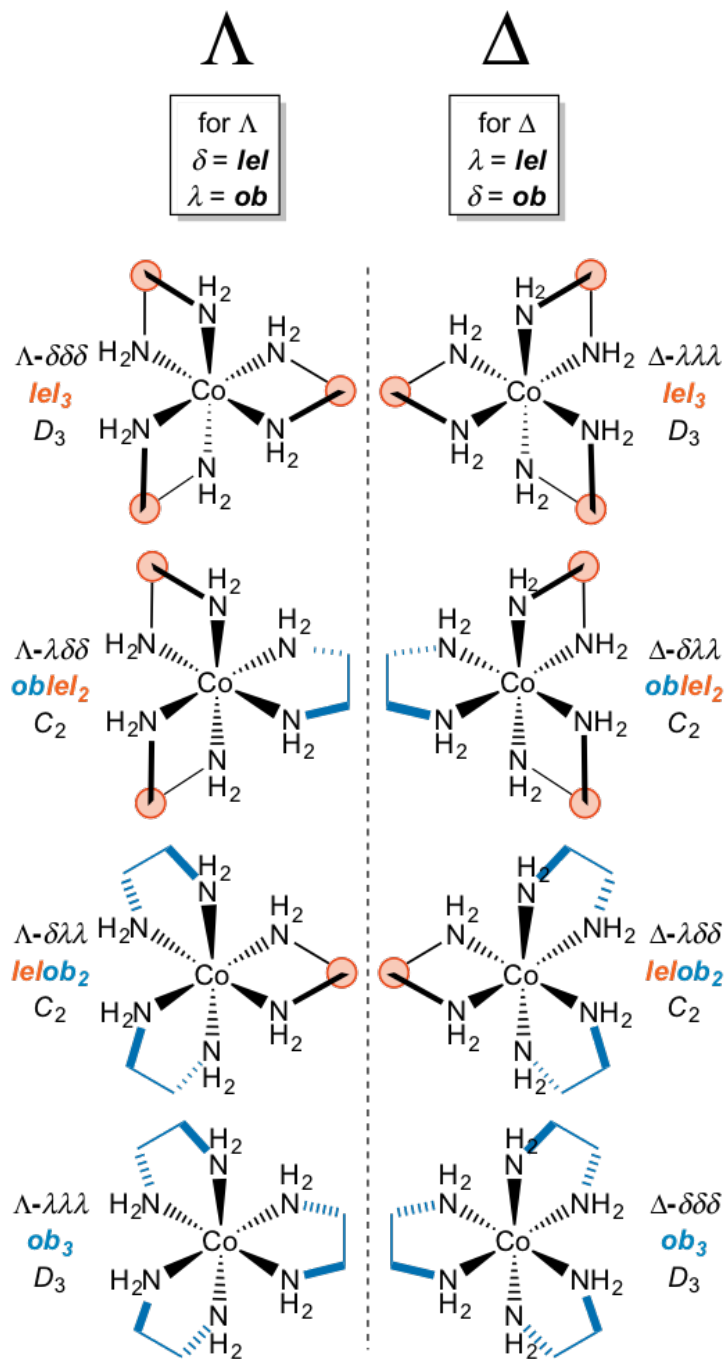


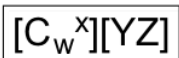
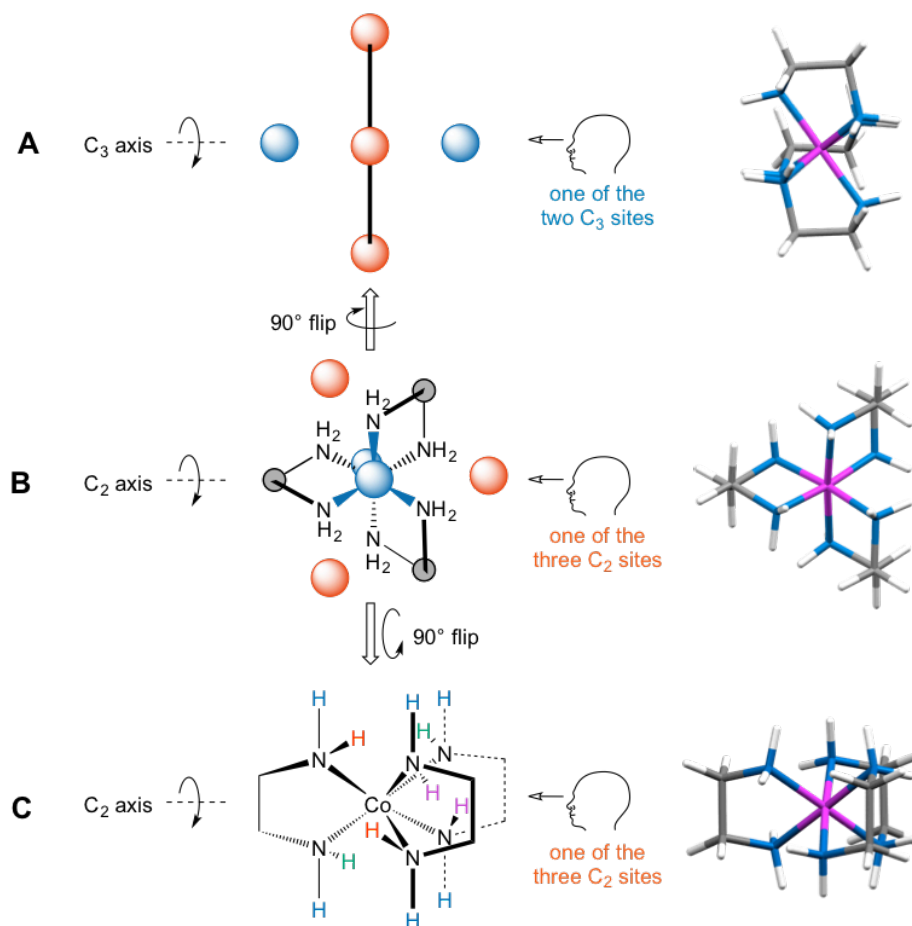
Figure 9.4 All possible stereoisomers of the $[\text{Co}(\text{en})_3]^{3+}$ trication.

9.3. A syntax for hydrogen bonding to the trication $[\text{Co}(\text{en})_3]^{3+}$

Certain views provide instructive starting points for the hydrogen bond classifications that follow. Some are illustrated in Figure 9.5 for $[\text{Co}(\text{en})_3]$ with a Δ - $\lambda\lambda\lambda$ configuration (lel_3 , D_3 symmetry). In Figure 9.5B (middle row), the C_3 symmetry axis is (as usual) perpendicular to the plane of the paper and highlighted with two blue spheres above and below the plane. Three synperiplanar nitrogen–hydrogen bonds, one from each chelate and together defining a C_3 binding site, point in the direction of the blue spheres. These NHH' units (all of which are pro-*S*; they would be pro-*R* in the enantiomer) are also readily visualized in Figure 9.1C,D. The Δ enantiomer in Figure 9.1C, a wire-frame representation, is repeated in Figure 9.5B (right). The three orange spheres in Figure 9.5B "hover" above the C_2 binding sites, each comprised of two nitrogen–hydrogen bonds from different chelates. These NHH' units (all of which are pro-*R*) are also readily visualized in Figure 9.1E,F.

In Figure 9.5A (top row), the structures in Figure 9.5B are rotated 90° about a vertical axis to bring the C_3 axis into the plane of the paper. The second blue sphere associated with C_3 binding sites is now better visible, but in the interest of clarity all the atoms and bonds have been omitted. The wire-frame structures in Figure 9.5B and A provide alternative points of reference. Figure 9.5C (bottom row) depicts a different 90° rotation of Figure 9.5B, now involving a horizontal axis. This nicely highlights each C_3 binding site with three vertically directed synperiplanar N–H bonds. The hydrogen atoms

associated with the C_2 binding sites are color-coded; the symmetry relationship between the two depicted in orange is particularly clear.



W = symmetry label of the N-H hydrogen bond donor (W = 2 or 3)
 X = number of H-bond accepting atoms engaged by a single N-H hydrogen bond donor (default = 1)
 Y = total number of H-bond accepting atoms engaged
 Z = type of atom that is accepting a hydrogen bond (only included if ambiguous)

Figure 9.5 Representations of the C_2 and C_3 binding sites of the Δ - $\lambda\lambda\lambda$ - $[\text{Co}(\text{en})_3]^{3+}$ trication, and a general nomenclature system for hydrogen bonding to an anion or molecule.

9.4. Various types of hydrogen bonding motifs for individual anions (or cocrystallized molecules) are summarized in Appendix G (section G.1 and G.2)

The general formula $[C_W^X][YZ]$ in Figure 9.5 (bottom) and further syntax are provided in Tables 17.1 through 17.3. The terms comprising the formula are defined as follows: (a) C_W denotes the origin of the NH hydrogen bond donor, the C_3 site or C_2 site; (b) X denotes the number of acceptor atoms of the anion that are engaged by the NH hydrogen bond donor (default = 1); (c) Y denotes the number of acceptor atoms of the anion engaged by the NH hydrogen bond donor; (d) Z denotes the type of atom that is accepting the hydrogen bond, which is only included in cases of potential ambiguity, such as with ambident anions. For a given salt, there will be a set of such formulae, as illustrated in the examples that follow.

Thus, when one N–H unit of a C_2 site binds to an anion X^- at a single acceptor atom, the representation $[C_2][1]$ is employed. For a corresponding interaction at a C_3 site, the representation $[C_3][1]$ is employed. When the same anion binds two or more N–H units via a single atom, representations such as $[C_2,C_2][1]$, $[C_3,C_3][1]$, and $[C_3,C_3,C_3][1]$ are employed. When such binding involves two distinct but like atoms of the anion, representations such as $[C_2,C_2][2]$ and $[C_3,C_3][2]$ may apply. When binding involves three distinct but like atoms of the anion, the representation $[C_3,C_3,C_3][3]$ may apply.

Of course, each like atom of an anion could make more than one hydrogen bond. Thus, there are additional manifolds of motifs along the lines of $[C_2^2, C_2][2]$ (three hydrogen bonds between two N–H units of a C_2 site and two like atoms of anion) or $[C_3^2, C_3^2, C_3][2]$ (five hydrogen bonds between three N–H units of a C_3 site and two like atoms of an anion). A reader who would like to see these relationships developed in a more systematic as opposed to intuitive way should consult Table 17.1 and Table 17.3 in Appendix G. The latter includes graphical representations.

It should also be possible for anions to hydrogen bond to both C_2 and C_3 sites. Complementary views of the three most likely motifs are depicted in Figure 9.6. First, the C_2 and C_3 N–H units can be on the same ethylenediamine ligand. The most easily conceptualized possibility involves the same NH_2 group, as shown in Figure 9.6A. In structures with crystallographic D_3 symmetry (*vide infra*), this $H\cdots H$ distance is typically 1.46 Å.²⁰ Alternatively, hydrogen bonding could involve a pseudoequatorial C_3 N–H unit of one NH_2 group, and a pseudoaxial C_2 N–H unit of the other (Figure 9.6B). In structures with crystallographic D_3 symmetry, this $H\cdots H$ distance is typically 3.73 Å.^{20b} This is much longer than in the preceding example, but the atoms can easily be bridged by delocalized multidentate anions.

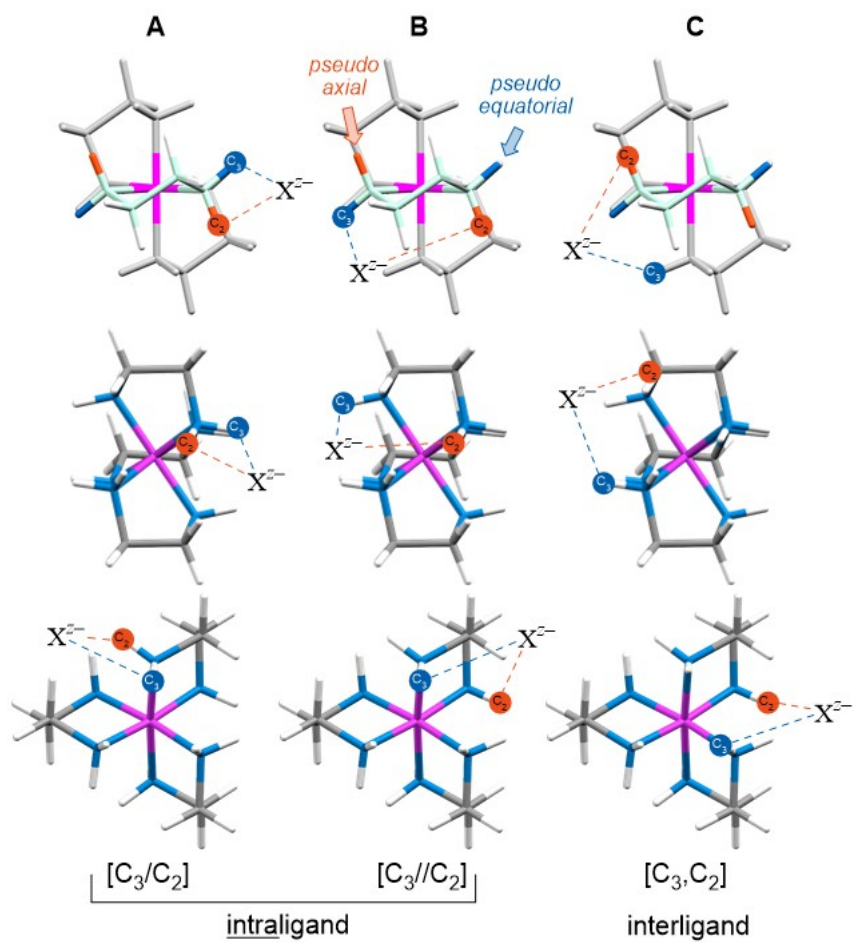


Figure 9.6 Anion binding modes involving hydrogen bonding to both the C_2 and C_3 sites of the Δ - $\lambda\lambda\lambda$ - $[\text{Co}(\text{en})_3]^{3+}$ trication.

As shown in Figure 9.6C, the C₂ and C₃ N–H units can also be on different ethylenediamine ligands. In structures with crystallographic D₃ symmetry, this H···H distance is typically 2.95 Å.^{20b} With regard to nomenclature, these motifs are designated as summarized in Figure 9.6. The binding sites are separated by commas for the *interligand* case ([C₃,C₂]), and one or two slashes for the *intra*ligand cases ([C₃/C₂] for the shorter contact in Figure 9.6A; [C₃//C₂] for the longer contact in Figure 9.6B).²¹

Some illustrative examples are presented in Figure 9.7 using the enantiomer of a nitrate salt analyzed below. In Figure 9.7A–C, the nitrate anion occupies a position near the blue sphere in Figure 9.5B — i.e. in the vicinity of the C₃ site, but not symmetrically arrayed. In Figure 9.7A, one oxygen atom of the nitrate anion is bound to one N–H unit of the C₃ site, and is thus designated [C₃][1]. In Figure 9.7B, one oxygen atom binds to the same N–H unit of the C₃ site, and the same oxygen atom as well as a second one binds to a different N–H unit of the C₃ site. This motif is designated [C₃²,C₃][2].

In Figure 9.7C, one oxygen atom is bound to all three N–H units of the C₃ site. A second oxygen atom binds to one. This might have been designated [C₃²,C₃,C₃][2]. However, this would also be consistent with an alternative motif in which the two oxygen atoms each make two hydrogen bonds. Therefore it is designated [C₃²,C₃,C₃][1,3:2], with the alternative motif then being [C₃²,C₃,C₃][2,2:2]. The first two integers in the second square bracket represent the numbers of hydrogen bonds to each oxygen atom.

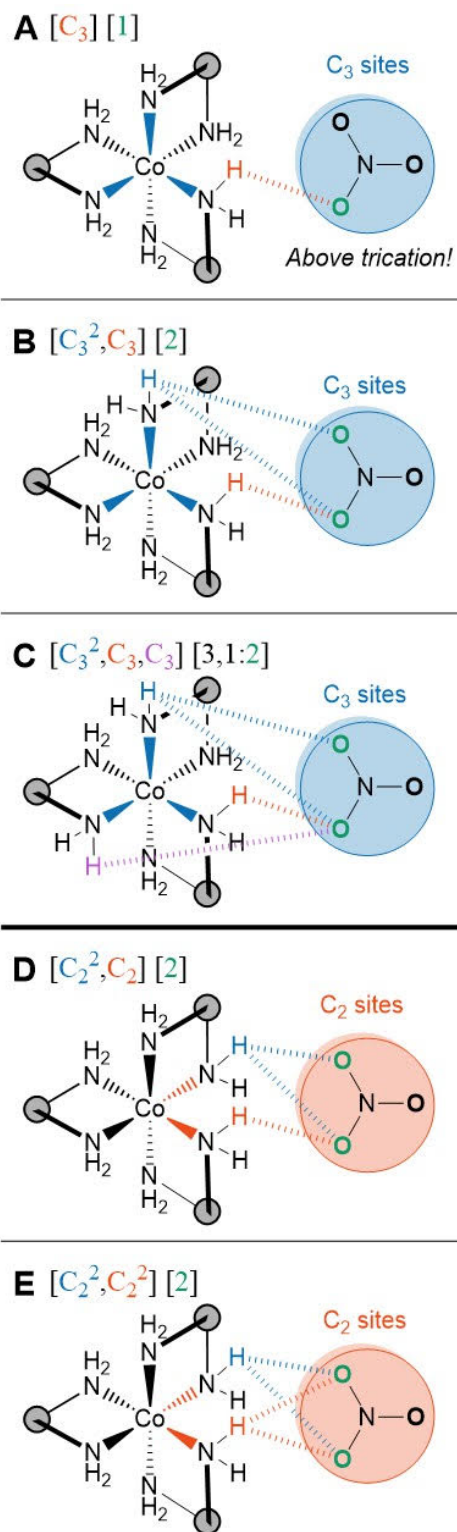


Figure 9.7 Representative hydrogen bonding motifs for the Δ - $\lambda\lambda\lambda$ - $[\text{Co}(\text{en})_3]^{3+}$ trication (Iel_3, D_3) and the nitrate anion.

9.5. Overview of crystallographically characterized salts of the trication $[\text{Co}(\text{en})_3]^{3+}$

9.5.1. General procedures and comments

The data in Table 17.3 in Appendix G summarizes the 150 unique crystal structures containing the trication $[\text{Co}(\text{en})_3]^{3+}$ that have been deposited in the Cambridge Structural Database (CSD). There are furthermore nineteen duplicate crystal structures, as listed in Table 17.4 (Appendix G). Of the 150, six are lacking atomic coordinates, and in two the trication is severely disordered. Hence, 142 $[\text{Co}(\text{en})_3]^{3+}$ salts are amenable to detailed analyses, and a few more to partial analyses. The 27 structures in the following sections 9.5.2 to 9.5.8 are representative. They are arranged in order of increasing charge and/or complexity of the counter anions.

All anions as well as cocrystallized water molecules that hydrogen bond to a given trication are considered. In many cases, these species also hydrogen bond to adjacent trications. However, these are not enumerated. Rather, the priority is to visualize all second coordination sphere interactions about a single trication.

For determining the presence or absence of hydrogen bonds, the default parameters in the program Mercury have been employed.²² These take into account the van der Waals radius of the acceptor atom,²³ so different atoms have different cutoff distances. Since hydrogen bonding is not an "all or nothing" property, the cutoff distances in the structures in sections 9.5.2 to 9.5.8 were increased by 5%. No additional hydrogen bonds were revealed.

Some of the crystal structures in sections 9.5.2 to 9.5.8 were determined using enantiopure Λ -[Co(en)₃]³⁺ salts, and others using racemates. In the latter cases, only the Λ enantiomers have been depicted. Crystal structures of enantiopure Δ -[Co(en)₃]³⁺ salts have also been determined, but these are less common (reflecting the manner that the resolution in Scheme 9.1 is most often applied). Only one example is presented in the text (4.7.2), and the Λ/Δ ratio in Table 17.3 (Appendix G) is 32:12 (21% and 8% of all structurally characterized [Co(en)₃]³⁺ salts).

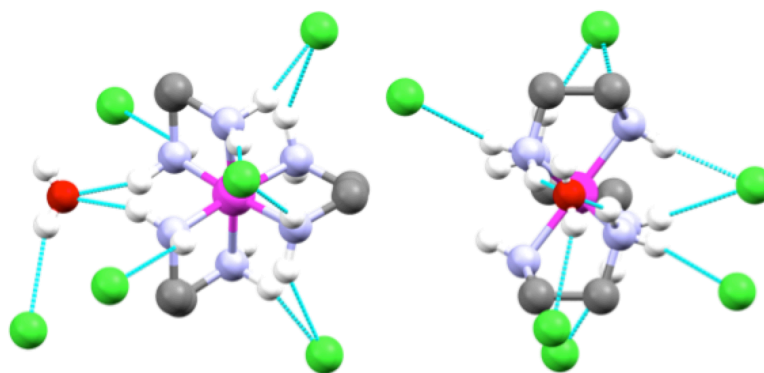
For all structures, two views are given. One is always labeled as along the C₃ axis, even though the idealized C₃ axes evident in Figure 9.1A-D translate in only a few cases to crystallographic C₃ axes (for mixed *lellob* systems, this is denoted as a pseudo C₃ axis; *vide supra*). The other is a view down one of the three C₂ axes (or for mixed *lellob* systems, the only C₂ axis). Again, in only a few cases do these correspond to crystallographic C₂ axes.

9.5.2. Salts with three monoanions (point charge)

Note that for cases in which the anion can be approximated as a point charge, the generalized hydrogen bonding nomenclature [C_W^X][YZ] (Figure 9.5) will reduce to [C_W^X][1].

9.5.2.1. Λ - $\delta\delta\delta$ -[Co(en)₃]³⁺ 3Cl⁻·H₂O (*lel*₃)

The structure and hydrogen bonding interactions of the enantiopure monohydrated trichloride salt, Λ - $\delta\delta\delta$ -[Co(en)₃]³⁺ 3Cl⁻·H₂O (*lel*₃), are shown in Figure 9.8.²⁴ Each trication forms hydrogen bonds with six Cl⁻ anions and one H₂O molecule. All twelve N–H units are engaged in hydrogen bonding. There is a crystallographic C₂ axis corresponding to one idealized C₂ axis of the trication (right view). The two N–H units of two C₂ sites exhibit a single hydrogen bond to a chelating Cl⁻ anion. Those of the third C₂ site exhibit a single hydrogen bond to a chelating H₂O molecule. Each N–H unit of each C₃ site exhibits one hydrogen bond to either a chelating or non-chelating Cl⁻ anion.



H-bond acceptor	type of H-bond	number of similar interactions
Cl ⁻	[C ₃][1]	2
Cl ⁻	[C ₂ ,C ₂][1]	2
Cl ⁻	[C ₃ ,C ₃][1]	2
H ₂ O	[C ₂ ,C ₂][1]	1

Figure 9.8 Hydrogen bonding interactions in Λ - $\delta\delta\delta$ -[Co(en)₃]³⁺ 3Cl⁻·H₂O (*lel*₃) viewed along the C₃ axis (left) and a C₂ axis (right).

9.5.2.2. Λ - $\delta\delta\delta$ -[Co(en)₃]³⁺ 3Cl⁻·2.8H₂O (*lel*₃)

The structure and hydrogen bonding interactions of the polyhydrated trichloride salt Λ - $\delta\delta\delta$ -[Co(en)₃]³⁺ 3Cl⁻·2.8H₂O (*lel*₃) are shown in Figure 9.8.²⁵ This represents one of the two enantiomers in the crystallographically characterized racemate. There is a crystallographic C₃ axis corresponding to the idealized C₃ axis of the trication, and three crystallographic C₂ axes that do not pass through a trication. All twelve N–H units engage in hydrogen bonding to nine Cl⁻ anions. The two N–H units of all three C₂ sites exhibit a single hydrogen bond to a chelating Cl⁻ anion. Each N–H unit of one C₃ site exhibits a single hydrogen bond to a non-chelating Cl⁻ anion, and each N–H unit of the other C₃ site exhibits two hydrogen bonds to two chelating Cl⁻ anions.

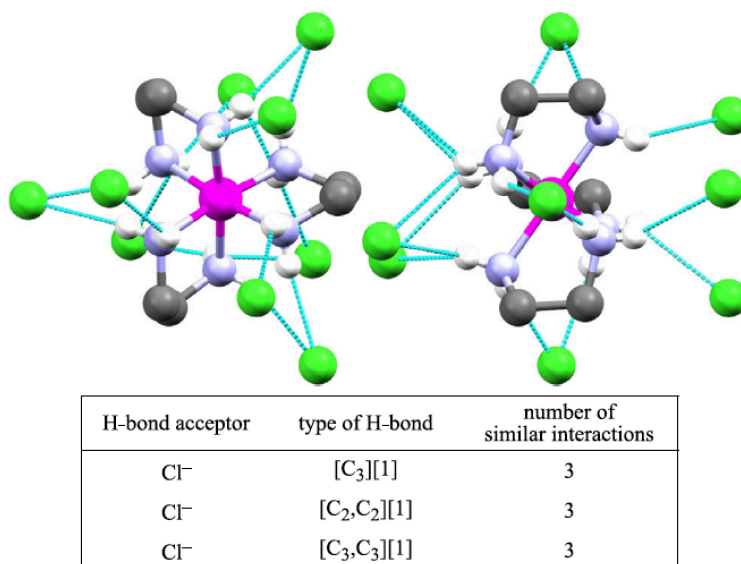


Figure 9.9 Hydrogen bonding interactions in Λ - $\delta\delta\delta$ -[Co(en)₃]³⁺ 3Cl⁻·2.8H₂O (*lel*₃) viewed along the C₃ axis (left) and a C₂ axis (right).

9.5.2.3. Λ - $\delta\delta\delta$ -[Co(en)₃]³⁺ 3Cl⁻ (*le*₃)

The structure and hydrogen bonding interactions of Λ - $\delta\delta\delta$ -[Co(en)₃]³⁺ 3Cl⁻ (*le*₃) are shown in Figure 9.10.²⁶ This represents one of the two enantiomers in the crystallographically characterized racemate. There is a crystallographic C₃ axis corresponding to the idealized C₃ axis of the trication, and three crystallographic C₂ axes that do not pass through a trication. All twelve N–H units are engaged in hydrogen bonding with nine Cl⁻ anions. The pattern is quite close to that of the previous structure (a polyhydrate), except that now each N–H unit of both C₃ sites exhibits two hydrogen bonds to two chelating Cl⁻ anions.

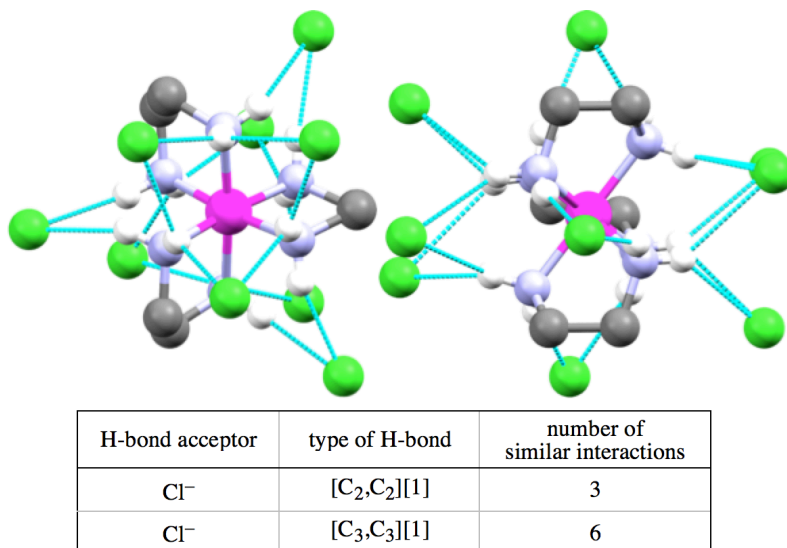


Figure 9.10 Hydrogen bonding interactions in Λ - $\delta\delta\delta$ -[Co(en)₃]³⁺ 3Cl⁻ (*le*₃) viewed along the C₃ axis (left) and a C₂ axis (right).

9.5.2.4. Λ - $\delta\delta\delta$ -[Co(en)₃]³⁺ 3Br⁻·H₂O (*lel*₃)

The structure and hydrogen bonding interactions of the enantiopure monohydrated bromide salt, Λ - $\delta\delta\delta$ -[Co(en)₃]³⁺ 3Br⁻·H₂O (*lel*₃), are shown in Figure 9.11.²⁷ All twelve N–H units engage in hydrogen bonding to four Br⁻ anions and one H₂O molecule. There is a crystallographic C₂ axis corresponding to one idealized C₂ axis of the trication (right view). The three N–H units of each C₃ site form a single hydrogen bond to a triply bridging Br⁻ anion. The two N–H units of two C₂ sites exhibit a single hydrogen bond to a chelating Br⁻ anion. Those of the third C₂ site exhibit a single hydrogen bond to a chelating H₂O molecule.

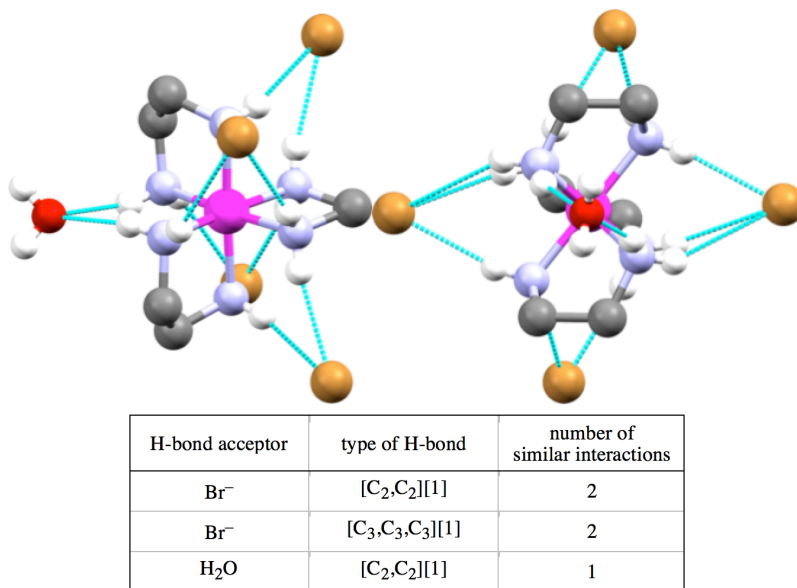
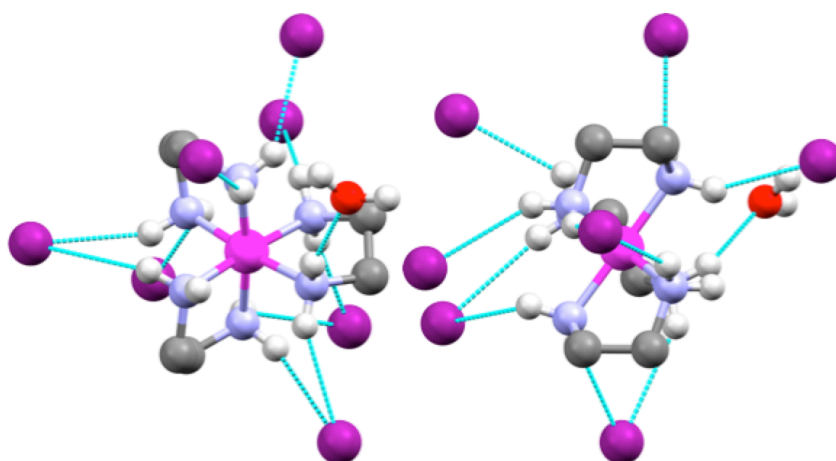


Figure 9.11 Hydrogen bonding interactions in Λ - $\delta\delta\delta$ -[Co(en)₃]³⁺ 3Br⁻·H₂O (*lel*₃) viewed along the C₃ axis (left) and a C₂ axis (right).

9.5.2.5. Λ - $\lambda\delta\delta$ -[Co(en)₃]³⁺ 3I⁻·H₂O (*oblel*₂)

The structure and hydrogen bonding interactions of the enantiopure monohydrated iodide salt, Λ - $\lambda\delta\delta$ -[Co(en)₃]³⁺ 3I⁻·H₂O (*oblel*₂), are shown in Figure 9.12.²⁸ Although one might have thought that this complex would be isostructural with the preceding tribromide salt, it crystallizes instead in an *oblel*₂ orientation — i.e. with one chelate in an *ob* as opposed to a *lel* conformation. Despite the lower symmetry, a pseudo C₃ reference axis remains (*vide supra*).

The trication forms hydrogen bonds to seven I⁻ anions and one H₂O molecule. In contrast to the preceding halide salts, only eleven N–H units are engaged in hydrogen bonding; one C₃ N–H unit remains free. Some of the I⁻ anions are singly hydrogen bonded, and others doubly; no pattern is apparent. The H₂O molecule is engaged by one C₃ N–H unit.



H-bond acceptor	type of H-bond	number of similar interactions
I ⁻	[C ₂][1]	2
I ⁻	[C ₂ ,C ₂][1]	2
I ⁻	[C ₃][1]	2
I ⁻	[C ₃ ,C ₃][1]	1
H ₂ O	[C ₃][1]	1

Figure 9.12 Hydrogen bonding interactions in Λ - $\delta\delta\delta$ -[Co(en)₃]³⁺ 3I⁻·H₂O (*obel*₃) viewed along the pseudo C₃ axis (left) and a C₂ axis (right).

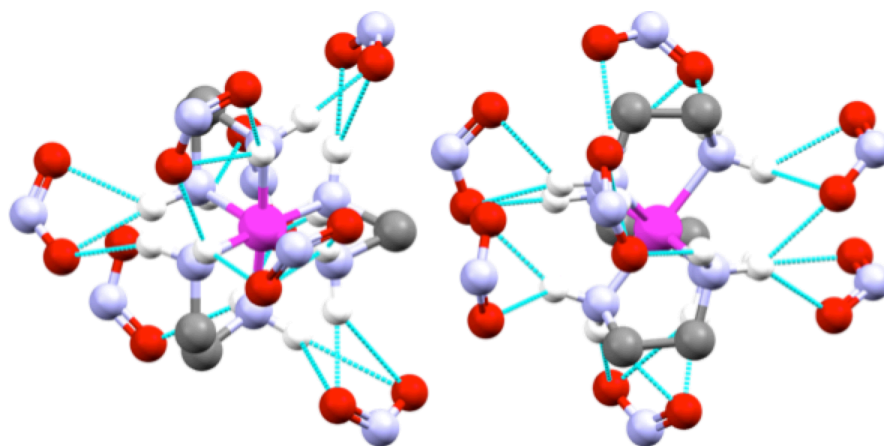
9.5.3. Salts with three monoanions (delocalized)

Now possibilities for the hydrogen bonding nomenclature [C_W^X][YZ] (Figure 9.5) include [C_W^X][1Z] and [C_W^X][2Z] (and potentially but also much less frequently higher values of Y).

9.5.3.1. Λ - $\delta\delta\delta$ -[Co(en)₃]³⁺ 3NO₃⁻ (*lel*₃)

The structure and hydrogen bonding interactions of the enantiopure nitrate salt, Λ - $\delta\delta\delta$ -[Co(en)₃]³⁺ 3NO₃⁻ (*lel*₃), are shown in Figure 9.13.²⁹ All twelve N–H units are engaged in hydrogen bonding to seven NO₃⁻ anions. Most of these interactions were depicted in Figure 9.7. At one C₃ site, two oxygen atoms from each of two NO₃⁻ anions

exhibit a total of six hydrogen bonds to the three N–H units. At the other, two oxygen atoms of one NO_3^- anion exhibit four hydrogen bonds to the three N–H units, and one oxygen atom of another exhibits a single hydrogen bond to one N–H unit. At each C_2 site, two oxygen atoms of a NO_3^- anion bind to both N–H units, either by three or four hydrogen bonds.

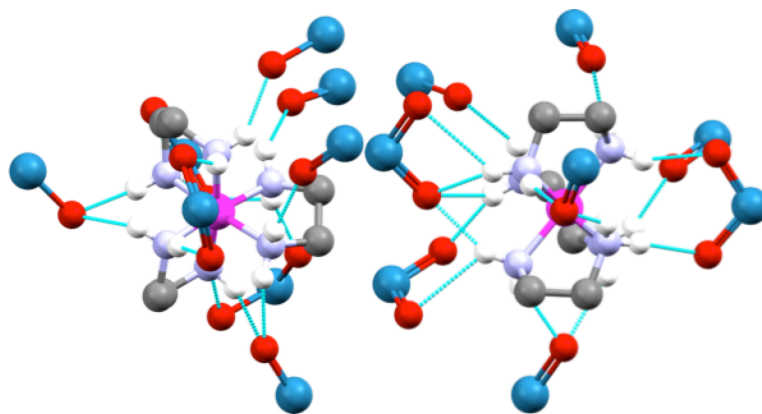


H-bond acceptor	type of H-bond	number of similar interactions
NO_3^-	$[\text{C}_2^2, \text{C}_2][2]$	2
NO_3^-	$[\text{C}_2^2, \text{C}_2^2][2]$	1
NO_3^-	$[\text{C}_3][1]$	1
NO_3^-	$[\text{C}_3^2, \text{C}_3][2]$	2
NO_3^-	$[\text{C}_3^2, \text{C}_3, \text{C}_3][3, 1:2]$	1

Figure 9.13 Hydrogen bonding interactions in $\Lambda\text{-}\delta\delta\delta\text{-}[\text{Co}(\text{en})_3]^{3+} 3\text{NO}_3^- (\text{lel}_3)$ viewed along the C_3 axis (left) and a C_2 axis (right). The distal oxygen atoms of the NO_3^- anions have been omitted for clarity.

9.5.3.2. Λ - $\lambda\delta\delta$ -[Co(en)₃]³⁺ 3ReO₄⁻ (*oblel*₂)

The structure and hydrogen bonding interactions of the enantiopure perrhenate salt, Λ - $\lambda\delta\delta$ -[Co(en)₃]³⁺ 3ReO₄⁻ (*oblel*₂), are shown in Figure 9.14.³⁰ As with the salt in section 9.5.2.5, the complex crystallizes in an *oblel*₂ orientation. All twelve N–H units are engaged in hydrogen bonding to eight ReO₄⁻ anions. The six C₂ N–H units are singly hydrogen bonded to the oxygen atoms of four ReO₄⁻ anions (two chelating, two non chelating). Each C₃ site interacts with two ReO₄⁻ anions, one of which chelates two N–H units via a O–Re–O linkage. The remaining ReO₄⁻ anion is either singly hydrogen bonded to the third N–H unit, or quadruply hydrogen bonded to all three N–H units via a O–Re–O linkage.

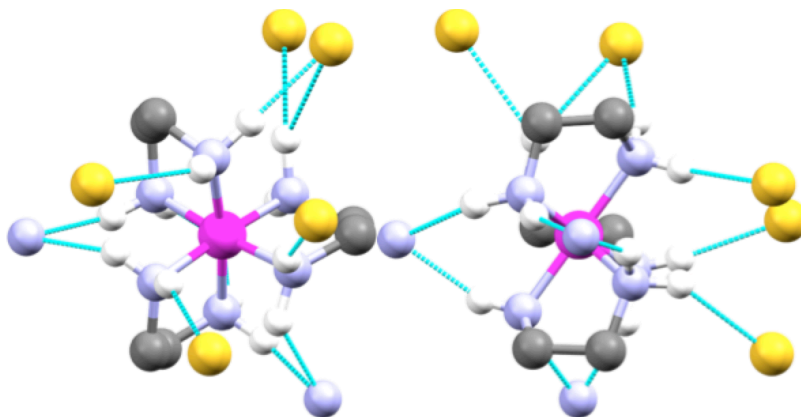


H-bond acceptor	type of H-bond	number of similar interactions
ReO ₄ ⁻	[C ₂][1]	2
ReO ₄ ⁻	[C ₂ ,C ₂][1]	2
ReO ₄ ⁻	[C ₃][1]	1
ReO ₄ ⁻	[C ₃ ,C ₃][2]	2
ReO ₄ ⁻	[C ₃ ² ,C ₃ ,C ₃][3,1:2]	1

Figure 9.14 Hydrogen bonding interactions in the Λ - $\lambda\delta\delta$ -[Co(en)₃]³⁺ 3ReO₄⁻ (*oblel*₂) viewed along the pseudo C₃ axis (left) and the C₂ axis (right). Non-interacting oxygen atoms of the ReO₄⁻ anions have been omitted for clarity.

9.5.3.3. Λ - $\delta\delta\delta$ -[Co(en)₃]³⁺ 3SCN⁻ (*le*₃)

The structure and hydrogen bonding interactions of the thiocyanate salt, Λ - $\delta\delta\delta$ -[Co(en)₃]³⁺ 3SCN⁻ (*le*₃) are shown in Figure 9.15.³¹ This represents one of the two enantiomers in the crystallographically characterized racemate. All twelve N–H units are engaged in hydrogen bonding to eight SCN⁻ anions. At one C₃ site, the nitrogen atom of a single SCN⁻ anion hydrogen bonds to all three N–H units. At the other C₃ site, the sulfur atoms of three SCN⁻ anions each hydrogen bond to one of the three N–H units. At two C₂ sites, a nitrogen atom of a SCN⁻ anion chelates the N–H units. At the third C₂ site, the sulfur atom of a SCN⁻ anion chelates the NH units, and the sulfur atom of a second SCN⁻ anion hydrogen bonds a single N–H unit.



H-bond acceptor	type of H-bond	number of similar interactions
SCN ⁻	[C ₂][1S]	1
SCN ⁻	[C ₂ ,C ₂][1N]	2
SCN ⁻	[C ₂ ,C ₂][1S]	1
SCN ⁻	[C ₃][1S]	3
SCN ⁻	[C ₃ ,C ₃ ,C ₃][1N]	1

Figure 9.15 Hydrogen bonding interactions in the Λ - $\delta\delta\delta$ -[Co(en)₃]³⁺ 3SCN⁻ (*le*₃) viewed along the C₃ axis (left) and the C₂ axis (right). Non-coordinating atoms of the anions have been omitted for clarity.

9.5.4. Salts with three monoanions (two types)

9.5.4.1. Λ - $\delta\delta\delta$ -[Co(en)₃]³⁺ Cl⁻2I⁻·H₂O (*le*₃)

The structure and hydrogen bonding interactions of the mixed chloride/diiodide salt, Λ - $\delta\delta\delta$ -[Co(en)₃]³⁺ Cl⁻2I⁻·H₂O (*le*₃) are shown in Figure 9.16.³² This represents one of the two enantiomers in the crystallographically characterized racemate. All twelve N–H units are engaged in hydrogen bonding to six I⁻ anions and three Cl⁻ anions. At one C₃ site, all three N–H units are doubly hydrogen bonded to one of three Cl⁻ anions. On the opposite C₃ site, all three N–H units are doubly hydrogen bonded to one of three I⁻ anions. The former motif was seen in the trichloride salts in 9.5.2.2 and 9.5.2.3, but the latter was not seen in the triiodide salt in 9.5.2.5. The two N–H units of each C₂ site chelate to a single I⁻ anion.

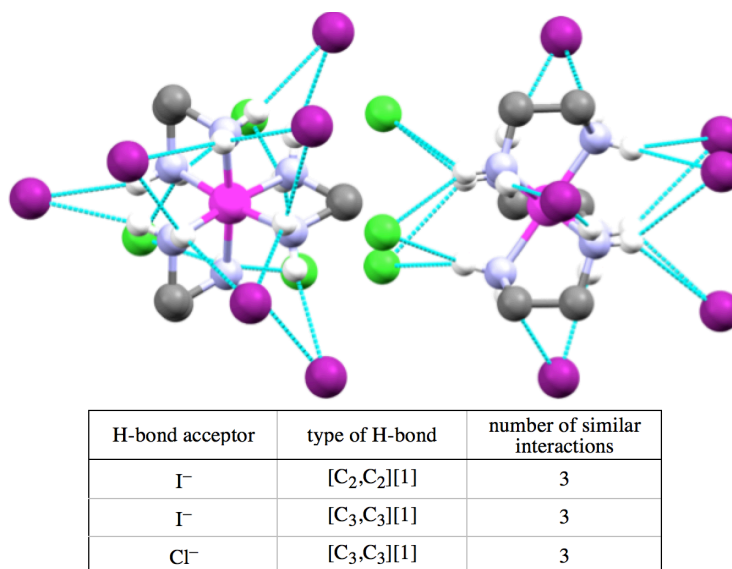
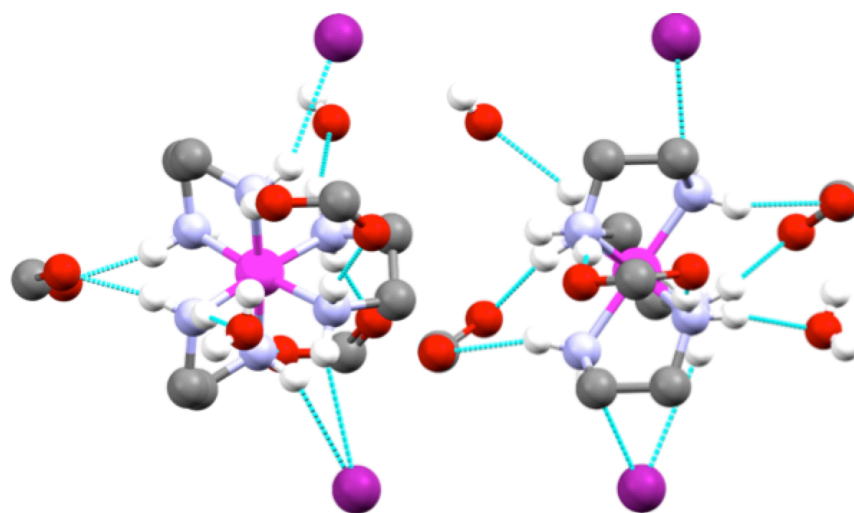


Figure 9.16 Hydrogen bonding interactions in the Λ - $\delta\delta\delta$ -[Co(en)₃]³⁺ Cl⁻2I⁻·H₂O (*le*₃) viewed along the C₃ axis (left) and the C₂ axis (right).

9.5.5. Salts with two anions (one monoanion and one dianion)

9.5.5.1. Λ - $\lambda\delta\delta$ -[Co(en)₃]³⁺ I⁻CO₃²⁻·4H₂O (*oblel*₂)

The structure and hydrogen bonding interactions of the tetrahydrated mixed iodide/carbonate salt, Λ - $\lambda\delta\delta$ -[Co(en)₃]³⁺ I⁻CO₃²⁻·4H₂O (*oblel*₂), are shown in Figure 9.17.³³ This represents one of the two enantiomers in the crystallographically characterized racemate. As with 9.5.2.5 and 9.5.3.2, the complex crystallizes in an *oblel*₂ orientation. Eleven of the twelve N–H units are engaged in hydrogen bonding to three CO₃²⁻ dianions, two I⁻ anions, and two H₂O molecules. At both C₃ sites, two N–H units bind to separate oxygen atoms of a CO₃²⁻ dianion. The third N–H unit binds to a H₂O molecule. Each of the C₂ sites engage in different hydrogen bonding motifs. In one, the two N–H units chelate to single I⁻ anion. In the second, the N–H units are chelated by a OCO linkage of a CO₃²⁻ dianion. In the third, the N–H units separately bind to an I⁻ anion and a H₂O molecule.

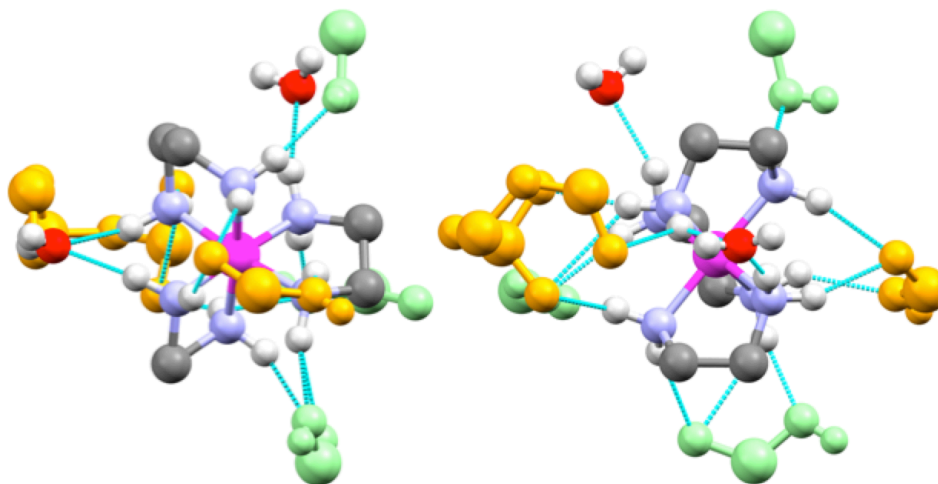


H-bond acceptor	type of H-bond	number of similar interactions
I ⁻	[C ₂][1]	1
I ⁻	[C ₂ ,C ₂][1]	1
CO ₃ ²⁻	[C ₂ ,C ₂][2]	1
CO ₃ ²⁻	[C ₃ ,C ₃][2]	2
H ₂ O	[C ₃][1]	2

Figure 9.17 Hydrogen bonding interactions in the Λ - $\lambda\delta\delta$ -[Co(en)₃]³⁺ I⁻CO₃²⁻·4H₂O (*oblel*₂) viewed along the pseudo C₃ axis (left) and the C₂ axis (right). One non-interacting oxygen atom of each carbonate anion has been omitted for clarity.

9.5.5.2. Λ - $\lambda\delta\delta$ -[Co(en)₃]³⁺ B₅O₆(OH)₄⁻ B₈O₁₀(OH)₆²⁻·5H₂O (*oblel*₂)

The structure and hydrogen bonding interactions of the pentahydrated bis(borate) salt, Λ - $\lambda\delta\delta$ -[Co(en)₃]³⁺ B₅O₆(OH)₄⁻ B₈O₁₀(OH)₆²⁻·5H₂O (*oblel*₂) are shown in Figure 9.18.³⁴ This represents one of the two enantiomers in the crystallographically characterized racemate. As with 9.5.2.5 and 9.5.3.2, and 9.5.5.1, the complex crystallizes in an *oblel*₂ orientation. All twelve N–H units are engaged in hydrogen bonding to two octaboron dianions and three pentaboron monoanions.



H-bond acceptor	type of H-bond	number of similar interactions
$B_5O_6(OH)_4^-$	$[C_2][1]$	1
$B_5O_6(OH)_4^-^a$	$[C_2^2, C_2][2]$	1
$B_5O_6(OH)_4^-$	$[C_3, C_3][1]$	1
$B_8O_{10}(OH)_6^{2-}^a$	$[C_3, C_3, C_3][2]$	1
$B_8O_{10}(OH)_6^{2-}^b$	$[(C_3^2/C_2), C_3][3]$	1
H_2O	$[C_2][1]$	1
H_2O	$[C_2, C_2][1]$	1

Figure 9.18 Hydrogen bonding interactions in the Λ - $\lambda\delta\delta$ - $[Co(en)_3]^{3+} B_5O_6(OH)_4^- B_8O_{10}(OH)_6^{2-} \cdot 5H_2O$ (*oblet*₂) viewed along the pseudo C_3 axis (left) and the C_2 axis (right). The larger borate dianion is colored orange and the smaller borate monoanion is colored light green. In both cases, some non-interacting atoms have been omitted for clarity. ^a Two of the hydrogen bonds involve BOB linkages, and one a BOH linkage. ^b Two of the hydrogen bonds involve BOB linkages, and two BOH linkages.

All three C_2 sites exhibit different hydrogen bonding motifs. The two N–H units of one make separate hydrogen bonds to a H_2O molecule and a $B_5O_6(OH)_4^-$ monoanion. The two N–H units of another make a total of three hydrogen bonds to a $B_5O_6(OH)_4^-$ monoanion. The two N–H units of the third chelate a H_2O molecule, and make a third hydrogen bond to a $B_8O_{10}(OH)_6^{2-}$ dianion. This initiates a unique motif, as this dianion further hydrogen bonds to two N–H units of a C_3 site; one involves a O–B–O chelate

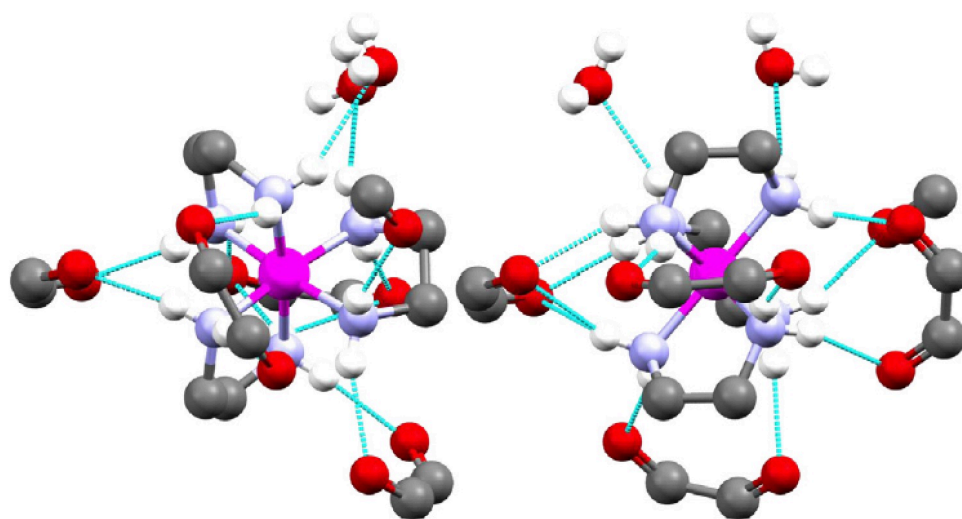
interaction with the same ethylenediamine ligand (see Figure 9.6A), and the other a B–O–H interaction with a different ethylenediamine ligand (see Figure 9.6C). This may provide a model for the interactions of Lewis basic substrates with an extended catalytic site, or the binding of a multifunctional product. Two N–H units on this site also chelate to an oxygen atom of a $B_5O_6(OH)_4^-$ monoanion. The three N–H units of the remaining C_3 site make a total of three hydrogen bonds to two oxygen atoms of another $B_8O_{10}(OH)_6^{2-}$ dianion.

9.5.6. Salts with achiral dianions

9.5.6.1. Λ - $\lambda\delta\delta$ - $[Co(en)_3]^{3+} \cdot 1.5C_4O_4^{2-} \cdot 4.5H_2O$ (*oblel_2*)

The structure and hydrogen bonding interactions of the polyhydrated squarate salt, Λ - $\lambda\delta\delta$ - $[Co(en)_3]^{3+} \cdot 1.5C_4O_4^{2-} \cdot 4.5H_2O$ (*oblel_2*), are shown in Figure 9.19.³⁵ This represents one of the two enantiomers in the crystallographically characterized racemate. As with 9.5.2.5, 9.5.3.2, 9.5.5.1, and 9.5.5.2 the complex crystallizes in an *oblel_2* Λ - $\delta\delta\delta$ - $[Co(en)_3]^{3+} \cdot 1.5p$ - $C_6H_4(CO_2)_2^{2-} \cdot 10H_2O$ (*lel_3*) orientation. All twelve N–H units are engaged in hydrogen bonding to five $C_4O_4^{2-}$ dianions and two H_2O molecules. One C_3 site is occupied by one $C_4O_4^{2-}$ dianion, two oxygen atoms of which each make two hydrogen bonds (two to one N–H unit, one to two N–H units). The other C_3 site is occupied by two $C_4O_4^{2-}$ dianions; two oxygen atoms of one dianion chelate two N–H units, and one oxygen atom of the other bonds to the remaining N–H unit. For two C_2

sites, both N–H units chelate to two oxygen atoms of a $C_4O_4^{2-}$ dianion. For the third, each N–H unit is singly hydrogen bonded to separate H_2O molecules.

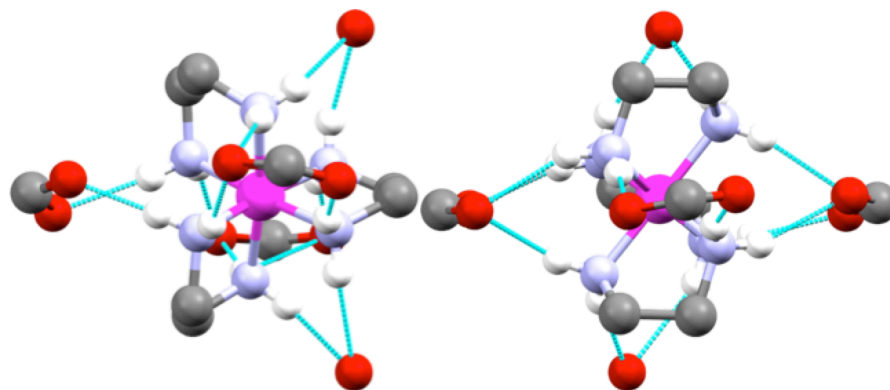


H-bond acceptor	type of H-bond	number of similar interactions
$C_4O_4^{2-}$	$[C_2, C_2][2]$	2
$C_4O_4^{2-}$	$[C_3][1]$	1
$C_4O_4^{2-}$	$[C_3, C_3][2]$	1
$C_4O_4^{2-}$	$[C_3^2, C_3, C_3][2, 2:2]$	1
H_2O	$[C_2][1]$	2

Figure 9.19 Hydrogen bonding interactions in the Λ - $\lambda\delta\delta$ - $[Co(en)_3]^{3+} 1.5C_4O_4^{2-} \cdot 4.5H_2O$ (*oblel*₂) viewed along the pseudo C_3 axis (left) and the C_2 axis (right). Several non-interacting atoms of the squarate anions have been omitted for clarity.

9.5.6.2. Λ - $\delta\delta\delta$ -[Co(en)₃]³⁺ 1.5*p*-C₆H₄(CO₂)₂²⁻·10H₂O (*le*₃)

The structure and hydrogen bonding interactions of the enantiopure decahydrated terephthalate salt, Λ - $\delta\delta\delta$ -[Co(en)₃]³⁺ 1.5*p*-C₆H₄(CO₂)₂²⁻·10H₂O (*le*₃), are shown in Figure 9.20.³⁶ All twelve N–H units are engaged in hydrogen bonding to three *p*-C₆H₄(CO₂)₂²⁻ dianions and two H₂O molecules. At each C₃ site, the three N–H units interact with both oxygen atoms of a single carboxylate moiety, although in one case there are three hydrogen bonds and in the other case four (two for each oxygen atom). At each C₂ site, the two N–H units form a chelate. In one case, this involves the two oxygen atoms of a carboxylate; in the other two cases, this involves a H₂O molecule.

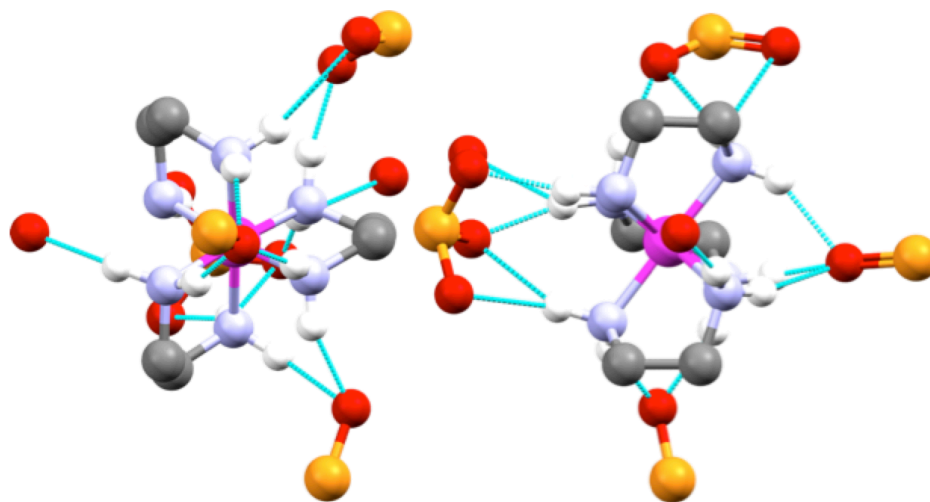


H-bond acceptor	type of H-bond	number of similar interactions
<i>p</i> -C ₆ H ₄ (CO ₂) ₂ ²⁻	[C ₂ ,C ₂][2]	1
<i>p</i> -C ₆ H ₄ (CO ₂) ₂ ²⁻	[C ₃ ,C ₃ ,C ₃][2]	1
<i>p</i> -C ₆ H ₄ (CO ₂) ₂ ²⁻	[C ₃ ² ,C ₃ ,C ₃][2,2:2]	1
H ₂ O	[C ₂ ,C ₂][1]	2

Figure 9.20 Hydrogen bonding interactions in the Λ - $\delta\delta\delta$ -[Co(en)₃]³⁺ 1.5*p*-C₆H₄(CO₂)₂²⁻·10H₂O (*le*₃) viewed along the C₃ axis (left) and the C₂ axis (right). The hydrogen atoms of the H₂O molecules and the C₆H₄ moieties of the terephthalate dianions have been omitted for clarity.

9.5.6.3. Λ - $\delta\delta\delta$ -[Co(en)₃]³⁺ 1.5HPO₄²⁻·4.5H₂O (*lel*₃)

The structure and hydrogen bonding interactions of the polyhydrated hydrogen phosphate salt Λ - $\delta\delta\delta$ -[Co(en)₃]³⁺ 1.5HPO₄²⁻·4.5H₂O (*lel*₃) are shown in Figure 9.21.³⁷ This represents one of the two enantiomers in the crystallographically characterized racemate. Due to disorder, it is not possible to analyze hydrogen bonding to one N–H unit, but all of the others are clearly engaged. At one C₃ site, all three N–H units are hydrogen bonded to a single oxygen atom of a HPO₄²⁻ dianion. At the other, the three N–H units make a total of four hydrogen bonds involving three oxygen atoms of the HPO₄²⁻ dianion; one of the N–H units also hydrogen bonds to a H₂O molecule. At one C₂ site, the two N–H units chelate to a single oxygen atom of a HPO₄²⁻ dianion. A second C₂ site is similar, but with an additional hydrogen bond involving one N–H unit and a second oxygen atom of the HPO₄²⁻ dianion.



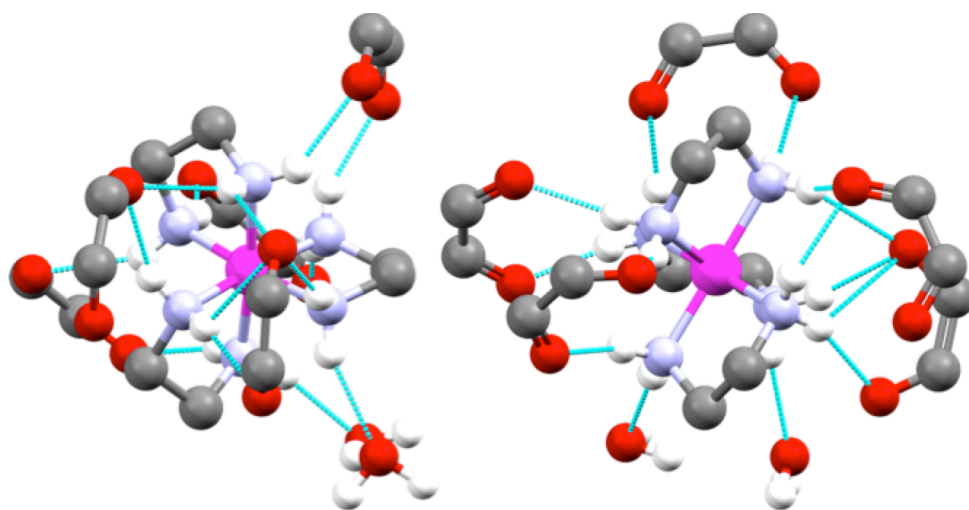
H-bond acceptor	type of H-bond	number of similar interactions
HPO_4^{2-}	$[\text{C}_2, \text{C}_2][1]$	1
HPO_4^{2-}	$[\text{C}_2^2, \text{C}_2][2]$	1
HPO_4^{2-}	$[\text{C}_3, \text{C}_3, \text{C}_3][1]$	1
HPO_4^{2-}	$[\text{C}_3^2, \text{C}_3, \text{C}_3][3]$	1
H_2O	$[\text{C}_2][1]$	1
H_2O	$[\text{C}_3][1]$	1

Figure 9.21 Hydrogen bonding interactions in the Λ - $\delta\delta\delta$ - $[\text{Co}(\text{en})_3]^{3+} 1.5\text{HPO}_4^{2-} \cdot 4.5\text{H}_2\text{O}$ (*lel*₃) viewed along the C_3 axis (left) and the C_2 axis (right). The hydrogen atoms of the H_2O molecules and HPO_4^{2-} dianions, and non-interacting oxygen atoms of the latter, have been omitted for clarity.

9.5.6.4. Λ - $\delta\lambda\lambda$ -[Co(en)₃]³⁺ 1.5C₅O₅²⁻·3H₂O (*lelob*₂)

The structure and hydrogen bonding interactions of the trihydrated croconate salt, Λ - $\delta\lambda\lambda$ -[Co(en)₃]³⁺ 1.5C₅O₅²⁻·3H₂O (*lelob*₂), are shown in Figure 9.22.³⁸ The cyclic croconate dianion is the next higher homolog of squarate. Figure 9.22 shows one of the two enantiomers in the crystallographically characterized racemate. This is the only salt presented in the text in which the trication [Co(en)₃]³⁺ crystallizes in a *lelob*₂ orientation.

All twelve N–H units are engaged in hydrogen bonding to five C₅O₅²⁻ dianions and two H₂O molecules. The two N–H units of one C₂ site each hydrogen bond to separate H₂O molecules. The N–H units of another C₂ site chelate a O–C–C–O linkage of a C₅O₅²⁻ dianion. The N–H units of the third C₂ site each hydrogen bond to a single oxygen atom of separate C₅O₅²⁻ dianions. However, in a rare motif, one of these oxygen atoms further hydrogen bonds to a N–H unit of a C₃ site. This involves two different ethylenediamine ligands, per Figure 9.6C. With the other C₅O₅²⁻ dianion, a second oxygen atom hydrogen bonds to a N–H unit of the opposite C₃ site. This also involves two different ethylenediamine ligands, but now the N–H units are spanned by four atoms as opposed to one. An additional C₅O₅²⁻ dianion completes the hydrogen bonding at each C₃ site (one uses two oxygen atoms to chelate two N–H units, and the other uses two oxygen atoms to make four hydrogen bonds involving all three N–H units).



H-bond acceptor	type of H-bond	number of similar interactions
$C_5O_5^{2-}$	$[C_3, C_2][1]$	1
$C_5O_5^{2-}$	$[C_2, C_2][2]$	1
$C_5O_5^{2-}$	$[C_3, C_2][2]$	1
$C_5O_5^{2-}$	$[C_3, C_3][2]$	1
$C_5O_5^{2-}$	$[C_3^2, C_3, C_3][3, 1:2]$	1
H_2O	$[C_2][1]$	2

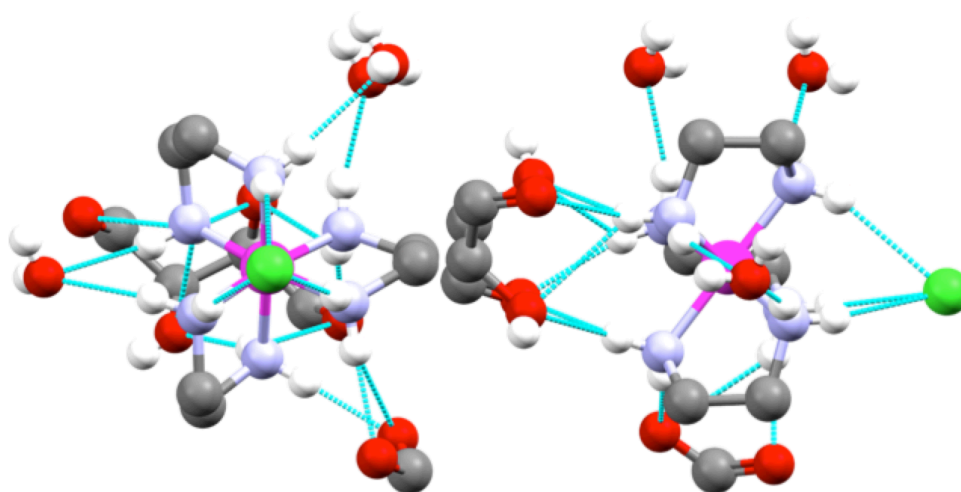
Figure 9.22 Hydrogen bonding interactions in the Λ - $\delta\lambda\lambda$ - $[Co(en)_3]^{3+} \cdot 1.5C_5H_5^{2-} \cdot 3H_2O$ (*lelob*₂) viewed along the pseudo C_3 axis (left) and the C_2 axis (right). Several atoms of the $C_5O_5^{2-}$ dianions have been omitted for clarity.

9.5.7. Salts with chiral tartrate dianions

As noted above, there is a series of papers in which the relative ability of a given enantiomer of the trication $[Co(en)_3]^{3+}$ or substituted derivatives to hydrogen bond to a given enantiomer of the tartrate dianion is critiqued.¹²⁻¹⁵ The analyses that follow are restricted to the modes of hydrogen bonding.

9.5.7.1. Λ - $\delta\delta\delta$ -[Co(en)₃]³⁺ Cl⁻(R,R)-tart²⁻·5H₂O (*lel*₃)

The structure and hydrogen bonding interactions of the enantiopure pentahydrated mixed chloride/tartrate salt, Λ - $\delta\delta\delta$ -[Co(en)₃]³⁺ Cl⁻(R,R)-tart²⁻·5H₂O (*lel*₃), are shown in Figure 9.23.^{15a} All twelve N–H units are engaged in hydrogen bonding to two (R,R)-tart²⁻ dianions, one Cl⁻ anion, and two H₂O molecules. At one C₃ site, all three N–H units hydrogen bond to a single chloride ion, a motif seen in 9.5.2.4 and 9.5.6.3 above. At the other, the three N–H units bind to four oxygen atoms of a single (R,R)-tart²⁻ dianion (O=C–CHOH–CHOH–C=O) via a total of seven hydrogen bonds. At one C₂ site, the two N–H units make three hydrogen bonds to the two oxygen atoms of a carboxylate group. At the other C₂ sites, there is hydrogen bonding either to one (chelating) or two (non-chelating) H₂O molecules.



H-bond acceptor	type of H-bond	number of similar interactions
(<i>R,R</i>)-tart ²⁻	[C ₂ ² ,C ₂][2]	1
(<i>R,R</i>)-tart ²⁻	[C ₃ ³ ,C ₃ ² ,C ₃ ²][2,2,2,1:4]	1
Cl ⁻	[C ₃ ,C ₃ ,C ₃][1]	1
H ₂ O	[C ₂][1]	2
H ₂ O	[C ₂ ,C ₂][1]	1

Figure 9.23 Hydrogen bonding interactions in the Λ - $\delta\delta\delta$ -[Co(en)₃]³⁺ Cl⁻(*R,R*)-tart²⁻·5H₂O (*le*₃) viewed along the C₃ axis (left) and the C₂ axis (right). Most non-interacting atoms of the tartrate dianions have been omitted for clarity.

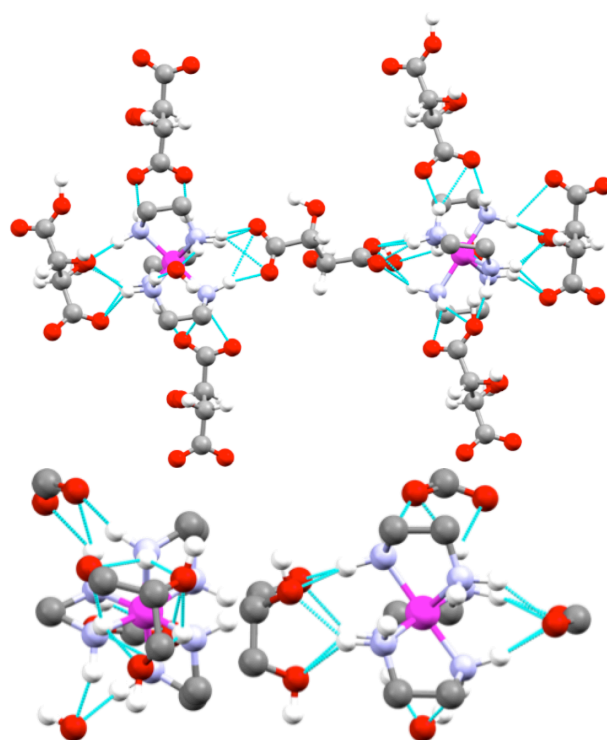
9.5.7.2. Δ - $\lambda\lambda\lambda$ -[Co(en)₃]³⁺ 1.5(*R,R*)-tart²⁻·5.75H₂O (*le*₃)

The structure and hydrogen bonding interactions of the enantiopure polyhydrated tartrate salt, Δ - $\lambda\lambda\lambda$ -[Co(en)₃]³⁺ 1.5(*R,R*)-tart²⁻·5.75H₂O, are shown in Figure 9.24.^{15e} This complex lacks the chloride anion found in the previous example in section 9.5.7.1. There are two independent trications in the unit cell, which are linked as shown at the top of Figure 9.24, and separately depicted in the middle and bottom. Of the N–H units, ten and twelve are engaged in hydrogen bonding, respectively.

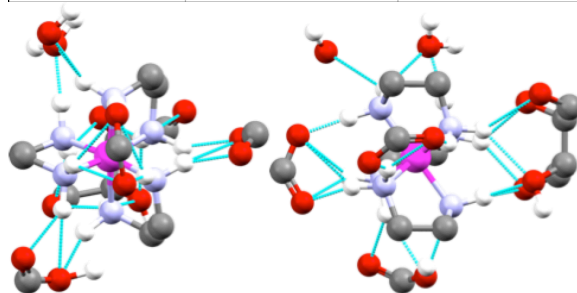
With the first trication (middle), all three C₂ sites are different. In one, the two N–H units chelate a H₂O molecule. In another, the N–H units make three hydrogen

bonds to two oxygen atoms of a carboxylate group. In the third, there is no hydrogen bonding, which is unique to all the structures surveyed. Each of the C₃ sites is occupied by a single tartrate dianion. In one, the three N–H units make a total of six hydrogen bonds to three oxygen atoms (O=C–CHOH–CHOH). In the other, the three N–H units make five hydrogen bonds to the two oxygen atoms of a carboxylate group.

With the second trication (bottom), the two N–H units of two C₂ sites each make three hydrogen bonds to two oxygen atoms of a carboxylate group.³⁹ The N–H units of the remaining C₂ site make three hydrogen bonds to two H₂O molecules (one chelating, one not). Each of the C₃ sites is again occupied by a single tartrate dianion. In one, the three N–H units make a total seven hydrogen bonds to four oxygen atoms (O=C–CHOH–CHOH–C=O); an identical motif was observed in section 9.5.7.1. In the other (as in the independent trication), the three N–H units make five hydrogen bonds to the two oxygen atoms of a carboxylate group.



H-bond acceptor	type of H-bond	number of similar interactions
(R,R) -tart ²⁻	[C ₂ ² ,C ₂][2]	1
(R,R) -tart ²⁻	[C ₃ ² ,C ₃ ² ,C ₃][3,2:2]	1
(R,R) -tart ²⁻	[C ₃ ² ,C ₃ ² ,C ₃ ²][2,2,2:3]	1
H ₂ O	[C ₂ ,C ₂][1]	1



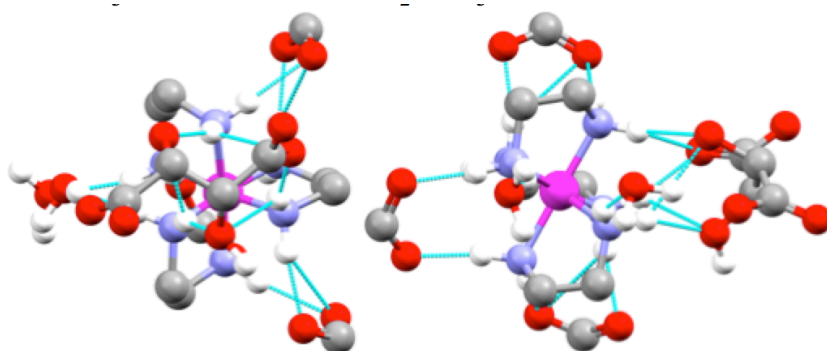
H-bond acceptor	type of H-bond	number of similar interactions
(R,R) -tart ²⁻	[C ₂ ² ,C ₂][2]	2
(R,R) -tart ²⁻	[C ₃ ² ,C ₃ ² ,C ₃][3,2:2]	1
(R,R) -tart ²⁻	[C ₃ ³ ,C ₃ ² ,C ₃ ²][2,2,2,1:4]	1
H ₂ O	[C ₂][1]	1
H ₂ O	[C ₂ ,C ₂][1]	1

Figure 9.24 Hydrogen bonding interactions in the two independent trications of Δ -λλλ-[Co(en)₃]³⁺ 1.5(*R,R*)-tart²⁻·5.75H₂O (*lél*₃) viewed along the C₃ axis (left middle, left bottom) and a C₂ axis (right middle, right bottom), or as linked together (top). In the middle and bottom representations, most non-interacting atoms of the tartrate dianions have been omitted for clarity.

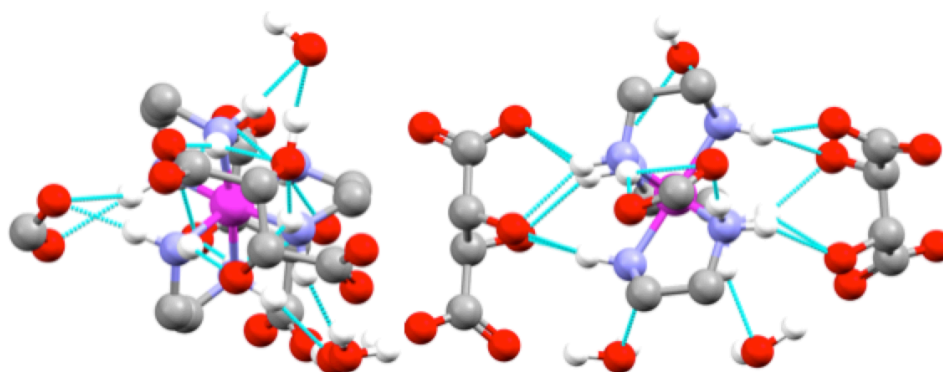
9.5.7.3. Λ - $\delta\delta\delta$ -[Co(en)₃]³⁺ 1.5(R,R)-tart²⁻·9.5H₂O (*lel*₃)

The structure and hydrogen bonding interactions of the enantiopure polyhydrated tartrate salt, Λ - $\delta\delta\delta$ -[Co(en)₃]³⁺ 1.5(R,R)- tart²⁻·9.5H₂O (*lel*₃), are shown in Figure 9.25.^{15e} This is simply a different hydrate — sometimes called a pseudopolymorph⁴⁰ — of the salt in section 9.5.7.2. As with 9.5.7.2, there are two independent trications in the unit cell, which are depicted in the top and bottom of Figure 9.25. The hydrogen bonding motifs do not break any new ground *vis-à-vis* the previous structure. Of the N–H units, eleven and twelve are engaged in hydrogen bonding, respectively.

For the first independent cation (top), two N–H units of one C₃ site chelate the O–C–O linkage of a carboxylate group; the third N–H unit exhibits no hydrogen bonding. The three N–H units of the other C₃ site make a total of six hydrogen bonds to three oxygen atoms of a tartrate dianion (O=C–CHOH–CHOH). The two N–H units of two C₂ sites each make three hydrogen bonds to the two oxygen atoms of separate carboxylate groups. In the third C₂ site, each N–H unit hydrogen bonds to an oxygen atom of a separate H₂O molecule.



H-bond acceptor	type of H-bond	number of similar interactions
H ₂ O	[C ₂][1]	2
H ₂ O	[C ₂ ,C ₂][1]	1
(<i>R,R</i>)-tart ²⁻	[C ₂ ² ,C ₂][2]	2
(<i>R,R</i>)-tart ²⁻	[C ₃ ,C ₃][2]	1
(<i>R,R</i>)-tart ²⁻	[C ₃ ² ,C ₃ ² ,C ₃ ²][2,2,2:3]	1



H-bond acceptor	type of H-bond	number of similar interactions
H ₂ O	[C ₂][1]	2
H ₂ O	[C ₂ ,C ₂][1]	1
(<i>R,R</i>)-tart ²⁻	[C ₂ ² ,C ₂][2]	1
(<i>R,R</i>)-tart ²⁻	[C ₃ ² ,C ₃ ² ,C ₃][2,2,1:3]	1
(<i>R,R</i>)-tart ²⁻	[C ₃ ² ,C ₃ ² ,C ₃ ²][2,2,2:3]	1

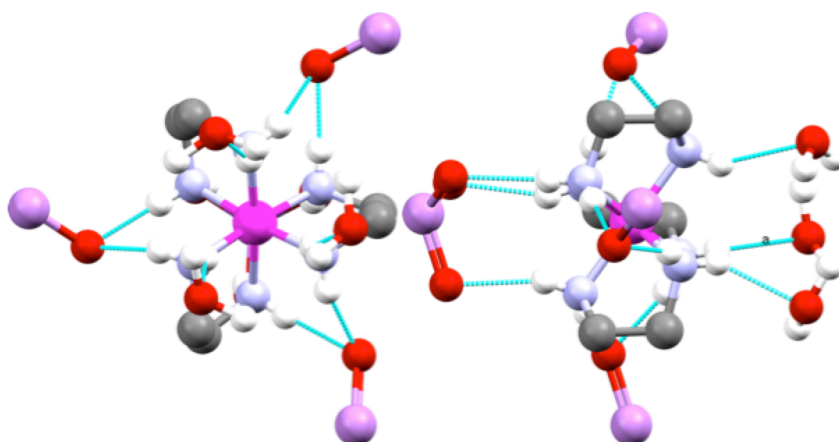
Figure 9.25 Hydrogen bonding interactions in the two independent trications of $\Lambda\text{-}\delta\delta\delta\text{-}[\text{Co}(\text{en})_3]^{3+}$ $1.5(\text{R,R})\text{-tart}^{2-}\cdot 9.5\text{H}_2\text{O}$ (*lel*₃) viewed along the C₃ axis (left middle, left bottom) and a C₂ axis (right middle, right bottom). Most non-interacting atoms of the tartrate dianions have been omitted for clarity.

For the second independent trication (bottom), three N–H units of one C_3 site make (as in the other trication) a total of six hydrogen bonds to three different oxygen atoms of a tartrate dianion ($\underline{O}=\underline{C}-\underline{C}\underline{H}\underline{O}\underline{H}-\underline{C}\underline{H}\underline{O}\underline{H}$). The three N–H units of the other C_3 site make five hydrogen bonds to the same three oxygen atoms of a second tartrate dianion. The two N–H units of one C_2 site make a total of three hydrogen bonds to the two oxygen atoms of a carboxylate. In another C_2 site, the N–H units chelate an oxygen atom of a disordered H_2O molecule. In the third C_2 site, each N–H unit hydrogen bonds to an oxygen atom of a separate H_2O molecule.

9.5.8. Salts with achiral dianions

9.5.8.1. Λ - $\delta\delta\delta$ - $[Co(en)_3]^{3+} AsO_4^{3-} \cdot 3H_2O$ (lel_3)

The structure and hydrogen bonding interactions of the trihydrated arsenate salt, Λ - $\delta\delta\delta$ - $[Co(en)_3]^{3+} AsO_4^{3-} \cdot 3H_2O$ (lel_3) are shown in Figure 9.26.⁴¹ This represents one of the two enantiomers in the crystallographically characterized racemate. There is a crystallographic C_3 axis corresponding to the idealized C_3 axis of the trication. All twelve N–H units engage in hydrogen bonding to four arsenate anions and three H_2O molecules. The AsO_4^{3-} trianions exhibit only two hydrogen bonding motifs. The two N–H units of all three C_2 sites chelate to an AsO_4^{3-} oxygen atom. The three N–H units of one C_3 site each hydrogen bond to a different oxygen atom of the AsO_4^{3-} anion. In the other C_3 site, each N–H unit hydrogen bonds to the oxygen atom of a separate H_2O molecule.



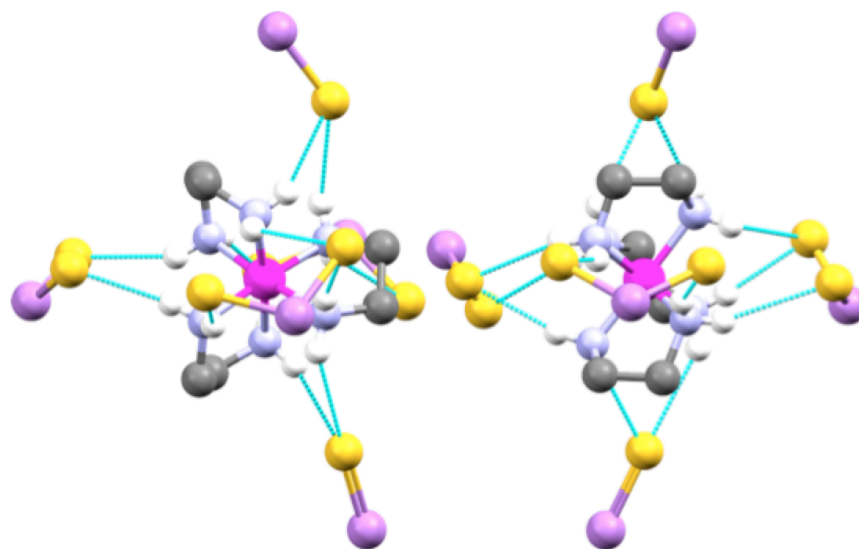
H-bond acceptor	type of H-bond	number of similar interactions
H ₂ O	[C ₃][1]	3
AsO ₄ ³⁻	[C ₂ ,C ₂][1]	3
AsO ₄ ³⁻	[C ₃ ,C ₃ ,C ₃][3]	1

Figure 9.26 Hydrogen bonding interactions in Λ - $\delta\delta\delta$ -[Co(en)₃]³⁺ AsO₄³⁻·3H₂O (*lel*₃) viewed along the C₃ axis (left) and a C₂ axis (right). Non-interacting oxygen atoms of the arsenate trianion have been omitted for clarity.

9.5.8.2. Λ - $\lambda\delta\delta$ -[Co(en)₃]³⁺ AsS₄³⁻ (*oblel*₂)

The structure and hydrogen bonding interactions of the tetrathioarsenate(V) salt, Λ - $\lambda\delta\delta$ -[Co(en)₃]³⁺ AsS₄³⁻ (*oblel*₂) are shown in Figure 9.27.⁴² This represents one of the two enantiomers in the crystallographically characterized racemate. As with salts in sections 9.5.2.5, 9.5.3.2, 9.5.5.1, 9.5.5.2, and 9.5.6.1 above, the complex crystallizes in an *oblel*₂ orientation. There is a crystallographic C₂ axis, but it does not correspond to the idealized C₂ axis of the trication. All twelve N–H units engage in hydrogen bonding to five AsS₄³⁻ trianions. Each of the three N–H units of each C₃ site hydrogen bond to

one of two sulfur atoms of a AsS_4^{3-} trianion. The two N–H units of each C_2 site hydrogen bond either to two sulfur atoms of a AsS_4^{3-} trianion, or the same sulfur atom.



H-bond acceptor	type of H-bond	number of similar interactions
AsS_4^{3-}	$[\text{C}_2, \text{C}_2][1]$	2
AsS_4^{3-}	$[\text{C}_2, \text{C}_2][2]$	1
AsS_4^{3-}	$[\text{C}_3, \text{C}_3, \text{C}_3][2]$	2

Figure 9.27 Hydrogen bonding interactions in $\Lambda\text{-}\lambda\delta\delta\text{-}[\text{Co}(\text{en})_3]^{3+} \text{AsS}_4^{3-}$ (*oblel*₂) viewed along the C_3 pseudoaxis (left) and a C_2 axis (right). Non-interacting sulfur atoms of the tetrathioarsenate trianion have been omitted for clarity.

9.5.8.3. $\Lambda\text{-}\delta\delta\delta\text{-}[\text{Co}(\text{en})_3]^{3+} \text{GaF}_6^{3-}$ (*lel*₃)

The structure and hydrogen bonding interactions of the enantiopure hexafluorogallate salt, $\Lambda\text{-}\delta\delta\delta\text{-}[\text{Co}(\text{en})_3]^{3+} \text{GaF}_6^{3-}$ (*lel*₃), are shown in Figure 9.28.⁴³

There are crystallographic C_3 and C_2 axes corresponding to the idealized C_3 and C_2 axes of the trication. All twelve N–H units engage in hydrogen bonding to five GaF_6^{3-}

trianions. The three N–H units of each C_3 site each bind to two of three *fac* oriented fluoride ions of a single GaF_6^{3-} trianion. The two N–H units of each C_2 site each bind to two (*cis*) fluoride ions of a single GaF_6^{3-} trianion.

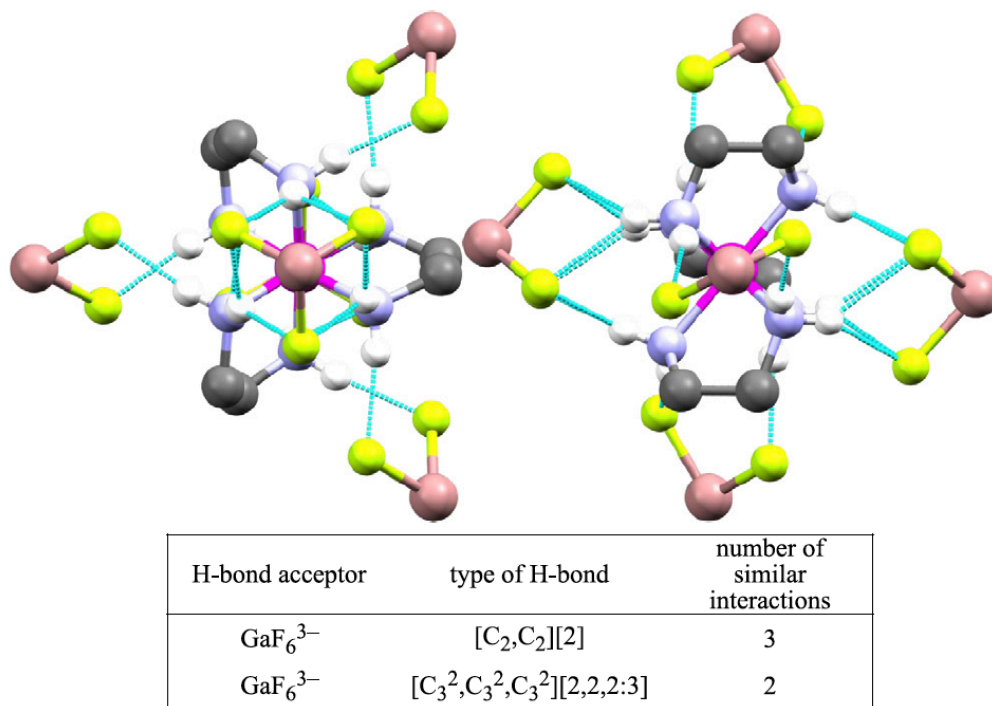
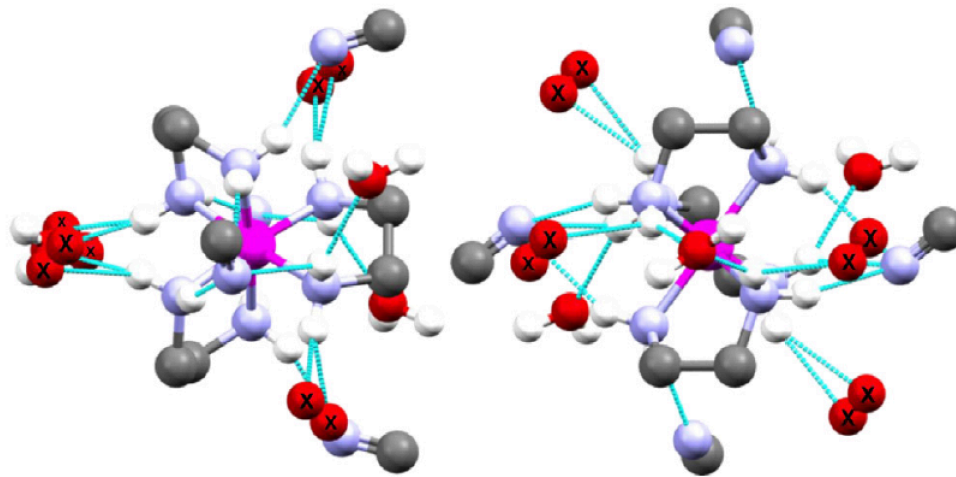


Figure 9.28 Hydrogen bonding interactions in $\Lambda\text{-}\delta\delta\delta\text{-}[\text{Co}(\text{en})_3]^{3+} \text{GaF}_6^{3-} (\text{tel}_3)$ viewed along the C_3 axis (left) and a C_2 axis (right). Non-interacting fluorine atoms of the hexafluorogallate trianion have been omitted for clarity.

9.5.8.4. Λ - $\lambda\delta\delta$ -[Co(en)₃]³⁺ Co(CN)₆³⁻·5H₂O (*oblel*₂)

The structure and hydrogen bonding interactions of the pentahydrated hexacyanocobaltate salt, Λ - $\lambda\delta\delta$ -[Co(en)₃]³⁺ Co(CN)₆³⁻·5H₂O (*oblel*₂) are shown in Figure 9.29.⁴⁴ This represents one of the two enantiomers in the crystallographically characterized racemate. As with 9.5.2.5, 9.5.3.2, 9.5.5.1, 9.5.5.2, 9.5.6.1, and 9.5.8.2 above the complex crystallizes in an *oblel*₂ orientation. Although some disorder is apparent as described in the following paragraph, there is a crystallographic C₂ axis corresponding to the idealized C₂ axis of the trication (right view).

The three N–H units of each C₃ site are hydrogen bonded to the same nitrogen atom of a cyanide ligand. In addition, one N–H unit of each C₃ site also hydrogen bonds to the oxygen atom of a H₂O molecule. The two N–H units of two C₂ sites are separately hydrogen bonded to a H₂O molecule and the nitrogen atom of a cyanide ligand. The N–H units of the third C₂ site bind three H₂O molecules (one chelating, two not). The four non-chelating H₂O molecules associated with the C₂ sites (labeled with "X" in Figure 9.29) are disordered over two positions, and furthermore engage in hydrogen bonding with the N–H units of neighboring trications.



H-bond acceptor	type of H-bond	number of similar interactions
H ₂ O ^a	[C ₂][1]	4
H ₂ O	[C ₃][1]	2
H ₂ O	[C ₂ ,C ₂][1]	1
Co(CN) ₆ ³⁻	[C ₂][1N]	2
Co(CN) ₆ ³⁻	[C ₃ ,C ₃ ,C ₃][1N]	2

Figure 9.29 Hydrogen bonding interactions in Λ - $\lambda\delta\delta$ -[Co(en)₃]³⁺ Co(CN)₆³⁻·5H₂O (*ob*lel₂) viewed along the pseudo C₃ axis (left) and the C₂ axis (right). Except for the interacting CN units, the Co(CN)₆³⁻ trianions have been omitted for clarity. Disordered H₂O molecules are denoted with an X.^a Although this salt has a stoichiometry of five H₂O molecules per trication, there are seven H₂O molecules in the second coordination sphere, four of which are shared with neighboring trications and disordered over two positions (each highlighted with an "X").

9.5.8.5. Λ - $\delta\delta\delta$ -[Co(en)₃]³⁺ Λ -Rh(C₂O₄)₃³⁻ (*le*l₃)

The structure and hydrogen bonding interactions of the enantiopure Λ -tris(oxalate)rhodate(III) salt, Λ - $\delta\delta\delta$ -[Co(en)₃]³⁺ Λ -Rh(C₂O₄)₃³⁻ (*le*l₃), are shown in Figure 9.30.⁴⁵ Note that the tris(chelate) trianion now also has helical (Λ/Δ) chirality. The crystal structure bears a number of similarities to that of the arsenate salt in 9.5.8.1. There is a crystallographic C₃ axis corresponding to the idealized C₃ axis of the trication (which also contains the C₃ axis of the trianion). All twelve N–H units are engaged in

hydrogen bonding to five trianions in one of two motifs. The two N–H units of all three C₂ sites chelate to a carbonyl oxygen atom of an oxalate ligand. The three N–H units of each C₃ site each bind to two of three fac oriented Rh–O linkages.

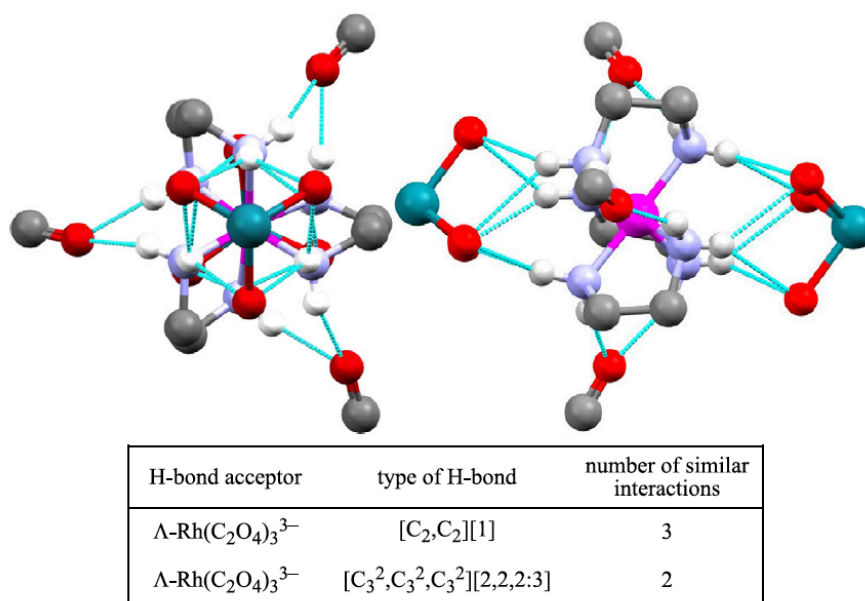
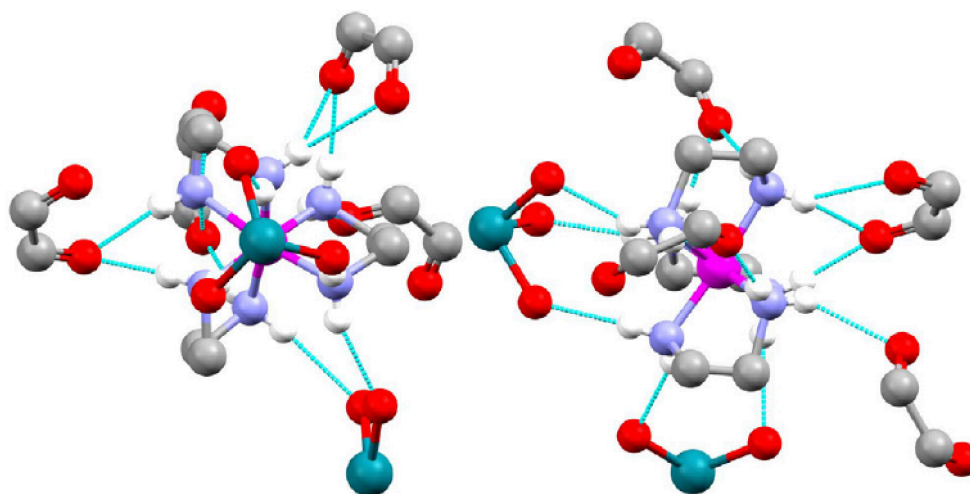


Figure 9.30 Hydrogen bonding interactions in $\Delta\text{-}\delta\delta\delta\text{-}[\text{Co}(\text{en})_3]^{3+} \Delta\text{-Rh}(\text{C}_2\text{O}_4)_3^{3-} (\text{lel}_3)$ viewed along the C₃ axis (left) and a C₂ axis (right). Non-interacting atoms of the trianion have been omitted for clarity.

9.5.8.6. $\Lambda\text{-}\delta\delta\delta\text{-}[\text{Co}(\text{en})_3]^{3+} \Delta\text{-Rh}(\text{C}_2\text{O}_4)_3^{3-} (\text{lel}_3)$

The structure and hydrogen bonding interactions of the enantiopure Δ -tris(oxalate)rhodate(III) salt, $\Lambda\text{-}\delta\delta\delta\text{-}[\text{Co}(\text{en})_3]^{3+} \Delta\text{-Rh}(\text{C}_2\text{O}_4)_3^{3-} (\text{lel}_3)$, are shown in Figure 9.31.⁴⁵ The CIF file for this salt did not indicate any hydrogen atoms. Hence, they were introduced in idealized positions using the program OLEX2.⁴⁶ This complex is diastereomeric with that in 9.5.8.5 (opposite $\text{Rh}(\text{C}_2\text{O}_4)_3^{3-}$ chirality), and has an

identical degree of hydration. As is easily seen with a quick glance at the "type of H-bond" entries in Figure 9.30 and Figure 9.31, the second coordination spheres markedly differ, with only one type of hydrogen bond (a single $[C_2, C_2][1]$ linkage) common to each.



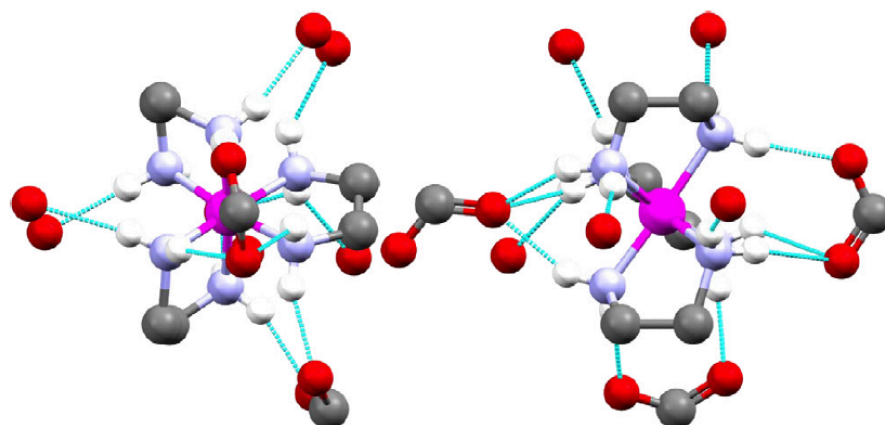
H-bond acceptor	type of H-bond	number of similar interactions
$\Delta\text{-Rh}(\text{C}_2\text{O}_4)_3^{3-}$	$[C_2, C_2][1]$	1
$\Delta\text{-Rh}(\text{C}_2\text{O}_4)_3^{3-}$	$[C_2, C_2][2]$	1
$\Delta\text{-Rh}(\text{C}_2\text{O}_4)_3^{3-}$	$[C_2^2, C_2][2]$	1
$\Delta\text{-Rh}(\text{C}_2\text{O}_4)_3^{3-}$	$[C_3][1]$	1
$\Delta\text{-Rh}(\text{C}_2\text{O}_4)_3^{3-}$	$[C_3^2, C_3][2]$	1
$\Delta\text{-Rh}(\text{C}_2\text{O}_4)_3^{3-}$	$[C_3, C_3, C_3][3]$	1

Figure 9.31 Hydrogen bonding interactions in $\Lambda\text{-}\delta\delta\delta\text{-}[\text{Co}(\text{en})_3]^{3+} \Delta\text{-Rh}(\text{C}_2\text{O}_4)_3^{3-} (\text{lel}_3)$ viewed along the C_3 axis (left) and a C_2 axis (right). Non-interacting atoms of the trianion have been omitted for clarity.

All twelve N–H units are engaged in hydrogen bonding to six trianions. The three C₂ sites exhibit different motifs. In one, the two N–H units chelate a carbonyl oxygen atom of an oxalate ligand. In another, the two N–H units make a total of three hydrogen bonds to the two oxygen atoms of a O=C–C=O moiety. In the third, the NH units bind a separate oxygen atom of a O–Rh–O linkage. At one C₃ site, each N–H unit makes one hydrogen bond to a different oxygen atom of three facially directed Rh–O linkages. At the other, one N–H unit makes a single hydrogen bond to a carbonyl oxygen atom of an oxalate ligand. The other two N–H units make a total of three hydrogen bonds to the two oxygen atoms of a O=C–C=O moiety.

9.5.8.7. Λ - $\delta\delta\delta$ -[Co(en)₃]³⁺ C₆H₃(CO₂)₃³⁻·5.55H₂O (*oblel*₂)

The structure and hydrogen bonding interactions of the polyhydrated benzene-1,3,5-tricarboxylate (trimesate) salt, Λ - $\lambda\delta\delta$ -[Co(en)₃]³⁺ C₆H₃(CO₂)₃³⁻·5.55H₂O (*oblel*₂), are shown in Figure 9.32.³⁶ This represents one of the two enantiomers in the crystallographically characterized racemate. The H₂O molecules about the Δ enantiomer (but not the Λ enantiomer) are disordered. As with 9.5.2.5, 9.5.3.2, 9.5.5.1, 9.5.5.2, 9.5.6.1, 0, and 9.5.8.4, the complex crystallizes in an *oblel*₂ orientation.



H-bond acceptor	type of H-bond	number of similar interactions
H ₂ O	[C ₂][1]	4
H ₂ O	[C ₃][1]	1
C ₆ H ₃ (CO ₂) ₃ ³⁻	[C ₂ ,C ₂][2]	1
C ₆ H ₃ (CO ₂) ₃ ³⁻	[C ₃ ,C ₃ ,C ₃][2]	1
C ₆ H ₃ (CO ₂) ₃ ³⁻	[C ₃ ,C ₃ ,C ₃][1]	1

Figure 9.32 Hydrogen bonding interactions in Λ - $\lambda\delta\delta$ -[Co(en)₃]³⁺ (C₆H₃)(CO₂)₃³⁻·5.55H₂O (*oblel*₂) viewed along the pseudo C₃ axis (left) and a C₂ axis (right). Non-interacting atoms of the trianion have been omitted for clarity.

All twelve N–H units engage in hydrogen bonding to three tris(carboxylate) trianions and five H₂O molecules. At two C₂ sites, each N–H unit hydrogen bonds to the oxygen atom of a separate H₂O molecule. At the third, the N–H units chelate the O–C–O linkage of a carboxylate group. At one C₃ site, the three N–H units interact with both oxygen atoms of a carboxylate group via three hydrogen bonds. At the other C₃ site, each N–H unit hydrogen bonds to the same oxygen atom of a carboxylate group, and one N–H unit makes an additional hydrogen bond with the oxygen atom of a H₂O molecule.

9.5.8.8. Λ - $\delta\delta\delta$ -[Co(en)₃]³⁺ P₃O₉³⁻·2H₂O (*lel*₃) (from racemic salt)

The structure and hydrogen bonding interactions of the dihydrated cyclotriphosphate salt, Λ - $\delta\delta\delta$ -[Co(en)₃]³⁺ P₃O₉³⁻·2H₂O (*lel*₃) are shown in Figure 9.33.⁴⁷ This represents one of the two enantiomers in the crystallographically characterized racemate. All twelve N–H units are engaged in hydrogen bonding to four P₃O₉³⁻ trianions and one H₂O molecule. The three N–H units of both C₃ sites hydrogen bond to two different oxygen atoms of a P₃O₉³⁻ trianion (1,5-relationship). The two N–H units of two C₂ sites chelate to a single oxygen atom of a P₃O₉³⁻ trianion. The N–H units of the third C₂ site chelate the oxygen atom of a H₂O molecule.

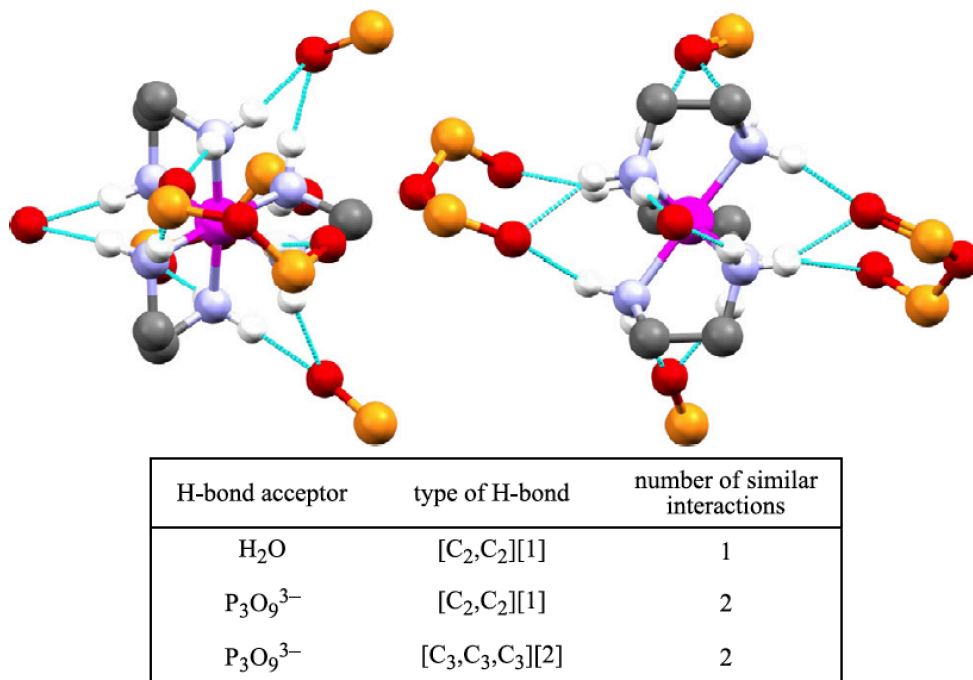


Figure 9.33 Hydrogen bonding interactions in Λ - $\delta\delta\delta$ -[Co(en)₃]³⁺ P₃O₉³⁻·2H₂O (*lel*₃) viewed along the C₃ axis (left) and a C₂ axis (right). Most non-interacting atoms of the trianion have been omitted for clarity.

9.5.8.9. Λ - $\delta\delta\delta$ -[Co(en)₃]³⁺ P₃O₉³⁻·2H₂O (*lel*₃) (from enantiopure salt)

The structure and hydrogen bonding interactions of the enantiopure dihydrated cobalt cyclotriphosphate salt, Λ - $\delta\delta\delta$ -[Co(en)₃]³⁺ P₃O₉³⁻·2H₂O (*lel*₃), are depicted in Figure 9.34.⁴⁷ The bonding motifs are very similar to those of the racemate in 9.5.8.8, which is also a dihydrate. All twelve N–H units are engaged in hydrogen bonding to four P₃O₉³⁻ trianions and one H₂O molecule. The C₃ sites exhibit the same interactions as with the racemate. However, the two N–H units of one C₂ site no longer chelate to a single oxygen atom of a P₃O₉³⁻ trianion. Rather, they form three hydrogen bonds to two oxygen atoms with a 1,3-relationship.

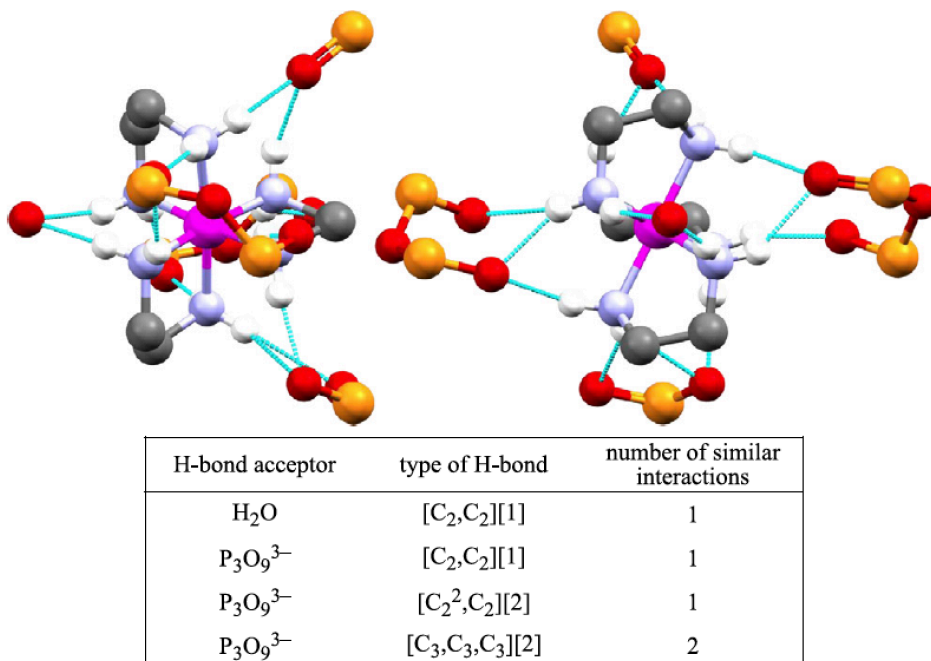


Figure 9.34 Hydrogen bonding interactions in Λ - $\delta\delta\delta$ -[Co(en)₃]³⁺ P₃O₉³⁻·2H₂O (*lel*₃) viewed along the C₃ axis (left) and a C₂ axis (right). Most non-interacting atoms of the trianion have been omitted for clarity.

9.6. Additional structural information and generalizations

9.6.1. General remarks and scope of hydrogen bonding

As noted above, Table 17.3 in Appendix G summarizes the 150 unique crystal structures containing the trication $[\text{Co}(\text{en})_3]^{3+}$, and 142 of these are amenable to detailed analyses (a few more to partial analyses). The anions or other features in about one third of these can be regarded (at least from an organic chemist's perspective) as *mondo bizzarro* (e.g. $\text{Zn}_6\text{P}_8\text{O}_{32}\text{H}_8^{3-}$,⁴⁸ $\text{V}_3\text{P}_3\text{BO}_{19}^{5-}\text{H}_2\text{PO}_4^-$,⁴⁹ $[(\text{Co}^{\text{II}}\text{O}_6)\text{Mo}_6^{\text{VI}}\text{O}_{18}(\text{As}_3^{\text{III}}\text{O}_3)_2]^{4-}$,⁵⁰ $[\text{Ru}_2(\text{C}_2\text{H}_4\text{O}_7\text{P}_2)_2\text{Cl}_2]^{5-}$,⁵¹ *trans*- $\text{CdBr}_4\text{Cl}_2^{4-}$,⁵² $\text{Zr}_4\text{F}_{22}\text{O}_2^{10-}$,⁵³ $\text{SiMo}_8\text{V}_4\text{O}_{40}(\text{VO})_2^{6-}$,⁵⁴ $\text{In}_3(\text{H}_2\text{PO}_4)_6(\text{HPO}_4)_3^{3-}$.⁵⁵ Additional exotica include eight different small molecule clathrates of $[\text{Co}(\text{en})_3]^{3+} \cdot 3\text{Cl}^-$ that have been structurally characterized.⁵⁶ These types of unusual species were generally excluded from sections 9.5.2 to 9.5.8, but not from further analyses below.

An important initial remark is that the N–H units of the $[\text{Co}(\text{en})_3]^{3+}$ trications of all 150 structures are extensively hydrogen bonded. Indeed, in sections 9.5.2 to 9.5.8 it was rather unusual to find cases in which all twelve of the N–H units were not engaged in hydrogen bonding. The N–H donor strengths must be substantial, as they interact with a variety of weak hydrogen bond acceptors. Although the hydrogen bond accepting strengths of many anions have been quantified,⁵⁷ relatively few of those in Table 17.3 have been ranked. Some of the extensively delocalized anions in the previous paragraph, as well as GaF_6^{3-} (section 9.5.8.3) or AuCl_4^- and SiF_6^{2-} (Table 17.3), are likely among the weakest.

Four crystal structures with perchlorate anions — a very feeble hydrogen bond acceptor⁵⁷ — can be found in Table 17.3 (Appendix G). One is of the mixed perchlorate/oxalate salt $[\text{Co}(\text{en})_3]^{3+} \text{ClO}_4^- \text{C}_2\text{O}_4^{2-}$ (entry 70).⁵⁸ Although carboxylate anions are good hydrogen bond acceptors,⁵⁷ the perchlorate anion competes, binding in a $[\text{C}_3, \text{C}_3][1]$ mode with $\text{N}-\text{H}\cdots\text{O}$ distances of 2.596 and 2.707 Å. Two others involve cocrystals of $[\text{Co}(\text{en})_3]^{3+} 3\text{ClO}_4^-$ and a neutral palladium penicillimate complex.⁵⁹ One lattice (entry 65) features two independent trications, many $\text{N}-\text{H}$ units of which interact with donor atoms of the penicillin moiety. However two perchlorate anions hydrogen bond to one trication ($[\text{C}_3][1]$, $\text{N}-\text{H}\cdots\text{O}$ 2.169 Å; $[\text{C}_3, \text{C}_2][2]$, $\text{N}-\text{H}\cdots\text{O}$ 2.197, 2.536 Å), and one to the other ($[\text{C}_2, \text{C}_2][2]$, $\text{N}-\text{H}\cdots\text{O}$ 2.144, 2.340 Å). Hydrogen bonding to perchlorate is evident in another structure (entry 77), but severe disorder precludes further analyses.

9.6.2. Types of hydrogen bonding

In the 27 salts in sections 9.5.2 to 9.5.8, a number of very common hydrogen bonding motifs are apparent. For example, many anions and H_2O molecules interact with two $\text{N}-\text{H}$ units of the same C_2 binding site, or multiple $\text{N}-\text{H}$ units from the same C_3 binding site. However, taking the opposite perspective, H_2O molecules never interact with multiple $\text{N}-\text{H}$ units originating from both C_2 and C_3 binding sites. Anions only do so in a few special cases involving larger species with multiple acceptor sites.

The most likely modes by which anions might interact with two $\text{N}-\text{H}$ units from different C_2 and C_3 binding sites have been summarized in Figure 9.6. The first, denoted

[C₃/C₂], entails anion binding to the N–H units of the same NH₂ group. This motif is unequivocally absent in the 27 salts in sections 9.5.2 to 9.5.8, and no examples have been found in the remaining structures (Table 17.3 in Appendix G). We have also interrogated, using software tools associated with the Cambridge Structural Database, the crystal structures of all 6259 primary and secondary organoammonium halides, [RNH₃]⁺ X⁻ and [RR'NH₂]⁺ X⁻. Interestingly, none showed hydrogen bonding of the halide anion to two geminal N–H units.⁶⁰ Hence, this motif appears to be intrinsically disfavored, presumably due to stereoelectronic reasons and/or angular requirements.

Although rare, it is possible to bridge the geminal N–H units of organoammonium halides with unusual larger anions that feature multiple acceptor sites.^{65,66} Interestingly, a more complicated variant, [(C₃²/C₂),C₃][3], occurs in section 9.5.5 (Figure 9.18). Here a large borate dianion, B₈O₁₀(OH)₆²⁻, bridges the C₃ and C₂ sites. The C₃ N–H unit is chelated by two oxygen atoms of the dianion, and the dianion makes an additional hydrogen bond with another C₃ N–H unit.

The second type of hydrogen bonding in Figure 9.6, involving an anion and non-geminal N–H units from the same ligand [C₃//C₂], is not found in any of the salts in sections 9.5.2 to 9.5.8 or Table 17.3. The distance between the N–H units is much too great to be bridged by a single atom. However, hydrogen bonding to a structurally extended anion, like the borate in the previous example, should in principle be feasible. The third type of hydrogen bonding in Figure 9.6, involving an anion and C₃ and C₂ sites on different ligands [C₃,C₂], is seen in 9.5.6.4 (Figure 9.22). Here the cyclic

croconate dianion, $C_5O_5^{2-}$, provides two variants: one in which a single oxygen atom binds to the two N–H units ($[C_3,C_2][1]$), and another in which two different oxygen atoms bind to the two N–H units ($[C_3,C_2][2]$).

9.6.3. Possible connections to catalysis

The ensemble of second coordination sphere binding motifs embodied in the preceding $[Co(en)_3]^{3+}$ salts do not directly bear on the mechanisms of any catalytic reactions. However, they certainly point to the viability of coordinating two reactive substrates to a single C_2 site, or to a single C_3 site. They are also entirely consistent with the initial binding of one substrate to a C_2 site and the other to a C_3 site. However, this might lead to a transition state or product that spans C_2 and C_3 sites. While there do not seem to be any steric or electronic impediments to such an assembly, this has much less precedent among the crystal structures.

Interestingly, sixteen of the 27 structures in sections 9.5.2 to 9.5.8 are hydrates. The conspicuous lack of other molecules of crystallization simply reflects the fact that all of these salts are prepared under aqueous conditions. With the recent syntheses of many lipophilic salts,^{6,67} the stage is now set to attempt the cocrystallization of guest molecules that are also substrates for catalysis. Strong interactions with substrates are evident by NMR in solution.^{7a} Their binding modes are likely to provide better starting points for the development of mechanistic models, including rationales for the observed enantioselection.

9.6.4. Other stereochemical issues

Consider the relative frequencies of the various *le/ob* orientations outlined in Figure 9.4. Well over half the $[\text{Co}(\text{en})_3]^{3+}$ salts crystallize in *lel*₃ orientations, per the following distribution: *lel*₃, 81; *oblel*₂, 35; *lelob*₂, 14; *ob*₃, 4 (134 total). There are an additional seven salts that crystallize with two independent trications, one with a *lel*₃ orientation and the other with an *oblel*₂ orientation. There are also an additional three salts that crystallize with two independent cations, one with a *lel*₃ orientation and the other with a *lelob*₂ orientation. Taking all of the independent trications in this series of 144 compounds, the overall distribution becomes *lel*₃, 99; *oblel*₂, 48; *lelob*₂, 18; *ob*₃, 4 (169 total).

Although it is by no means a proof, this distribution suggests that *lel*₃ orientations have the greatest thermodynamic stabilities, and *ob*₃ orientations the lowest thermodynamic stabilities. This is in agreement with available experimental and computational literature.^{18,19} Finally, we note that the salts in which larger anions span C₃ and C₂ binding sites (9.5.5.2, Figure 9.18; 9.5.6.4, Figure 9.22) possess *oblel*₂ and *lelob*₂ orientations. Perhaps in these lower symmetry structures, the distances between the hydrogen atoms of the N–H units, or other geometric features, are more conducive to this motif (the analysis in Figure 9.6 is for *lel*₃ orientations).

9.7. Concluding remarks

The $[\text{Co}(\text{en})_3]^{3+}$ trication is a hydrogen bond donor extraordinaire. Adducts readily form with counter anions and H_2O molecules in the solid state. These usually engage all twelve N–H units, even when the anions include very poor hydrogen bond acceptors. These properties presumably extend to many other cationic metal complexes of primary and secondary amines. There is good NMR evidence that most of these interactions remain extant in solution.⁶⁷

In the preceding sections, some generalizations could be offered about relatively common or less common hydrogen bonding motifs. However, the main take-home lesson of this review is the diversity of hydrogen bonding motifs. Insight regarding the energetics of various binding modes is currently being sought through computational studies.⁶⁸ Perhaps the situation is not too different from that in nucleic acid chemistry, where Watson-Crick, Hoogsteen, and reverse Hoogsteen base pairs — as well as other hydrogen bonding arrangements — can all be encountered and serve as determinants of biological function, depending upon circumstances.⁶⁹ In any case, an essential analytical step has been taken in the quest for insight as to how $[\text{Co}(\text{en})_3]^{3+}$ and related cations might bind and activate organic substrates in catalysis.

9.8. References

(1) G. L. Miessler, D. A. Tarr, *Inorganic Chemistry*, third ed.; Pearson Prentice Hall: Upper Saddle River, New Jersey, 2004, pp. 299-321. (b) A. K. De, *Inorganic Chemistry*, ninth ed.; New Age International Publishers: New Delhi, 2003, pp. 88-108.

(2) (a) Borer, L. L.; Russell, J. G.; Settlage, R. E. Experiments with Tris(ethylenediamine)cobalt(III) Compounds: ^{59}Co NMR and the Resolution of Enantiomeric $[\text{Co}(\text{en})_3]^{3+}$ Ion and Analysis by Formation of Diastereomeric Ion Pairs. *J. Chem. Educ.* **2002**, *79*, 494-497. (b) Ernst, K-H.; Wild, F. R. W. P.; Blacque, O.; Berke, H. Alfred Werner's Coordination Chemistry: New Insights from Old Samples. *Angew. Chem. Int. Ed.* **2011**, *50*, 10780-10787; Alfred Werners Koordinationschemie: neue Erkenntnisse aus alten Proben. *Angew. Chem.* **2011**, *123*, 10970-10977.

(3) (a) Werner, A. Zur Kenntnis des asymmetrischen Kobaltatoms. I. *Chem. Ber.* **1911**, *44*, 1887-1898. V. L. King is listed as an author for the experimental section. (b) Werner, A. Zur Kenntnis des asymmetrischen Kobaltatoms. II. *Chem. Ber.* **1911**, *44*, 2445-2455. (c) Werner, A. Zur Kenntnis des asymmetrischen Kobaltatoms. III. *Chem. Ber.* **1911**, *44*, 3272-3278. (d) Werner, A. Zur Kenntnis des asymmetrischen Kobaltatoms. IV. *Chem. Ber.* **1911**, *44*, 3279-3284. (e) Werner, A. Zur Kenntnis des asymmetrischen Kobaltatoms. V. *Chem. Ber.* **1912**, *45*, 121-130.

(4) (a) Broomhead, J. A.; Dwyer, F. P.; Hogarth, J. W. Dextro-Tris(ethylenediamine)cobalt(III) Iodide by a Partial Asymmetric Synthesis. *Inorg. Synth.* **1960**, *6*, 183-186. (b) Nakazawa, H.; Yoneda H. Chromatographic study of optical

resolution: II. Separation of optically active cobalt (III) complexes using potassium antimony *d*-tartrate as eluent. *J. Chromatogr. A.* **1978**, *160*, 89-99.

(5) Ehnbohm, A.; Ghosh, S. K.; Lewis, K. G.; Gladysz, J. A. Octahedral Werner complexes with substituted ethylenediamine ligands: a stereochemical primer for a historic series of compounds now emerging as a modern family of catalysts. *Chem. Soc. Rev.* **2016**, *45*, 6799-6811.

(6) Ganzmann, C.; Gladysz, J. A. Phase Transfer of Enantiopure Werner Cations into Organic Solvents: An Overlooked Family of Chiral Hydrogen Bond Donors for Enantioselective Catalysis. *Chem. Eur. J.* **2008**, *14*, 5397-5400.

(7) (a) Lewis, K. G.; Ghosh, S. K.; Bhuvanesh, N.; Gladysz, J. A. Cobalt(III) Werner Complexes with 1,2-Diphenylethylenediamine Ligands: Readily Available, Inexpensive, and Modular Chiral Hydrogen Bond Donor Catalysts for Enantioselective Organic Synthesis. *ACS Cent. Sci.* **2015**, *1*, 50-56. (b) Ghosh, S. K.; Ganzmann, C.; Bhuvanesh, N.; Gladysz, J. A. Werner Complexes with ω -Dimethylaminoalkyl Substituted Ethylenediamine Ligands: Bifunctional Hydrogen-Bond-Donor Catalysts for Highly Enantioselective Michael Additions. *Angew. Chem. Int. Ed.* **2016**, *55*, 4356-4360; Werner-Komplexe mit ω -Dimethylaminoalkyl-substituierten Ethylendiaminliganden: bifunktionale H-Brückendonor-Katalysatoren für hoch enantioselektive Michael-Additionen. *Angew. Chem.* **2016**, *128*, 4429-4433. (c) Kumar, A.; Ghosh, S. K.; Gladysz, J. A. Tris(1,2-diphenylethylenediamine)cobalt(III) Complexes: Chiral Hydrogen Bond Donor Catalysts for Enantioselective α -Aminations of 1,3-Dicarbonyl Compounds. *Org. Lett.* **2016**, *18*, 760-763.

(8) (a) Taylor, M. S.; Jacobsen, E. N. Asymmetric Catalysis by Chiral Hydrogen-Bond Donors. *Angew. Chem. Int. Ed.* **2006**, *45*, 1520-1543; Asymmetrische Katalyse durch chirale Wasserstoffbrückendonoren. *Angew. Chem.* **2006**, *118*, 1550-1573. (b) Doyle, A. G.; Jacobsen, E. N. Small-Molecule H-Bond Donors in Asymmetric Catalysis. *Chem. Rev.* **2007**, *107*, 5713-5743. (c) Yu, X.; Wang, W. Hydrogen-Bond-Mediated Asymmetric Catalysis. *Chem. Asian J.* **2008**, *3*, 516-532.

(9) See also (a) Thomas, C.; Gladysz, J. A. Highly Active Families of Catalysts for the Ring-Opening Polymerization of Lactide: Metal Templated Organic Hydrogen Bond Donors Derived from 2-Guanidinobenzimidazole. *ACS Catalysis*, **2014**, *4*, 1134-1138. (b) Scherer, A.; Mukherjee, T.; Hampel, F.; Gladysz, J. A. Highly Active Families of Catalysts for the Ring-Opening Polymerization of Lactide: Metal Templated Organic Hydrogen Bond Donors Derived from 2-Guanidinobenzimidazole. *Organometallics* **2014**, *33*, 6709-6722. (c) Mukherjee, T.; Ganzmann, C.; Bhuvanesh, N.; Gladysz, J. A. Syntheses of Enantiopure Bifunctional 2-Guanidinobenzimidazole Cyclopentadienyl Ruthenium Complexes: Highly Enantioselective Organometallic Hydrogen Bond Donor Catalysts for Carbon–Carbon Bond Forming Reactions. *Organometallics* **2014**, *33*, 6723-6737.

(10) (a) Chen, L.-A.; Xu, W.; Huang, B.; Ma, J.; Wang, L.; Xi, J.; Harms, K.; Meggers, E. Asymmetric Catalysis with an Inert Chiral-at-Metal Iridium Complex. *J. Am. Chem. Soc.* **2013**, *135*, 10598-10601. (b) Chen, L.-A.; Tang, X.; Xi, J.; Xu, W.; Gong, L.; Meggers, E. Chiral-at-Metal Octahedral Iridium Catalyst for the Asymmetric Construction of an All-Carbon Quaternary Stereocenter. *Angew. Chem. Int. Ed.* **2013**,

52, 14021-14025; *Angew. Chem.* **2013**, *125*, 14271-14275. (c) Ma, J.; Ding, X.; Hu, Y.; Huang, Y.; Gong, L.; Meggers, E. Metal-templated chiral Brønsted base organocatalysis. *Nat. Commun.* **2014**, *5*, 4531 (d) Huo, H.; Fu, C.; Wang, C.; Harms, K.; Meggers, E. Metal-templated enantioselective enamine/H-bonding dual activation catalysis. *Chem. Commun.* **2014**, *50*, 10409-10411. (e) Liu, J.; Gong, L.; Meggers, E. Asymmetric Friedel-Crafts alkylation of indoles with 2-nitro-3-arylacrylates catalyzed by a metal-templated hydrogen bonding catalyst. *Tetrahedron Lett.* **2015**, *56*, 4653-4656. (f) Hu, Y.; Zhou, Z.; Gong, L.; Meggers, E. Asymmetric aza-Henry reaction to provide oxindoles with quaternary carbon stereocenter catalyzed by a metal-templated chiral Brønsted base. *Org. Chem. Front.* **2015**, *2*, 968-972. (g) Xu, W.; Shen, X.; Ma, Q.; Gong, L.; Meggers, E. Restricted Conformation of a Hydrogen Bond Mediated Catalyst Enables the Highly Efficient Enantioselective Construction of an All-Carbon Quaternary Stereocenter. *ACS Catal.* **2016**, *6*, 7641-7646. (h) Xu, W.; Arieno, M.; Löw, H.; Huang, K.; Xie, X.; Cruchter, T.; Ma, Q.; Xi, J.; Huang, B.; Wiest, O.; Gong, L.; Meggers, E. Metal-Templated Design: Enantioselective Hydrogen-Bond-Driven Catalysis Requiring Only Parts-per-Million Catalyst Loading. *J. Am. Chem. Soc.* **2016**, *138*, 8774-8780.

(11) Maleev, V. I.; North, M.; Larionov, V. A.; Fedyanin, I. V.; Savel'yeva, T. F.; Moscalenko, M. A.; Smolyakov, A. F.; Belokon, Y. N. Chiral Octahedral Complexes of Cobalt(III) as "Organic Catalysts in Disguise" for the Asymmetric Addition of a Glycine Schiff Base Ester to Activated Olefins. *Adv. Synth. Catal.* **2014**, *356*, 1803-1810.

(12) Mizuta, T.; Toshitani, K.; Miyoshi, K.; Yoneda, H. Structural Study of Optical Resolution. 14. Highly Efficient Chiral Discrimination of the *lel*₃-Tris(*trans*-1,2-

cyclohexanediamine)cobalt(III) Ion Attained with the *d*-(*R,R*)-Tartrate Ion Assuming an Anomalous Conformation. *Inorg. Chem.* **1990**, *29*, 3020-3026.

(13) See also (a) Ogino, K.; Saito, U. Association Involving Optically Active Ions. I. Association Constants of Tris(ethylenediamine)cobalt(III) and Tartrate Ions. *Bull. Chem. Soc. Jpn.* **1967**, *40*, 826-829. (b) Yoneda, H.; Taura, T. Stereoselectivity in ion-pair formation. I. Association constants of Λ - and Δ -[Co(en)₃]³⁺ with L- and *meso*-tartrates from CD measurements. *Chem. Lett.* **1977**, 63-66.

(14) Yoneda, H. Mechanism of chromatographic separation of optically active metal complexes. *J. Chromatogr. A.* **1984**, *313*, 59-91.

(15) (a) Templeton, D. H.; Zalkin, A.; Ruben H. W.; Templeton, L. K. Anomalous scattering by cobalt and chlorine and crystal structure of (+)-tris(ethylenediamine)cobalt(III) chloride (+)-tartrate pentahydrate. *Acta Cryst.* **1979**, *B35*, 1608-1613. (b) Magill, L. S.; Korp, J. D.; Bernal, I. Crystal Structure and Absolute Configuration of Tartrate Derivatives. 2. [Λ -($\delta\delta\delta$)-Co(en)₃]³⁺ [(+)₅₈₉-(*R,R*)-tart²⁻] Cl⁻·5H₂O. *Inorg. Chem.* **1981**, *20*, 1187-1192. (c) Tada, T.; Kushi, Y.; Yoneda, H. Structural study of optical resolution V. The crystal structure of hydrogen tris(ethylenediamine)cobalt(III) *d*-tartrate trihydrate. *Chem. Lett.* **1977**, 379-382. (d) Kushi, Y.; Kuramoto, M.; Yoneda, H. Structural study of optical resolution I. The crystal structure of hydrogen tris(ethylenediamine)cobalt(III) bromide *d*-tartrate pentahydrate *Chem. Lett.* **1976**, 135-136. (e) Mizuta, T.; Tada, T.; Kushi, Y.; Yoneda, H. Crystal structures of the racemic tartrate and the two *d*-tartrate salts of the tris(ethylenediamine)cobalt(III) complex. *Inorg. Chem.* **1988**, *27*, 3836-3841.

(16) To the best of our knowledge, atomic coordinates or related data are not available for Λ -[Co(en)₃]³⁺·H₃O⁺ 2(R,R)-tart²⁻·2H₂O reported in reference 15c and Λ -[Co(en)₃]³⁺ Br⁻(R,R)-tart²⁻·5H₂O reported in reference 15d.

(17) Etter, M. C. Encoding and decoding hydrogen-bond patterns of organic compounds. *Acc. Chem. Res.* **1990**, 23, 120-126.

(18) Corey, E. J.; Bailar, J. C. Jr. The Stereochemistry of Complex Inorganic Compounds. XXII. Stereospecific Effects in Complex Ions. *J. Am. Chem. Soc.* **1959**, 81, 2620-2628.

(19) Jorge, F. E.; Autschbach, J.; Ziegler, T. On the Origin of Optical Activity in Tris-diamine Complexes of Co(III) and Rh(III): A Simple Model Based on Time-Dependent Density Function Theory. *J. Am. Chem. Soc.* **2005**, 127, 975-985.

(20) (a) There would be a range of values in structures of lower symmetry. (b) The C–H and N–H bond lengths in crystal structures are commonly underestimated (ca. 10%); therefore, this distance, which is taken from structures with N–H bond lengths of 0.90 Å (vs. >1.00 Å as typically determined by other methods), must be slightly lower than the true distance.

(21) In the interest of uniformity, some additional conventions are followed: (a) The N–H units of the higher symmetry binding site are specified first, giving any "tie" to the N–H unit that bonds to the greatest number of anion atoms. For example, [C₃²,C₃,C₂][2] is written in preference to [C₃,C₂,C₃²][2], even though either representation is unambiguous. (b) In a list, [C₂,C₂][1] takes priority over [C₃][1]

because the latter has only one N–H unit engaged in hydrogen bonding. Similarly, $[C_3][1]$ takes precedence over $[C_2^3][1]$ (value for W weighted over that of X), and $[C_2][2]$ takes precedence over $[C_2][1]$ (higher Y value used as tiebreaker). Thus, an illustrative descending order of hierarchy would be $[C_3^2, C_3^2][2]$, $[C_3^2, C_3^2][1]$, $[C_3^2, C_3][1]$, $[C_3, C_2][1]$, $[C_2, C_2][1]$, $[C_3^2][1]$, $[C_3][1]$, $[C_2^3][1]$, $[C_2^2][2]$, $[C_2^2][1]$, $[C_2][1]$.

(22) Macrae, C. F.; Bruno, I. J.; Chisholm, J. A.; Edgington, P. R.; McCabe, P.; Pidcock, E.; Rodriguez-Monge, L.; Taylor, R.; van de Streek, J.; Wood, P. A. *Mercury CSD 2.0 — new features for the visualization and investigation of crystal structures*. *J. Appl. Cryst.* **2008**, *41*, 466-470.

(23) Bondi, A. van der Waals Volumes and Radii. *J. Phys. Chem.* **1964**, *68*, 441-451.

(24) Iwata, M.; Nakatzu, K.; Saito, Y. The crystal structure of (+)D-tris(ethylenediamine)cobalt(III) chloride monohydrate, (+)D- $[Co(en)_3]Cl \cdot 3H_2O$. *Acta Cryst.* **1969**, *B25*, 2562-2571.

(25) Whuler, A.; Brouty, C.; Spinat, P.; Herpin, P. Etudes structurales des complexes racémiques hydratés $(\pm)\text{-Co(en)}_3\text{Cl}_3$ et $(\pm)\text{-Cr(en)}_3\text{Cl}_3$. *Acta Cryst.* **1975**, *B31*, 2069-2076.

(26) Ueda, T.; Bernard, G. M.; McDonald, R.; Wasylshen, R. E. Cobalt-59 NMR and X-ray diffraction studies of hydrated and dehydrated (+/-)-

tris(ethylenediamine) cobalt(III) chloride. *Solid State Nucl. Magn. Reson.* **2003**, *24*, 163-183.

(27) Nakatsu, K.; The Crystal Structure of D-Tris-ethylenediamine-cobalt(III) Bromide Monohydrate, D-[Co en₃]Br₃·H₂O, and the Absolute Configuration of the D-Tris-ethylenediamine-cobalt(III) Ion, D-[Co en₃]³⁺. *Bull. Chem. Soc. Jpn.* **1962**, *35*, 832-834.

(28) Matsuki, R.; Shiro, M.; Asahi, T.; Asai, H.; Absolute configuration of Λ-(+)₅₈₉-tris-(ethylenediamine)-cobalt(III) triiodide monohydrate. *Acta Cryst.* **2001**, *E57*, 448-450.

(29) Witiak, D.; Clardy, J. C.; Martin Jr. D. S. The crystal structure of (+)-D-tris(ethylenediamine)cobalt(III) nitrate. *Acta Cryst.* **1972**, *B28*, 2694-2695.

(30) Baidina, I. A.; Filatov, E. Y.; Makotchenko, E. V.; Smolentsev, A. I. Synthesis and structure investigation of Co(III) complex salts with the perrhenate anion. *J. Struct. Chem.* **2012**, *53*, 112-118.

(31) Brouty, P. C.; Spinat, P.; Whuler, A.; Herpin, P. Structure du complexe racémique (±)-Co(en)₃(SCN)₃. Etude des liaisons hydrogène. *Acta Cryst.* **1976**, *B32*, 2153-2159.

(32) Zhang, Z.-J.; Zheng, F.-K.; Fu, M. L.; Guo, G.-C.; Huang, J.-S. A new cobalt(III) ethylenediamine complex with mixed halide counter-anions, [Co(en)₃](Cl)(I)₂·H₂O. *Acta Cryst.* **2005**, *E61*, m89-m91.

(33) Brewer, G.; Butcher, R. J.; Jasinski, J. P. Tris(ethane-1,2-diamine- κ^2,N,N')-cobalt(III) carbonate iodide tetrahydrate. *Acta Cryst.* **2010**, *E66*, m1148-m1149.

(34) Altahan, M. A.; Beckett, M. A.; Coles, S. J.; Horton, P. N. A New Decaoxidooctaborate(2-) Anion, $[B_8O_{10}(OH)_6]^{2-}$: Synthesis and Characterization of $[Co(en)_3][B_5O_6(OH)_4][B_8O_{10}(OH)_6]\cdot 5H_2O$ (en = 1,2-Diaminoethane). *Inorg. Chem.* **2015**, *54*, 412-414.

(35) Yeşilel, O. Z.; Ölmez, H.; Soylu, S. Synthesis and Spectrothermal Studies of Thermochromic Diamine Complexes of Cobalt(III), Nickel(II) and Copper(II) Squarate. Crystal Structure of $[Co(en)_3](sq)_{1.5}\cdot 6H_2O$. *Trans. Met. Chem.* **2006**, *31*, 396-404.

(36) Liebig, T. J.; Ruschewitz, U. Supramolecular Polymers with $[Co(en)_3]^{3+}$ Cores (en = ethylenediamine). *Cryst. Growth Des.* **2012**, *12*, 5402-5410.

(37) Duesler, E. N.; Raymond, K. N. Conformational effects of intermolecular interactions. Structure of tris(ethylenediamine)cobalt(III) monohydrogen phosphate nonahydrate. *Inorg. Chem.* **1971**, *10*, 1486-1492.

(38) Wang, C.-C.; Yeh, C.-T.; Cheng, Y.-T.; Chen, I.-H.; Lee, G.-H.; Shih, W.-J.; Sheu, H.-S.; Fedorov, V. E.; A hydrogen-bonded and π - π assembled 3D supramolecular network, $[Co(en)_3]\cdot 1.5(C_5O_5)$, with 1D microporous hydrophilic channels showing reversible water ad/desorption property. *CrystEngComm* **2012**, *14*, 4637-4643.

(39) One of these carboxylates appears to be protonated in the CIF file provided in the supporting information of the published article, but this is believed to be an

artifact of the refinement (similarly, what would logically be a H₂O molecule in the lattice is missing a hydrogen atom).

(40) Nangia, A. Pseudopolymorph: Retain This Widely Accepted Term. *Cryst. Growth Des.* **2006**, *6*, 2-4.

(41) Rius, J.; Gali, S. Tris(ethylenediamine) cobalt (III) arseniate trihydrate Co(C₂H₈N₂)₃AsO₄·3H₂O. *Cryst. Struct. Commun.* **1982**, *11*, 829-831.

(42) Hu, Z.; Dang, L.-Q.; Bao, D.-H.; An, Y.-L. Tris(ethylenediamine)cobalt(III) tetrathioarsenate(V). *Acta Cryst.* **2006**, *E62*, m2756-m2757.

(43) Loiseau, T.; Serpaggi, F.; Ferey, G. Crystal structure of tris(ethylenediamine-*N,N'*)cobalt(III) hexafluorogallate, Co(C₂H₈N₂)₃[GaF₆]. *Z. Kristallogr. New Cryst. St.* **2004**, *219*, 469-470.

(44) Serada, O.; Stoeckli-Evans, H. *Private Communication to the Cambridge Structural Database (CSD)* **2008**. See (a)
http://webo.csd.ccdc.cam.ac.uk/display_csd_entry.php?identifier=WOQDUC (b)
http://webo.csd.ccdc.cam.ac.uk/display_csd_entry.php?identifier=WOQFAK.

(45) Kuroda, R. Chiral discriminations and crystal packing. Two diastereomeric compounds involving complex ions of *D*₃ symmetry, Tris(ethylenediamine)cobalt(III) and Tris(oxalato)rhodate(III). *Inorg. Chem.* **1991**, *30*, 4954-4959.

(46) Dolomanov, O. V.; Bourhis, L. J.; Gildea, R. J.; Howard, J. A. K.; Puschmann, H. *OLEX2*: a complete structure solution, refinement and analysis program. *J. Appl. Cryst.* **2009**, *42*, 339-341.

(47) Nakashima, T.; Mishiro, J.; Ito, M.; Kura, G.; Ikuta, Y.; Matsumoto, N.; Nakajima, K.; Kojima, M. Homochiral Column Structure of *rac*- and Λ -Tris(ethylenediamine)cobalt(III) Cyclotriphosphate Dihydrate in Crystal Structures and Cation-Anion Association in Aqueous Solution. *Inorg. Chem.* **2003**, *42*, 2323-2330.

(48) (a) Yu, J. H.; Wang, Y.; Shi, Z.; Xu, R. R. Hydrothermal Synthesis and Characterization of Two New Zinc Phosphates Assembled about a Chiral Metal Complex: $[\text{Co}^{\text{II}}(\text{en})_3]_2[\text{Zn}_6\text{P}_8\text{O}_{32}\text{H}_8]$ and $[\text{Co}^{\text{III}}(\text{en})_3][\text{Zn}_8\text{P}_6\text{O}_{24}\text{Cl}]\cdot 2\text{H}_2\text{O}$. *Chem. Mater.* **2001**, *13*, 2972-2978.

(49) Wang, Y.; Yu, J. H.; Pan, Q. H.; Du, Y.; Zou, Y. C.; Xu, R. R. Synthesis and Structural Characterization of 0D Vanadium Borophosphate $[\text{Co}(\text{en})_3]_2[\text{V}_3\text{P}_3\text{-BO}_{19}][\text{H}_2\text{PO}_4]\cdot 4\text{H}_2\text{O}$ and 1D Vanadium Oxides $[\text{Co}(\text{en})_3][\text{V}_3\text{O}_9]\cdot \text{H}_2\text{O}$ and $[\text{Co}(\text{dien})_2][\text{V}_3\text{O}_9]\cdot \text{H}_2\text{O}$ Templated by Cobalt Complexes: Cooperative Organization of the Complexes and the Inorganic Networks. *Inorg. Chem.* **2004**, *43*, 559-565.

(50) He, Q. L.; Wang, E. B. Hydrothermal synthesis and crystal structure of a new molybdenum(VI) arsenate(III), $\text{Co}^{\text{III}}(\text{en})_3\text{H}_3\text{O}[(\text{Co}^{\text{II}}\text{O}_6)\text{Mo}^{\text{VI}}_6\text{O}_{18}(\text{As}^{\text{III}}_3\text{O}_3)_2]\cdot 2\text{H}_2\text{O}$. *Inorg. Chim. Acta.* **1999**, *295*, 244-247.

(51) Peng, Y.; Li, Y. Z.; Bao, S. S.; Zheng, L. M. Bis[tris(ethylenediamine)cobalt(III)]dichlorobis[μ -(1-hydroxyethylidene)diphosphonato-(4-)]diruthenium(II,III)(*Ru-Ru*) chloride trihydrate. *Acta Cryst.* **2004**, *C60*, M302-M304.

(52) Sharma, R. P.; Shashni, R.; Singh, A.; Venugopalan, P.; Yu, J.; Guo, Y. A.; Ferretti, V. A rational synthesis of a new discrete anion [*trans*-CdBr₄Cl₂]⁴⁻ and its comparison with newly synthesized anion [CdBr₆]⁴⁻. *J. Mol. Struct.* **2011**, *1006*, 121-127.

(53) Du, Y.; Yu, J. H.; Chen, Y.; Yang, Y. H. Mesostructured molecular solid material |Co(en)₃|(Zr₂F₁₁H₂O) with enhanced photoelectronic effect. *Dalton Trans.* **2009**, 6736-6740.

(54) Lu, Y. K.; Tian, M. M.; Xu, S. G.; Lu, R. Q.; Liu, Y. Q. Bis[tris(ethylenediamine-κ²N,N')cobalt(III)] octakis-μ₃-oxidohexadeca-μ₂-oxido-tetradeca-μ₁₂-tetraoxosilicato-octa-molybdenum(VI)hexavanadium(IV,V) hexahydrate. *Acta Cryst.* **2011**, *E67*, M1776-U1523.

(55) Du, Y.; Yu, J. H.; Wang, Y.; Pan, Q. H.; Zou, Y. C.; Xu, R. R. [Co(en)₃][In₃(H₂PO₄)₆(HPO₄)₃]·H₂O: A new layered indium phosphate templated by cobalt complex. *J. Solid State Chem.* **2004**, *177*, 3032-3037.

(56) Takamizawa, S.; Akatsuka, T.; Ueda, T. Gas-Conforming Transformability of an Ionic Single-Crystal Host Consisting of Discrete Charged Components. *Angew. Chem. Int. Ed.* **2008**, *47*, 1689-1692; *Angew. Chem.* **2008**, *120*, 1713-1716.

(57) (a) Lungwitz, R.; Spange, S. A. *New. J. Chem.* **2008**, *32*, 392-394. (b) Cláudio, A. F. M.; Swift, L.; Hallett, J. P.; Welton, T.; Coutinho, J. A. P.; Freire, M. G. Extended scale for the hydrogen-bond basicity of ionic liquids. *Phys. Chem. Chem. Phys.* **2014**, *16*, 6593-6601.

(58) Cai, J. W.; Zhang, Y. F.; Hu, X. P.; Feng, X. L. Tris(ethylenediamine-*N,N'*)cobalt(III) oxalate perchlorate dihydrate. *Acta Cryst.* **2000**, *C56*, 661-663.

(59) Hirai, Y.; Nagao, Y.; Igashira-Kamiyama, A.; Konno, T. Enantioselective/Anion-Selective Incorporation of Tris(ethylenediamine) Complexes into 2D Coordination Spaces between Tripalladium(II) Supramolecular Layers with D-Penicillamine. *Inorg. Chem.* **2011**, *50*, 2040-2042.

(60) Three "hits" had peripheral relevance (REFCODEs: VOCWEP,⁶¹ MURHUE,⁶² ECEBOC.⁶³ For example, one structure featured a [RR'NH₂]⁺ moiety with two N···H···Br inter-actions involving the same bromide ion (H···Br 2.136 Å and 1.824 Å).⁶¹ However, the N···H···Br angles (111.9°, 89.9°) were lower than the 120° cutoff commonly assigned to hydrogen bonds.⁶⁴ The same held for a primary ammonium iodide (H···I 2.351 Å and 2.420 Å; N···H···I 103.1°, 98.4°)⁶² and chloride (H···Cl 2.202 Å and 2.345 Å; N···H···I 110.0°, 100.34°).⁶³

(61) Menif, R.; Reibenspies, J.; Martell, A. E. Synthesis, protonation constants, and copper(II) and cobalt(II) binding constants of a new octaaza macrobicyclic cryptand: (MX)₃(TREN)₂. Hydroxide and carbonate binding of the dicopper(II) cryptate and crystal structures of the cryptand and of the carbonato-bridged dinuclear copper(II) cryptate. *Inorg. Chem.* **1991**, *30*, 3446-3454.

(62) Vinciguerra, B.; Zavalij, P. Y.; Isaacs, L. Synthesis and Recognition Properties of Cucurbit[8]uril Derivatives. *Org. Lett.* **2015**, *17*, 5068-5071.

(63) Mulagaleev, R. F.; Leshok, D. Y.; Starkov, A. K.; Matsulev, A. N.; Kirik, S. D. *Private Communication to the Cambridge Structural Database (CSD)* **2016**.

(64) (a) Taylor, R.; Kennard, O. *Acc. Chem. Res.* **1984**, *17*, 320-326; see especially Figure 2. (b) Wood, P. A.; Allen, F. H.; Pidcock, E. Hydrogen-bond directionality at the donor H atom—analysis of interaction energies and database statistics. *CrystEngComm* **2009**, *11*, 1563-1571.

(65) (a) Zarychta, B.; Bujak, M.; Zaleski, J. Phase Transitions and Distortion of $[\text{BiCl}_6]^{3-}$ Octahedra in $(\text{C}_3\text{H}_5\text{NH}_3)_3[\text{BiCl}_6]$ — DSC and Single-Crystal X-Ray Diffraction Studies. *Z. Naturforsch. B.* **2004**, *59*, 1029-1034. (b) Tacke, R.; Burschka, C.; Richter, I.; Wagner, B.; Willeke, R. Lewis Acidity Expressed in Neutral Electron-Rich Aluminum(III) Complexes: An Example of Ligand-Defined Catalysis. *J. Am. Chem. Soc.* **2000**, *122*, 8480-8485.

(66) (a) Jiang, W.; Sattler, D.; Rissanen, K.; Schalley, C. A. [4]Pseudorotaxanes with Remarkable Self-Sorting Selectivities. *Org. Lett.* **2011**, *13*, 4502-4505. (b) Bu, X. H.; Feng, P. Y.; Stucky, G. D. Host-Guest Symmetry and Charge Matching in Two Germanates with Intersecting Three-Dimensional Channels. *Chem. Mater.* **2000**, *12*, 1505-1507.

(67) Ghosh, S. K.; Lewis, K. G.; Kumar, A.; Gladysz, J. A. Syntheses of Families of Enantiopure and Diastereopure Cobalt Catalysts Derived from Trications of the Formula $[\text{Co}(\text{NH}_2\text{CHArCHArNH}_2)_3]^{3+}$. *Inorg. Chem.* **2017**, *56*, 2304-2320.

(68) Ehnbohm, A. work in progress, Texas A&M University.

(69) Sessler, J. L.; Lawrence, C. M.; Jayawickramarajah, J. Molecular recognition *via* base-pairing. *Chem. Soc. Rev.* **2007**, *36*, 314-325.

10. SUMMARY

This work has overall forged a stronger bond between computational and experimental aspects of chemistry with rich examples demonstrating this. Broadly defined, molecular devices in this work specifically imply molecular gyroscopes, wires, and molecular polygons, all of which have been investigated using computational tools. The spectroscopic ^{13}C NMR signatures in lengthy polyynes carbon chains can be challenging, or near impossible, to determine for an experimental chemist. However, herein, this work has unambiguously assigned the spectroscopic signatures, for simple $\text{H}(\text{C}\equiv\text{C})_n\text{H}$ type of species but then also applied the same theoretical model for larger and more intricate metal end capped systems of the formulae $\text{L}_y\text{M}(\text{C}\equiv\text{C})_n\text{Z}$ ($\text{M} = \text{Pt}$, $\text{Z} = \text{SiR}_3$). On the same theme, *molecular polygons* containing *polyynes* linkers have shown to be flexible and crystallize in both planar and puckered forms. The computational methods used herein deconvoluted their path of interconversion and also show both forms to be energetically accessible. More importantly, the theoretical insights developed show a strongly negatively charged space in the Pt_4C_{16} complexes $[(\text{R}_2\text{C}(\text{CH}_2\text{PPh}_2)_2)[\overline{\text{Pt}(\text{C}\equiv\text{C})_2}]_4$, suggesting that the void core would be susceptible for cation binding. This was later evidenced with yet unpublished crystallographic X-ray data, characterizing various solvates of ammonium salts binding to the core of the Pt_4C_{16} complexes.

This work has evidenced a mechanism of interconversion of cage compounds that can be formed when *molecular gyroscopes* are stripped of their metal center. The remaining macrobicyclic "cages" of the type $P((CH_2)_n)_3P$ have two lone pairs that either can face outwards or inwards in the two limiting conformations termed "*out,out*" and "*in,in*". Interestingly, and analogous to turning a shirt inside out, these two forms can interchange by a simple process called *homeomorphic isomerization* where one of the three $(CH_2)_n$ linkers is threaded through the "loop" spanned by the remaining two linkers. This mechanism was examined as detailed in this work and shown to be operable for cages of the size $n > 13$ and the different NMR ^{31}P chemical shift signals that experimentalist observe match the computational models.

Molecular gyroscopes provide an almost unbound scene of properties to investigate. A new aspect is that they can be paired with *two* rotators, forming a molecular structure, which can be likened to a gearbox with molecular spur gear, where each metal center (if it can rotate) constitutes one gear. The steric features of each of these metal centers is important in order to evaluate whether these molecular entities can function like a gearbox or if it is static due to steric constraints. Our computational insight provided understanding as steric boundaries allowed for the rotator to be static or dynamic. Critical spectroscopic signatures in challenging infrared $\nu_{C\equiv O}$ bands were further unambiguously assigned using computations.

Ultimately, the synergism between computations and experiments are becoming increasingly important, not only due to the many advancements of the fundamental theoretical models thus leading to improved results, yet, the entire field has undergone a

paradigmatic shift due to the very recent advancements of machine learning and artificial intelligence. The ever-increasing role of artificial intelligence and automation is likely merely the beginning of a new era, even more profoundly uniting experimental and theoretical chemistry.

APPENDIX A

A.1. Additional crystallographic data

The three independent molecules found in the unit cell of crystalline *trans-7c* are depicted in Figure 11.1.

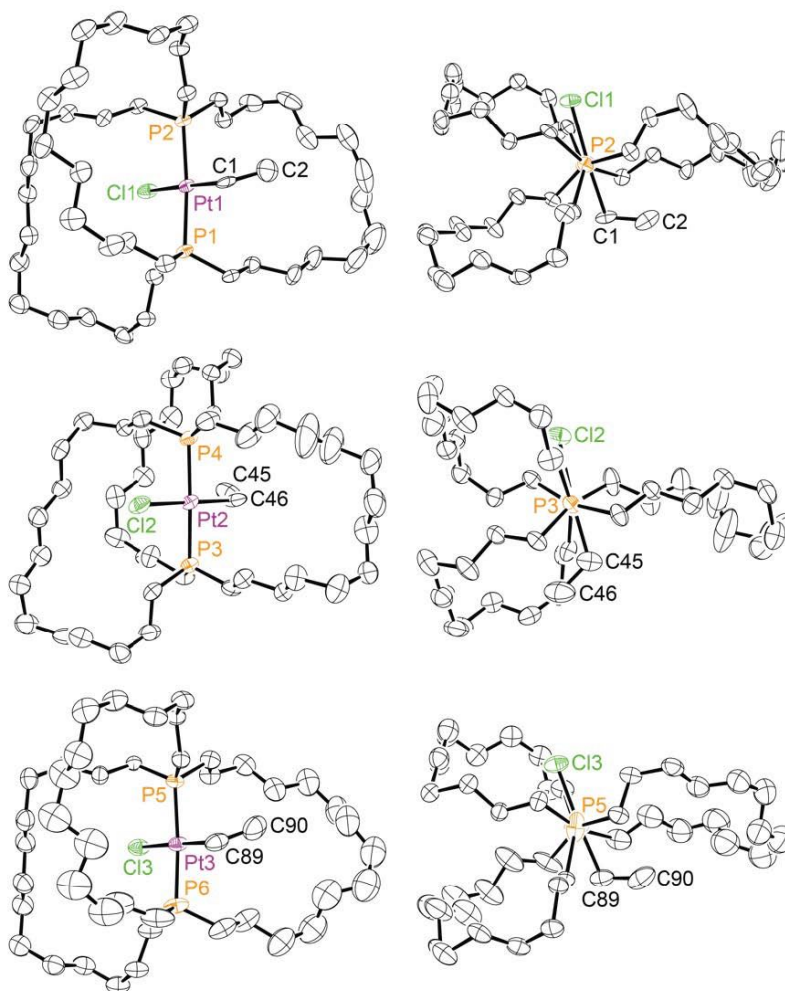


Figure 11.1 Thermal ellipsoid plots of the molecular structure of *trans-7c* (50% probability level, three independent molecules).

A.2. Computational section

A.2.1. General considerations

The general computational methodology employed is outlined in Figure 11.2. The conformational spaces of all species were first sampled using molecular mechanics and simulated annealing (MM/MD), following a protocol reported in an earlier study.¹ This method is fast and has the ability to sample hundreds of thousands of conformations; however, the inherent level of theory is based on force fields. Several of the structures were submitted for Born Oppenheimer Molecular Dynamics (BOMD) (QM/MD), where the forces for the Newtonian trajectories are computed in each time frame (on-the-fly) using Density Functional Theory (DFT).^{2,3} Because the end results varied very little between the techniques, the BOMD data will not be presented.

Structures were sampled and extracted from both techniques and were further optimized using DFT. The same level of theory in the DFT optimizations was used in the BOMD calculations. Ten low-energy conformations throughout each trajectory were extracted from the MM/MD simulated annealing simulation for subsequent DFT optimization. The MD simulations allow sampling of structures over time, and at elevated temperatures, matching experimental conditions.

All extracted structures were subjected to DFT optimizations (in the gas phase) at the B3LYP/6-311+G(d) level of theory.^{4,5} Grimme's dispersion corrections (GD3BJ) were crucial to establish conformations also found crystallographically.^{1b,6} An ultrafine grid, (routeline command "int=ultrafine"), which is the default in Gaussian 16, was employed.⁷ Subsequent single point corrections using implicit solvent models (SMD) in

toluene and *o*-C₆H₄Cl₂ (in addition to gas phase) were performed.⁸ All DFT extracted species were also separately subjected to frequency calculations and the statistical mechanical corrections were made for $T = 298$ and 414 K [141 °C]. The results are plotted in the main text (Figure 3.5 and Figure 3.6) for the full complexes and acyclic models, respectively.

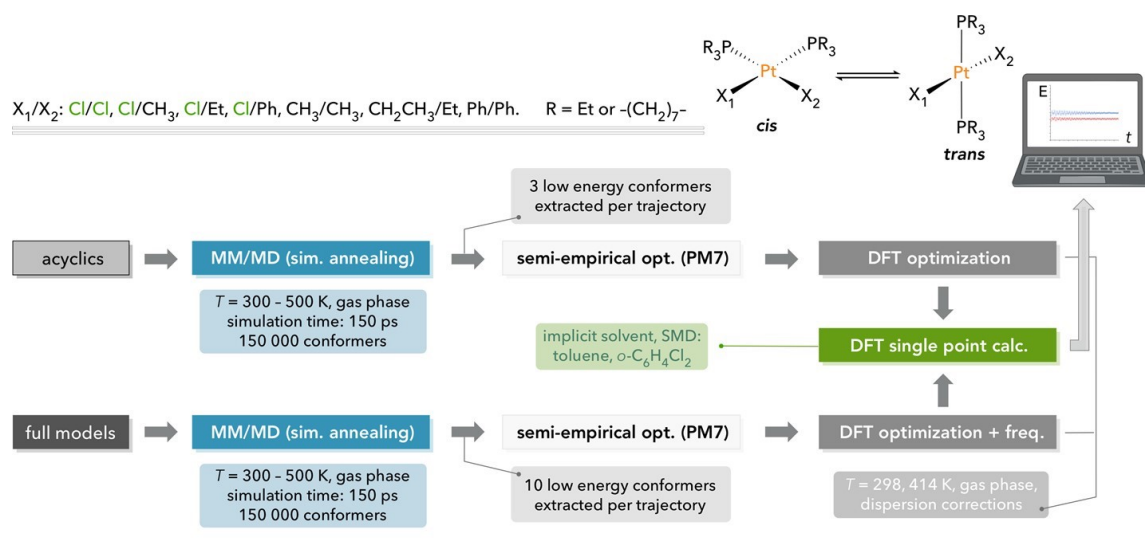


Figure 11.2 A graphical overview of the computational sequence used in this study.

Due to the elevated temperature, and thus access to higher vibrational modes, certain bonds can be elongated in the extracted structures (in particular for the modern BOMD method). Thus, a semiempirical (PM7) optimization was performed on all extracted species from the QM/MD and MM/MD simulations computations before subjecting them to DFT optimizations, in order to accelerate the latter.⁹

A.2.2. Details of the simulated annealing (MM/MD) calculations

The simulated annealing calculations employed the Forcite module in MaterialsStudio™ with NVT ensembles using random initial velocities, initial temperatures of 300 K, mid-cycle temperatures of 500 K, heating ramps per cycle is five, and 10,000 dynamic steps per ramp.¹⁰ Thus, the total number of steps was 15,000,000. The sampled structures were automatically geometry optimized after each cycle using the smart algorithm with a "fine" convergence tolerance (energy of 0.0001 kcal/mol, force of 0.005 kcal/mol·Å, displacement of 0.00005 Å, maximum of 10,000 iterations). The time steps in the annealing cycles were 1.0 femtoseconds, generating a total simulation time of 150 nanoseconds. The universal force fields¹¹ (UFF) was used with atom based electrostatics *and* van der Waals terms using cubic spline truncation, cutoff distances of 15.5 Å, spline widths of 1.0 Å, and buffer widths of 0.5 Å.

A.2.3. Simulated annealing MM/MD data:

The generated annealing MM/MD data for *cis* (×) and *trans* (○) platinum species *cis/trans-5c, 7c, 8c, 4c, 6c, 3c* are given in the same plot (Figure 11.3 and Figure 11.4). Each panel represents a different complex, and all were run in the gas phase. These data show that there is a large conformational space for each isomer at the 17-membered

macrocycle size ($n = 14$). It was found that this MD technique distorts and samples the conformational space better than the BOMD technique. This is presumably caused by the larger temperature range of the simulated annealing setup, subjecting species to cycling temperatures ranging from 300 to 500 K. The drawback of this methodology is that only gas phase calculations are available in the computational suite in MaterialsStudio. Thus, it was decided to further pursue calculations using BOMD, although only for evaluative purposes (i.e. quality assurance). The MM/MD data in Figure 11.3 to Figure 11.6 shows the potential energy plotted in kcal/mol versus the simulation time in femtoseconds.

GaussView 6.1.1¹² was used to study the different trajectories and VMD 1.9.3¹³ was used to generate videos. CylView 1.0¹⁴ was used to visualize specific frames and computational models throughout the study, including the DFT data.

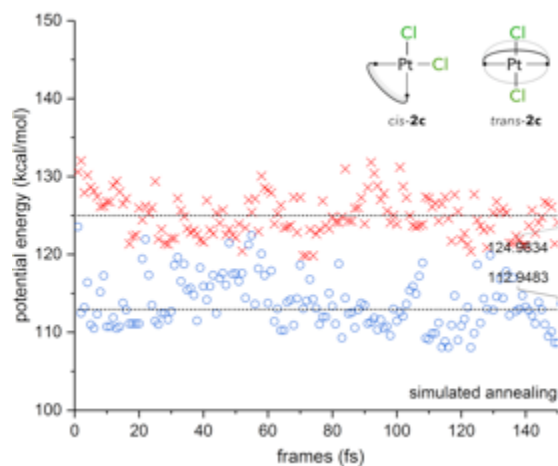


Figure 11.3 Molecular dynamics simulations (MM/MD, simulated annealing) of *cis-2c* (×) and *trans-2c* (○). The trajectories are run in the gas phase.

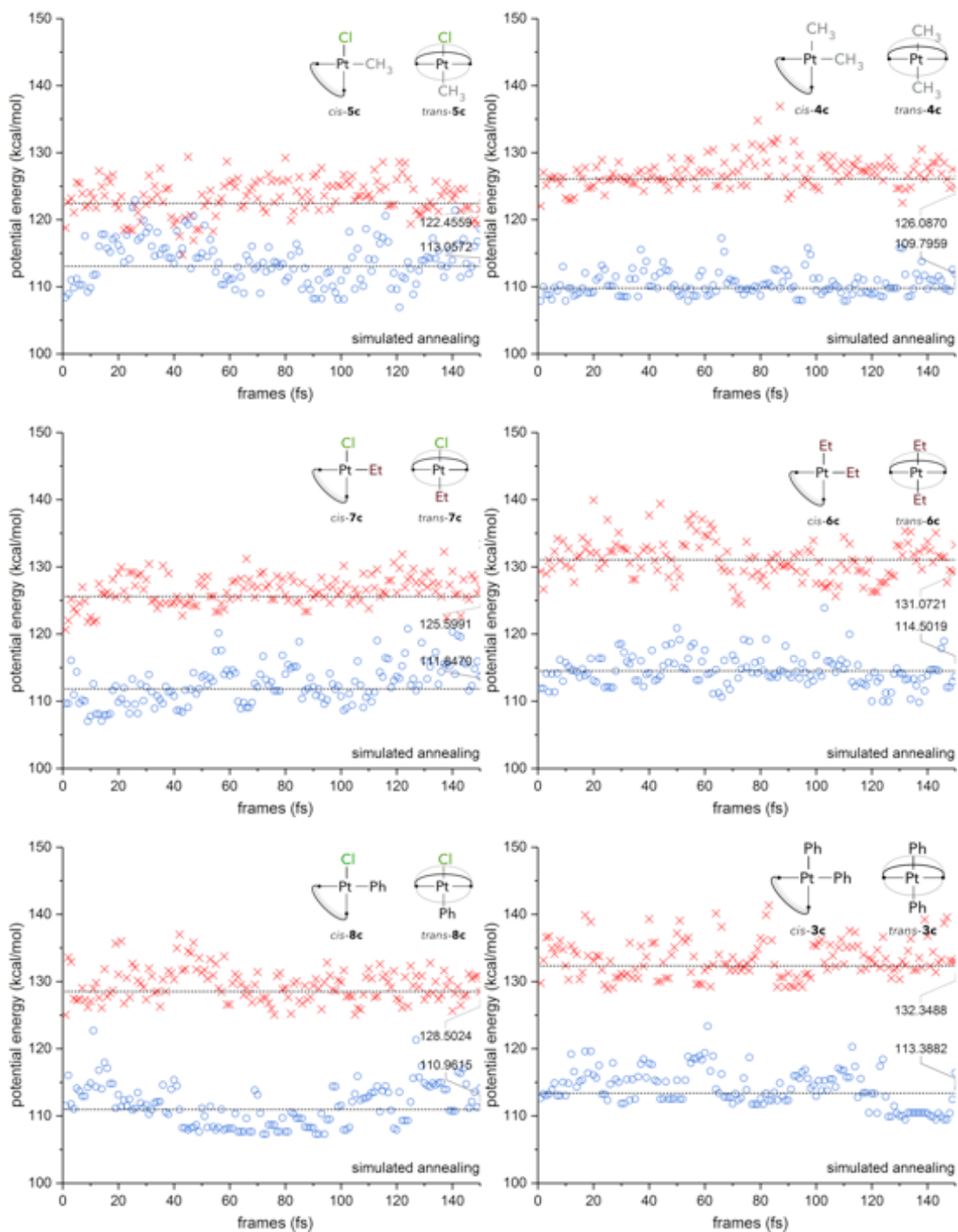


Figure 11.4 Molecular dynamics simulations (MM/MD, simulated annealing) of *cis/trans*-**5c**, **7c**, **8**, **4c**, **6c**, **3c**. The trajectories are run in the gas phase.

Truncated models using $\text{P}(\text{CH}_2\text{CH}_3)_3$ ligands were constructed to understand electronic effects and avoid bias from macrocyclic cages with large degrees of freedom. The simpler $\text{P}(\text{CH}_3)_3$ analogue could have been used; however, the electronic effect exerted by $\text{P}(\text{CH}_2)_{14}$ is better represented by $\text{P}(\text{CH}_2\text{CH}_3)_3$.¹⁵ These species were subjected to the same type of calculation conditions as the full models discussed in the preceding sections (see Figure 11.5 and Figure 11.6 for the results). This allows one to accurately map the electronic contributions of different ligands.

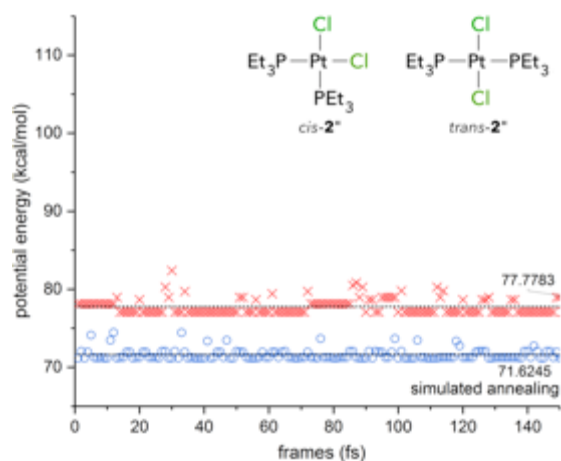


Figure 11.5 Molecular dynamics simulations (MM/MD, simulated annealing) of acyclic *cis-2''* (×) and *trans-2''* (○). The trajectories are run in the gas phase.

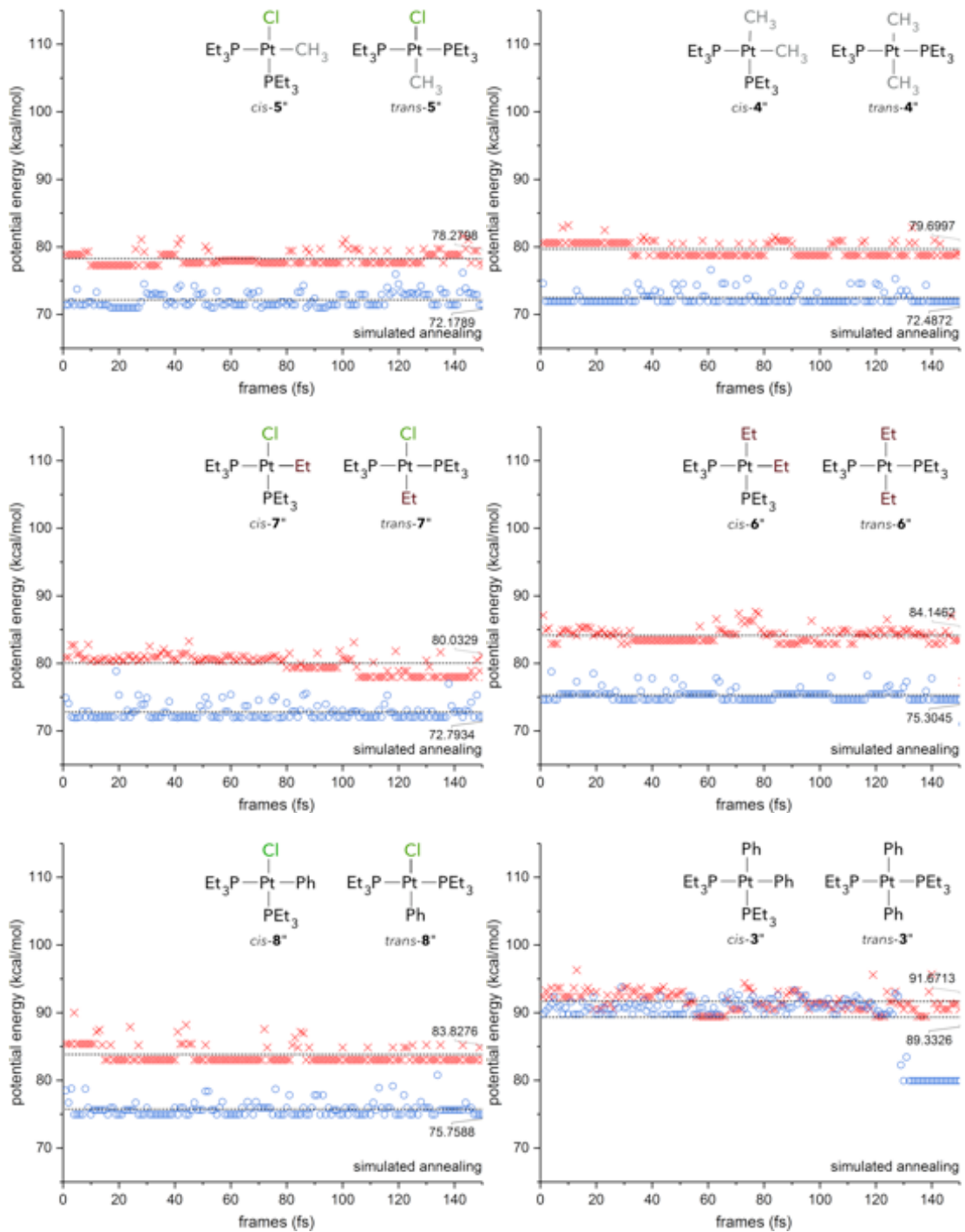


Figure 11.6 Molecular dynamics simulations (MM/MD, simulated annealing) of acyclic *cis/trans-5**, *7**, *8**, *4**, *6**, *3**. The trajectories are run in the gas phase.

A.2.4. Details of the Born-Oppenheimer molecular dynamics (DFT/MD) simulations

The Born-Oppenheimer molecular dynamics (BOMD) simulations were performed at the B3LYP-GD3BJ/6-311+G(d)^{s04,s05} level of theory, and were only run for evaluative purposes (i.e. quality assurance of the MM/MD data). A fully relativistic effective core potential (ECP60MDF) paired with a correlation consistent triple- ζ -quality basis set (cc-pVTZ-PP) was used on the platinum atom.¹⁶ A benchmark study for the selected DFT level of theory is provided in section 0 and additional DFT details are found in section 0. Useful protocols for BOMD calculations featuring direct examples can be found in the supplementary information of references 02 and 03. Relevant information has been provided below. The BOMD calculations were all performed at temperatures ($T = 141$ °C) and in solvents (toluene, *o*-C₆H₄Cl₂), in addition to the gas phase ($T = 25$ °C).

In the currently used implementation of BOMD in Gaussian, all forces are quantum mechanically evaluated at each frame (using DFT). The BOMD calculations use the same level of theory as in the separate DFT optimizations (see section 0). The nuclear motion is non-quantized and the velocity Verlet integration algorithm is applied to the Newtonian equations of motion. A microcanonical ensemble is responsible for the propagation of the trajectories. Thus, the total energy (the sum of potential E_p and kinetic energy E_k) is conserved, as is the number of particles N and volume V . A random Maxwell-Boltzmann distribution assigns the initial velocity of each atom with E_k being adjusted depending on the simulation temperature ($T = 414$ K, 140 °C which was set to

match the experimental conditions). The zero point energy is not included in these calculations.

The temperature was implemented through the keyword "*nke*" (initial kinetic energy) as there is currently no implemented temperature thermostat in Gaussian. Equation (1) was used where N_{Atoms} is the total number of atoms of the system, k is the Boltzmann constant, and T is the given temperature.

$$nke = (N_{\text{Atoms}} - 1) \times \frac{3}{2} kT \quad (\text{eq. 1})$$

The following generic routine exemplifies the different parameters used in the BOMD calculations.

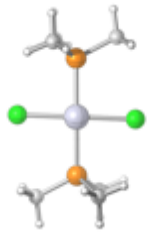
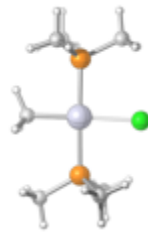
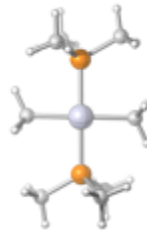
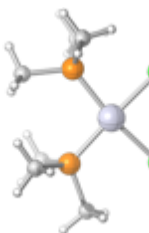
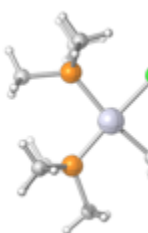
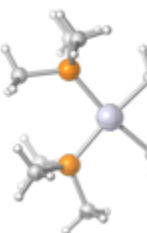
```
#p B3LYP/genecp iop(1/44=$random_seed) BOMD(gradientonly, stepsize=$n,  
sample=microcanonical, randomvelocity, maxpoints=$maxpoint, nke=$nke) empirical-  
dispersion=GD3BJ scrf=(smd,solvent=S), int=ultrafine.
```

The term *\$random_seed* determines the random number generation seeds. *\$maxpoint* is the total simulation time and one femtosecond step size is used. *S* is the given solvent, which in this study is toluene or *o*-C₆H₄Cl₂.

A.2.5. Benchmark study

A benchmark study was performed on the smallest *cis* and *trans* species carrying no chelating ligand, i.e. Cl/Cl, Cl/CH₃, and CH₃/CH₃, all with P(CH₃)₃. The data are recorded in Table 11.1. A variety of functionals and different families of basis sets were used. The data conclusively demonstrate that the choice of functional does not impact the energetic drastically and that the accuracy of the previously used level of theory [B3LYP-GD3BJ/6-311+G(d)] is sufficient to determine the relative energetics.

Table 11.1 Computed stability differences (kcal/mol) of key pairs of *cis/trans* species.

						
						
functional	basis set ^a	solvent ^b	dispersion correction ^c	Cl/Cl ^d (<i>cis</i> vs. <i>trans</i>)	Cl/CH ₃ ^d (<i>cis</i> vs. <i>trans</i>)	CH ₃ /CH ₃ ^d (<i>cis</i> vs. <i>trans</i>)
B3LYP	6-311+G(<i>d</i>)	gas	GD3BJ	-6.0	-5.3	2.3
TPSS	6-311+G(<i>d</i>)	gas	GD3BJ	-4.2	-3.9	3.4
CAM-	6-311+G(<i>d</i>)	gas	GD3BJ	-7.0	-5.9	1.6
M06	6-311+G(<i>d</i>)	gas	GD3	-6.7	-5.3	2.3
B3LYP	6-311+G(<i>d</i>)	H ₂ O	GD3BJ	6.1	-1.4	3.4
B3LYP	6-311+G(<i>d</i>)	C ₆ H ₆	GD3BJ	-1.6	-4.3	2.4
B3LYP	6-311+G(<i>d</i>)	Et ₂ O	GD3BJ	1.2	-3.3	2.7
B3LYP	6-311++G(<i>d</i>)	gas	GD3BJ	-6.0	-5.3	2.4
B3LYP	6-311++G(2 <i>d</i> ,2 <i>p</i>)	gas	GD3BJ	-5.2	-5.0	2.1
B3LYP	def2-SVP	gas	GD3BJ	-5.1	-4.8	2.4
B3LYP	def2-TZVP	gas	GD3BJ	-4.4	-4.5	2.0
B3LYP	def2-QZVP	gas	GD3BJ	-4.3	-4.6	1.8
B3LYP	cc-PVDZ	gas	GD3BJ	-5.6	-5.2	2.6
B3LYP	cc-PVQZ	gas	GD3BJ	-4.5	-4.6	2.0
ωB97X-D	6-311+G(<i>d</i>)	gas	—	-6.8	-5.9	1.6

^a The platinum atom was fitted with a triple- ζ -quality basis set (cc-pVTZ-PP) paired with a fully relativistic effective core potential (ECP60MDF). ^b Truhlar's universal continuum solvation model (SMD) was used. ^c Grimme's empirical dispersion corrections with Becke-Johnson damping were used in all applicable cases except for incompatible functionals. ^d Relative total electronic energy between the *cis/trans* species in which the *cis* dichloride, monochloride, and dimethyl complexes are set to zero (0 kcal/mol).

A.2.6. Electronic structure theory, DFT

Electronic structure calculations employed the Gaussian (revision C.01) program package using the ultrafine grid (99,590) to enhance accuracy.⁷ Gas phase geometries were optimized using DFT. The B3LYP⁴ functional was paired with an all-electron triple- ζ -quality 6-311+G(d)⁵ basis set on all atoms except platinum. For platinum a fully relativistic effective core potential (ECP60MDF) was paired with a correlation consistent triple- ζ -quality basis set (cc-pVTZ-PP).¹⁶ The choice of functional and basis set was based on a previous study for similar structures where good agreement was reached between experiment and theory (structural and energetic data). A benchmark study (section 0) was further undertaken to showcase that there were small variations in relative energies among commonly used functionals and even higher quality basis set. Dispersion corrections were implemented using the D3 version of Grimme's dispersion function with Becke-Johnson damping (referred to as GD3BJ).^{s06} These are critical for the correct folding of the ligand scaffolds as can be shown in the model structure in Figure 11.7. A sample input file for an optimization is provided after the reference section.

Selected computed structures (one conformation per complex) are provided in a separate concatenated *xyz* formatted text file in the published supplementary information. These files can be easily opened using a variety of free software, e.g. Mercury.^{s17} The bond distance data provided in Figure 3.7 is based on an average of three computed conformers per complex.

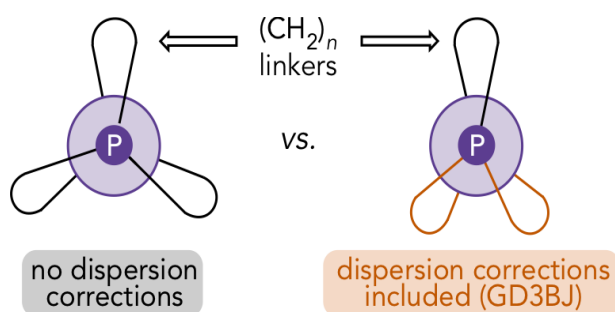


Figure 11.7. Views of gyroscope like complexes showing attractions between two $(\text{CH}_2)_n$ bridges if dispersion corrections are used.

A.2.7. Energetics of excised diphosphine ligands, single point calculation (DFT)

To further probe the origin of the energy differences associated with the *cis*/parachute and *trans*/gyroscope isomers (ca. 6.6 kcal/mol with $(\text{CH}_2)_{14}$ bridges; see Figure 3.5 and Figure 3.6), and respond to a reviewer inquiry, additional computations involving $\text{P}((\text{CH}_2)_{14})_3\text{P}$, $\text{H}_2\text{P}(\text{CH}_2)_{14}\text{PH}_2$ and $\text{HP}((\text{CH}_2)_{14})_2\text{PH}$ species were submitted. First, the PtX_2 or PtXX' fragments were excised from the complexes in Figure 3.5, leaving only the $\text{P}((\text{CH}_2)_{14})_3\text{P}$ scaffolds. These were computed at the same level of theory as in the preceding DFT investigations, but only single-point calculations were performed, keeping all atoms fixed. The relative electronic energies of the $\text{P}((\text{CH}_2)_{14})_3\text{P}$ species stemming from the *cis/trans* complexes are presented in Figure 11.8 (average difference = -4.6 kcal/mol). Note that only *one* of the 10 conformers from each complex was computed. The PtX_2 or PtXX' fragment designations are retained in Figure 11.8 to identify the complex of origin.

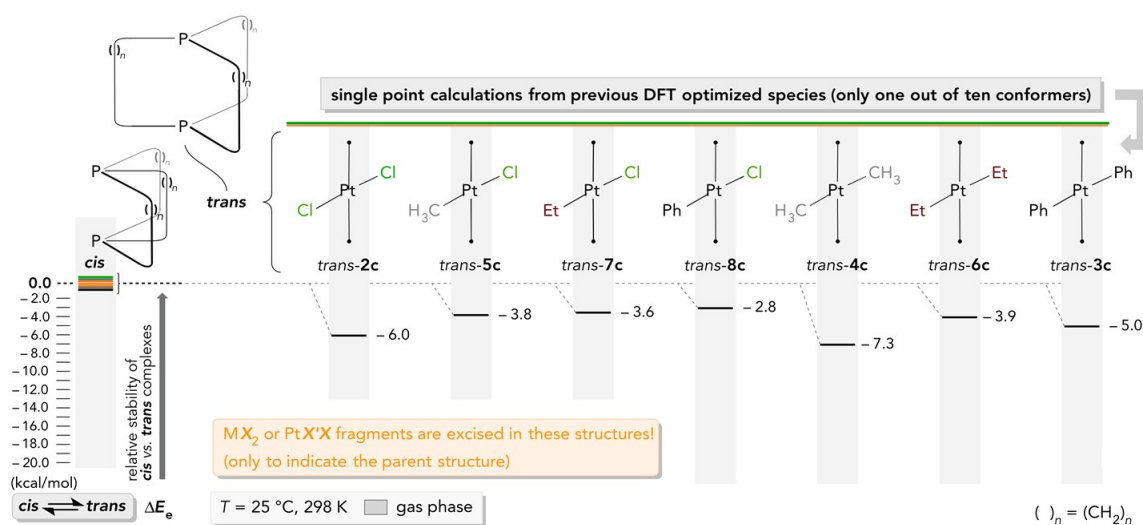
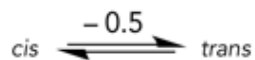


Figure 11.8. Structures and relative electronic energies from single point energy calculations on $P((CH_2)_{14})_3P$ scaffolds excised from the platinum complexes indicated.

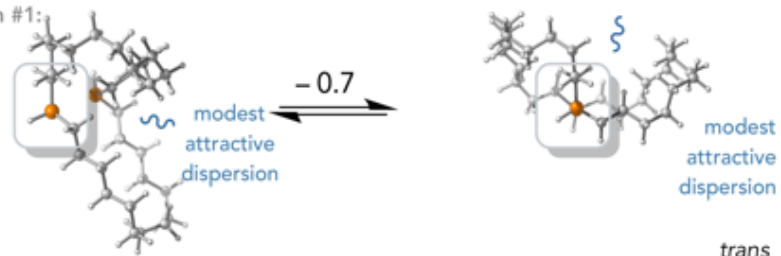
Next, single-point calculations on the $H_2P(CH_2)_{14}PH_2$ and $HP((CH_2)_{14})_2PH$ systems derived from *cis/trans-2c* were carried out. The electronic energy differences between the *cis/trans* species are shown in Figure 11.9, together with the "three stranded" $P((CH_2)_{14})_3P$ species from *cis/trans-2c*. The energetic differences are minimal in $H_2P(CH_2)_{14}PH_2$, but much greater in both the $HP((CH_2)_{14})_2PH$ and $P((CH_2)_{14})_3P$ systems. In all equations, *trans* isomers are favored. This suggests that interactions between the chains are important for understanding energetic differences in these diphosphine scaffolds.

one strand: average energy: -0.5 kcal/mol favoring the *trans* species excised from *cis/trans-2c*



two strands: average energy: -2.5 kcal/mol favoring the *trans* species excised from *cis/trans-2c*

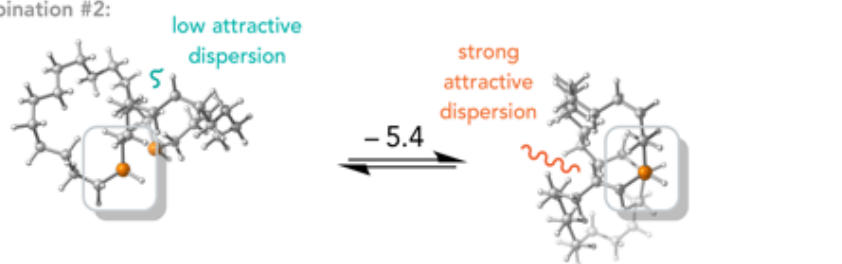
combination #1:



cis

trans

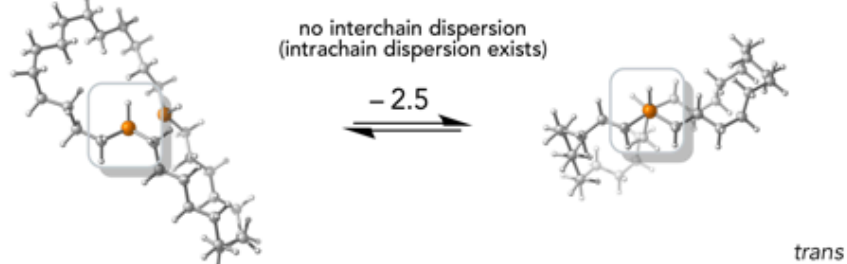
combination #2:



cis

trans

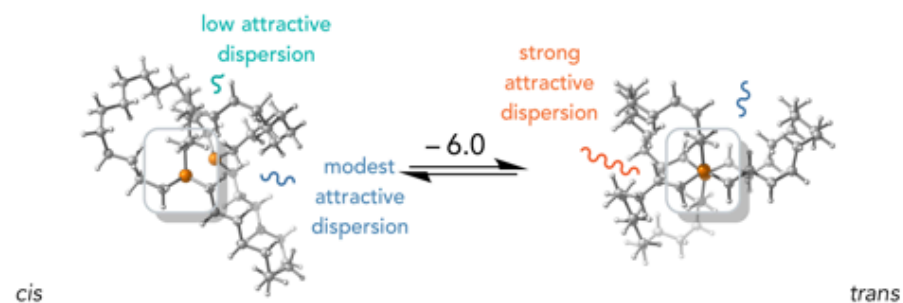
combination #3:



cis

trans

three strands: -6.0 kcal/mol favoring the *trans* species excised from *cis/trans-2c*



cis

trans

Figure 11.9. Structures and relative electronic energies from single point energy calculations of the diphosphines $\text{H}_2\text{P}(\text{CH}_2)_{14}\text{PH}_2$, $\text{HP}((\text{CH}_2)_{14})_2\text{PH}$, and $\text{P}((\text{CH}_2)_{14})_3\text{P}$ derived from the parent platinum complexes *cis/trans-2c*.

A.3. References

(1) Joshi, H.; Kharel, S.; Ehnbohm, A.; Skopek, K.; Hess, G. D.; Fiedler, T.; Hampel, F.; Bhuvanesh, N.; Gladysz, J. A. Three-Fold Intramolecular Ring Closing Alkene Metatheses of Square Planar Complexes with *cis* Phosphorus Donor Ligands $P(X(CH_2)_mCH=CH_2)_3$ ($X = -$, $m = 5-10$; $X = O$, $m = 3-5$): Syntheses, Structures, and Thermal Properties of Macrocyclic Dibrigehead Diphosphorus Complexes. *J. Am. Chem. Soc.* **2018**, *140*, 8463-8478.

(2) Pu, M.; Sanhueza, I. A.; Senol, E.; Schoenebeck, F. Divergent Reactivity of Stannane and Silane in the Trifluoromethylation of Pd^{II} : Cyclic Transition State versus Difluorocarbene Release. *Angew. Chem. Int. Ed.* **2018**, *57*, 15081-15085.

(3) Scattolin, T.; Pu, M.; Schoenebeck, F. Investigation of $(Me_4N)SCF_3$ as a Stable, Solid and Safe Reservoir for $S=CF_2$ as a Surrogate for Thiophosgene. *Chem. Eur. J.* **2018**, *24*, 567-571.

(4) (a) Becke, A. D. Density-functional exchange-energy approximation with correct asymptotic behavior. *Phys. Rev. A*, **1988**, *38*, 3098-3100. (b) Becke, A. D. Density-functional thermochemistry. III. The role of exact exchange. *J. Chem. Phys.* **1993**, *98*, 5648-5652. (c) Lee, C.; Yang, W.; Parr, R. G. Development of the Colle-Salvetti correlation energy formula into a functional of the electron density. *Phys. Rev. B.* **1988**, *37*, 785-789.

(5) References for Pople type basis set "**6-311G**" are as follows (an addition of "d" adds polarization functions of *d*-type to C, "p" adds *p*-type polarization functions to C and H atoms, and "+/++" indicates added diffuse functions): (a) McLean, A. D.;

Chandler, G. S. Contracted Gaussian basis sets for molecular calculations. I. Second row atoms, $Z = 11-18$. *J. Chem. Phys.* **1980**, *72*, 5639-5648. (b) Raghavachari, K.; Binkley, J. S.; Seeger, R.; Pople, J. A. Self-consistent molecular orbital methods. XX. A basis set for correlated wave functions. *J. Chem. Phys.* **1980**, *72*, 650-654.

(6) Grimme, S.; Ehrlich, S.; Goerigk, L. Effect of the damping function in dispersion corrected density functional theory. *J. Comput. Chem.* **2011**, *32*, 1456-1465.

(7) Gaussian 16, *Revision C.01*, Frisch, M. J.; Trucks, G. W.; Schlegel, H. B.; Scuseria, G. E.; Robb, M. A.; Cheeseman, J. R.; Scalmani, G.; Barone, V.; Petersson, G. A.; Nakatsuji, H.; Li, X.; Caricato, M.; Marenich, A. V.; Bloino, J.; Janesko, B. G.; Gomperts, R.; Mennucci, B.; Hratchian, H. P.; Ortiz, J. V.; Izmaylov, A. F.; Sonnenberg, J. L.; Williams-Young, D.; Ding, F.; Lipparini, F.; Egidi, F.; Goings, J.; Peng, B.; Petrone, A.; Henderson, T.; Ranasinghe, D.; Zakrzewski, V. G.; Gao, J.; Rega, N.; Zheng, G.; Liang, W.; Hada, M.; Ehara, M.; Toyota, K.; Fukuda, R.; Hasegawa, J.; Ishida, M.; Nakajima, T.; Honda, Y.; Kitao, O.; Nakai, H.; Vreven, T.; Throssell, K.; Montgomery, J. A. Jr.; Peralta, J. E.; Ogliaro, F.; Bearpark, M. J.; Heyd, J. J.; Brothers, E. N.; Kudin, K. N.; Staroverov, V. N.; Keith, T. A.; Kobayashi, R.; Normand, J.; Raghavachari, K.; Rendell, A. P.; Burant, J. C.; Iyengar, S. S.; Tomasi, J.; Cossi, M.; Millam, J. M.; Klene, M.; Adamo, C.; Cammi, R.; Ochterski, J. W.; Martin, R. L.; Morokuma, K.; Farkas, O.; Foresman, J. B.; Fox, D. J. Gaussian, Inc. Wallingford CT, **2016**.

(8) Marenich, A. V.; Cramer, C. J.; Truhlar, D. G. Universal Solvation Model Based on Solute Electron Density and on a Continuum Model of the Solvent Defined by

the Bulk Dielectric Constant and Atomic Surface Tensions. *J. Phys. Chem. B.* **2009**, *113*, 6378-6396.

(9) PM7 (a) Christensen, A. S.; Kubař, T.; Cui, Q.; Elstner, M. Semiempirical Quantum Mechanical Methods for Noncovalent Interactions for Chemical and Biochemical Applications. *Chem. Rev.* **2016**, *116*, 5301-5337. (b) Stewart, J. J. P. Optimization of parameters for semiempirical methods VI: more modifications to the NDDO approximations and re-optimization of parameters. *J. Mol. Model.* **2013**, *19*, 1-32.

(10) Dassault Systèmes BIOVIA, Materials Studio, 6.0, San Diego: Dassault Systèmes, 2017.

(11) Rappé, A. K.; Casewit, C. J.; Colwell, K. S.; W. A. Goddard III, W. A.; Skiff, W. M. UFF, a full periodic-table force field for molecular mechanics and molecular-dynamics simulations. *J. Am. Chem. Soc.* **1992**, *114*, 10024-10035.

(12) GaussView, Version 6.1.1, Roy Dennington, Todd Keith, and John Millam, Semichem Inc. Shawnee Mission, KS, 2019.

(13) W. Humphrey, A. Dalke, and K. Schulten, VMD — Visual Molecular Dynamics, *J. Molec. Graphics*, **1996**, vol. 14, pp. 33-38. (<http://www.ks.uiuc.edu/Research/vmd/>)

(14) CYLview, 1.0b; Legault, C. Y. Université de Sherbrooke, 2009 (<http://www.cylview.org>)

(15) (a) Suresh, C. H.; Koga, N.; Quantifying the Electronic Effect of Substituted Phosphine Ligands via Molecular Electrostatic Potential. *Inorg. Chem.* **2002**, *41*, 1573-

1578. (b) Tolman, C. A. Steric effects of phosphorus ligands in organometallic chemistry and homogeneous catalysis. *Chem. Rev.* **1977**, *77*, 313-348.

(16) Figgen, D.; Peterson, K. A.; Dolg, M. Energy-consistent pseudopotentials and correlation consistent basis sets for the 5*d* elements Hf-Pt. *J. Phys. Chem.* **2009**, *130*, 164108.

(17) Macrae, C. F.; Bruno, I. J.; Chisholm, J. A.; Edgington, P. R.; McCabe, P.; Pidcock, E.; Rodriguez-Monge, L.; Taylor, R.; van de Streek, J.; Wood, P. A. Mercury CSD 2.0 — new features for the visualization and investigation of crystal structures. *J. Appl. Crystallogr.* **2008**, *41*, 466-470.

APPENDIX B

B.1. Computational section

B.1.1. General considerations

The general computational methodology employed is outlined in Figure 12.1. An all-electron triple- ζ -quality basis set def2-TZVP¹ was used on all atoms including iron. Thus, no pseudopotentials were used on the heavier elements. The basis set was paired with the TPSS functional,² which has been shown to closely reproduce the IR spectra of iron carbonyl complexes.³ All computations were performed using the Gaussian program suite, employing an ultrafine grid (99,590) to enhance accuracy.⁴ Complexes were first optimized and then subjected to frequency calculations to conduct a vibrational analysis. Single point calculations using Truhlar's SMD⁵ solvent model in CH₂Cl₂ and paired with Grimme's empirical dispersion corrections (version D3) with Becke-Johnson damping (GD3BJ)⁶ were carried out to obtain more accurate relative thermodynamic energies. Optimized structures were also used as input in scan calculations, which are discussed separately below.

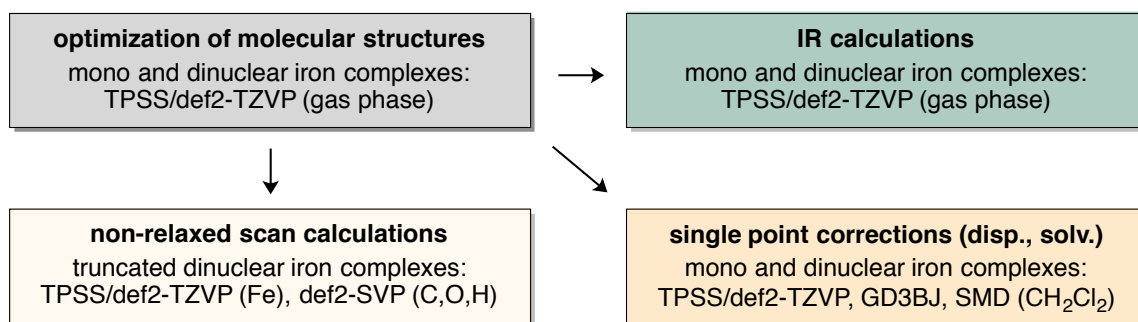


Figure 12.1 A graphical overview of the computational methods employed in this study.

B.1.2. IR spectra

IR spectra were computed for all iron complexes using the same basis set and level of theory from the geometry-optimized structures. These calculations had to be run separately from the geometry optimizations, and with additional memory (150 GB) in order to reach convergence. All structures were deemed to be local minima after the vibrational frequencies were inspected. A scaling factor of 0.9863 was used for all plotted computed data. These were matched based upon the most intense absorptions. This scaling factor was in accord with earlier reports using this functional and basis set combination.⁷ The calculated energies and single point corrections are summarized in Table 12.1. Key $\nu_{\text{C}\equiv\text{O}}$ band patterns are plotted with arrows indicating vibrational amplitudes in Figure 12.2 and Figure 12.3. The corresponding bands are summarized in Table 12.1. The spectra in the text are plotted with linewidths of 4 cm^{-1} unless noted.

All monoiron species $\textit{trans}\text{-}(\text{CO})_3\overline{\text{Fe}[\text{Ph}_2\text{P}(\text{CH}_2)_n\text{PPh}_2]}$ ($n = 1\text{-}6$) (Figure 12.2), which are denoted with prime numbers, exhibit one band in a higher frequency regime corresponding to a *symmetric* vibrational mode (**S**) and two near-degenerate bands in an intermediate to lower frequency regime corresponding to *asymmetric* vibrational modes (**A**). The frequency differences between the two latter bands differ, which can result in the lowest frequency band acquiring a shoulder. These two bands can also merge into a single band, as observed for **1'**. Irrespective of formal coordination geometry, the bands of **1'-5'** show similar relative intensities. However, the relative intensities can change markedly if the diphosphine adopts a *trans* geometry. This causes the high frequency band to lose intensity to the two lower frequency bands.

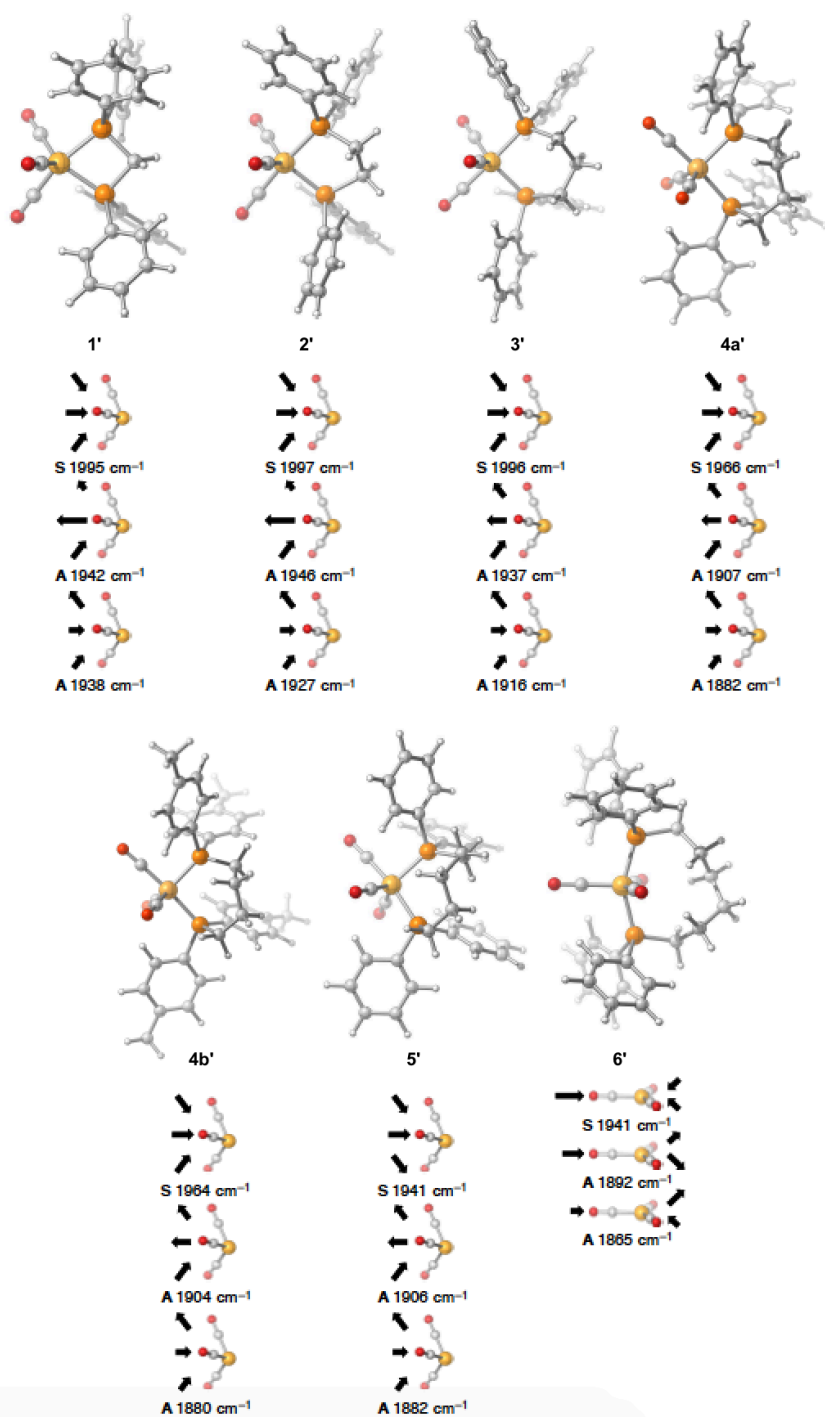


Figure 12.2 Computed structures and vibrational modes of *monoiron* complexes. The lengths of the arrows indicate the relative amplitude.

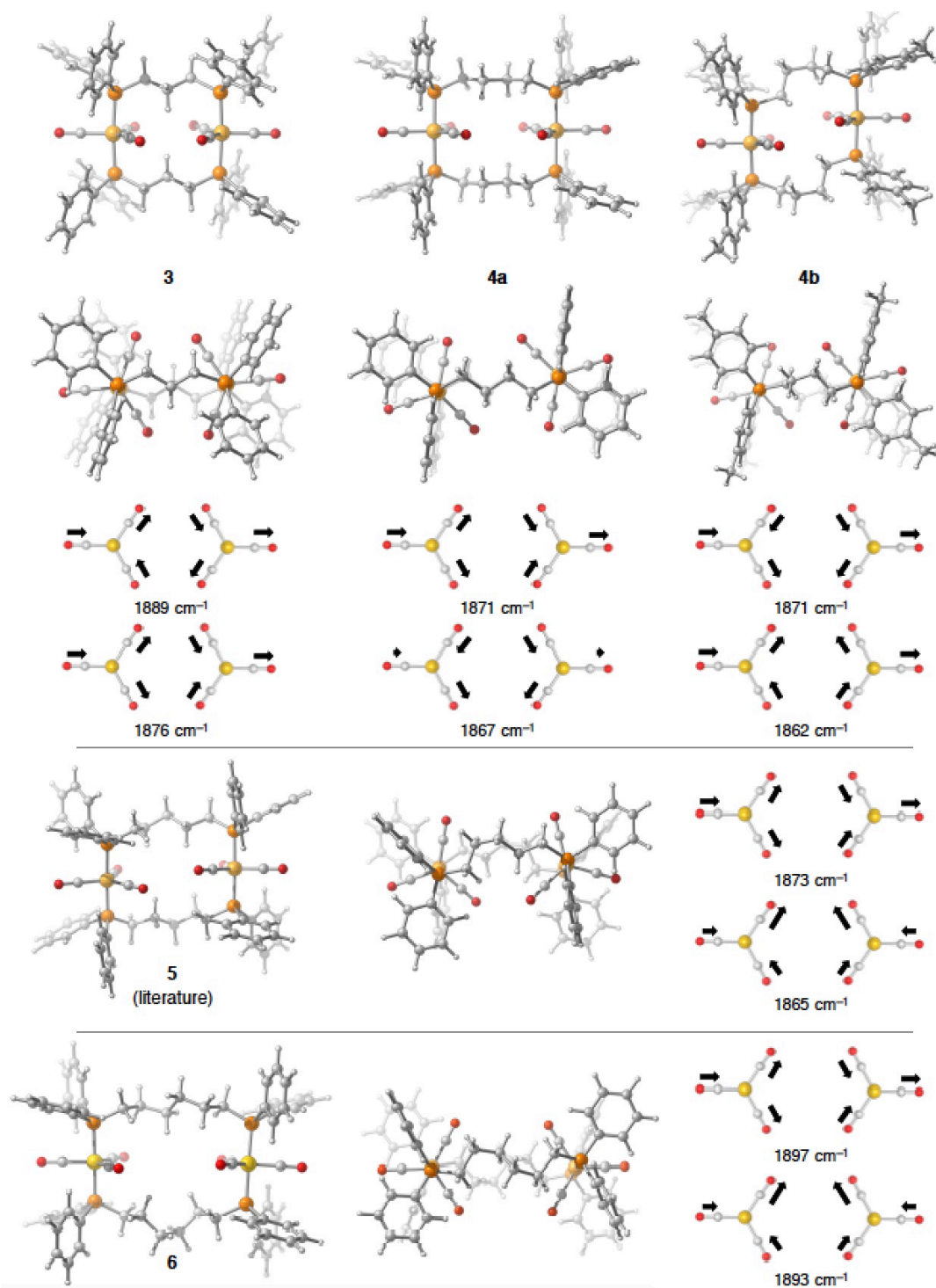


Figure 12.3 Computed structures and vibrational modes of *diiron* complexes. The lengths of the arrows indicate the relative amplitudes.

Table 12.1 Computed IR $\nu_{\text{C}\equiv\text{O}}$ bands and energies for iron carbonyl complexes.

complex	geometry	$\nu_{\text{C}\equiv\text{O}}$ (cm^{-1})	thermal correction to Gibbs energy ^a (Hartree)	electronic energy ^b (CH_2Cl_2 , GD3BJ) (Hartree)	total energy incorporating corrections (Hartree)
1'	sq pyr <i>cis</i> ^c	1968 s, 1915 s, 1911 s	0.343062	-3253.47868	-3253.13562
2'	sq pyr <i>cis</i> ^c	1970 s, 1919 m, 1901 s	0.372904	-3292.83741	-3292.46450
3'	tbp <i>cis</i>	1969 s, 1910 m, 1890 s	0.400573	-3332.17559	-3331.77502
4'a	tbp <i>cis</i>	1966 s, 1907 m, 1882 s	0.429289	-3371.50864	-3371.07935
4'b ^d	tbp <i>cis</i>	1964 s, 1904 m, 1880 s	0.522285	-3528.87724	-3528.35496
5'	tbp <i>cis</i>	1964 s, 1906 m, 1882 s	0.456635	-3410.84409	-3410.38745
6'	sq pyr <i>trans</i>	1941 w, 1892 m, 1865 s	0.482487	-3450.18500	-3449.70252
3	tbp <i>trans</i>	1939 w, 1889 sh, 1876 s	0.823204	-6664.38043	-6663.55722
4a	tbp <i>trans</i>	1933 w, 1871 sh, 1867 s	0.876875	-6743.04981	-6742.17293
4b	tbp <i>trans</i>	1930 w, 1871 s, 1862 s	1.067937	-7057.78633	-7056.71839
5	tbp <i>trans</i>	1935 w, 1873 sh, 1865 s	0.930600	-6821.73448	-6820.80388
6	tbp <i>trans</i>	1960 w, 1897 s, 1893 s	0.981384	-6900.40298	-6899.42159

^a These data were obtained through gas phase optimization and frequency analyses at 298.15 K. ^b These data were obtained from single point calculations using Truhlar's SMD solvation model and Grimme's empirical dispersion correction with Becke-Johnson damping. ^c See comments in Table 4.1 of the main text. ^d This species contained two small imaginary frequencies (less than 15 cm^{-1}) corresponding to the rotation of two methyl groups.

The diiron species have the same number of bands, although the relative intensities differ. The highest intensity bands of **3**, **4a,b**, and **5** are the lowest frequency bands, and are in turn at a slightly lower frequency than the lowest frequency bands of **3'**, **4'a,b**, and **5'**. The band patterns of **3**, **4a,b**, and **5** most closely resemble those of **6'**, a commonality that is likely rooted in the *trans* coordination geometries. Experimentally, the intermediate frequency band can appear as a shoulder on the low frequency band. The calculations sample only the lowest energy structure, whereas the experimental values reflect all accessible conformations under the measurement conditions.

B.1.3. Scan calculations and additional data

To visualize the relative energetics of certain limiting Fe(CO)/Fe(CO)₃ conformations in the diiron complexes, scan calculations were set up. The diphosphine ligand in the optimized structure of **3** was pruned down to PH₃ groups (no (CH₂)₃ segments), the P–Fe–P angles were set to 180°, and the Fe(CO)₃ conformations were fixed per the three orientations in Figure 12.4 (**A**, **B**, **C**). The energies of the assemblies were then interrogated while bringing the two fragments closer together in small increments. The wave functions and energetic data were calculated at each distance. The stability order **B** > **C** > **A** was always observed.

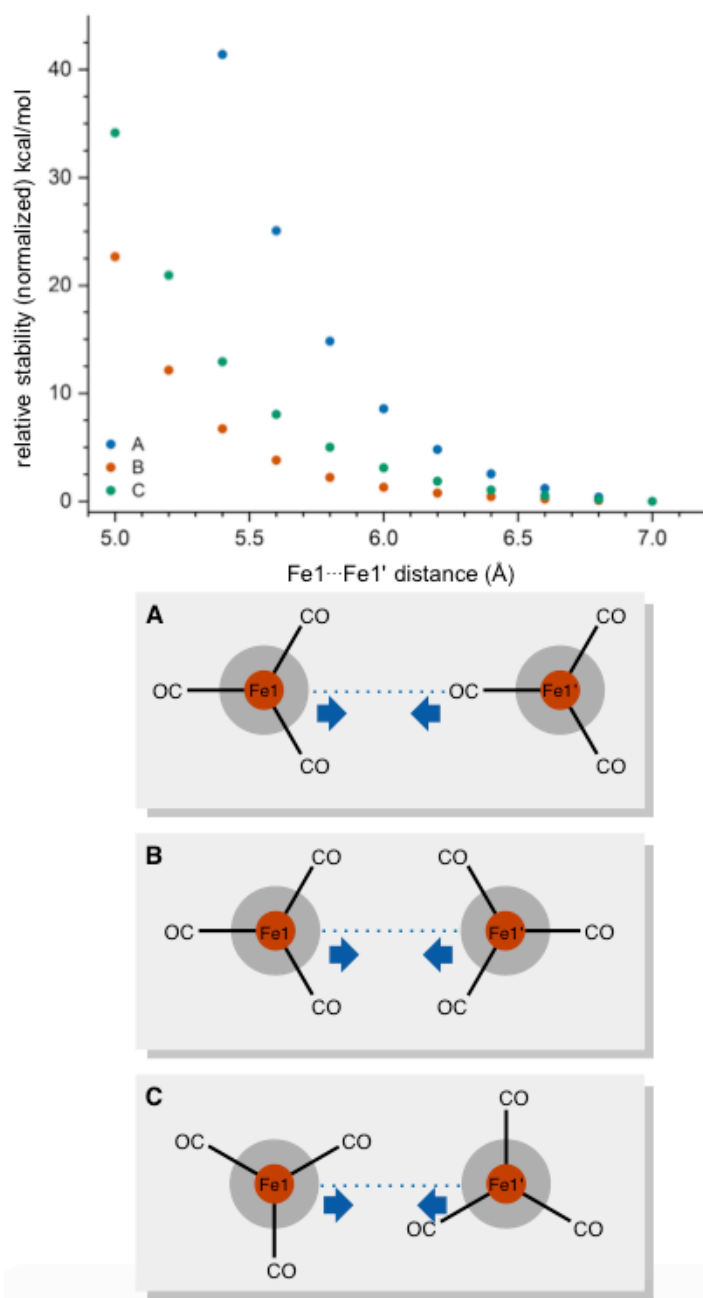


Figure 12.4 Three different setups for scanning the energy vs. Fe1...Fe1' interatomic distance with single point calculations at each increment.

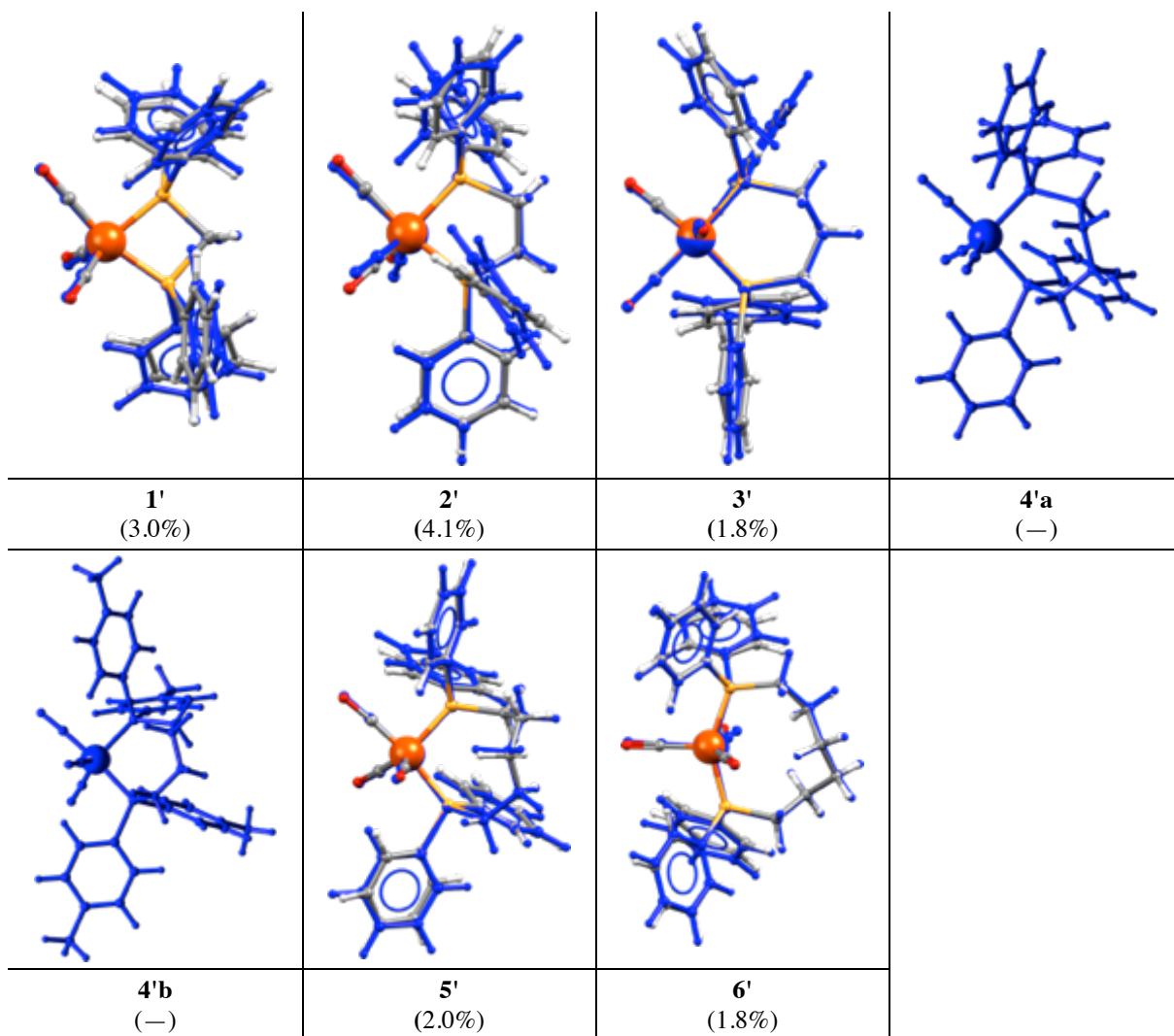


Figure 12.5 Computed structures of the monoiron complexes overlaid with crystal structures when available (RMSD values).

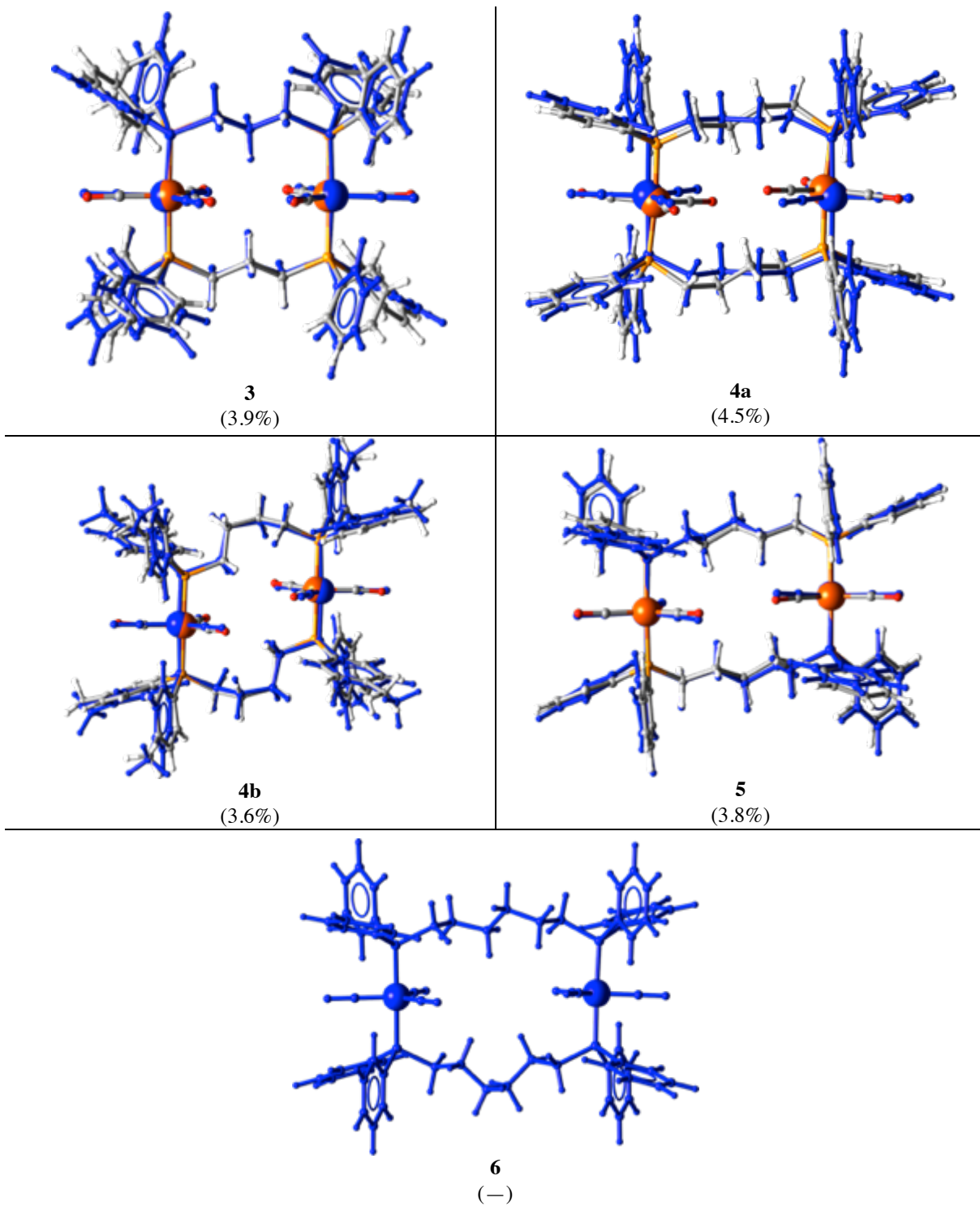


Figure 12.6 Computed structures of the diiron complexes overlaid with crystal structures when available (RMSD values).

Table 12.2 Key interatomic distances (Å) and angles (°) for computed structures of diiron complexes.^a

	3	4a	4b	5	6
Fe1–P1	2.230	2.233	2.231	2.229	2.224/2.231
Fe1–P2	2.227	2.233	2.235	2.227	2.231/2.224
Fe1–C1	1.782	1.779	1.776	1.779/1.777	1.778/1.778
Fe1–C2	1.782	1.784	1.783	1.784	1.783/1.783
Fe1–C3	1.168	1.777	1.778	1.777/1.779	1.778/1.779
C1–O1	1.166	1.170	1.172	1.168/1.171	1.169/1.169
C2–O2	1.167	1.166	1.167	1.166	1.167/1.167
C3–O3	1.168	1.170	1.169	1.171/1.168	1.170/1.169
Fe1–O1	2.948	2.949	2.947	2.947	2.947/2.947
Fe1–O2	2.949	2.950	2.950	2.951	2.950/2.950
Fe1–O3	2.947	2.946	2.946	2.947	2.947/2.948
C1–Fe1–C2	115.90	117.42	119.73	119.83/118.89	121.05/121.18
C1–Fe1–C3	125.35	123.47	121.93	121.27	119.27/118.85
C2–Fe1–C3	118.75	119.11	118.33	118.89/119.83	119.68/119.96
P1–Fe1–P2	174.76	172.79	173.43	177.76	178.25/177.85

^a When distances or angles differ about the two Fe(CO)₃ rotators, two values are given.

Table 12.3 Key interatomic distances (Å) and angles (°) for the computed structures of di iron complexes.^a

	3	4a	4b	5	6
radius of rotator ^b	4.47	4.47	4.47	4.47	4.47
Fe1...Fe1' ^c	5.954	6.949	6.509	7.609	8.517
P1...P2 ^c	4.452	4.457	4.458	4.456	4.455/4.454
P1...P2' ^c	5.763	6.892	6.373	7.567	8.452/8.719
O1...O3' ^c	3.331	4.251	3.807	3.414	5.531
O3...O3' ^c	5.749	7.523	7.038	6.907	7.738
P1-Fe1-P2/Fe1' vs. P1'-Fe1'-P2'/Fe1' ^d	0.00	0.00	0.00	14.94	12.00
P2-Fe1-Fe1'-P1' ^e	-1.75	-7.02	-5.61	-14.91	-10.8
P2-Fe1-Fe1'-P2' ^e	-180.0	-180.0	-180.0	163.54	167.8
P1-Fe1-Fe1'-P2' ^e	1.75	7.03	5.61	-14.91	-13.3
P1'-Fe1'-Fe1-P1' ^e	180.0	-180.0	180.0	166.65	168.2
Fe1-P2-C4-C5 ^e	-49.9	73.2	-81.9	64.2	63.4/68.6
P2-C4-C5-C6 ^e	167.6	-154.7	147.7	178.1	159.2/-169.7
C4-C5-C6-C7 ^e	—	-175.8	-77.4	62.7	65.2/67.5
C5-C6-C7-C8 ^e	—	—	—	164.5	76.0/170.5
C6-C7-C8-C9 ^e	—	—	—	—	63.2/-63.0
C _{ω-2} -C _{ω-1} -C _ω -P1' ^{e,f}	-175.7	-154.7	-171.3	-179.7	155.31/-137.2
C _{ω-1} -C _ω -P1'-Fe1' ^{e,g}	55.7	73.3	175.8	50.8	64.42/74.05

^a Calculated using standard programs such as Mercury. ^b Calculated by averaging the Fe-O distances and adding the van der Waals radius of oxygen (1.52 Å). ^c Non-bonded distance (Å). ^d Angle between two four-atom least squares planes (°). ^e Torsion angle (°). ^f This torsion angle is the counterpart to P2-C4-C5-C6; ω = 6, 7, 7, 8, and 9 for the respective entries. ^g This torsion angle is the counterpart to Fe1-P2-C4-C5; ω = 6, 7, 7, 8, and 9 for the respective entries.

B.2. References

(1) Weigend, F.; Ahlrichs, R. Balanced basis sets of split valence, triple zeta valence and quadruple zeta valence quality for H to Rn: Design and assessment of accuracy. *Phys. Chem. Chem. Phys.* **2005**, *7*, 3297-3305.

(2) Tao, J.; Perdew, J. P.; Staroverov, V. N.; Scuseria, G. E. Climbing the Density Functional Ladder: Nonempirical Meta-Generalized Gradient Approximation Designed for Molecules and Solids. *Phys. Rev. Lett.* **2003**, *91*, 146401.

(3) Representative studies validating the use of the TPSS functional and/or def2-TZVP basis set for IR calculations in related systems: (a) Brothers, S. M.; Darensbourg, M. Y.; Hall, M. B. Modeling Structures and Vibrational Frequencies for Dinitrosyl Iron Complexes (DNICs) with Density Functional Theory. *Inorg. Chem.* **2011**, *50*, 8532-8540. (b) Meng, L.; Liu, S.; Qin, Q.; Zeng, B.; Chi, C. Infrared Photodissociation Spectroscopy of Heteronuclear Arsenic–Iron Carbonyl Cluster Anions. *J. Phys. Chem. A* **2020**, *124*, 1158-1166. (c) Speelman, A. L.; Zhang, B.; Silakov, A.; Skodje, K. M.; Alp, E. E.; Zhao, J.; Hu, M. Y.; Kim, E.; Krebs, C.; Lehnert, N. Unusual Synthetic Pathway for an $\{\text{Fe}(\text{NO})_2\}^9$ Dinitrosyl Iron Complex (DNIC) and Insight into DNIC Electronic Structure via Nuclear Resonance Vibrational Spectroscopy. *Inorg. Chem.* **2016**, *55*, 5485-5501. (d) Pan, S.; Zhao, L.; Dias, H. V. R.; Frenking, G. Bonding in Binuclear Carbonyl Complexes $\text{M}_2(\text{CO})_9$ ($\text{M} = \text{Fe}, \text{Ru}, \text{Os}$). *Inorg. Chem.* **2018**, *57*, 7780-7791. (e) Karpal, C.; Harding, D. J.; Rayner, D. M.; Fielicke, A. Small Platinum Cluster Hydrides in the Gas Phase. *J. Phys. Chem. A* **2013**, *117*, 8230-8237.

(4) Frisch, M. J.; Trucks, G. W.; Schlegel, H. B.; Scuseria, G. E.; Robb, M. A.; Cheeseman, J. R.; Scalmani, G.; Barone, V.; Mennucci, B.; Petersson, G. A.; Nakatsuji, H.; Caricato, M.; Li, X.; Hratchian, H. P.; Izmaylov, A. F.; Bloino, J.; Zheng, G.; Sonnenberg, J. L.; Hada, M.; Ehara, M.; Toyota, K.; Fukuda, R.; Hasegawa, J.; Ishida, M.; Nakajima, T.; Honda, Y.; Kitao, O.; Nakai, H.; Vreven, T.; Montgomery, J. A. Jr.; Peralta, J. E.; Ogliaro, F.; Bearpark, M.; Heyd, J. J.; Brothers, E.; Kudin, K. N.; Staroverov, V. N.; Kobayashi, R.; Normand, J.; Raghavachari, K.; Rendell, A.; Burant, J. C.; Iyengar, S. S.; Tomasi, J.; Cossi, M.; Rega, N.; Millam, J. M.; Klene, M.; Knox, J. E.; Cross, J. B.; Bakken, V.; Adamo, C.; Jaramillo, J.; Gomperts, R.; Stratmann, R. E.; Yazyev, O.; Austin, A. J.; Cammi, R.; Pomelli, C.; Ochterski, J. W.; Martin, R. L.; Morokuma, K.; Zakrzewski, V. G.; Voth, G. A.; Salvador, P.; Dannenberg, J. J.; Dapprich, S.; Daniels, A. D.; Farkas, Ö.; Foresman, J. B.; Ortiz, J. V.; Cioslowski, J.; Fox, D. J. *Gaussian 09, Revision D.01*; Gaussian, Inc. Wallingford CT, **2009**.

(5) Marenich, A. V.; Cramer, C. J.; Truhlar, D. G. Universal Solvation Model Based on Solute Electron Density and on a Continuum Model of the Solvent Defined by the Bulk Dielectric Constant and Atomic Surface Tensions. *J. Phys. Chem. B* **2009**, *113*, 6378-6396.

(6) Grimme, S.; Ehrlich, S.; Goerigk, L. Effect of the damping function in dispersion corrected density functional theory. *J. Comput. Chem.* **2011**, *32*, 1456-1465.

(7) (a) Kesharwani, M. K.; Brauer, B.; Martin, J. M. L. Frequency and Zero-Point Vibrational Energy Scale Factors for Double-Hybrid Density Functionals (and Other Selected Methods): Can Anharmonic Force Fields Be Avoided?. *J. Phys. Chem. A*.

2015, *119*, 1701-1714. (b) Assefa, M. K.; Devera, J. L.; Brathwaite, A. D.; Mosley, J. D.; Duncan, M. A. Vibrational scaling factors for transition metal carbonyls. *Chem. Phys. Lett.* **2015**, *640*, 175-179.

APPENDIX C

C.1. General considerations

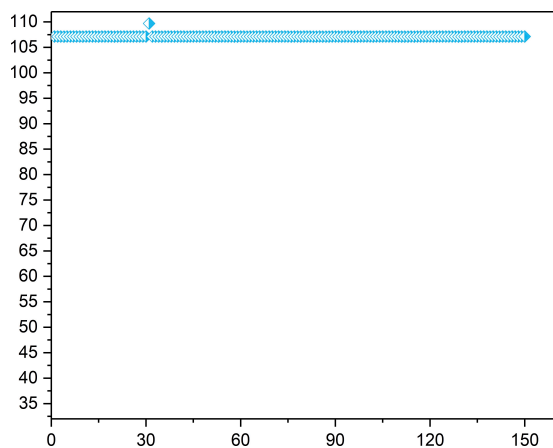
C.1.1. Simulated annealing

Model structures of ii_n , oo_n , and io_n were subjected to simulated annealing in order to sample the conformational space and identify the lowest energy conformer and the type of cage formed. The Materials Studio program package with the Forcite component was used.¹ The specific parameters used with the Forcite module were as follows: NVT ensemble with random initial velocities, initial temperature of 300 K, mid-cycle temperature of 500 K, 150 heating ramps per cycle, 5 dynamic steps per ramp. Thus, the total number of steps was 100,000. The sampled structures were automatically geometry optimized after each cycle using the smart algorithm with a fine convergence tolerance (energy of 0.0001 kcal/mol, force of 0.005 kcal/mol·Å, displacement of 0.00005 Å, maximum of 10,000 iterations; annealing time steps of 1.0 fs frames). Select high- and low energy frames from the simulated annealing were DFT optimized using the same level of theory as in section C.1.2. The correlation is shown in Figure 13.1.

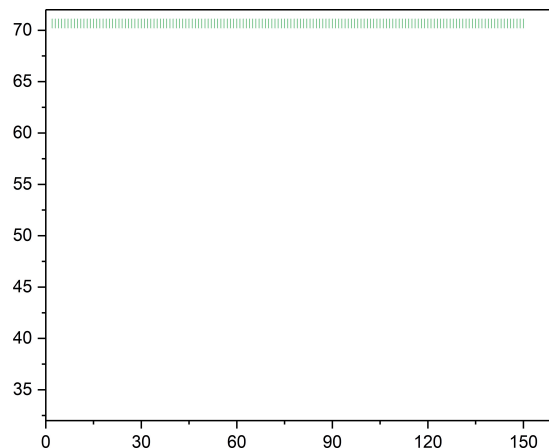
C.1.2. NMR calculations

Computations were performed using the Gaussian program package, employing an ultrafine grid (99,590) to enhance accuracy.² Gas phase geometries were optimized using DFT and the frequencies were analyzed to confirm that the structures were local minima. The B3LYP³ functional was employed with an all-electron 6-311+G(d)⁴ basis set on all atoms. Dispersion corrections were implemented using the D3 version of Grimme's dispersion function with Becke-Johnson damping (referred to as GD3BJ) during optimizations.⁵

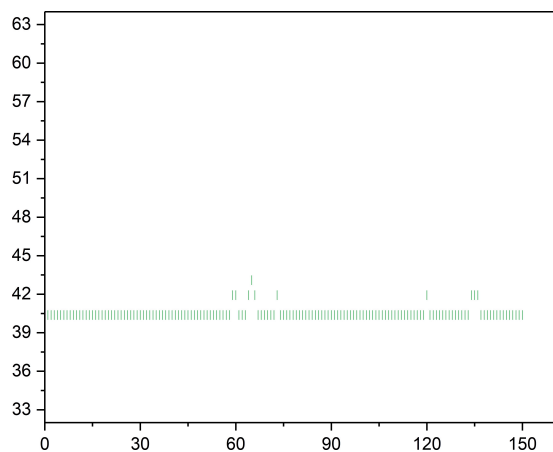
Table 13.1 Molecular dynamics simulation (simulated annealing) of ii_n , $n = 4, 5, 6, \dots, 20$. The different species are denoted as follows: \times (cross-chain) \circ (*out-out*) \mid (*in-in*) \diamond (*in-out*). The x -axes represent cumulative molecular structures and the y -axes represent potential energy (kcal/mol).



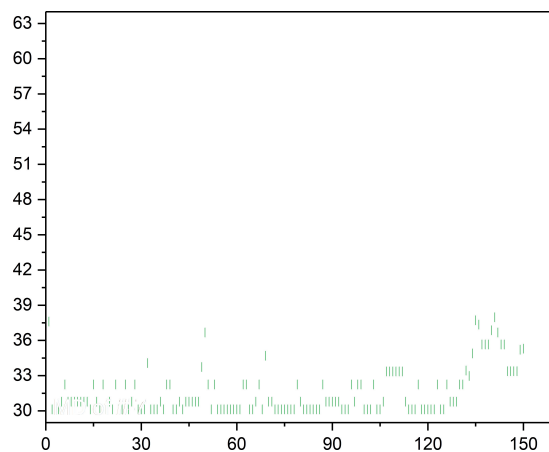
ii_4



ii_5

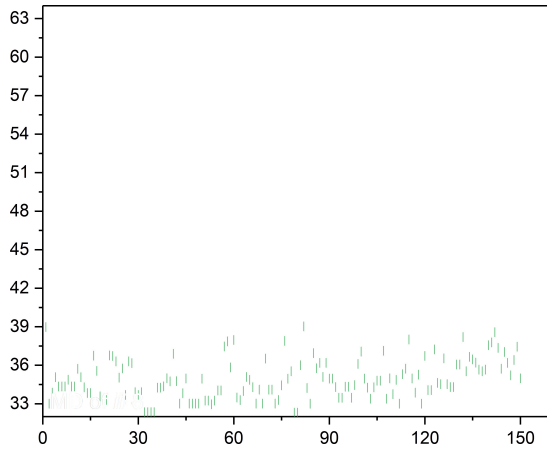


ii_6

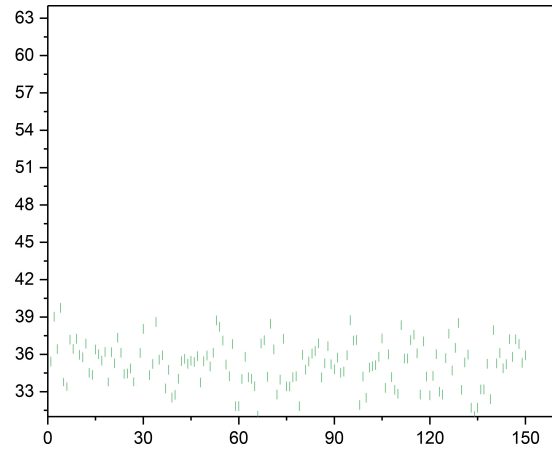


ii_7

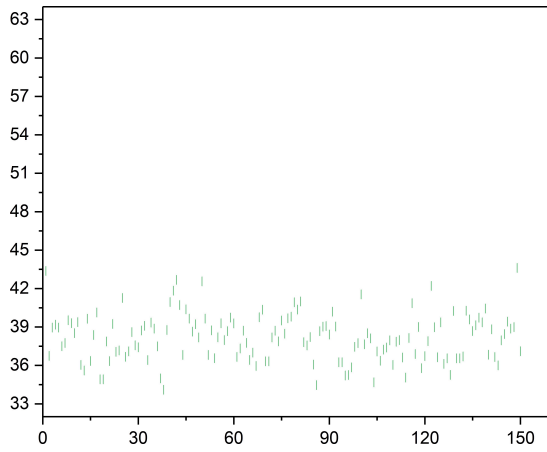
Table 13.1 *continued.*



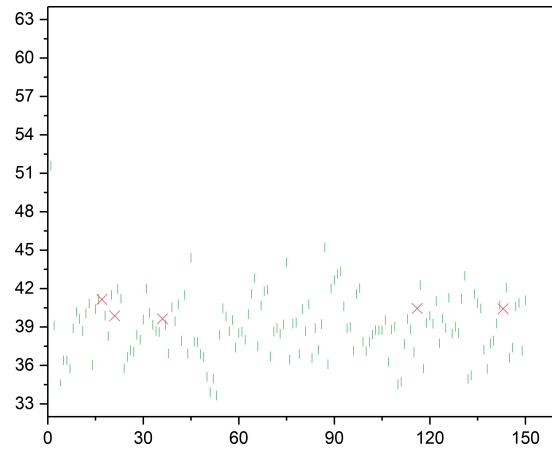
ii_8



ii_9

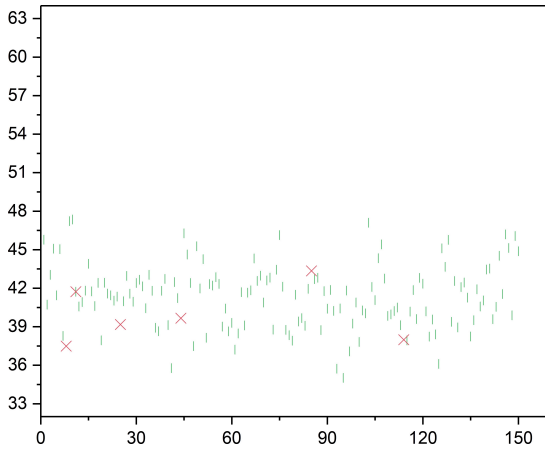


ii_{10}

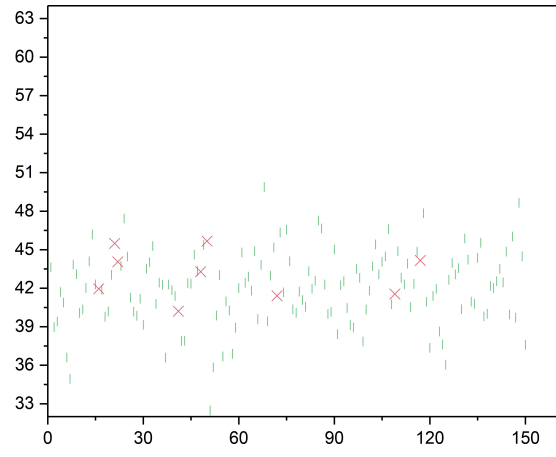


ii_{11}

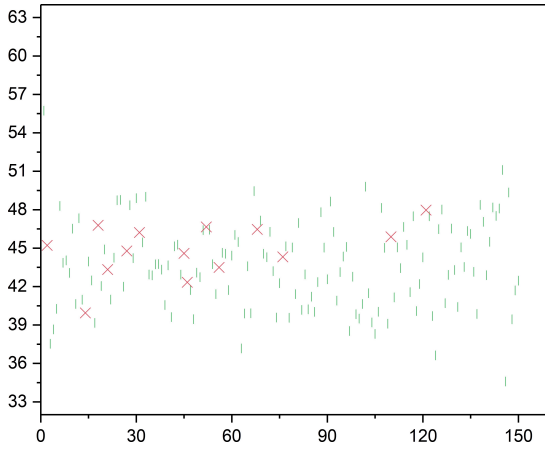
Table 13.1 *continued.*



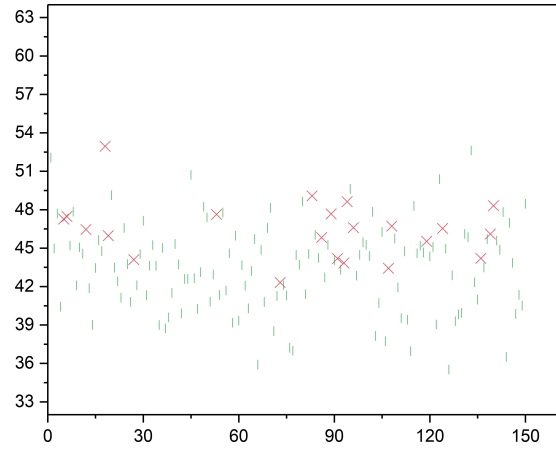
ii_{12}



ii_{13}

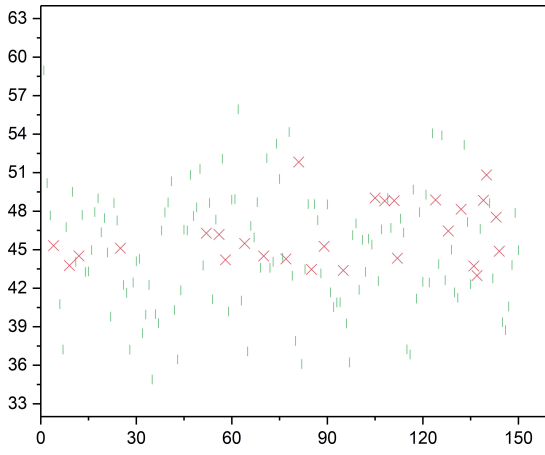


ii_{14}

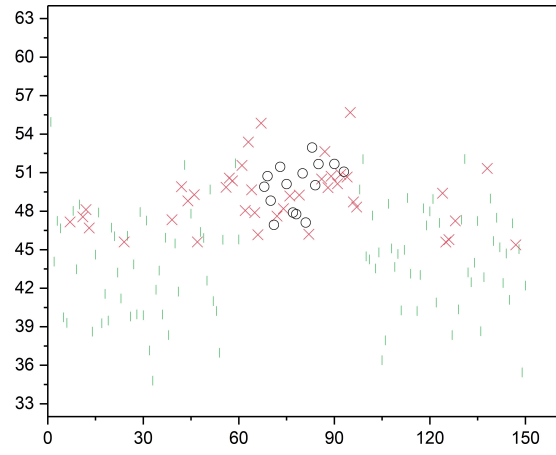


ii_{15}

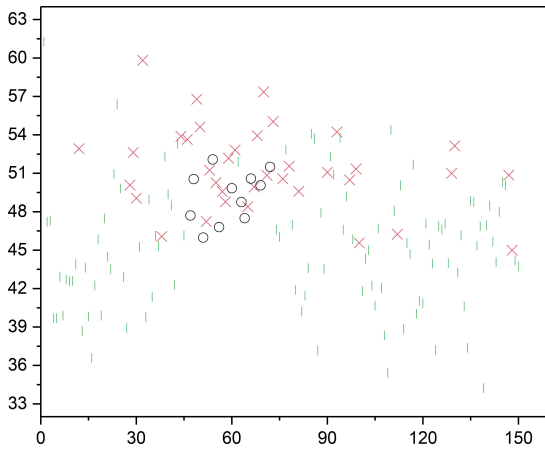
Table 13.1 *continued.*



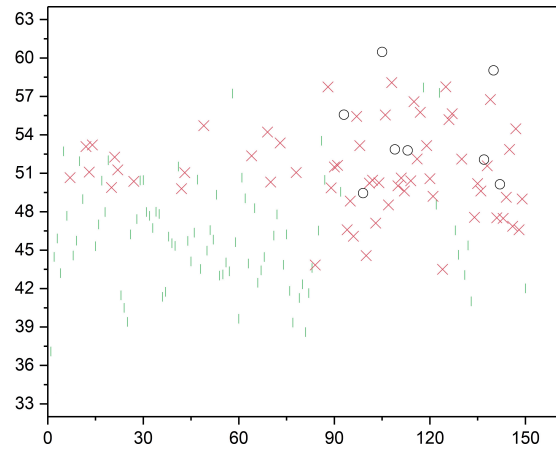
ii_{16}



ii_{17}

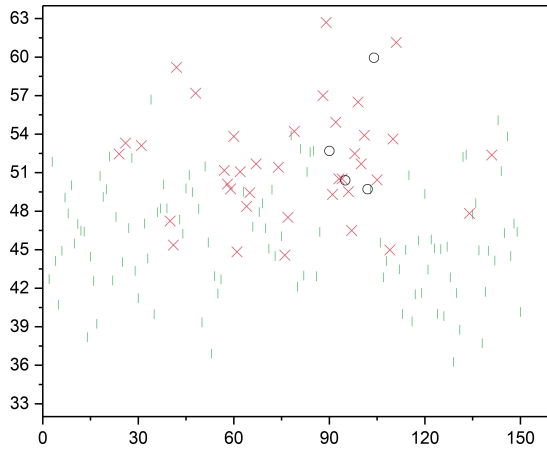


ii_{18}

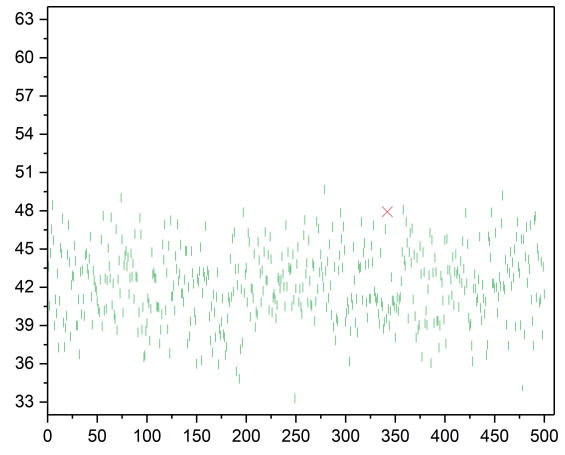


ii_{19}

Table 13.1 *continued.*

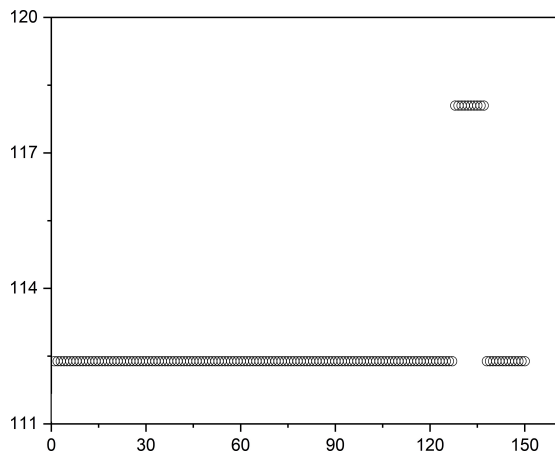


ii_{20}

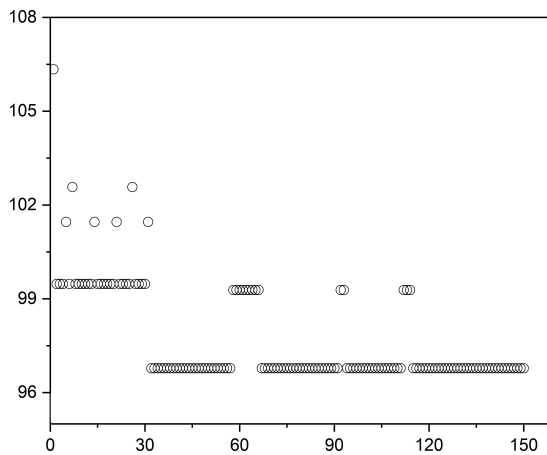


ii_{13} extended trajectory (500 frames)

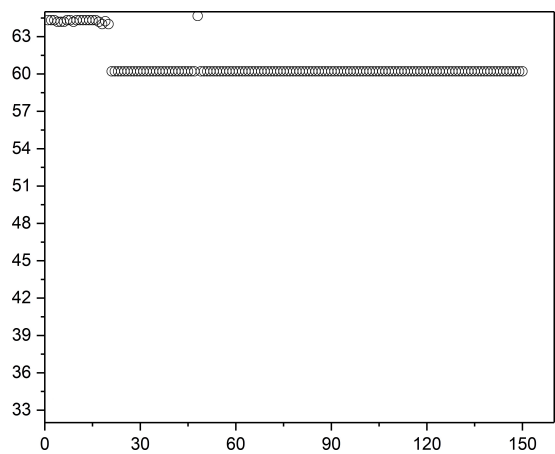
Table 13.2 Molecular dynamics simulation (simulated annealing) of oo_n , $n = 4, 5, 6, \dots, 20$. The different species are denoted as follows: \times (cross-chain) \circ (*out-out*) \mid (*in-in*) \diamond (*in-out*). The x -axes represent cumulative molecular structures and the y -axes represent potential energy (kcal/mol).



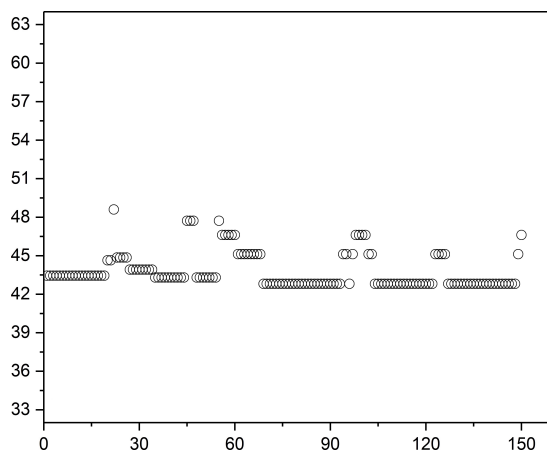
oo_4



oo_5

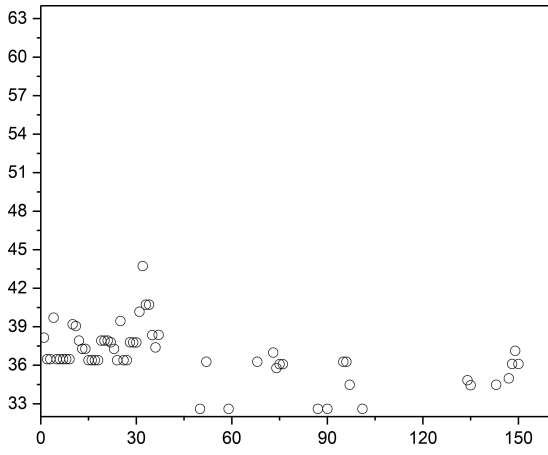


oo_6

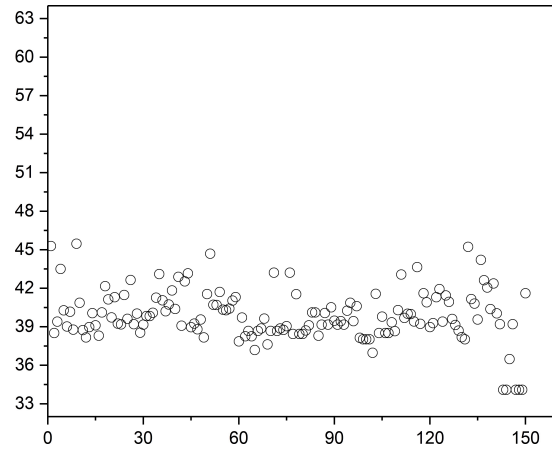


oo_7

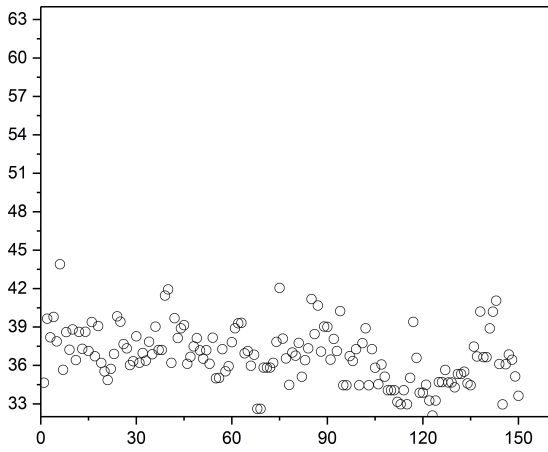
Table 13.2 *continued.*



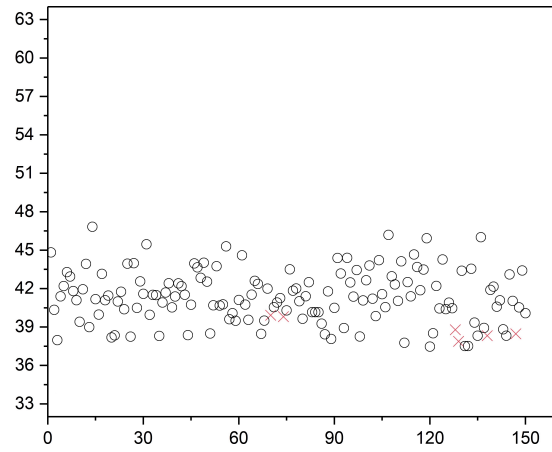
oo8



oo9

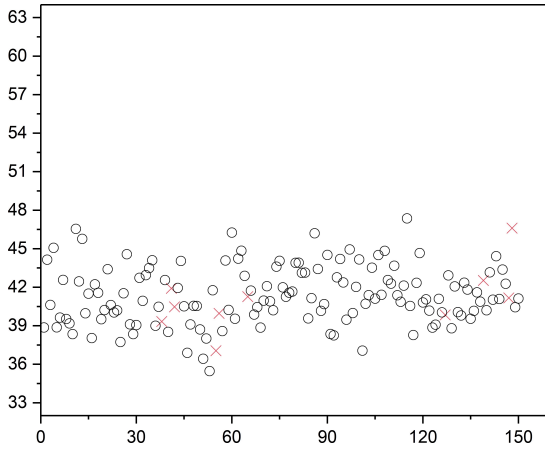


oo10

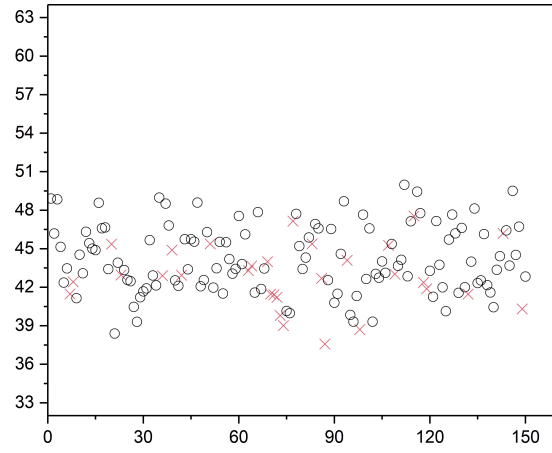


oo11

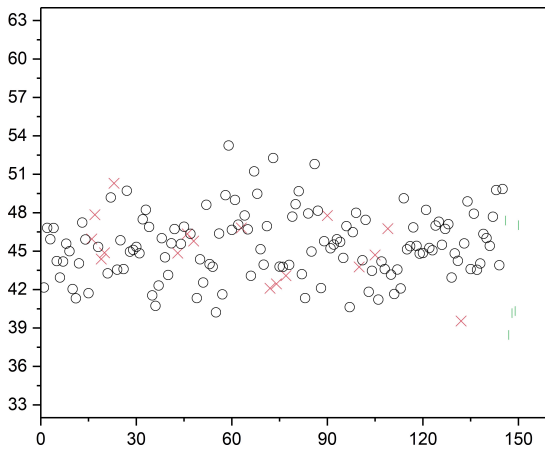
Table 13.2 continued.



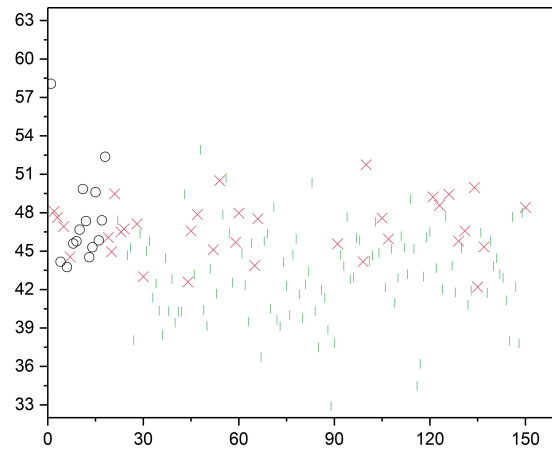
oo12



oo13

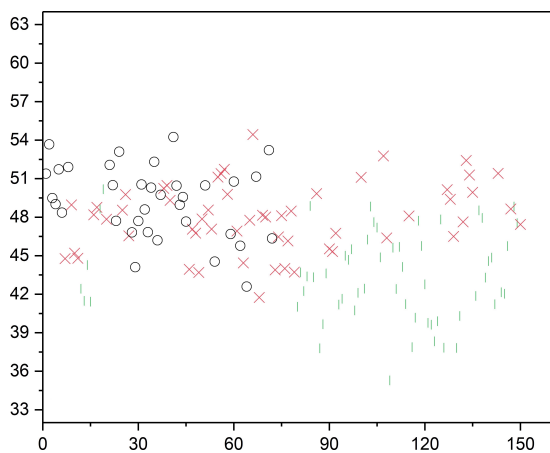


oo14

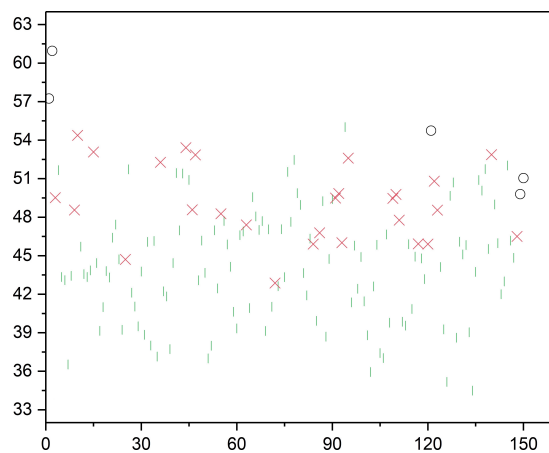


oo15

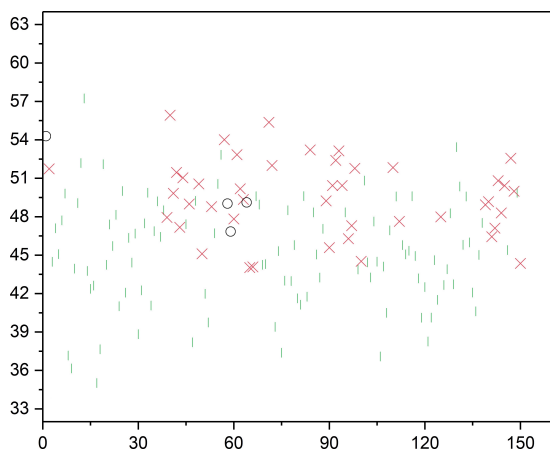
Table 13.2 *continued.*



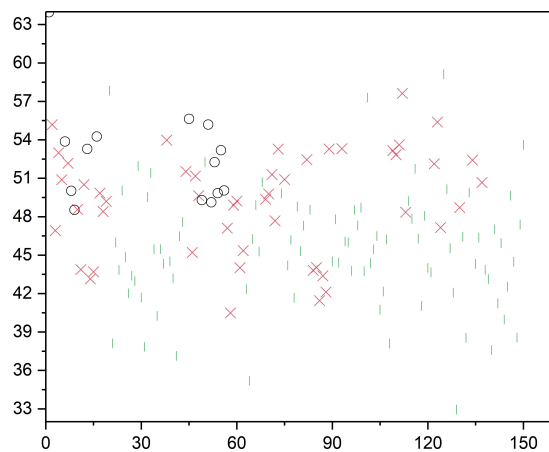
oo16



oo17



oo18



oo19

Table 13.2 continued.

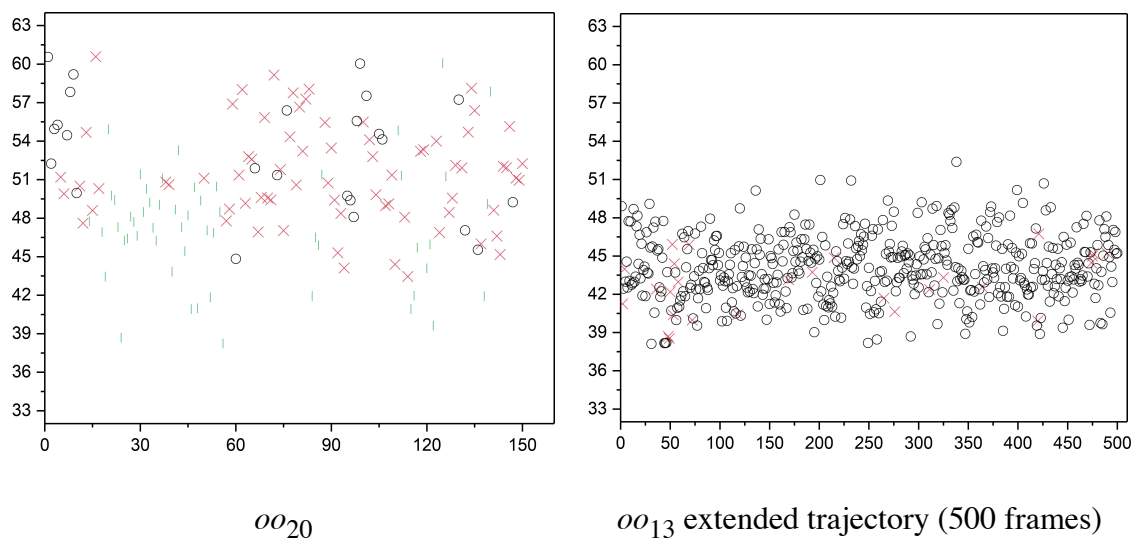


Table 13.3 Boltzmann averaged energies ($T = 298.15$ K) of ii_n vs. oo_n for $n = 5-20$.

n	Boltzmann averaged energies of ii_n (kcal/mol)	Boltzmann averaged energies of oo_n (kcal/mol)	Boltzmann averaged energy differences of ii_n vs. oo_n (kcal/mol)
5	70.7	96.8	-26.1
6	40.4	60.2	-19.8
7	30.2	42.9	-12.7
8	33.0	31.6	1.4
9	31.8	34.1	-2.3
10	35.0	40.2	-5.2
11	34.3	38.2	-3.9
12	35.6	36.1	-0.5
13	32.5	39.8	-7.3
14	34.7	39.0	-4.3
15	36.0	44.2	-8.2
16	33.3	42.8	-9.5
17	35.1	49.9	-14.8
18	34.5	49.1	-14.5
19	37.3	49.0	-11.7
20	36.6	45.0	-8.4

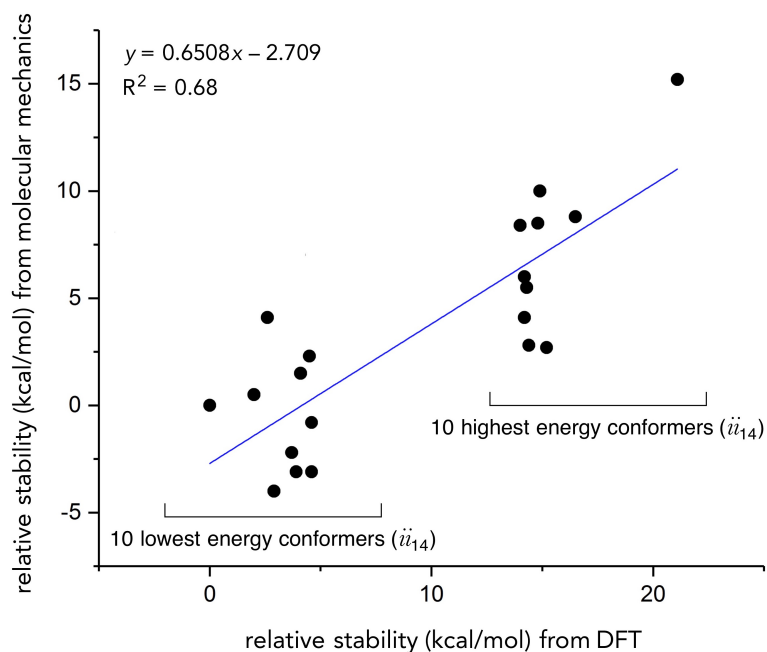


Figure 13.1 The ten lowest and highest energy (E_p) molecular mechanics ii_{14} frames have been DFT optimized. These isomers are not cumulative molecular structures and the energies are normalized to the lowest energy (E_p) frame.

C.2. References

- (1) Dassault Systèmes BIOVIA, Materials Studio, 6.0, San Diego: Dassault Systèmes, 2017.
- (2) Frisch, M. J.; Trucks, G. W.; Schlegel, H. B.; Scuseria, G. E.; Robb, M. A.; Cheeseman, J. R.; Scalmani, G.; Barone, V.; Mennucci, B.; Petersson, G. A.; Nakatsuji, H.; Caricato, M.; Li, X.; Hratchian, H. P.; Izmaylov, A. F.; Bloino, J.; Zheng, G.; Sonnenberg, J. L.; Hada, M.; Ehara, M.; Toyota, K.; Fukuda, R.; Hasegawa, J.; Ishida, M.; Nakajima, T.; Honda, Y.; Kitao, O.; Nakai, H.; Vreven, T.; Montgomery, J. A. Jr.; Peralta, J. E.; Ogliaro, F.; Bearpark, M.; Heyd, J. J.; Brothers, E.; Kudin, K. N.; Staroverov, V. N.; Kobayashi, R.; Normand, J.; Raghavachari, K.; Rendell, A.; Burant, J. C.; Iyengar, S. S.; Tomasi, J.; Cossi, M.; Rega, N.; Millam, J. M.; Klene, M.; Knox, J.

E.; Cross, J. B.; Bakken, V.; Adamo, C.; Jaramillo, J.; Gomperts, R.; Stratmann, R. E.; Yazyev, O.; Austin, A. J.; Cammi, R.; Pomelli, C.; Ochterski, J. W.; Martin, R. L.; Morokuma, K.; Zakrzewski, V. G.; Voth, G. A.; Salvador, P.; Dannenberg, J. J.; Dapprich, S.; Daniels, A. D.; Farkas, Ö.; Foresman, J. B.; Ortiz, J. V.; Cioslowski, J.; Fox, D. J. *Gaussian 09, Revision D.01*; Gaussian, Inc. Wallingford CT, **2009**.

(3) (a) Becke, A. D. Density-functional exchange-energy approximation with correct asymptotic behavior. *Phys. Rev. A*, **1988**, *38*, 3098-3100. (b) Becke, A. D. Density-functional thermochemistry. III. The role of exact exchange. *J. Chem. Phys.* **1993**, *98*, 5648-5652. (c) Lee, C.; Yang, W.; Parr, R. G. Development of the Colle-Salvetti correlation energy formula into a functional of the electron density. *Phys. Rev. B*, **1988**, *37*, 785-789.

(4) References for Pople type basis set "**6-311G**" are as follows (an addition of "d" adds polarization functions of *d*-type to C, "p" adds *p*-type polarization functions to C and H atoms, and "+/++" indicates added diffuse functions): (a) McLean, A. D.; Chandler, G. S. Contracted Gaussian basis sets for molecular calculations. I. Second row atoms, *Z* = 11-18. *J. Chem. Phys.* **1980**, *72*, 5639-5648. (b) Raghavachari, K.; Binkley, J. S.; Seeger, R.; Pople, J. A. Self-consistent molecular orbital methods. XX. A basis set for correlated wave functions. *J. Chem. Phys.* **1980**, *72*, 650-654.

(5) Grimme, S.; Ehrlich, S.; Goerigk, L. Effect of the damping function in dispersion corrected density functional theory. *J. Comput. Chem.* **2011**, *32*, 1456-1465.

APPENDIX D

D.1. Computational section for $\text{H}(\text{C}\equiv\text{C})_n\text{H}$ species treated in section 6.3

D.1.1. General considerations

The general computational methodology employed is outlined in Figure 14.1. First, validation methods were sought to ensure the accuracy of the results. A variety of functionals were compared by building dimeric conjugated polyynes $\text{H}(\text{C}\equiv\text{C})_n\text{H}$ ($n = 2-10$). For the starting geometries, C–C and C≡C bond lengths of 1.54 Å and 1.22 Å were used. Metrical parameters from crystal structures were not employed, as non-biased distances were desired for evaluating the functionals. Although the input structures possessed $D_{\infty h}$ symmetry, no constraints were applied in the calculations. The structures were optimized using each of the following functionals: BMK,¹ M06,² CAM-B3LYP,³ ω B97XD,⁴ PBE0,⁵ B3LYP,⁶ M06L,⁷ BLYP,^{6a,c} and BP86.^{6a,8} In all cases, a triple-zeta Pople basis set [6-311++G(d,p)]⁹ that has extra diffuse and polarization functions was used. All computations were performed with the Gaussian program package, employing the ultrafine grid (99,590) to enhance accuracy.¹⁰

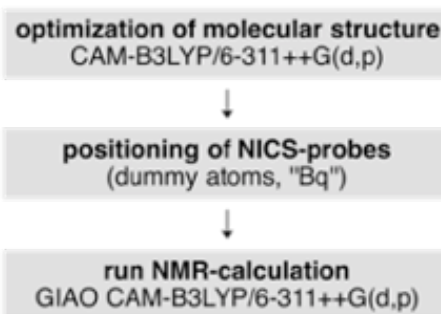


Figure 14.1 Graphical outline of the calculation sequence.

Results for the octayne $\text{H}(\text{C}\equiv\text{C})_8\text{H}$ were compared with the crystal structure of *t*-Bu(C \equiv C) $_8$ *t*-Bu (CCSD code LUMWAS).¹¹ Table 14.1 summarizes, for each functional, the *sum* of (1) the percent difference in the average C–C bond lengths, and (2) the percent difference in the average C \equiv C bond lengths. The underlying data are presented in Table 14.2. The CAM-B3LYP functional performed well (ranking second) and was used for subsequent calculations as it has been extensively employed for accurate NMR simulations.¹² The basis sets were then evaluated [6-311++G(d,p),⁹ 6-311+G(d),⁹ 6-311+G,⁹ and 6-31+G(d) in order of decreasing quality],¹³ and representative data are given in Table 14.3. The choice of basis set had little influence upon the NICS values (or bond lengths) unless they were small relative to the maximum values. This is also supported in related studies.¹⁴ However, it is important to use polarization functions and diffuse functions when computing NMR chemical shifts, so the best quality basis set (triple zeta) was used [6-311++G(d,p)].⁹ The functionals were also evaluated on the basis of their NICS values, but no significant difference was observed (Table 14.4). Importantly, in accord with the sign convention for NICS, the sign was inverted on values from the isotropic portion of the data.¹⁵

Table 14.1 The sum of (1) the percent difference in average C-C bond lengths, and (2) the percent difference in average C≡C bond lengths for those in the crystal structure of *t*-Bu(C≡C)₈*t*-Bu versus those computed for H(C≡C)₈H with various functionals.¹¹

functional	% difference ^a
ωB97XD	0.19
CAM-B3LYP	0.31
BMK	0.50
M06	1.20
PBE0	1.97
B3LYP	2.15
M06L	3.46
BLYP	4.14
BP86	4.37

^a This quantity is defined in the text and caption.

In addition to choosing an appropriate functional and basis set as described above, our methodology was also benchmarked versus two literature reports that produced NICS values. The first involved the classical example of benzene,¹⁵ and Figure 14.2 (first and second panels) depicts the high level of agreement. The second involved a cyclic conjugated heptyne,¹⁶ again with excellent agreement (Figure 14.2, third and fourth panels).¹⁷



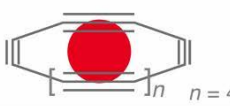
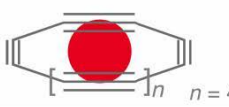
	ref 15 GIAO B3LYP/6-311+G*	this work GIAO CAM-B3LYP/6-311++G(d,p)	ref 16 GIAO M06/6-311++G(d,p)	this work GIAO CAM-B3LYP/6-311++G(d,p)
NICS (3.0)	● -2.0	● -1.7		
NICS (2.5)	● -3.0	● -2.7		
NICS (2.0)	● -4.9	● -4.5		
NICS (1.5)	● -7.6	● -7.4		
NICS (1.0)	● -10.2	● -10.3		
NICS (0.5)	● -9.8	● -9.8		
NICS (0.0)	● -8.0 	● -8.0 	-40.52 	-40.04 

Figure 14.2 Validation of the computational methods: benchmarking vs. literature results.

D.1.2. Procedure for Figure 14.4

The diterminal conjugated polyynes were aligned with the x axis, such that the y coordinate for any carbon or hydrogen atom was zero (see Figure 14.3). NICS probes were positioned with the same x/y coordinates as the center of each carbon and hydrogen atom (see Table 14.5 for the bond lengths employed). For each value of x , additional probes were placed at y values of 0.5, 1.0, 1.5, 2.0, 2.5, and 3.0 Å. For each y value, additional NICS probes were extended beyond the terminal carbon atoms at values of 2.0, 2.5, and 3.0 Å. In view of the $D_{\infty h}$ symmetries of these molecules, data points are depicted for only half of each structure (regions thus omitted are marked with "×"). The computed values for all compounds are shown in Figure 14.4. Table 14.6 summarizes the computed bond lengths that in turn define the x -values on the NICS grid. Both the optimized structures and the input files containing the NICS probes and their placement are provided as $.xyz$ files found in the published supplementary material.¹⁷

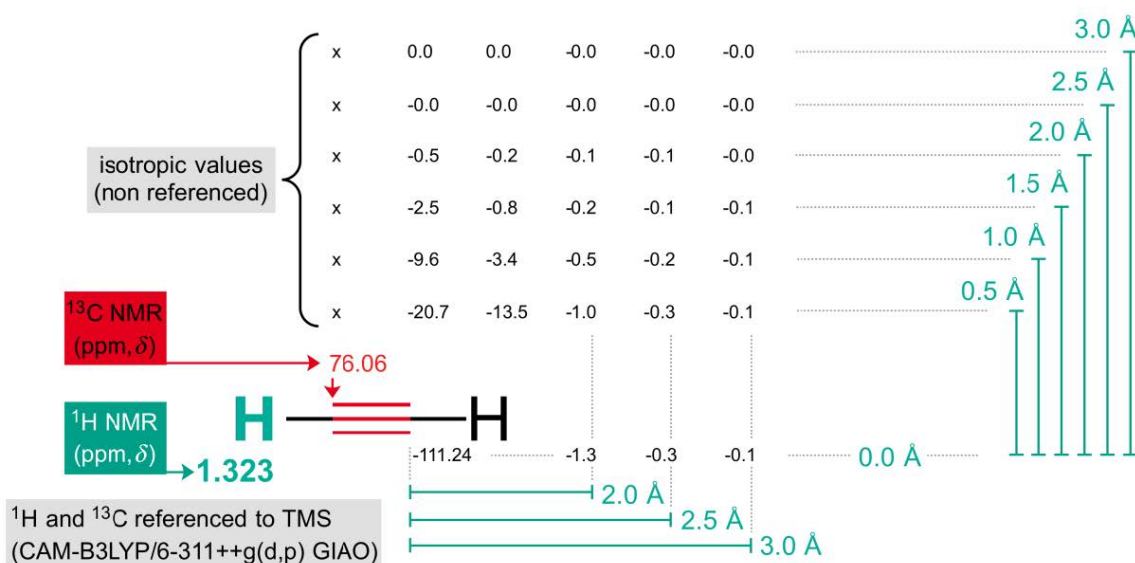


Figure 14.3 Graphical depiction of the different distances typically used in the NICS grid plots.

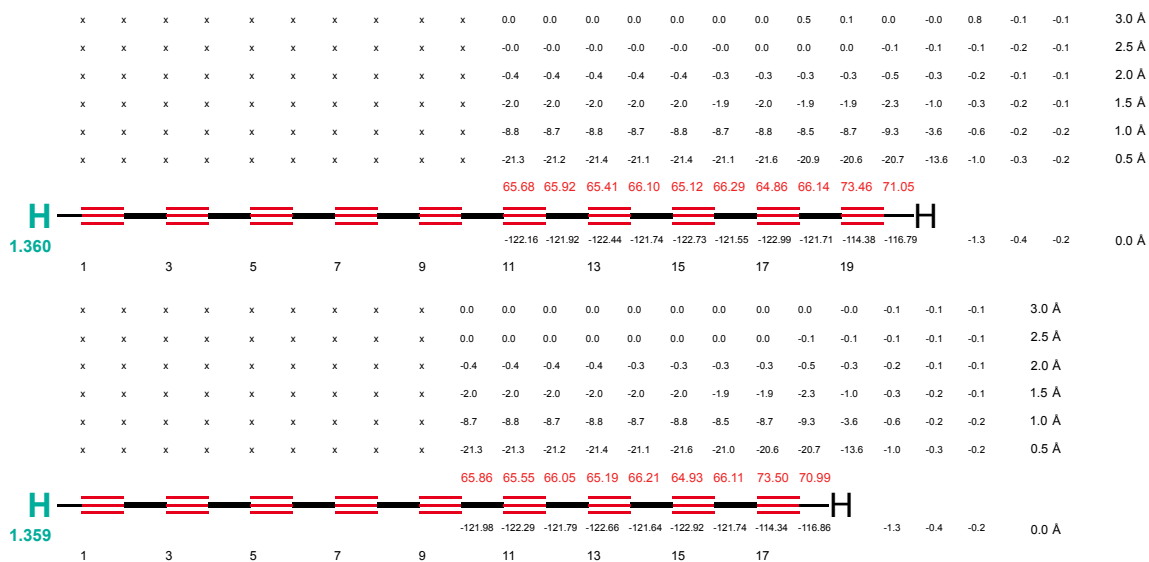


Figure 14.4 NICS grid plot for $\text{H}(\text{C}\equiv\text{C})_n\text{H}$ ($n = 10, 9$).

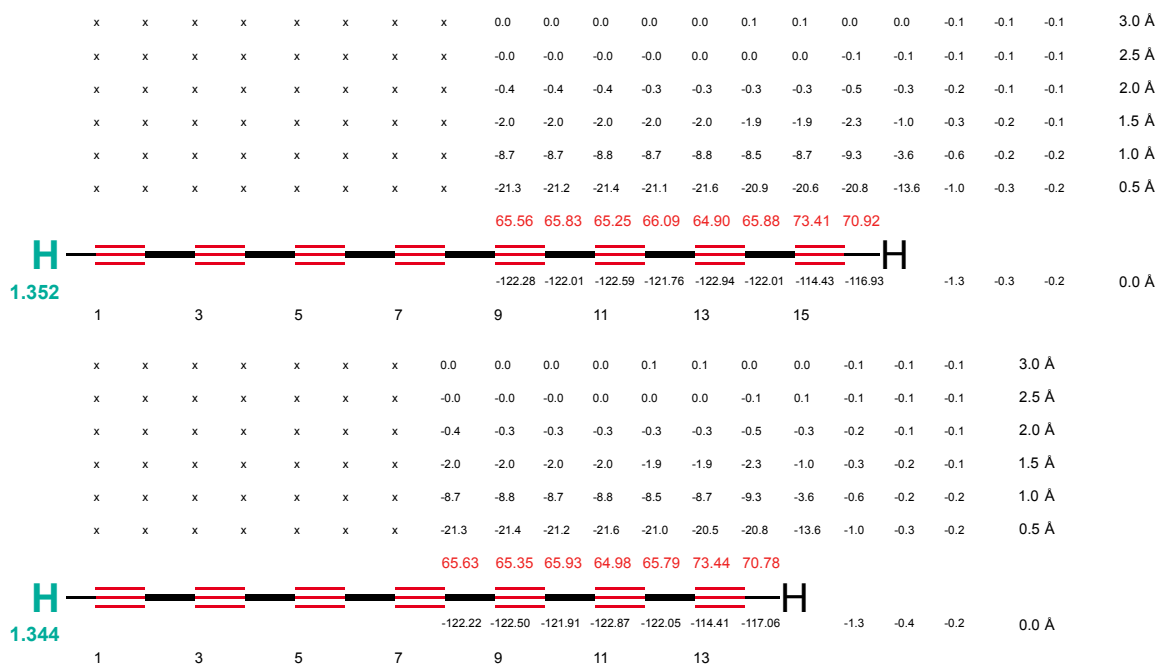


Figure 14.4 continued. NICS grid plot for $\text{H}(\text{C}\equiv\text{C})_n\text{H}$ ($n = 8, 7$).

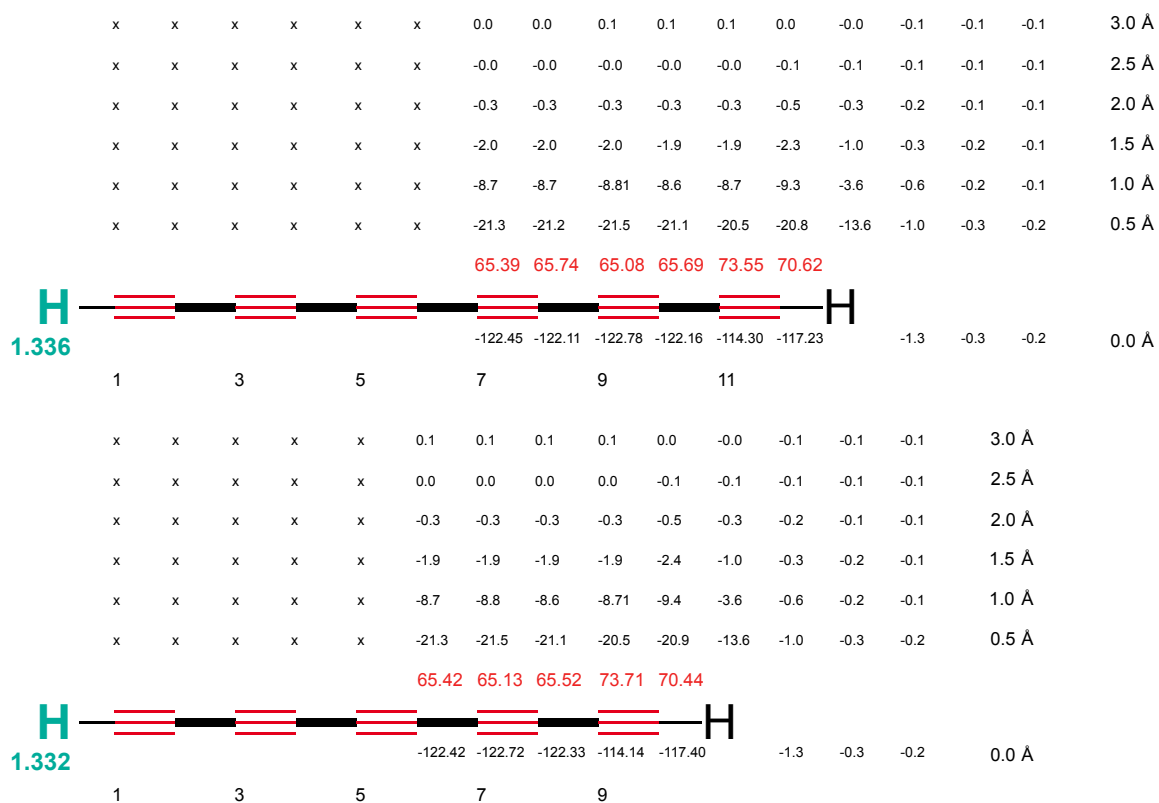


Figure 14.4 *continued*. NICS grid plot for $\text{H}(\text{C}\equiv\text{C})_n\text{H}$ ($n = 6, 5$).

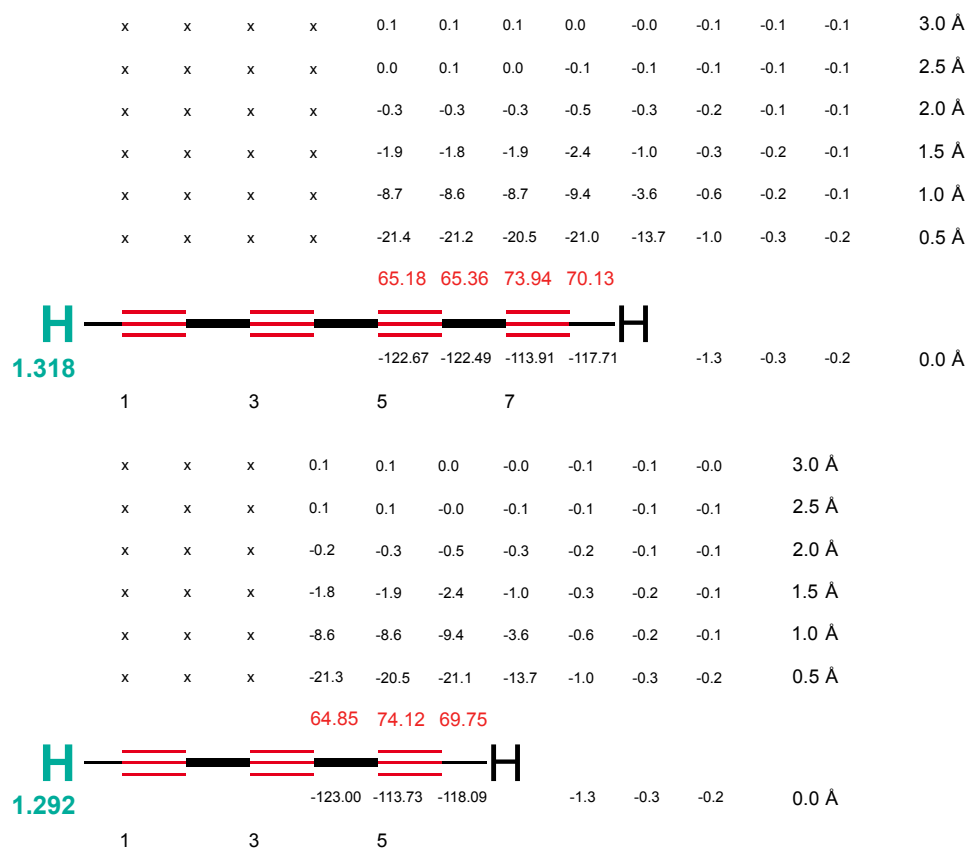


Figure 14.4. *continued*. NICS grid plot for $\text{H}(\text{C}\equiv\text{C})_n\text{H}$ ($n = 4, 3$).

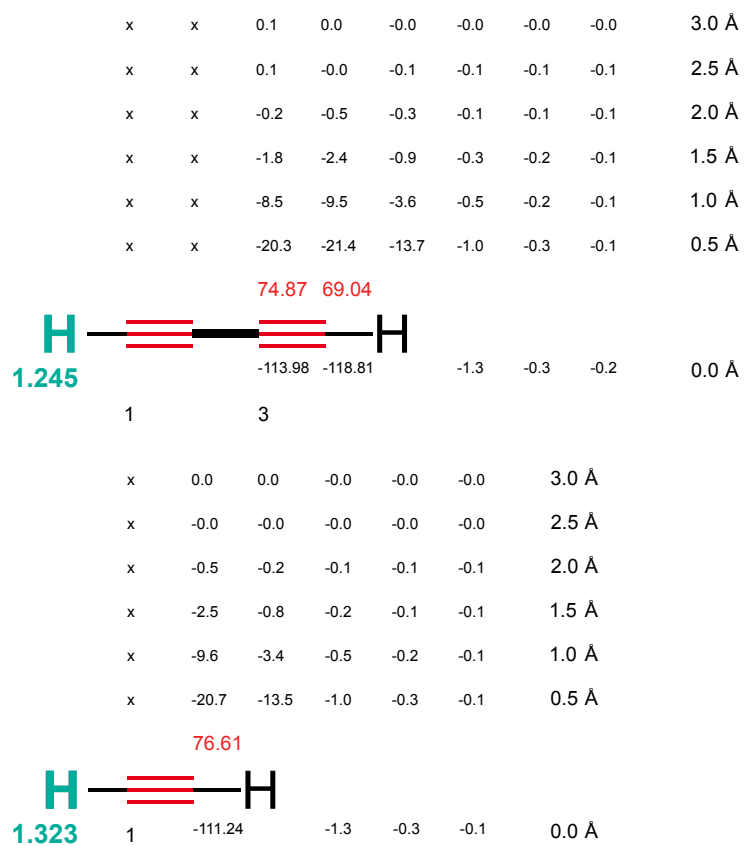


Figure 14.4. *continued.* NICS grid plot format for $\text{H}(\text{C}\equiv\text{C})_n\text{H}$ ($n = 2, 1$).

Table 14.2 Carbon-carbon bond distances (Å) in optimized structures of $\text{H}(\text{C}\equiv\text{C})_8\text{H}$ using nine different functionals compared to experimentally determined values in $t\text{-Bu}(\text{C}\equiv\text{C})_8t\text{-Bu}$.

functional:	experimental data		B3LYP		CAM-B3LYP		BLYP		BP86	
	C1-C2	N/A	1.208	N/A	1.211	N/A	1.201	N/A	1.225	N/A
C2-C3	1.367	N/A	1.350	N/A	1.3621	N/A	1.345	N/A	1.344	N/A
C3-C4	N/A	1.210	N/A	1.224	N/A	1.209	N/A	1.242	N/A	1.243
C4-C5	1.352	N/A	1.337	N/A	1.352	N/A	1.330	N/A	1.328	N/A
C5-C6	N/A	1.218	N/A	1.228	N/A	1.212	N/A	1.248	N/A	1.250
C6-C7	1.349	N/A	1.333	N/A	1.350	N/A	1.324	N/A	1.323	N/A
C7-C8	N/A	1.213	N/A	1.230	N/A	1.213	N/A	1.251	N/A	1.252
C8-C9	1.353	N/A	1.332	N/A	1.349	N/A	1.323	N/A	1.321	N/A
C9-C10	N/A	1.213	N/A	1.230	N/A	1.213	N/A	1.251	N/A	1.252
C10-C11	1.352	N/A	1.333	N/A	1.350	N/A	1.324	N/A	1.323	N/A
C11-C12	N/A	1.214	N/A	1.228	N/A	1.212	N/A	1.248	N/A	1.250
C12-C13	1.355	N/A	1.337	N/A	1.352	N/A	1.330	N/A	1.328	N/A
C13-C14	N/A	1.207	N/A	1.224	N/A	1.209	N/A	1.242	N/A	1.243
C14-C15	1.366	N/A	1.350	N/A	1.362	N/A	1.345	N/A	1.344	N/A
C15-C16	N/A	1.196	N/A	1.211	N/A	1.201	N/A	1.225	N/A	1.227
bond type:	C-C	C≡C	C-C	C≡C	C-C	C≡C	C-C	C≡C	C-C	C≡C
average:	1.355	1.212	1.212	1.223	1.354	1.209	1.332	1.242	1.331	1.243
deviation from exp. data (%):			1.249	1.270	0.064	0.246	1.753	2.387	1.859	2.507
sum of deviation from exp.			2.15		0.31		4.14		4.37	

Table 14.2. *continued.*

functional:	experimental data		PBE0		M06		M06L		ωB97xd		BMK	
C1-C2	N/A	1.208	N/A	1.210	N/A	1.207	N/A	1.215	N/A	1.204	N/A	1.205
C2-C3	1.350	N/A	1.350	N/A	1.354	N/A	1.340	N/A	1.363	N/A	1.361	N/A
C3-C4	N/A	1.210	N/A	1.222	N/A	1.217	N/A	1.229	N/A	1.211	N/A	1.216
C4-C5	1.338	N/A	1.338	N/A	1.342	N/A	1.326	N/A	1.355	N/A	1.350	N/A
C5-C6	N/A	1.218	N/A	1.227	N/A	1.221	N/A	1.235	N/A	1.214	N/A	1.219
C6-C7	1.334	N/A	1.334	N/A	1.339	N/A	1.321	N/A	1.352	N/A	1.347	N/A
C7-C8	N/A	1.213	N/A	1.228	N/A	1.222	N/A	1.237	N/A	1.214	N/A	1.220
C8-C9	1.333	N/A	1.333	N/A	1.338	N/A	1.319	N/A	1.352	N/A	1.346	N/A
C9-C10	N/A	1.213	N/A	1.228	N/A	1.222	N/A	1.237	N/A	1.214	N/A	1.220
C10-C11	1.334	N/A	1.334	N/A	1.339	N/A	1.321	N/A	1.352	N/A	1.347	N/A
C11-C12	N/A	1.214	N/A	1.227	N/A	1.221	N/A	1.235	N/A	1.214	N/A	1.219
C12-C13	1.338	N/A	1.338	N/A	1.342	N/A	1.326	N/A	1.355	N/A	1.350	N/A
C13-C14	N/A	1.207	N/A	1.222	N/A	1.217	N/A	1.229	N/A	1.211	N/A	1.216
C14-C15	1.350	N/A	1.350	N/A	1.354	N/A	1.340	N/A	1.363	N/A	1.361	N/A
C15-C16	N/A	1.196	N/A	1.210	N/A	1.207	N/A	1.215	N/A	1.204	N/A	1.205
bond type:	C-C	C≡C	C-C	C≡C	C-C	C≡C	C-C	C≡C	C-C	C≡C	C-C	C≡C
average:	1.339	1.212	1.339	1.222	1.345	1.217	1.328	1.229	1.357	1.211	1.352	1.216
deviation from exp. data (%):			1.152	0.820	1.152	0.820	0.799	0.404	2.044	1.416	0.101	0.093
sum of deviation from exp.			0.19		0.31		0.19				3.46	

Table 14.3 The effect of basis set on NICS values at three distances from the centers of the C1 and C2 atoms of $\text{H}(\text{C}\equiv\text{C})_4\text{H}$ using the CAM-B3LYP functional.

basis set	6-311++G(d,p)		6-311+G(d)		6-311+G		6-31+G(d)	
	C1	C2	C1	C2	C1	C2	C1	C2
NICS (3.0 Å)	0.1	0.0	0.0	0.1	0.0	0.1	0.0	0.1
NICS (2.0 Å)	-0.5	-0.3	-0.5	-0.3	-0.5	-0.3	-0.4	-0.2
NICS (1.0 Å)	-9.4	-8.7	-9.4	-8.6	-9.5	-8.9	-9.4	-8.6

Table 14.4 The effect of functional on NICS values at three distances from the centers of the C1 and C2 atoms of H(C≡C)₄H using the 6-311++G(d,p) basis set.

functional	B3LYP		CAM-B3LYP		BLYP		BP86		BMK	
	C1	C2	C1	C2	C1	C2	C1	C2	C1	C2
NICS (3.0 Å)	0.0	0.1	0.0	0.1	0.0	0.1	0.0	0.1	0.0	0.1
NICS (2.0 Å)	-0.5	-0.3	-0.5	-0.3	-0.5	-0.3	-0.5	-0.3	-0.5	-0.3
NICS (1.0 Å)	-9.3	-8.7	-9.3	-8.7	-9.3	-8.6	-9.3	-8.6	-9.3	-8.7
functional	PBE0		M06		M06L		ωB97xd			
	C1	C2	C1	C2	C1	C2	C1	C2		
NICS (3.0 Å)	0.0	0.1	0.0	0.1	0.0	0.1	0.0	0.1		
NICS (2.0 Å)	-0.5	-0.3	-0.5	-0.3	-0.5	-0.3	-0.5	-0.3		
NICS (1.0 Å)	-9.3	-8.7	-9.3	-8.7	-9.3	-8.6	-9.3	-8.7		

Table 14.5 Summary of the ^1H and ^{13}C NMR chemical shifts for $\text{H}(\text{C}\equiv\text{C})_n\text{H}$ ($n = 1-10$). All isotropic values have been corrected using TMS and the GIAO method at the CAM-B3LYP/6-311++G(d,p) level.

The TMS isotropic ^1H and ^{13}C values are 31.9766 and 187.8458, respectively.

n	C1	C2	C3	C4	C5	C6	C7	C8	C9	C10	C11	C12	C13	C14	C15	C16	C17	C18	C19	C20	^1H
10	71.05	73.46	66.14	64.85	66.29	65.11	66.10	65.41	65.92	65.68	65.68	65.92	65.41	66.10	65.11	66.29	64.85	66.14	73.46	71.05	1.360
9	70.98	73.50	66.11	64.92	66.21	65.19	66.05	65.55	65.86	65.86	65.55	66.05	65.19	66.21	64.92	66.11	73.50	70.98			1.359
8	70.91	73.41	65.87	64.90	66.09	65.25	65.83	65.56	65.56	65.83	65.25	66.09	64.90	65.87	73.41	70.91					1.352
7	70.78	73.43	65.79	64.97	65.93	65.34	65.62	65.62	65.34	65.93	64.97	65.79	73.43	70.78							1.344
6	70.61	73.55	65.68	65.08	65.74	65.39	65.39	65.74	65.08	65.68	73.55	70.61									1.336
5	70.44	73.71	65.51	65.12	65.42	65.42	65.12	65.51	73.71	70.44											1.332
4	70.13	73.94	65.35	65.17	65.17	65.35	73.94	70.13													1.318
3	69.75	74.11	64.85	64.85	74.11	69.75															1.292
2	69.03	73.86	73.86	69.03																	1.245
1	76.60	76.60																			1.323

Table 14.6 Summary of optimized bond lengths (Å) for H(C≡C)_nH (*n* = 1-10) at the CAM-B3LYP/6-311++G(d,p) level.

<i>n</i>	C–H	C1–C2	C2–C3	C3–C4	C4–C5	C5–C6	C6–C7	C7–C8	C8–C9	C9–	
10	1.06344	1.20160	1.36203	1.20982	1.35272	1.21251	1.35013	1.21341	1.34928	1.21372	1.34910
9	1.06344	1.20161	1.36207	1.20983	1.35278	1.21249	1.35022	1.21337	1.34945	1.21358	
8	1.06343	1.20161	1.36211	1.20981	1.35290	1.21245	1.35041	1.21323	1.34982		
7	1.06339	1.20161	1.36219	1.20978	1.35306	1.21233	1.35078	1.21290			
6	1.06328	1.20143	1.36187	1.20975	1.35382	1.21214	1.35200				
5	1.06333	1.20162	1.36273	1.20940	1.35410	1.21115					
4	1.06328	1.20147	1.36339	1.20868	1.35629						
3	1.60315	1.20098	1.36501	1.20662							
2	1.06307	1.19953	1.37210								
1	1.06337	1.19419									

D.2. Computational details for platinum polyne complexes in section 6.4

D.2.1. General considerations

When crystal structures were available, they were used as the starting geometries for computations. In other cases, related compounds generally with matching *sp* carbon chain lengths were employed. No constraints were applied in the calculations although several of the structures became less "bent" or more "linear" upon optimization. The structures were optimized using the BP86 functional¹ and with an increased SCF cycle maximum (scf = maxcycle = 1200). In previous work with the polyynes (section 6.3) $\text{H}(\text{C}\equiv\text{C})_n\text{H}$ ($n = 2-10$),¹⁷ BP86 was not the best performing functional. However, it afforded cleanly optimized wave functions for the compounds in this study, whereas other functionals (e.g. CAM-B3LYP)³ gave convergence difficulties.

A triple-zeta Pople basis set [6-311G(d)]⁹ with polarization functions was used for carbon, hydrogen, phosphorus, fluorine, and oxygen atoms. For platinum atoms, energy-consistent pseudopotentials (ECP) of the Stuttgart group, ECP60MDF (fully relativistic correction, 60 electrons in the core, 18 electrons treated fully), were paired with a double- ζ couple-cluster basis set (cc-pVDZ-PP VDZ-PP).¹⁸ All computations were performed with the Gaussian program package, which by default employs the ultrafine grid (99,590) to enhance accuracy.¹⁰ The fully optimized structures were then subjected to NMR computations using the same functional (BP86) and basis set. Tetramethylsilane (TMS) was optimized and its ¹³C NMR spectrum was analogously computed. All NMR chemical shifts from the compounds were then scaled to TMS by

taking the difference of computed chemical shift between the reference and the compound of interest. Results are summarized in Table 6.1 and Table 6.2 (see the main text section 6.4).

D.3. References

- (1) **BMK**-functional: Boese, D. A.; Martin, J. M. L. Development of density functionals for thermochemical kinetics. *J. Chem. Phys.* **2004**, *121*, 3405-3416.
- (2) **M06**-functional: Zhao, Y.; Truhlar, D. G. The M06 suite of density functionals for main group thermochemistry, thermochemical kinetics, noncovalent interactions, excited states, and transition elements: two new functionals and systematic testing of four M06-class functionals and 12 other functionals. *Theor. Chem. Acc.* **2008**, *120*, 215-241.
- (3) **CAM-B3LYP**-functional: Yanai, T.; Tew, P. D.; Handy, N. C. A new hybrid exchange–correlation functional using the Coulomb-attenuating method (CAM-B3LYP). *Chem. Phys. Lett.* **2004**, *393*, 51-57.
- (4) **ωB97XD**-functional: Chai, J.-D.; Head-Gordon, M. Long-range corrected hybrid density functionals with damped atom–atom dispersion corrections. *Phys. Chem. Chem. Phys.* **2008**, *10*, 6615-6620.
- (5) **PBE0**-functional: Adamo, C.; Barone, V. Toward reliable density functional methods without adjustable parameters: The PBE0 model. *J. Chem. Phys.* **1999**, *110*, 6158-6170.
- (6) **B3LYP**, **BLYP**, and **BP86** functionals: (a) Becke, A. D. Density-functional exchange-energy approximation with correct asymptotic behavior. *Phys. Rev. A*, **1988**, *38*, 3098-3100. (b) Becke, A. D. Density-functional thermochemistry. III. The role of exact exchange. *J. Chem. Phys.* **1993**, *98*, 5648-5652. (c) Lee, C.; Yang, W.; Parr, R. G.

Development of the Colle-Salvetti correlation energy formula into a functional of the electron density. *Phys. Rev. B*, **1988**, *37*, 785-789.

(7) **M06L**-functional: Zhao, Y.; Truhlar, D. G. A new local density functional for main-group thermochemistry, transition metal bonding, thermochemical kinetics, and noncovalent interactions. *J. Chem. Phys.* **2006**, *125*, 194101-194118.

(8) **BP86**-functional: Perdew, J. P. Density-functional approximation for the correlation energy of the inhomogeneous electron gas. *Phys. Rev. B*, **1986**, *33*, 8822-8824.

(9) References for Pople type basis set "**6-311G**" are as follows (an addition of "d" adds polarization functions of *d*-type to C, "p" adds *p*-type polarization functions to C and H atoms, and "+/++" indicates added diffuse functions): (a) McLean, A. D.; Chandler, G. S. Contracted Gaussian basis sets for molecular calculations. I. Second row atoms, *Z* = 11-18. *J. Chem. Phys.* **1980**, *72*, 5639-5648. (b) Raghavachari, K.; Binkley, J. S.; Seeger, R.; Pople, J. A. Self-consistent molecular orbital methods. XX. A basis set for correlated wave functions. *J. Chem. Phys.* **1980**, *72*, 650-654.

(10) Frisch, M. J.; Trucks, G. W.; Schlegel, H. B.; Scuseria, G. E.; Robb, M. A.; Cheeseman, J. R.; Scalmani, G.; Barone, V.; Mennucci, B.; Petersson, G. A.; Nakatsuji, H.; Caricato, M.; Li, X.; Hratchian, H. P.; Izmaylov, A. F.; Bloino, J.; Zheng, G.; Sonnenberg, J. L.; Hada, M.; Ehara, M.; Toyota, K.; Fukuda, R.; Hasegawa, J.; Ishida, M.; Nakajima, T.; Honda, Y.; Kitao, O.; Nakai, H.; Vreven, T.; Montgomery, J. A. Jr.; Peralta, J. E.; Ogliaro, F.; Bearpark, M.; Heyd, J. J.; Brothers, E.; Kudin, K. N.; Staroverov, V. N.; Kobayashi, R.; Normand, J.; Raghavachari, K.; Rendell, A.; Burant,

J. C.; Iyengar, S. S.; Tomasi, J.; Cossi, M.; Rega, N.; Millam, J. M.; Klene, M.; Knox, J. E.; Cross, J. B.; Bakken, V.; Adamo, C.; Jaramillo, J.; Gomperts, R.; Stratmann, R. E.; Yazyev, O.; Austin, A. J.; Cammi, R.; Pomelli, C.; Ochterski, J. W.; Martin, R. L.; Morokuma, K.; Zakrzewski, V. G.; Voth, G. A.; Salvador, P.; Dannenberg, J. J.; Dapprich, S.; Daniels, A. D.; Farkas, Ö.; Foresman, J. B.; Ortiz, J. V.; Cioslowski, J.; Fox, D. J. *Gaussian 09, Revision D.01*; Gaussian, Inc. Wallingford CT, **2009**.

(11) Chalifoux, W. A.; McDonald, R.; Ferguson, M. J.; Tykwinski, R. R. *tert*-Butyl-End-Capped Polyynes: Crystallographic Evidence of Reduced Bond-Length Alternation. *Angew. Chem. Int. Ed.* **2009**, *48*, 7915-7919; Polyine mit *tert*-Butyl-Endgruppen: kristallographischer Nachweis einer reduzierten Bindungslängenalternanz. *Angew. Chem.* **2009**, *121*, 8056-8060.

(12) Toomsalu, E.; Burk, P. Critical test of some computational methods for prediction of NMR ^1H and ^{13}C chemical shifts. *J. Mol. Model.* **2015**, *21*, 244-244.

(13) References for Pople type basis set "**6-31G**" are as follows (an addition of "d" adds polarization functions of *d*-type to C, "p" adds *p*-type polarization functions to C and H atoms. "+/++" indicates added diffuse functions): (a) Ditchfield, R.; Hehre, W. J.; Pople, J. A. Self-Consistent Molecular-Orbital Methods. IX. An Extended Gaussian-Type Basis for Molecular-Orbital Studies of Organic Molecules. *J. Chem. Phys.* **1971**, *54*, 724-728. (b) Hehre, W. J.; Ditchfield, R.; Pople, J. A. Self-Consistent Molecular Orbital Methods. XII. Further Extensions of Gaussian-Type Basis Sets for Use in Molecular Orbital Studies of Organic Molecules. *J. Chem. Phys.* **1972**, *56*, 2257-2261. (c) Hariharan, P. C.; Pople, J. A. The Influence of Polarization Functions on Molecular

Orbital Hydrogenation Energies. *Theor. Chem. Acc.* **1973**, *28*, 213-222. (d) Hariharan, P. C.; Pople, J. A. Accuracy of AH_n equilibrium geometries by single determinant molecular orbital theory. *Mol. Phys.* **1974**, *27*, 209-214. (e) Gordon, M. S. The isomers of silacyclopropane. *Chem. Phys. Lett.* **1980**, *76*, 163-168. (f) Francl, M. M.; Pietro, W. J.; Hehre, W. J.; Binkley, J. S.; Gordon, M. S.; DeFrees, D. J.; Pople, J. A. Self-consistent molecular orbital methods. XXIII. A polarization-type basis set for second-row elements. *J. Chem. Phys.* **1982**, *77*, 3654-3665. (g) Binning, Jr. R. C.; Curtiss, L. A. Compact Contracted Basis Sets for Third-Row Atoms: Ga-Kr. *J. Comp. Chem.* **1990**, *11*, 1206-1216. (h) Blaudeau, J.-P.; McGrath, M. P.; Curtiss, L. A.; Radom, L. Extension of Gaussian-2 (G2) theory to molecules containing third-row atoms K and Ca. *J. Chem. Phys.* **1997**, *107*, 5016-5021. (i) Rassolov, V. A.; Pople, J. A.; Ratner, M. A.; Windus, T. L. 6-31G* basis set for atoms K through Zn. *J. Chem. Phys.* **1998**, *109*, 1223-1229. (j) Rassolov, V. A.; Ratner, M. A.; Pople, J. A.; Redfern, P. C.; Curtiss, L. A. 6-31G* Basis Set for Third-Row Atoms. *J. Comp. Chem.* **2001**, *22*, 976-984.

(14) Klod, S.; Kleinpeter, E. *Ab initio* calculation of the anisotropy effect of multiple bonds and the ring current effect of arenes—application in conformational and configurational analysis. *J. Chem. Soc. Perkin Trans. 2*, **2001**, 1893-1898.

(15) Chen, Z.; Wannere, C. S.; Corminboeuf, C.; Puchta, R.; von Ragué Schleyer, P. Nucleus-Independent Chemical Shifts (NICS) as an Aromaticity Criterion. *Chem. Rev.* **2005**, *105*, 3842-3888.

(16) Remya, K.; Suresh, C. H. Carbon rings: a DFT study on geometry, aromaticity, intermolecular carbon–carbon interactions and stability. *RSC Adv.* **2016**, *6*, 44261-44271.

(17) Ehnbohm, A.; Hall, M. B.; Gladysz, J. A. Origin of Shielding and Deshielding Effects in NMR Spectra of Organic Conjugated Polyynes. *Org. Lett.* **2019**, *21*, 753-757.

(18) Figgen, D.; Peterson, K. A.; Dolg, M.; Stoll, H. Energy-consistent pseudopotentials and correlation consistent basis sets for the 5d elements Hf–Pt. *J. Chem. Phys.* **2009**, *130*, 164108.

APPENDIX E

E.1. Computational section

E.1.1. General considerations

Validation methods were initially sought to ensure the accuracy of the results. However, it had previously been shown that the functionals ω B97X-D¹ and CAM-B3LYP² gave the best agreement with experimental C–C and C \equiv C bond lengths in diterminal conjugated polyynes H(C \equiv C)_nH ($n = 2-10$).³ The same protocol was applied in a study specifically addressing spectroscopic properties of platinum polyynyl complexes,⁴ again with good agreement between experimental and computed data. Most calculations were performed using the Gaussian program package, employing the ultrafine grid (99,590) to enhance accuracy.⁵

This study mainly used the triple- ζ Pople basis set [6-311G(d)]⁶ on all non-platinum atoms. Other families of basis sets (e.g. def2-SVP, def2-SV(P), def2-SV, and def2-TZVP)⁷ were evaluated for optimization of the full Pt₄C₁₆ complex **4a**. However, these led to convergence problems with the ω B97X-D and CAM-B3LYP functionals. It was further reasoned that polarization functions on the hydrogen atoms would not be necessary, as these are located only in the periphery, and thus should not significantly impact spectroscopic data. For platinum atoms, energy-consistent pseudopotentials (ECP) of the Stuttgart group, ECP60MWB (quasi relativistic correction, 60 electrons in the core, 18 electrons treated fully), with its matching basis set (ECP60MWB) were

used.⁸ Refer to Table 15.1 for specific details regarding the exact basis set used for different tasks as smaller variations were applied.

Throughout this section, experimental and model compounds are numbered as in the main text. In **4'a**, the PPh groups of **4a** have been replaced by PMe groups. The analogous Pt₃C₁₂ and Pt₅C₂₀ complexes are referred to as **7'a** and **8'a**. Computations were carried out on both the experimental bis(butadiynyl) complexes **3a,b** as well as the PMe analogs **3'a,b**. Most of the geometry-optimized species are depicted in Figure 15.1.

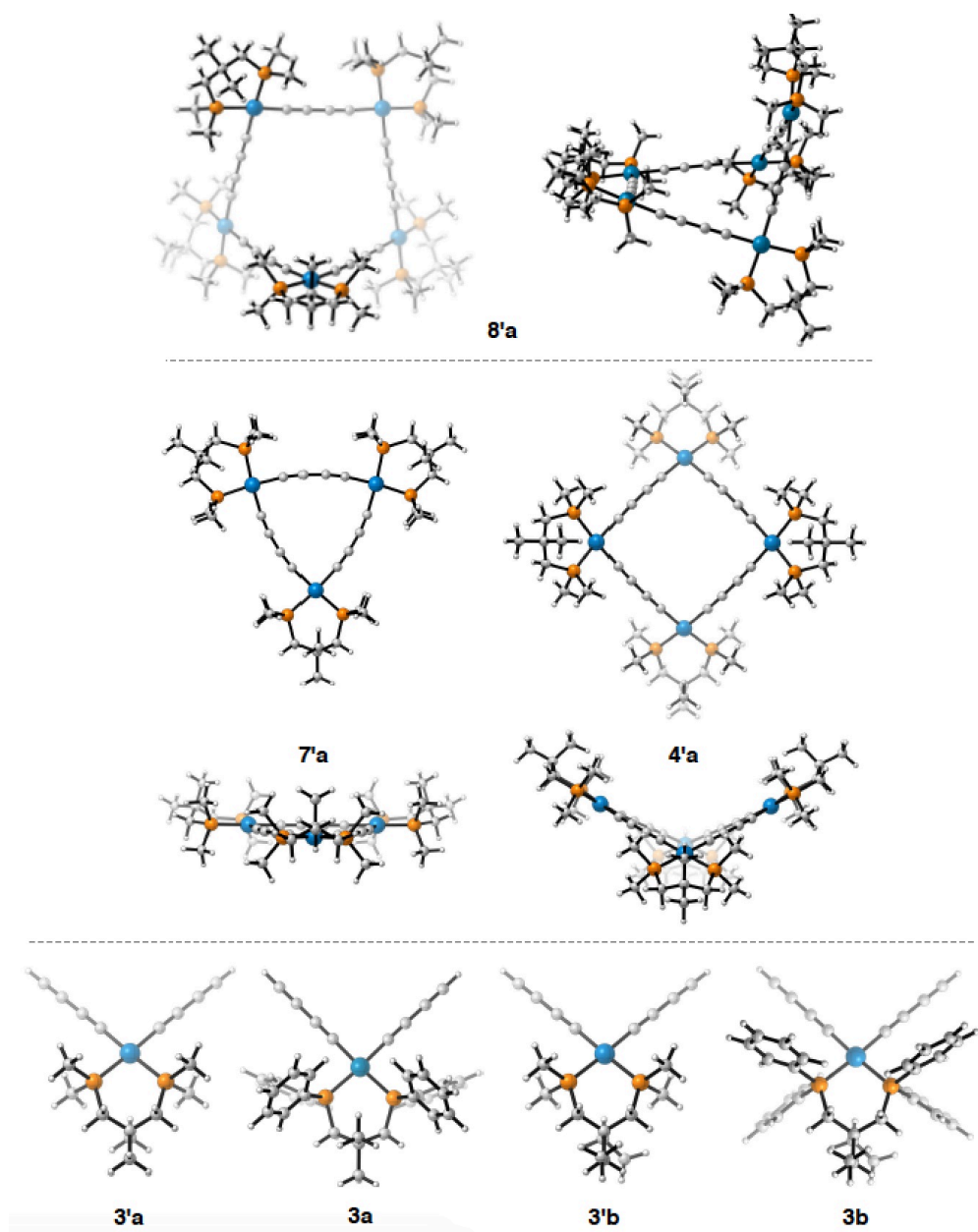


Figure 15.1 Views of computed structures.

E.1.2. Conformational and constitutional equilibria

All cyclic polyplatinum species were challenging to converge and a wide variety of computational methods and theory levels had to be used before suitable structures were obtained. Planar symmetrized starting geometries of **4'a** and other Pt_nC_{4n} complexes were constructed in addition to using (for **4'a**) the puckered crystal structures. Optimizing these structures using DFT never resulted in fully puckered minima. Semi-empirical methods (PM6) were first employed in order to get closer to the experimental puckered geometry. Converged geometries from the semi-empirical calculations were then subjected to appropriate DFT optimizations. Due to the small energetic difference between planar and puckered **4'a** obtained by the CAM-B3LYP/6-311G(d) (gas phase) method, a multitude of single point calculations with different theoretical models were carried out. The resulting electronic energies are provided in Table 15.1.

Table 15.1 Computed stability differences (kcal/mol) between planar and puckered isomers of **4'a**.^a

entry	functional	basis set	solvent ^b	dispersion correction ^c	4'a (planar)	4'a (puckered)
1	wB97X-D	6-31G(d) ^d	gas phase	—	0	-0.2
2	wB97X-D	6-31G(d) ^d	SMD/H ₂ O	—	0	0.4
3	wB97X-D	6-31G(d) ^d	SMD/C ₆ H ₆	—	0	-0.8
4	wB97X-D	6-311G(d) ^d	gas phase	—	0	1.9
5	wB97X-D	def2-SVP ^d	gas phase	—	0	-3.0
6	wB97X-D	6-31G(d) ^e	gas phase	—	0	0.0
7	CAM-B3LYP	6-31G(d) ^d	gas phase	GD3BJ ^c	0	-0.8
8	wB97X-D	cc-pVDZ ^d	gas phase	—	0	-3.5
9	wB97X-D	6-311+G(d) ^d	SMD/H ₂ O	—	0	0.4
10	wB97X-D	6-31G(d) ^d	SMD/Et ₂ O	—	0	-0.5
11	wB97X-D	6-31G(d) ^d	SMD/CH ₂ Cl ₂	—	0	-0.2
12	wB97X-D	6-31G(d) ^d	SMD/MeOH	—	0	0.0
13	wB97X-D	6-31G(d) ^d	SMD/THF	—	0	-0.2
14	B3LYP	6-31G(d) ^d	MeOH	GD3BJ ^c	0	-0.2
15	TPSS	6-31G(d) ^d	MeOH	GD3BJ ^c	0	-2.6
16	CAM-B3LYP	6-31G(d) ^d	MeOH	GD3BJ ^c	0	1.0
17	PBE	6-31G(d) ^d	MeOH	GD3BJ ^c	0	-5.8
18	wB97X-D	6-311G(d) ^e	MeOH	—	0	2.0
19	wB97X-D	cc-pVTZ ^e	MeOH	—	0	3.6

^a Single point calculations from a geometry optimized structure at the CAM-B3LYP/6-311G(d) level of theory. ^b Truhlar's universal continuum solvation model (SMD) was used. ^c Grimme's empirical dispersion corrections with Becke-Johnson damping were used in all applicable cases except for incompatible functionals (wB97X-D). ^d The basis set ECP60MWB was used for platinum with the same ECP. ^e The basis set cc-pVTZ-PP was used for platinum with the ECP60MDF ECP.

Transition state searches were carried out.¹⁰ One could be found for a truncated model with two PH₃ ligands in place of each chelating diphosphine (**4''**). It exhibited an intermediate non-planar geometry (164.9° angle between the planes defined in Figure 7.4). A frequency analysis confirmed that it showed *one* imaginary mode, which was distributed over the entire Pt₄C₁₆ moiety with large displacement vectors at each platinum corner. Two diagonally disposed platinum corners are bending upwards, while the other two bend downwards.

Another objective was to establish the thermodynamics of various equilibria involving **4'a**, **7'a**, and **8'a**. Calculations employed the free energies from the frequency calculations of these species in gas phase.

E.1.3. Computed UV-visible spectra

Simulated UV-visible data were sought for a variety of reasons. TD-DFT calculations were set up using 30 excited states (singlets) for all involved species and employing the same CAM-B3LYP/6-311G(d) level of theory. The excitations were added in increments of 10 until no observable qualitative differences in spectral features could be noted. A full list of interpreted transitions is provided in Table 15.2. The intensities (*y*-axis) of the spectra were scaled uniformly (factor of $6 \cdot 10^{-5}$). A scaling factor was further applied to the *x*-axis in order to match the highest intensity band of **3a** with that of computed **3'a**. This complex was used as the scaling standard because of its unambiguous geometry. All spectra were plotted with a 600 cm⁻¹ linewidth. The resulting UV-visible simulations are depicted in Figure 7.6 and Figure 15.2.

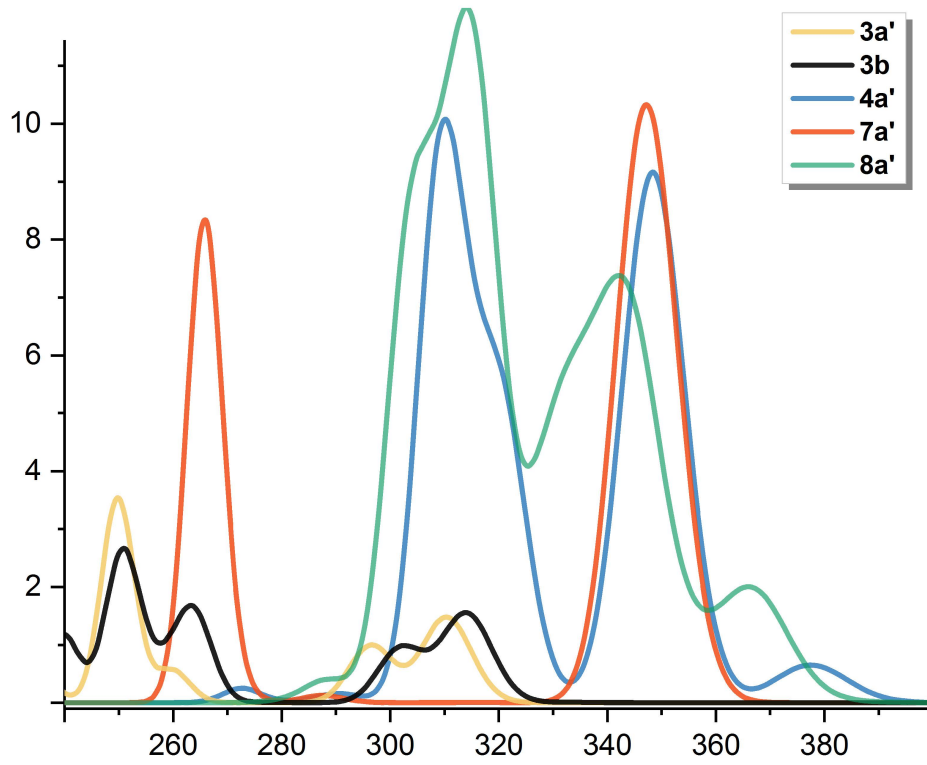


Figure 15.2 Computed UV-visible spectra of **3'a**, **3b**, **4'a**, **7'a**, and **8'a**.

Table 15.2 Computed wavelengths (λ , nm), oscillator strengths (f), main compositions, and main assignments for the UV-visible electronic excitations of **3'a**, **7'a**, **4'a**, and **8'a**. Unless noted, only contributions larger than 10% are presented. The associated orbitals are plotted in Figures 15.3-15.6.

λ^a (f)	main composition	main assignment
3'a		
295.5 (0.0907) ^b	73% HOMO-3 → LUMO 11% HOMO-1 → LUMO+7	Pt(5d), π → Pt(6p), π^* Pt(5d), π → Pt(5d), π^*
310.4 (0.1353) ^b	82% HOMO → LUMO 07% HOMO-2 → LUMO+7	Pt(5d), π → Pt(6p), π^* Pt(5d), π → Pt(5d), π^*
7'a		
265.73 (0.3742) ^b	31% HOMO-5 → LUMO 08% HOMO-3 → LUMO+10 09% HOMO-2 → LUMO+9 09% HOMO-1 → LUMO+13	Pt(5d), π → Pt(p) Pt(5d), π → Pt(5d), π^* , ligand Pt(5d), π → Pt(5d), π^* , ligand π → Pt(5d), π^* , ligand
265.85 (0.3759) ^b	32% HOMO-4 → LUMO 08% HOMO-3 → LUMO+13 08% HOMO-2 → LUMO+10 10% HOMO-1 → LUMO+14	Pt(5d), π → Pt(p) Pt(5d), π → Pt(5d), π^* , ligand Pt(5d), π → Pt(5d), π^* , ligand π → Pt(5d), π^* , ligand
347.14 (0.4750) ^b	83% HOMO-5 → LUMO 06% HOMO → LUMO+4 10% HOMO → LUMO+5	Pt(5d), π → Pt(6p) Pt(5d), π → Pt(6p), π^* Pt(5d), π → Pt(6p), π^*
347.22 (0.4744) ^b	83% HOMO-4 → LUMO 10% HOMO → LUMO+4 06% HOMO → LUMO+5	Pt(5d), π → Pt(6p) Pt(5d), π → Pt(6p), π^* Pt(5d), π → Pt(6p), π^*
4'a		
273.07 (0.0174)	54% HOMO-1 → LUMO+4 11% HOMO-4 → LUMO+3 16% HOMO-3 → LUMO+1	Pt(5d), π → Pt, ligand scaffold Pt(5d), π → Pt, ligand scaffold Pt(5d), π → Pt, ligand scaffold
291.05 (0.0115)	51% HOMO-1 → LUMO+2 19% HOMO → LUMO+1	Pt(5d), π → ligand scaffold Pt(5d), π → Pt, ligand scaffold
309.33 (0.3447)	20% HOMO-7 → LUMO+5 26% HOMO-6 → LUMO+7 17% HOMO-4 → LUMO+5	Pt(5d), π → Pt(6p), π^* Pt(5d), π → Pt(6p), π^* Pt(5d), π → Pt(6p), π^*
309.57 (0.3499)	13% HOMO-7 → LUMO+6 10% HOMO-5 → LUMO 26% HOMO-5 → LUMO+7 11% HOMO-4 → LUMO+6 12% HOMO-3 → LUMO+5	Pt(5d), π → Pt(6p), π^* Pt(5d), π → Pt(6p) Pt(5d), π → Pt(6p), π^* Pt(5d), π → Pt(6p), π^* Pt(5d), π → Pt(6p), π^*
310.38 (0.1953)	23% HOMO-7 → LUMO 21% HOMO-6 → LUMO+5 11% HOMO-5 → LUMO+1 17% HOMO-5 → LUMO+6 21% HOMO-4 → LUMO+7	Pt(5d), π → Pt(6p) Pt(5d), π → Pt(6p), π^* Pt(5d), π → Pt, ligand scaffold Pt(5d), π → Pt(6p), π^* Pt(5d), π → Pt(6p), π^*
320.10 (0.2416)	22% HOMO-3 → LUMO+5 37% HOMO-2 → LUMO+7 20% HOMO → LUMO+5	Pt(5d), π → Pt(6p), π^* Pt(5d), π → Pt(6p), π^* Pt(5d), π → Pt(6p), π^*
320.41 (0.2307)	13% HOMO-4 → LUMO+5 14% HOMO-4 → LUMO+6 36% HOMO-1 → LUMO+7 12% HOMO → LUMO+6	Pt(5d), π → Pt(6p), π^* Pt(5d), π → Pt(6p), π^* Pt(5d), π → Pt(6p), π^* Pt(5d), π → Pt(6p), π^*

Table 15.2 continued.

λ^a (f)	main composition	main assignment
348.33 (0.4064)	41% HOMO-5 → LUMO 31% HOMO → LUMO+5	Pt(5d), π → Pt(6p) Pt(5d), π → Pt(6p), π^*
348.52 (0.4104)	42% HOMO-6 → LUMO 11% HOMO → LUMO+1 22% HOMO → LUMO+6	Pt(5d), π → Pt(6p) Pt(5d), π → Pt, ligand scaffold Pt(5d), π → Pt(6p), π^*
377.43 (0.0277)	17% HOMO-4 → LUMO+6 13% HOMO-3 → LUMO+5 52% HOMO-2 → LUMO	Pt(5d), π → Pt(6p), π^* Pt(5d), π → Pt(6p), π^* Pt(5d), π → Pt(6p), π^*
377.55 (0.0319)	23% HOMO-4 → LUMO+5 52% HOMO-1 → LUMO	Pt(5d), π → Pt(6p) Pt(5d), π → Pt(6p), π^* Pt(5d), π → Pt(6p)
8'a		
288.13 (0.0136)	24% HOMO-3 → LUMO+1 10% HOMO-3 → LUMO+2 15% HOMO-2 → LUMO+3 24% HOMO-2 → LUMO+4 14% HOMO-2 → LUMO+5	Pt(5d), π → Pt, ligand scaffold Pt(5d), π → Pt, ligand scaffold Pt(5d), π → Pt, ligand scaffold Pt(5d), π → Pt, ligand scaffold Pt(5d), π → Pt, ligand scaffold
301.80 (0.1725)	11% HOMO-9 → LUMO+2 39% HOMO-9 → LUMO+9 13% HOMO-6 → LUMO+9	Pt(5d), π → Pt, ligand scaffold Pt(5d), π → Pt(6p), π^* Pt(5d), π → Pt(6p), π^*
303.87 (0.4598)	12% HOMO-9 → LUMO+9 20% HOMO-7 → LUMO+7	Pt(5d), π → Pt(6p), π^* Pt(5d), π → Pt(6p), π^*
309.60 (0.2169)	15% HOMO-9 → LUMO+7 16% HOMO-6 → LUMO+9 15% HOMO → LUMO+9	Pt(5d), π → Pt(6p), π^* Pt(5d), π → Pt(6p), π^* Pt(5d), π → Pt(6p), π^*
314.09 (0.5188)	10% HOMO-9 → LUMO 18% HOMO-8 → LUMO+7 14% HOMO-7 → LUMO+8 21% HOMO-4 → LUMO+9	Pt(5d), π → Pt(6p), π^* Pt(5d), π → Pt(6p), π^* Pt(5d), π → Pt(6p), π^* Pt(5d), π → Pt(6p), π^*
316.85 (0.4730)	27% HOMO-4 → LUMO+9 16% HOMO-3 → LUMO+9	Pt(5d), π → Pt(6p), π^* Pt(5d), π → Pt(6p), π^*
330.49 (0.2848)	18% HOMO-6 → LUMO 20% HOMO-3 → LUMO+7 10% HOMO → LUMO+9	Pt(5d), π → Pt(6p), π^* Pt(5d), π → Pt(6p), π^* Pt(5d), π → Pt(6p), π^*
336.34 (0.2285)	10% HOMO-2 → LUMO+6 29% HOMO-2 → LUMO+7 12% HOMO-2 → LUMO+9 22% HOMO-1 → LUMO+7	Pt(5d), π → Pt, ligand scaffold Pt(5d), π → Pt(6p), π^* Pt(5d), π → Pt(6p), π^* Pt(5d), π → Pt(6p), π^*
343.17 (0.1485)	10% HOMO-9 → LUMO 11% HOMO-2 → LUMO+7 10% HOMO-2 → LUMO+8 10% HOMO → LUMO+3 21% HOMO → LUMO+8	Pt(5d), π → Pt(6p), π^* Pt(5d), π → Pt(6p), π^* Pt(5d), π → Pt(6p), π^* Pt(5d), π → Pt, ligand scaffold Pt(5d), π → Pt(6p), π^*
345.10 (0.3458)	10% HOMO-8 → LUMO 50% HOMO-1 → LUMO+9	Pt(5d), π → Pt(6p), π^* Pt(5d), π → Pt(6p), π^*
366.93 (0.1650)	14% HOMO-2 → LUMO 14% HOMO-1 → LUMO 47% HOMO → LUMO	Pt(5d), π → Pt(6p), π^* Pt(5d), π → Pt(6p), π^* Pt(5d), π → Pt(6p), π^*

^a All absorptions are scaled by a factor of 1.095 based on matching the intense 310 nm signal of **3'a** with the intense 304 nm signal of **3a**. ^b Additional transitions were analyzed due to an abundance of weak absorptions.

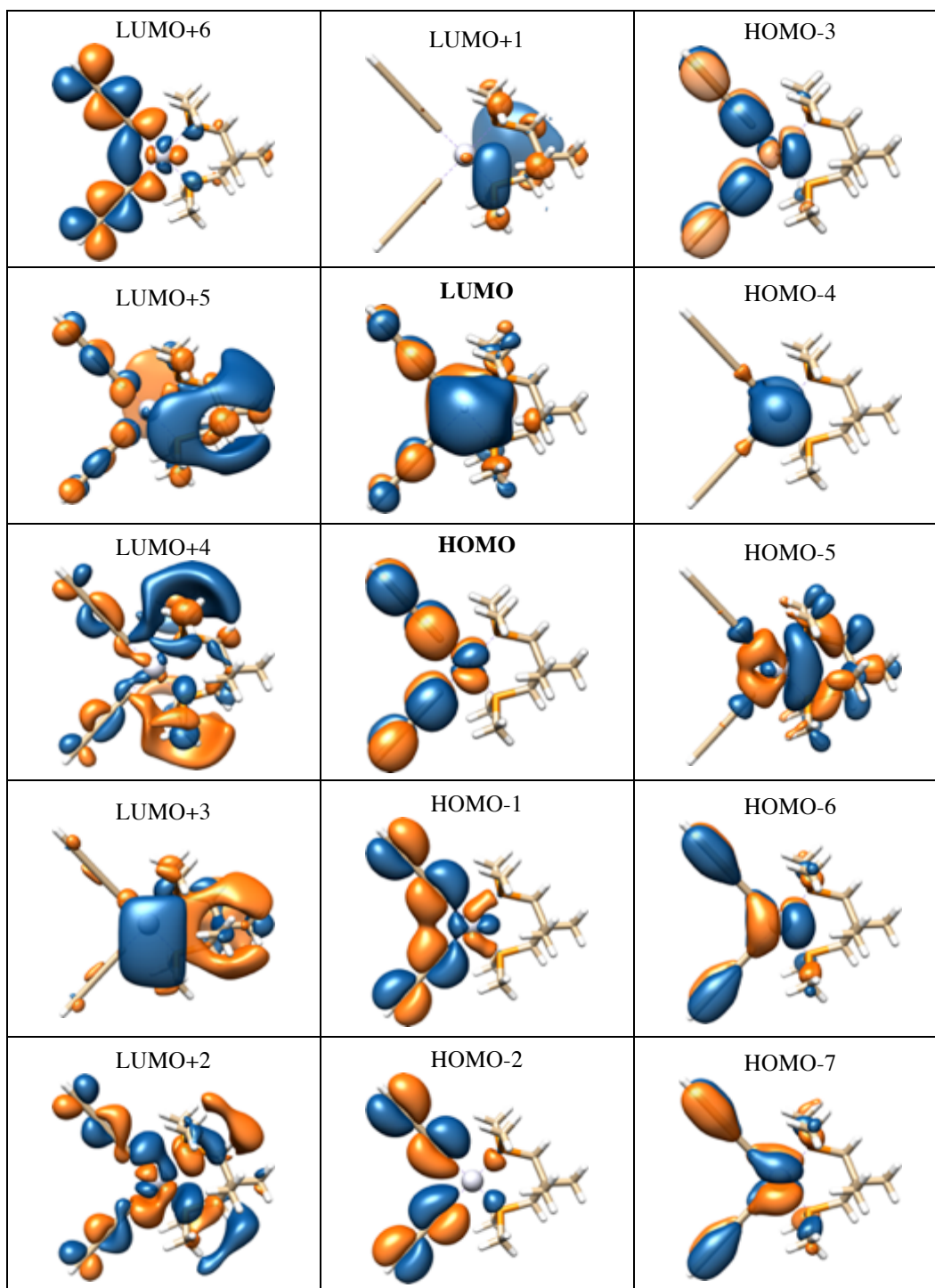


Figure 15.3 Selected frontier molecular orbitals of **3'a** relevant to Table 15.2.

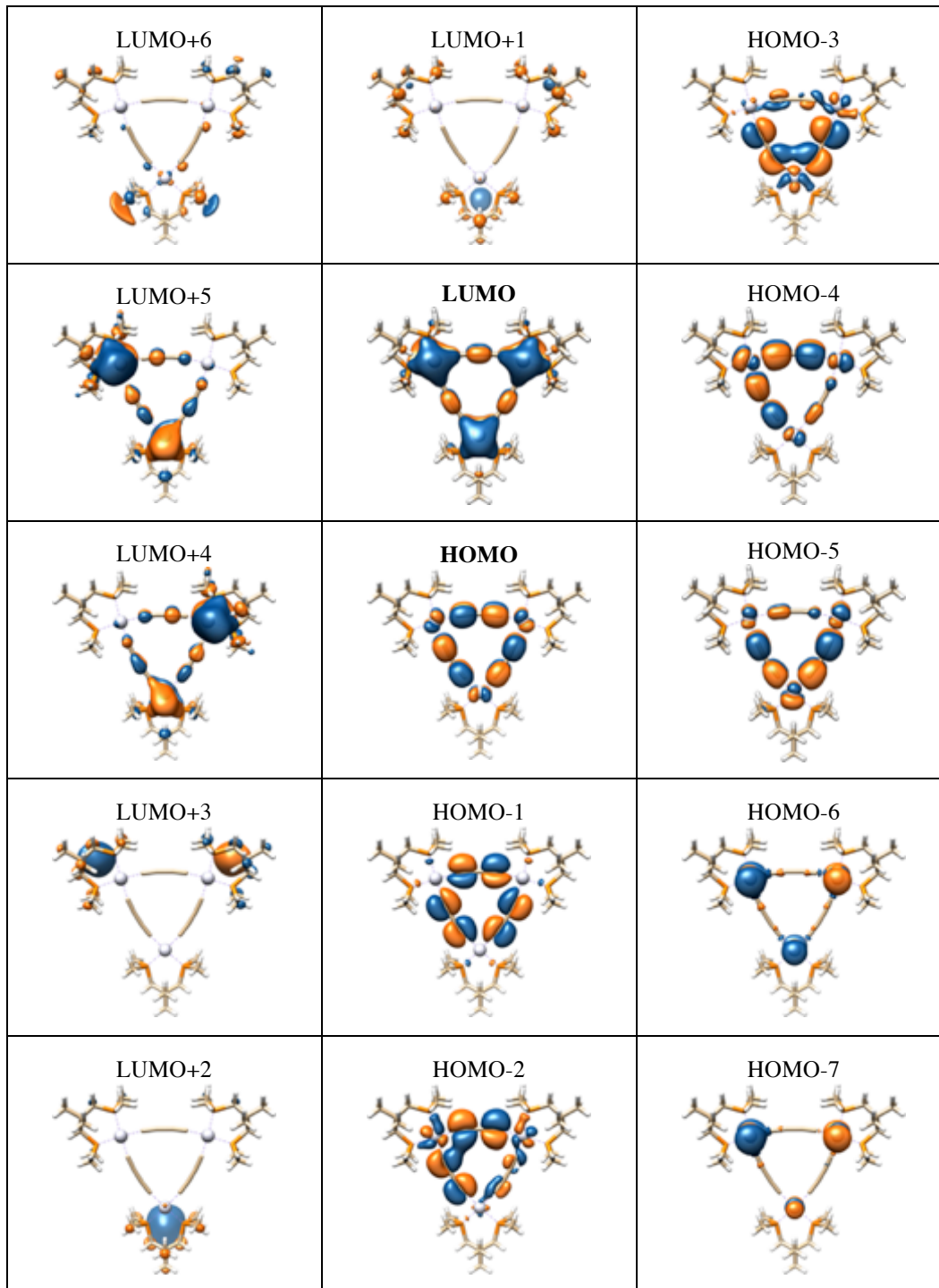


Figure 15.4 Selected frontier molecular orbitals of **7'a** relevant to Table 15.2.

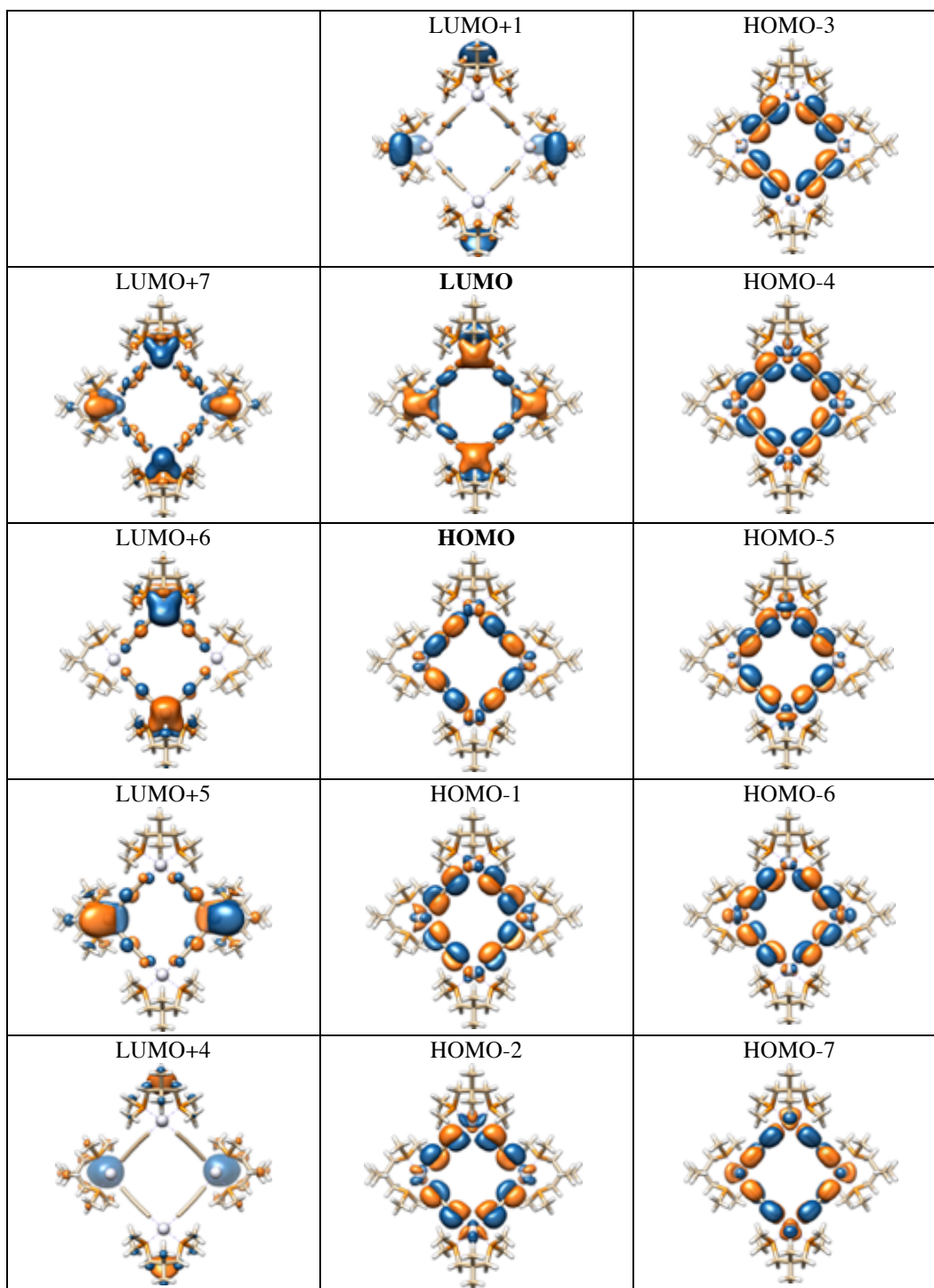


Figure 15.5 Selected frontier molecular orbitals of **4'a** relevant to Table 15.2.

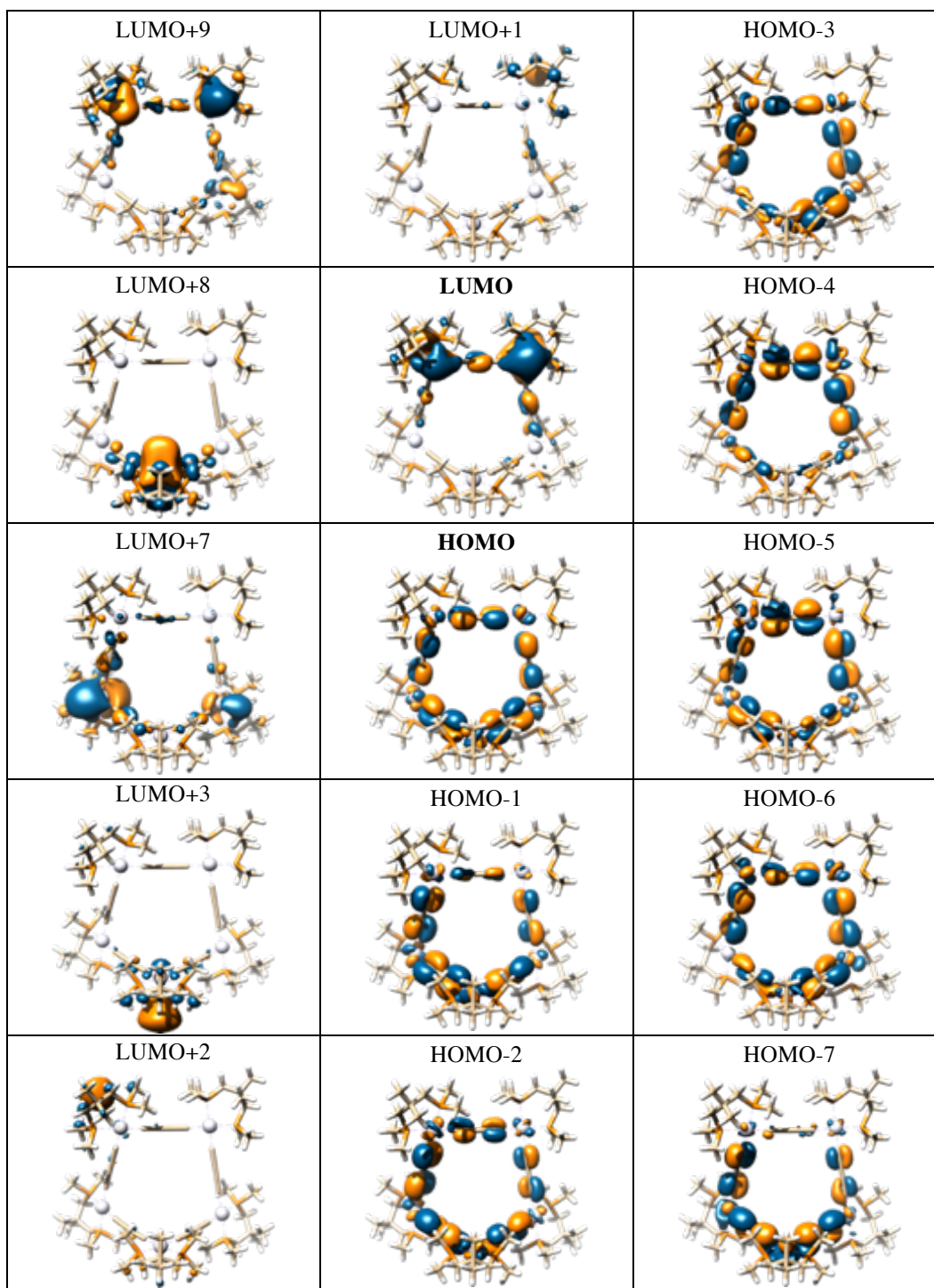


Figure 15.6 Selected frontier molecular orbitals of **8'a** relevant to Table 15.2.

E.1.4. Electrostatic potential surfaces

Electrostatic potential surface maps (Figure 15.7) were generated for the polyplatinum complexes and other relevant species from the DFT optimized structures at the CAM-B3LYP/6-311G(d) level of theory using the default settings in Gaussian. All plots were rendered using a density of $r = 0.004 \text{ e}\cdot\text{au}^{-3}$ and surfaces were rendered with a fixed isovalue to facilitate comparisons. The surface scales were fixed to a range of -0.011 to 0.011 au using a coarse grid.

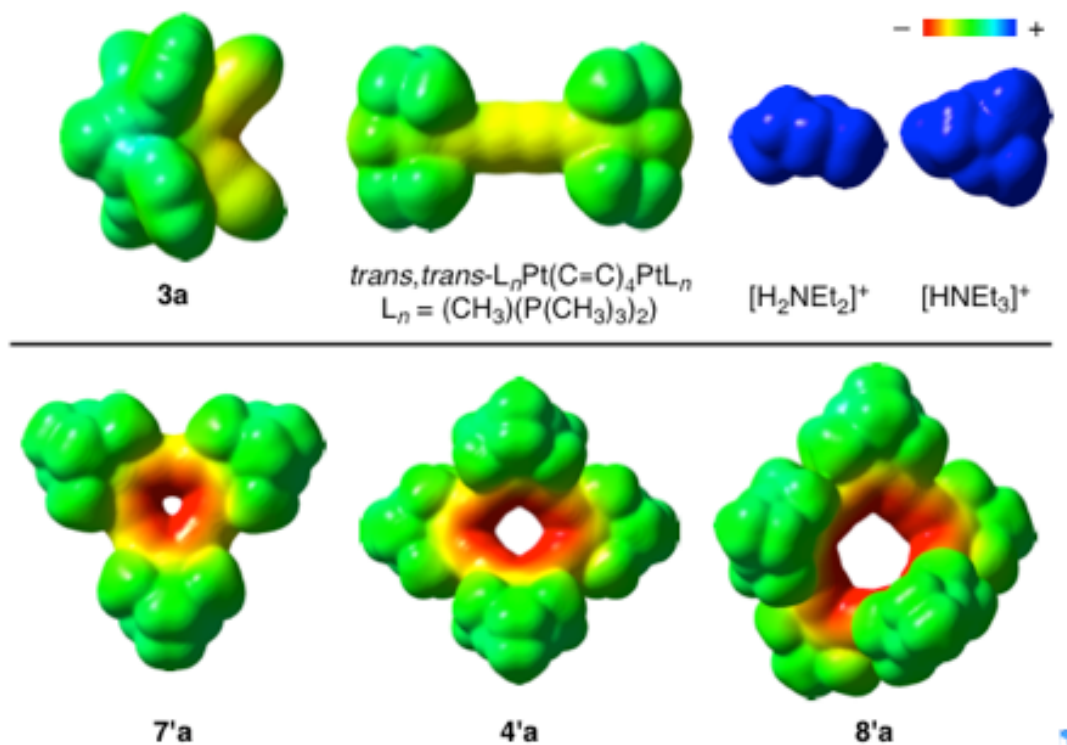


Figure 15.7 Electrostatic potential surface plots for selected DFT optimized species.

E.1.5. Structural data

Experimental structures were overlaid with the model computed structures, excising any atoms not contained in the model. These were compared using the *Molecular Overlay* function in the program Mercury, as shown in Figure 15.8. The RMSD values were then calculated. Additional comparisons of experimental and computed structures are given in Table 15.3 and Table 15.4.

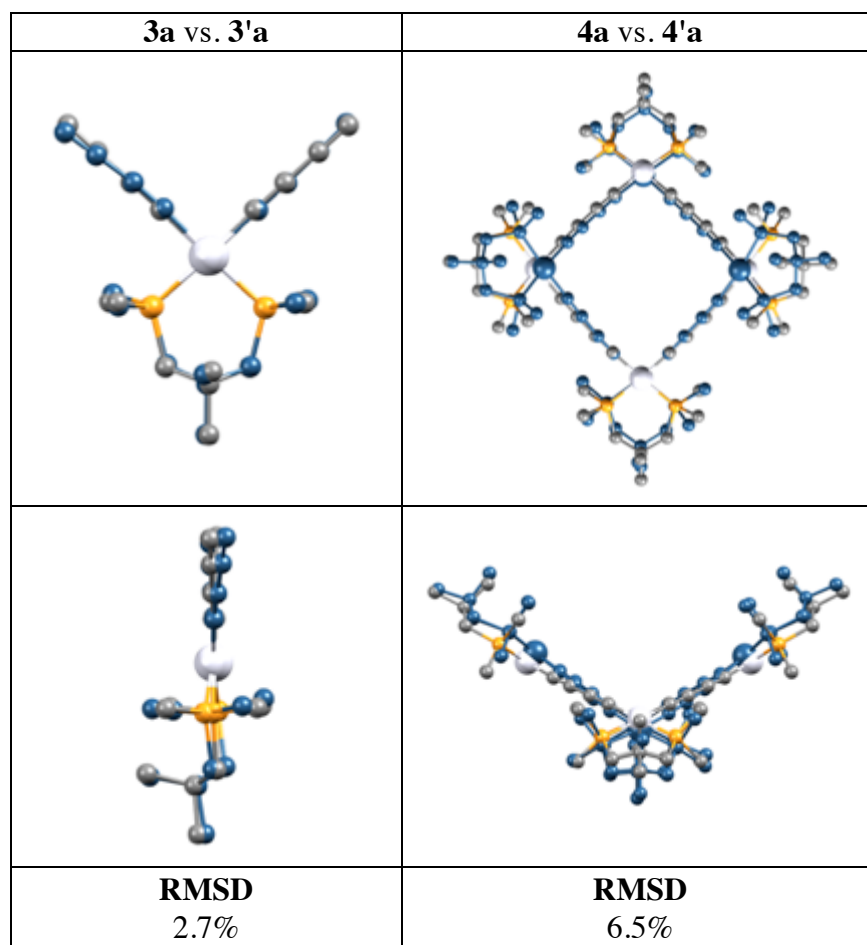


Figure 15.8 Overlays of experimental and computed structures, truncating the former for atoms not included in the latter. The hydrogen atoms have been removed for clarity.

Table 15.3 Key crystallographic distances (Å) and angles (°) for **3a**·CH₂Cl₂ and the corresponding metrics computed for **3a**, **3'a**, **3b**, and **3'b**.^a Computed data are have compound numbers shown in brackets.

	3a ·CH ₂ Cl ₂	3a ^b	3'a ^c	error dev. (%) ^d	3b	3'b ^c
Pt1–C4	1.998(4)	1.993	1.998	0.0%	1.993	1.998
Pt1–C8	2.004(4)	1.993	1.998	0.5%	1.994	1.999
Pt1–P2	2.2912(10)	2.326	2.31	0.8%	2.323	2.308
Pt1–P3	2.2870(9)	2.326	2.31	1.0%	2.329	2.311
C4≡C5	1.212(5)	1.214	1.215	0.0%	1.214	1.215
C5–C6	1.387(5)	—	—	—	—	—
C6≡C7	1.178(5)	1.214	1.215	3.1%	1.214	1.215
C8≡C9	1.211(5)	1.202	1.202	0.8%	1.202	1.202
C9–C10	1.376(6)	—	—	—	—	—
C10≡C11	1.188(5)	1.202	1.202	0.7%	1.203	1.202
C4–Pt1–C8	90.65(14)	89.40	90.99	0.5%	89.30	90.96
Pt1–C4–C5	174.2(3)	178.55	177.81	2.1%	178.75	177.78
C4–C5–C6	175.1(4)	179.48	179.85	2.5%	179.56	179.85
C5–C6–C7	179.8(6)	179.68	179.62	0.1%	179.72	179.62
Pt1–C8–C9	175.6(3)	178.55	177.82	1.1%	178.63	177.86
C8–C9–C10	178.2(4)	179.48	179.82	1.1%	179.07	179.84
C9–C10–C11	178.9(4)	179.68	179.62	0.3%	179.47	179.62
P2–Pt–P3	96.06(3)	96.31	96.19	0.1%	96.21	95.96

^a For the atom numbering, see Figure 7.1. ^c Computed structure of **3a**. ^c In these molecules, the PPh groups of the unprimed analogs have been replaced by PMe groups. ^d For **3'a** and **3a**·CH₂Cl₂.

Table 15.4 Key crystallographic distances (Å) and angles (°) for **4a**, and corresponding metrics computed for **4'a**, **7'a**, and **8'a**.^a Computed data are have compound numbers shown in brackets.

	4a	4'a	error dev. (%) ^b	7'a	8'a
Pt1–C1	2.006(6)	2.000	0.3	2.002	2.002
Pt1–C16	1.998(7)	2.000	0.1	—	—
Pt1–C12	—	—	—	2.002	—
Pt1–C20	—	—	—	—	1.998
Pt2–C4	2.001(6)	2.000	0.1	2.002	2.003
Pt2–C5	2.010(6)	2.000	0.5	2.003	1.999
Pt3–C8	2.008(6)	2.000	0.4	2.003	2.000
Pt3–C9	2.009(6)	2.000	0.5	2.002	1.999
Pt4–C12	2.022(6)	2.000	1.1	—	1.999
Pt4–C13	1.998(6)	2.000	0.1	—	1.999
Pt5–C16	—	—	—	—	1.999
Pt5–C17	—	—	—	—	1.999
Pt1–P1	2.2825(15)	2.297	0.6	2.294	2.300
Pt1–P2	2.2819(14)	2.297	0.7	2.294	2.298
Pt2–P3	2.2810(15)	2.297	0.7	2.294	2.299
Pt2–P4	2.2809(16)	2.297	0.7	2.295	2.299
Pt3–P5	2.2771(15)	2.297	0.9	2.295	2.299
Pt3–P6	2.2812(15)	2.297	0.7	2.293	2.300
Pt4–P7	2.2770(14)	2.297	0.9	—	2.298
Pt4–P8	2.2787(15)	2.297	0.8	—	2.298
Pt5–P9	—	—	—	—	2.298
Pt5–P10	—	—	—	—	2.298
C1≡C2	1.231(9)	1.217	1.3	1.216	1.217
C2–C3	1.377(9)	1.373	0.3	1.373	1.373
C3≡C4	1.212(9)	1.217	0.3	1.216	1.217
C5≡C6	1.192(8)	1.217	2.0	1.216	1.217

Table 15.4 *continued.*

	4a	4'a	error dev. (%) ^b	7'a	8'a
C6–C7	1.408(9)	1.373	2.5	1.373	1.374
C7≡C8	1.187(8)	1.217	2.5	1.216	1.217
C9≡C10	1.208(8)	1.217	0.7	1.216	1.217
C10–C11	1.376(9)	1.373	0.3	1.373	1.372
C11≡C12	1.180(8)	1.217	3.0	1.216	1.217
C13≡C14	1.218(8)	1.217	0.2	—	1.216
C14–C15	1.372(9)	1.373	0.1	—	1.372
C15≡C16	1.220(9)	1.217	0.3	—	1.217
C17≡C18	—	—	—	—	1.217
C18–C19	—	—	—	—	1.372
C19≡C20	—	—	—	—	1.217
C16–Pt1–C1	86.1(2)	90.3	4.9	—	—
C12≡Pt1≡C1	—	—	—	87.43	—
C20≡Pt1≡C1	—	—	—	—	91.80
C4–Pt2–C5	88.6(2)	90.24	1.8	87.54	92.46
C8–Pt3–C9	86.5(2)	90.3	4.4	87.48	92.15
C12–Pt4–C13	88.3(2)	90.23	2.3	—	90.58
C16≡Pt5≡C17	—	—	—	—	90.43
Pt1–C1–C2	176.5(5)	177.35	0.5	172.61	176.19
C1–C2–C3	177.4(7)	177.34	0.1	173.3	178.94
C2–C3–C4	177.9(6)	177.32	0.4	173.39	179.16
C3–C4–Pt2	176.6(5)	177.29	0.4	172.83	176.18
Pt2–C5–C6	179.4(6)	177.27	1.2	172.72	175.89
C5–C6–C7	177.9(7)	177.33	0.4	173.35	178.74
C6–C7–C8	177.0(8)	177.34	0.1	173.28	178.61
C7–C8–Pt3	173.6(5)	177.38	2.1	172.64	175.49
Pt3–C9–C10	174.7(5)	177.36	1.5	172.89	175.55
C9–C10–C11	177.7(7)	177.34	0.2	173.44	178.48
C10–C11–C12	179.6(8)	177.32	1.3	173.41	178.19
C11–C12–Pt4	174.1(5)	177.28	1.8	—	176.80
C11–C12–Pt1	—	—	—	172.74	—
Pt4–C13–C14	176.9(5)	177.27	0.2	—	175.44
C13–C14–C15	177.9(7)	177.33	0.4	—	176.74
C14–C15–C16	177.6(7)	177.35	0.2	—	176.65
C15–C16–Pt1	177.0(5)	177.37	0.2	—	—
C15–C16–Pt5	—	—	—	—	174.77
Pt5–C17–C18	—	—	—	—	175.87
C17–C18–C19	—	—	—	—	177.65
C18–C19–C20	—	—	—	—	177.92
C19–C20–Pt1	—	—	—	—	175.60
Pt1–Pt2	7.811	7.792	0.2	7.676	7.800
Pt2–Pt3	7.785	7.792	0.0	7.675	7.795
Pt3–Pt4	7.772	7.792	0.3	—	7.795
Pt1–Pt4	7.790	7.792	0.2	—	10.399
Pt1–Pt3	10.144	10.370	2.2	7.677	11.895
Pt2–Pt4	9.735	10.339	5.8	—	11.696
Pt4–Pt5	—	—	—	—	7.769
Pt1–Pt5	—	—	—	—	7.787
Pt3–Pt5	—	—	—	—	10.514
Pt2–Pt5	—	—	—	—	11.455

^aThe atom numbering can be inferred from that in Table 7.5. ^bFor **4a** and **4'a**.

E.2. References

(1) J Chai, J.-D.; Head-Gordon, M. Long-range corrected hybrid density functionals with damped atom–atom dispersion corrections. *Phys. Chem. Chem. Phys.* **2008**, *10*, 6615-6620.

(2) Yanai, T.; Tew, P. D.; Handy, N. C. A new hybrid exchange–correlation functional using the Coulomb-attenuating method (CAM-B3LYP). *Chem. Phys. Lett.* **2004**, *393*, 51-57.

(3) Ehnbohm, A.; Hall, M. B.; Gladysz, J. A. Origin of Shielding and Deshielding Effects in NMR Spectra of Organic Conjugated Polyynes. *Org. Lett.* **2019**, *21*, 753-757.

(4) Weisbach, N.; Kuhn, H.; Amini, H.; Ehnbohm, A.; Hampel, F.; Reibenspies, J. H.; Hall, M. B.; Gladysz, J. A. Triisopropylsilyl (TIPS) Alkynes as Building Blocks for Syntheses of Platinum Triisopropylsilylpolyynyl and Diplatinum Polyynediyl Complexes. *Organometallics* **2019**, *38*, 3294-3310.

(5) Frisch, M. J.; Trucks, G. W.; Schlegel, H. B.; Scuseria, G. E.; Robb, M. A.; Cheeseman, J. R.; Scalmani, G.; Barone, V.; Mennucci, B.; Petersson, G. A.; Nakatsuji, H.; Caricato, M.; Li, X.; Hratchian, H. P.; Izmaylov, A. F.; Bloino, J.; Zheng, G.; Sonnenberg, J. L.; Hada, M.; Ehara, M.; Toyota, K.; Fukuda, R.; Hasegawa, J.; Ishida, M.; Nakajima, T.; Honda, Y.; Kitao, O.; Nakai, H.; Vreven, T.; Montgomery, J. A. Jr.; Peralta, J. E.; Ogliaro, F.; Bearpark, M.; Heyd, J. J.; Brothers, E.; Kudin, K. N.; Staroverov, V. N.; Kobayashi, R.; Normand, J.; Raghavachari, K.; Rendell, A.; Burant, J. C.; Iyengar, S. S.; Tomasi, J.; Cossi, M.; Rega, N.; Millam, J. M.; Klene, M.; Knox, J. E.; Cross, J. B.; Bakken, V.; Adamo, C.; Jaramillo, J.; Gomperts, R.; Stratmann, R. E.;

Yazyev, O.; Austin, A. J.; Cammi, R.; Pomelli, C.; Ochterski, J. W.; Martin, R. L.; Morokuma, K.; Zakrzewski, V. G.; Voth, G. A.; Salvador, P.; Dannenberg, J. J.; Dapprich, S.; Daniels, A. D.; Farkas, Ö.; Foresman, J. B.; Ortiz, J. V.; Cioslowski, J.; Fox, D. J. *Gaussian 09, Revision D.01*; Gaussian, Inc. Wallingford CT, **2009**.

(6) References for Pople type basis set "**6-311G**" are as follows (an addition of "d" adds polarization functions of *d*-type to C, "p" adds *p*-type polarization functions to C and H atoms, and "+/++" indicates added diffuse functions): (a) McLean, A. D.; Chandler, G. S. Contracted Gaussian basis sets for molecular calculations. I. Second row atoms, $Z = 11-18$. *J. Chem. Phys.* **1980**, *72*, 5639-5648. (b) Raghavachari, K.; Binkley, J. S.; Seeger, R.; Pople, J. A. Self-consistent molecular orbital methods. XX. A basis set for correlated wave functions. *J. Chem. Phys.* **1980**, *72*, 650-654.

(7) Weigend, F.; Ahlrichs, R. Balanced basis sets of split valence, triple zeta valence and quadruple zeta valence quality for H to Rn: Design and assessment of accuracy. *Phys. Chem. Chem. Phys.* **2005**, *7*, 3297-3305.

(8) (a) Andrae, D.; Häussermann, U.; Dolg, M.; Stoll, H.; Preuss, H. Energy-adjusted *ab initio* pseudopotentials for the second and third row transition elements. *Theor. Chim. Acta* **1990**, *77*, 123-141. (b) Martin, J. M. L.; Sundermann, A. Correlation consistent valence basis sets for use with the Stuttgart-Dresden-Bonn relativistic effective core potentials: The atoms Ga-Kr and In-Xe. *J. Chem. Phys.* **2001**, *114*, 3408-3420.

(9) Marenich, A. V.; Cramer, C. J.; Truhlar, D. G. Universal Solvation Model Based on Solute Electron Density and on a Continuum Model of the Solvent Defined by

the Bulk Dielectric Constant and Atomic Surface Tensions. *J. Phys. Chem. B.* **2009**, *113*, 6378-6396.

(10) The planar and puckered forms of **4**" were optimized in the CAM-B3LYP functional. However, the transition state structure of **4**" was optimized using the BP86 functional and subsequently evaluated through a single point calculation, using the same methodology as applied to other species.

*****APPENDIX F

F.1. Stereoisomers of $[\text{Co}(pn)_3]^{3+}$ trications comprised of all combinations of (*R*)-*pn* and (*S*)-*pn* ligands

A brief introduction to Figure 16.1 and Figure 16.2 is provided to aid the reader. The major objective is to couple each three dimensional structure to a unique and unambiguous stereochemical descriptor.

First, each trication is viewed along the formal C_3 axis (see text). Second, for each cobalt configuration (Λ , Δ), the triangles **X** and **XI** are defined, the apices of which "point" to the three chelate ligands. The first stereochemical designation in each sequence of three (λ vs. δ ; *R* vs. *S*; *ob* vs. *lel*) is given for the apex labeled "1", followed by "2" and "3". For consistency, if there is one unlike λ/δ configuration (e.g. $\lambda\delta\delta$ or $\delta\lambda\lambda$), it is assigned to apex 1. Note that there are some fixed relationships between metal configurations, chelate conformations, and perspectives (*ob*, *lel*), as summarized by the box in Figure 16.1.

In any case, 24 structures, corresponding to those summarized in Table 16.1, result. The unique stereochemical descriptors are highlighted in the boxes underneath each structure.

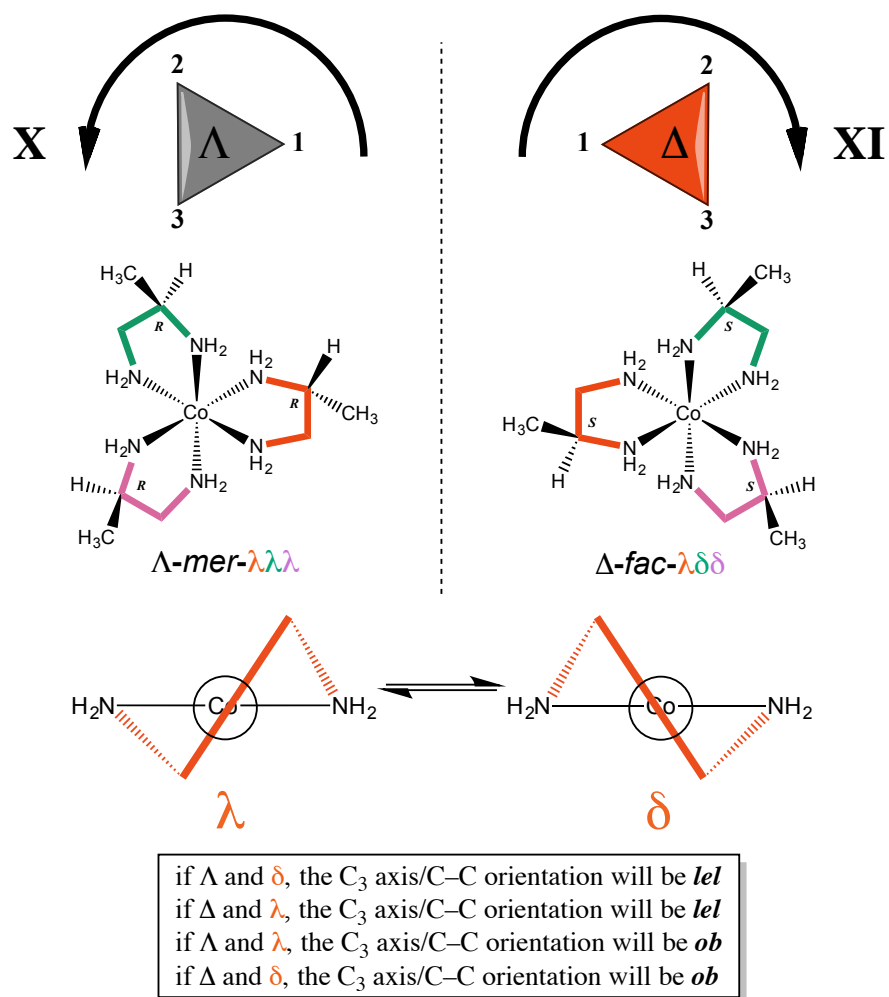


Figure 16.1 Conventions used in designating chelate stereochemistry (*R* vs. *S*; λ vs. δ ; *ob* vs. *lel*) in the structural representations in Figure 16.2 and some "short cuts" involving these relationships.

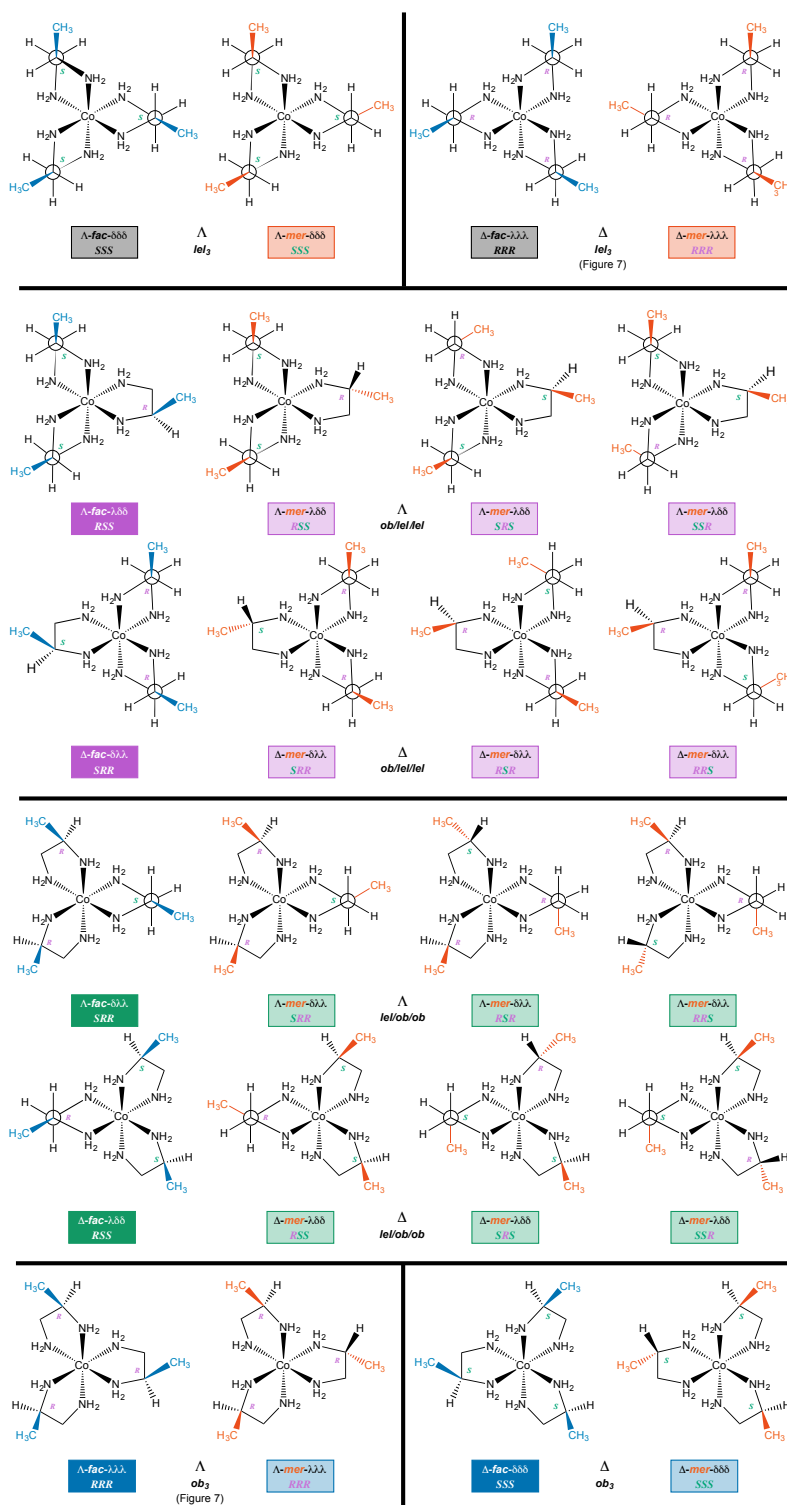


Figure 16.2 The 24 stereoisomers of the $[\text{Co}(\text{pn})_3]^{3+}$ trication summarized in Table 16.1, allowing all combinations of *R* (purple labels) and *S* (turquoise labels) *pn* ligands. The methyl groups are depicted in blue for *fac* isomers, and in vermilion for *mer* isomers.

F.2. Stereoisomers of $[\text{Co}(\text{cis-}chxn)_3]^{3+}$ trications (i.e. comprised only of *R,S-chxn* or *meso* ligands)

In order to couple each three-dimensional structure to a unique and unambiguous stereochemical descriptor, the conventions outlined in Figure 16.1 and the preceding text are adopted. One then views the formal C_3 axis from in front of the plane of the paper to order the two *RS* stereocenters of each chelate. As illustrated in Figure 16.3, one obtains the reverse order if the axis is viewed from behind the plane of the paper.

The first stereochemical designation in each sequence of three (λ vs. δ ; *RS* vs. *SR*; *ob* vs. *lel*) is given for the apex labeled "1", followed by "2" and "3". Some 24 structures, summarized in Table 16.1, result. Each is assigned a number (1 through 24). The unique stereochemical descriptors are highlighted in the boxes beside each structure. The boxes are color coded according to the *ob/lel* pattern.

For each cobalt configuration (Λ/Δ), the stereoisomers exhibit two *lel*₃, four *lel*_{2ob}, four *lelob*₂, and two *ob*₃ orientations. One from each group is *fac* isomer, and the others are *mer*. A representative pair of enantiomers is as follows: $\Lambda\text{-mer-}\lambda\delta\delta\text{-SR/SR/RS}$ and $\Delta\text{-mer-}\delta\lambda\lambda\text{-RS/RS/SR}$ (structures **6** and **18** in Figure 16.4); both feature *lel*_{2ob} orientations.

Structures that are related by a single cyclohexane "ring flip" are summarized in Table 16.2. These link to give the four separate families of stereoisomers noted in Figure 16.4 (two for each cobalt Λ/Δ configuration). The "ring flip" relationships are also coded by the circled letters close to each of the three apices/cyclohexane rings of each structure

(i.e. F, F', F" for structure **6** in Figure 16.4). The structure that results from a "ring flip" of the nearby cyclohexane is labeled on the left side of the colored boxes with the letter of the apex/cyclohexane ring that "flipped".

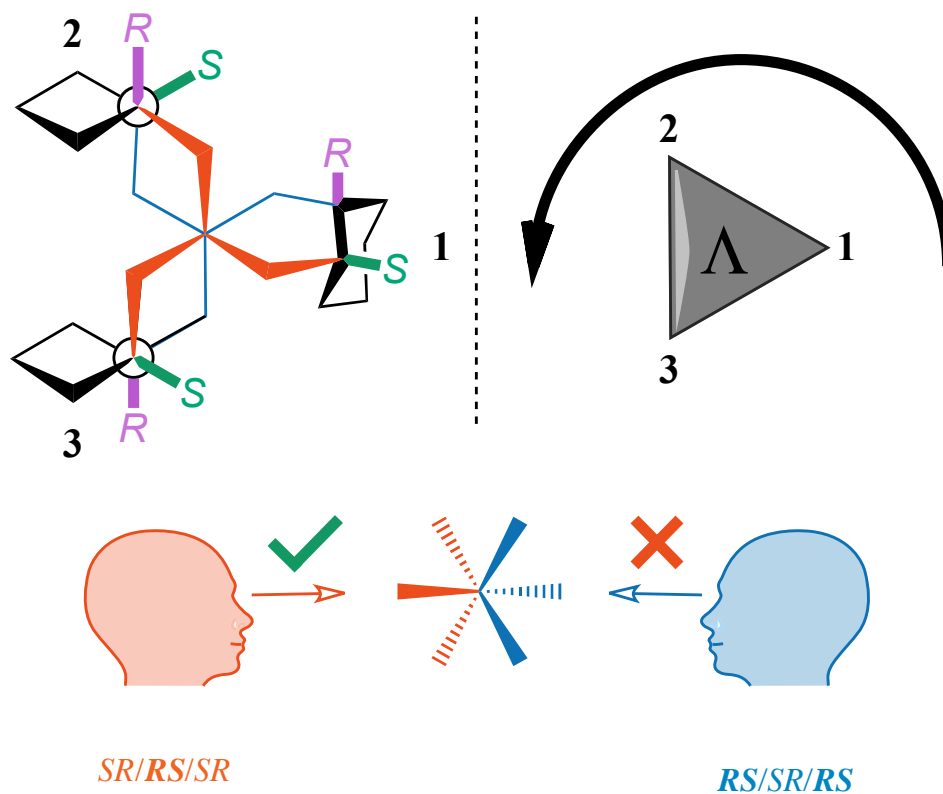


Figure 16.3 Conventions used in designating chelate stereochemistry in the structural representations in Figure 16.4. The procedure is analogous to that in Figure 16.1 except it is important to consistently view the C_3 axes from in front of the plane of the paper to "order" the *SR/RS* configurations of the chelate ring stereocenters.

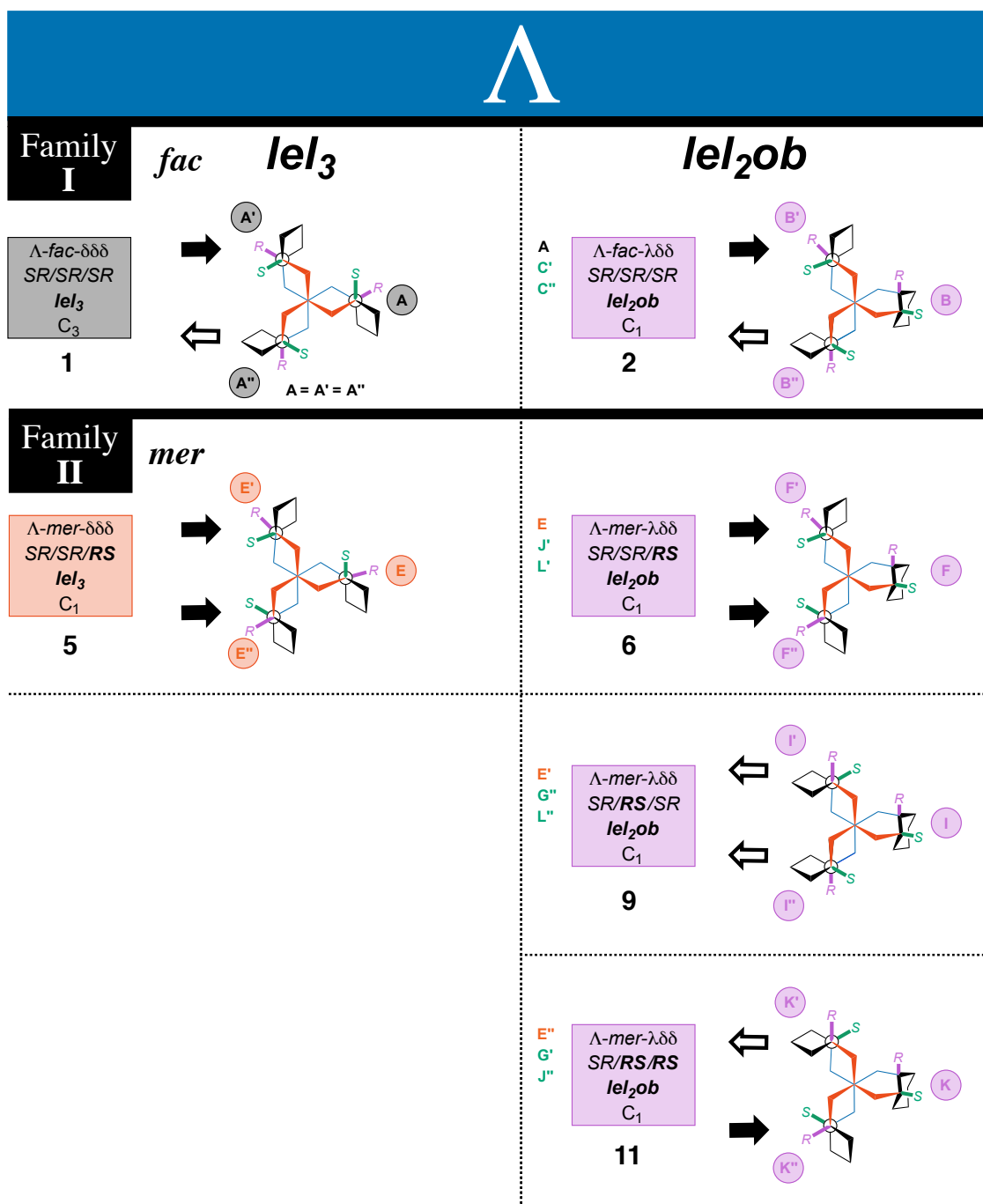


Figure 16.4 The 24 stereoisomers of the $[\text{Co}(\text{cis-}chxn)_3]^{3+}$ trication ($\text{cis-}chxn = R,S\text{-}chxn$) summarized in Table 16.1. In each vertical series, the λ/δ configuration of the chelate at apex 1 (Figure 16.3) is kept constant while the configurations in the remaining chelates are varied, as denoted by the arrows \Leftarrow/\Rightarrow (for $\lambda\delta\delta$ and $\delta\lambda\lambda$ systems apex 1 is also set as the unlike configuration). Bold lines separate the families of isomers described in the preceding text. There is extensive color-coding that carries over to Table 16.1, but the conventions are left to be empirically discerned.

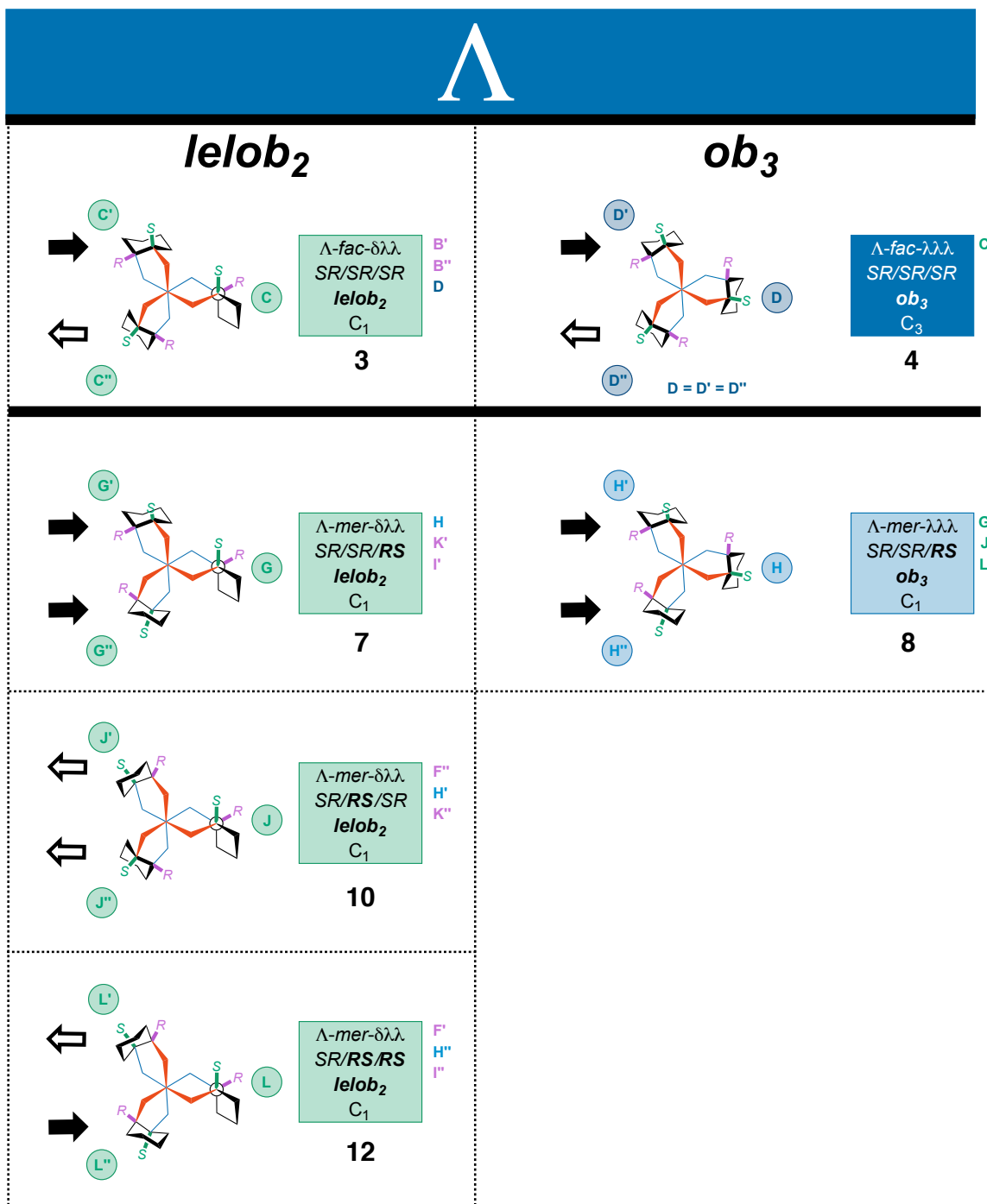


Figure 16.4 continued.

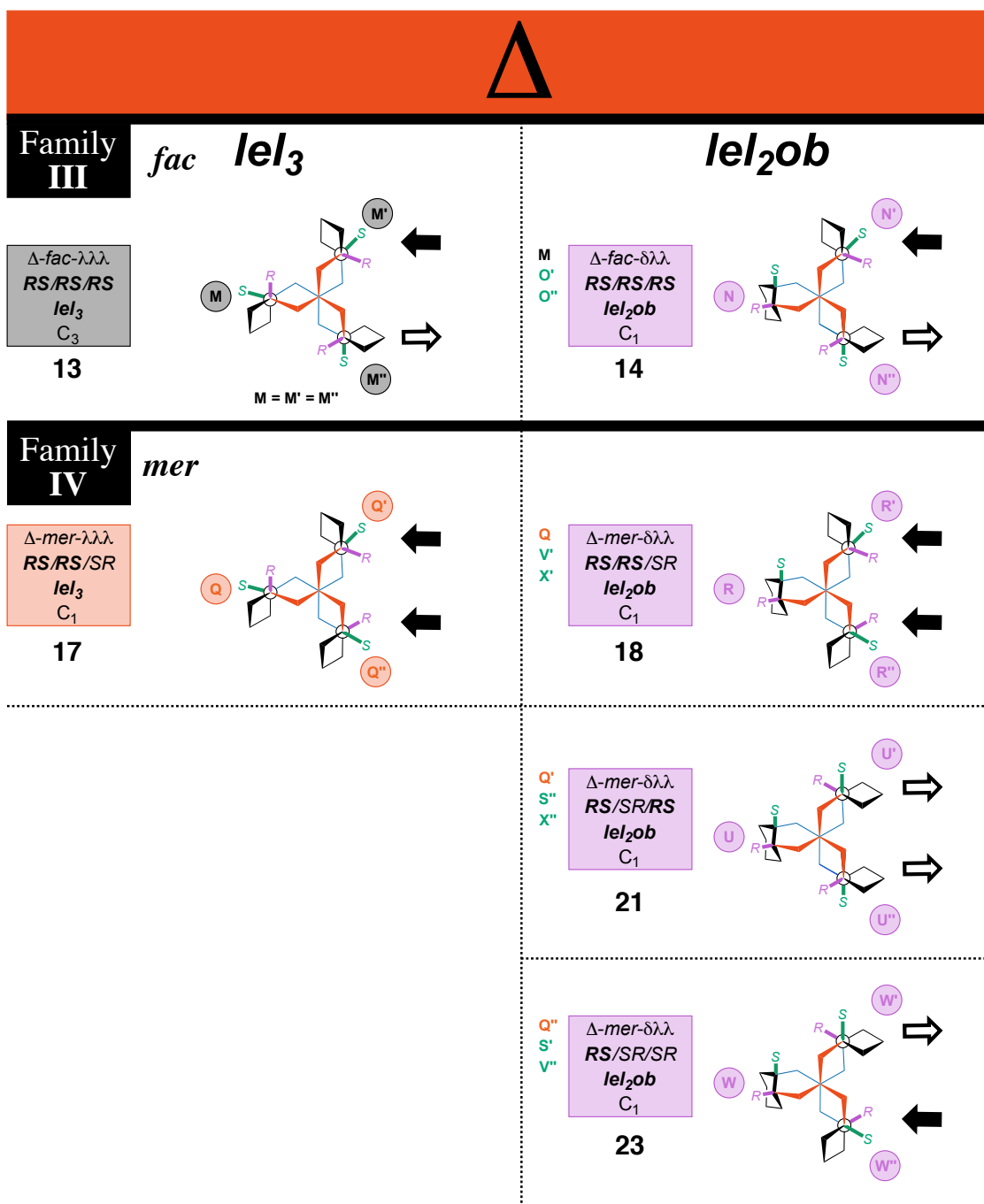


Figure 16.4 continued.

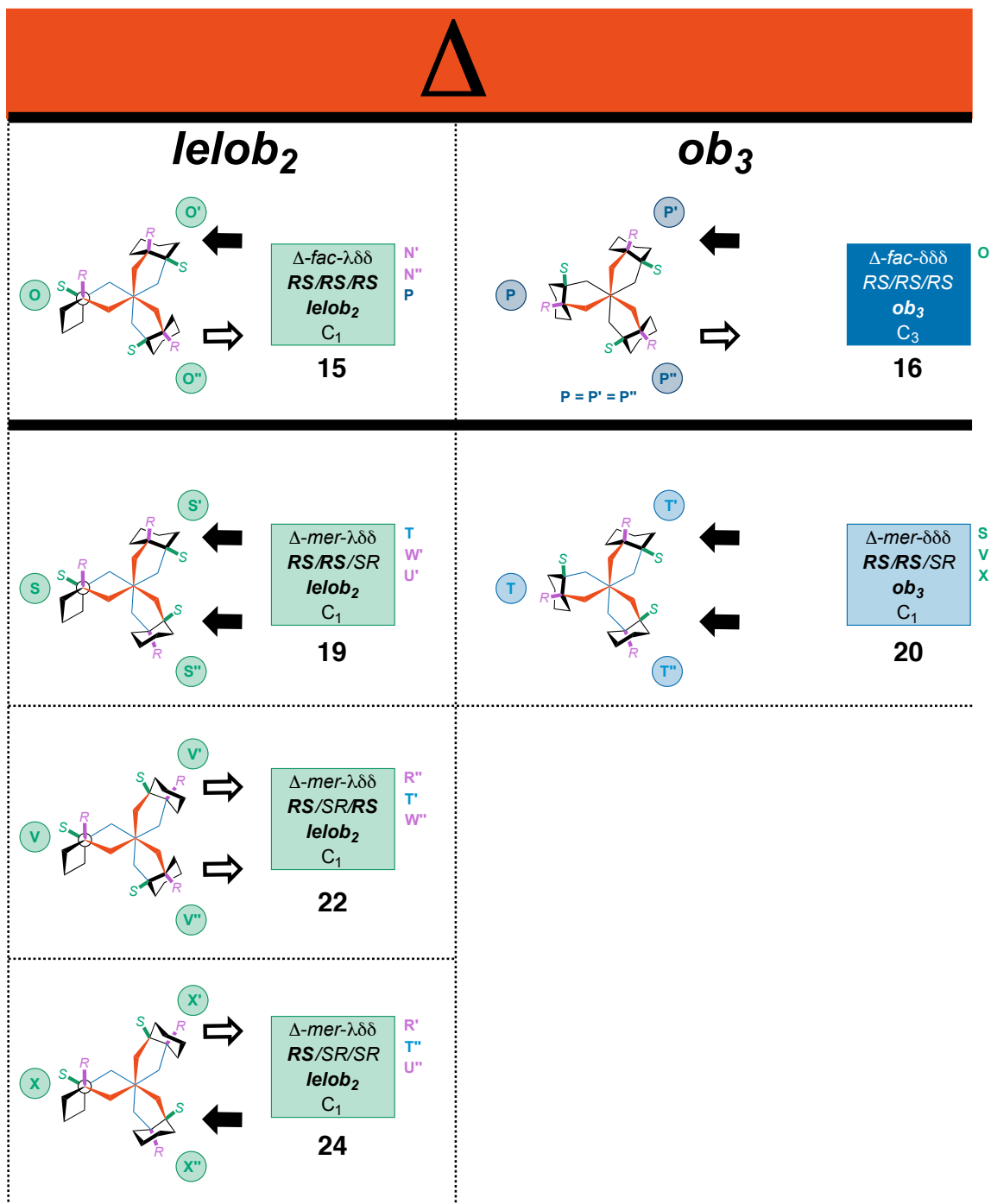


Figure 16.4 *continued*.

Table 16.1 Summary of the stereoisomers of the $[\text{Co}(\text{cis-chn})_3]^{3+}$ trication.

structure number (Figure 16.4)	cobalt configuration	ligand configurations	chelate conformations	perspective down the C_3 axis ^a	geometrical type isomers
1	Λ	<i>SR/SR/SR</i>	$\delta\delta\delta$	<i>lel₃</i>	<i>fac</i>
5	Λ	<i>SR/SR/RS</i>	$\delta\delta\delta$		<i>mer</i>
17	Δ	<i>RS/RS/SR</i>	$\lambda\lambda\lambda$		<i>mer</i>
13	Δ	<i>RS/RS/RS</i>	$\lambda\lambda\lambda$		<i>fac</i>
2	Λ	<i>SR/SR/SR</i>	$\lambda\delta\delta$	<i>lel_{2ob}</i>	<i>fac</i>
6	Λ	<i>SR/SR/RS</i>	$\lambda\delta\delta$		<i>mer</i>
9	Λ	<i>SR/RS/SR</i>	$\lambda\delta\delta$		<i>mer</i>
11	Λ	<i>SR/RS/RS</i>	$\lambda\delta\delta$		<i>mer</i>
23	Δ	<i>RS/SR/SR</i>	$\delta\lambda\lambda$		<i>mer</i>
21	Δ	<i>RS/SR/RS</i>	$\delta\lambda\lambda$		<i>mer</i>
18	Δ	<i>RS/RS/SR</i>	$\delta\lambda\lambda$		<i>mer</i>
14	Δ	<i>RS/RS/RS</i>	$\delta\lambda\lambda$		<i>fac</i>
3	Λ	<i>SR/SR/SR</i>	$\delta\lambda\lambda$	<i>lelob₂</i>	<i>fac</i>
7	Λ	<i>SR/SR/RS</i>	$\delta\lambda\lambda$		<i>mer</i>
10	Λ	<i>SR/RS/SR</i>	$\delta\lambda\lambda$		<i>mer</i>
12	Λ	<i>SR/RS/RS</i>	$\delta\lambda\lambda$		<i>mer</i>
24	Δ	<i>RS/SR/SR</i>	$\lambda\delta\delta$		<i>mer</i>
22	Δ	<i>RS/SR/RS</i>	$\lambda\delta\delta$		<i>mer</i>
19	Δ	<i>RS/RS/SR</i>	$\lambda\delta\delta$		<i>mer</i>
15	Δ	<i>RS/RS/RS</i>	$\lambda\delta\delta$		<i>fac</i>
4	Λ	<i>SR/SR/SR</i>	$\lambda\lambda\lambda$	<i>ob₃</i>	<i>fac</i>
8	Λ	<i>SR/SR/RS</i>	$\lambda\lambda\lambda$		<i>mer</i>
20	Δ	<i>RS/RS/SR</i>	$\delta\delta\delta$		<i>mer</i>
16	Δ	<i>RS/RS/RS</i>	$\delta\delta\delta$		<i>fac</i>

^a Or an equivalent axis as defined in the text.

Table 16.2 A grid of the structure numbers for the 24 stereoisomers in Figure 16.4 with "x" indicating those that can be interconverted by a single cyclohexane "ring flip". The specific ring can be inferred from additional coding in Figure 16.4. The sets of structures interconverted by "x" are considered families of conformational stereoisomers.

	1	2	3	4	5	6	7	8	9	10	11	12	13	14	15	16	17	18	19	20	21	22	23	24	
1		x																							
2	x		x																						
3		x		x																					
4			x																						
5						x			x	x															
6					x					x		x													
7							x	x			x														
8							x			x		x													
9					x		x					x													
10						x		x			x														
11					x		x			x															
12						x		x	x																
13														x	x	x									
14														x		x									
15															x		x								
16																x									
17																	x	x			x				
18																		x				x			x
19																			x	x			x		
20																				x			x		x
21																		x		x					x
22																			x		x			x	
23																				x				x	
24																					x	x			x

APPENDIX G

G.1. Syntax and nomenclature summaries

Table 17.1 Syntax for hydrogen bonding interactions between the $[\text{Co}(\text{en})_3]^{3+}$ trication and anions or solvent molecules.

hydrogen bond motif	C_2 N–H	C_3 N–H	<i>interligand</i> C_2, C_3 N–H	<i>intra</i> ligand (C_2/C_3) N–H ^a	<i>intra</i> ligand $(\text{C}_2//\text{C}_3)$ N–H ^b
one N–H unit binds to anion at a single atom	[C ₂][1]	[C ₃][1]	—	—	—
two N–H units bind to anion at a single atom	[C ₂ ,C ₂][1]	[C ₃ ,C ₃][1]	[C ₃ ,C ₂][1]	[(C ₃ /C ₂)] [1]	[(C ₃ //C ₂)] [1]
three N–H units bind to anion at a single atom	—	[C ₃ ,C ₃ ,C ₃][1]	[C ₃ ,C ₃ ,C ₂][1] ^c <i>or</i> [C ₃ ,C ₂ ,C ₂][1] ^c	[C ₃ ,(C ₃ /C ₂)] [1] ^c <i>or</i> [(C ₃ /C ₂),C ₂][1] ^c	[C ₃ ,(C ₃ //C ₂)] [1] ^c <i>or</i> [(C ₃ //C ₂),C ₂][1] ^c
one N–H unit bind to anion at two different atoms	[C ₂ ²][2]	[C ₃ ²][2]	—	—	—
two N–H units bind to anion at two different atoms	[C ₂ ,C ₂][2]	[C ₃ ,C ₃][2]	[C ₃ ,C ₂][2]	[(C ₃ /C ₂)] [2]	[(C ₃ //C ₂)] [2]
three N–H units bind to anion at two different atoms	—	[C ₃ ,C ₃ ,C ₃][2]	[C ₃ ,C ₃ ,C ₂][2] <i>or</i> [C ₃ ,C ₂ ,C ₂][2]	[C ₃ ,(C ₃ /C ₂)] [2] <i>or</i> [(C ₃ /C ₂),C ₂][2]	[C ₃ ,(C ₃ //C ₂)] [2] <i>or</i> [(C ₃ //C ₂),C ₂][2]
one N–H unit binds to anion at three different atoms	[C ₂ ³][3]	[C ₃ ³][3]	—	—	—
two N–H units bind to anion at three different atoms	[C ₂ ² ,C ₂][3]	[C ₃ ² ,C ₃][3]	[C ₃ ,C ₂ ²][3] <i>or</i> [C ₃ ² ,C ₄][3]	[(C ₃ ² /C ₂)] [3] <i>or</i> [(C ₃ //C ₂ ²)] [3]	[(C ₃ ² //C ₂)] [3] <i>or</i> [(C ₃ //C ₂ ²)] [3]
three N–H units bind to anion at three different atoms	—	[C ₃ ,C ₃ ,C ₃][3]	[C ₃ ,C ₃ ,C ₂][3] <i>or</i> [C ₃ ,C ₂ ,C ₂][3]	[C ₃ ,(C ₃ /C ₂)] [3] <i>or</i> [(C ₃ /C ₂),C ₂][3]	[C ₃ ,(C ₃ //C ₂)] [3] <i>or</i> [(C ₃ //C ₂),C ₂][3]
miscellaneous motifs from section 9.5					
three N–H units bind to anion at two different atoms with each atom of the anion making two hydrogen bonds	—	[C ₃ ² ,C ₃ ,C ₃][2,2:2]	—	—	—
three N–H units bind to anion at two different atoms, with one atom making two hydrogen bonds and the other making one.	—	[C ₃ ² ,C ₃ ,C ₃][1,3:2]	—	—	—

^a The N–H bonds are geminal (NH₂; see Figure 9.6) ^b The N–H bonds involve different nitrogen atoms on the same ligand (see Figure 9.6). ^c Considering the substantial distance at which the third N–H unit will be from the other two, this will be a rare motif.

G.2. Representations of the motifs cataloged in Table 17.1

Table 17.2 Syntax using Λ - $\delta\delta\delta$ -[Co(en)₃]³⁺ (*lel*₃) and a hypothetical triatomic anion (green) in which all atoms are capable of hydrogen bonding.





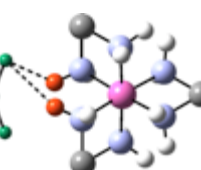
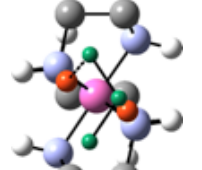
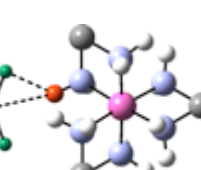
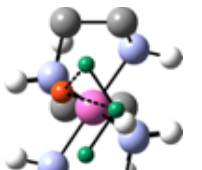
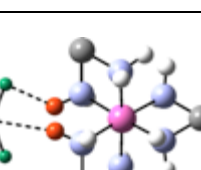
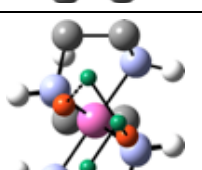
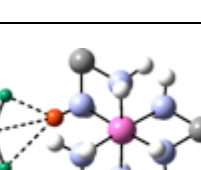
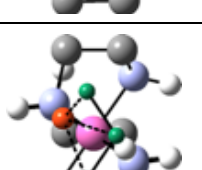
	perspective from C ₃ site	perspective from C ₂ site	designation
0			reference structure of the trication [Co(en) ₃] ³⁺ with the C ₂ and C ₃ hydrogen atoms in vermilion and blue, respectively ^a
1			[C ₂][1]
2			[C ₂ ,C ₂][1]
3			[C ₂ ²][2]
4			[C ₂ ,C ₂][2]
5			[C ₂ ³][3]

Table 17.2 *continued.*

	perspective from C_3 site	perspective from C_2 site	designation
6			$[C_2^2, C_2][3]$
7			$[C_3][1]$
8			$[C_3, C_3][1]$
9			$[C_3, C_3, C_3][1]$
10			$[C_3^2][2]$
11			$[C_3, C_3][2]$

Table 17.2 *continued*.

	perspective from C_3 site	perspective from C_2 site	designation
12			$[C_3, C_3, C_3][2]$
13			$[C_3^3][3]$
14			$[C_3^2, C_3][3]$
15			$[C_3, C_3, C_3][3]$
16			$[C_3, C_2][1]$
17			$[C_3, C_3, C_2][1]$

Table 17.2 *continued*.

	perspective from C_3 site	perspective from C_2 site	designation
18			$[C_3, C_2, C_2][1]$
19			$[C_3, C_2][2]$
20			$[C_3, C_3, C_2][2]$
21			$[C_3, C_2, C_2][2]$
22			$[C_3, C_2^2][3]$
23			$[C_3^2, C_2][3]$

Table 17.2 *continued*.

	perspective from C_3 site	perspective from C_2 site	designation
24			$[C_3, C_3, C_2][3]$
25			$[C_3, C_2, C_2][3]$
26			$[(C_3/C_2)][1]$
27			$[C_3, (C_3/C_2)][1]$
28			$[(C_3/C_2), C_2][1]$
29			$[(C_3/C_2)][2]$

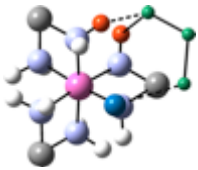

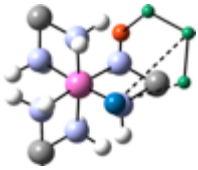

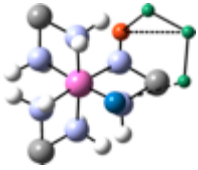
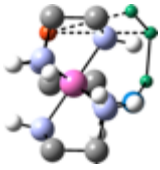
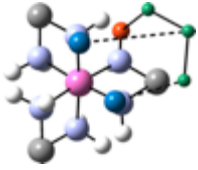

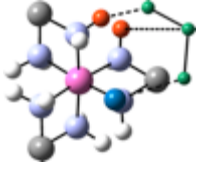

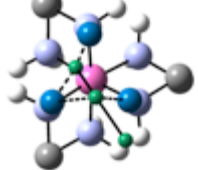
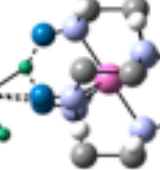
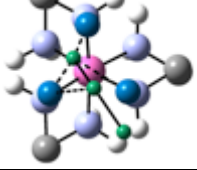
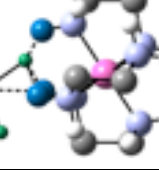
Table 17.2 *continued*.

	perspective from C_3 site	perspective from C_2 site	designation
30			$[C_3, (C_3/C_2)] [2]$
31			$[(C_3/C_2), C_2] [2]$
32			$[(C_3^2/C_2)] [3]$
33			$[(C_3/C_2^2)] [3]$
34			$[C_3, (C_3/C_2)] [3]$
35			$[(C_3/C_2), C_2] [3]$

Table 17.2 *continued.*

	perspective from C ₃ site	perspective from C ₂ site	designation
36			$[(C_3//C_2)][1]$
37			$[C_3, (C_3//C_2)][1]$
38			$[(C_3//C_2), C_2][1]$
39			$[(C_3//C_2)][2]$
40			$[C_3, (C_3//C_2)][2]$

Table 17.2 *continued*.

	perspective from C ₃ site	perspective from C ₂ site	designation
41			$[(C_3//C_2),C_2][2]$
42			$[(C_3^2//C_2)][3]$
43			$[(C_3//C_2^2)][3]$
44			$[C_3,(C_3//C_2)][3]$
45			$[(C_3//C_2),C_2][3]$
46			$[C_3^2,C_3,C_3]$ [2,2:2]
47			$[C_3^2,C_3,C_3]$ [3,1:2]

^a In subsequent formulae, this color format is maintained for the N–H hydrogen atoms that bind to the anion.

Table 17.3 Crystal structures containing the $[\text{Co}(\text{en})_3]^{3+}$ trication in the Cambridge Structural Database (CSD) minus duplicates.^a The identities of the salts can be found in the supplementary information of the published article.

entry	ref	CSD refcode	<i>ob/lel</i> orientation	cobalt configuration	space group
1	1	ABIXIT	<i>oblel</i> ₂	Λ, Δ	<i>P</i> -31 <i>c</i>
2	2	ACUBAB	<i>ob</i> ₃	Λ, Δ	<i>P</i> -31 <i>c</i>
3	3	ARILES	<i>lel</i> ₃	Λ, Δ	<i>C</i> 2/ <i>c</i>
4	4	BESFAG	<i>lel</i> ₃	Λ, Δ	<i>P</i> -1
5	5	BIRSUO ^b	<i>lel</i> ₃	Λ, Δ	<i>P</i> -3
6	6	BIWLIC	<i>lel</i> ₃	Λ, Δ	<i>I</i> -42 <i>d</i>
7	7	CASTAS	<i>lel</i> ₃	Λ	<i>I</i> 2 ₁ 2 ₁ 2 ₁
8	8	COCRCL	<i>lel</i> ₃	Λ	<i>P</i> 321
9	9	COCREN	<i>lel</i> ₃	Λ	<i>P</i> 112 ₁
10	10	COENCF	<i>oblel</i> ₂	Λ, Δ	<i>P</i> 21/ <i>n</i>
11	11	COENCH ^b	<i>lel</i> ₃	Λ	<i>P</i> 4 ₃ 2 ₁ 2
12	12	COENCL	<i>lel</i> ₃	Λ	<i>P</i> 32 ₁
13	13	COENSI	<i>lel</i> ₃	Λ, Δ	<i>P</i> 2 ₁ / <i>n</i>
14	14	COENTC ^b	<i>lel</i> ₃	Λ, Δ	<i>Pbca</i>
15	15	COENTD ^c	<i>lel</i> ₃	Λ	<i>c</i>
16	16	COTENC ^b	<i>lel</i> ₃	Λ, Δ	<i>P</i> -3 <i>c</i> 1
17	17	CUDGEN	<i>ob</i> ₃	Λ, Δ	<i>P</i> 6/ <i>mcc</i>
18	18	DUCYIL ^b	<i>oblel</i> ₂	Λ, Δ	<i>P</i> -1
19	19	EDANEC ^b	<i>oblel</i> ₂	Λ	<i>P</i> 2 ₁ 2 ₁ 2 ₁
20	20	EDCOBR ^b	<i>lel</i> ₃	Λ	<i>P</i> 4 ₃ 2 ₁ 2
21	21	EGOXII	<i>oblel</i> ₂	Λ, Δ	<i>P</i> 2 ₁ / <i>c</i>
22	22	ENCCUC10 ^d	<i>lelob</i> ₂	Λ, Δ	<i>Pbca</i>
23	23	ENCOCD	<i>lel</i> ₃	Λ, Δ	<i>P</i> 2 ₁ / <i>c</i>
24	24	ENCOCT ^b	<i>lel</i> ₃	Λ	<i>P</i> 1
25	25	ENCOFD ^c	<i>c</i>	<i>c</i>	<i>c</i>
26	26	ENCOIH	<i>lelob</i> ₂	Λ, Δ	<i>Pbca</i>
27	27	ENCOPB	<i>lel</i> ₃ + <i>oblel</i> ₂ ^e	Λ, Δ ^e	<i>P</i> 2 ₁
28	28	ENCOPC	<i>lelob</i> ₂	Λ, Δ	<i>P</i> 2 ₁ / <i>c</i>
29	29	ENCOPN ^b	<i>lel</i> ₃	Λ, Δ	<i>Pnma</i>
30	30	ENCOSN	<i>oblel</i> ₂	Λ, Δ	<i>Pbca</i>
31	31	ENCOTT ^c	<i>c</i>	<i>c</i>	<i>P</i> 2 ₁
32	32	ENCTAR ^c	<i>c</i>	<i>c</i>	<i>P</i> 1
33	33	ENICON	<i>oblel</i> ₂	Δ	<i>P</i> 2 ₁ 2 ₁ 2 ₁
34	34	EPAXOJ	<i>lel</i> ₃	Λ, Δ	<i>C</i> 2/ <i>c</i>
35	35	EXOVAO	<i>lel</i> ₃ + <i>oblel</i> ₂	Λ, Δ	<i>P</i> -1
36	36	FAHHIH	<i>lel</i> ₃	Λ, Δ	<i>P</i> -1
37	36	FAHHON	<i>oblel</i> ₂	Λ, Δ	<i>C</i> 2/ <i>c</i>
38	37	FASHUE	<i>lel</i> ₃	Λ, Δ	<i>P</i> 2 ₁ / <i>c</i>
39	37	FASJAM	<i>lel</i> ₃	Λ, Δ	<i>P</i> 2 ₁ / <i>c</i>
40	38	FAXMEX ^b	<i>lel</i> ₃	Λ, Δ	<i>P</i> 6 ₃ 22

Table 17.3 *continued.*

entry	ref	CSD refcode	ob/lel orientation	cobalt configuration	space group
41	39	FIRQIH ^b	lel ₃	Λ	P ₆ 322
42	40	GAPHUA	lel ₃	Λ,Δ	P ₂ 1 ₂ 1 ₂ 1
43	41	GAXKIB ^b	lelob ₂	Λ,Δ	C2/c
44	42	GEPGEO ^b	oblel ₂	Λ,Δ	P ₄ 2bc
45	43	GINLUK ^b	lel ₃	Λ	P ₂ 1 ₂ 1 ₂ 1
46	43	GINMAR ^b	lel ₃	Δ	P1
47	44	GIXRIP	lel ₃	Λ,Δ	P-3c1
48	44	GIXROV	lel ₃	Λ,Δ	P-3c1
49	44	GIXRUB	lel ₃	Λ,Δ	P-3c1
50	44	GIXSAI	lel ₃	Λ,Δ	P-3c1
51	44	GIXSEM	lel ₃	Λ,Δ	P-3c1
52	44	GIZLIL	lel ₃	Λ,Δ	P-3c1
53	44	GIZLOR	lel ₃	Λ,Δ	P-3c1
54	44	GIZLUX	lel ₃	Λ,Δ	P-3c1
55	45	GULNEH	lelob ₂	Λ,Δ	C2/m
56	46	GUZNIY ^b	lel ₃	Λ,Δ	P ₂ 1/n
57	46	GUZNOE ^b	lel ₃	Λ	P21
58	47	HAJCOM	lel ₃	Λ,Δ	P-1
59	48	HEQWIL	oblel ₂	Λ,Δ	C2/c
60	49	HEYVAJ	oblel ₂	Λ,Δ	Pn2 ₁ a
61	50	HEYVEN	lel ₃	Λ,Δ	C2/c
62	51	IGOZEK	lel ₃	Λ,Δ	P ₂ 1/c
63	52	IRIRAC ^b	lel ₃	Λ,Δ	P-3c1
64	53	IYIBIC	lelob ₂	Δ	P ₂ 1 ₂ 1 ₂ 1
65	53	IYIBOI	lelob ₂	Λ	P ₂ 1 ₂ 1 ₂ 1
66	54	IZEQUZ ^c	^c	^c	C2/c
67	55	JIMRUT	lel ₃	Λ,Δ	Pnna
68	56	LALDUZ	oblel ₂	Λ,Δ	P-1
69	57	LITSOW	oblel ₂	Λ	P ₂ 1 ₂ 1 ₂ 1
70	58	LIYMUB	lel ₃	Λ,Δ	P ₂ 1/n
71	59	MARGAP	oblel ₂	Λ,Δ	P-1
72	60	MOMWOB	lel ₃	Λ,Δ	P-1
73	60	MOMWUH	lelob ₂	Λ,Δ	P ₂ 1/n
74	61	MOTXID	oblel ₂	Λ,Δ	Cmc2 ₁
75	61	MOTXOJ	lel ₃	Λ,Δ	P ₂ 1/c
76	62	MUTWUU	oblel ₂	Λ,Δ	C2/c
77	63	NAXTUC	oblel ₂	^f	P ₂ 1/c
78	64	NAZZEU	lel ₃	Λ,Δ	C2/c
79	65	NEJDEM ^b	oblel ₂	Λ,Δ	Pnma
80	66	NEKHUG	lelob ₂	Λ,Δ	Pmna
81	67	NIHNEZ	oblel ₂	Λ,Δ	Pna2 ₁

Table 17.3 *continued.*

entry	ref	CSD refcode	ob/lel orientation	cobalt configuration	space group
82	68	NONKAC	lel_3	Λ	$C222_1$
83	69	NOYQOH	$oblel_2$	Λ, Δ	$Pca2_1$
84	70	OBIWAZ	$oblel_2$	Λ, Δ	$Pnma$
85	71	OKOQOW	$oblel_2$	Λ, Δ	$P2_1/n$
86	72	OLANOE	$oblel_2$	Λ, Δ	$P2_1/n$
88	74	PEJGAO	lel_3	Λ	$P2_1$
89	74	PEJGES ^b	lel_3	Λ	$P1$
90	74	PEJGIW	$oblel_2$	Λ, Δ	$P-1$
91	74	PEJGOC ^b	$oblel_2$	Λ, Δ	$P2_1/c$
92	74	PEJGUI	lel_3	Δ	$C2$
93	75	PERHIE	$oblel_2$	Λ, Δ	$P2_1/c$
94	75	PESVEP	$oblel_2$	Λ, Δ	$P2_1/c$
95	76	PEVXAP	$lel_3 + oblel_2$	Δ	$P1$
96	77	PIBFEL	lel_3	Λ	$P2_1$
97	77	PIBFIP	lel_3	Δ	$P2_12_12_1$
98	77	PIBFOV	lel_3	Λ	$P2_12_12_1$
99	78	PIMXIS	$lelob_2$	Λ	$R3$
100	79	POVPEV	lel_3	Λ, Δ	$P2_1/c$
101	80	QATWIT	$lelob_2$	Δ	$P2_12_12_1$
102	81	QORFIM	lel_3	Λ, Δ	$C2/c$
103	82	REGSIG	$lel_3 + oblel_2$	Λ, Δ	$P2/a$
104	83	RUBDEY	lel_3	Λ, Δ	$C2/c$
105	84	SADQUL	$lelob_2$	Λ, Δ	$Pbca$
106	85	SAETCO	lel_3	Λ	$P3$
107	86	SAFFIQ	$oblel_2$	Λ, Δ	$P-1$
108	87	SATKEE	lel_3	Λ, Δ	$Cmc2_1$
109	88	SAYKUY	$lelob_2$	Λ, Δ	$P2_1/a$
110	89	SINQUB	lel_3	Λ	$I2$
111	89	SINRIQ	lel_3	Λ	$I2$
112	90	SOZFIW ^b	lel_3	Λ	$R3$
113	90	SOZFOC ^b	lel_3	Λ	$P2_1$
114	91	SUYFIC ^b	$oblel_2$	Λ, Δ	$Pna2_1$
115	92	TAKHOD	lel_3	Λ, Δ	$P2_1/c$
116	93	TEDDOV	lel_3	Λ, Δ	$Pb3$
117	94	TENCON ^b	lel_3	Λ	$P2_12_12_1$
118	95	TIFDOC	$oblel_2$	Λ, Δ	$C2/c$
119	95	TIFDUI	$oblel_2 + lelob_2$	Δ	$P2_1$
120	96	TUZGEA	lel_3	Δ	$P2_12_12_1$
121	97	UNAVIP	lel_3	Λ	$P2_12_12_1$
122	97	UNAVOV	$lel_3 + oblel_2$	Λ, Δ	$P-1$
123	97	UNAVUB	ob_3	Λ, Δ	$P-1$
124	97	UNAWAI	lel_3	Λ	$P2_12_12_1$

Table 17.3 *continued.*

entry	ref	CSD refcode	<i>obl/lel</i> orientation	cobalt configuration	space group
125	97	UNAWEM	lel_3	Λ, Δ	$P2_1/c$
126	97	UNAWIQ	lel_3	Λ, Δ	$P2_1/n$
127	97	UNAWOW	$lel_3 + oblel_2$	Λ, Δ	$P-1$
128	98	UQUNIE	$oblel_2$	Λ, Δ	$P-1$
129	99	VISHOW	lel_3	Λ, Δ	$C2/c$
130	100	WACMIX	lel_3	Λ, Δ	$P2_1/c$
131	101	WESRER	ob_3	Λ	$P2_1, 2_1 2$
132	102	WILREP	lel_3	Λ, Δ	$C2/c$
133	102	WILRIT	$oblel_2$	Λ, Δ	$P2_1/c$
134	102	WIMJEI	lel_3	Δ	$P3_2$
135	102	WIPBUT	lel_3	Λ, Δ	$C2$
136	103	WOQDUC ^b	$oblel_2$	Λ, Δ	$C2/c$
137	103	WOQFAK	lel_3	Λ, Δ	$P2_1/c$
138	104	WUQKEZ	lel_3	Λ	$P1$
139	104	WUQKID	lel_3	Λ	$P1$
140	104	WUQKOJ	$lel_3 + oblel_2$	Δ	$P1$
141	105	XAGWEI ^f	f	f	$P2_1/m$
142	106	XEMSEP ^b	$oblel_2$	Δ	$P1$
143	107	XONLIV	$lel_3 + lelob_2$	Λ, Δ	$P2_1/c$
144	108	YEMFOM	$lelob_2$	Λ	$P6_5 22$
145	109	YIVHIU	lel_3	Λ, Δ	$Pna2_1$
146	110	YURJOL	lel_3	Λ, Δ	$Pna2_1$
147	111	YUXPOW	lel_3	Λ, Δ	$P2_1/c$
148	43	ZZZAZY	lel_3	Λ, Δ	$P2_1/n$
149	112	ZZZUZM ^c	c	c	$P4_1 32$
150	112	ZZZVXG ^c	c	Λ, Δ	$P-3c1$

^a Dications [cobalt(II)] have been excluded. ^b This salt is analyzed in the main text. ^c The atomic coordinates for this salt are not available in the CSD, precluding certain assignments. ^d For duplicate structures in the CSD, an Arabic numeral is generally appended to the refcode. For this salt (refcode ENCCUC10), there is no corresponding structure that lacks the "10". Hence, it is included in the table of unique structures. In a private communication, a CSD representative confirmed this, but also indicated that there are plans to reinstate some structures with lower numerals that were deleted earlier. ^e This crystal contains both orientations ($oblel_2$ for the Λ enantiomer, lel_3 for the Δ enantiomer). ^f The high degree of disorder in this structure precludes certain assignments.

Table 17.4 Duplicate crystal structures containing the $[\text{Co}(\text{en})_3]^{3+}$ trication in the Cambridge Structural Database (CSD).

entry	ref	CSD Refcode	<i>obl/lel</i> orientation	cobalt configuration	space group
151	113	ACUBAB01 ^a	<i>a</i>	<i>a</i>	<i>P</i> -31 <i>c</i>
152	114	ACUBAB02 ^a	<i>a</i>	<i>a</i>	<i>P</i> -31 <i>c</i>
153	9	COCREN01	<i>lel</i> ₃	Λ	<i>P</i> 112 ₁
154	15	COENTC01 ^a	<i>a</i>	Λ,Δ	<i>a</i>
155	15	COENTD01 ^a	<i>a</i>	Λ	<i>a</i>
156	115	COENTD10	<i>lel</i> ₃	Λ	<i>P</i> 2 ₁ 2 ₁ 2 ₁
157	16	COTENC01	<i>lel</i> ₃	Λ,Δ	<i>P</i> -3 <i>c</i> 1
158	116	ENCOCT01	<i>lel</i> ₃	Λ	<i>P</i> 1
159	25	ENCOFD01 ^a	<i>a</i>	<i>a</i>	<i>a</i>
160	25	ENCOFD02 ^a	<i>a</i>	<i>a</i>	<i>P</i> 2 ₁ / <i>n</i>
161	117	ENCOPB01	<i>lel</i> ₃ + <i>obl</i> <i>lel</i> ₂ ^b	Λ,Δ ^b	<i>P</i> 21
162	44	GIZLIL01	<i>lel</i> ₃	Λ,Δ	<i>P</i> -3 <i>c</i> 1
163	44	IRIRAC01	<i>lel</i> ₃	Λ,Δ	<i>P</i> -3 <i>c</i> 1
164	67	NIHNEZ01	<i>obl</i> <i>lel</i> ₂	Λ,Δ	<i>P</i> 4 ₂ <i>bc</i>
165	118	PIMXIS01	<i>lelob</i> ₂	Λ	<i>R</i> 32
166	119	SAETCO01	<i>lel</i> ₃	Λ	<i>P</i> 3
167	3	TUZGEA01	<i>lel</i> ₃	Δ	<i>P</i> 2 ₁ 2 ₁ 2 ₁
168	96	TUZGEA02	<i>lel</i> ₃	Δ	<i>P</i> 2 ₁ 2 ₁ 2 ₁
169	43	ZZZAZY10	<i>lel</i> ₃	Λ,Δ	<i>P</i> 21/ <i>n</i>

^a The atomic coordinates for this salt are not available in the CSD, precluding certain assignments. ^b This crystal contained both orientations (*obl**lel*₂ for the Λ enantiomer, *lel*₃ for the Δ enantiomer).

G.3. References

(1) He, X.; Zhang, P.; Song, T. Y.; Mu, Z. C.; Yu, J. H.; Wang, Y.; Xu, J. N. Hydrothermal synthesis and structure of a molybdenum(VI) phosphate cluster and a three dimensional cobalt molybdenum(V) phosphate. *Polyhedron* **2004**, *23*, 2153-2159.

(2) Yu, J. H.; Wang, Y.; Shi, Z.; Xu, R. R. Hydrothermal Synthesis and Characterization of Two New Zinc Phosphates Assembled about a Chiral Metal Complex: $[\text{Co}^{\text{II}}(\text{en})_3]_2[\text{Zn}_6\text{P}_8\text{O}_{32}\text{H}_8]$ and $[\text{Co}^{\text{III}}(\text{en})_3][\text{Zn}_8\text{P}_6\text{O}_{24}\text{Cl}]\cdot 2\text{H}_2\text{O}$. *Chem. Mater.* **2001**, *13*, 2972-2978.

(3) Wang, Y.; Yu, J. H.; Pan, Q. H.; Du, Y.; Zou, Y. C.; Xu, R. R. Synthesis and Structural Characterization of 0D Vanadium Borophosphate $[\text{Co}(\text{en})_3]_2[\text{V}_3\text{P}_3\text{BO}_{19}][\text{H}_2\text{PO}_4]\cdot 4\text{H}_2\text{O}$ and 1D Vanadium Oxides $[\text{Co}(\text{en})_3][\text{V}_3\text{O}_9]\cdot \text{H}_2\text{O}$ and $[\text{Co}(\text{dien})_2][\text{V}_3\text{O}_9]\cdot \text{H}_2\text{O}$ Templated by Cobalt Complexes: Cooperative Organization of the Complexes and the Inorganic Networks. *Inorg. Chem.* **2004**, *43*, 559-565.

(4) Barnes, J. C.; Paton, J. D. Tris(ethylenediamine)cobalt(III) Dihydrogen Tetrahydrofuran-tetra-carboxylate Trihydrogen Tetrahydrofuran-tetracarboxylate Hydrate (1:1:1:2½). *Acta Crystallogr. Sect. B: Struct. Sci.* **1982**, *38*, 1588-1591.

(5) Reference supplied by communication from the authors to the CSD: Rius, J.; Gali, S. *Cryst. Struct. Commun.* **1982**, *11*, 829-834.

(6) Jasper, J. D.; Wilkinson, A. P. Synthesis of Low-Dimensional Aluminophosphates from Higher Dimensional Precursors: Conversion of $\Lambda, \Delta\text{-Co}(\text{en})_3[\text{Al}_3\text{P}_4\text{O}_{16}]\cdot x\text{H}_2\text{O}$ to the Chain Compound $\Lambda, \Delta\text{-Co}(\text{en})_3[\text{AlP}_2\text{O}_8]\cdot x\text{H}_2\text{O}$. *Chem. Mater.* **1998**, *10*, 1664-1667.

(7) Chen, P.; Li, J. Y.; Yu, J. H.; Wang, Y.; Pan, Q. H.; Xu, R. R. The synthesis and structure of a chiral 1D aluminophosphate chain compound: d -Co(en)₃[AlP₂O₈] \cdot 6.5H₂O. *J. Solid State Chem.* **2005**, *178*, 1929-1934.

(8) Whuler, A.; Brouty, C.; Spinat, P.; Herpin, P. Etude Structurale du Complexe Racémique Actif Hydraté [(+)-Co(en)₃(-)-Cr(en)₃]Cl₆ \cdot 6,1H₂O. *Acta Crystallogr. Sect. B: Struct. Sci.* **1976**, *32*, 194-198.

(9) Brouty, C.; Whuler, A.; Spinat, P.; Herpin, P. Détermination Structurale à 293 et 133 K du Complexe Racémique Actif [(+)-Co(en)₃(-)-Cr(en)₃](SCN)₆ \cdot n H₂O. *Acta Crystallogr. Sect. B: Struct. Sci.* **1977**, *33*, 2563-2572.

(10) Bok, L. D. C.; Basson, S. S.; Leipoldt, J. G. The Crystal Structure of Tris (ethylenediamine) cobalt(III) Hexacyanoferrate(III) Dihydrate, CO(C₂H₈N₂)₃[F(CN)₆] \cdot 2H₂O. *Z. Anorg. Allg. Chem.* **1972**, *389*, 307-314.

(11) Iwata, M.; Nakatzu, K.; Saito, Y. The Crystal Structure of (+)D-Tris(ethylenediamine)cobalt(III) Chloride Monohydrate, (+)_D-[Co(en)₃]Cl₃ \cdot H₂O. *Acta Crystallogr. Sect. B: Struct. Sci.* **1969**, *B 25*, 2562-2571.

(12) Whuler, A.; Brouty, C.; Spinat, P. Etude Structurale du Complexe Racémique Actif [(+)-Co(en)₃(-)-Cr(en)₃]Cl₆ \cdot 6.1H₂O à 123 K. *Acta Crystallogr. Sect. B: Struct. Sci.* **1978**, *34*, 425-429.

(13) Reference supplied by communication from the authors to the CSD: Smolin, Y. I.; Shepelev, Y. F.; Pomes, R.; Khobbel, D.; Viker, V. *Kristallografiya* **1975**, *20*, 917-924.

(14) Brouty, C.; Spinat, P.; Whuler, A.; Herpin, P. Structure du Complexe Racémique (4-)-Co(en)₃(SCN)₃. Etude des Liaisons Hydrogène. *Acta Crystallogr. Sect. B: Struct. Sci.* **1976**, *32*, 2153-2159.

(15) Reference supplied by communication from the authors to the CSD: Brouty, C.; Spinat, P.; Whuler, A. *C.R. Acad. Sci. Ser. IIC: Chim.* **1979**, *288*, 257-259.

(16) Studies on Crystals of Metallic Tris-ethylenediamine-complexes. I. The Crystal Structure of DL-Tris-ethylenediamine-cobalt (III) Chloride Tri-hydrate, [Coen₃]Cl₃·3H₂O. Nakatsu, K.; Saito, Y.; Kuroya, H. *Bull. Chem. Soc. Jpn.* **1956**, *29*, 428-434.

(17) He, Q. L.; Wang, E. B. Hydrothermal synthesis and crystal structure of a new molybdenum(VI) arsenate(III), Co^{III}(en)₃H₃O[(Co^{II}O₆)Mo^{VI}₆O₁₈(As^{III}₃O₃)₂]-·2H₂O. *Inorg. Chim. Acta.* **1999**, *295*, 244-247.

(18) Altahan, M. A.; Beckett, M. A.; Coles, S. J.; Horton, P. N. A New Decaoxidooctaborate(2-) Anion, [B₈O₁₀(OH)₆]²⁻: Synthesis and Characterization of [Co(en)₃][B₅O₆(OH)₄][B₈O₁₀(OH)₆]-5H₂O (en = 1,2-Diaminoethane). *Inorg. Chem.* **2015**, *54*, 412-414.

(19) Matsuki, R.; Shiro, M.; Asahi, T.; Asai, H. Absolute configuration of Λ-(+)₅₈₉-tris(ethylenediamine)cobalt(III) triiodide monohydrate. *Acta Crystallogr. Sect. E: Struct. Rep. Online* **2001**, *57*, m448-m450.

(20) Nakatsu, K. The Crystal Structure of D-Tris-ethylenediamine-cobalt(III) Bromide Monohydrate, D-[Co en₃]Br₃·H₂O, and the Absolute Configuration of the D-

Tris-ethylenediamine-cobalt(III) Ion, D-[Co en₃]³⁺. *Bull. Chem. Soc. Jpn.* **1962**, *35*, 832-839.

(21) Qiao, J.; Zhang, L. R.; Liu, L.; Yua, Y.; Bi, M. H.; Huo, Q. S.; Liu, Y. L. Solvothermal synthesis and structure of a novel 3D zincophosphate-I₃Co(en)₃[Zn₄(HPO₃)₅(H₂PO₃)] containing helical chains. *J. Solid State Chem.* **2008**, *181*, 2908-2913.

(22) Hodgson, D. J.; Hale, P. K.; Hatfield, W. E. The Crystal and Molecular Structure of Tris(ethylenediamine)cobalt(III) Di- μ -chloro-bis(trichlorocuprate(II)) Dichloride Dihydrate, [Co(N₂C₂H₈)₃]₂[Cu₂Cl]₂Cl₂·2H₂O. *Inorg. Chem.* **1971**, *10*, 1061-1067.

(23) Veal, J. T.; Hodgson, D. J. The Crystal and Molecular Structure of Tris(ethylenediamine)cobalt(III) Hexachlorocadmate(II) Dichloride Dihydrate, [Co(N₂C₂H₈)₃]₂[CdCl₆]₂Cl₂·2H₂O. *Inorg. Chem.* **1972**, *11*, 597-600.

(24) Templeton, D. H.; Zalkin, A.; Ruben, H. W.; Templeton, L. K. Anomalous Scattering by Cobalt and Chlorine and Crystal Structure of (+)-Tris(ethylenediamine)cobalt(III) Chloride (+)-Tartrate Pentahydrate. *Acta Crystallogr. Sect. B: Struct. Sci.* **1979**, *35*, 1608-1613.

(25) Spinat, P.; Whuler, A.; Brouty, C. Données cristallographiques des formes polymorphes du complexe racémique de fluorure de tris(éthylènediamine)cobalt(III). *J. Appl. Crystallogr.* **1981**, *14*, 211-212.

(26) Whuler, A.; Spinat, P.; Brouty, C. Structure de l'iodure de Tris(éthylènediamine)cobalt(III) Monohydraté. *Acta Crystallogr. Sect. B: Struct. Sci.* **1980**, *36*, 1086-1091.

(27) Aquilino, A.; Cannas, M.; Christini, A.; Marongiu, G. A Novel Chain Structure in the $[\text{Pb}_2\text{Cl}]_5$ -Anion; Crystal and Molecular Structure of $[\text{Co}(\text{NH}_2\text{CH}_2\text{CH}_2\text{NH}_2)]_3[\text{Pb}_2\text{Cl}_9]\text{Cl}\cdot 3\text{H}_2\text{O}$. *J. Chem. Soc. Chem. Commun.* **1978**, 347-348.

(28) Enemark, J. H.; Quinby, M. S.; Reed, L. L.; Steuck, M. J.; Walthers, K. K. The Crystal and Molecular Structure of Tris(ethylenediamine)cobalt Pentacyanonitrosylchromate Dihydrate, $[\text{Co}(\text{C}_2\text{H}_8\text{N}_2)_3][\text{Cr}(\text{CN})_5(\text{NO})]\cdot 2\text{H}_2\text{O}$. *Inorg. Chem.* **1970**, *9*, 2397-2403.

(29) Duesler, E. N.; Raymond, K. N. Conformational Effects of Intermolecular Interactions. The Structure of Tris(ethylenediamine)cobalt(III) Monohydrogen Phosphate Nonahydrate. *Inorg. Chem.* **1971**, *10*, 1486-1492.

(30) Haupt, H. J.; Huber, F.; Preut, H. Darstellung und Kristallstruktur von Tris(äthylendiamin)kobalt(III)-trichlorostannat(III)-dichlorid, $[\text{Co}(\text{en})_3][\text{SnCl}_3]\text{Cl}_2$. *Z. Anorg. Allg. Chem.* **1976**, *422*, 255-260.

(31) Tada, T.; Kushi, Y.; Yoneda, H. STRUCTURAL STUDY OF OPTICAL RESOLUTION V. THE CRYSTAL STRUCTURE OF HYDROGEN TRIS(ETHYLENEDIAMINE) COBALT(III) D-TARTRATE TRIHYDRATE. *Chem. Lett.* **1977**, 379-382.

- (32) Kushi, Y.; Kuramoto, M.; Yoneda, H. STRUCTURAL STUDY OF OPTICAL RESOLUTION I. THE CRYSTAL STRUCTURE OF HYDROGEN TRIS(ETHYLENEDIAMINE) COBALT(III) BROMIDE D-TARTRATE PENTAHYDRATE. *Chem. Lett.* **1976**, 135-136.
- (33) Rohrbaugh, W. J.; Jacobson, R. A. Tris(ethylenediamine)cobalt(III) Tetrakis(isothioeyanato)cobaltate(II) Nitrate. *Acta Crystallogr. Sect. B: Struct. Sci.* **1977**, 33, 3254-3256.
- (34) Baidina, I. A.; Makotchenko, E. V. CRYSTAL STRUCTURE OF $[\text{Co}(\text{N}_2\text{C}_2\text{H}_8)_3][\text{AuBr}_4]_2\text{Br}$ BIS(TETRABROMOAUROATE(III)TRIS(ETHYLENEDIAMINE) COBALT(III) BROMIDE. *J. Struct. Chem.* **2010**, 51, 187-189.
- (35) Peng, Y.; Li, Y. Z.; Bao, S. S.; Zheng, L. M. Bis[tris(ethylenediamine)cobalt(III)]dichlorobis[μ -(1-hydroxyethylidene) diphosphonato(4-)]diruthenium(II,III)(Ru–Ru) chloride trihydrate. *Acta Crystallogr. Sect. C: Cryst. Struct. Commun.* **2004**, 60, M302-M304.
- (36) Keene, T. D.; Hursthouse, M. B.; Price, D. J. Recurrent H-bond graph motifs between metal tris-ethylenediamine cations and uncoordinated oxalate anions: Fitting a three pin plug into a two pin socket. *CrystEngComm* **2012**, 14, 116-123.
- (37) Sharma, R. P.; Shashni, R.; Singh, A.; Venugopalan, P.; Yu, J.; Guo, Y. A.; Ferretti, V. A rational synthesis of a new discrete anion $[\text{trans-CdBr}_4\text{Cl}_2]^{4-}$ and its comparison with newly synthesized anion $[\text{CdBr}_6]^{4-}$. *J. Mol. Struct.* **2011**, 1006, 121-127.
- (38) Zhang, Z. J.; Zheng, F. K.; Fu, M. L.; Guo, G. C.; Huang, J. S. A new cobalt(III) ethylenediamine complex with mixed halide counter-anions,

[Co(en)₃](Cl)(I)2·H₂O. *Acta Crystallogr. Sect. E: Struct. Rep. Online* **2005**, *61*, M89-M91.

(39) Reference supplied by communication from the authors to the CSD: Loiseau, T.; Serpaggi, F.; Ferey, G. Z. *Kristal-New Cryst. St.* **2004**, *219*, 469-470.

(40) Fuertes, A.; Miravittles, C.; Ibanez, R.; Martineztamayo, E.; Beltranporter, A. Structure of the Active Racemic Complex [(±)Co(en)₃](C₂O₄)I·1.5H₂O: a hydrogen-Bond-Induced Case of Asymmetry. *Acta Crystallogr. Sect. C: Cryst. Struct. Commun.* **1988**, *44*, 417-421.

(41) Wang, C. C.; Yeh, C. T.; Cheng, Y. T.; Chen, I. H.; Lee, G. H.; Shih, W. J.; Sheu, H. S.; Fedorov, V. E. A hydrogen-bonded and π-π assembled 3D supramolecular network, [Co(en)₃]⁺·1.5(C₅O₅)⁻, with 1D microporous hydrophilic channels showing reversible water ad/de-sorption property. *CrystEngComm* **2012**, *14*, 4637-4643.

(42) Hu, Z.; Dang, L. Q.; Bao, D. H.; An, Y. L. Tris(ethylenediamine)cobalt(III) tetrathioarsenate(V). *Acta Crystallogr. Sect. E: Struct. Rep. Online* **2006**, *62*, M2756-M2757.

(43) Mizuta, T.; Tada, T.; Kushi, Y.; Yoneda, H. Crystal Structures of the Racemic Tartrate and the Two *d*-Tartrate Salts of the Tris(ethylenediamine)cobalt(III) Complex. *Inorg. Chem.* **1988**, *27*, 3836-3841.

(44) Takamizawa, S.; Akatsuka, T.; Ueda, T. Gas-Conforming Transformability of an Ionic Single-Crystal Host Consisting of Discrete Charged Components. *Angew. Chem. Int. Ed.* **2008**, *47*, 1689-1692; *Angew. Chem.* **2008**, *120*, 1713-1716.

(45) Beznischenko, A. O.; Makhankova, V. G.; Kokozay, V. N.; Dyakonenko, V. V.; Shishkin, O. V. Direct synthesis of Co/Mn complex with Co-semisepulchrate entity. *Inorg. Chem. Commun.* **2009**, *12*, 473-475.

(46) Nakashima, T.; Mishiro, J.; Ito, M.; Kura, G.; Ikuta, Y.; Matsumoto, N.; Nakajima, K.; Kojima, M. Homochiral Column Structure of *rac*- and Λ -Tris(ethylenediamine)cobalt(III) Cyclotriphosphate Dihydrate in Crystal Structures and Cation-Anion Association in Aqueous Solution. *Inorg. Chem.* **2003**, *42*, 2323-2330.

(47) Reference supplied by communication from the authors to the CSD: Kang, J.; Pyo, S.; Yun, H.; Do, J. Z. *Kristal-New Cryst. St.* **2011**, *226*, 353-354.

(48) Kirubavathy, S. J. C. S. *Private Communication to the Cambridge Structural Database (CSD)*. **2013**.

(49) Zabel, M.; Poznyak, A. L.; Pavlovskii, V. I. CRYSTAL STRUCTURE OF [ETHYLENEDIAMINE-*N,N'*-DI(3-PROPIONATO)COPPER(II)]TRIS[DICHLOROMERCURY(II)] [Cu(Eddp)(HgCl₂)₃]_n. *J. Struct. Chem.* **2007**, *48*, 968-972.

(50) Makotchenko, E. V.; Baidina, I. A.; Naumov, D. Y. SYNTHESIS AND CRYSTAL STRUCTURE OF TRIS(ETHYLENEDIAMINE)COBALT(III)BIS(TETRACHLORO-AURATE(III)) CHLORIDE. *J. Struct. Chem.* **2006**, *47*, 499-503.

(51) Du, Y.; Yu, J. H.; Chen, Y.; Yang, Y. H. Mesostructured molecular solid material [Co(en)₃][Zr₂F₁₁H₂O] with enhanced photoelectronic effect. *Dalton Trans.* **2009**, 6736-6740.

(52) Ueda, T.; Bernard, G. M.; McDonald, R.; Wasylishen, R. E. Cobalt-59 NMR and X-ray diffraction studies of hydrated and dehydrated (\pm)-tris(ethylenediamine) cobalt(III) chloride. *Solid State Nucl. Magn. Reson.* **2003**, *24*, 163-183.

(53) Hirai, Y.; Nagao, Y.; Igashira-Kamiyama, A.; Konno, T. Enantioselective/Anion-Selective Incorporation of Tris(ethylenediamine) Complexes into 2D Coordination Spaces between Tripalladium(II) Supramolecular Layers with D-Penicillamate. *Inorg. Chem.* **2011**, *50*, 2040-2042.

(54) Zeng, Q. X.; Xu, J. Q.; Yang, G. Y.; Li, Y. F.; Cui, X. B.; Zhao, X. L.; Li, C. B. Synthesis and Structure of a Tetracapped Keggin Polyarsenomolybdovanadate $[\text{Co}(\text{en})_3][\text{Co}(\text{en})_2(\text{H}_2\text{O})_2]_2 \cdot [\text{Mo}^{\text{V}}_4\text{Mo}^{\text{VI}}_4\text{V}^{\text{IV}}_8\text{O}_{40}(\text{AsO}_4)]$. *Chem. J. Chinese. U.* **2001**, *22*, 1800-1802.

(55) Wang, Y.; Yu, J. H.; Du, Y.; Xu, R. R. Two layered gallophosphates assembled about the chiral metal complexes: $\text{Co}(\text{en})_3 \cdot \text{Ga}_3\text{P}_4\text{O}_{16} \cdot 5\text{H}_2\text{O}$ and *trans*- $\text{Co}(\text{dien})_2 \cdot \text{Ga}_3\text{P}_4\text{O}_{16} \cdot 3\text{H}_2\text{O}$. *J. Solid State Chem.* **2004**, *177*, 2511-2517.

(56) Pan, Q. H.; Chen, Q. A.; Song, W. C.; Hu, T. L.; Bu, X. H. Template-directed synthesis of three new open-framework metal(II) oxalates using Co(III) complex as template. *CrystEngComm* **2010**, *12*, 4198-4204.

(57) Reference supplied by communication from the authors to the CSD: Poznyak, A. L.; Burshtein, I. F. *Russ. J. Inorg. Chem.* **1999**, *44*, 1381-1389.

(58) Cai, J. W.; Zhang, Y. F.; Hu, X. P.; Feng, X. L. Tris(ethylenediamine-*N,N'*)cobalt(III) oxalate perchlorate dihydrate. *Acta Crystallogr. Sect. C: Cryst. Struct. Commun.* **2000**, *56*, 661-663.

(59) Lin, J. M.; Qiu, Y. X.; Chen, W. B.; Yang, M.; Zhou, A. J.; Dong, W.; Tian, C. E. Unusual π - π -stacking interactions between 5,5'-azotetrazolate(AT) anions in six AT based 3d metal photochromic complexes. *CrystEngComm* **2012**, *14*, 2779-2786.

(60) Faoro, E.; de Oliveira, G. M.; Lang, E. S. Attainment of new Te^{II} and Te^{IV} iodides by unexpected removal of the mesityl group of [mesTeI₂]⁻: Synthesis and structural features of [TeI₄][Co(en)₃]₂·I, [TeI₆][Co(en)₃]₂·I, [{TeI₆}{Te₂I₁₀}]₂·[Co(NH₃)₆]₂·2I·6H₂O and [(mesTeI₂)₂(μ -I₂)]₂·[Co(bpy)₃]₂·I₃·2CHCl₃ (mes = 2,4,6-trimethylphenyl; en = ethylenediamine; bpy = bipyridine). *Polyhedron* **2009**, *28*, 63-68.

(61) Matiková-Mal'arová, M.; Černák, J.; Massa, W.; Varret, F. Three Co(III)-Fe(II) complexes based on hexacyanoferrates: Syntheses, spectroscopic and structural characterizations. *Inorg. Chim. Acta*. **2009**, *362*, 443-448.

(62) Das, B.; Baruah, J. B. Cooperativity on selective products in one pot reactions of 2,6-pyridinedicarboxylic acid and ethylenediamine with metal ion. *Inorg. Chem. Commun.* **2010**, *13*, 350-352.

(63) Wang, Y. Q.; Cao, R.; Bi, W. H.; Li, X.; Li, X. J.; Wang, Y. L. Two Hydrogen-bonded Supramolecular Frameworks of the 4,4'-Diazido-2,2'-stilbene Disulfonate Anion. *Z. Anorg. Allg. Chem.* **2005**, *631*, 2309-2311.

(64) Du, Y.; Yang, M.; Yu, J. H.; Pan, Q. H.; Xu, R. R. An Unexpected Photoelectronic Effect From [Co(en)₃]₂(Zr₂F₁₂)(SiF₆)·4H₂O, a Compound Containing an H-Bonded Assembly of Discrete [Co(en)₃]³⁺, (Zn₂F₁₂)⁴⁻, and (SiF₆)²⁻. *Angew. Chem. Int. Ed.* **2005**, *44*, 7988-7990; *Angew. Chem.* **2008**, *117*, 8202-8204.

(65) Yeşilel, O. Z.; Ölmez, H.; Soylu, S. Synthesis and spectrothermal studies of thermochromic diamine complexes of cobalt(III), nickel(II) and copper(II) squarate. Crystal structure of [Co(en)₃](sq)1.5·6H₂O. *Transition Met. Chem.* **2006**, *31*, 396-404.

(66) Psaroudakis, N.; Terzis, A.; Raptopoulou, C. P.; Mertis, C. Redox chemistry of the [Re₃(μ-Cl)₃X₉]³⁻ halides (X = Cl or Br); isolation and structural characterization of the [{Re₃(μ-Cl)₃Br₆(H₂O)(μ-O)₂ }²⁻ cluster anion. *J. Chem. Soc. Dalton Trans.* **1997**, 3299-3304.

(67) Wang, M. F.; Yue, C. Y.; Yuan, Z. D.; Lei, X. W. Two polymorphs of tris(ethylenediamine)cobalt(III) tetrathioantimonate(V). *Acta Crystallogr. Sect. C: Cryst. Struct. Commun.* **2013**, *69*, 855-858.

(68) Gray, M. J.; Jasper, J. D.; Wilkinson, A. P.; Hanson, J. C. Synthesis and Synchrotron Microcrystal Structure of an Aluminophosphate with Chiral Layers Containing Λ Tris(ethylenediamine)cobalt(III). *Chem. Mater.* **1997**, *9*, 976-980.

(69) Reference supplied by communication from the authors to the CSD: Haussühl, S.; Schreuer, J. Z. *Kristallogr.* **1998**, *213*, 161-167.

(70) Lu, Y. K.; Tian, M. M.; Xu, S. G.; Lu, R. Q.; Liu, Y. Q. Bis[tris(ethylenediamine-κ²N,N')-cobalt(III)] octakis-μ-3-oxido-hexadeca-μ₂-oxido-tetradeca-μ₁₂-tetraoxosilicato-octamolybdenum(VI)hexavanadium(IV,V) hexahydrate. *Acta Crystallogr. Sect. E: Struct. Rep. Online* **2011**, *67*, M1776-U1523.

(71) Thuéry, P.; Rivière, E.; Harrowfield, J. Counterion-Induced Variations in the Dimensionality and Topology of Uranyl Pimelate Complexes. *Cryst. Growth Des.* **2016**, *16*, 2826-2835.

(72) Kotov, V. Y.; Ilyukhin, A. B. Dissolution of water-insoluble $[\text{Co}(\text{en})_3]_2\text{I}_2[\text{Fe}(\text{CN})_6]\cdot 4.6\text{H}_2\text{O}$ in a saturated $\text{K}_4[\text{Fe}(\text{CN})_6]$ solution. *Mendeleev Commun.* **2003**, *13*, 169-170.

(73) Ma, Y.; Lu, Y.; Wang, E. B.; Xu, X. X.; Guo, Y. Q.; Bai, X. L.; Xu, L. Hydrothermal synthesis and crystal structure of a novel three-dimensional supramolecular network containing cyclic water hexamers: $[\text{Co}(\text{en})_3]_4\text{-}[\text{P}_2\text{Mo}_5\text{O}_{23}]_2\cdot 9\text{H}_2\text{O}$ (en = ethylenediamine). *J. Mol. Struct.* **2006**, *784*, 18-23.

(74) Liebig, T. J.; Ruschewitz, U. Supramolecular Polymers with $[\text{Co}(\text{en})_3]^{3+}$ Cores (en = ethylenediamine). *Cryst. Growth Des.* **2012**, *12*, 5402-5410.

(75) Mal'arová, M.; Trávníček, Z.; Zbořil, R.; Černák, J. $[\text{Co}(\text{en})_3][\text{Fe}(\text{CN})_6]\cdot \text{H}_2\text{O}$ and $[\text{Co}(\text{en})_3][\text{Fe}(\text{CN})_6]$: A dehydration process investigated by single crystal X-ray analysis, thermal analysis and Mössbauer spectroscopy. *Polyhedron* **2006**, *25*, 2935-2943.

(76) Aschwanden, S.; Schmalle, H. W.; Reller, A.; Oswald, H. R. PREPARATION, CRYSTAL STRUCTURE, AND THERMAL BEHAVIOUR OF COBALT-ETHYLENEDIAMINE-VANADATE. *Mater. Res. Bull.* **1993**, *28*, 575-590.

(77) Lappin, A. G.; Haller, K. J.; Warren, R. M. L.; Tatehata, A. X-ray and Molecular Structure of the Diastereomeric Pair $[\Lambda\text{-Co}(\text{en})_3][\Delta\text{-Co}(\text{en})(\text{ox})_2]_2\cdot 3\text{H}_2\text{O}$ and

$[\Delta\text{-Co(en)}_3][\Delta\text{-Co(en)(ox)}_2]_2\cdot\text{H}_2\text{O}$ and Comparisons with $[\Lambda\text{-Co(en)}_3][\Delta\text{-Co(gly)(ox)}_2]\Gamma\cdot\text{H}_2\text{O}$. *Inorg. Chem.* **1993**, *32*, 4498-4504.

(78) Morón, M. C.; Palacio, F.; Pons, J.; Casabó, J.; Solans, X.; Merabet, K. E.; Huang, D.; Shi, X.; Teo, B. K.; Carlin, R. L. Bimetallic Derivatives of $[\text{M(en)}_3]^+$ Ions (M = Cr, Co): An Approach to Intermolecular Magnetic Interactions in Molecular Magnets. *Inorg. Chem.* **1994**, *33*, 746-753.

(79) Myrczek, J. A Change of Crystallization Pathway from D_2O Solution. The structure of $\{[\text{Co(en)}_3]_2\cdot\text{D}_2\text{O}\}_2(\text{C}_2\text{O}_4)$ (I). *Pol. J. Chem.* **1997**, *71*, 844-847.

(80) Sharma, R. P.; Lata, K.; Singh, A.; Venugopalan, P.; Ferretti, V. Isolation of a new anion, $[\text{CdBr}_4(\text{C}_7\text{H}_5\text{O}_2)]^{3-}$: Synthesis, single crystal X-ray structure determination and DFT calculations of $[\text{Co(en)}_3][\text{CdBr}_4(\text{C}_7\text{H}_5\text{O}_2)]\cdot\text{H}_2\text{O}$. *Inorg. Chem. Commun.* **2012**, *15*, 185-189.

(81) Yang, G. Y.; Sevov, S. C. $[\text{Co(en)}_3][\text{B}_2\text{P}_3\text{O}_{11}(\text{OH})_2]$: A Novel Borophosphate Templated by a Transition-Metal Complex. *Inorg. Chem.* **2001**, *40*, 2214-2215.

(82) Reference supplied by communication from the authors to the CSD: Zabel, M.; Poznyak, A. L.; Pavlovskii, V. I. *Russ. J. Inorg. Chem.* **2005**, *50*, 1362-1368.

(83) Chen, P.; Li, J. Y.; Xu, J.; Duan, F. Z.; Deng, F.; Xu, R. R. Synthesis, structure and NMR characterization of a new monomeric aluminophosphate $[\delta\lambda\text{-Co(en)}_3]_2[\text{Al}(\text{HPO}_4)_2(\text{H}_{1.5}\text{PO}_4)_2(\text{H}_2\text{PO}_4)_2](\text{H}_3\text{PO}_4)_4$ containing four different types of monophosphates. *Solid State Sci.* **2009**, *11*, 622-627.

(84) Feng, M. L.; Xiong, W. W.; Ye, D.; Li, J. R.; Huang, X. Y. A Series of Novel Organically Templated Germanium Antimony Sulfides. *Chem. Asian J.* **2010**, *5*, 1817-1823.

(85) Nakatsu, K.; Shiro, M.; Saito, Y.; Kuroya, H. Studies on Crystals of Metallic Tris-ethylenediamine-complexes. II. The Crystal Structure of Sodium D-Tris-ethylenediamine-cobalt (III) Chloride Hexahydrate, 2D-[Co(en)₃]Cl₃·NaCl·6H₂O. *Bull. Chem. Soc. Jpn.* **1957**, *30*, 158-164.

(86) Zhang, Z.; Wang, F. X.; Liao, S. Q. Tris(ethylenediamine-κ²N,N')cobalt(III) aquatris(oxalato-κ²O1,O2)indate(III). *Acta Crystallogr. Sect. E: Struct. Rep. Online* **2012**, *68*, M65-M66.

(87) Goforth, A. M.; Hipp, R. E.; Smith, M. D.; Peterson, L.; zur Loye, H. C. Tris(ethylenediamine)cobalt(III) nonaiododibismuthate. *Acta Crystallogr. Sect. E: Struct. Rep. Online* **2005**, *61*, M1531-M1533.

(88) House, D. A.; Mckee, V.; Robinson, W. T. The Structures of [Co(en)₃][HgCl₄I] and *cis*-[Co(en)₂(NH₃)(py)][Hg₂Cl₇] — Complexes Containing Novel Halomercury(II) Anions. *Inorg. Chim. Acta.* **1989**, *160*, 71-76.

(89) Stalder, S. M.; Wilkinson, A. P. Synthesis and Characterization of a Chiral 3D-Framework Material: *d*-Co(en)₃[H₃Ga₂P₄O₁₆]. *Chem. Mater.* **1997**, *9*, 2168-2173.

(90) Kuroda, R. Chiral Discriminations and Crystal Packing. Two Diastereomeric Compounds Involving Complex Ions of *D*₃ Symmetry, Tris(ethylenediamine)cobalt(III) and Tris(oxalato)rhodate(III). *Inorg. Chem.* **1991**, *30*, 4954-4959.

(91) Brewer, G.; Butcher, R. J.; Jasinski, J. P. Tris(ethane-1,2-diamine- κ^2N,N')-cobalt(III) carbonate iodide tetrahydrate. *Acta Crystallogr. Sect. E: Struct. Rep. Online* **2010**, *66*, M1148-U988.

(92) Reference supplied by communication from the authors to the CSD: Kokunov, Y. V.; Detkov, D. G.; Gorbunova, Y. E.; Ershova, M. M.; Mikhailov, Y. N. *Russ. J. Inorg. Chem.* **2002**, *47*, 1459-1462.

(93) Podberezskaya, N. V.; Romanenko, G. V.; Tychinskaya, I. I. THREE-LAYERED CLOSE PACKING IN THE CRYSTAL STRUCTURE OF TRIS(ETHYLENEDIAMINE)-COBALT(III)HEXANITRORHODATE(III) HYDRATE, $[\text{Co}(\text{en})_3] [\text{Rh}(\text{NO}_2)_6] \cdot 3\text{H}_2\text{O}$, en = $\text{C}_2\text{H}_8\text{N}_2$. *J. Struct. Chem.* **1996**, *37*, 114-119.

(94) Witiak, D.; Clardy, J. C.; Martin, D. S. 94. The Crystal Structure of (+)D-Tris(ethylenediamine)cobalt(III) Nitrate. *Acta Crystallogr. Sect. B: Struct. Sci.* **1972**, *B 28*, 2694-2699.

(95) Iwamura, M.; Tsukuda, T.; Morita, M. Energy-Transfer Process in Crystals of Chiral and Racemic Double Complex Salts of $[\text{Co}(\text{ethylenediamine})_3] [\text{Tb}(\text{2,6-pyridinedicarboxylate})_3]$. *Bull. Chem. Soc. Jpn.* **2007**, *80*, 1140-1147.

(96) Khan, M. I.; Yohannes, E.; Doedens, R. J.; Golub, V. O.; O'Connor, C. J. Templated synthesis of a chiral solid: Synthesis and characterization of $\{\text{Co}(\text{H}_2\text{N}(\text{CH}_2)_2\text{NH}_2)_3\}[\text{V}_3\text{O}_9] \cdot \text{H}_2\text{O}$, containing a new type of chiral vanadium oxide chain. *Inorg. Chem. Commun.* **2005**, *8*, 841-845.

(97) Dey, C.; Das, R.; Pachfule, P.; Poddar, P.; Banerjee, R. Structural and Selective Gas Adsorption Studies of Polyoxometalate and Tris(ethylenediamine) Cobalt(III) Based Ionic Crystals. *Cryst. Growth Des.* **2011**, *11*, 139-146.

(98) Tong, J. Y.; Pan, Q. H. Tris(ethylenediamine)cobalt(III)diformato-dioxalatoindate(III) dihydrate. *Acta Crystallogr. Sect. E: Struct. Rep. Online* **2011**, *67*, M579-U704.

(99) Kuratieva, N. V.; Tereshkin, I. O.; Khranenko, S. P.; Gromilov, S. A. CRYSTAL STRUCTURE OF $[\text{Co}(\text{en})_3]_2(\text{W}_7\text{O}_{24}) \cdot 6\text{H}_2\text{O}$. *J. Struct. Chem.* **2013**, *54*, 1133-1136.

(100) Asnani, M.; Ramanan, A.; Vittal, J. J. Hydrothermal synthesis and structural characterization of a vanadium (V) borophosphate cluster containing solid: $[\text{Co}(\text{en})_3][\text{enH}_2]\{\text{V}_3\text{BP}_3\text{O}_{19}\} \cdot 4.5\text{H}_2\text{O}$. *Inorg. Chem. Commun.* **2003**, *6*, 589-592.

(101) Warren, R. M. L.; Haller, K. J.; Tatehata, A.; Lappin, A. G. Chiral Discrimination in the Reduction of $[\text{Co}(\text{edta})]^-$ by $[\text{Co}(\text{en})_3]^{2+}$ and $[\text{Ru}(\text{en})_3]^{2+}$. X-ray Structure of $[\Lambda\text{-Co}(\text{en})_3][\Delta\text{-Co}(\text{edta})]_2\text{Cl} \cdot 10\text{H}_2\text{O}$. *Inorg. Chem.* **1994**, *33*, 227-232.

(102) Chen, P.; Li, J. Y.; Duan, F. Z.; Yu, J. H.; Xu, R. R.; Sharma, R. P. Syntheses and Characterizations of Three Low-Dimensional Chloride-Rich Zincophosphates Assembled about $[d\text{-Co}(\text{en})_3]^{3+}$ and $[dl\text{-Co}(\text{en})_3]^{3+}$ Complex Cations. *Inorg. Chem.* **2007**, *46*, 6683-6687.

(103) Serada, O. S. E. H. *Private Communication to the Cambridge Structural Database (CSD)*. **2008**.

(104) Ohta, N.; Fuyuhiko, A.; Yamanari, K. Crystal structure and chiral recognition of supramolecular complex composed of tris(1,2-diaminoethane)cobalt(III) carbonate and α -cyclodextrin, $[\text{Co}(\text{en})_3]_2(\text{CO}_3)_3 \cdot 2(\alpha\text{-CDX})$. *Chem. Commun.* **2010**, *46*, 3535-3537.

(105) Du, Y.; Yu, J. H.; Wang, Y.; Pan, Q. H.; Zou, Y. C.; Xu, R. R. $[\text{Co}(\text{en})_3][\text{In}_3(\text{H}_2\text{PO}_4)_6(\text{HPO}_4)_3] \cdot \text{H}_2\text{O}$: A new layered indium phosphate templated by cobalt complex. *J. Solid State Chem.* **2004**, *177*, 3032-3037.

(106) Baidina, I. A.; Filatov, E. Y.; Makotchenko, E. V.; Smolentsev, A. I. SYNTHESIS AND STRUCTURE INVESTIGATION OF CO(III) COMPLEX SALTS WITH THE PERRHENATE ANION. *J. Struct. Chem.* **2012**, *53*, 112-118.

(107) Zhu, M. L.; Lu, L. P.; Yang, P. 107. Crystal Structure Analysis of Tetras[(-tris(ethylenediamine) cobalt(III)] tris[hexacyanoruthenate(II)]. *Chinese J. Struct. Chem.* **2002**, *21*, 396-401.

(108) Wang, Y.; Chen, P.; Li, J. Y.; Yu, J. H.; Xu, J.; Pan, Q. H.; Xu, R. R. Chiral Layered Zincophosphate $[d\text{-Co}(\text{en})_3]\text{Zn}_3(\text{H}_{0.5}\text{PO}_4)_2(\text{HPO}_4)_2$ Assembled about $d\text{-Co}(\text{en})_3^{3+}$ Complex Cations. *Inorg. Chem.* **2006**, *45*, 4764-4768.

(109) Morgan, K.; Gainsford, G.; Milestone, N. A Novel Layered Aluminum Phosphate $[\text{Co}(\text{en})_3\text{Al}_3\text{P}_4\text{O}_{16} \cdot 3\text{H}_2\text{O}]$ Assembled about a Chiral Metal Complex. *J. Chem. Soc. Chem. Commun.* **1995**, 425-426.

(110) Zheng, L. J.; Zhang, J. J.; Liu, Z. H. Crystal Structure and Thermal Behavior of $\text{Co(en)}_3[\text{B}_4\text{O}_5(\text{OH})_4]\text{Cl}\cdot 3\text{H}_2\text{O}$ and $[\text{Ni(en)}_3][\text{B}_5\text{O}_6(\text{OH})_4]_2\cdot 2\text{H}_2\text{O}$. *Chin. J. Chem.* **2009**, *27*, 494-500.

(111) Reference supplied by communication from the authors to the CSD: Rakov, I. E.; Kokunov, Y. V.; Gorbunova, Y. E.; Mikhailov, Y. N.; Buslaev, Y. A. *Koord. Khim.* **1995**, *21*, 16-19.

(112) Reference supplied by communication from the authors to the CSD: ter Berg, J. *Recl. Trav. Chim. Pays-Bas.* **1939**, *58*, 93-98.

(113) Reference supplied by communication from the authors to the CSD: Yu, J. H.; Wang, Y.; Shi, Z.; Xu, R. R. *Chin. J. Inorg. Chem.* **2002**, *18*, 51-55.

(114) Reference supplied by communication from the authors to the CSD: Yu J.; Wang, Y. S. Z.; Xu, R. *Conference* **2001**, 178. ()

(115) Brouty, C.; Spinat, P.; Whuler, A. Détermination Structurale de $[(+)\text{Co(en)}_3(-)\text{Cr(en)}_3](\text{SCN})_6$, Forme Orthorhombique. *Acta Crystallogr. Sect. B: Struct. Sci.* **1980**, *36*, 2037-2041.

(116) Magill, L. S.; Korp, J. D.; Bernal, I. Crystal Structure and Absolute Configuration of Tartrate Derivatives. 2. $[\Lambda(\delta\delta\delta)\text{-Co(en)}_3][(+)\text{ }_{589}\text{-}(R,R)\text{-tart}^{2-}]\text{Cl}\cdot 5\text{H}_2\text{O}$. *Inorg. Chem.* **1981**, *20*, 1187-1192.

(117) Reference supplied by communication from the authors to the CSD: Haupt, H. J.; Huber, F. Z. *Anorg. Allg. Chem.* **1978**, *442*, 31-40.

(118) Marsh, R. E. The space groups of point group C_3 : some corrections, some comments. *Acta Crystallogr. Sect. B: Struct. Sci.* **2002**, *58*, 893-899.

(119) Farrugia, L. J.; Peacock, R. D.; Stewart, B. Redetermination of the double salt Λ -[tris(ethylenediamine)cobalt(III)trichloride]-sodium chloride-water(2/1/6). *Acta Crystallogr. Sect. C: Cryst. Struct. Commun.* **2000**, *56*, 149-151.

fin